Springer Series in Surface Sciences 66

Jan Toporski
Thomas Dieing
Olaf Hollricher *Editors*

Confocal Raman Microscopy

Second Edition

Springer

Springer Series in Surface Sciences

Volume 66

This series covers the whole spectrum of surface sciences, including structure and dynamics of clean and adsorbate-covered surfaces, thin films, basic surface effects, analytical methods and also the physics and chemistry of interfaces. Written by leading researchers in the field, the books are intended primarily for researchers in academia and industry and for graduate students.

More information about this series at http://www.springer.com/series/409

Jan Toporski · Thomas Dieing
Olaf Hollricher
Editors

Confocal Raman Microscopy

Second Edition

Springer

Editors
Jan Toporski
Wissenschaftliche Instrumente und Technologie GmbH
Ulm
Germany

Olaf Hollricher
Wissenschaftliche Instrumente und Technologie GmbH
Ulm
Germany

Thomas Dieing
Ulm
Germany

ISSN 0931-5195 ISSN 2198-4743 (electronic)
Springer Series in Surface Sciences
ISBN 978-3-319-75378-2 ISBN 978-3-319-75380-5 (eBook)
https://doi.org/10.1007/978-3-319-75380-5

Library of Congress Control Number: 2018931495

Originally published as volume 158 in the series: Springer Series in Optical Sciences

Printed on acid-free paper

This Springer imprint is published by Springer Nature
The registered company is Springer International Publishing AG
The registered company address is: Gewerbestrasse 11, 6330 Cham, Switzerland

Preface to the Second Edition

Toward the end of the Editorial of the first Edition of *Confocal Raman Microscopy*, we stipulated it would be our intention to keep this book as up-to-date as possible in order to provide our readership with a window into the state of the art of confocal Raman microscopy. At the time of writing the Editorial then, we were aiming to keep pace with technological advancement. This in itself is still a very valid motivation to date, given that confocal Raman microscopy refers to a method, enabled by technology which continuously evolves.

When we started our considerations for the second Edition of *Confocal Raman Microscopy* and began to accrue an overview of what had changed in technology and been released to the scientific community, we soon realized that the most prominent advancement had taken place in the scientific realms, rather than merely in technology. Cutting-edge technology enables highest impact scientific discoveries, yet it cannot drive the scientific motivation to apply this method to any given field of research. As we surveyed and compiled publications on the subject matter from the years since publication of the one Edition of *Confocal Raman Microscopy* until recently, we found ourselves exposed to high numbers and high impact of scientific work that featured confocal Raman microscopy at its core or as a crucial component.

This reflects the versatility of the method itself, the quality of the information that can be acquired with it, and its growing popularity within the greater scientific community. As a natural consequence, the composition and contents of this two Edition of *Confocal Raman Microscopy* provide updates on technology and instrumental infrastructure but, more importantly, significantly expands on the scientific contents. The volume has nearly doubled in number of chapters, which—following a historical overview on C. V. Raman's life and discovery—lead us to introduce subsections on Theory & Technology, Novel Materials, Geosciences, Life and Pharmaceutical Sciences, Material Sciences, and Correlative Microscopy, containing a total of 23 chapters.

We are looking back at a rather successful one Edition of *Confocal Raman Microscopy*, evidenced by a continuously increasing number of citations and references to the book as a whole, or individual chapters. We are confident that the two

Edition of *Confocal Raman Microscopy* will build on this and makes a not insignificant contribution to establishing the method of confocal Raman microscopy even further in the scientific community. Our readership's discoveries drive the technique's development and further its adoption by the scientific community at large. We look forward to seeing where *Confocal Raman Microscopy* goes next.

Ulm, Germany
January 2018

Thomas Dieing
Jan Toporski
Olaf Hollricher

Preface to the First Edition

Readers of this book are aware that the theory of the Raman effect has been known for over 80 years, though routine Raman spectroscopy experiments were performed only after almost another half century of technological development. Since then, the analytical potential of this specific light-scattering effect has been explored for decades and resulted in a wealth of scientific publications. It took another major step in technical development toward the end of the second millennium that allowed the three-dimensional chemometric characterization of materials with high sensitivity and diffraction-limited resolution by combining confocal microscopy and Raman spectroscopy. With the inception of the resulting high-resolution confocal Raman microscopy as a novel analytical technique, new realms for the application of this method were defined and new research goals formulated. This has resulted in an expanding pool of experience and expertise.

The motivation to compile this book largely emerged from the observation that among the substantial portfolio of excellent publications of monographs on Raman spectroscopy, there are few dedicated to confocal Raman microscopy or even high-resolution confocal Raman imaging. Encouraged additionally by conversation and discussion with experts in the field of confocal Raman microscopy, we realized the demand for a reference work that condenses background information on physical, technical, hardware, and software aspects that serve as prerequisites for high-end analytical microscopy equipment. Equally important are comprehensive data evaluation methods to further and foster data processing, permitting advancement of research by simply providing tools to obtain novel results and make new discoveries.

The goal of this book therefore is to provide the best possible overview of the theoretical and practical facts and issues associated with confocal Raman microscopy. With the incorporation of over a dozen contributions from expert scientists and research groups spanning a wide range of applications in academic research as well as industry-driven research and development, this first edition of "confocal Raman microscopy" provides a comprehensive frame of reference for anyone involved in research employing confocal Raman microscopy. Aiming to keep pace with technological advancement, it is our intention to keep this book as up-to-date

as possible in order to provide our readership with the current state of the art in confocal Raman microscopy. We therefore welcome any constructive comments or suggestions for all future editions.

Ulm, Germany
May 2010

Thomas Dieing
Jan Toporski
Olaf Hollricher

Contents

Contributors

Mansoor Amiji Department of Pharmaceutical Sciences and Center for Pharmaceutical Biotechnology and Nanomedicine, Northeastern University, Boston, MA, USA

Malgorzata Baranska Faculty of Chemistry, Jagiellonian University, Krakow, Poland; Jagiellonian Centre for Experimental Therapeutics, Jagiellonian University, Krakow, Poland

Adolfo del Campo Electroceramic Department, Instituto de Cerámica y Vidrio, Madrid, Spain

Tatyana Chernenko Department of Chemistry and Chemical Biology, Northeastern University, Boston, MA, USA

Dana Cialla Institut für Physikalische Chemie, Friedrich-Schiller-Universität Jena, Jena, Germany

Thomas Dieing WITec GmbH, Ulm, Germany

Max Diem Department of Chemistry and Chemical Biology, Northeastern University, Boston, MA, USA

Benjamin Dietzek Institut für Physikalische Chemie, Friedrich-Schiller-Universität Jena, Jena, Germany; Institut für Photonische Technologien e.V., Jena, Germany

Jose F. Fernandez Electroceramic Department, Instituto de Cerámica y Vidrio, Madrid, Spain

Marc Fries Astromaterials Acquisition and Curation Office, NASA Johnson Space Center, Houston, TX, USA

Notburga Gierlinger Department of Biomaterials, Max-Planck-Institute of Colloids and Interfaces, Golm, Germany; Johannes Kepler University, Institute of Polymer Science, Linz, Austria

Thomas F. Haefele Technical Research and Development, Novartis Pharma AG, Basel, Switzerland

Olaf Hollricher WITec GmbH, Ulm, Germany

Hailong Hu WITec GmbH, Beijing Representative Office, Chaoyang District, Beijing, People's Republic of China

Wolfram Ibach WITec GmbH, Ulm, Germany

Nathalie Jung Institute of Pharmaceutical Technology and Buchmann Institute for Molecular Life Sciences, Goethe University, Frankfurt am Main, Germany; Department of Drug Delivery, Helmholtz Centre for Infection Research (HZI) and Helmholtz Institute for Pharmaceutical Research Saarland (HIPS), Saarbruecken, Germany

Alain Jungen Micro and Nanosystems, ETH Zurich, Zurich, Switzerland; Nicronex Ltd., Luxembourg, Luxembourg

Agnieszka Kaczor Faculty of Chemistry, Jagiellonian University, Krakow, Poland; Jagiellonian Centre for Experimental Therapeutics, Jagiellonian University, Krakow, Poland

Amit Kale Department of Pharmaceutical Sciences and Center for Pharmaceutical Biotechnology and Nanomedicine, Northeastern University, Boston, MA, USA

Wolfgang Kiefer Institute for Physical and Theoretical Chemistry, University of Würzburg, Würzburg, Germany; Eisingen Laboratory for Applied Raman Spectroscopy (ELARS), Eisingen, Germany

Kamila Kochan Faculty of Chemistry, Jagiellonian University, Krakow, Poland; Jagiellonian Centre for Experimental Therapeutics, Jagiellonian University, Krakow, Poland

Joachim Koenen WITec GmbH, Ulm, Germany

Andrey V. Korsakov Sobolev Institute of Geology and Mineralogy, Siberian Branch, Russian Academy of Sciences, Novosibirsk, Russian Federation

Stefan Lorkowski Institute of Nutrition and Abbe Center of Photonics, Friedrich Schiller University Jena, Jena, Germany

Katarzyna Majzner Faculty of Chemistry, Jagiellonian University, Krakow, Poland; Jagiellonian Centre for Experimental Therapeutics, Jagiellonian University, Krakow, Poland

Katarzyna M. Marzec Jagiellonian Centre for Experimental Therapeutics, Jagiellonian University, Krakow, Poland; Center for Medical Genomics (OMICRON), Jagiellonian University Medical College, Krakow, Poland

Admir Masic Department of Civil and Environmental Engineering, MIT, Cambridge, MA, USA

Christian Matthäus Department of Chemistry and Chemical Biology, Northeastern University, Boston, MA, USA; Leibniz Institute of Photonic Technology (Leibniz-IPHT), Jena, Germany; Institute of Physical Chemistry and Abbe Center of Photonics, Friedrich Schiller University Jena, Jena, Germany

Lara Milane Department of Pharmaceutical Sciences and Center for Pharmaceutical Biotechnology and Nanomedicine, Northeastern University, Boston, MA, USA

Miloš Miljković Department of Chemistry and Chemical Biology, Northeastern University, Boston, MA, USA

Jörg Müller WITec GmbH, Ulm, Germany

Christoph Neumann JARA-FIT and 2nd Institute of Physics, RWTH Aachen University, Aachen, Germany

Marta Z. Pacia Faculty of Chemistry, Jagiellonian University, Krakow, Poland; Jagiellonian Centre for Experimental Therapeutics, Jagiellonian University, Krakow, Poland

Kurt Paulus Technical Research and Development, Novartis Pharma AG, Basel, Switzerland

Simona Cintă Pînzaru Biomolecular Physics Department, Babes-Bolyai University, Cluj-Napoca, Romania

Jürgen Popp Leibniz Institute of Photonic Technology (Leibniz-IPHT), Jena, Germany; Institute of Physical Chemistry and Abbe Center of Photonics, Friedrich Schiller University Jena, Jena, Germany

Luis Quintero College of Engineering, University of Puerto Rico, Mayagües, PR, USA

Fernando Rubio-Marcos Electroceramic Department, Instituto de Cerámica y Vidrio, Madrid, Spain

Sebastian Schlücker Department of Chemistry and Center for Nanointegration Duisburg-Essen (CENIDE), University of Duisburg-Essen, Essen, Germany

Ute Schmidt WITec GmbH, Ulm, Germany

Michael Schmitt Institut für Physikalische Chemie, Friedrich-Schiller-Universität Jena, Jena, Germany

Ze Xiang Shen Division of Physics and Applied Physics, School of Physical and Mathematical Sciences, School of Materials Science and Engineering, Nanyang Technological University, Singapore, Singapore

Ralph Spolenak Laboratory of Nanometallurgy, Department of Materials, ETH Zurich, Zurich, Switzerland

Christoph Stampfer Peter Grünberg Institute (PGI-9), Forschungszentrum Jülich, Jülich, Germany

Andrew Steele Geophysical Laboratory of the Carnegie Institution of Washington, Washington, DC, USA

Clara Stiebing Leibniz Institute of Photonic Technology (Leibniz-IPHT), Jena, Germany; Institute of Physical Chemistry and Abbe Center of Photonics, Friedrich Schiller University Jena, Jena, Germany

Vladimir Torchilin Department of Pharmaceutical Sciences and Center for Pharmaceutical Biotechnology and Nanomedicine, Northeastern University, Boston, MA, USA

Branko Vukosavljevic Institute of Pharmaceutical Technology and Buchmann Institute for Molecular Life Sciences, Goethe University, Frankfurt am Main, Germany

James C. Weaver Wyss Institute for Biologically Inspired Engineering, Harvard University, Cambridge, MA, USA

Thomas Wermelinger Laboratory of Nanometallurgy, Department of Materials, ETH Zurich, Zurich, Switzerland

Guillaume Wille BRGM, Orleans Cedex 2, France

Maike Windbergs Institute of Pharmaceutical Technology and Buchmann Institute for Molecular Life Sciences, Goethe University, Frankfurt am Main, Germany; Department of Drug Delivery, Helmholtz Centre for Infection Research (HZI) and Helmholtz Institute for Pharmaceutical Research Saarland (HIPS), Saarbruecken, Germany

Klaus Wormuth SurModics, Inc., Eden Prairie, MN, USA

Ting Yu Division of Physics and Applied Physics, School of Physical and Mathematical Sciences, Nanyang Technological University, Singapore, Singapore

Yuying Zhang Department of Chemistry and Center for Nanointegration Duisburg-Essen (CENIDE), University of Duisburg-Essen, Essen, Germany

Part I
Introduction

Chapter 1
Raman's Discovery in Historical Context

Simona Cintă Pînzaru and Wolfgang Kiefer

Abstract In this introductory chapter a short historical description of C.V. Raman himself and of the effect which bears his name will be given. Based on various publications from Indian colleagues, some remarkable facts on Raman as well as on his discovery are highlighted. Following an illustrated description of how the first "Raman light" was detected using the sunlight as an excitation source, the way in which the 1930 Nobel prize winner has been recognized worldwide by his physics colleagues is recounted. Furthermore, some important contributions to the theoretical and experimental developments after the discovery are pointed out. As is well known, the introduction of the laser as a light source brought about a renaissance in Raman spectroscopy. A short list detailing some of the remarkable progress in laser Raman spectroscopy is then provided.

1.1 One in About a Million

When light is scattered by a material, only about one photon in a million (0.0001%) is inelastically scattered. To collect and analyze these inelastically-scattered photons in the early 20th century, when lasers, charge-coupled devices and software tools had yet to be developed it was very challenging. Searching for a light analogue to the Compton effect and critically observing the splendid blue color of the Mediterranean Sea during a voyage in Europe, a young Indian physicist supposed that

S. C. Pînzaru (✉)
Biomolecular Physics Department, Babes-Bolyai University,
Kogalniceanu 1, 400084 Cluj-Napoca, Romania
e-mail: simona.cinta@phys.ubbcluj.ro

W. Kiefer
Institute for Physical and Theoretical Chemistry, University of Würzburg,
Am Hubland, 97074 Würzburg, Germany
e-mail: wolfgang.kiefer@uni-wurzburg.de

W. Kiefer
Eisingen Laboratory for Applied Raman Spectroscopy (ELARS),
97249 Eisingen, Germany

J. Toporski et al. (eds.), *Confocal Raman Microscopy*, Springer Series
in Surface Sciences 66, https://doi.org/10.1007/978-3-319-75380-5_1

inelastically-scattered light could be observed and imagined an optical setup to record it. He showed that the inelastically-scattered light reveals structural information about those molecular species that scattered it.

This chapter includes a brief excursion into the early days of Raman spectroscopy, soon after the first results were recorded through a spectrograph onto a photographic plate, and highlights the scientific context of the Raman effect's discovery and its subsequent impact and developments. It becomes evident that this approach should be connected through some biographical data and the scientific context in which the protagonist of this important scientific achievement, Sir Chandrasekhara Venkata Raman lived and worked.

Newcomers to the field of Raman spectroscopy and current students usually start with a basic definition such as "Raman spectroscopy is a spectroscopic technique based on inelastic scattering of monochromatic light, usually from a laser source, by materials." When Raman spectroscopy was born there were no laser sources. After the development of laser sources and efficient detection systems, Raman spectroscopy research began to flourish. Nowadays, not only physicists, but also chemists, biologists, pharmacologists, toxicologists, mineralogists, artists, engineers, forensic scientists, environmental scientists and clinicians are increasingly interested in, or have already employed some Raman spectroscopy techniques. Advanced research in interdisciplinary fields such as nanobiotechnology, smart sensors, medical diagnostics, drug delivery carriers, personalized medicine, advanced materials or astrobiology, just to mention a few, employ linear or non-linear Raman spectroscopy techniques. It is now difficult to identify a research field in which Raman spectroscopy is not involved. For most users, a "black box" spectrometer and a user-friendly interface provide valuable tools for obtaining the desired Raman spectral information. This type of spectrometer continues to be improved for increased sensitivity, flexibility and capability. In both cases, a retrospective look at the origin of Raman spectroscopy may provide a glimpse into their future developments.

1.2 The Young C.V. Raman and the Discovery of the Effect Named After Him

Chandrasekhara Venkata Raman (C.V. Raman) was an Indian physicist born on November 7th, 1888 in a small village called Thiruvanaikaval in southern India in the state of Tamil Nadu. The pictures in the Fig. 1.1a, b show the house and the room where Raman first saw the light of day.

He studied physics at Presidency College in Madras and Fig. 1.1c shows his picture as a student taken around 1905. After he obtained his Master of Arts in 1907, his poor health prevented him from continuing his education abroad in England, and with limited opportunities in physics in India, he began working as an assistant accountant general in the Indian Finance Department. In his early Calcutta days he

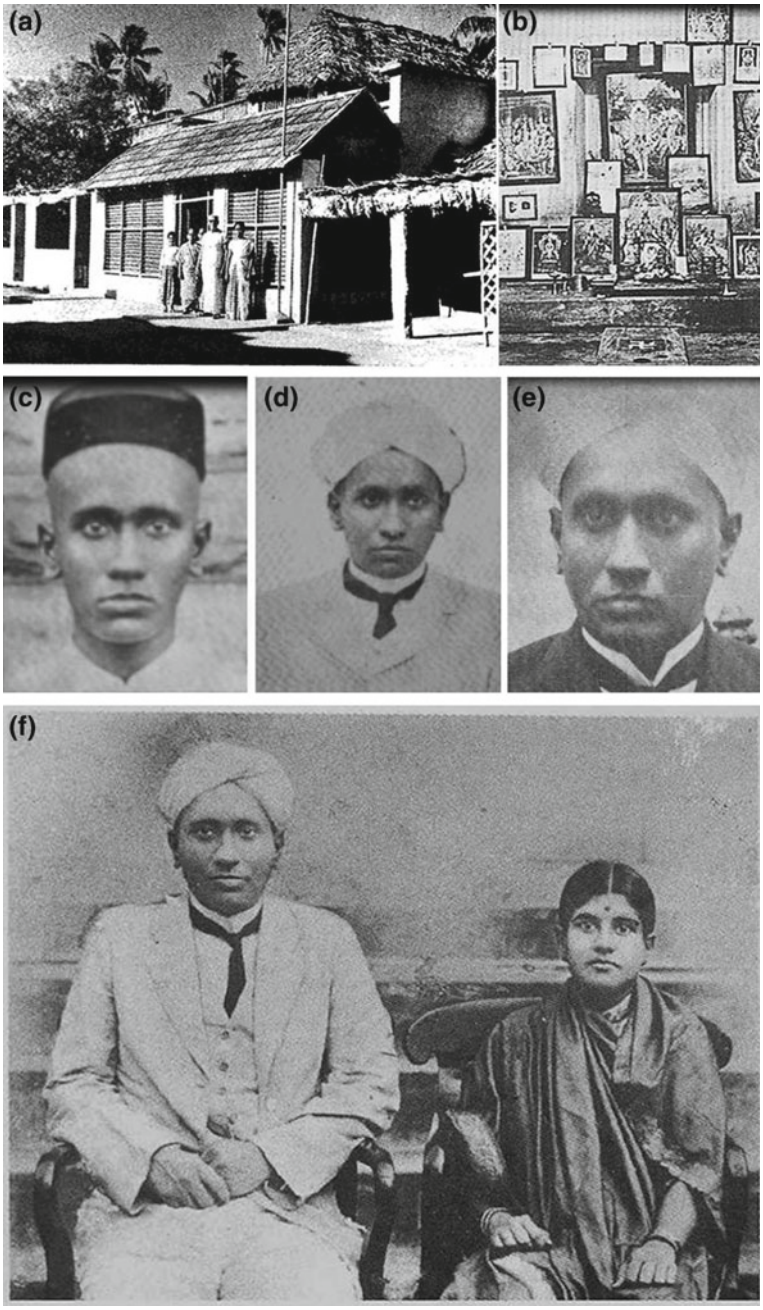

Fig. 1.1 Pictures of the house (**a**) and the room (**b**) where C.V. Raman first saw the light of day. Pictures reproduced from [1, 2], respectively. Pictures of C.V. Raman as a student of physics at the Presidency College in Madras, taken around 1905 (**c**), as an assistant accountant general (Calcutta, 1909, (**d**)) and as professor of physics at Calcutta University in 1924 (**e**) [1]. C.V. Raman and his wife, Lokasundari, in his early Calcutta days (**f**) [2]

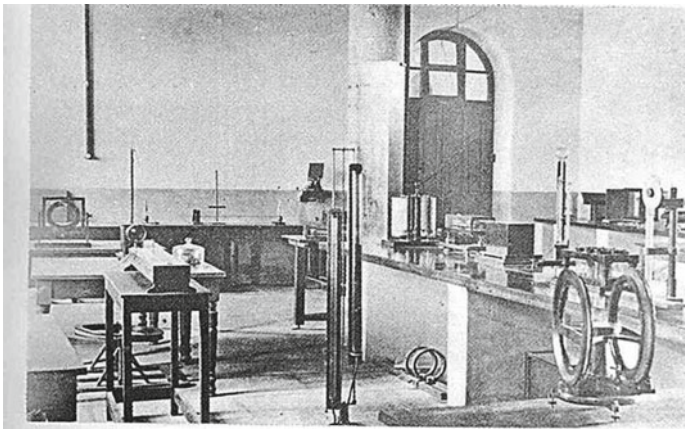

Fig. 1.2 Physics laboratory in India around 1928 [1]

Fig. 1.3 The Indian Association for the Cultivation of Science (IACS) in Calcutta (Raja S.C. Mullick Road), the institution where C.V. Raman discovered the effect named after him. Note that the original building in which the discovery actually took place was then located on Bow Bazar Street, also in Calcutta. It seems that no picture exists of the IACS building at that time [3]

married Lokasundari Ammal (Fig. 1.1f). In 1917 he accepted the position of Palit Chair of Physics at Calcutta University.

A typical physics laboratory in India around 1928 is shown in Fig. 1.2. Most of the time, C.V. Raman worked at the laboratories of the Indian Association for the Cultivation of Science (IACS) in Calcutta, the oldest research institute in India (Fig. 1.3). The original building of the IACS where he actually discovered the effect named after him was located in Calcutta at 210 Bow Bazar Street. Figure 1.4 shows Raman in his office and private library at IACS.

Fig. 1.4 C.V. Raman in his office and private library at the Indian Association for the Cultivation of Science in Calcutta

Raman's discovery was not by accident; he had been searching for precisely that sort of light scattering effect for many years. Indications of this include:

1. A voyage to Europe during the summer months of 1921 gave Raman the opportunity to observe the wonderful blue color of the Mediterranean Sea; Raman searched for an explanation for this phenomenon over several years.
2. He intensified his search for evidence of inelastic scattering of light scattering when he heard of Compton's discovery of the scattering of X-rays by electrons in 1922.

The Raman effect had already been predicted in theory by Adolf Smekal (Fig. 1.5a) in 1923 [4]. Smekal held a professorial position in physics at Karl Franzens University in Graz, Austria until 1959.

Smekal published his paper in Naturwissenschaften, entitled "*Die Quantentheorie der Dispersion*" (The Quantum Theory of Dispersion) and the very first book on the Raman effect was entitled "*Der Smekal-Raman Effekt*" (The Smekal-Raman Effect), published by Fritz Kohlrausch (Fig. 1.5b, c) in 1931 [5]. Kohlrausch was a professor at the Technical University in Graz.

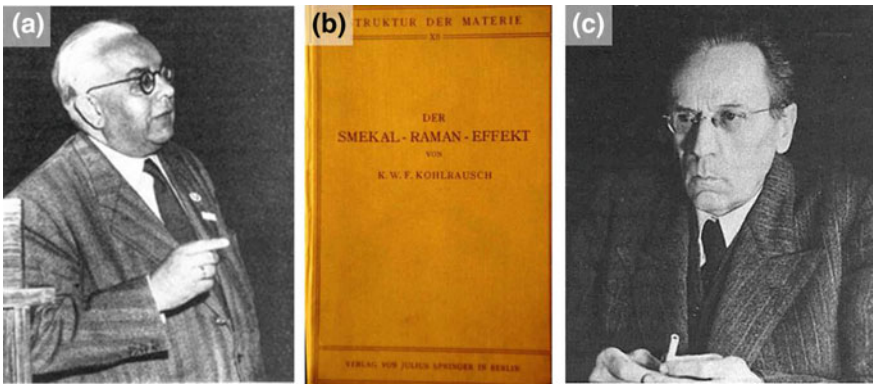

Fig. 1.5 Adolf Gustav Stephan Smekal, an Austrian physicist who predicted the Raman effect by theoretical means in 1923 (**a**); The very first book on the Raman effect was entitled "*Der Smekal-Raman Effekt*" (The Smekal-Raman Effect) (**b**) and was published by Fritz Kohlrausch (**c**) in 1931. Pictures reproduced with permission from Springer Nature

1.3 Observation of the Raman Effect with Sunlight - A Detailed Look at the First Raman Paper, "A New Type of Secondary Radiation"

The first paper on the Raman effect, "A New Type of Secondary Radiation" by C.V. Raman and K.S. Krishnan [6], was submitted by cable to Nature on February 16, 1928 and published on March 31, 1928. A snap shot of the one-page historical manuscript together with pictures of its co-authors is shown in Fig. 1.6.

Let us have a closer look at the paper entitled "*A New Type of Secondary Radiation*." It is notable that it refers to the Compton effect and therefore both elastically and inelastically scattered light should be expected. The sunlight was converged successively by a telescope objective of 18 cm aperture diameter and 230 cm focal length and by a second lens of 5 cm focal length. The sample (liquid or dust-free gas) was placed in the focus of the second lens. To detect the presence of modified scattered radiation, the method of complementary filters was used.

As shown in the (a)–(e) sequence in Fig. 1.7, the experimental set-up for the first observation of inelastic light scattering (Raman light) employed sunlight as the excitation source.

By means of a blue-violet filter in the excitation path (Fig. 1.7b), blue light was observed at 90°. Similarly, with a yellow-green filter in the excitation path (Fig. 1.7c), green-yellow light was observed at 90°. With both color filters in the excitation path (Fig. 1.7d), no light was observed at 90°. With a blue-violet filter in the excitation path and a yellow-green filter in the detection path, the inelastically scattered (Raman) light

A New Type of Secondary Radiation.

If we assume that the X-ray scattering of the 'unmodified' type observed by Prof. Compton corresponds to the normal or average state of the atoms and molecules, while the 'modified' scattering of altered wave-length corresponds to their fluctuations from that state, it would follow that we should expect also in the case of ordinary light two types of scattering, one determined by the normal optical properties of the atoms or molecules, and another representing the effect of their fluctuations from their normal state. It accordingly becomes necessary to test whether this is actually the case. The experiments we have made have confirmed this anticipation, and shown that in every case in which light is scattered by the molecules in dust-free liquids or gases, the diffuse radiation of the ordinary kind, having the same wave-length as the incident beam, is accompanied by a modified scattered radiation of degraded frequency.

The new type of light scattering discovered by us naturally requires very powerful illumination for its observation. In our experiments, a beam of sunlight was converged successively by a telescope objective of 18 cm. aperture and 230 cm. focal length, and by a second lens of 5 cm. focal length. At the focus of the second lens was placed the scattering material, which is either a liquid (carefully purified by repeated distillation *in vacuo*) or its dust-free vapour. To detect the presence of a modified scattered radiation, the method of complementary light-filters was used. A blue-violet filter, when coupled with a yellow-green filter and placed in the incident light, completely extinguished the track of the light through the liquid or vapour. The reappearance of the track when the yellow filter is transferred to a place between it and the observer's eye is proof of the existence of a modified scattered radiation. Spectroscopic confirmation is also available.

Some sixty different common liquids have been examined in this way, and every one of them showed the effect in greater or less degree. That the effect is a true scattering and not a fluorescence is indicated in the first place by its feebleness in comparison with the ordinary scattering, and secondly by its polarisation, which is in many cases quite strong and comparable with the polarisation of the ordinary scattering. The investigation is naturally much more difficult in the case of gases and vapours, owing to the excessive feebleness of the effect. Nevertheless, when the vapour is of sufficient density, for example with ether or amylene, the modified scattering is readily demonstrable.

C. V. Raman.
K. S. Krishnan.

210 Bowbazar Street,
Calcutta, India,
Feb. 16.

Prof. C V Raman

Prof. K S Krishnan

Fig. 1.6 The manuscript entitled "*A New Type of Secondary Radiation*" submitted by cable to Nature by C.V. Raman and K.S. Krishnan on February 16, 1928 and published on March 31, 1928. Reprinted by permission from Macmillan Publishers Ltd: Nature [6], copyright 1928

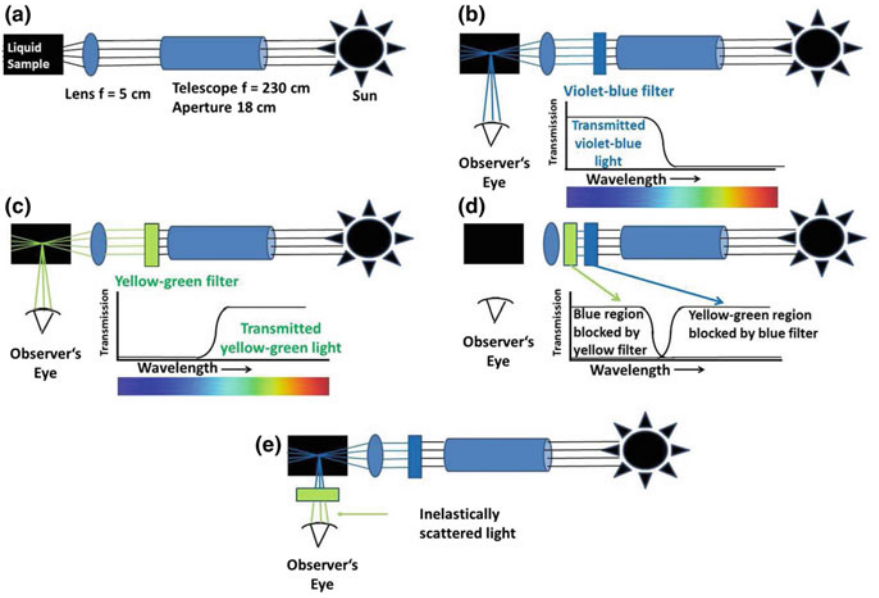

Fig. 1.7 Experimental set-up for the first observation of inelastically scattered (Raman) light - The method of complementary filters: **a** Using sunlight as the excitation source; **b** by means of a blue-violet filter in the excitation path, blue light was observed at 90°; **c** with a yellow-green filter in the excitation path, green-yellow light was observed at 90°; **d** with both color filters in the excitation path, no light was observed at 90°; **e** with a blue-violet filter in the excitation path and a yellow-green filter in the detection path, the inelastically scattered (Raman) light was observed at 90°

was observed at 90° (Fig. 1.7e). The observed yellow-green light was the first proof of the existence of modified light: "inelastically scattered light by molecules," later called Raman scattered light. Raman and Krishnan provided evidence of scattered light from 60 common liquid samples. They had already mentioned that spectroscopic confirmation was also available [6].

In the next step, Raman used a mercury lamp as the excitation source and observed the scattered light through a spectroscope (Fig. 1.8).

Shortly afterwards he used the Hilger quartz spectrograph (20 cm focal length) shown in Fig. 1.9. With this spectrograph the first Raman spectrum was photographed. The IACS in Calcutta, India, still keeps this instrument on display.

Raman was awarded the Nobel Prize in 1930 for his work: "On the Diffusion of Light" and for the discovery of the effect named after him. Figure 1.10 shows the ceremony at which Sir C.V. Raman received the Nobel Prize along with the Nobel Diploma from the King of Sweden.

Fig. 1.8 Next step: Mercury lamp (S) and a simple hand spectroscope (SP) used for observing Raman spectra of liquid samples in large sample cells (L). Raman used his eye as the detector

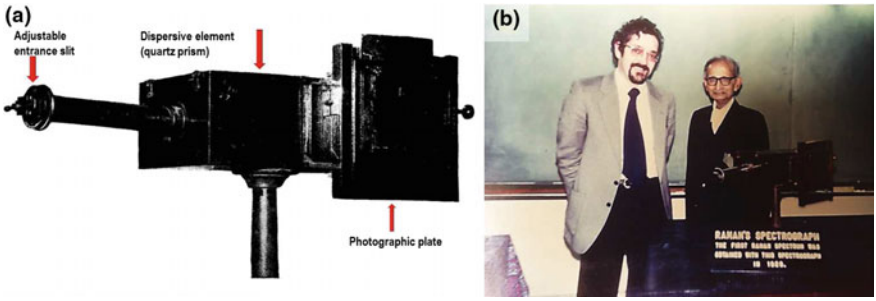

Fig. 1.9 **a** The first spectrograph used by C.V. Raman (Hilger quartz spectrograph, 20 cm focal length) with which Raman acquired the first Raman spectrum. (Courtesy: Indian Association for the Cultivation of Science and Birla Industrial & Technological Museum, Calcutta). **b** W. Kiefer (left) and S.C. Sirkar (right), one of last coworkers of Raman, with Raman's spectrograph. Picture taken in 1978. Pictures source: W. Kiefer's personal collection

It should be pointed out that Subrahmanyan Chandrasekhar, a nephew of C.V. Raman, received the Nobel Prize for Physics in 1983 for "Theoretical Studies on the Structure and Evolution of the Stars" He shared the prize with William A. Fowler. The uncle and his nephew are seen together in Fig. 1.11.

There are two stories that attest to the character of this incredible man, namely his audacity and unshakeable self-confidence.

First story: Raman was elected a Fellow of the Royal Society in 1924. At the ceremony recognizing him, he is known to have said that while he appreciated

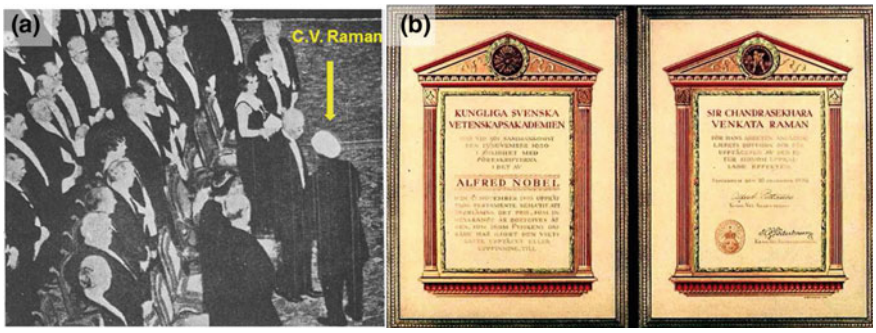

Fig. 1.10 **a** C.V. Raman receiving the Nobel Prize in 1930 from the King of Sweden [3]. **b** The Nobel Diploma (Reproduced from [2], section "Raman's World of Colors")

Fig. 1.11 Uncle and nephew, both Noble laureates in physics: C.V. Raman and S. Chandrasekhar [2]

the honor bestowed upon him he did not consider it the highest honor and that he would get the Nobel Prize for India within five years.

Second story: In 1930 the Nobel Prizes were announced in the second or third week in November. The Nobel Prize ceremony is always on December 10th, the day of Nobel's death. It would have been impossible for Raman to reach Stockholm in time for the ceremony from Calcutta by steam ship after receiving the news by telegram from the Nobel Committee in mid-November. It is now a historical fact that Raman had booked two tickets for himself and his wife already in July that year to enable them to reach Stockholm in early December.

Fig. 1.12 The proud and self-confident C.V. Raman (left side) and the modest Jawaharlal Nehru, the first Prime Minister of India (right side) [2]

A picture in Fig. 1.12 illustrates on the left the proud, self-confident C.V. Raman and on the right, the modest first Prime Minister of India, Jawaharlal Nehru, a remarkable figure in Indian politics.

1.4 Recognition of Raman's Work by Other Scientists

Raman was recognized as an important physicist worldwide after receiving the Nobel Prize. He met with many great physicists of his time. To evoke the famous names in physics, Fig. 1.13 presents a collage of images of C.V. Raman accompanied by Arnold Sommerfeld (1928), Niels Bohr, Robert Millikan (1940), Werner Heisenberg, Wolfgang Pauli, Paul Andre Maurice Dirac, Louis de Broglie, Robert S. Mulliken and Linus Pauling.

During the celebration of the silver jubilee of the discovery of the Raman effect in 1953, Albert Einstein mentioned to a press correspondent: "*C.V. Raman was the first to recognize and demonstrate that the energy of a photon can undergo a partial transformation within matter. I still recall vividly the deep impression that the discovery made on all of us*."

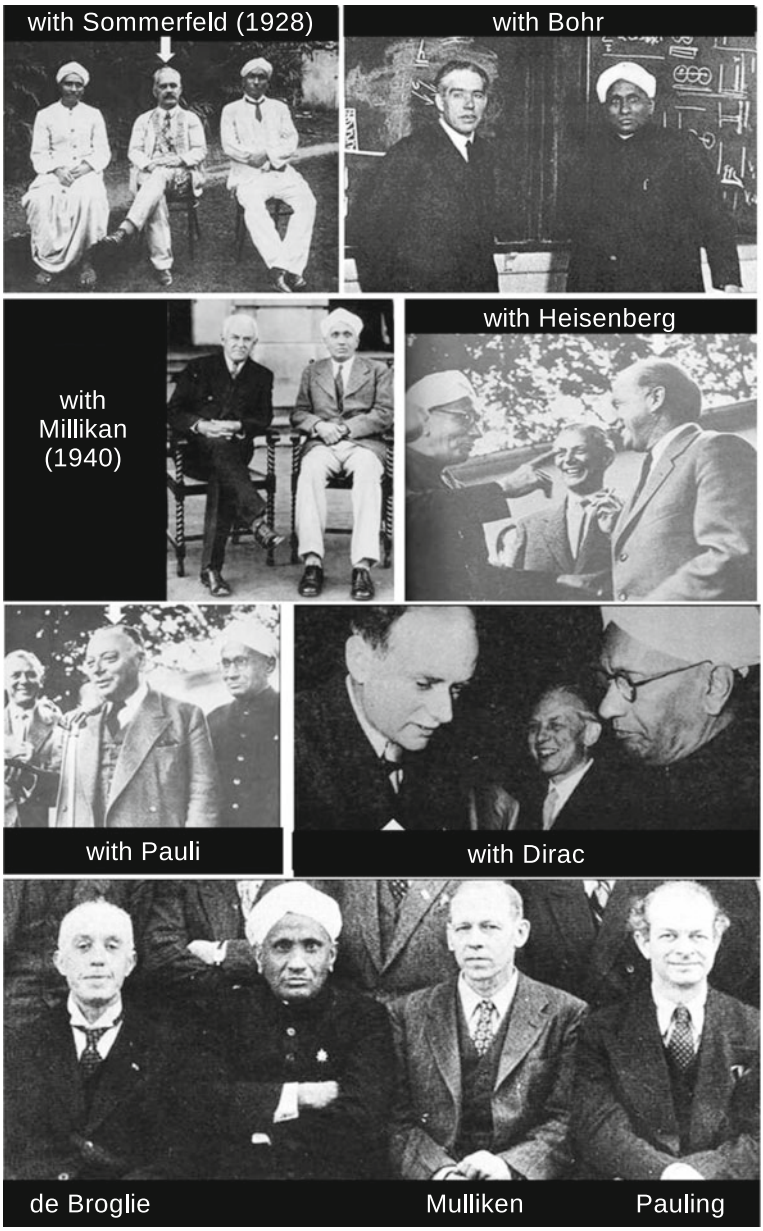

Fig. 1.13 Raman's meetings with other great physicists of his time: Arnold Sommerfeld (1928), Niels Bohr, Robert Millikan (1940), Werner Heisenberg, Wolfgang Pauli, Paul Dirac, Louis de Broglie, Robert S. Mulliken and Linus Pauling. Adapted from figures taken from [2, 7]

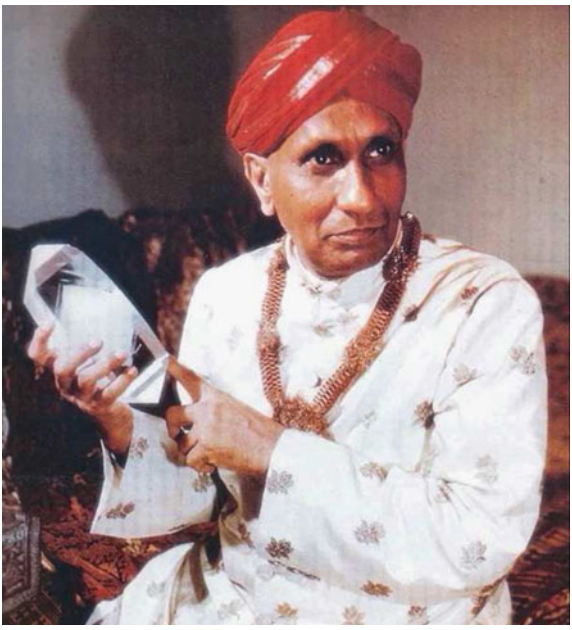

Fig. 1.14 Crystals always fascinated Raman. Here he holds a large quartz crystal (Reproduced from [2], section "Raman's World of Colors")

1.5 Raman's Fascination with Crystals and His Time at the Raman Research Institute in Bangalore

Crystals always held a fascination for Raman. He was enthralled by the light and colors created by nature. He set up in his research institute an exhibition of crystals emitting a spectacular glow under UV illumination to be admired by his guests. Figure 1.14 shows a picture of Raman with a large quartz crystal in his hands.

He spent many years studying diamond. The largest diamond (borrowed from a wealthy Indian Maharajah) he and his student S. Bhagavantam studied was 140 carats (=28 g). All papers on the diamond are collected in Raman's book, "The Diamond" [8], which he published shortly before he died on November 21st, 1970 at the age of 82. Raman had sent a copy of his book with a personal dedication to one of the authors. A snap shot of the page bearing his signature is shown in Fig. 1.15.

In 1933 the Indian Government built a special research institute for C.V. Raman in Bangalore, which is now called the Raman Research Institute. Raman was the director of the institute from 1933 until his death in 1970. An original video supplied by the Raman Research Institute in Bangalore, India, recorded in 1968 is available on the internet, presenting a special interview with Dr. C.V. Raman about his book "The Physiology of Vision" and his latest discovery on the origin of floral colors [9, 10].

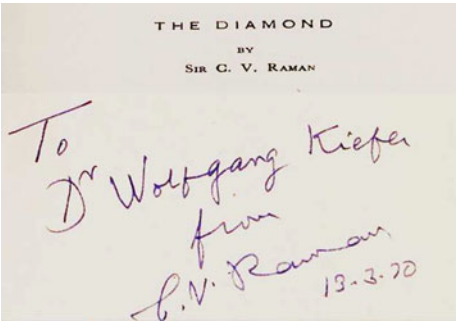

Fig. 1.15 Snap shot of the first page of the book "The Diamond" authored by C.V. Raman with a personal dedication to W.K. Photo: W. Kiefer

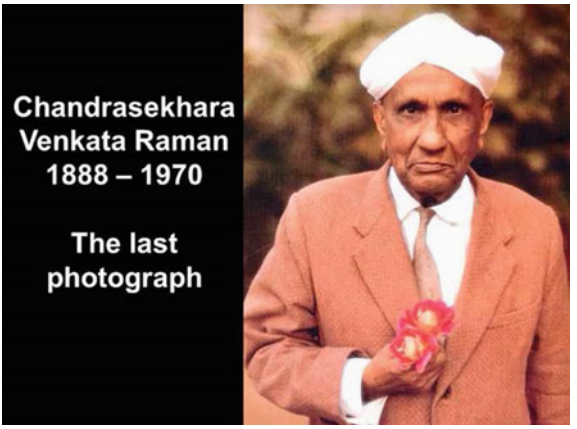

Fig. 1.16 Sir Chandrasekhara Venkata Raman (1888–1970) (Reproduced from [2] with permission from Springer Nature)

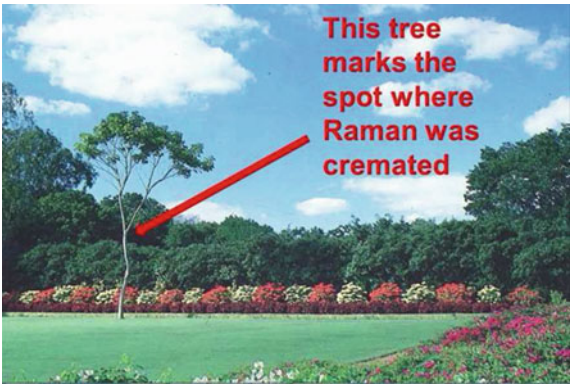

Fig. 1.17 The lawn of the Raman Research Institute in Bangalore (Reproduced from [2], section "Raman's World of Colors")

> Nature you see at her best in a garden. It is up to us to try to understand what she does and why she does it. See the real science... Real science begins when you are really interested in something. (Sir C.V. Raman)

The last photograph of Sir C.V. Raman is shown in Fig. 1.16. He was cremated on the lawn of the Raman Research Institute. A tree marks the spot where Raman was cremated (Fig. 1.17).

1.6 Some Important Contributions to Theoretical and Experimental Developments After Raman's Discovery

Among the theoretical contributions, the first comprehensive theory is detailed in the 170-page article entitled "*Rayleigh-Streuung und Raman-Effekt*" from the German book published in 1934 by Placzek [11] entitled "*Quantenmechanik der Materie und Strahlung, Teil II*" (Quantum Mechanics of the Matter and Radiation, Vol. II), which treats explicitly Rayleigh scattering and the Raman effect, including the quantum mechanical description. Placzek's article is still a valuable reference for anybody interested in the theory of the Raman effect. It is highly recommended for beginners.

Important early developments in Raman instrumentation include the construction of stronger light sources and more efficiently resolving spectrometers. The so-called "Toronto burner" (Fig. 1.18) was a high power mercury arc lamp used for many years before the development of the laser. The helically formed mercury-discharge lamp surrounded the liquid sample cells while the Raman scattered light was observed along the axis of the liquid tube cell (Fig. 1.18b).

The Steinheil spectrograph with recorder adapter was a powerful three-prism device that became the first photoelectric recorder of Raman spectra (Fig. 1.19). In the focal plane of this spectrometer, the spectrum could be either photographed or photo-electrically recorded. The photomultiplier attached (PM) was moved along the spectral focal plane and the collected photo-current was a function of time.

In 1956 C.V. Raman visited the Steinheil Company in Munich, Germany. In Fig. 1.20a, Raman is shown in the company of Josef Behringer, one of the pioneers of resonance Raman scattering theories and a representative of the Steinheil Company, while in Fig. 1.20b he is in discussion with Professors J. Brandmüller and J. Behringer from the University of Munich. Professor Behringer and Professor Herbert Moser published a comprehensive textbook entitled "*Einführung in die Ramanspektroskopie*" (Introduction to Raman Spectroscopy) [14], for which C.V. Raman wrote the foreword. This book was "The Bible" for many students involved in Raman spectroscopy in the pre-laser era.

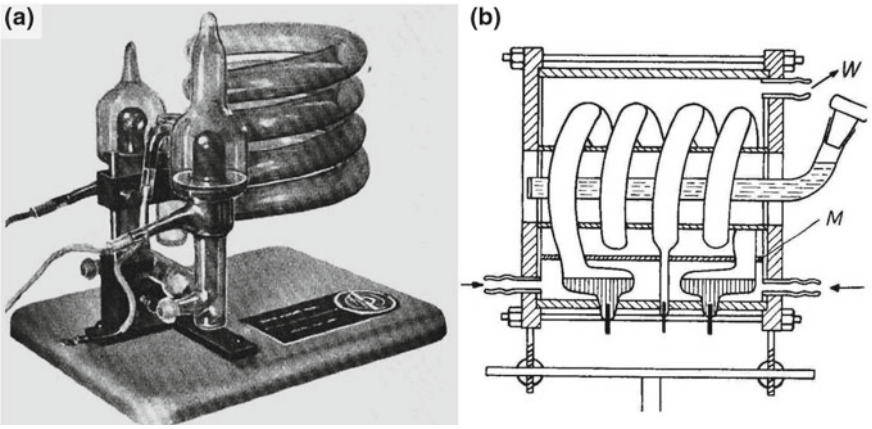

Fig. 1.18 The high power mercury arc lamp in the pre-laser era: the Toronto burner (table view) (**a**) and schematic representation of the helical light resulting from the mercury arc discharge surrounding the liquid cell containing the sample (**b**). Raman scattering was collected along the liquid cell axis. Reproduced from [12, 13]

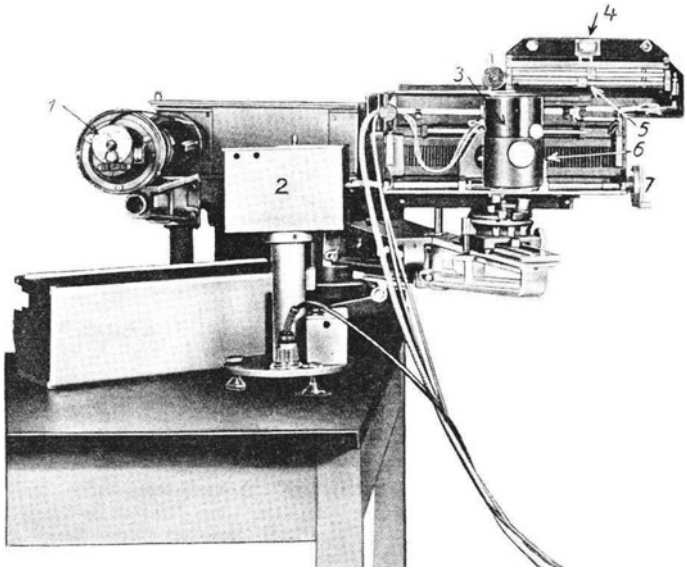

Fig. 1.19 The Steinheil spectrograph with photoelectric recorder for Raman spectra. It was a powerful three-prism device. 1-entrance slit, 2-gears, 3-photomultiplier (PM), 4-sledge scale, 5-limit stopper, 6-exit slit in front of PM, 7-handwheel. Reproduced from [14] with permission of Springer Nature

Fig. 1.20 **a** C.V. Raman visiting C.A. Steinheil & Söhne GmbH in Munich, Germany (1956). Left: Josef Behringer, one of the pioneers of Resonance Raman Spectroscopy and the representative of the Steinheil Company (middle). **b** C.V. Raman in discussion with Professors J. Behringer (middle) and J. Brandmüller (right) from the University of Munich. Pictures supplied in 1956 by Steinheil GmbH to Prof. Brandmüller and forwarded to W. Kiefer through H.W. Schrötter, Munich

1.7 The First Laser-Raman Spectra

The renaissance of Raman spectroscopy began in 1960 shortly after the laser was invented. The first laser-excited Raman spectrum was shown by S.P.S. Porto and D.L. Wood from Bell Labs at the Symposium of Molecular Structure and Spectroscopy, organized by Ohio State University in Columbus, Ohio in 1961. Their contributed paper entitled "*The Optical MASER as a Raman Source*" described the equipment including a high-intensity ruby maser, a Raman cell coated with $BaSO_4$ and a high-speed grating spectrograph. The Raman spectrum of benzene was obtained with an effective exposure time of several milliseconds. The main difficulties encountered include the temperature dependence of the maser frequency and the strong fluorescent emission lines from the ruby crystal in the spectral range where the most important Raman lines occur.

1.8 Development of Modern Laser-Raman Spectroscopy and Conclusion

The main development of modern laser-Raman spectroscopy was of course the first realization of laser. This breakthrough along with several other remarkable

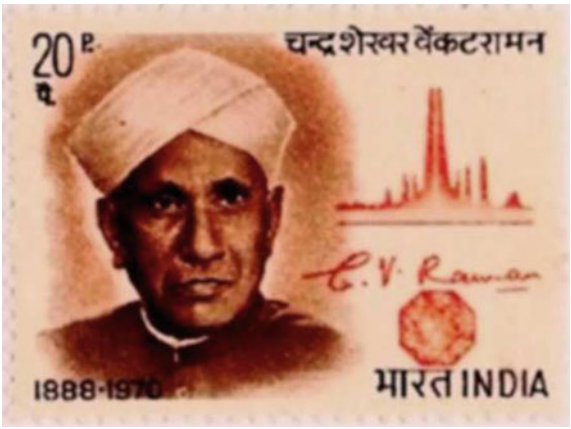

Fig. 1.21 The Indian stamp (1971) showing the Stokes and anti-Stokes regions of the Raman spectrum of CCl_4. Picture taken by W. Kiefer from his stamp collection

developments (still applied in modern laser-Raman spectroscopy) are briefly and chronologically summarized as follows:

1960 First realization of laser
1965 Dual-grating monochromators
1973 Coherent anti-Stokes Raman spectroscopy (CARS)
1977 Surface-enhanced Raman spectroscopy (SERS)
1980 Micro-Raman spectroscopy
1985 Fourier-transform Raman spectroscopy
1990 Nitrogen-cooled CCD cameras
1990 Holographic notch filters
1995 Femtosecond time-resolved Raman spectroscopy and fs-CARS
1998 Tip-enhanced Raman spectroscopy (TERS)

1.9 Conclusion

In conclusion we offer some advice to the reader.

- Get infected by the virus *Ramanus spectroscopus*!
- Do both, experiment and theory;
- Follow the advice our master C.V. Raman gave us: "*The essence of science is independent thinking and hard work*." Maybe then a stamp will be created to honor you as was done in 1971 for C.V. Raman (Fig. 1.21).

Acknowledgements W.K. thanks the Raman Research Institute in Bangalore for providing the interview film and the audio of Raman's lectures.

References

1. G. Venkataraman, *Journey into Light: Life and Science of C.V. Raman* (Indian Academy of Sciences, Bangalore, 1988). https://books.google.nl/books?id=YaTvAAAAMAAJ
2. S. Ramaseshan, C.R. Rao (eds.), *C.V. Raman, A Pictoral Biography* (Indian Academy of Sciences, Bangalore, 1998)
3. U. Ghatak, S. Mukherjee, A. Chaudhuri, S. Banerjee, S. Bhattacharyya, S. Goch, M. Bagchi, *A Century* (Indian Association for the Cultivation of Science, Calcutta, 1980)
4. A. Smekal, Naturwissenschaften **11**(43), 873 (1923)
5. K.W.F. Kohlrausch, *Der Smekal-Raman-Effekt*, vol. 12 (Springer, 1931)
6. C.V. Raman, K.S. Krishnan, Nature **121**, 501 (1928)
7. D. Long, Int. Rev. Phys. Chem. **7**(4), 317 (1988)
8. C.V. Raman, The diamond. A private book published by the author containing a collection of journal publications on the diamond. An electronic version is available from wolfgang.kiefer@uni-wuerzburg.de
9. C.V. Raman, in *Proceedings of the Indian Academy of Sciences-Section B*, vol. 58 (Springer, Berlin, 1963), pp. 104–113
10. C.V. Raman, *The Physiology of Vision* (Indian Academy of Sciences, Bangalore, 1968)
11. G. Placzek, *Rayleigh-Streuung und Raman-Effekt* (Akad. Verlag-Ges, An electronic version is available from wolfgang.kiefer@uni-wuerzburg.de, 1934), pp. 275–374
12. J. Kemp, J. Jones, R. Durkee, JOSA **42**(11), 811 (1952)
13. H. Moser, Colloquium über Ramaspektroskopie. cited in [14] (1955)
14. J. Brandmüller, H. Moser, *Einführung in die Ramanspektroskopie* (Dietrich Steinkopff Verlag, 1962)

Part II
Theory and Technology

Chapter 2
High Resolution Optical and Confocal Microscopy

Olaf Hollricher and Wolfram Ibach

Abstract In this chapter, the theory of optical image formation in an optical microscope is described and the difference between conventional and confocal microscopy is explained. The selection of the appropriate pinhole diameter is discussed in detail, as the pinhole diameter is crucial in obtaining the highest depth resolution as well as optimizing collection efficiency, because the Raman signal is typically very weak.

2.1 Introduction

More than 2000 years ago, Seneca[1] described the magnifying properties of water-filled glass spheres. Since that time, many researchers have known that all convex lenses can be used to magnify objects, but it took more than a millennium until further improvements lead to the combination of several lenses to form an optical microscope. It is often said, that Dutch spectacle maker Hans Janssen and his son Zacharias[2] were the first to develop the optical microscope by combining several lenses to form an optical microscope. It could, however, also have been the Dutch-German lens-maker Hans Lippershey[3] or even Galileo Galilei.[4] Galileo combined a convex and a concave lens for his microscopes in 1609. Christiaan Hygens,[5] also a Dutch scientist, developed the first achromatic objective in the late 17th century by combining two lenses of different kinds of glass, which was a big step forward.

Up to the 19th century, progress in quality and resolution was slow because microscopes were built using experience and trail-and-error, not scientific knowledge.

[1] Lucius Annaeus Seneca the younger (∗ around 4 BC, † 65 AD).
[2] Zacharias Janssen (∗ around 1588, † around 1631).
[3] Hans Lippershey (∗ around 1570, † September 1619).
[4] Galileo Galilei (∗ 15.02.1564, † 08.01.1642).
[5] Christiaan Hygens (∗ 14.04.1629, † 08.07.1695).

O. Hollricher (✉) · W. Ibach
WITec GmbH, Lise-Meitner-Strasse 6, 89081 Ulm, Germany
e-mail: olaf.hollricher@witec.de

J. Toporski et al. (eds.), *Confocal Raman Microscopy*, Springer Series in Surface Sciences 66, https://doi.org/10.1007/978-3-319-75380-5_2

Around 1873, Ernst Abbe,[6] Prof. of Physics in Jena, Germany, developed his theory of optical image formation which was the basis of understanding the physics behind the optical microscope. His combined work with Carl Zeiss,[7] who was a precision mechanic and Otto Schott,[8] who had a Ph.D. in chemistry and used his knowledge to develop glass with different optical properties, lead to the development of the diffraction-limited optical microscope as it is known today. The resolution of the optical microscope remained nearly constant since the advent of Abbe's diffraction theory and is still about half of the wavelength of the excitation light.

During the 20th century, many new imaging techniques were introduced, such as fluorescence microscopy, interference microscopy, phase contrast and dark-field illumination which made the optical microscope a powerful analytical tool, but the most important development of recent years is the confocal microscope.[9]

The principle underlying confocal imaging was patented by Marvin Minsky in 1957 (US patent 3013467), but it was not until the late 1980s that it became a standard technique. In confocal microscopy, a point-like light source (typically a laser) is focused onto the sample and the image of this spot is detected through a small pinhole in front of the detector. As the pinhole is located in the image plane of the microscope, the pinhole is confocal with the illuminating spot.

An image of the sample can only be obtained by either scanning the sample or the excitation spot point by point and line by line. This makes a confocal microscope much more complex than a conventional microscope, but the additional complexity is far outweighed by the advantage of having the detected light restricted to a small area around the focal point. Therefore, scattered light from above or below the focal point does not contribute to the image.

Although an increase in lateral resolution of a factor of ≈ 1.4 ($\sqrt{2}$) can be achieved by convolution of the excitation spot with the pinhole aperture, this resolution enhancement can only be achieved at a high price: the pinhole must be so small that 95% of the light is lost. The main advantage of confocal microscopy as compared to conventional microscopy is therefore the depth resolution and the much higher image contrast due to stray-light suppression.

This chapter provides an introduction to the theory of confocal image formation.

The first section describes the theory of image formation in an optical microscope and the differences between conventional and confocal microscopy are explained. The next section describes the choice of the appropriate pinhole diameter, suitable for highest depth and lateral resolution. Factors that need to be taken into account in order to achieve optimum results will also be explained.

---

[6] Ernst Karl Abbe, (∗ 23.1.1840, † 14.1.1905).

[7] Carl Zeiss (∗ 11.9.1816, † 3.12.1888).

[8] Otto Schott (∗ 17.12.1851, † 27.8.1935).

[9] "confocal" from "konfokal": (lat.) with equal focal points.

2.2 Introduction to Theoretical Considerations in High Resolution Microscopy

All confocal imaging techniques, for example, confocal Raman microscopy or confocal 2-photon microscopy are based on a point to point image formation. A detailed overview of these methods can be found in [1].

In this section, a theoretical background for this technique will be provided. The electromagnetic field distribution in the focus of an objective will be calculated, which is the starting point for the mathematical description of image formation. Furthermore, the fundamental difference between confocal microscopy and confocal Raman microscopy with its range of excitation possibilities will be discussed.

2.3 Introduction to Confocal Microscopy

In confocal microscopy, a point-like light source is focused with a lens or an objective onto a sample. The spatial extension of the focus spot on the sample is determined by the wavelength λ and the quality of the image formation. The image spot is then focused through the same (or a second) lens onto an aperture (pinhole) in front of a detector. The size of the pinhole is chosen so that only the central part of the focus can pass through the pinhole and reach the detector.

One can see in Fig. 2.1 that rays that do not come from the focal plane will not be able to pass through the pinhole. From this simple geometric representation, two

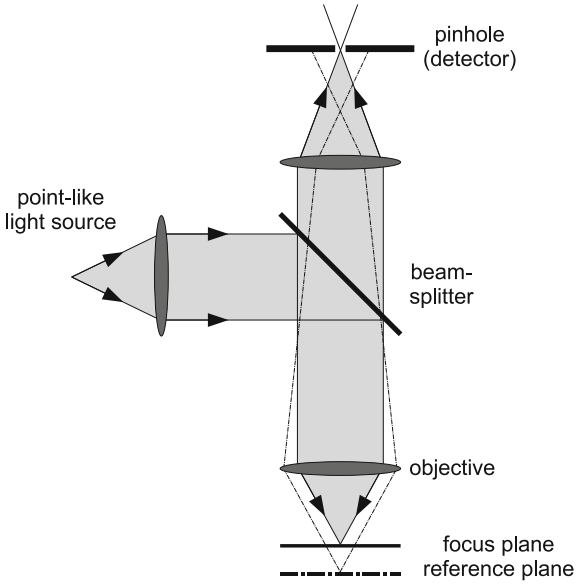

Fig. 2.1 Principal setup of a confocal microscope

advantages of confocal microscopy can already be seen. First, through scanning of the sample with respect to the objective, a three-dimensional image of the sample can be obtained. This is not possible in conventional microscopy. Second, only light from the focal plane will hit the detector. Therefore, image contrast is strongly enhanced.

Additionally, by choosing an appropriate pinhole diameter, the lateral resolution can be increased by up to a factor of $\sqrt{2}$.

2.4 Electromagnetic Scattering in Optical Systems

In this section, the basic principles necessary for calculating the field distribution in the focus are provided. A detailed discussion can be found in the articles of Wolf [2, 3]. Figure 2.2 shows the geometry used to illustrate this.

S_0 is the origin of a monochromatic wave with frequency ω and S_1 its image, obtained with geometric ray optics. The field distribution in the focus is described in the Cartesian coordinate system with origin in S_1. Starting point is the HELMHOLTZ-EQUATION

$$\Delta \boldsymbol{E} + k^2 \boldsymbol{E} = \boldsymbol{0},$$

which describes the space-dependent component of the electrical field.

$$\boldsymbol{E}(P,t) = \Re\left\{\boldsymbol{e}(P)e^{-i\omega t}\right\}$$

In general, the HELMHOLTZ-EQUATION can be satisfied by

$$\boldsymbol{e}(P) = \int_{-\infty}^{\infty}\int_{-\infty}^{\infty} e^{ik(s_x x + s_y y)}\left\{\boldsymbol{U}(s_x, s_y)e^{iks_z z} + \boldsymbol{V}(s_x, s_y)e^{-iks_z z}\right\} ds_x ds_y \qquad (2.1)$$

where s_z is given by the condition ${s_x}^2 + {s_y}^2 + {s_z}^2 = 1$.

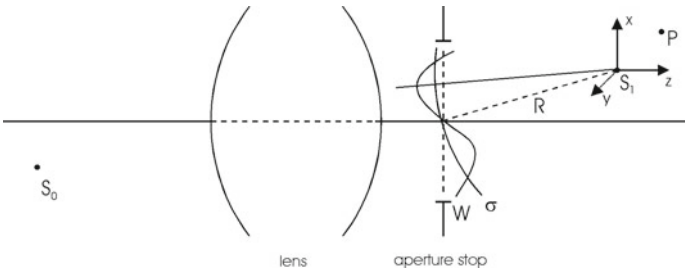

Fig. 2.2 Imaging geometry

$\boldsymbol{U}(s_x, s_y)$ and $\boldsymbol{V}(s_x, s_y)$ are arbitrary functions that have to fulfill the KIRCHHOFF BOUNDARY CONDITIONS. For the magnetic field

$$\boldsymbol{H}(P, t) = \Re\left\{\boldsymbol{h}(P)e^{-i\omega t}\right\}$$

similar expressions can be found.

As described in [2], an approximate solution for the electrical field in the plane of the aperture can be found with the method of stationary phase. This leads to two general solutions:

$$\boldsymbol{e}(P) = -\frac{ik}{2\pi}\iint\limits_{\Omega}\frac{\boldsymbol{a}(s_x, s_y)}{s_z}e^{ik\{\Phi(s_x,s_y)+s_x x+s_y y+s_z z\}}ds_x ds_y \tag{2.2}$$

$$\boldsymbol{h}(P) = -\frac{ik}{2\pi}\iint\limits_{\Omega}\frac{\boldsymbol{b}(s_x, s_y)}{s_z}e^{ik\{\Phi(s_x,s_y)+s_x x+s_y y+s_z z\}}ds_x ds_y \tag{2.3}$$

Here, the functions $\boldsymbol{a}(s_x, s_y)$, $\boldsymbol{b}(s_x, s_y)$ and $\Phi(s_x, s_y)$ take the part of $\boldsymbol{U}(s_x, s_y)$ and $\boldsymbol{V}(s_x, s_y)$. These two functions have the following meaning:

The abberation function $\Phi(s_x, s_y)$ is a measure how strongly the real wavefront W deviates from the ideal spherical wavefront σ. The factor $\boldsymbol{a}(s_x, s_y)$ determines the amplitude of the field. In the geometrical optic, this is the intensity of the light beam. Along every beam $\boldsymbol{a}(s_x, s_y)$ is independent of the position of the aperture.

All three numbers $\boldsymbol{a}$, $\boldsymbol{b}$ and Φ can be determined by Ray-Tracing algorithms.

Equations (2.2) and (2.3) represent the addition of planar waves inside the aperture. In contrast, using the HUYGENS-FRESNEL PRINCIPLE one would add spherical waves.

2.5 3D-Intensity Distribution in the Focus

In the literature one can find two different descriptions for the field distribution in the focus. One describes the electrical field as a scalar and is correct only for small aperture angles. The vector description from Richards and Wolf [4] is more appropriate for the nature of light. Here, the field distribution is a function of the aperture angle α, and therefore can also be applied to systems with large aperture angles.

If one compares small and large aperture angles one sees that the electrical energy density in the focal plane is no longer radially symmetric, but depends on the original polarization direction. Additionally, the energy density in the secondary maxima and minima get larger.

2.5.1 Large Aperture Angles

For an abberation free system ($\Phi(s_x, s_y) = 0$), a system without wavefront errors, all components of the electrical field in the focus can be derived from (2.2) and (2.3). To simplify the calculation the point S_0 (Fig. 2.2) is shifted to infinity. This point is the origin of an electrical field which is polarized in x-direction ($\phi_P = 0$). Therefore, the image of S_0 lies exactly in the focal plane of the lens S_1. A change of the transmission of the lens due to its surface curvature, which could be calculated with the FRESNEL FORMULAS is neglected. Therefore, the surface curvature of the lens must be sufficiently small.

Because of the symmetry of the system, it is appropriate to change to spherical coordinates.

$$x = r_P \sin\theta_P \cos\phi_P, \qquad y = r_P \sin\theta_P \sin\phi_P, \qquad z = r_P \cos\theta_P$$

The origin of the coordinate system is the geometrical focus point S_1. We also change to so-called optical coordinates

$$\left.\begin{aligned} u &= k r_P \cos\theta_P \sin^2\alpha = k z \sin^2\alpha \\ v &= k r_P \sin\theta_P \sin\alpha \;\; = k\sqrt{x^2+y^2}\sin\alpha \end{aligned}\right\} \tag{2.4}$$

with

$k = \frac{2\pi}{\lambda}$: absolute value of the wave vector
$0° < \alpha < 90°$: half of the aperture angle

to eliminate the wavelength dependence. With these coordinates, the spatially dependent component of the electrical and magnetica field can be written as

$$\left.\begin{aligned} e_x(u,v) &= -iA(I_0 + I_2\cos 2\phi_P) \\ e_y(u,v) &= -iAI_2 \sin 2\phi_P \\ e_z(u,v) &= -2AI_1 \cos\phi_P \end{aligned}\right\} \tag{2.5}$$

$$\left.\begin{aligned} h_x(u,v) &= -iAI_2 \sin 2\phi_P \\ h_y(u,v) &= -iA(I_0 - I_2\cos 2\phi_P) \\ h_z(u,v) &= -2AI_1 \sin\phi_P \end{aligned}\right\}. \tag{2.6}$$

Herein, I_0, I_1 and I_2 are defined over the integrals

$$\left.\begin{aligned} I_0(u,v) &= \int_0^\alpha \cos^{\frac{1}{2}}\theta \sin\theta(1+\cos\theta) J_0\left(\tfrac{v\sin\theta}{\sin\alpha}\right) e^{iu\cos\theta/\sin^2\alpha} d\theta \\ I_1(u,v) &= \int_0^\alpha \cos^{\frac{1}{2}}\theta \sin^2\theta J_1\left(\tfrac{v\sin\theta}{\sin\alpha}\right) e^{iu\cos\theta/\sin^2\alpha} d\theta \\ I_2(u,v) &= \int_0^\alpha \cos^{\frac{1}{2}}\theta \sin\theta(1-\cos\theta) J_2\left(\tfrac{v\sin\theta}{\sin\alpha}\right) e^{iu\cos\theta/\sin^2\alpha} d\theta \end{aligned}\right\} \tag{2.7}$$

The parameter $A = \frac{kfl_0}{2} = \frac{\pi f l_0}{\lambda}$ is a constant containing the focal length f of the lens and the amplitude l_0 of the incoming light. The symbol J_n stands for the Bessel function of order n.

With these equations it is possible to calculate all properties that are important for microscopy. The electrical, magnetic and total energy distribution have the forms

$$\left.\begin{aligned} \langle w_e(u,v,\phi_P)\rangle &= \tfrac{A^2}{16\pi}\left\{|I_0|^2 + 4|I_1|^2\cos^2\phi_P + |I_2|^2 + 2\cos 2\phi_P \Re(I_0 I_2{}^*)\right\} \\ \langle w_m(u,v,\phi_P)\rangle &= \tfrac{A^2}{16\pi}\left\{|I_0|^2 + 4|I_1|^2\sin^2\phi_P + |I_2|^2 - 2\cos 2\phi_P \Re(I_0 I_2{}^*)\right\} \\ \langle w(u,v,\phi_P)\rangle &= \tfrac{A^2}{8\pi}\left\{|I_0|^2 + 2|I_1|^2 + |I_2|^2\right\} \end{aligned}\right\}. \tag{2.8}$$

As expected, the total energy density is independent of the angle ϕ_P. Not as obvious from the equations, but given by the symmetry of the arrangement is that the electrical energy distribution becomes the magnetic energy distribution when turned by 90°.

Also interesting is the POYNTING[10]-VECTOR $\boldsymbol{S}$ that describes the energy flux density of the electromagnetic field in the propagation direction. It's time average can be calculated with the equations

$$\left.\begin{aligned} \langle S_x\rangle &= \tfrac{cA^2}{4\pi}\cos\phi_P \Im\{I_1(I_2{}^* - I_0{}^*\} \\ \langle S_y\rangle &= \tfrac{cA^2}{4\pi}\sin\phi_P \Im\{I_1(I_2{}^* - I_0{}^*\} \\ \langle S_z\rangle &= \tfrac{cA^2}{8\pi}\left\{|I_0|^2 - |I_2|^2\right\} \end{aligned}\right\} \tag{2.9}$$

For the case of the electrical energy density (2.8) we will discuss what happens to the field distribution with increasing aperture angle. In Fig. 2.3 the electrical energy density is shown in the focal plane ($u = 0$) for different aperture angles α as a function of the optical coordinate v. The case $\alpha = 0°$ corresponds to the case of Sect. 2.5.2, the transition to small aperture angles. For $\alpha = 90°$ the light comes from the complete half space. A cut through the center of the profile, as well as a 10-fold magnification is shown above and to the right of each graphic. The initial polarization of the electrical field is horizontal.

In Fig. 2.3 one can see that the electrical energy density drastically changes with increasing aperture angle. The width of the field distribution as a measure of the optical resolution becomes strongly anisotropic. In the cut through the center, parallel to the direction of polarization, one can see even for small aperture angles that the minima don't return to zero. The side maxima get larger with increasing aperture angle and reach a relative height of 4.3% for $\alpha = 90°$. This is more than twice the value at $\alpha = 0°$ (1.8%).

Figure 2.4 shows the field distribution in the axial direction. The figure shows a cut through the electrical field distribution w_e vertical to the focal plane. The position of the focusing lens would be above (or below) the figure. In the left image, the polarization of the electrical field is horizontal (in the image plane), while in the right image it is pointing out of the image plane.

[10]The Poynting-vector was defined by John Henry Poynting.

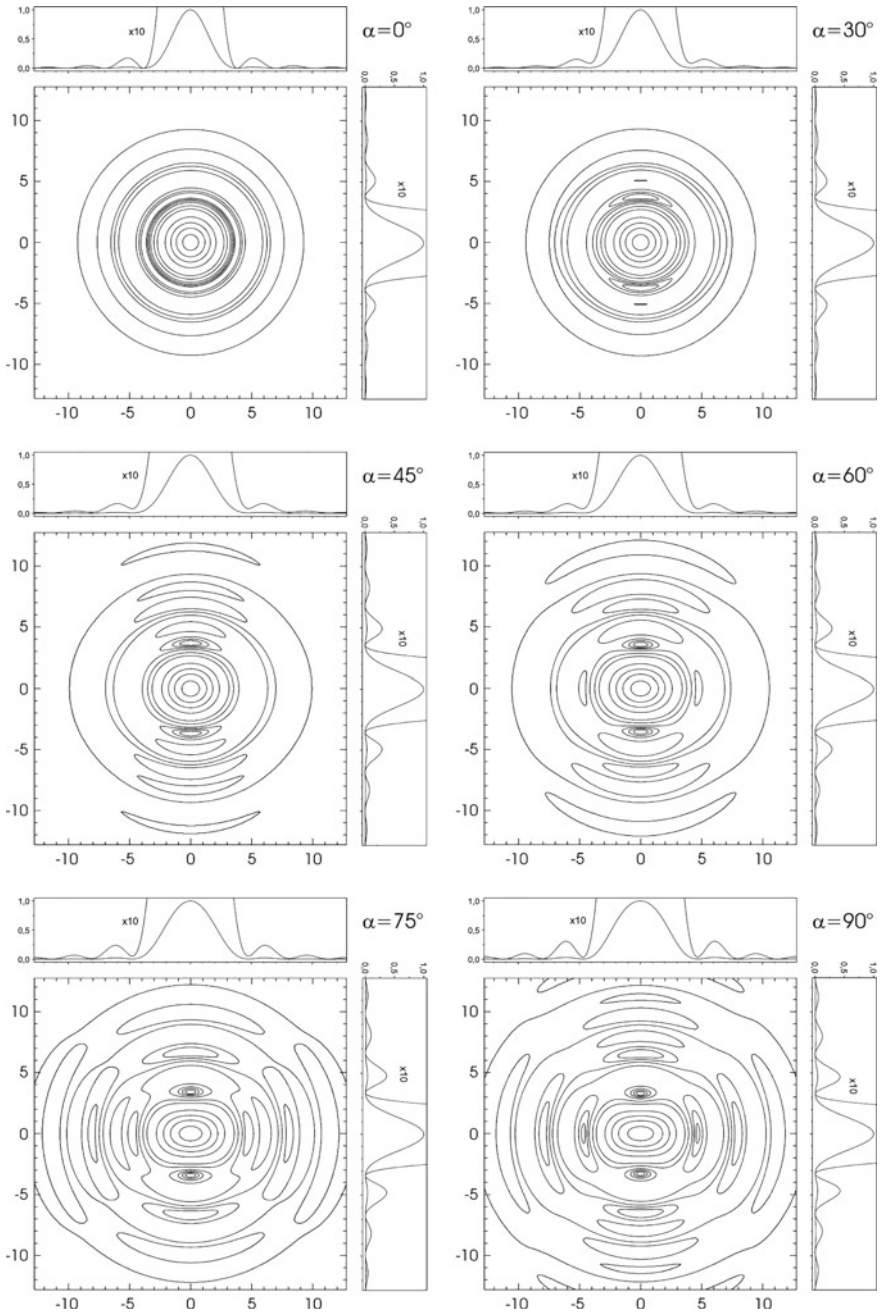

Fig. 2.3 Electrical energy density $w_e(u, v, \phi_P)$ in the focal plane ($u = 0$) for different aperture angles α as a function of v. The initial polarization of the electrical field is horizontal ($\phi_P = 0$). The contour lines show the heights 0.002, 0.005, 0.01, 0.02, 0.05, 0.1, 0.3, 0.5, 0.7 and 0.9. A cut through the center of the profile, as well as a 10-fold magnification is shown above and to the right of each graphic

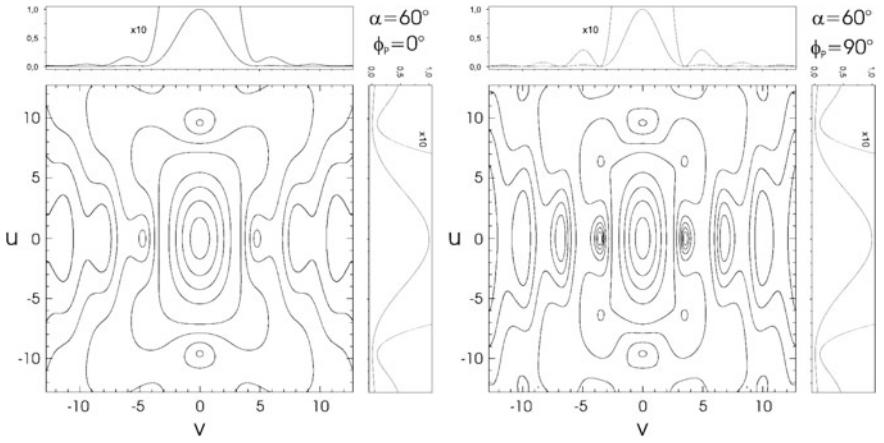

Fig. 2.4 Cut through the electrical energy density $w_e(u, v, \phi_P)$ for $\alpha = 60°$. The optical coordinate u is plotted vertical, while the optical coordinate v is plotted horizontal. In the left image, the polarization of the electrical field is horizontal (in the image plane), while in the right image it is pointing out of the image plane. The contour lines show the heights 0.002, 0.005, 0.01, 0.02, 0.05, 0.1, 0.3, 0.5, 0.7 and 0.9

Again one can see that the electrical energy distribution is highly anisotropic. Even in the axial direction the minima do not return to zero.

2.5.2 *Transition to Small Aperture Angles*

The theory in the last paragraph is appropriate to describe vector properties of light, but it is too complicated for a simple understanding. If one permits only small aperture angles I_1 and I_2 can be set zero, because for small x the relation $J_n(x) \sim x^n$ is fulfilled. The equations (2.5) and (2.6) simplify to

$$\begin{aligned} e_x &= h_y = -iAI_0 \\ e_y &= e_z = h_x = h_z = 0\,. \end{aligned}$$

The initial polarization is preserved for small aperture angles. I_0 can be written so that the integral becomes independent of α

$$\left.\begin{aligned} I_0(u, v) &= \alpha^2 e^{\frac{iu}{\alpha^2}} h(u, v) \\ h(u, v) &= 2\int_0^1 \rho J_0(\rho v)\, e^{\frac{1}{2}iu\rho^2} d\rho \end{aligned}\right\}\,. \tag{2.10}$$

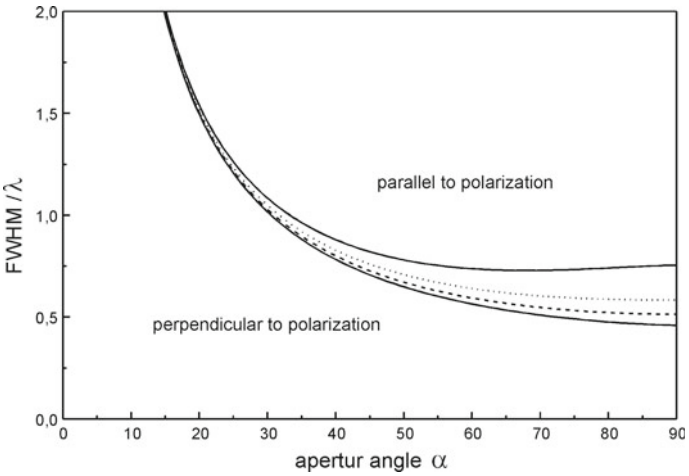

Fig. 2.5 Full width at half maximum (FWHM) of the field distribution in the focal plane, solid lines: electrical energy density, dotted line: total energy density, dashed line: electrical or total energy density for small aperture angles

The function $h(u, v)$ is called the 3-D Point Spread Function (PSF). It is normalized, so that $h(0, 0) = 1$. The PSF can be interpreted as a Greens function that describes the image of an infinitely small point. The approximation of small aperture angles simplifies the theoretical calculation, but is unfortunately coupled with a strong restriction. As a comparison, Fig. 2.5 shows the full width at half maximum (FWHM) of the electrical energy density at $u = 0$ as a function of the aperture angle. The dashed line corresponds to the theory for small aperture angles, whereas the solid lines represent the correct theory for a cut parallel and vertical to the polarization direction. The width of the total energy density w (2.8) is shown as a dotted line. The total energy density w is better suitable for a comparison, because w is radially symmetric, as is the field distribution for small aperture angles.

As expected, all curves are equal for small aperture angles. With increasing α the difference between the curves becomes greater and greater. At an aperture angle of only $\alpha = 40°$ the deviation between the curves is larger than 4%.

Oil- and water-immersion objectives can not be adequately described by this theory, because their aperture angle is typically between 55° and 70°. For this case, the deviation of the FWHM is more than 10%.

In Fig. 2.5 one can also see that an increase of the aperture angle above 70° results in only a very small increase in resolution. A technical realization above this angle is therefore of little use.

2.6 Theory of Image Formation

One of the most important properties of a confocal system is the point spread function (PSF), which is mainly determined by the microscope objective. This can be the electrical, magnetic or total energy density in the focus. If a sample system couples only to the x-component of the electrical field, the PSF of the excitation would only contain this component. The PSF of the detection can be different. This depends on the emitted light itself, and on the properties of the detector. Of course it would be better if one could measure the PSF for every application. In this case, a deconvolution of the image would be possible without additional assumptions. In [5] a simple interferometric measurement setup is described that makes the measurement of the PSF possible. As a result, one not only finds the amplitude of the function $h(u, v)$, but also the phase. The phase is especially important for a coherent image formation.

In the following paragraphs, h_1 stands for the PSF of the excitation and h_2 for the PSF of the detection. For simplification, both functions should be only scalar values. The modification of the light due to the sample can also be described by the scalar function $\tau(x, y, z)$. In general, τ is a complex function that influences the amplitude and phase of the electromagnetic field.

2.6.1 Microscope

The formation of the image in a microscope with point-like excitation and a large detector is far more complicated than the image formation in a confocal system (with a point-like detector). The reason is that the image formation is partially coherent. Both extremes can be mathematically described as following:

$$I = |h_1|^2 \otimes |\tau|^2 \qquad \text{incoherent image formation} \tag{2.11}$$

$$I = |h_1 \otimes \tau|^2 \qquad \text{coherent image formation.} \tag{2.12}$$

The difference between both cases is that for an incoherent image formation the intensities, and for the coherent image formation the amplitudes have to be added. This difference can be illustrated with the following example. Consider the image formation of two points separated by the distance of the Rayleigh limit.[11]

For the incoherent image formation, the two points are easily resolved (minimum). In the case of the coherent image formation, both points can no longer be separated (see Fig. 2.6).

The imaging quality of the detection, described by function h_2 is not important here.

[11] The Rayleigh criterion says that two points can be optically resolved if one point sits in the first minimum of the PSF of the second point.

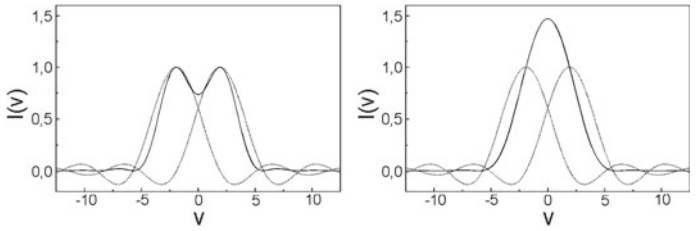

Fig. 2.6 Intensity distribution of two points that fulfil the Rayleigh criterion, left: incoherent image formation after (2.11), right: coherent image formation after (2.12)

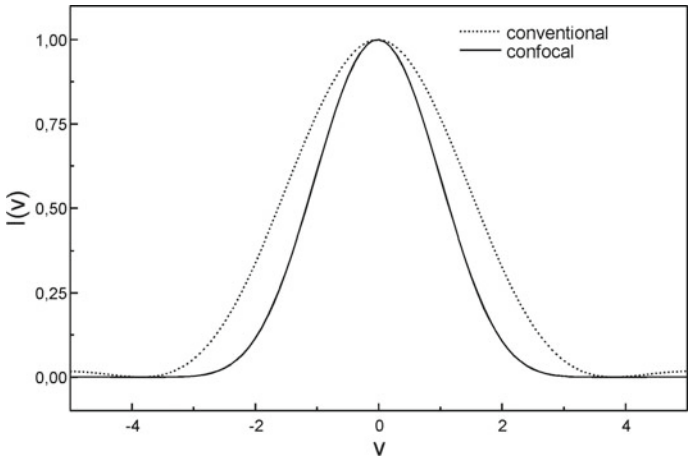

Fig. 2.7 Comparison of the intensity PSFs: $I_{conventional} = \left(\frac{2J_1(v)}{v}\right)^2$, $I_{confocal} = \left(\frac{2J_1(v)}{v}\right)^4$

2.6.2 Confocal Microscope

Due to the point-like excitation and detection, the image formation in a confocal microscope must be described as coherent. This can be illustrated using the following equation

$$I = |(h_1 h_2) \otimes \tau|^2 \tag{2.13}$$

after [6]. The product $h_{eff} = h_1 h_2$ is called the effective PSF of the optical system. If one inserts the delta function $\delta(\boldsymbol{x})$ for τ, one gets the intensity point spread function. This function is plotted in Fig. 2.7 for a conventional and a confocal microscope. The FWHM differs roughly by a factor of $\sqrt{2}$.

2.6.3 Confocal Raman Microscope

The image formation of a confocal Raman microscope is strongly different from the case in Sect. 2.6.2. This is due to the nature of Raman scattering.

The Raman scattering is proportional to the excitation intensity $|h_1|^2$ and the Raman generation $f(x, y, z)$. The resulting equation for the intensity distribution of the resulting image in a confocal Raman microscope is therefore [7]

$$I = |h_{eff}|^2 \otimes f \tag{2.14}$$

with

$$\begin{aligned} h_{eff} &= h_1(u, v) h_2\left(\tfrac{u}{\beta}, \tfrac{v}{\beta}\right) \\ \beta &= \tfrac{\lambda_2}{\lambda_1} \end{aligned}.$$

The optical coordinates u and v refer to the wavelength λ_1 of the excitation light. This theory is not completely correct, because the wavelength of the Raman light has a certain frequency distribution and not only a single wavelength λ_2. In principle, one must integrate over all Raman wavelengths. If the Raman wavelength is mostly distributed around a certain wavelength λ_x the error will be small if one replaces λ_2 with λ_x. A complete Raman spectrum is very complicated and for an exact solution the complete spectrum has to be taken into account.

2.7 Image Formation for Light Scattering

In the following two sections, the resolution of a confocal microscope as a function of pinhole size will be discussed. Since the achievable resolution strongly depends on the sample properties, these statements can not be taken as valid in general but are true only under ideal conditions. For all calculations, the point spread function $h(u, v)$ (2.10) was used.

2.7.1 Scattering Point

In the following, we consider the scenario of Fig. 2.8, in which a scattering point is scanned laterally across the excitation focus.

Up to now, all calculations have been performed for an infinitesimally small point detector. Now we replace this point detector with a real two-dimensional detector of radius v_P. This is the reason why the PSF h_2 in (2.15) has to be convolved with the detector function D, to obtain the effective PSF for the detection.

Since we consider only a single scattering point in the object space, the convolution with the object itself is not necessary. After [8] we obtain the intensity distribution

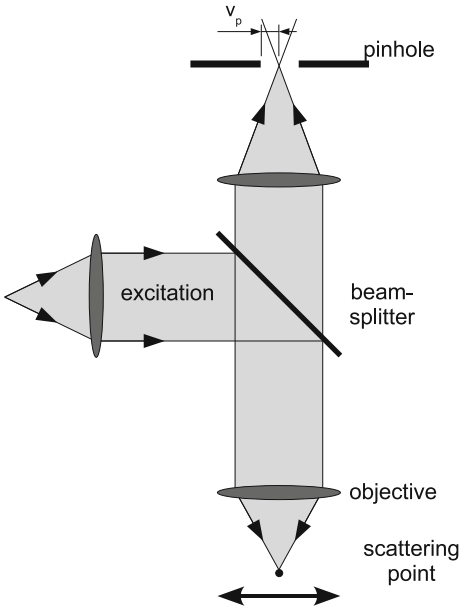

Fig. 2.8 Confocal setup for a scattering point

through

$$I = |h_1|^2(|h_2|^2 \otimes D). \tag{2.15}$$

The FWHM of $I\,(u = 0, v)$ is plotted in Fig. 2.9 as a function of the detector radius v_P. As can be seen, the detector radius should be below $v_P = 0.5$ for highest resolution. If the detector radius is larger than approximately $v_P = 4$, the resolution will be the same as for conventional microscopy. Even in this case, stray light suppression remains as an advantage over conventional microscopy.

2.7.2 *Reflection at a Mirror*

The quality of the image can be easily checked by acquiring the signal while a mirror is scanned axially through the focus (Fig. 2.10).

Since the entire mirror plane reflects the light, the following integral [8] must be calculated

$$I_{plane}(u) = \int_0^{v_p} |h(2u, v)|^2 v dv. \tag{2.16}$$

From Fig. 2.11 one can see that there is no loss in depth resolution up to a detector radius of $v_P = 2.5$. If the detector radius gets larger than $v_P = 3.5$ the depth resolution decreases linearly with increasing detector radius.

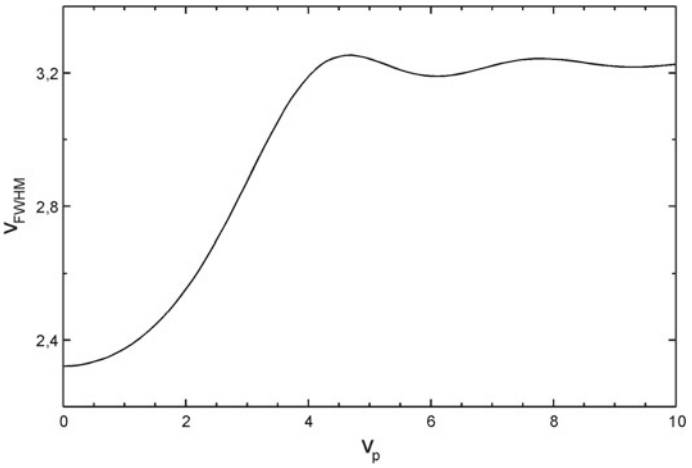

Fig. 2.9 Lateral resolution of a scattering point as a function of detector size v_P

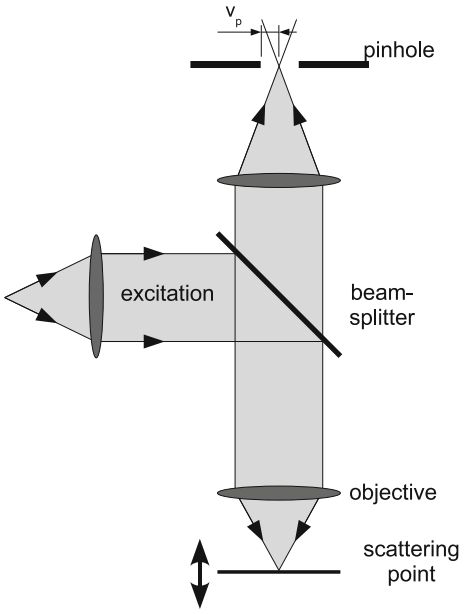

Fig. 2.10 Confocal setup for reflection at a mirror surface

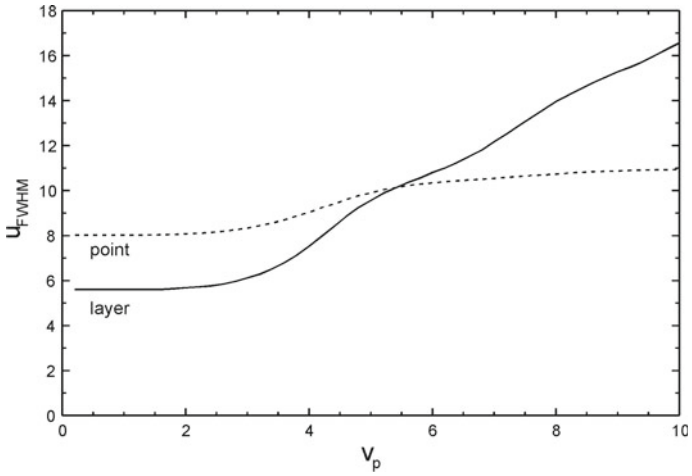

Fig. 2.11 Comparison of the depth resolution for a point and a reflecting layer as a function of detector size v_P

The depth resolution of a reflecting point shows a different behavior. For small detector radii, the resolution is worse than for a reflecting layer, but for larger radii the width becomes nearly constant. At $v_p = 10$, the depth resolution is no better than for a conventional microscope with point-like excitation, but if a homogeneous layer is investigated, no axial resolution is possible with a conventional microscope.

Since no lens abberations are taken into account, (2.16) is symmetric to $u = 0$. In reality, the distribution usually looks different. There will be drastic deviations if the setup is not optimized for the objective, or the cover glass correction is not considered. An incorrect pinhole position is also immediately visible.

2.8 Image Formation for Raman Scattering

As discussed in Sect. 2.6.3, the image formation for Raman emissions is very different from the case of a scattering object. As an example, the resolution for a Raman emitting point and a Raman emitting layer will be calculated analogue to the last section.

2.8.1 Raman Emitting Point

Equation (2.14) is the basis for the curves shown in Fig. 2.12. v_P is the detector radius.

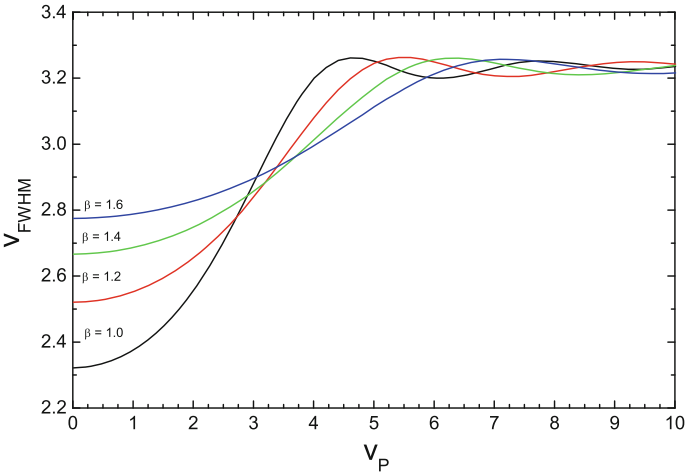

Fig. 2.12 Lateral resolution for a Raman emitting point as a function of detector size v_P for different β

The Raman emission wavelength is usually shifted by a certain factor relative to the excitation wavelength. This is taken into account by the parameter β, which is the ratio between the Raman and excitation wavelengths. For $\beta = 1$ the resolution is the same as for a scattering point. With increasing shift of the Raman wavelength, the resolution decreases. If a small loss in resolution is accepted, one sees that the pinhole size should not be adjusted to the excitation, but to the Raman wavelength. If the wavelength shift is large, one should use a larger pinhole in order to avoid an unnecessary loss in signal.

For large pinhole sizes, all curves converge. Here again the case of a conventional microscope with point-like excitation is approached. In this case, the resolution is determined only by the excitation wavelength.

For 532 nm excitation, β is between 1 and 1.25, while for 785 nm excitation β can be as high as 1.4 (@ 3600 rel. cm^{-1}).

2.8.2 *Raman Emission of a Layer*

The axial resolution at a Raman emitting layer differs strongly from the resolution at a reflecting surface. The reason is not mainly due to the wavelength shift but rather due to the incoherent image formation.

To calculate the axial point spread function $I_{CF}(u)$ of a Raman emitting layer in a confocal microscope, one must integrate over the intensity point spread function $I(u, v, \beta)$ (after [9]):

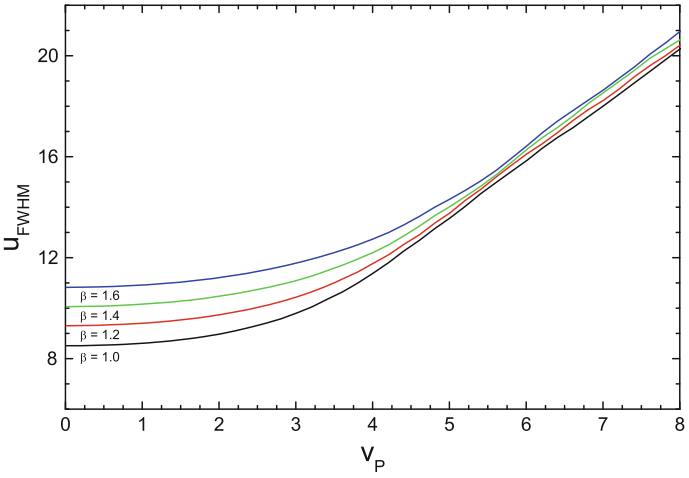

Fig. 2.13 Depth resolution at a Raman emitting layer for different β as a function of detector size v_P

$$I_{CF}(u) = \int_0^\infty I(u, v, \beta) v dv$$

The best depth resolution achievable at a reflecting surface was $u = 5.6$, whereas the best depth resolution for a Raman emitting layer without a wavelength shift is only $u = 8.5$ (Figs. 2.11 and 2.13). This becomes even worse with increasing wavelength shift β. Again, the detector size can be up to $v_P = 2.5$ without a loss in resolution.

2.9 Pinhole Size

Confocal Microscopes typically have two output ports where one output port is equipped with an adjustable fiber coupler for multi-mode fibers or an adjustable pinhole. The core of the multi-mode fiber acts as a pinhole for confocal microscopy in the first case. The system needs to allow for lateral adjustment of the fiber so that maximum collection efficiency can be achieved.

The fiber additionally needs to be protected against mechanical strain and shielded from room light. With the fiber it is simple to direct the light to any detector, e.g. a PMT or a spectrometer.

The lateral position of the pinhole must be adjusted with micrometer precision (typical pinhole size 10–100 µm) while the focus position is not very critical.

If ΔG is the object size and M the magnification of the objective, then the lateral image size is given by $\Delta B = \Delta G \cdot M$. But what about the axial magnification? From the image equation for thin lenses one gets the relation

$$
\begin{aligned}
|\Delta b| &\approx |\Delta g| M^2 \\
\Delta b &\ll b \qquad : \textit{image distance} \\
\Delta g &\ll g \qquad : \textit{object distance}
\end{aligned}
\tag{2.17}
$$

Without the diffraction limit, an object of an axial extension of 200 nm would have a length of 2 mm in the image space at a magnification of $M = 100$. Since the magnification M is quadratic in (2.17), the depth of focus is very high and the axial position of the pinhole is not critical.

The choice of the pinhole size is very important in Raman experiments. On one hand the signal should be as high as possible, while on the other hand the image should be confocal.

The size of the pinhole, in optical coordinates, should not exceed $v_{P_{max}} = 2.5$ to avoid a loss in z-resolution. To obtain the highest lateral resolution, the pinhole size should be below $v_{P_{max}} = 0.5$.

In practice, the pinhole size can be up to $v_{P_{max}} = 4$ without significantly changing depth resolution and up to $v_{P_{max}} = 2$ without significantly changing lateral resolution. As shown in Sect. 2.7.1, for $v_{P_{max}} > 4$, only the resolution of a conventional microscope remains.

For the experiment, the relation

$$
\frac{M}{N_A} \geq \frac{\pi d_0}{v_{P_{max}} \lambda}
$$

must be fulfilled, where M is the magnification, d_0 the diameter of the pinhole and N_A the numerical aperture of the objective. The left side of this equation is defined by the objective and the beam path. In Table 2.1, the parameter $\frac{M}{N_A}$ is calculated for several typical objectives.

The right side of (2.9) is defined by the wavelength and the pinhole size itself (Table 2.2).

With the help of these tables, the correct pinhole size can be determined for any experiment. If an objective with a magnification of 100× and a numerical aperture of 0.9 is used at a wavelength of 532 nm, the optimum pinhole size would be 50 µm for maximum depth resolution and 10 µm for maximum lateral resolution.

In real experiments, one must usually find a compromise between resolution and collection efficiency. When a very small pinhole is used, the collection efficiency is strongly reduced. This is plotted in Fig. 2.14.

This graphic shows the intensity on the detector as a function of pinhole size, normalized to the total intensity in the image plane [$u = 0$ in (2.16)]. One can see

Table 2.1 M/N_A for different objectives

Objective	10/0.25	20/0.4	40/0.6	60/0.8	100/0.9	100/1.25	100/1.4
M/N_A	53	50	67	75	111	80	71

Table 2.2 $\frac{\pi d_0}{2{,}5\lambda}$ for typical wavelengths and pinhole sizes

Wavelength (nm)	440	488	532	633	785
$d_0 = 10\,\mu\text{m}$	29	26	24	20	16
$d_0 = 25\,\mu\text{m}$	71	64	59	50	40
$d_0 = 50\,\mu\text{m}$	142	129	118	99	80
$d_0 = 100\,\mu\text{m}$	286	258	236	199	160
$d_0 = 200\,\mu\text{m}$	571	515	472	397	320

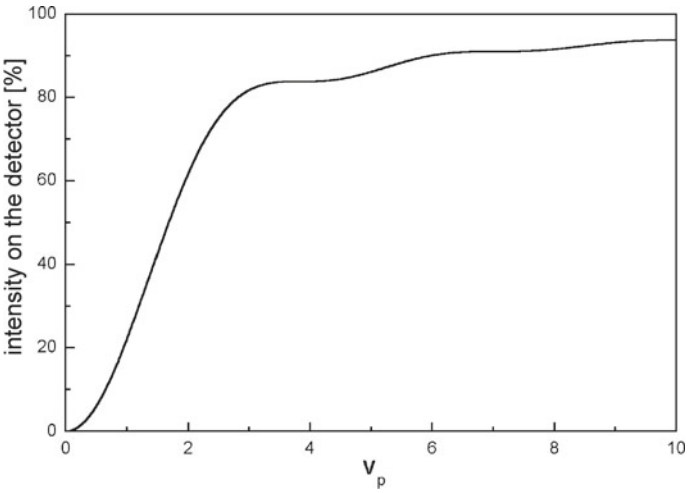

Fig. 2.14 Collection efficiency as a function of pinhole size normalized to the total power in the image plane

that the collection efficiency is about 75% for maximum depth resolution ($v_P = 2.5$), but only 6% for maximum lateral resolution $v_P = 0.5$.

For a scattering point (Sect. 2.7.1, $\beta = 1$), the gain in resolution between using a pinhole size of $v_P = 2.5$ and $v_P = 0.5$ is only about 16%, while for a Raman-emitting sample with $\beta = 1.2$ (Sect. 2.8.2) the gain in resolution is only about 8%, but for both cases the detected intensity is reduced by a factor of 12.5.

References

1. J.B. Pawley, *Handbook of Biological Confocal Microscopy*, 2nd edn. (Plenum Press, New York, 1995)
2. E. Wolf, Proc. R. Soc. Lond. A **253**, 358 (1959)
3. E. Wolf, Proc. Phys. Soc. **74**, 269 (1959)
4. B. Richards, E. Wolf, Proc. R. Soc. Lond. A **253**, 358 (1959)

5. R. Juškaitis, T. Wilson, J. Microsc. **189**, 8 (1998)
6. T. Wilson, *Confocal Microscopy* (Academic Press, 1990), Chap. IV.2. The imaging of simple objects, pp. 25–30
7. T. Wilson, *Confocal Microscopy* (Academic Press, 1990), Chap. IV.2. The imaging of simple objects, pp. 41–45
8. T. Wilson, A.R. Carlini, Opt. Lett. **12**, 227 (1987)
9. C.J.R. Sheppard, M. Gu, Optik **86**(3), 104 (1990)

Chapter 3
Introduction to the Fundamentals of Raman Spectroscopy

Benjamin Dietzek, Dana Cialla, Michael Schmitt and Jürgen Popp

Abstract The goal of this chapter is to provide a general introduction to the principles of Raman spectroscopy. The chapter will therefore begin with a theoretical description of the Raman effect i.e. the classical electrodynamic treatment of Raman scattering, the discussion of the Raman intensities and the quantum mechanical picture. Enhancement mechanisms for Raman Microscopy will be discussed in the second part and resonant Raman as well as surface-enhanced Raman spectroscopy will then be explained in detail.

3.1 Introduction

During the last decade Raman spectroscopy has matured to become one of the most powerful techniques in analytical science due to its molecular sensitivity, its ease of implementation and the fact that in contrast to IR absorption spectroscopy the presence of water is not hindering its applicability. The use of Raman spectroscopy originating in physics and chemistry has spread and now includes a variety of applications in biology and medicine revealing the molecular signature of diseases and individual bacteria, ultrafast spectroscopy to unravel the sub-picosecond dynamics of structural rearrangements during chemical reaction and has reached for the stars - with the upcoming implementation of Raman spectrometers in the Mars-missions of ESA and NASA [1]. Furthermore, latest developments have merged the chemical sensitivity and specificity of Raman scattering with the high spatial resolution of confocal microscopy yielding chemical images of a sample.

B. Dietzek (✉) · D. Cialla · M. Schmitt · J. Popp
Institut für Physikalische Chemie, Friedrich-Schiller-Universität Jena,
Helmholtzweg 4, 07743 Jena, Germany
e-mail: Benjamin.Dietzek@uni-jena.de; Benjamin.dietzek@ipht-jena.de

D. Cialla
e-mail: juergen.popp@uni-jena.de; juergen.popp@ipht-jena.de

B. Dietzek · J. Popp
Institut für Photonische Technologien e.V., Albert-Einstein-Strasse 9,
07745 Jena, Germany

J. Toporski et al. (eds.), *Confocal Raman Microscopy*, Springer Series
in Surface Sciences 66, https://doi.org/10.1007/978-3-319-75380-5_3

In this chapter, the fundamentals of Raman spectroscopy will be explained.

First, we will discuss the classical picture of light scattering, which in the special case of inelastic scattering will correspond to Raman scattering. The classical discussion is followed by a quantum mechanical description of light-scattering based on perturbation theory, and a description of effects, that enhance the weak Raman effect, like Resonance Raman (RR) and Surface Enhanced Raman Scattering (SERS).

3.2 Classical Picture of Light Scattering

In this chapter, the classical picture of light scattering, i.e. the classical picture of interaction between an oscillating electromagnetic field and a molecular system will be discussed. Generally, the primary incident electric field will disturb the electronic charge distribution in the molecule and thereby induce a dipole moment even in the case of an unpolar molecular system. The sum of the induced dipole moments will act as a macroscopic polarization, which represents the source for a secondary electric field irradiated by the molecules. This secondary field represents the scattered light. Within this quite general and qualitative framework it is clear that all scattering processes originate from the interaction of an electromagnetic field with the electronic subsystem of the sample. In order to understand how this interaction reveals information on the nuclear subsystem of the sample, i.e. structural information and normal coordinates, we will turn to a more quantitative yet still classical description of the matter-field interaction.

3.2.1 Frequency-Dependence of Raman Scattering

This description starts with the formula for the induced dipole moment μ, which can be written as:

$$\vec{\mu} = \tilde{\alpha}\vec{E} \tag{3.1}$$

Here μ the molecular dipole induced by the external electric field E, which is characterized by its vector amplitude E_0 and its oscillation frequency ω_0.[1] The real part of the field may thus be expressed as:

$$\vec{E} = \vec{E}_0 \cdot \cos(\omega_0 t) \tag{3.2}$$

The proportionality factor between the external field and the induced dipole moment in (3.1) is the molecular polarizability, α, which is physically related to the extent to

[1] As in all practical modern applications of Raman scattering a laser is used as the excitation light source, the terms excitation light and laser light as well as excitation frequency, ω_0 and laser frequency are used synonymously.

which the driving field is able to disturb the electron density of the sample out of its equilibrium configuration, i.e. the configuration in the absence of an external field.[2]

However, the polarizability of an electronic system is not a static quantity. Nuclear motion will modify the polarizability as the electron density adiabatically adjusts to the momentarily nuclear geometry to overall minimize the energy of the system. To formalize this effect, the polarizability is expanded into a Taylor series around the equilibrium nuclear geometry Q_0, where Q represents the group of all individual normal modes q.[3]

$$\alpha = \alpha(Q) = \alpha_0 + \sum_{q=1}^{N} \left[\left(\frac{\partial \alpha}{\partial q} \right)_{q_0} \cdot q + \frac{1}{2} \left(\frac{\partial^2 \alpha}{\partial q \partial q'} \right)_{q_0 q_0'} \cdot q \cdot q' + O\left(q^3\right) \right] \tag{3.3}$$

In turn, oscillations with a characteristic frequency ω_q along each normal coordinate q can be excited, thus

$$q = q_0 \cdot \cos(w_q t) \tag{3.4}$$

Inserting (3.2) and (3.3) into (3.1) yields:

$$\mu(t) = \left[\alpha_0 + \left(\frac{\partial \alpha}{\partial q} \right)_{q_0} \cdot q_0 \cdot \cos(\omega_q t) \right] \cdot E_0 \cdot \cos(\omega_0 t) \tag{3.5}$$

Here, without loss of generality, we reduced the sum over all normal modes to a representative mode q and further truncated the Taylor-expansion in (3.3) after the term linear in the mode displacement. This approximation is referred to as electrical harmonic approximation. Using the trigonometric formula for the product of two cosine functions (3.5) can be re-written as

$$\mu(t) = \alpha_0 \cdot E_0 \cdot \cos(\omega_0 t) + \frac{1}{2} \left(\frac{\partial \alpha}{\partial q} \right)_{q_0} \cdot q_0 \cdot E_0 \cdot \cos\left[(\omega_0 - \omega_q) t \right] + \frac{1}{2} \left(\frac{\partial \alpha}{\partial q} \right)_{q_0} \cdot q_0 \cdot E_0 \cdot \cos\left[(\omega_0 + \omega_q) t \right] \tag{3.6}$$

This formula already constitutes the conceptual core of Raman scattering as a limiting case of general light scattering. As can be seen, the time-dependent induced dipole moment, which will act as a secondary source of (scattered) radiation contains three distinct frequency terms:

1. The first one, $\alpha_0 \cdot E_0 \cdot \cos(\omega_0 t)$, oscillates at the same frequency as the incident radiation and thus will be responsible for scattered light at this frequency, i.e.

[2] We note that μ and E are vector quantities, while α represents a 3rd rank tensor. Keeping this in mind, vector notation is dropped from now on.

[3] In the derivation presented here, molecular rotations are neglected as classical theory does not yield discrete excitation energies for molecular rotations.

elastic *Rayleigh scattering*. This term does not contain any information on the nuclear molecular degrees of freedom and is non-zero for all molecules due to the non-vanishing polarizability of the electronic molecular sub-system.
2. The second term in (3.6) oscillates with the difference between the laser and the molecular normal mode frequency. Hence, the radiation emitted by the induced dipole moment is red-shifted with respect to the excitation frequency. This term representing inelastic light scattering contains information about the molecular system via its dependence on ω_q. It is the source of the *Stokes scattering* that is usually presented as the Raman spectrum.
3. Finally, the time-dependence of the third term is characterized by the sum $\omega_0 + \omega_q$. Thus, it represents a source for radiation, which is blue shifted with respect to the laser frequency. This so-called *anti-Stokes scattering*, is identical to the Stokes-spectrum, but has a strongly reduced intensity due to the Boltzmann-factor that describes the population of the thermally excited vibrational states.

3.2.2 *Classical "Selection Rule" and Comparison to IR Absorption*

In contrast to the elastic Rayleigh scattering, which classically depends on the equilibrium polarizability of the molecule, the inelastically scattered light stems from the non-zero derivative of the electronic polarizability at the equilibrium geometry along the q-th normal coordinate, i.e. $\left(\frac{\partial \alpha}{\partial q}\right)_{q_0} \neq 0$. This relation provides an intuitive "selection rule" for Raman scattering of small molecules, which is useful in conceptually discriminating Raman scattering from infrared absorption.

Let us begin the discussion considering the symmetric stretching vibration of a homo-diatomic molecule, i.e. considering actually the only vibration of such molecule. Due to the symmetry of the system it does not have a permanent dipole moment in its equilibrium geometry. This zero-dipole moment is not changed upon small changes along the normal coordinate. Hence, the derivative of the dipole moment is zero and the vibration (see Fig. 3.1a) is not IR active.[4]

However, the polarizability of the molecule changes as a function of the nuclear displacement as can be qualitatively deduced from the limiting situations[5]: For zero internuclear distance the electron density resembles the density of a single atom, while at infinite internuclear distance the situation compares to two individual atoms of half mass. The latter having a larger polarizability than the former one. Thus, the polarizability can be expected to increase monotoneously along the normal coordinate and hence to have a non-zero derivative at the equilibrium position. In turn, the vibration is Raman active.

[4]This is different for a hetero-diatomic molecule, which has a permanent dipole moment, whose derivative at the equilibrium position is non-zero.

[5]For the derivation of a quantitative expression of the polarizability tensor the reader is referred to the section on the quantum mechanical picture of Raman scattering.

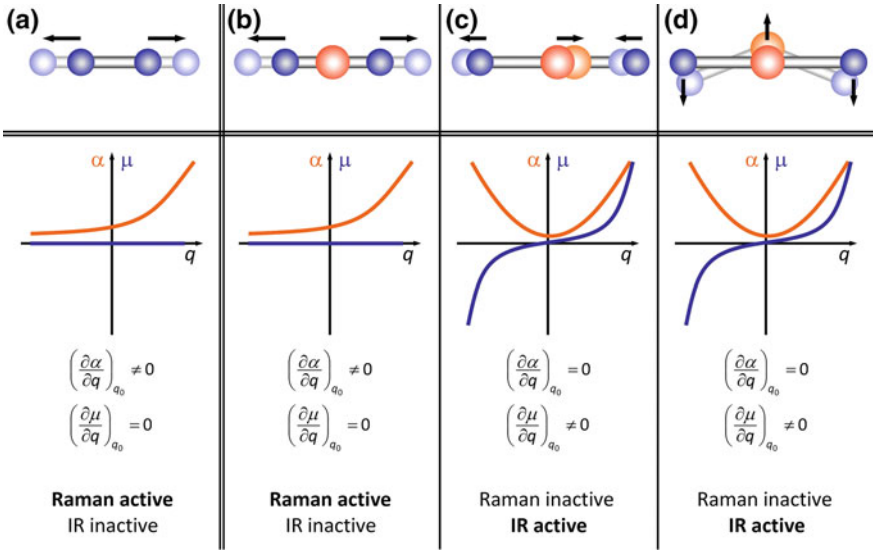

Fig. 3.1 The derivatives of polarizability (red) and dipole moment (blue) are schematically depicted for the normal modes of a two (**a**) and a three atomic molecule (**b–d**). Based on these intuitive considerations, conclusions on the IR and Raman activity of the modes can be drawn

The situation is slightly more complex for the linear triatomic molecule considered in Fig. 3.1b–d. In this case we shall consider the molecular dipole moment and polarizability in first order approximation as the sum of bond dipole moments and bond polarizability, respectively. For the symmetric stretch vibration (Fig. 3.1b) the dipole moment changes as individual bonds are identical but opposite in sign yielding a constant dipole moment along the reaction coordinate. This results in no infrared absorption activity of this vibration. In contrast and according to the arguments presented for the homo dinuclear molecule above, the molecular polarizability changes along the reaction coordinate giving rise to the Raman activity of this mode.

The situation is different for the antisymmetric stretching (Fig. 3.1c) and bending vibrations (Fig. 3.1d). In these cases it is obvious that the dipole moment will change sign, when the systems passes through the equilibrium configuration, thus $\left(\frac{\partial\alpha}{\partial q}\right)_{q_0} \neq 0$ and both vibrations are IR active. The changes of the polarizability along the mode are also non-zero but symmetric upon inversion of the sign of the reaction coordinate. Hence, the changes of the polarizability for small displacements can be approximated to be harmonic and $\left(\frac{\partial\alpha}{\partial q}\right)_{q_0} = 0$. Therefore, both the asymmetric stretch and the bending vibrations are Raman inactive. In principle, a similar conceptual approach of dissecting molecular dipoles and polarizabilities into bond dipoles and bond polarizabilities can be pursued for large molecules as well. However, this rapidly becomes cumbersome and is therefore not discussed further.

3.2.3 Scattered Raman Intensity

Having discussed the origin of the frequency dependence of the Raman spectrum and the classical "selection rules", we will now focus on a derivation of the intensities observed in a Raman spectroscopic experiment. The considerations start from the oscillating induced dipole moment. For the simplicity of the discussion, we only consider the part of the dipole moment, which oscillates at $\omega_0 - \omega_q$ and gives rise to the Stokes radiation:

$$\mu^{Stokes}(t) \propto \left(\frac{\partial\alpha}{\partial q}\right)_{q_0} \cdot q_0 \cdot E_0 \cdot \cos\left[(\omega_0 - \omega_q)t\right] \tag{3.7}$$

Each oscillating induced dipole serves as a Hertzian dipole, i.e. as an antenna emitting the secondary oscillation. The total power emitted by a Hertzian dipole is:

$$P = \frac{|\ddot{\mu}|^2}{6\pi \cdot \varepsilon_0 \cdot c^3} = \frac{q_0^2}{12\pi \cdot \varepsilon_0 \cdot c^3} \cdot \left(\frac{\partial\alpha}{\partial q}\right)_{q_0}^2 \cdot \left(\omega_0 - \omega_q\right)^4 \cdot E_0^2 \tag{3.8}$$

In the second identity, a temporal average over the oscillating part of $|\ddot{\mu}|^2 \propto \cos^2(\omega t)$ has been performed. The scattered intensity observed in a Raman experiment is proportional to the overall power emitted by the induced dipole moment, hence:

$$I_{Stokes} \propto \left(\frac{\partial\alpha}{\partial q}\right)_{q_0}^2 \cdot \left(\omega_0 - \omega_q\right)^4 \cdot E_0^2 \tag{3.9}$$

Equation (3.9), which together with (3.6) constitutes the central result of the classical discussion of Raman scattering, illustrates the dependence of the observed scattered intensity on molecular and experimental parameters. In order to be visible in a Raman spectrum, the molecular polarizability needs to change along the normal mode with a non-zero gradient at the equilibrium geometry. Thus, the gradient of the polarizability determines the Raman scattering intensity in contrast to the equilibrium polarizability, α_0, which is roughly independent of the molecular species and influences the Rayleigh scattering term only. While $\left(\frac{\partial\alpha}{\partial q}\right)_{q_0}$ and ω_q provide molecular information about the system under study, ω_0 and E_0^2 are the experimental parameters that influence the intensities observed in the experiment. An increase of the laser power as well as the laser frequency will lead to more intense Raman scattering being observed.

Furthermore, (3.7) offers a roadway to the design of experiments with controlled Raman enhancement: Resonance Raman spectroscopy and surface enhanced Raman scattering. In resonance Raman scattering the laser frequency ω_0 is tuned into an electronic resonance of the system under study. The frequency-dependence of $\left(\frac{\partial\alpha}{\partial q}\right)_{q_0}$, which becomes apparent only in a full quantum mechanical description of the molecular properties, then results in an increase of the scattered intensity and a reduction

of spectral complexity compared to non-resonant Raman scattering. In the case of surface enhanced Raman scattering, the molecular species is brought into close contact with a metallic surface, which increases the Raman scattering cross section by up to 15 orders of magnitude. As will be described in detail later, this effect is due to a combination of a field enhancement (E_0) and a chemical enhancement, which originates in surface induced changes of the molecular polarizability.

3.2.4 Short Falls of the Classical Picture

While the classical picture of light-matter interactions outlined above yields an intuitive understanding of the number of lines and line-positions in a Raman spectrum and the relative amplitudes of Stokes and anti-Stokes lines, the non-quantized approach has some severe short falls. To give an obvious example, it does not provide any description for rotational Raman spectra for the simple reason that classical theory does not assign discrete frequencies to rotational transitions. Furthermore, a classical treatment does not offer a connection between the Raman scattering tensor $(\alpha_{ij})_k$ and the transition dipole moments, the molecular Hamiltonian and the frequency of the incident field. Thus, prominent and analytically important processes such as resonance Raman scattering and surface enhanced Raman scattering are not explained within the classical theory. This information results naturally from a quantum mechanical perturbation theory approach to light-matter interactions and is considered in the following.

3.3 Raman Cross-Section Enhancement Mechanisms

The classical description of the scattered Raman intensity as presented in (3.9) provides an immediate starting point for the discussion of mechanisms to enhance the Raman scattering cross-section. As the enhancement of Raman scattering is of utmost importance for the detection of trace amounts of analytes abundant in biological samples [2, 3], contaminations found in products or pollutants in air [4, 5] or drinking water, the remainder of this chapter briefly introduces and discusses the two central and frequently used Raman enhancement mechanisms. The starting point of this discussion is (3.9), which reveals that the inelastically scattered intensity is proportional to the square of (i) the polarizability and (ii) the electric field. Consequently, the mechanisms routinely used to boost the Raman cross-section address these two entities and can be conceptually divided into resonance Raman scattering and surface enhanced Raman scattering.

We will start the discussion reviewing the concepts of resonance Raman (RR) scattering and presenting two prominent applications from our group. Finally we will close this chapter by presenting the basics of surface enhanced Raman scattering

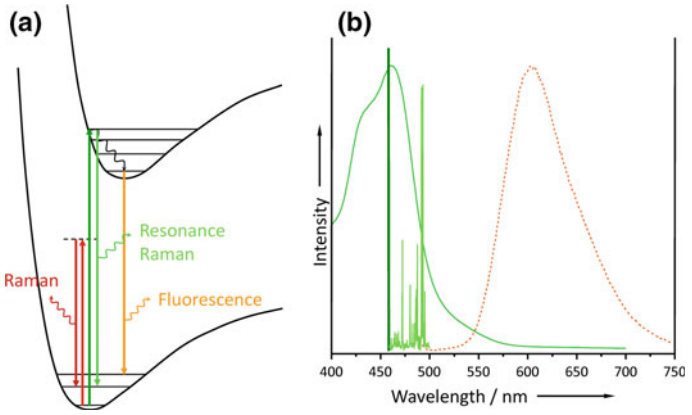

Fig. 3.2 **a** Energy level diagram and dipole transitions illustrating Raman, resonance Raman and fluorescence. **b** Schematic comparison of absorption (solid, green) and emission spectrum (dotted, red) and a Raman spectrum excited in resonance (light green) with the ground-state absorption spectrum

(SERS), surveying the variety of metallic substrates used in the application of SERS and highlight some biological applications of this intriguing technique.

3.3.1 Resonant Raman Scattering

In resonance Raman (RR) scattering the excitation-wavelength is chosen to fall within an electronic absorption of the molecule under investigation Fig. 3.2.

In this case and in contrast to non-resonant Raman scattering, not only inelastically scattered light but also fluorescence/luminenscence is observed.[6] As the cross-section for fluorescence is about six orders of magnitude larger than the resonance Raman cross-section the observation of Stokes-scattered light is in many cases hampered by the presence of fluorescence. However, in cases of large fluorescence Stokes-shifts (like in carbon-nanotubes) or pre-resonant RR excitation wavelengths both processes can be observed. Another experimental approach to suppress fluorescence and obtain a pure RR signal is based on the different time-dependences of both signals; while RR scattering originates from the excited-state wave packet prior to dephasing, it appears within a time-window of roughly 20 fs after excitation. In contrast, typical fluorescence lifetimes are in the order of some hundred ps to ns. Hence, the use of an

[6] It can be shown (see S. Mukamel, Principles of Nonlinear Optics and Spectroscopy, Oxford University Press (1995)), that in the case of no dephasing of the excited-state wavefunction RR scattering and fluorescence are identical. In the - in most experimental situations realistic - case of dephasing being present RR scattering is associated with the emission of the initial coherent excited-state wavefunction prior to dephasing, while fluorescence reflects the emission of the incoherent wavefunction after dephasing.

ultrafast Kerr-shutter could enable the observation of the RR signal without emission contributions.

A more formalized description of RR scattering starts from (3.9) with the notion, that the electric field is going to be treated classically, while the polarizability is given based on quantum mechanics and in particular perturbation theory [6]. In contrast to the notion in (3.9), it has to be kept in mind, that α presents a complex valued quantity. Thus within the quantum mechanical treatment, the absolute square of α enters the corresponding formula. As Raman scattering presents a two-photon process, second-order perturbation theory has to be applied. On this basis Kramer and Heisenberg (1925) and Dirac (1927) derived a quantum mechanical description of the molecular polarizability:

$$\left(\alpha_{\rho\sigma}\right)_{fi} = \sum_{r} \left\{ \frac{\langle f|\mu_\rho|r\rangle\langle r|\mu_\sigma|i\rangle}{\hbar\omega_{ri} - \hbar\omega_0 - i\Gamma_r} + \frac{\langle f|\mu_\sigma|r\rangle\langle r|\mu_\rho|i\rangle}{\hbar\omega_{rf} - \hbar\omega_0 - i\Gamma_r} \right\} \tag{3.10}$$

In here, r and s denote the polarization of the incident and scattered light, respectively, while $|i\rangle$, $|r\rangle$ and $|f\rangle$ refer to the initial, intermediate and final state of the Raman scattering process, ω_0 is the laser frequency and ω_{ri}, ω_{rf} quantify the energetic differences between the respective states. The damping constant Γ_r has been introduced phenomenologically in order to mimic the homogeneous line-widths of the respective band. While the first term in the sum represents the "intuitive" order of events within the scattering process, i.e. the "absorption" of a photon is followed by "emission" of the Stokes photon, the second term represents the reversed order of events, i.e. the Stokes photon is "emitted" prior to the interaction of the system with the pump, and formally follows from perturbation theory.

If - as in the case of RR scattering - the excitation wavelength is chosen to be resonant with a molecular electronic transition, the denominator of the first term becomes small and this term dominantly contributes to the molecular polarizability and thus to the observed Raman scattering. Under these circumstances, the polarizability is determined by the transition dipoles of the two transitions involved in the process and the lifetime of the intermediate state, which is inversely proportional to Γ. Hence, in electronic resonance:

$$\left(\alpha_{\rho\sigma}\right)_{fi} = \sum_{r} \left\{ \frac{\langle f|\mu_\rho|r\rangle\langle r|\mu_\sigma|i\rangle}{\hbar\omega_{ri} - \hbar\omega_0 - i\Gamma_r} \right\} \tag{3.11}$$

This expression can be further simplified by invoking the Born-Oppenheimer approximation, i.e. factorization of the total wavefunctions $|i\rangle$, $|r\rangle$ and $|f\rangle$ into an electronic part $|\varepsilon_g\rangle$, $|\varepsilon_e\rangle$ and a vibrational wavefunction $|v_{i,f,r}\rangle$. Hence,

$$\begin{aligned} |i\rangle &\approx |\varepsilon_g\rangle \cdot |v_i\rangle \\ |r\rangle &\approx |\varepsilon_e\rangle \cdot |v_r\rangle \\ |f\rangle &\approx |\varepsilon_g\rangle \cdot |v_f\rangle \end{aligned} \tag{3.12}$$

Furthermore, the Herzberg-Teller and Condon-approximations are invoked, which involve a Taylor-expansion of the transition dipole moment as a function of the vibrational coordinates and a truncation of the expansion after the constant term. Hence, the transition dipole moment is assumed to be independent of nuclear displacement. Formally, the combination of both the Herzberg-Teller and the Condon-approximation yield:

$$\begin{aligned} \langle f|\mu_\rho|r\rangle &= \langle v_f|\overbrace{\langle\varepsilon|\mu_\rho|\varepsilon'\rangle}^{\approx \overline{\mu}^{(0)}_{\rho,\varepsilon\varepsilon'}}|v_{\varepsilon'}\rangle \\ \langle r|\mu_\sigma|i\rangle &= \langle v_{\varepsilon'}|\overbrace{\langle\varepsilon'|\mu_\sigma|\varepsilon\rangle}^{\approx \overline{\mu}^{(0)}_{\sigma,\varepsilon'\varepsilon}}|v_i\rangle \end{aligned} \tag{3.13}$$

and hence the polarizability

$$\left(\alpha_{\rho\sigma}\right)_{fi} = \sum_{\varepsilon'} \overline{\mu}^{(0)}_{\rho\varepsilon\varepsilon'} \overline{\mu}^{(0)}_{\rho\varepsilon'\varepsilon} \sum_{v_{\varepsilon'}} \frac{\langle v_f|v_{\varepsilon'}\rangle\langle v_{\varepsilon'}|v_i\rangle}{\hbar\omega_{ri} - \hbar\omega_0 - i\,\Gamma_{\varepsilon' v_{\varepsilon'}}} \tag{3.14}$$

as well as the vibronic part of the polarizability tensor, which we are concerned about in the context of Raman spectroscopy:

$$\left(\alpha_{\rho\sigma}\right)_{fi} = \sum_{\varepsilon'} \frac{\langle v_f|v_{\varepsilon'}\rangle\langle v_{\varepsilon'}|v_i\rangle}{\hbar\omega_{ri} - \hbar\omega_0 - i\,\Gamma_{\varepsilon' v_{\varepsilon'}}} \tag{3.15}$$

While (3.10)–(3.15) allow an immediate grasp of the physics behind RR scattering, it is extremely cumbersome to evaluate the formulas quantitatively as the sum has to be performed over all possible, i.e. real and virtual, intermediate states. To obtain a description of the RR cross-section that is numerically easier to tackle, the Fourier-transformation of the *sum-over-states* approach of Kramer, Heisenberg, and Dirac is reconsidered. This procedure yields the time-dependent description of RR scattering with

$$\left(\alpha_{\rho\sigma}\right)_{fi} = \frac{i}{\hbar} \int_0^\infty \langle v_f|v_i(t)\rangle e^{i(\omega_0+\omega_i)t-\Gamma t}\, dt \tag{3.16}$$

Equation (3.16) relates the RR scattering cross-section to the time-dependent overlap of the excited-state vibrational wavefunction $|v_i(t)\rangle$ with the final ground-state wavefunction $|v_f\rangle$. The time-dependence of this quantity derives from the fact, that upon interaction with the electronically resonant pump-photon, the initial ground-state wavefunction $|v_i\rangle$ is transferred to the electronically excited state. In this electronic potential $|v_i\rangle$ does not represent an eigenfunction of the Hamiltonian and consequently the propagation with the excited-state Hamiltonian $\hat{H}_{ex}$ results in a structural change of the wavefunction over time.

$$|v_i(t)\rangle = e^{\frac{i\hat{H}_{ex}t}{\hbar}}|v_i\rangle \tag{3.17}$$

It can be shown, that $\langle v_f|v_i(t)\rangle$ and thus the RR cross-section is directly proportional to the displacement parameter Δ which is a measure of how far a molecule has to move in one state in order to reach the geometry of the other state.

Hence, those modes are visible in the spectrum, which undergo the largest geometry change upon electronic excitation. These are the modes, which are coupled to the absorption and show the steepest gradient at the Franck-Condon point of absorption. Thus, quantitative RR band analysis allows for the characterization of the excited-state geometry [7, 8], while non-resonant Raman scattering is limited to study ground-state structures of molecules.

Besides its intrinsic potential to study the structure of electronically excited-states, RR scattering offers some further advantages in analytics as the resonance enhancement of the Raman cross-section boosts the intensity of the scattered light by up to eight orders of magnitude and consequently leads to a drastic improvement of the signal-to-noise ratio. Thus, the detection of analytes is possible in concentrations a couple of orders of magnitude lower than in non-resonant Raman scattering. Furthermore, only those modes are resonantly enhanced, that are coupled to the electronic excitation, which leads to a drastic reduction of the spectral complexity. Finally, RR offers advantages in studying mixtures of various analytes and chromophores as, by tuning the excitation wavelength into the absorption of a particular analyte, only the vibrational modes of this particular molecular system will become visible in the spectrum. The selective excitation of chromophores in RR scattering is furthermore of utmost advantage, when studying systems of more than a single chromophore in biological or biomimetic systems. It is not uncommon, that chromophore-selective excitation is relevant for the biological/biomimetic function of a system. Therefore, it is extremely important to study the excited-state geometries and ultrafast initial dynamics of individual subunits of a larger system.

In conclusion, RR extends the potential of non-resonant Raman scattering to interrogate molecular structure to the study of excited-state structure and ultrafast sub-20 fs dynamics upon photoexcitation. Employing a pump-wavelength within an electronic resonance of a molecular species boosts the Raman cross-section of the modes, which are coupled to the particular electronic transition. Thereby, the RR spectrum is less complex and concentration of analytes several orders of magnitude lower than compared to non-resonant Raman scattering can be detected.

3.3.2 Advantages and Applications of Resonance Raman Scattering

Since resonance Raman scattering occurs via enhanced scattering involving an excited electronic state, the technique can be used to gain information about the molecular structure and dynamic of the excited electronic state. From the excitation

profile (plot of intensity of resonantly enhanced modes vs. excitation wavelength) one can determine the strength of the interactions between the electronic excited state and the vibrational modes, the atomic displacement Δ between ground and excited state, and thus the change in bond length and bond angles when going from the ground to the excited state. From the overtone progression of totally symmetric vibrations, or combinations of them, the anharmonicity constant and harmonic frequencies of the appropriate vibrations can be calculated [9, 10]. However, resonance Raman spectroscopy is not only used because of its high power for photochemical analysis, but rather because of its high sensitivity and selectivity. By electronic resonance enhancement the intensity of the scattered light can be increased by a factor of 10^6 compared to non-resonant Raman excitation. This improves the signal-to-noise ratio and allows the detection of substances in solution at low concentrations ($10^{-3} - 10^{-5}$ M). As the enhancement results from a coupling of the vibrational modes (most of the time totally symmetric vibrational modes) to an electronically excited state, it is possible to exclusively select vibrational modes from certain chromophores by choosing an appropriate wavelength. Figure 3.3 illustrates this selectivity for guanosine-5'-monophosphate as an example.

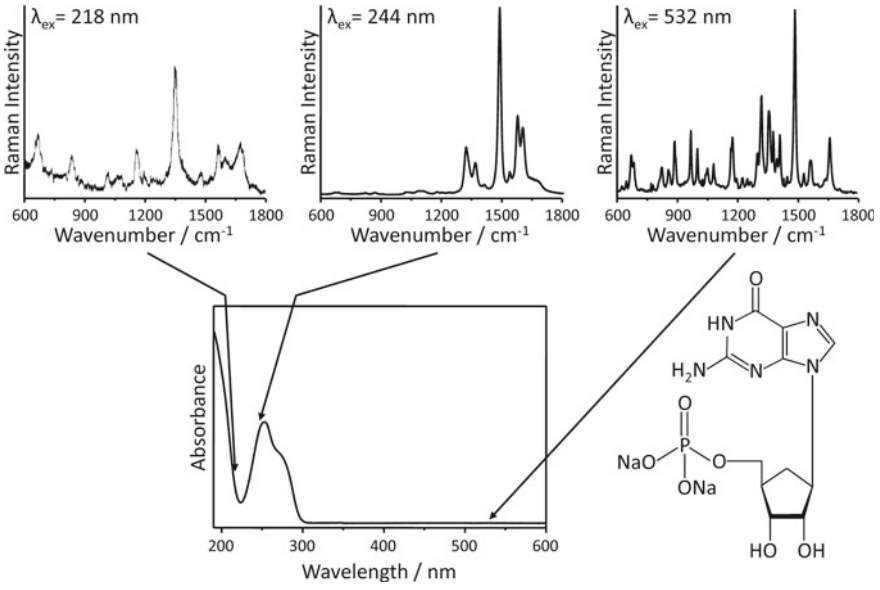

Fig. 3.3 Selectivity of resonance Raman spectroscopy. (Bottom) UV/vis absorption spectrum of guanosine-5'-monophosphate (structure shown on the right). The arrows mark three different excitation wavelengths applied to record the Raman spectra (shown in the Top) the off-resonance Raman spectrum excited at 532 nm on the right, and the resonance Raman spectra excited at 244 nm (middle) and 218 nm (left) involving two different electronic transitions. (Spectrum excited at 218 nm taken from [11])

By varying the Raman excitation wavelength to be resonant with different electronic transitions, selective excitation of different chromophores is possible. The off-resonance Raman spectrum excited at 532 nm (top right in Fig. 3.3) shows a very complex vibrational structure, since all Raman active vibrations contribute to this spectrum. When exciting at 244 nm, only those vibrational bands are enhanced that couple to the $\pi - \pi^*$ transition centered around 253 nm. The spectrum is much simpler and special focus can be put selectively on those enhanced vibrations. A different enhancement pattern is found in the resonance Raman spectrum excited at 218 nm allowing one to investigate a different site within the molecule. This site-specificity due to the application of different Raman excitation frequencies allows the study of smaller subunits in larger assemblies, as e.g. probing the active center in proteins which is pivotal for the function of the respective molecules, or the selective excitation of macromolecules such as proteins or DNA in the presence of other molecules, as e.g. in whole cells. The simplification of rich vibrational spectra from complex systems can also reduce the overlap of vibrational bands. When using excitation wavelengths in the deep UV (<250 nm), fluorescence, which is often a problem in biological samples, is energetically far enough away from the scattered light and does not interfere with the Raman signal. This is illustrated in Fig. 3.4.

In case resonance Raman spectroscopy occurs via the same electronic excited states where the fluorescence emission originates (Fig. 3.4a), the Raman signals are often masked by the broad and featureless fluorescence spectra. This is especially the case when the Stokes shift, i.e. the energy difference between the absorption maximum and the fluorescence maximum, is only small (Fig. 3.4c). In UV-resonance Raman spectroscopy, energy-rich UV-light is used, so that higher electronic excited states are incorporated. Raman scattering occurs within the first few femtoseconds (10^{-15} s) directly from the high electronic state. The fluorescence process occurs only on a time scale of nanoseconds (10^{-9} s), and therefore the molecule can relax to the lowest excited electronic state via radiationless processes.

Since fluorescence occurs in most cases from the lowest-energy excited state (Kasha's rule), the Raman and fluorescence signals are well separated on the energy scale as shown in Fig. 3.4b. The high sensitivity, selectivity and the absence of interfering fluorescence brought forth various applications of the resonance Raman technique in biological, biochemical and medicinal research in the last years. The techniques was successfully applied to study DNA conformation, native structures of proteins and peptides, the local environment of biological chromophores (such as hemoglobin, bacterio rhodopsin, carotinoids, just to name some of them [12–23]) in-situ and in dilute aqueous solutions, and for the differentiation and identification of various bacteria, fungi and algae [24–26].

Despite all the advantages experimental difficulties arise due to strong absorption of the excitation light which can cause thermal decomposition and unwanted photoreactions of the sample. Reabsorption of the scattered light makes a quantitative evaluation of the Raman intensity difficult and internal standards have to be used [27].

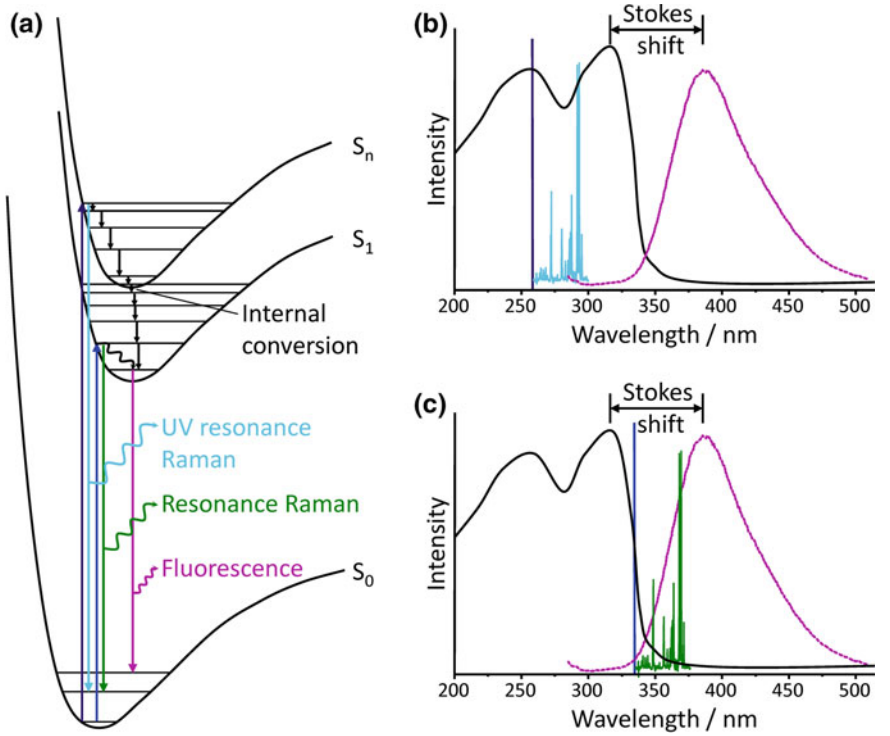

Fig. 3.4 Resonance Raman spectroscopy and fluorescence. **a** Energy level diagram (dark blue arrows: excitation, light blue and green arrow: Raman scattering, pink: fluorescence). **b** Excitation to higher electronic states. Fluorescence and Raman signals do not interfere. **c** Excitation at the high wavelength edge of the absorption band. The Stokes shift is small and therefore the Raman and fluorescence signal overlap

3.3.3 Surface Enhanced Raman Scattering

Since its first observation by Fleischmann and coworkers in 1974 [28], surface enhanced Raman scattering (SERS) has matured into a widely used analytical tool in spectroscopy and microscopy [29, 30]. SERS was first observed for pyridine adsorbed on a silver electrode in an electrolyte cell. Subsequent experiments concluded an enhancement of the Raman scattering by roughly five orders of magnitude [31, 32].

Since SERS has been reported for molecules adsorbed on metallic structures formed of e.g. silver, gold, aluminium, copper, palladium and platinum [33, 34] an empirical correlation between the surface roughness of the metallic structure and the SERS enhancement has been established [30, 35, 36]. Especially adsorbance of a molecule on noble metal nano-particles with strong surface curvature and roughness enhances its Raman scattering cross-section by up to 15 orders of magnitude. At the

same time the complexity of the Raman spectrum is typically reduced down to some prominent marker bands. Enhancement factors of up to 10^{15} ultimately allow for the detection of Raman signals from single molecules [37, 38] and sparked the use of SERS as an analytical tool in living-cell diagnostic [39, 40] and nano-sensors [41, 42].

3.3.3.1 Enhancement Mechanisms

As discussed above, Raman scattering can be classically understood on the basis of induced dipole moments. Therefore, the Raman intensity corresponds to the total power emitted by such Hertzian dipole and is thus proportional to the square of the second time derivative of the induced dipole moment μ. μ itself is defined as product of the molecular polarizability α and the electromagnetic field of the incident laser beam E [see (3.1)]. This gives rise to two complementary and multiplicative enhancement mechanisms, the interplay of which is still subject to discussions. The two conceptually distinct mechanisms, which are conventionally considered to account for the SERS effect, are: (1) an electromagnetic mechanism for an enhancement of E and (2) a chemical mechanism for an enhancement of α:

1. Electromagnetic enhancement, which accounts for enhancement factors of up to 10^{11}, results from the excitation of localized surface plasmons within the metal nanoparticles which serve as SERS substrates. The metallic nanoparticles are smaller in size than the wavelength of the excitation light, i.e. typically sizes of up to 100 nm are used. Thus they act as dipoles, in a qualitative same way as the molecules in the Raman scattering process discussed above, and constitute the source for localized strong fields. The excited surface plasmons enhance both the local laser field experienced by a molecule, E_0, and the Stokes shifted light scattered by the molecule. Thus, the nanoparticle acts as an antenna efficiently amplifying the Raman signal [43, 44].
   The simplest formalized treatment of the electromagnetic mechanism involves the quasistatic treatment of an isolated metallic nanosphere (dielectric constant ε_i) embedded in a surrounding medium (dielectric constant ε_0). In Fig. 3.5 a schematic illustration is depicted. The incident laser light excites a plasmon on the surface of the nanoparticle.
   The localized surface plasmon (LSP) resonance is characterized by the frequency, with which the plasmon oscillates locally on the surface of the nanoparticle. The nanoparticle itself acts as an antenna and the LSP irradiates a strong electromagnetic field $\vec{E}_{LM}$ directly on the surface of the nanoparticle with a range of a few nanometers, which in the quasistatic approximation for an isolated nanosphere can be described as

$$E_{LM}^2 = E_0^2 |g|^2 \left(1 + 3\cos^2\theta\right) \tag{3.18}$$

   wherein E_0 denotes the amplitude of the incident electromagnetic field, and θ the angle relative to the applied field direction. The angle dependence encoded

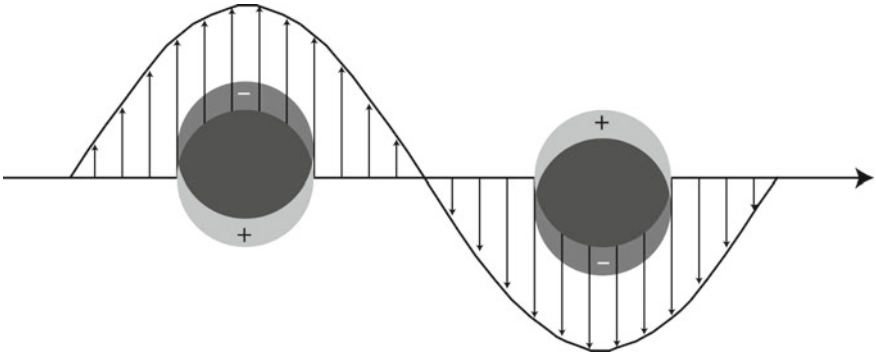

Fig. 3.5 Oscillation of free charges upon excitation of a localized surface plasmon in a metal nanoparticle. The arrows indicate the electric field

in (3.18) relates to the fact that in the approximation used the nanoparticle acts as a Hertzian dipole and reflects the latter irradiation characteristics. The important factor $g = \frac{\varepsilon_i - \varepsilon_0}{\varepsilon_i + 2\varepsilon_0}$ reveals that the strongest field enhancement, i.e. the largest values of E_{LM}^2 for a given experimental geometry, is observed if the plasmon resonance relation is met, i.e. $\Re(\varepsilon_i) \approx -2\varepsilon_0$ and $\Im(\varepsilon_i) \ll 1$. In theory, the proportionality between the field strengths of the LSP irradiation and the incoming field shows that extremely high Raman scattering intensities of molecules close to the surface can be achieved. However, an attempt to experimentally do so is often impractical due to burning of the sample [45, 46].

Not only the incident electric field is amplified by the LSP. Additionally, the Raman scattered light of analyte molecules in close proximity to the surface, $\vec{E}_{Dip}$, can be interacting with the induced electromagnetic field $\vec{E}_{LM}$ on the nanoparticle surface and yields in $\vec{E}_{SC}$. Thus the SERS intensity is additional enhanced by the contribution of $\vec{E}_{Dip}$ and $\vec{E}_{SC}$ [46]. See Fig. 3.6 for an illustration.

2. Chemical enhancement on the other hand can be understood as a surface-induced resonance Raman effect resulting from the chemisorption of a molecule on the metal surface. Due to chemisorption, the electronic structure of the substrate is disturbed allowing for a resonant excitation of a surface-induced electronically excited charge-transfer state. A simplified mechanism, as proposed in the literature [47, 48], is based on the formation of a surface complex upon chemisorption of a molecule on the metal layer. The formed surface complex is characterized by its charge-transfer character either transferring charge from the conduction band of the metal to unoccupied molecular orbitals or vice-versa. In this context, chemical enhancement can thus be understood by a surface-induced resonance Raman effect along the lines discussed above in the general context of resonance Raman scattering.

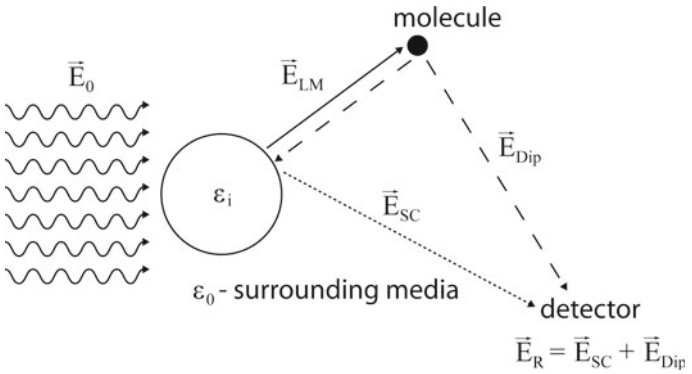

Fig. 3.6 Schematic illustration of the origin of electromagnetic enhancement of Raman scattering for molecules in close proximity to a nanoparticle surface

Despite of the conceptual differences, an exact separation of the two distinct enhancement processes is extremely challenging and experimentally very difficult, as any parameter easily changed in the experimental design will have an influence on both mechanisms. A detailed understanding of the chemical enhancement and a reliable separation from purely electromagnetic enhancement is thus not only relevant for fundamental reasons but also crucial for the design of analytical tools. Since both enhancement mechanisms are multiplicative, unexpected chemical enhancements can easily lead to quantitatively and qualitatively wrong analytical conclusions. For the sake of simply increasing the Raman scattering cross-section, surface enhanced resonance Raman scattering (SERRS) can be employed. Here, the excitation wavelength is not only in resonance with the surface plasmon absorption but more importantly also resonant to the electronic absorption of the adsorbed molecules. Thus, surface enhancement of the Raman signal appears combined with the adsorbate intrinsic enhancement of the scattering due to the dispersion of $\left(\frac{\partial\alpha}{\partial q}\right)_{q_0}$. As SERRS further enhances the scattering cross-section and thus allows for a lowering of the detection limit of a particular analyte, it has been implemented to study drug absorption and protein properties [49].

3.3.3.2 SERS Active Substrates

Substrates used for SERS have to meet the following requirements aside from the plasmon resonance condition, i.e. $\Re(\varepsilon_i) \approx -2\varepsilon_0$ and $\Im(\varepsilon_i) \ll 1$, which is particularly well met for silver, gold and copper when working with excitation in the visible spectral region: Due to an increased field enhancement at strongly curved surfaces (lightning rod effect), the substrates should reveal sharp features or a significant nano-roughness. A different way of enhancing local fields is to place two

(or more) nano-particles/structures in close proximity, so that high fields are produced at the interface between the particles. Furthermore, in order to be applicable in bio-analytical chemistry, SERS substrates need to be (i) non-toxic and chemically compatible with the analytes or cells which are subject to detection, (ii) temporally stable, i.e. show no aggregation, which alters the enhancement during the course of the experiment and (iii) reproducible and (iv) ideally low cost and easily preparable.

Besides the conventional use of metal colloids, nanoparticles and roughened surfaces, recent experimental efforts have been devoted to the design of highly reproducible SERS substrates with well defined shapes and hence exactly controlled plasmonic properties. Pursuing this research goal, basically two independent experimental approaches have been followed: nanosphere lithography and electron beam lithography. *Nanosphere lithography* was pioneered by Fischer and Zingsheim, who demonstrated that a nanosphere containing solvent can be evaporated in a controlled way to form a dense monolayer on a substrate, which is subsequently used as a mask for a metal layer deposition. Van Duyne demonstrated the use of self-assembled sphere masks to produce highly organized particle arrays. Defect-free silver arrays of sizes up to 25 μm^2 have been reported, which revealed enhancement factors of more than 10^7 for benzenethiol on these arrays [50].

Metal deposition without removal of the nanospheres forms the basis of an approach conventionally referred to as *films over nanospheres*. Using the latter technique, substrates with enhancement factors of up to 10^6 have been designed. The use of multilayer silver-gold films-over-nanosphere substrates allows to combine the high SERS enhancement typically observed for silver with the enhanced long term stability typically associated with gold substrates [51, 52]. *Electron beam lithography* routinely produces highly reproducible patterns of a variety of materials. Structures that have been demonstrated in the literature include square and hexagonal arrays composed of ellipsoids, cylinders and trigonal prisms as well as nanowires [53–58]. Another recently pursued approach in designing novel SERS materials, especially in connection with on-chip point-of-care protein diagnostics, is the use of *enzymatic silver deposition*. In this technique, a streptavidin peroxidase complex (SAPK) is coupled to a biotin-modified oligonucleotide immobilized on a glass surface due to the biotin-streptavidin interaction. The enzymatic silver deposition, which is caused by the enzymatic activity of the peroxidase, yields in the formation of nanostructures with sharp edges as depicted in Fig. 3.7 [59].

3.3.3.3 Application of SERS

The significant enhancement of the scattering cross-section in SERS has sparked the use of SERS as an analytical tool.

First experiments demonstrate the capability of combining SERS with microfluidic devices in order to develop novel lab-on-a-chip devices. Popp and coworkers presented a proof of principle experiment for the application of a liquid/liquid

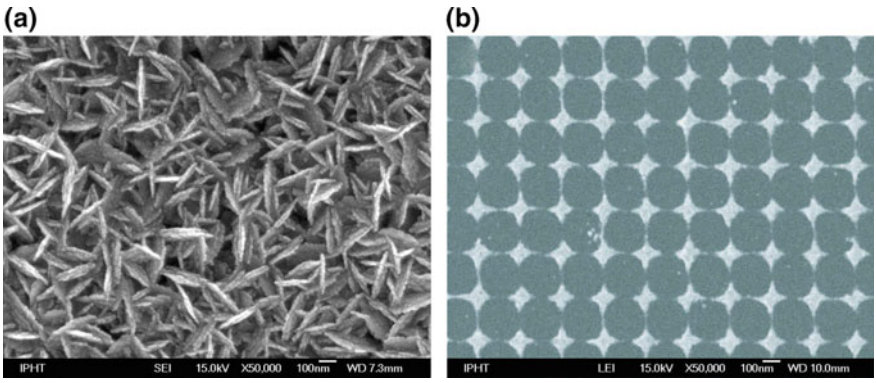

Fig. 3.7 Two examples of novel SERS substrates are depicted. **a** Enzymatic grown metal particles and **b** substrates manufactured by electron-beam lithography

microsegmented flow for serial high-throughput microanalytical systems with promising applications in clinical chemistry, pharmaceutical research and analytical chemistry. They combined microspectral SERS analysis with reproducible sample volumes down to 180nl and showed that their approach offers the capability of quantifying analytes by analysing the SERS spectra [2, 60].

The combination of SERS spectroscopy readout and atomic force microscopy (AFM) or scanning tunnelling microscopy (STM) yielded a novel microscopic technique called tip-enhance Raman scattering TERS [61]. TERS combines the high spatial and topological resolution of AFM with the chemical sensitivity of Raman scattering. Employing a near-field optical effect, TERS is capable of resolving structures smaller than the diffraction limit of the laser light used. TERS investigations on the spectral composition of the surface of *Staphylococcus epidermis* quantified the nanoscale heterogeneity of the bacterial surface with spatial resolution as small $50 \times 50\,\mathrm{nm}^2$ [39, 40]. The chemical sensitive characterization of bacterial cell walls offer promising roadways to the design of novel drugs designed to selectively target a particular bacterium. Another recent highlight of TERS micro-spectroscopy was performed by Bailo and Deckert, who presented SERS spectra of a single-stranded RNA homopolymer of cytosine with a spatial resolution down to a couple of nucleobases [62]. Their experiment presents a benchmark in the application of TERS to directly monitor DNA transcription - a key process for the understanding of transcription errors and related diseases.

Another milestone in bringing TERS spectroscopy into the lifescience and in particular into the field of biomedical diagnostics has been recently presented by Deckert, Popp and coworkers [63]. Their work revealed the high potential that lies in the combination of extremely high spatial resolution (20 nm) and chemical sensitivity intrinsic to TERS. Using the Raman enhancement on the tip surface the authors succeeded in recording Raman spectra of the surface of a single *tobacco mosaic* virus. The recorded spectra were comparable to Raman spectra taken on bulk virus

material and revealed the chemical composition - i.e. dominant contributions of RNA and proteins - of the virus. While the SERS-active tip interacts predominantely with the protein containing capsid, the range of the evanescent field of several nanometers allows for additional Raman bands of the RNA from the inside of the virus to be observed in the data. These results open new possibilities for the fast detection and identification of single virus particles, which is not achievable by conventional methods, and potentially study the interaction of viruses with cells and drugs.

Yet another intriguing application of SERS in analytical science shall be mentioned that has been presented by van Duyne and coworkers [64]. In their work SERS was used as the read-out mechanism to quantify the in vitro concentration of glucose in solution within the clinically relevant concentration range of less than 10 mM. Their apparatus consisted of a roughened silver surface, which was modified with a hydrophilic partition layer. The latter was implemented to facilitate the preconcentration of glucose and various small analytes. The in vivo implementation of their glucose sensor allowed for online monitoring of the glucose level in anesthetized rats proving the capability of SERS based devices to operate within a clinical procedure.

Finally, we want to mention an application that combines both Raman cross-section enhancement mechanisms discussed so far, i.e. the combination of resonance Raman and surface enhanced Raman scattering SERRS (surface enhanced resonance Raman scattering) for DNA sequence analysis [49]. The basic concept in using SERRS for identification of specific DNA sequences is to couple the spectroscopic read-out with a biological essay. In this technique, the DNA fragment is chemically linked to a dye molecule which it turn is terminated to a noble metal surface by means of a covalently attached surface-seeking group. Hence, the dye, which might or might not be a fluorescent molecule, is covalently attached to the DNA fraction to be labelled and brought into close proximity of the noble metal surface. Therefore, characteristic Raman modes of the dye are enhanced. The biochemical essay ensures that the presence of a particular dye can be correlated with the presence of a particular DNA fragment and hence, indirect DNA sensitivity is achieved. The dominant attractiveness of this technique is its high sensitivity in terms of absolute detection limits, which is reported to be in the range between 10^{-9} and 10^{-12} M, depending on the use of the particular SERRS-marker and the metallic surface providing the Raman enhancement. Thus, the detection limit of SERRS in the DNA detection exceeds the sensitivity of a fluorescence read-out by roughly one to three orders of magnitude [49].

This brief and far-from-complete overview over recent applications and ongoing developments of surface-enhanced (resonance) Raman scattering demonstrates the enormous potential of Raman spectroscopy for biomedical analysis. Subsequent chapters in this book will provide further and more detailed insight into selected areas of Raman applications in the lifescience.

References

1. M. Schmitt, J. Popp, J. Raman Spectrosc. **37**(1–3), 20 (2006)
2. K.R. Ackermann, T. Henkel, J. Popp, ChemPhysChem **8**(18), 2665 (2007)
3. K.R. Strehle, D. Cialla, P. Rösch, T. Henkel, M. Köhler, J. Popp, Anal. Chem. **79**(4), 1542 (2007)
4. P. Rösch, M. Harz, M. Schmitt, K.D. Peschke, O. Ronneberger, H. Burkhardt, H.W. Motzkus, M. Lankers, S. Hofer, H. Thiele, J. Popp, Appl. Environ. Microbiol. **71**(3), 1626 (2005)
5. P. Rösch, M. Harz, K.D. Peschke, O. Ronneberger, H. Burkhardt, A. Schüle, G. Schmauz, M. Lankers, S. Hofer, H. Thiele, H.W. Motzkus, J. Popp, Anal. Chem. **78**(7), 2163 (2006)
6. B. Schrader (ed.), *Infrared and Raman Spectroscopy, Methods and Applications* (Wiley-VCH, 1995), Chapter Application of non-classical Raman spectroscopy, p. 465
7. A.V. Szeghalmi, M. Erdmann, V. Engel, M. Schmitt, S. Amthor, V. Kriegisch, G. Noell, R. Stahl, C. Lambert, D. Leusser, D. Stalke, M. Zabel, J. Popp, J. Am. Chem. Soc. **126**(25), 7834 (2004)
8. S. Lochbrunner, A. Szeghalmi, K. Stock, M. Schmitt, J. Chem. Phys. **122**, 244315 (2005)
9. R.J.H. Clark, P.D. Mitchell, J. Am. Chem. Soc. **95**(25), 8300 (1973)
10. W. Kiefer, H.J. Bernstein, J. Mol. Spectrosc. **43**, 366 (1972)
11. S.P.A. Fodor, R.P. Rava, T.R. Hays, T.G. Spiro, J. Am. Chem. Soc. **107**, 1520 (1985)
12. S.A. Asher, Anal. Chem. **65**, A201 (1993)
13. J.M. Benevides, S.A. Overman, G.J.J. Thomas, J. Raman Spectrosc. **36**, 279 (2005)
14. T. Egawa, S.R. Yeh, J. Inorg. Biochem. **99**(1), 72 (2005)
15. J.R. Kincaid, *Porphyrin Handbook*, vol. 7 (2000), p. 225
16. J.R. Kincaid, K. Czarnecki, *Comprehensive Coordination Chemistry II*, vol. 2 (2004), p. 131
17. T. Kitagawa, Y. Mizutani, Coord. Chem. Rev. **135/136**, 685 (1994)
18. T. Kitagawa, J. Porphyrins Phthalocyanines **6**(4), 301 (2002)
19. R. Schweitzer-Stenner, J. Raman Spectrosc. **32**(9), 711 (2001)
20. T.G. Spiro, *Biological Applications of Raman Spectroscopy* (Wiley, New York, 1987), vol. 3, Chapter Resonance Raman spectra of heme and metalloproteins
21. T.G. Spiro, C.A. Grygon, J. Mol. Struct. **173**, 79 (1988)
22. G.J.J. Thomas, Annu. Rev. Biophys. Biomol. Struct. **28**, 1 (1999)
23. R. Withnall, *Protein-Ligand Interactions, Structure and Spectroscopy: A Practical Approach* (Oxford University Press, Oxford, 2001), Chapter Protein-ligand interactions studied by Raman and resonance Raman spectroscopy
24. K. Gaus, P. Rösch, R. Petry, K.D. Peschke, O. Ronneberger, H. Burkhardt, K. Baumann, J. Popp, Biopolymers **82**(4), 286 (2006)
25. R.M. Jarvis, R. Goodacre, F.E.M.S. Microbiol, Lett. **232**, 127 (2004)
26. E.C. Lopez-Diez, R. Goodacre, Anal. Chem. **76**(3), 585 (2004)
27. Z.Q. Wen, S.A. Overman, G.J.J. Thomas, Biochemistry **36**, 7810 (1997)
28. M. Fleischmann, P.J. Hendra, A.J. McQuillan, Chem. Phys. Lett. **26**(2), 163 (1974)
29. R. Petry, M. Schmitt, J. Popp, ChemPhysChem **4**(1), 14 (2003)
30. K. Hering, D. Cialla, K. Ackermann, T. Dörfer, R. Möller, H. Schneidewind, R. Mattheis, W. Fritzsche, P. Rösch, J. Popp, Anal. Bioanal. Chem. **390**(1), 113 (2008)
31. M.G. Albrecht, J.A. Creighton, J. Am. Chem. Soc. **99**(15), 5215 (1977)
32. D.L. Jeanmaire, R.P. Van Duyne, J. Electroanal. Chem. Interfacial Electrochem. **84**(1), 1 (1977)
33. M.J. Banholzer, J.E. Millstone, L. Qin, C.A. Mirkin, Chem. Soc. Rev. **37**(5), 885 (2008)
34. B. Ren, G.K. Liu, X.B. Lian, Z.L. Yang, Z.Q. Tian, Anal. Bioanal. Chem. **388**(1), 29 (2007)
35. K. Kneipp, H. Kneipp, I. Itzkan, R.R. Dasari, M.S. Feld, J. Phys.: Condens. Matter **14**(18), R597 (2002)
36. P.L. Stiles, J.A. Dieringer, N.C. Shah, R.P. Van Duyne, Annu. Rev. Anal. Chem. **1**, 601 (2008)
37. K. Kneipp, Y. Wang, H. Kneipp, L.T. Perelman, I. Itzkan, R.R. Dasari, M.S. Feld, Phys. Rev. Lett. **78**(9), 1667 (1997)
38. S.M. Nie, S.R. Emery, Science **275**(5303), 1102 (1997)

39. U. Neugebauer, P. Rösch, M. Schmitt, J. Popp, C. Julien, A. Rasmussen, C. Budich, V. Deckert, ChemPhysChem **7**(7), 1428 (2006)
40. U. Neugebauer, U. Schmid, K. Baumann, W. Ziebuhr, S. Kozitskaya, V. Deckert, M. Schmitt, J. Popp, ChemPhysChem **8**(1), 124 (2007)
41. R. Gessner, P. Rösch, W. Kiefer, J. Popp, Biopolymers **67**(3), 327 (2002)
42. R. Gessner, P. Rösch, R. Petry, M. Schmitt, M.A. Strehle, W. Kiefer, J. Popp, Analyst **129**(12), 1193 (2004)
43. W.A. Murray, W.L. Barnes, Adv. Mater. **19**(22), 3771 (2007)
44. K.A. Willets, R.P. Van Duyne, Annu. Rev. Phys. Chem. **58**, 267 (2007)
45. G.C. Schatz, R.P. Van Duyne, *Handbook of Vibrational Spectroscopy* (Wiley, Chichester, 2002), Chapter Electromagnetic Mechanism of Surface-enhanced Spectroscopy, pp. 759–774
46. M. Kerker, D.S. Wang, H. Chew, Appl. Opt. **19**(24), 4159 (1980)
47. J.F. Arenas, I. Lopez-Tocon, J.L. Castro, S.P. Centeno, M.R. Lopez-Ramirez, J.C. Otero, J. Raman Spectrosc. **36**(6/7), 515 (2005)
48. A. Otto, J. Raman Spectrosc. **36**(6/7), 497 (2005)
49. D. Graham, K. Faulds, Chem. Soc. Rev. **37**(5), 1042 (2008)
50. A.J. Haes, C.L. Haynes, A.D. McFarland, G.C. Schatz, R.P. van Duyne, S. Zou, MRS Bull. **30**(5), 368 (2005)
51. X. Zhang, J. Zhao, A.V. Whitney, J.W. Elam, R.P. Van Duyne, J. Am. Chem. Soc. **128**(31), 10304 (2006)
52. J. Stropp, G. Trachta, G. Brehm, S. Schneider, J. Raman Spectrosc. **34**(1), 26 (2003)
53. C.L. Haynes, A.D. McFarland, L. Zhao, R.P. Van Duyne, G.C. Schatz, L. Gunnarsson, J. Prikulis, B. Kasemo, M. Kaell, J. Phys. Chem. B **107**(30), 7337 (2003)
54. G. Laurent, N. Felidj, J. Aubard, G. Levi, J.R. Krenn, A. Hohenau, G. Schider, A. Leitner, F.R. Aussenegg, J. Chem. Phys. **122**(1), 011102/1 (2005)
55. L. Billot, M. Lamy de la Chapelle, A.S. Grimault, A. Vial, D. Barchiesi, J.L. Bijeon, P.M. Adam, P. Royer, Chem. Phys. Lett. **422**(4–6), 303 (2006)
56. K. Li, L. Clime, B. Cui, T. Veres, Nanotechnology **19**(14), 145305/1 (2008)
57. D. Cialla, U. Hübner, H. Schneidewind, R. Möller, J. Popp, ChemPhysChem **9**, 758 (2008)
58. U. Hübner, R. Boucher, H. Schneidewind, D. Cialla, J. Popp, Microelectron. Eng. **85**, 1792 (2008)
59. K.K. Hering, R. Möller, W. Fritzsche, J. Popp, ChemPhysChem **9**(6), 867 (2008)
60. K.R. Strehle, D. Cialla, P. R'sch, T. Henkel, M. K'hler. J. Popp Anal. Chem. **79**(4), 1542 (2007)
61. E. Bailo, V. Deckert, Chem. Soc. Rev. **37**(5), 921 (2008)
62. E. Bailo, V. Deckert, Angew. Chem. Int. Ed. **47**(9), 1658 (2008)
63. D. Cialla, T. Deckert-Gauding, C. Budich, M. Laue, R. M'ller, D. Naumann, V. Deckert. J. Popp J. Raman Spectrosc. **40**(3), 240 (2008)
64. C.L. Haynes, C.R. Yonzon, X. Zhang, R.P. Van Duyne, J. Raman Spectrosc. **36**(6/7), 471 (2005)

Chapter 4
Raman Instrumentation for Confocal Raman Microscopy

Olaf Hollricher

Abstract Raman spectroscopy is a weak scattering technique in which typically less than one in a million excitation photons give rise to a single Raman photon. The situation is even more difficult in confocal Raman microscopy, as the detection volume is reduced by the small pinhole and thousands of spectra must be collected in a short period of time. Therefore, careful design of the excitation and detection optics, as well as the appropriate choice of spectrometer and detector is important for successful experiments. As detectors and instrumentation in this field continue to quickly evolve, a snap-shot of state of the art Raman equipment and instrumentation will be provided.

4.1 Introduction

Raman scattering is typically a very weak effect due to the non-resonant interaction of the exciting photons with the molecules involved in the scattering process. Therefore, the number of Raman photons in a given measurement geometry is limited and any progress in technology that leads to a higher collection efficiency is very important.

Although the Raman effect was already discovered in 1928 by Chandrasekara Raman [1], who was awarded the Nobel price in physics two years later, routine Raman spectroscopic experiments were not possible until the development of the laser in the 1960s [2].

In the 1970s and 80s, the development of charge coupled devices (CCDs) [3, 4] replaced photomultiplier tubes (PMTs) and enabled multi-channel detection. Willard S. Boyle and George E. Smith received the Nobel Price in Physics 2009 for the invention of the CCD camera.

As silicon detectors have a much higher quantum efficiency (QE) compared to PMTs in the visible and near-infrared regions of the spectrum and CCDs are available as linear detectors, this has reduced measurement times by at least three orders of magnitude. Before, the Raman band of interest had to be scanned across a PMT, a

O. Hollricher (✉)
WITec GmbH, Lise-Meitner-Strasse 6, 89081 Ulm, Germany
e-mail: olaf.hollricher@witec.de

J. Toporski et al. (eds.), *Confocal Raman Microscopy*, Springer Series in Surface Sciences 66, https://doi.org/10.1007/978-3-319-75380-5_4

point detector only sensitive to a very narrow wavelength range selected by the exit slit of the spectrometer.

With the introduction of the CCD, the exit slit of the spectrometer could be replaced by a linear CCD detector, enabling the acquisition of 1000 channels (or more) at the same time.

4.2 The Development of Raman Microscopes

In the 90s, companies first combined a Raman spectrometer with an optical microscope and established so-called micro-Raman spectroscopy. The microscope was used to focus the excitation light to a small spot a few micrometers in diameter to obtain a Raman spectrum from a microscopic area. For the first time, Raman spectra could be obtained from samples of only a few micrometers in diameter. The advantage of using a microscope objective instead of a simple lens is the high collection efficiency for the Raman signal due to the high NA[1] of the microscope objective. On the other hand, as one focuses the light to a microscopic spot, care must be taken to not heat the sample and thermally destroy it with an overly intense laser beam.

In a further approach, the micro-Raman instruments were equipped with stepper motor driven positioning stages to raster scan the sample and collect Raman spectra at a given number of sample positions. This technique, which was called Raman mapping, could be used to extract the relevant chemical information from each spectrum and to create a map of the distribution of the chemical components in a sample with a lateral resolution of a few micrometers.

As the acquisition of typical Raman spectra using these instruments could take several seconds integration time (or even much longer, depending on the required S/N ratio and scattering efficiency of the sample), general understanding was that this technique is very slow and creating a Raman map of a sample takes hours, if not days, to acquire [5]. If one uses an integration time of only 1 s per spectrum, a 60×60 pixel Raman map takes $60 \times 60 = 3600\,\text{s} = 1\,\text{h}$ for the integration alone. Adding the time required to position the sample with a stepper motor stage, as well as the readout time for the CCD and the time for the backward scan, the total time required for this experiment can be easily twice as long. Keeping a system stable with an accuracy of better than 1 μm over this time scale is already a challenge and a 60×60 pixel map is only a very small image. A $200 \times 200 = 40{,}000$ spectra image under these conditions is virtually impossible if the integration time per spectrum is not dramatically lowered. If one wants to establish Raman imaging as a routine technique, the integration time per spectrum must be reduced to 100 ms per spectrum or even less.

Therefore, multiplex setups were developed to increase the acquisition speed similar to the transition from the single point, zero dimensional PMT to the one dimensional CCD.

[1] Numerical aperture = sine of half of the acceptance angle of the objective.

Instead of illuminating a single point and scanning this point across the entire sample area, one idea is to illuminate a complete line and project this line onto the entrance slit of a spectrometer. Using an imaging spectrometer, the vertical axis of the CCD camera could be used for position information and the horizontal axis for energy dispersion. With this technique, one could acquire hundreds of spectra along the illuminated line at the same time. This technique is called "line imaging".

Another approach is to homogeneously illuminate the sample as a whole and acquire the desired spectral information without a spectrometer by sending the light through a (tunable) narrowband filter onto an imaging CCD. A single exposure collects the Raman light of the whole sample and scanning is no longer necessary. It is not possible to collect a complete Raman spectrum at every image point. Instead, the spectral information must be gained by taking several images at different filter pass-band positions. This technique is called "global imaging".

Although these techniques appear to increase detection speed through their multiplex advantages by several orders of magnitude, they have severe disadvantages that in most cases prevent their useful application.

One main disadvantage is that neither technique is confocal, so that there is either a slit instead of a round pinhole, or no pinhole at all. "Confocal" is defined as "having the same focus" and describes an optical microscope in which the sample is illuminated with a point source and the image of this point is detected through a pinhole in front of the detector. The illuminating point source and the pinhole are both positioned in the same focal plane. An image of the sample is obtained by either scanning the laser focus point by point and line by line across the sample or by scanning the sample under the laser spot. As the signal is detected through a pinhole, only light originating from the focal plane can reach the detector. Light emitted above or below the focal plane is not in focus in the pinhole plane and therefore does not contribute to the image. The theory of confocal microscopy is described in Chap. 1.

4.3 Confocality

The natural enemy of Raman spectroscopy is fluorescence. As fluorescence is a resonant interaction of light with electronic sample states, the efficiency of fluorescence can easily be 6 orders of magnitude higher than that of the Raman interaction. If the sample shows fluorescence at the excitation wavelength used for Raman, in most cases the fluorescence intensity is so high that no Raman signal can be detected.

Therefore it is extremely important to reduce the fluorescence background as much as possible by either using an excitation wavelength at which the sample does not show fluorescence, or by reducing the detection volume.

Unfortunately it is not always possible to find an excitation wavelength at which there is no fluorescence, because of the high efficiency of the fluorescence process compared to Raman scattering. In these cases, the confocal detection setup limits the collection of fluorescence to photons emitted from the focal plane. This dramatically

reduces the fluorescence background signal, so that in many cases Raman images can be obtained, where non-confocal techniques only detect fluorescence.

If the fluorescence is caused by impurities and not the sample itself, very often the fluorescence is bleached due to the high excitation intensity in the focal plane. In these cases, a confocal Raman image gives often very useful results, while non-confocal techniques would still collect too much fluorescence from areas above and below the focal plane.

As the confocal detection principle limits the detected light to the focal plane, it also allows the analysis of transparent samples in 3D and an optical cross section to be performed without cutting the sample in half. If the sample is a thin layer on top of a supporting substrate, only a confocal setup allows the separation of the signal from the sample from the background signal of the substrate. A less than 1 μm thin polymer sample on a cover glass (170 μm thickness) will give a more than 100 times smaller Raman signal than the glass substrate itself and can hardly be analyzed with a non-confocal technique.

Non-confocal techniques might have their niche applications, but the confocal setup is so far the most versatile technique that delivers the best results in terms of spatial resolution and background suppression.

4.4 Throughput of a Confocal Raman Microscope

It is extremely important to optimize the throughput of the confocal Raman microscope to allow confocal Raman imaging in reasonable amounts of time because the Raman signal is usually very weak. Figure 4.1 shows a sketch of a typical Raman microscope system consisting of an excitation laser, a microscope and a spectrometer with CCD detector. Scanning movement of the sample is performed with a piezo-scanner which is very fast and extremely accurate when equipped with position sensors.

To optimize the Raman signal, every part of the system must be optimized for the highest transmission and efficiency. It is very easy to lose an order of magnitude in sensitivity if the components are not properly chosen. If a single spectrum is desired, it is usually not important whether the necessary integration time is 1 s or 10 s, but it makes a big difference if an image takes 15 min or 2.5 h.

In the following sections, points of specific importance are described.

4.4.1 Laser Wavelength

The Raman scattering intensity is proportional to ν^4, where ν is the frequency of the exciting laser radiation. Excitation at 400 nm therefore leads to a 16 times higher Raman signal than excitation at 800 nm. On the other hand, many samples show

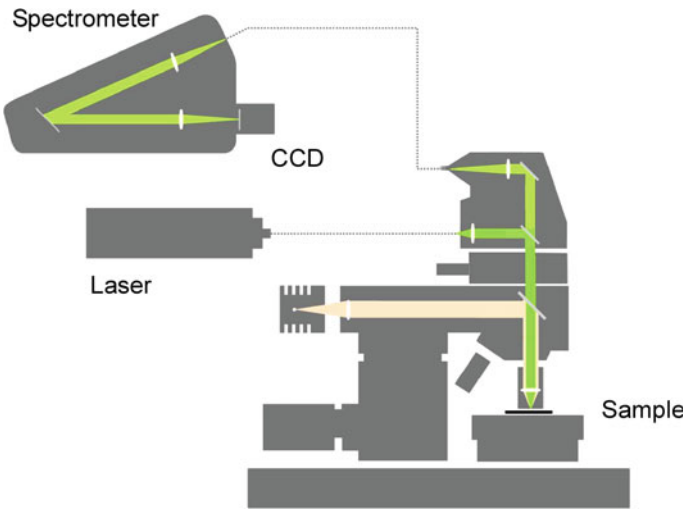

Fig. 4.1 Typical layout of a Raman microscope with a fiber-coupled laser source and spectrometer

strong fluorescence when excited in the UV or blue region of the spectrum and low fluorescence when excited in the red or NIR region of the spectrum.

The shorter the excitation wavelength, the higher the lateral resolution, because the resolution is given by $\Delta x = 0.61 \times \lambda / NA$ with Δx being the shortest distinguishable distance between two points, λ the wavelength and NA the numerical aperture of the objective used. This relation also shows that the numerical aperture is equally important. Good objectives with a very high NA are easily available in the range from 400 to 900 nm. For UV wavelengths below 350 nm, Raman scattering is very high, but the number of available objectives is limited and their NA is typically very small. Also, sample damage due to the high photon energy is starting to be a problem. At long wavelengths, lateral resolution decreases and the Raman efficiency drops strongly, but fluorescence is less likely.

A laser suitable for Raman microscopy should

- have a Gaussian beam shape (single longitudal mode, TEM00), so that it can be focused to a diffraction limited spot,
- be linearly polarized, to allow the observation of polarization dependent sample properties,
- have a very narrow line shape of well below $1\,\mathrm{cm}^{-1}$, to avoid broadening of the Raman lines,
- be very stable in frequency (variation $< 0.01\,\mathrm{cm}^{-1}$) to allow stress measurements with high accuracy,
- be very stable in intensity (<1–2% power fluctuations), to allow accurate and comparable measurements of concentrations,

just to name a few of the essential properties.

4.4.2 Excitation Power

The Raman signal is proportional to the excitation power, but the excitation laser power should be chosen well below the point where absorption leads to thermal decomposition of the sample. The acceptable laser power depends on laser wavelength, sample properties (absorption, thermal conductivity) and other imaging conditions (laser focus diameter etc.). It can vary from a few μW to several 100 mW. If the sample is transparent, the typically acceptable power for green excitation will be on the order of 10 mW for a 300 nm spot size.

4.4.3 Objective

To obtain the highest possible collection efficiency in combination with the best spatial resolution, one should use an objective with the highest numerical aperture applicable under the measurement conditions. One must also pay attention to the transmission characteristics of the microscope objective at the excitation wavelength. A good microscope objective might have 80–90% transmission at 500 nm wavelength, but only 40% or even less at 900 nm. The reason for this is that antireflection coatings that have less than 0.5% reflectivity in the visible can be far more reflective in the IR. This is particularly important, as the light must pass through the objective twice.

The sample flatness need to be considered as well when choosing the correct objective since a high NA objective will have a good depth resolution and collect from only a narrow height in the Z direction. This in turn means, that a sample with a high topography will sometimes be in focus on the sample surface and sometimes not. In this case using an objective with a lower NA might be beneficial.

4.4.4 Microscope Throughput

The throughput of the microscope is as important as the throughput of the objective itself. The light must pass through the microscope twice, therefore the losses are squared. Fewer optical components with optimized throughput result in lower losses.

The laser beam is coupled into the microscope with a dichroic or holographical beamsplitter. The reflectivity of this beamsplitter should be as high as possible for the laser excitation wevelength, while its transmission for the Raman light should be high as well. With today's coating technology, dichroic filters are available that have a reflectivity $>95\%$ at the laser wavelength and at the same time a transmission of about 98% for the Stokes-shifted Raman light above approximately 150 rel. cm^{-1}. If one needs to get closer to the Rayleigh line, holographic beamsplitters must be used, but it is only a matter of time until coating technology will allow holographic filters

to be completely replaced. Holographic filters will then only be needed if detection of the Anti-Stokes Raman spectrum is necessary.

For efficient suppression of the Rayleigh line, an edge- or notch-filter which reduces the laser line intensity by 6 orders of magnitude while having a throughput of >95% for the Stokes-shifted Raman lines should be used.

4.4.5 Coupling Between Microscope and Spectrometer

It might sound trivial, but the optical coupling between microscope and spectrometer is extremely important because it has to serve several functions. The first obvious task is that it must couple the light effectively from the microscope into the spectrometer. If this is done with metallic mirrors that have 85% average reflectivity, after only 4 mirrors 50% of the signal is lost.

Additionally, the light must be coupled into the entrance slit of the spectrometer and its aperture must be transformed into the entrance aperture of the spectrometer. A higher divergence than the acceptance angle of the spectrometer will result in enormous losses, a smaller divergence will result in a reduced resolution because the grating is only partly illuminated.

For an effective confocal setup, the confocal pinhole size must be chosen according to the diameter of the point spread function on the image side of the objective. As an example, a 100× objective with NA = 0.9 at 633 nm excitation wavelength will produce a diffraction-limited airy disc of 43 µm in the image plane. A confocal pinhole diameter of 50 µm will be in this case nearly ideal for maximum depth resolution and high collection efficiency. The illuminating NA in the image plane for the objective above is NA = 0.009 (0.9/100 = 0.009, because the product of magnification and NA is a constant (Étendue)[2]), while a typical f = 300 mm spectrometer has an entrance aperture of NA = 0.125 (f/4).

To match the entrance aperture of the spectrometer, an additional intermediate magnification of 14× is needed which introduces losses and is subject to misalignment. A single multi-mode optical fiber with, in this case, 50 µm core diameter can be used to fulfill all these purposes. The fiber serves

1. as a pinhole, because only the core guides and transports the light,
2. as a light guide with extremely high efficiency (the only losses are 4% entrance and exit losses if non-coated entrance and exit surfaces are used),
3. as an entrance slit for the spectrometer and
4. as an aperture matching device, because the exit aperture of the fiber (NA = 0.12) exactly matches that of the spectrometer, if a f/4 spectrometer is used.

[2]The Étendue is a conserved quantity in optical systems. It basically characterizes how "spread out" the light is in area and angle.

4.4.6 Spectrometer Throughput

Most commercially available spectrometers have a throughput (including gratings) of only 30–35% (@532 nm), although the gratings have an efficiency of up to 80%. This means that more than 50% of the light is lost in the coatings of the spectrometer mirrors. The reason for this is that most spectrometers are not optimized for the small frequency range of the Raman signal, but should work from UV to IR. Optimizing the spectrometer for the wavelength range of interest can therefore double the throughput [6].

4.4.7 Gratings

The grating in a spectrometer disperses the signal onto the CCD detector by deflecting each wavelength at a slightly different angle. The number of grooves per mm determines the dispersion characteristics. A high number of grooves/mm (lines/mm) results in a high dispersion and a high resolution, but also distributes the signal over a large number of CCD pixels. As, with very few exceptions, the narrowest lines of typical samples for confocal Raman microscopy have a width (FWHM = full width at half maximum) of not less than 2–3 cm^{-1} so that a spectrometer with a resolution of about 1 cm^{-1} is a good compromise.

It is useful to be able to switch between multiple gratings so that the user can use one grating with a dispersion that is matched to the detector size in order to ensure that the full Raman spectrum (−100 to 3600 rel. cm^{-1}) is covered by the detector, as well as a high resolution grating that delivers approximately 1 cm^{-1} resolution.

To optimize the efficiency, gratings are typically "blazed" for a certain wavelength. This means that the grooves are angled so that the grating efficiency can reach 80% for the first diffraction order. The grating efficiency sets the upper limit of the throughput of the spectrometer. A typical grating efficiency for a 600 lines/mm grating with a blaze wavelength of 500 nm is shown in Fig. 4.2.

As can be seen, the grating efficiency peaks at the blaze wavelength and shows a strong drop-off with shorter wavelengths. With longer wavelengths, the falloff is less steep, but if this grating is used at 785 nm excitation, the efficiency is reduced by a factor of 2–3.

4.4.8 CCD Detector

The detector is one of the key components of a Raman microscope and choosing the correct CCD strongly affects the performance of the instrument.

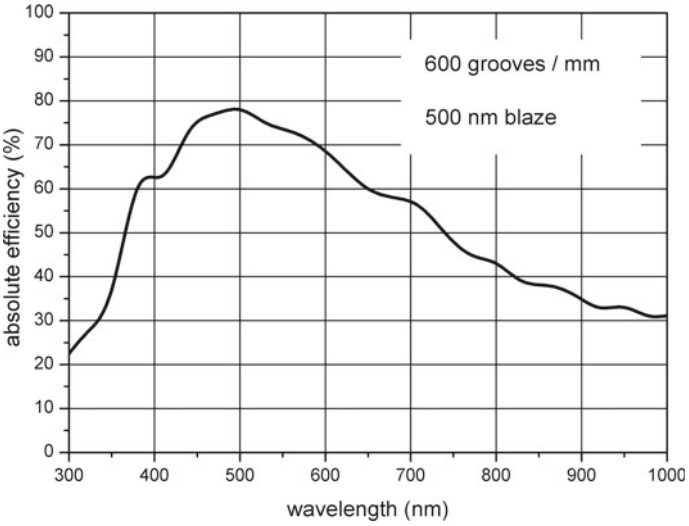

Fig. 4.2 Typical absolute reflection efficiency into the first order for unpolarized light of a 600 lines/mm grating blazed for 500 nm

CCD cameras are available in a wide variety of detector sizes, uncooled or cooled, with Peltier or liquid Nitrogen (LN) cooling, front-or back-illuminated, as deep-depletion models or with a UV coating, just to mention a few of the hundreds of variations.

A CCD (charge coupled device) detector consists of an array of light sensitive Si-photodiodes, each connected to a capacitor. In the photodiode, every detected photon creates an electron-hole pair which is separated by the internal electric field and the electrons are stored in the capacitor. A typical detector size for a spectroscopic detector is 1024 × 127 pixels (pixels per line × pixels per column), with a pixel size of 26 µm × 26 µm.

The first important characteristic of the detector is its quantum efficiency (QE), which is the percentage of detected photons to total incoming photons. As the light sensitive area of a CCD is partially blocked by electrical interconnection lines, the QE of a typical (front illuminated) detector is about 45% @ 500 nm. To increase the detection efficiency, many scientific detectors are available as back-illuminated devices, which means they are etched to about 17 µm thickness and the light is incident from the backside. With this technique and a proper anti-reflection (AR) coating, a QE of more than 90% can be achieved (@ 500 nm).

A comparison of QE curves for typical front- and back-illuminated detectors is shown in Fig. 4.3.

The QE determines the signal that is detected in a Raman experiment. Equally important is the noise in the signal or the noise created in the detector itself, because the signal to noise ratio (S/N) determines the quality of a measurement.

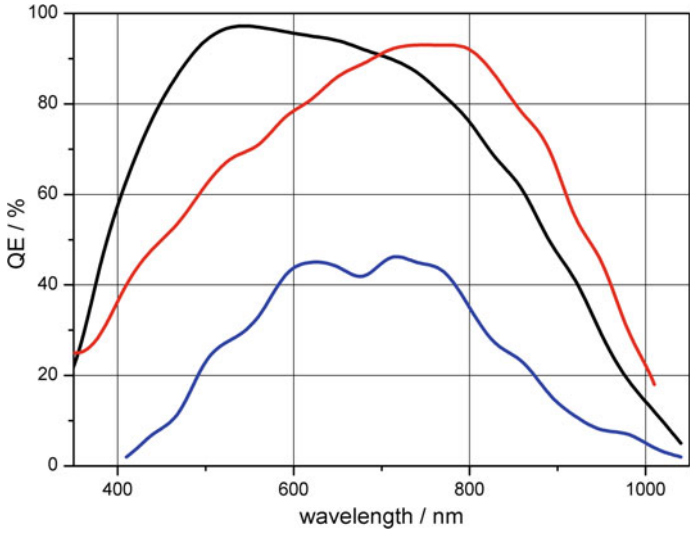

Fig. 4.3 Typical QE curves for back-illuminated (black), back-illuminated deep-depletion (red) and standard front-illuminated (blue) CCD detectors as a function of wavelength

The primary noise sources in a background-free measurement (no fluorescence or other background signal) are:

- σ_s (shot noise) = $\sqrt{\text{signal}(e^-)}$
- σ_t (thermal noise) = $\sqrt{\sharp \text{ of thermally created electrons}}$
- σ_r (readout noise) = noise created by the readout amplifier during the amplification and digitization process

Ideally, the noise should be dominated by the shot noise of the signal itself. Every other noise source should be as small as possible.

Thermal noise is created by thermally excited carriers in the detector itself and can be strongly reduced by cooling the detector. At −60 °C, the typical background signal due to thermally excited electrons is 0.01 electrons/pixel/s for a back-illuminated CCD. Therefore, thermal noise (which is the square root of the number of thermally created electrons) can be neglected up to integration times of a few minutes if the detector is kept at −60 °C or below. As the integration times in a throughput optimized confocal Raman microscope are usually well below 1s/spectrum, thermal noise is generally not a limiting factor.

A CCD temperature of −60 to −70 °C is easily achieved with a good Peltier cooler, and more recently even −90 °C has become possible, so that LN cooling is nearly obsolete.

More important is the readout noise of the readout amplifier in the detector itself. The readout noise is expressed in electrons and depends on the quality of the readout amplifier, as well as the readout speed. For longer integration times (>50 ms), a slow readout amplifier is sufficient. A high-end 33 kHz readout amplifier produces a noise

floor of less than 4 electrons. At 100 kHz readout speed, the readout noise of the best cameras on in the order of 10 electrons, while at 2.5 MHz readout speed it can easily be 35 electrons.

Using a 1024 × 127 pixel detector with a 33 kHz readout amplifier, the minimum integration time will be about 32 ms (31 spectra/s). An image consisting of 256 lines with 256 spectra each (65635 spectra) obtained with this integration time will take about 2100 s = 35 min acquisition time (retrace not counted). The noise of 4 electrons per pixel is equal to the shot noise of 16 electrons/pixel signal (18 photons/pixel signal @90% QE).

If a 100 kHz readout amplifier is used, the minimum integration time is reduced from 32 to about 12 ms (83 spectra/s) and the image can be acquired in 790 s ≈ 13 min, but the readout noise is then equal to the shot noise of a signal of 100 electrons/pixel (111 photons/pixel @ 90% QE).

If a 2.5 MHz readout amplifier is used, the integration time can be further reduced to below 1 ms (1000 spectra/s) and the acquisition time can be as low as 65 s ≈ 1 min, but of course the available signal is reduced by a factor of 32 compared to the first, and a factor of 12 compared to the second example due to the lower integration time per spectrum. The readout noise increases dramatically and now dominates the shot noise of every signal below 1225 electrons/pixel (1361 photons/pixel @90% QE).

As one can see, especially at very short integration times (fast scanning), the readout noise starts to dominate all other noise sources and the signal is very often no longer shot noise limited.

The signal to noise ratio (S/N) for such CCD detectors can be calculated with

$$S/N = \frac{\text{Signal}}{\sqrt{\text{Signal} + \sigma_R^2 + \sigma_T^2}} \tag{4.1}$$

where σ_R is the readout noise and σ_T the thermal noise, which can be excluded in this case. If an experiment requires a S/N ratio of 10 at 32 ms integration time using the 33 kHz readout amplifier, this would mean a signal of 114 electrons/pixel (127 photons /pixel = 3969 photons/pixel/s) would be necessary. An ideal detector without any readout noise would achieve a S/N ratio of 10.68 (114/sqr(114)), so that the readout noise would only add 7% to the total noise.

At 12 ms integration time using the same conditions, the 100 kHz readout amplifier must be used and as the integration time is shorter, the signal is reduced by a factor of 2.7 (=32 ms/12 ms). One would in this case detect only 43 electrons/pixel. This, together with a readout noise of 10 electrons for the 100 kHz readout amplifier, leads to a S/N ratio of 3.6 ($S/N = 43/\sqrt{10^2 + 43}$). This signal is still detectable, but without readout noise the S/N ratio would be 6.6, which means that the S/N ratio is already reduced by a factor of nearly 2, just because of the readout noise.

At even shorter integration times, which means lower signal levels, things become even worse. At 1 ms integration time using the 2.5 MHz readout amplifier (35 electrons readout noise), the experiment would deliver only 3.56 electrons/pixel which

leads to a S/N ratio of only 0.1 ($S/N = 3.56/\sqrt{35^2 + 3.56}$). Without readout noise, the S/N ratio would be 1.89, nearly a factor of 20 higher. A signal with a S/N ratio of 1.89 can be easily detected, while this cannot be said for a signal with a S/N ratio of only 0.1.

In the examples above, the digitization noise was neglected. After the readout amplification, the signal is digitized with typically 16 bit resolution in a scientific spectroscopic CCD. The A/D rate is expressed in electrons per A/D count and is usually chosen for maximum S/N without losing too much sensitivity. If a typical CCD has a saturation signal of 650,000 electrons per pixel, the amplification should be about 10 electrons/AD count (650,000/16 bit). Thus the "single bit uncertainty" or "digitization error" is also 10 electrons and is equal to the readout noise for a 100 kHz amplifier. This then already adds 41% ($1/\sqrt{1+1} = 1.41$) to the readout noise, which means the readout noise is effectively $\sqrt{2}$ larger. Therefore, many CCDs have an additional amplifier with e.g. 2× or 4× amplification before digitization, so that the noise added by digitization can be reduced (at the cost of dynamic range).

Ideally one would wish to have a detector that has 100% QE, no thermal noise, no readout noise or any other noise source. This ideal detector would always be shot noise limited, which is as good as physics allows. A back-illuminated CCD with good cooling comes very close to this ideal detector if used with long integration times. In terms of QE and thermal noise one could already call it ideal.

Recent developments in CCD technology have lead to a detector that comes even closer to what would be an ideal detector, at least in a certain wavelength range. This detector is called an EMCCD (electron multiplying CCD).

4.4.8.1 EMCCD

An electron multiplying CCD (EMCCD) is a normal CCD with an additional readout register that is driven with a much higher clock voltage than a normal CCD readout register. Due to this high clock voltage, electron multiplication through impact ionization is achieved with an adjustable total amplification of the signal of up to 1000 times. While shifting the carriers from pixel to pixel in the readout register, the probability for the generation of an excess carrier is extremely low (max. 1.0043), but as this process is repeated 1600 times, the total amplification can be as high as $1.0043^{1600} = 1000$. With this multiplication process, it is always possible to amplify the signal above the readout noise so that the S/N ratio is always limited by the Poisson noise of the signal, even if a very fast readout amplifier is used. The signal is then called shot noise limited.

As an example, a 1600 × 200 pixel EMCCD with a 2.5 MHz readout amplifier can be read out in only 1.3 ms (=760 spectra/s) without being limited by readout noise, as in a normal CCD.

If the readout is restricted to a few lines of the CCD chip, even more than 1300 spectra/s are possible (<700 µs integration time/spectrum).

As demonstrated in the example above, the readout noise is only important for very low signals below a few hundred electrons/pixel, as is typical for short integration

times. If the signal is not dominated by readout noise (large signal, long integration time), the "normal" readout register can be used and the EMCCD behaves like a state-of-the-art back-illuminated CCD.

Although an EMCCD camera is extremely sensitive and capable of detecting single photons, it cannot be used as a single photon detection device such as a photomultiplier because it lacks a discriminator. A certain number of generated carriers can originate from a different number of photons. This is taken into account in the so-called excess noise factor which adds a factor of 1.4 to the total noise of an EMCCD camera. Despite this factor, an EMCCD can still enhance the S/N ratio compared to a standard CCD, especially for very low signal levels and fast readouts.

Figure 4.4 shows the calculated S/N ratio versus signal (photons per pixel) for an EMCCD compared to a conventional CCD with 4, 10 and 35 electrons readout noise (33, 100 kHz and 2.5 MHz readout speed). An excess noise factor of 1.4 was taken into account for the EMCCD. It was assumed that both cameras had 90% QE.

Figure 4.5 shows the improvement of the S/N ratio of an EMCCD compared to a normal CCD with 4, 10 and 35 electrons readout noise.

As one can see, the S/N ratio obtained with an EMCCD is improved for signal levels up to 18 (111; 1362) photons/pixel compared to a standard CCD with 4 (10; 35) electrons readout noise.

A signal of 18 electrons or even less seems to be extremely small and that is certainly true if one is accustomed to working with single Raman spectra. As far as

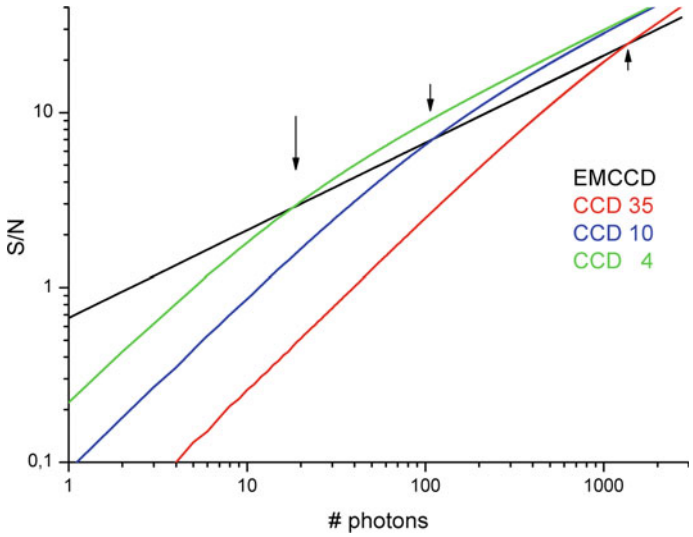

Fig. 4.4 Signal/Noise ratio for a back-illuminated EMCCD detector compared to conventional back-illuminated CCD cameras with different readout noise levels (4, 10 and 35 electrons) as is typical for slow (33 kHz), medium (100 kHz) and fast (2.5 MHz) readout speeds as a function of photons per pixel. The arrows indicate the number of photons (18, 111, 1362) below which the S/N ratio of the EMCCD exceeds that of a conventional detector at the various readout noise levels

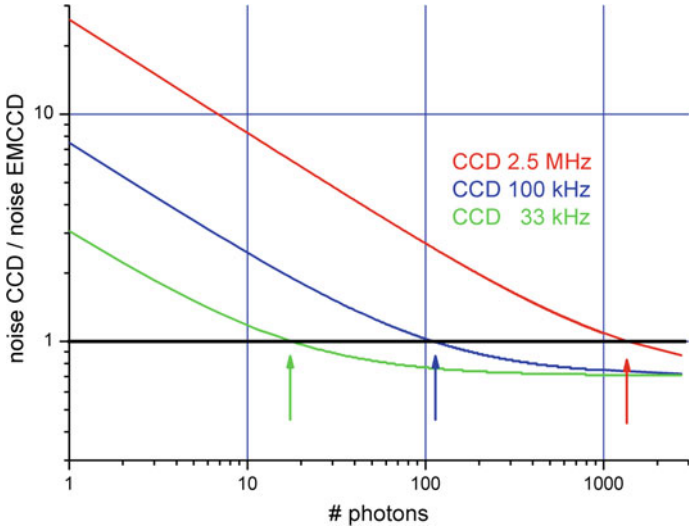

Fig. 4.5 Improvement of the S/N ratio for a back-illuminated EMCCD detector compared to conventional back-illuminated CCD cameras with different readout noise levels (4, 10 and 35 electrons) as is typical for slow (33 kHz), medium (100 kHz) and fast (2.5 MHz) readout speed as a function of photons per pixel. The arrows indicate the number of photons (18, 111, 1362) below which the S/N ratio of the EMCCD exceeds that of a conventional detector at the various readout noise levels

confocal Raman microscopy is concerned, things are different. Here, a large number of spectra (>10,000) are acquired and stored and similar spectra with a very low S/N ratio can be averaged to generate a single spectrum with a high S/N ratio. In a confocal Raman measurement, even a S/N ratio of less than 0.1 in the individual spectra can be sufficient to identify unknown species if one knows which of the spectra have to be averaged or if multi-variate analysis methods are employed.

Example of an EMCCD Measurement

In order to illustrate the effect of the EMCCD gain, the following test was performed.

The sample for the tests presented here was an ultra-thin poly(methyl methacylate) (PMMA) film spin-coated onto a glass substrate. The layer was scratched and the PMMA removed in some areas of the sample (in the center of the figures below). Here the height of the sample layer was determined by AFM to be 7.1 nm. Additionally, a needle-shaped contamination was found on the surface with a thickness of 4.2 nm. The origin and material composition of this contamination layer was not known initially, but could be determined by the confocal Raman measurements.

The results presented in Fig. 4.6 were obtained by acquiring 200 × 200 Raman spectra in a 50 × 50 μm scan range and integrating the intensity of the CH stretching band of PMMA at around 3000 rel. cm^{-1}. Excitation power was 20 mW @532 nm using a 100×, NA = 0.9 objective.

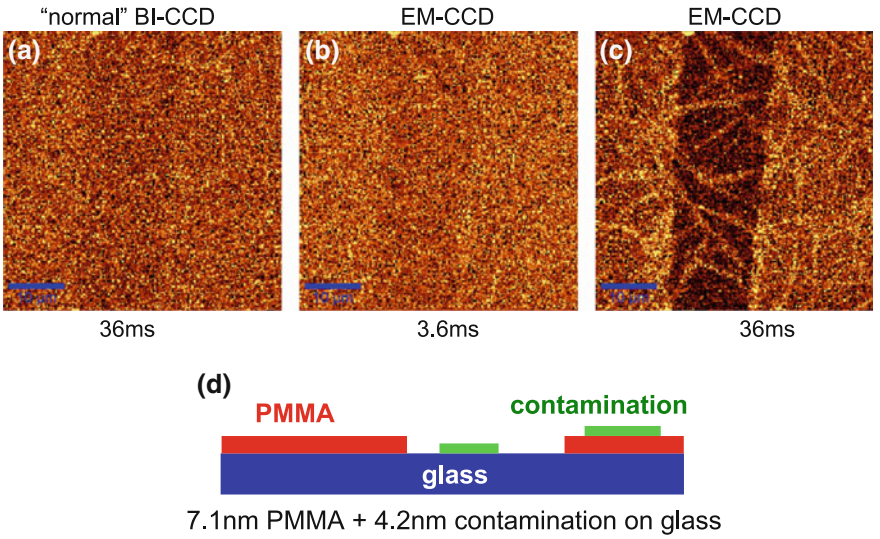

Fig. 4.6 Confocal Raman Images of a 7.1 nm PMMA layer on glass obtained at the CH stretching band around 2950 rel. cm^{-1}: **a** back-illuminated CCD, **b**, **c** EMCCD. Scale bar: 10 µm. **d** Schematic of the sample

Figure 4.6a was obtained with a standard back-illuminated (BI) CCD using a 62 kHz readout amplifier and 36 ms integration time per spectrum. With a little imagination, the scratch in the center of the image is barely visible, but the S/N ratio is much smaller than 1.

Figure 4.6b shows the same part of the sample imaged with an EMCCD with a gain of approximately 600. The image shows nearly the same S/N, but now the integration time was only 3.6 ms, 10 times faster than in Fig. 4.6a. The complete image acquisition took 25 min for Fig. 4.6a, but only 3.4 min for Fig. 4.6b. Figure 4.6c was taken with the EMCCD, though now with the same integration time as in Fig. 4.6a. One can not only clearly see the scratch, but also the contamination in the form of a needle-like structure across the PMMA and glass surface which will be discussed later. Figure 4.6d shows a sketch of the sample.

For the next images, the sample was turned upside down and an oil immersion objective with NA = 1.4 was used. The integration time was 7 ms/spectrum resulting in a total acquisition time of only 5.4 min. (including 0.3 s/line for the back-scan). Figure 4.7 shows 12 images acquired under the same conditions with different gain settings ranging from 16× to 1000×.

Again, the signal around the CH stretching band was integrated to obtain the images. As one can see, the S/N ratio strongly increases up to a gain setting of about 200×. Above this, no further improvement in S/N is visible in the images.

In Fig. 4.8, the S/N ratio of the signal from the CH stretching band of the PMMA is plotted against the EMCCD gain. The standard deviation of the signal was interpreted as noise. As one can see, the signal increases up to a gain of 300×, which appears

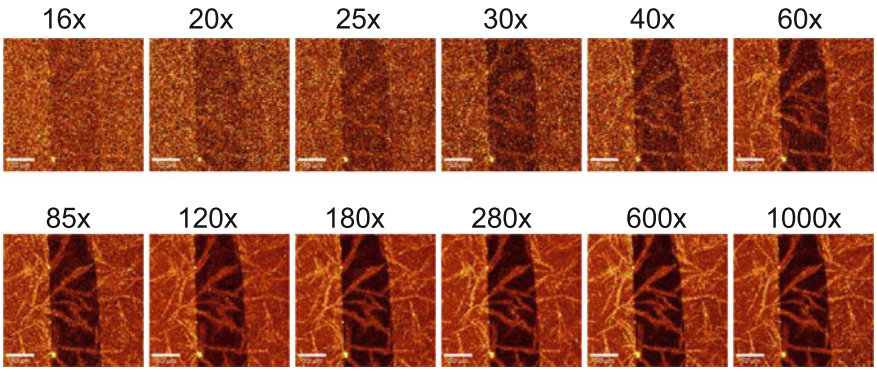

Fig. 4.7 Comparison of confocal Raman images acquired with different settings of the EMCCD gain

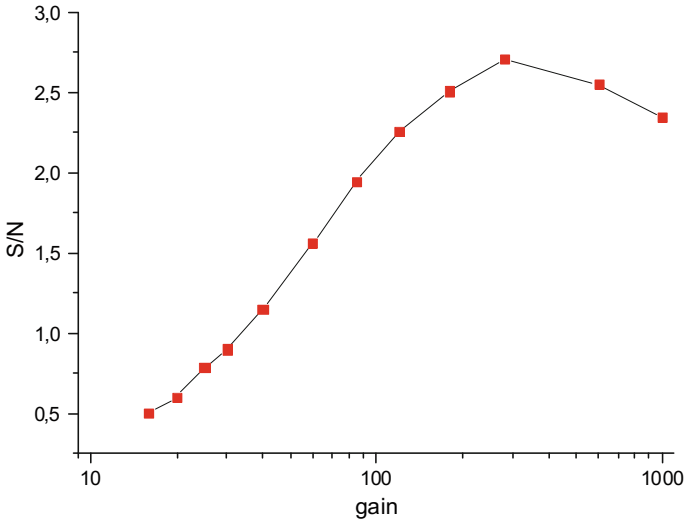

Fig. 4.8 S/N of the signal from the CH stretching band of PMMA plotted against the EMCCD gain.

to be the optimum setting. Above this value, the S/N value slightly decreases again. Using the appropriate gain factor, the overall improvement is more than a factor of 5.

Due to the limited confocal depth resolution, none of the spectra obtained was a pure PMMA spectrum or a pure spectrum of the contamination layer. However, by averaging all spectra acquired in the area of the scratch with no contamination present, a pure glass spectrum was obtained. By subsequent subtraction of the glass spectrum from the PMMA spectrum as well as from the spectrum of the contamination, pure PMMA and contamination spectra could be calculated. These spectra were used for a basis analysis, in which each measured spectrum is fitted as a linear combination

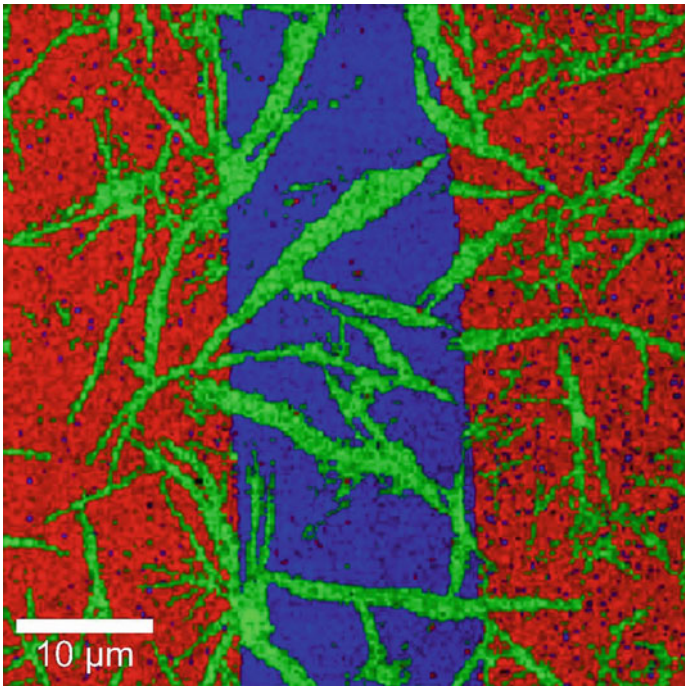

Fig. 4.9 Confocal Raman image of a 7.1 nm PMMA layer (red) and a 4.2 nm contamination layer (green) on glass (blue). 200 × 200 spectra, 7 ms integration time per spectrum. Total acquisition time: 5.4 min

of basic spectra [7, 8]. Using this technique, three images with the distribution of the three components (glass, PMMA and contamination) could be obtained which were then color-coded (blue = glass, red = PMMA and green = contamination) to visualize their distribution (Fig. 4.9).

Figure 4.10 shows the spectra of the different components. From this, the green spectrum (contamination) could be easily identified as an alkane spectrum.

The sample was prepared for the AFM thickness investigation several weeks before the Raman measurement and stored in a polystyrene (PS) container. These PS containers are produced by injection molding and alkane is used to coat the mold for better separation. As the sample was stored (perhaps in a warm environment), part of the alkane evaporated and condensed onto the sample, which explains the needle-like structure and the fact that the coating also covers the scratch.

The maximum peak intensity of the PMMA band at 2950 rel. cm^{-1} in Fig. 4.10 is 28 counts. The signal integrated over the complete CH stretching region (about 330 cm^{-1} or 150 pixels) is 1965 counts. The EM gain for this measurement was about 600×, so the 1965 counts correspond to only 98 electrons (109 photons) total. This corresponds to an average of 0.65 electrons (0.7 photons) per pixel and 1.4 photons maximum per CCD pixel in each spectrum recorded. This is possible because

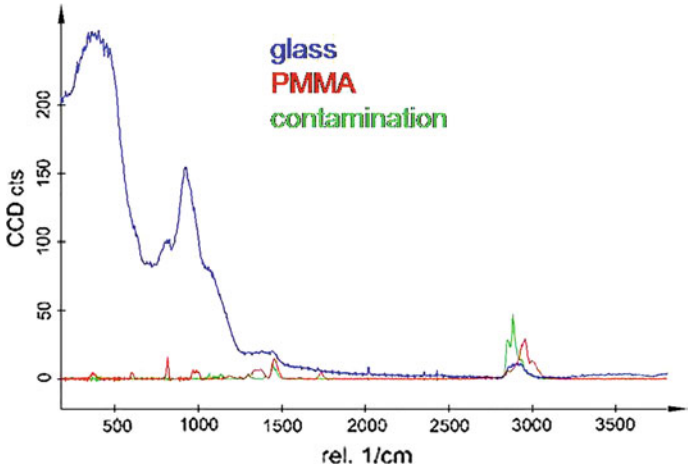

Fig. 4.10 Raman spectra as calculated from the Raman measurement in Fig. 4.9

approximately 20,000 spectra were averaged to calculate the PMMA spectrum shown in Fig. 4.10, so the overall signal is 20,000 times greater. However, only spectra in which PMMA could be detected were taken. For this, the signal per spectrum must be strong enough to show the distribution of the PMMA in the Raman image, which enables one to select the correct spectra for averaging. As can be seen from Fig. 4.7, 0.7 photons per EMCCD pixel are more than enough to visualize the distribution of the PMMA layer in this example and to choose the appropriate spectra for the averaging process.

The result would have been even more impressive if a substrate with no background signal in the CH stretching regime would have been used. As can be seen from Fig. 4.10, the glass substrate has a small Raman band with about half of the signal of PMMA and about one third of the alkane signal in exactly the same area. It is obvious that the confocality of the Raman system is crucial for investigating thin layers. Even with the best confocal setup, the information depth is at least 500 nm, which means that 500 nm of glass contributes to the Raman signal. As the Raman signal is proportional to the amount of material, a standard (non-confocal) setup would have collected a glass signal more than 300 times greater (170 µm cover glass thickness), making detection of the thin coating layers impossible, even with much longer integration times.

4.5 Conclusion

Confocal Raman imaging is an extremely powerful technique that has applications in a variety of scientific fields. The confocality is important for the suppression of unwanted fluorescence background as well as backgrounds from substrates which

may otherwise completely mask the signal of a thin coating layer. Good confocality additionally allows depth scans to be performed with a high level of depth resolution.

Because of the large number of spectra in an image, integration times per spectrum must be kept as short as possible. Therefore, the system as a whole should be optimized for the highest throughput to maximize the S/N ratio in the spectra obtained. The large number of spectra helps to obtain high quality spectra even if a single spectrum might contain hardly any signal.

Using an EMCCD, the spectra can be kept nearly shot noise limited even at extremely low signal levels. The distribution of a 7.1 nm PMMA as well as a 4.2 nm Alkane layer on a glass substrate could be easily detected and identified with an integration time of only 7 ms per spectrum. This reduced the overall acquisition time to a total of only 5.4 min for a 200 × 200 (=40,000) spectra confocal Raman image. The diffraction limited spatial resolution in this confocal image was 230 nm using a NA = 1.4 oil immersion objective at 532 nm excitation. For very small signals that are dominated by the CCD's readout noise, the use of an EMCCD can improve the S/N ratio by a factor of more than 10 compared to the best available standard CCD's, while for larger signals the electron multiplying circuit can simply be switched off and all properties of a standard (back-illuminated) CCD remain.

References

1. C. Raman, Indian J. Phys. **2**, 387 (1928)
2. T. Maiman. US Patent♯ 3353115 (1961). Apr 13
3. W. Boyle, G. Smith, Bell Syst. Tech. J. **49**, 587 (1970)
4. S. Sze, *Physics of Semiconductor Devices* (1981), p. 407
5. I. Lewis, H. Edwards (eds.), *Handbook of Raman Spectra* (Dekker, 2001)
6. T. Dieing, O. Hollricher, Vib. Spectro. **48**, 22 (2008)
7. U. Schmidt, S. Hild, O. Hollricher, Macromol. Symp. **230**, 133 (2005)
8. U. Schmidt, W. Ibach, J. Mueller, O. Hollricher, SPIE Proc. **6616**(1), 66160E (2007)

Chapter 5
Software Requirements and Data Analysis in Confocal Raman Microscopy

Thomas Dieing and Wolfram Ibach

Abstract In confocal Raman microscopy experiments, hundreds of thousands of spectra are commonly acquired in each measurement. Every spectrum carries a wealth of information on the material at the position where the spectrum is recorded. From each of these spectra the relevant information can be extracted to allow i.e. the determination of the various phases present in the sample, variations in the strain state, or temporal evolutions. For this purpose, the spectra need to be prepared (i.e. background subtraction) before the relevant information can be extracted using appropriate filters and algorithms. This information can then be visualized as an image, which can be further processed and exported for the presentation of the results of the experiment. In this chapter, the requirements of the software in terms of handling the data streams and maintaining the spatial and spectral correlation between the spectra and the created images are illustrated. Spectral data processing features, simple and multi-variant algorithms for image creation as well as advanced data processing features are discussed.

5.1 Introduction

In the previous chapters the theoretical background as well as the instrumentation requirements for a confocal Raman microscope were illustrated. In addition to the hardware, software enabling the data handling and analysis plays a crucial role in enabling the acquisition and presentation of results of confocal Raman data.

Generally, the software included with commercially available confocal Raman microscopes facilitates data acquisition as well as data evaluation to varying degrees. Other software available on the market is purely focused on data evaluation.

T. Dieing (✉) · W. Ibach
WITec GmbH, Lise-Meitner-Strasse 6, 89081 Ulm, Germany
e-mail: thomas.dieing@witec.de

W. Ibach
e-mail: wolfram.ibach@witec.de

J. Toporski et al. (eds.), *Confocal Raman Microscopy*, Springer Series in Surface Sciences 66, https://doi.org/10.1007/978-3-319-75380-5_5

The requirements for the software for data acquisition are described in Sect. 5.2 before a general description of the data sets acquired in confocal Raman microscopy experiments is presented in Sect. 5.3.

Once the data is acquired, it can be treated in various ways. In most cases, a pre-processing will first take place such as cosmic ray removal, background subtraction or normalization of the spectra. These are usually applied to both single spectra as well as multi-spectral data sets and are described in Sect. 5.4. Multi-spectral data sets are then commonly evaluated further to extract the information in a way that it can be displayed. For data sets originating from confocal Raman microscopy experiments, where at each image pixel a full spectrum was recorded, this evaluation will result in an image or a 3D stack. This image generation can be performed using either single-variant or multi-variant methods. The resulting images and masks can then be evaluated further in combination with the multi-spectral data set in order to obtain, for example, average spectra originating from certain areas on the sample. Combining the information contained in single spectra with the multi-spectral data sets allows further enhancement of the image contrast. These steps are described in Sects. 5.5, 5.6 and 5.7. Combining the images generated allows the information contained in various images to be displayed in one multi-colored image (Sect. 5.8). From these images, phase separation and/or mixing can easily be identified.

In Sect. 5.9 it will be illustrated that even very noisy spectra acquired with extremely little signal can be treated through the described methods to extract the relevant information and obtain images with excellent contrast.

All the above mentioned data processing techniques will be shown using a few sample systems which are introduced together with the acquisition parameters in Sect. 5.10.

5.2 Requirements for Data Acquisition Software

The requirements for any data acquisition software for confocal Raman microscopy are extensive. The main tasks can, however, be sorted into several groups, which will be described in the following.

5.2.1 Data Acquisition

5.2.1.1 Acquisition of Spectra

For the acquisition of spectral data the software must first read and store the data acquired by the spectroscopic CCD camera. While this may at first appear straight froward, it can already pose some significant challenges for the software.

Consider a spectroscopic CCD camera with 1600×200 pixels. Such cameras can be readout in a full vertical binning mode, by reading out only a certain region

of interest or by reading out the entire chip as an image. The first cases, however, allow a significantly faster readout. A single spectrum readout from such a CCD camera will in this case consist of 1600 integer values, which corresponds to a size of 2×1600 Bytes $= 3200$ Bytes per spectrum if using a 16-bit AD converter.

State-of-the-art CCD cameras such as EMCCDs can acquire single spectra in extremely short times (i.e. 0.66 ms has already been demonstrated [1]). This corresponds to more than 1500 spectra per second. The software must therefore be capable of handling this data stream of 1500 spectra/s $\times$ 3200 Bytes/spectrum $\approx$ 4.6 MB/s. The challenge for the data acquisition software is, that most modern cameras are connected to the PC via USB and thus the data stream needs to be handled by the processor which at the same time needs to be able to manage all other tasks for the control of the microscope. Additionally, the data stream must be handled in a way that allows data acquisition without interruptions. If the software needs pauses after a certain number of acquired spectra to process and/or store the data, the advantage of the fast data acquisition is lost.

If the entire CCD chip of the camera must be readout (i.e. due to the necessity to acquire a reference, calibration spectrum with each spectrum recorded) the data stream would multiply by the vertical size of the chip (200 in the example above) thus lowering the maximum acquisition speed significantly. In addition a shutter would be needed in this case to block the light during the readout process.

An additional challenge for the software is memory space required by the spectra recorded. If, for example, a Raman image of 4096×4096 spectra is recorded, this results in a data amount of

$$4096 \times 4096 \text{ spectra} \times 3200 \text{ Byte/spectrum} \approx 56 \text{ GB}.$$

While such pure two-dimensional scans with more than 16 million spectra are rarely performed (see for example [2]), it sets a bench mark for the performance of the respective software package. Even more so, since large data sets are easily accumulated once the scans are performed in three dimensions. Once scanning for example a data set of $500 \times 500 \times 50$ spectra the software has to handle 12.5 million spectra as well. Note also that once data processing starts, the data is typically transformed from integer (2 bytes) to float (4 bytes) to increase the accuracy of the calculations. This almost triples the storage space needed per spectrum because it is convenient to keep the data of each processing step in order to allow an easy retracing of the data evaluation steps taken.

Adding to the issue of memory space is that many analysis methods such as multivariate analysis require a substantial additional amount. Programmers must therefore balance computation time against available memory.

5.2.1.2 Control of the Microscope and Sample Positioning

In addition to the acquisition of the spectra discussed in the previous section, the software also needs to control all other parameters of the microscope. These are, but

are not limited to, the control of the positioning of the grating within the spectrometer as well as the control over the position at which the spectra are recorded. The latter is either done by moving the sample through the focussed laser spot or by moving the laser spot itself. Since high resolution objectives with high numerical apertures and magnifications are often used, sample scanning has the advantage that the image size is not limited by the field of view.

In order to achieve high resolution images, it is necessary to perform this positioning with a high level of accuracy from both the control electronics as well as the controlling software. The software should also allow the acquisition of white light

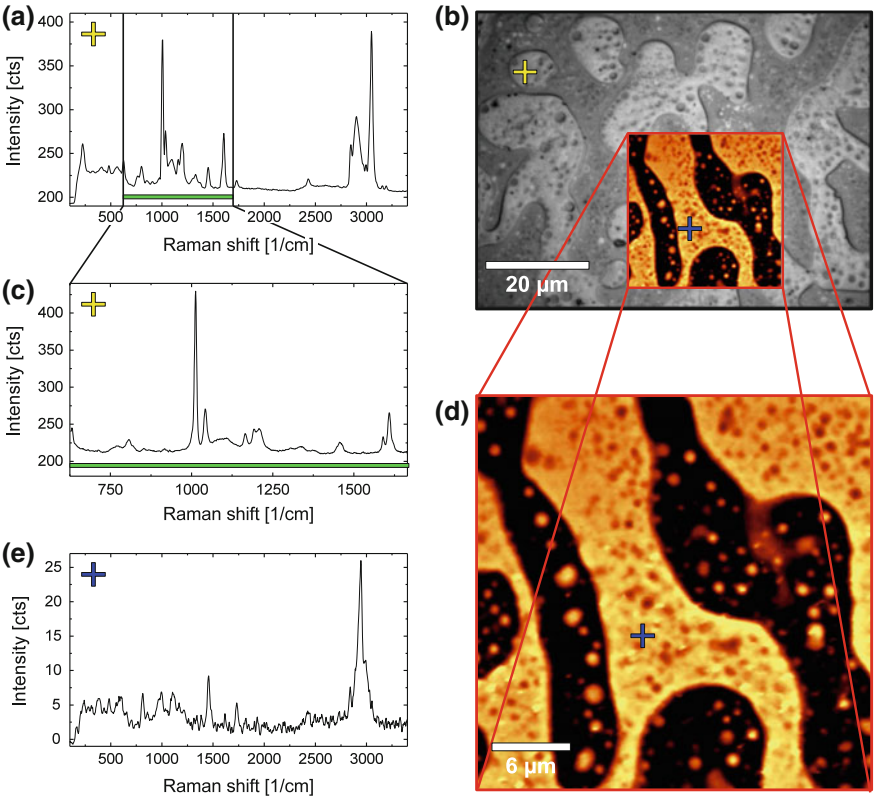

Fig. 5.1 Spectral and spatial correlation within the data acquisition software. The spectra recorded (**a**, **c**, **e**) are linked to the position where they are recorded as indicated by the yellow and blue crosses. The spatial correlation between the video image (**b**) and the confocal Raman image (**d**) is indicated by the red box and the Raman image is overlaid onto the white light image in this example. Additionally, the spectral axes are correlated for spectra recorded with different gratings as indicated by the green bar for a spectrum recorded using a 600 g/mm grating (**a**) and an 1800 g/mm grating (**c**). **e** Shows one of the spectra recorded for the confocal Raman image (**d**) and its position correlation (blue cross)

images at the position where measurements are taken as well as white light stitching images over areas larger than the field of view of the objective.

5.2.2 *Correlation of Spatial and Spectral Data*

Apart from the above discussed data acquisition, the software needs to establish correlations between and among the data acquired. For example: The software should be capable of indicating where the spectra were recorded on the bitmap representing the white light image of the sample. Also, after the generation of a confocal Raman image though i.e. an integral filter over a certain spectral region, the software needs to allow the display of the spectra at each position of the image by a simple mouse click to facilitate the analysis. Additionally, if spectra were taken with different gratings (and thus different spectral resolutions), the software needs to be able to correlate these spectra with each other. Figure 5.1 displays these correlations using the example of several measurements on a polymer blend sample (PS-PMMA on glass).

5.3 Description of the Data Sets Acquired in Confocal Raman Microscopy

Data acquired in confocal Raman measurements are generally five or even six dimensional. The dimensions are:

- The spatial X, Y and Z coordinate of the point where the spectrum was recorded (typically given in μm).
- The spectral position given as the wavenumber (cm^{-1}), relative wavenumber (rel. cm^{-1}) or wavelength (typically given in nm)
- the intensity recorded at this spatial and spectral position (typically given in CCD counts or counts per second [cps])
- Time may also be present as a sixth dimension.

Such a data set is sometimes referred to as a *hyperspectral data set*.

Individual spectra can of course be displayed in a straightforward way (Intensity vs. spectral position) with the coordinates (and time if applicable) added in writing.

Displaying data sets containing more than one spectrum, however, becomes more complicated. Line scans (spectra collected along a single line) as well as time series (spectra recorded at the same position as a function of time) are sometimes displayed in a so-called waterfall display as shown in Fig. 5.2.

For confocal Raman image scans, an entire Raman spectrum is collected at every image point. A confocal Raman image scan consisting of 400×400 points will therefore contain $400 \times 400 = 160{,}000$ individual spectra. One may distinguish between a single image scan, in which the spectra are recorded in one layer in 3D

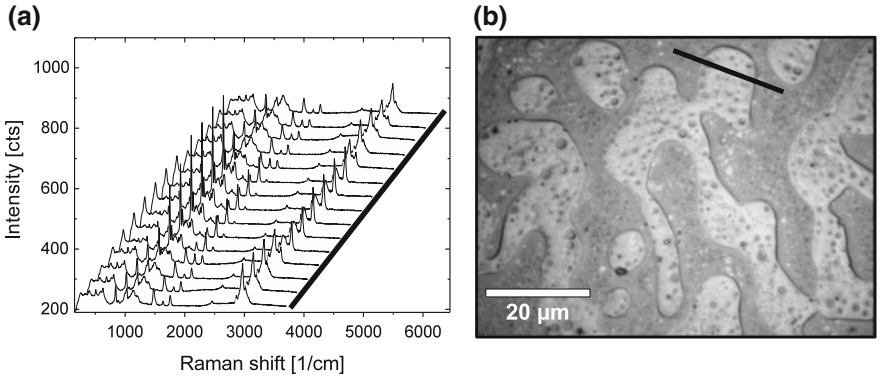

Fig. 5.2 Display of a line scan recorded along the line represented in red in the video image (**b**), in the form of a waterfall plot (**a**)

space, and a multi-layered or stack scan, in which several parallel layers offset by a specific distance are recorded.

In either case, the information contained within each spectrum needs to be reduced to a single value, which will then determine the coloring of the pixel at this position (see also Sect. 5.5).

In the case of an image stack one can then display each layer of the stack individually or combine them with software in order to display the distribution in three dimensions. Some examples of this can be found in Chap. 21 by Thomas Wermelinger and Ralph Spolenak, in Chap. 11 by Andrey Korsakov as well as in Chap. 6 by Thomas Dieing.

5.4 Pre-processing of Raman Spectra

Pre-processing of Raman spectra refers to the treatment of the Raman spectra before the generation of images or final presentation of the spectra. The steps described below are universal to spectra recorded and should generally be followed before any further processing.

5.4.1 Cosmic Ray Removal

Cosmic rays are high energy particles from outer space which interact with atoms and molecules in the Earth's atmosphere. Due to their high energy, a large number (often called a shower) of particles are generated upon this impact which are mainly charged mesons. These quickly decay into muons. Due to their relativistic speeds (and thus

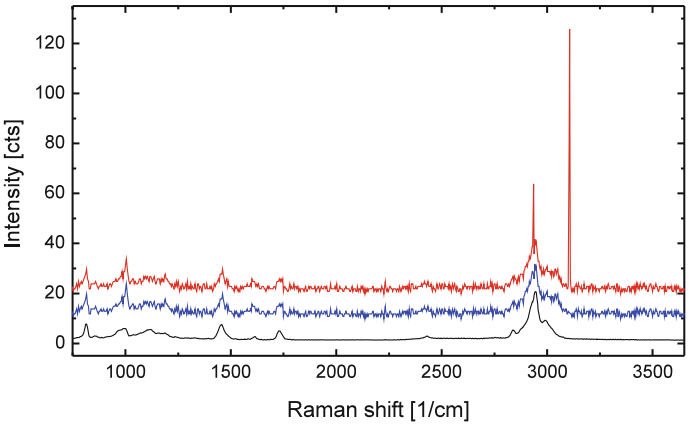

Fig. 5.3 Cosmic Ray removal. The red spectrum was recorded with a short integration time and shows two cosmic rays near 3000 rel. cm^{-1}. The blue spectrum is the same as the red, but after having undergone cosmic ray removal, and the black spectrum is the spectrum of this component (PMMA) recorded with a longer integration time for a better signal to noise ratio

the time dilation) some of these muons reach the surface of the Earth. Despite this exact reaction path, the term "cosmic ray" is also used (even if not 100% correct) for the muons interacting with devices on the Earth's surface and for simplicity, this term will be used in the following as well.

If such a cosmic ray hits a CCD detector it will generate a false signal in the shape of a very sharp peak in the spectrum that is not related to the Raman signal. An example can be seen in red in Fig. 5.3.

Cosmic rays can be filtered out as shown in Fig. 5.3 and described below. There is, however, also the possibility to minimize the amount of cosmic rays recorded through the readout method of the CCD camera. As already described in Sect. 5.2.1.1, one method is the full vertical binning mode, which is the fastest readout method. In this case, all pixels are used even though typically only a few % of the pixels are exposed to the Raman signal. If one limits the readout to the few lines in the detector at which the Raman photons hit the CCD camera, one typically excludes more than 90% of the pixels from the readout. This will of course reduce the probability of recording a cosmic ray. The disadvantages of this method is that it is a slower readout method and that during the readout, the light hitting the camera cannot be recorded. This method is therefore recommended for single spectra, whereas for Raman imaging it is not very suitable.

Once the spectra are recorded, various mathematical methods can be used to filter the cosmic rays from the spectra. In these, two principal approaches can be distinguished. These will be discussed in the following.

5.4.1.1 Spectral Cosmic Ray Removal

Filtering spectra in the spectral domain for cosmic rays has the advantage that this method works for true, one-shot exposures as well as for multiple accumulations, time series or Raman image scans.

The principle of this method is that each pixel is compared to its adjacent pixels and if it exceeds a certain threshold, then it is identified as a cosmic ray. This method is heavily dependent on the size of the filter (=the number of adjacent pixels taken into account) and the threshold (or multiplicative factor). Therefore, any spectroscopic software should allow the adjustment of these values as well as the preview of the resulting spectrum to allow the user to select the correct parameters.

While this method can be problematic when using very sharp atomic emission lines, it works very well for Raman spectra in which (with only few exceptions) the natural line widths (FWHM) are typically $>3\,\mathrm{cm}^{-1}$. Additionally, Raman lines typically display a relative broad base of the peaks similar to Lorenzian curves. The Raman lines therefore have a certain rise, which is beneficial for this type of detection algorithm. It of course also depends on the spectral resolution of the spectrometer used.

Other methods for cosmic ray removal involving further computational methods are reviewed in the literature (i.e. [3]), but discussing these would exceed the scope of this chapter.

5.4.1.2 Temporal Cosmic Ray Removal

Removal of cosmic rays based on variations over time is also a very popular method. In this case spectra recorded one after another are compared and each pixel is compared to its variation in the time domain.

This method works well when evaluating single spectra with various acquisitions on the same position. It requires that there are only negligible changes from spectrum to spectrum. If the sample changes its spectral signature in a rapid way (for example due to a chemical process taking place), the usage of this type of algorithm is problematic.

For confocal Raman imaging data sets, this method should not be applied. The user must be aware, that in this case the spectra are not only recorded at different times, but also at different spatial positions. In this case it additionally depends on the compositional variation of the sample compared to the resolution of the scan. If the changes from spectrum to spectrum are too dramatic, one faces again the problem that the algorithm might filter out real peaks.

5.4.2 Smoothing

Smoothing is a common practice used to reduce the noise potentially associated with a recorded spectrum.

Most smoothing algorithms rely on the fact that spectral data (in our case Raman) is assumed to vary somewhat gradually when going from spectral data point to data point, whereas noise associated with the spectrum typically changes very quickly. In this case, it can be useful to replace each value by a value calculated from the surrounding values in order to reduce the noise. Therefore, most filters for this purpose can be considered as low pass filters. Independent of the filter used, care must be taken in order to avoid alteration of the true Raman signal. Overly extensive smoothing for example will result in a "smearing" of the Raman peaks, thus altering their height and/or width. Additionally, small shoulder peaks might be lost.

The various filters which can be applied to the data essentially differ most significantly in the way that the replacement value is calculated. Most filters will allow the definition of how many values are taken into account around the value to be replaced. The software should allow the user a preview of the results in order to facilitate the choice of parameters.

The following filters are a typical selection of those used to smooth spectral data:

1. **Moving Average**:
   This filter is arguably the simplest filter for smoothing. For this filter a definable number of values to the left and right of the current value are averaged and the current value is replaced. Then this "window" moves to the next value and so on. For very slow changing signals (as might be the case in photoluminescence [PL]) this filter can be suitable.
2. **Weighted Average**:
   This filter differs from the *Moving Average* in that it does not take each value with the same weight, but multiplies each one with a binomial weighting factor or a Gaussian distribution. Table 5.1 shows the distribution of the binomial coefficients for the average calculation for various filter sizes.
   This filter ensures that the resulting value is closer to the real value as compared to the *Moving Average* filter even if the signal is changing more rapidly.

Table 5.1 Matrices for the graph average filter

Filter size	Range	Filter coefficients
1	3	$\frac{1}{4}(1, 2, 1)$
2	5	$\frac{1}{16}(1, 4, 6, 4, 1)$
3	7	$\frac{1}{64}(1, 6, 15, 20, 15, 6, 1)$
4	9	$\frac{1}{256}(1, 8, 28, 56, 70, 56, 28, 8, 1)$

3. **Median**:
   The median filter is generally less influenced by single data points that fall out of range of the "normal" signal. For example, if a cosmic ray is within the search window, the median filter will be less influenced by this than an average filter. This filter is a good choice for removing spikes in a line graph without heavy rounding of the edges of Raman peaks.
4. **Savitzky-Golay**:
   The Savitzky-Golay filter (sometimes also known as *DISPO (Digital Smoothing Polynomial)* filter) essentially uses the surrounding values in a weighted way and fits a polynomial through these points in order to determine the "fitted" value at the current position. While the smoothing of this filter will not be as strong as, for example, a *Moving Average* filter, it will smooth the data considerably while largely maintaining the curve shape (peak width, peak intensities, …). A detailed discussion of the functionality as well as examples of this filter can be found in [4]. This filter has the additional advantage of allowing the calculation of the derivative of the spectrum, which can be useful for peak location (see black vertical lines in Fig. 5.4). Figure 5.4 shows an example of the usage of the Savitzky-Golay filter.
   The use of this filter is especially recommended if the widths of the peaks in the spectrum are comparable.
5. **Wavelet transformation techniques**:
   Wavelet transformation is a mathematical technique somewhat similar to Fourier transformation but with the advantage that both time and frequency information are maintained. Wavelets consist essentially of a family of basic functions which can be used to model the signal. Each level of the wavelet decomposition will

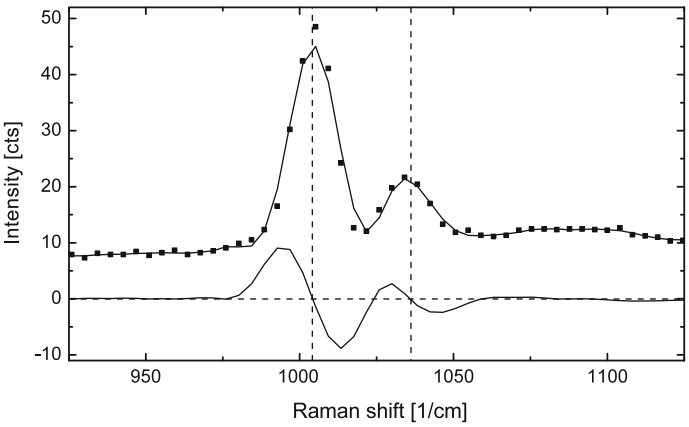

Fig. 5.4 Effect of the Savitzky-Golay filter. The black squares in the top spectrum correspond to the data points recorded from the CCD camera and the solid line shows the spectrum after smoothing using the Savitzky-Golay filter. The bottom curve is the derivation of the spectrum obtained through the Savitzky-Golay filter

result in an *approximation* and a *detail* result. The *approximation* result is then used as the basis for the next decomposition and this is repeated until a defined threshold. By using the correct combination of the *detail* results (one available per decomposition level) and the *approximation* result (only the last one is typically used here) one can perform the reconstruction (or inverse discrete wavelet transformation [IDWT]) to obtain a spectrum with either a strong noise reduction, a removed background or both. More detailed descriptions as well as some illustrative examples can be found in [5, 6].

6. **Maximum entropy filter**:
   The maximum entropy method uses the fact that certain aspects of the instrument functionality are known. Through this, neighboring pixels in a spectrum are not statistically independent anymore and a filtering of these values is therefore possible.

5.4.2.1 Smoothing in Raman Imaging

The filters discussed above can be applied to single spectra as well as to entire spectral data sets. In the case of Raman imaging, the experimenter can also take the spatial correlation between various spectra into account. In other words: For pure spectral filtering only the spectrally neighboring pixels are taken into account, whereas for Raman imaging, the spatially neighboring pixels may also be used. This is especially true for the case of the *Median* and *Average* filters.

Images generated from Raman data (see Sect. 5.5) can also be smoothed and most image filtering methods can be applied to the images. A wide variety of filtering methods is described in [7]. For Raman images, the most prominent filters are the 2D variation for the median and the average filter, but also anisotropic filters [8] or fourier filters are used at times.

5.4.3 Background Subtraction and Subtraction of Reference Spectra

Any Raman spectra read from a CCD camera show some background signal. The sources of the background can be divided into two main categories, and the recommended removal of this background may differ somewhat. These two categories as well as the respective background removal are described below.

5.4.3.1 Background Originating from the CCD Camera

A CCD camera generally adds a DC voltage to the detected signal in order ensure that the A/D converter, which converts the analog charge into a digital signal, will

not receive a negative voltage due to noise. This results in a constant background of typically a few hundred to a few thousand CCD counts.

Most cameras additionally have a slight non-flat background due to various reasons within the hardware and electronics of the CCD such as inhomogeneities in the chip itself or a non-homogenous cooling of the CCD chip.

Removal of a background originating from the CCD camera

The constant background originating from the CCD camera can be subtracted quite easily by subtracting the constant value added by the camera. One can, for example, find this value by averaging the part where the Raman edge filter is still blocking the signal but no Rayleigh peak is present.

The non-flat background of the CCD camera is best eliminated by the subtraction of a reference or "dark" spectrum. A dark spectrum is ideally recorded using exactly the same integration parameters as were used for the recoding of the Raman spectrum. To minimize the noise of the "dark" spectrum, it is recommended to record it with the same integration time as the Raman spectrum, but to use many accumulations using this integration time. The software then needs of offer a simple functionality to calculate $[Raman\ Spectrum] - [Dark\ Spectrum]$. However, the raw data should still be available to the user.

5.4.3.2 True Signal Background

There are very few "real world" materials that will show a complete zero background in their Raman spectrum. Good confocality of the system, however, will largely reduce this background as described in the earlier chapters. Nevertheless, a remaining background such as fluorescence or some signal from the substrate often underlies the Raman spectrum.

Removal of signal background

There are several ways to subtract the background from the recorded spectrum and the methods below can be applied to both single spectra ass well as 2D or 3D data sets. Some of the most prominent are:

Single-Pass Polynomial Background Subtraction

For this type of background subtraction, a polynomial needs to be fitted to the spectrum and subtracted. Care must be taken to ensure, however, that the regions of the spectrum containing Raman peaks are not included in the values used to calculate the fit of the polynomial. This selection can either be done automatically through a peak recognition routine, or manually though defining the regions in the spectrum where no peaks are present. The order of the polynomial is then the next variable which needs to be adjusted. Using a very high (i.e. 9th order) polynomial often fits the data well at first glace, but will often introduce "wave"-like artifact oscillations around the 0 value of the background. Using an order that is too low, on the other hand, might not allow the polynomial to follow the spectrum closely enough.

Contact Line Background Subtraction

This algorithm removes the lower contact line of the spectra. It can be visualized as an object moving underneath the spectrum where the contact point with the spectrum defines the value to be subtracted. The size of the object needs to be controlled in this case to ensure, that only the background and not wide Raman peaks are subtracted. This method has the big advantage, that the position of the contact can be shifted into the noise level of the spectrum. It thus works even on noisy spectra and can follow a virtually arbitrarily shaped background.

Wavelet Transformation Techniques

The principals of wavelet transformation techniques have already been described in Sect. 5.4.2. Through the appropriate combination of the *detail* results (one available per decomposition level) and the *approximation* result (only the last one is typically used here) one can subtract the background. In this the *approximation* result is generally omitted from the reconstruction.

5.5 Image Generation

Confocal Raman imaging data sets (as described in Sect. 5.3) are typically five to six-dimensional and thus the dimensionality needs to be reduced in order to display the information. As stated earlier, the dimensions are:
X, Y, Z, wavenumber, intensity and time.

Considering a typical Raman Image, which is a single scan along one plane, the dimensionality reduces to the two directions of the plane (let us assume X and Y for simplicity), the wavenumber and the intensity. While this is still a four-dimensional data set, we can in a quite straightforward way display the information from this.

For the image generation two main methods may be distinguished: Univariate and Multivariate analysis. The primary difference is that for a univariate analysis one spectrum at a time is evaluated and used for the generation of one data point per resulting image. In contrast to this all spectra in the data set play a role for each data point in the case of the multivariate data analysis. Typical uni- and multivariate methods will be described in the following sections.

5.5.1 Univariate Image Generation

As stated above, in univariate data analysis, each spectrum determines one value of the corresponding pixel in the image or the images. The value of these pixels can be determined by simple filters or by fitting procedures.

5.5.1.1 Simple Filters

Simple filters typically evaluate a certain part of the spectrum. Figure 5.5 shows an example of an integrated intensity (sum) filter evaluating the integrated intensity of various specific peaks found in the image scan of an oil-water-alkane immersion. The resulting images (Fig. 5.5c–e) show in more brightly colored areas the high intensities of these peaks and in darker colored areas the low intensities. Other types of filters can evaluate, for example, the peak width or the peak position and display this as an image.

It should be noted that many of the filters used allow the extraction of a large amount of information from the data. However, there is also the danger of misinterpretation. The list below shows some typical simple filters and their usage as well as considerations which should be taken into account to avoid misinterpretations.

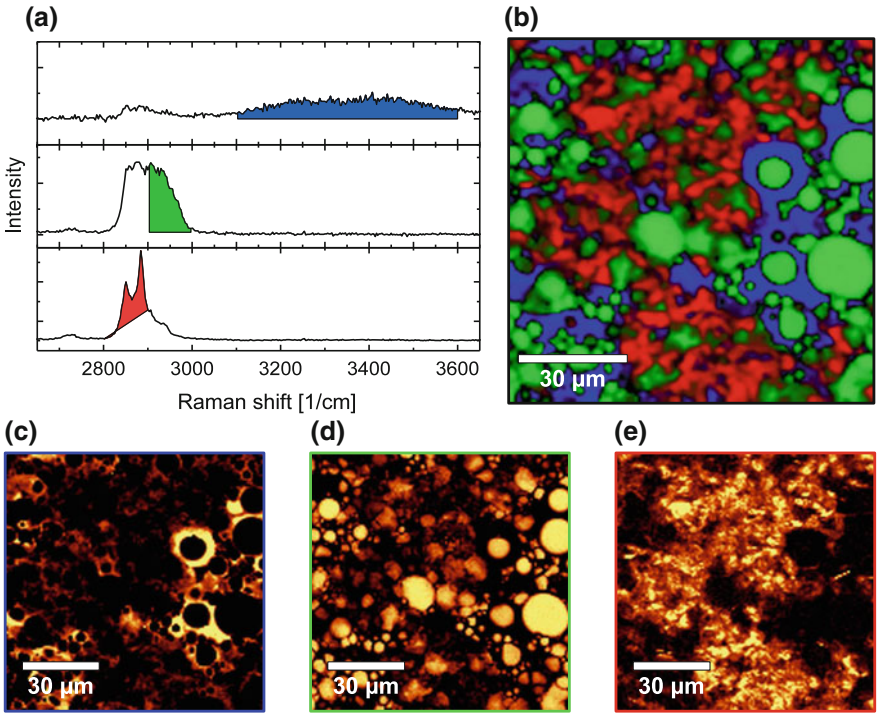

Fig. 5.5 Usage of an integrated intensity filter with an oil-water-alkane immersion. The spectra (**a**) are integrated in three different spectral areas. The water peak (blue) is evaluated without background subtraction and results in image (**c**). The oil peak is integrated as shown in green with the pixels adjacent the higher wavenumber side of the peak used as the background level and results in image (**d**). The Alkane is using pixels to the left and right of the integration area for background calculation (red) and results in image (**e**). Image (**b**) shows the combined image of (**c**), (**d**) and (**e**)

- **Integrated Intensity Filter (Sum Filter)**

  Information Content:
  A typical measure of the amount and scattering strength of a certain material within the focus.
  Misinterpretation Dangers:

– Other materials present in the sample might also have peaks at this position.
– The amount of material between the objective and the focal point might change and this would also have an influence on the absolute intensity of the peak.
– The polarization direction of the laser relative to the structure can also have an influence on this peak intensity.
– If the software does not provide good background subtraction methods, then changes in the background such as a change in fluorescence can influence the result.

- **Peak Width (i.e. FWHM)**

  Information Content:
  A measure of the crystallinity and the structural orientation relative to the polarization direction of the laser. Also, inhomogeneous peak broadening can occur in samples under stress for example.
  Misinterpretation Dangers:

– Non-resolved shoulder peaks can influence this result.
– If the software does not provide good background subtraction methods, then changes in the background can influence the result.

- **Peak Position (i.e. Center of Mass position)**

  Information Content:
  A measure for the strain within a material and for the general chemical neighborhood of the molecule
  Misinterpretation Dangers:

– Non-resolved shoulder peaks can influence this result
– If the software does not provide good background subtraction methods, then changes in the background can influence the result.

Simple filters have the advantage of being relatively low in processor load and thus they can be applied during ongoing data acquisition.

5.5.1.2 Fitting Filters

Fitting filters are a more sophisticated way of extracting the information required from the spectra. In this case part of the spectrum is fitted to a mathematical model. Most models are peak functions, which should be motivated by the theoretical description of the Raman lines. Depending on the state (solid, liquid or gas) and the environment

of the molecules observed by Raman spectroscopy, the line shape of the emitted Raman line can lie anywhere between a Gaussian and a Lorenzian curve.

Voigt curves represent a convolution between Lorenzian and Gaussian curves and Pseudo-Voigt curves are calculated by

$$m_u \times Gauss + (1 - m_u) \times Lorenzian.$$

Here m_u is the profile shape factor.

In addition to the above discussed mixture of Lorenzian and Gaussian line profiles, the Raman curves may also be distorted by the local sample environment. If Silicon (Si) is for example exposed to high power laser radiation, one can detect a peak distortion of the first order Si peak. Instrument functions will play an additional role. The change of the signal due to these instrument functions is heavily dependent on the microscope and spectrometer design [9] and it will depend on the instrument if this needs to be taken into account for peak fitting.

For these reasons, there is not one perfect peak function which can be used to perfectly match all Raman peaks. Table 5.2 shows some common fitting filters and which information can be obtained through them.

As can be seen from Table 5.2, all of the filters listed deliver more than one result per curve fitted. Therefore, the results after applying such filters to a confocal Raman image data set are multiple images as can be seen in Fig. 5.6. In addition to the results described in Table 5.2, the software should provide an error image in

Table 5.2 Fitting filters for spectral data

Filter	Information content (results)
Linear fit	– Slope – Offset
Quadratic fit	– Peak position – Curvature – Peak intensity
Gaussian fit	– Peak position – Width – Integrated intensity – Offset
Lorenzian fit	– Peak position – Width – Integrated intensity – Offset
Pseudo Voigt fit	– Peak position – Width (Gaussian and Lorenzian) – Integrated intensity – Offset – Profile shape factor

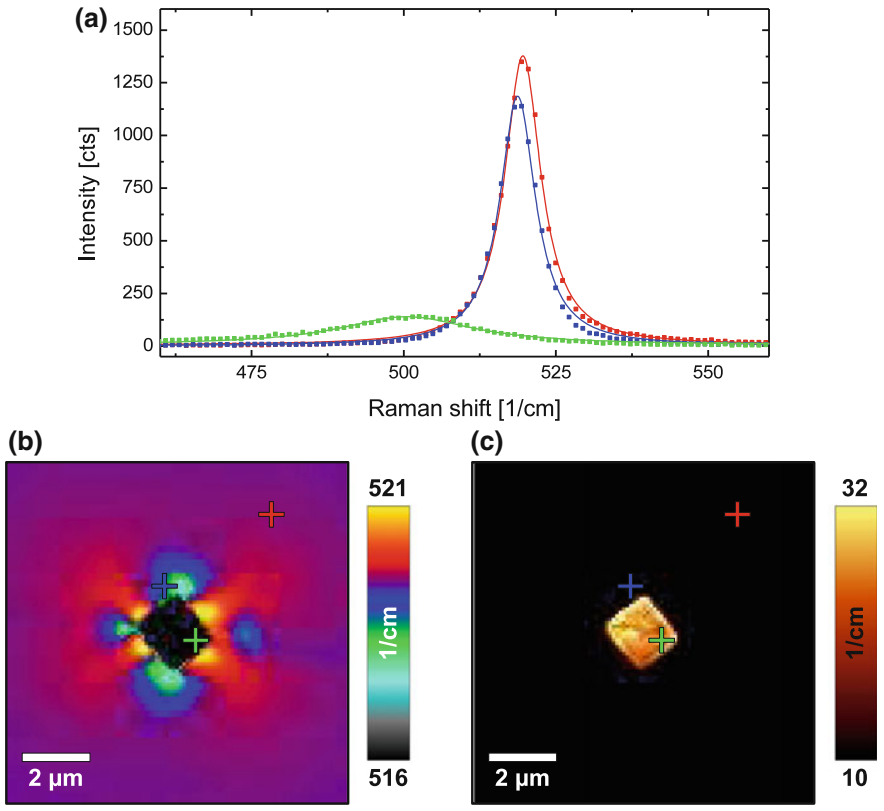

Fig. 5.6 Lorenzian fitting of 1st order Si peaks around a Vickers indent. The spectra (**a**) are extracted from the points indicated by the corresponding colors in the images. **b** Shows the position of the 1st order Si peaks and **c** shows the width of the line. Both are results from a Lorenzian fit

order to allow the user to quickly determine if the fitting error in a certain region is larger due to, for example, a line distortion. In Fig. 5.6a confocal Raman image was recorded of a Vickers indent in Si and the resulting spectra were fitted using a Lorenzian function. The peak shift as well as the broadening can clearly be seen from the spectra (Fig. 5.6a) as well as from the images (Fig. 5.6b, c).

The accuracy of a fit heavily depends on the signal to noise ratio of the data acquired. A noisy data set can never achieve the same accuracy when compared to a data set with high signal to noise ratio. An easy test of the accuracy for a given system, laser power and integration time is the consecutive recording of i.e. 1000 spectra on the same sample position. After the fit of all of these spectra one can for example plot the position in a histogram and determine the standard deviation of the measurement (see for example Fig. 6.1 in Chap. 6). As a consequence, measurements for the exact determination of a peak shift and/or a peak broadening tend to require a longer

integration time per spectrum than scans, wherein different phases are determined based on the presence of certain Raman bands.

5.5.2 Multivariate Image Generation

As mentioned in a previous section, multivariate image generation uses the information of the entire hyperspectral data set for the determination of the value (and thus the color) of each image pixel. In the following the two most commonly used multivariate data analysis methods for the analysis of Raman spectra are presented. First the so-called *Principal Component Analysis* is discussed. This method is not only used for image generation, but also for data reduction and distinction of sample properties based on the principal components.

The second method described is the *Cluster Analysis* which can be used for direct image generation or average spectra calculation for further data analysis (see for example Sect. 5.7).

Vertex component analysis (VCA) is another multivariate method which finds the most dissimilar spectra in the data set as described in Chap. 13 by Christian Matthäus et al.

5.5.2.1 Principal Component Analysis

Principal Component Analysis (PCA) was first proposed in 1901 by Karl Pearson [10]. However, only the use of computers allowed its usage as we know it today due to the large computational effort required by the method. PCA is the underlying method for many other multivariate methods since it is very effective for data reduction. In this way a spectrum consisting of 1600 pixels and thus 1600 dimensions can often be reduced to approximately 4–6 dimensions. In some cases, this is then also the number of different components in the sample, since all the other spectra are a linear combination of the pure component spectra (see also Sect. 5.7).

In the following this reduction is explained in a greatly simplified way. The user is referred to, for example, [11, 12] for further reading and detailed explanation of the method.

Principal function of the PCA

If we assume a single spectrum consisting of 1600 pixels, then this spectrum can be described as a single point in 1600-dimensional space. Each of the CCD pixels belongs to one axis within the 1600-dimensional space and the value recorded at this CCD pixel is the coordinate along this axis. If we now look at a confocal Raman image, then we might have for example 150 × 150 (=22,500) spectra and we will thus have 22,500 points in our 1600-dimensional space. Now let us consider a Raman peak which is present in some of the spectra. As most Raman peaks are significantly wider than a single pixel the pixels describing this peak are

not statistically independent. Furthermore, most Raman spectra consist of more than one peak. Therefore the pixels which will increase if such a Raman spectrum is recorded are linked. In our 1600-dimensional space, this corresponds to a certain direction called the "Eigenvector". Analyzing the entire data set will result in a variety of such Eigenvectors. These directions span a subspace in the 1600 dimensional space wherein all spectra can be found. These directions are orthogonal to each other, but cannot be identified as pure components, since for example, they might point in the negative direction. Each of those Eigenvectors has a certain "importance" called the "Eigenvalue". The magnitude of each Eigenvalue depends on the amount of variation within the data set explained by this direction. There is a strong spread in their value and some might be hundreds of times the value of others. Sorting them by value allows the quick determination of the relevant directions (=the principal components). If the sample consists, for example, of three components, then three principal components should describe the dataset sufficiently, while the other directions should then only describe noise. PCA can only work if the dataset is not dominated by noise. Otherwise, even the principal components with the highest Eigenvalues will only describe noise and thus all directions are equally good or bad.

Results from a PCA

Following the PCA, one can extract a variety of results. The most commonly used for the analysis of confocal Raman data are:

Reduced Data set:

Each of the 22,500 spectra used for the PCA is now described through principal components. As mentioned above a relatively small number of components is sufficient to describe the spectrum clearly. We can therefore export these "spectra of components" which now consist of only a few pixels instead of 1600 at each image pixel and use this for further investigation such as cluster analysis, which will then be much faster.

Images of the principal components:

Each of the spectra used for the analysis can be described by a weighted combination of the principal components. If we now consider only one component, then this will result in one value per image pixel and we can of course display this, which then corresponds to the Raman image describing the abundance of a certain spectrum (direction) within the data set.

Reconstructed spectra from the principal components:

If we calculate the spectra using for example only 5 components, then we will find spectra with much lower noise. Due to the fact that the noise is statistical and will not be described by one of the first approximately 20 directions, the noise will be reduced. Please note here, that this is only true if the spectra are recorded with a sufficient signal to noise ratio (S/N). For a S/N close to 1, no PCA is possible. In this case the noise would determine the "directions" of the principal components.

Cross correlation plots of various components:

If we consider our spectra again and plot a point for each spectrum at a corresponding position in a coordinate system of principal component A versus principal component B (or C, D, …) we can visualize the correlation between the components. We might have clearly separated point clusters, or we might have them aligned along a diagonal, for example. Such representations are often referred to as "score-score" plots or - using the loadings - a loadings plots [13–15].

5.5.2.2 Non-negative Matrix Factorization (NMF)

The results obtained through Principal Component Analysis generally contain spectra which show positive and negative peaks. This is mathematically absolutely correct, but cannot represent real Raman spectra. The Non-Negative Matrix Factorization (NMF) overcomes this limitation by only allowing results with positive values. For this the vectors describing the dataset encompass the whole dataset while only pointing in positive directions. For this, the offset vector needs to be defined differently. In PCA this offset vector is the average spectrum of the entire dataset while for NMF the offset vector represents spectral features present in all spectra (such as for example a glass background due to the substrate). Figure 5.7 illustrates schematically the major difference between NMF and PCA.

Here the offset vector for NMF and PCA are shown in green and the corresponding vectors describing the data set in this two-dimensional example are plotted in blue and red. While the red vector for the PCA result shows a negative component, all components are positive in case of the NMF. An important aspect in NMF is to find the vectors which closest encompass the data set, since "wider" vectors would also represent a mathematically correct solution, but would not be a close physical

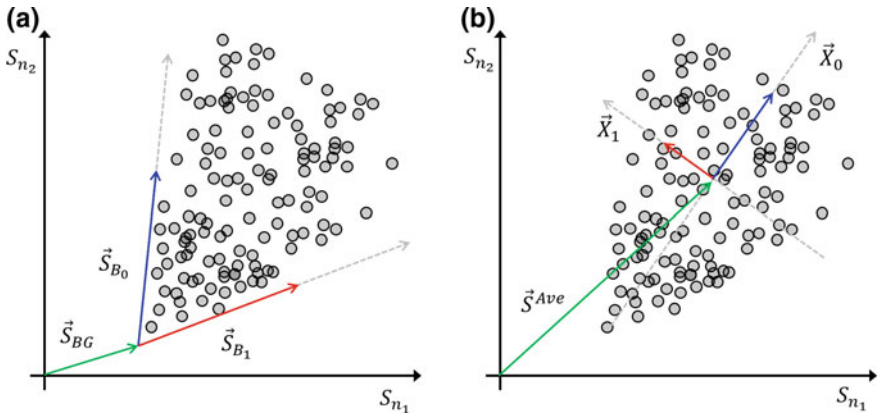

Fig. 5.7 Schematic illustration of the principal difference of the NMF (**a**) compared to the PCA (**b**)

representation of the dataset. If implemented correctly in the software, this method represents a powerful tool, especially when analyzing samples with varying degrees of mixed spectra. The result of the NMF are the describing spectra and the abundance images for each component.

5.5.2.3 Multivariate Curve Resolution (MCR)

In contrast to NMF is the MCR a method, which by its definition does not prevent parts of the resulting spectra to be negative. For this reason constraints have to be applied to the algorithm to ensure, that only positive results are obtained. MCR is often used in conjunction with the alternating least squares (ALS) algorithm, but it is to some degree more sensitive to noise of the spectra when compared to NMF. As for NMF, the results of the algorithm are the describing spectra and the abundance images for each component.

5.5.2.4 Cluster Analysis

Cluster analysis applied to confocal Raman images is essentially the sorting of the tens of thousands of spectra in a data set according to their similarities. As a result one gets a certain number of areas or masks which indicate where the spectra belonging to the various clusters were acquired as well as the average spectra of each cluster. Other applications also include the identification of bacteria strands and even their position in their life cycle or the identification of pathogenic cells [16].

Cluster analysis has the advantage of being an automated and objective method to find similar regions in spectral data sets. It can, however, require significant processing power and time.

There are various ways of clustering the data and each has its advantages and disadvantages. In the following, some clustering principles are briefly introduced before two typical clustering methods as well as one variation are described. For detailed descriptions of cluster analysis, the reader is referred to the literature, for example, [12].

Distance calculation in cluster analysis

As already introduced in Sect. 5.5.2.1, each spectrum can be seen as a single point in 1600-dimensional space (if the spectra contain 1600 pixels). For a confocal Raman image, this might be tens of thousands of points and the cluster analysis tries to group (or cluster) these points. The clustering is mainly dependent on the distance between the points. Spectra which differ significantly from each other will be further apart in the 1600-dimensional space than spectra that are similar or even close to identical. The distance therefore determines which spectrum belongs to which cluster.

There are various ways of defining the distance between the spectra. The Euclidean and the Manhattan distance calculation are but two examples of methods which work well for Raman imaging.

Care must be taken if some of the spectra in the data set contain a high fluorescence background, because depending on the distance calculation method, the fluorescence might have a quite strong influence on the clustering. The background of the spectra should in general be subtracted prior to cluster analysis.

Hierarchical cluster analysis

As indicated by the name, hierarchical cluster analysis creates a hierarchy of clusters. This hierarchy is often represented by a tree. In this analogue, the trunk represents the main cluster containing all spectra. Following this, the clusters are split up int sub-clusters of various sizes (the branches) and these into further sub-clusters (smaller branches, then twigs, smaller twigs, …). The leaves are then the individual spectra in the data set.

In order to calculate the clusters one either starts at the base cluster and splits this up (divisive clustering) or with the individual spectra and merges them together (agglomerative clustering). Now the distance between the clusters must also be taken into account and there are again a variety of methods to calculate this distance such as the maximum distance between elements of each cluster, the minimum distance between elements of each cluster or the mean distance between elements of each cluster. Once the cluster tree is calculated the height, or extraction level, must be defined and from this the masks and average spectra can be extracted.

While this method is almost completely unsupervised (with the exception of the extraction level) it requires a huge amount of processing power and/or time.

K-means cluster analysis

The K-means cluster analysis is often assigned to the partial clustering methods. It differs from the hierarchical cluster analysis in that the number of clusters must be selected prior to the clustering. However, the method can also then be applied to the sub-clusters in order to sort them further into sub-clusters and thus generate a pseudo-hierarchical cluster tree as shown in Fig. 5.8. Here an oil-water-alkane immersion is first clustered into three clusters before the three clusters were again split up into sub-clusters. In this example one can clearly see the mixed phases which are partly due to edge effects and positions at which the laser spot hit the boundary between two phases. Note that water does not exist as a pure component in this sample but is always to some degree mixed with the Alkane.

Once the number of clusters (N) is defined for the K-Means cluster analysis, the algorithm first defines N centers in the 1600-dimensional space and assigns each point (spectrum) the center closest to it. Then the centroid (one might also call it an average spectrum) for each group is computed. Following this the spectra are again sorted according to their distance to the calculated centroids and then the procedure is repeated. The algorithm is typically stopped once the assignment of the points (spectra) to their group ceases to change.

While this method needs somewhat more supervision than hierarchical clustering and is heavily dependent on the selection of the N initial centers, it requires much less processing power and is thus significantly faster than i.e. hierarchical cluster analysis.

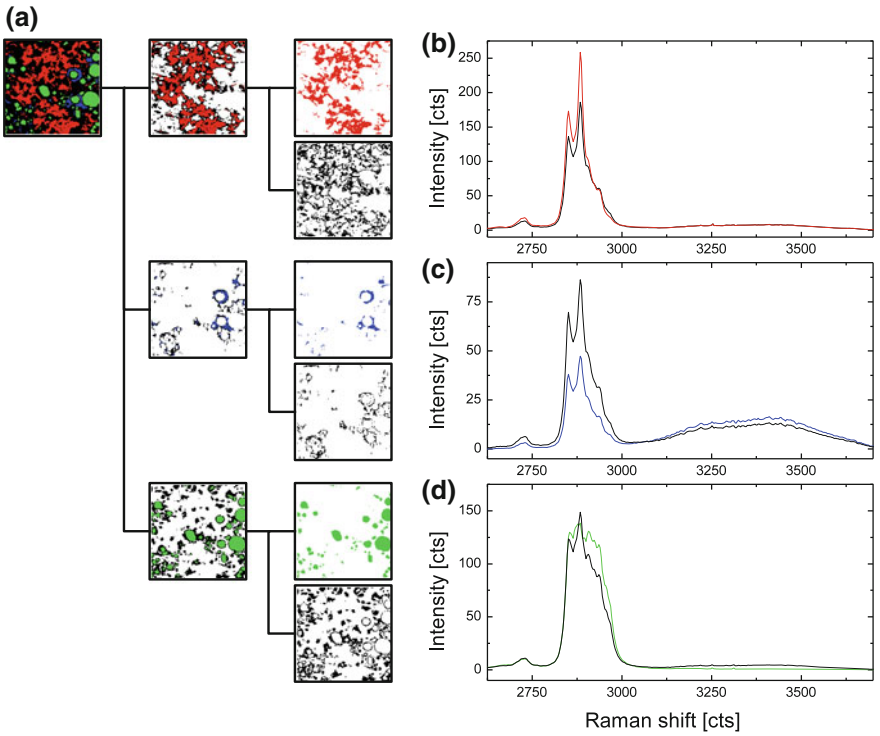

Fig. 5.8 K-means cluster analysis of an oil-water-alkane immersion. **a** Cluster tree with the root cluster on the left, the first level of clusters in the middle and a further division into sub-clusters on the right. The sub-clusters each show a mixed phase marked in black. **b** Alkane spectrum (red) and the mixed phase (black) as extracted from the top two clusters. **c** Mixed Alkane and water spectrum (blue) and the mixed phase (black) as extracted from the middle two clusters. The water phase does not exist as a pure phase in this sample. **d** Oil spectrum (green) and the mixed phase (black) as extracted from the bottom two clusters

Fuzzy clustering

In the hierarchical and K-means cluster algorithms, each spectrum either belongs to a cluster or does not. This is why the image output of these algorithms are binary masks (one for each cluster extracted).

In fuzzy clustering, the spectra can belong "to a certain degree" to a cluster. If a spectrum is located inside the cluster, then it belongs more to this cluster than one on the edge of it. Image outputs of this algorithm display this variation and are therefore not binary, but each pixel value typically has a value between 0 and 1 (or 100%).

This method instantly shows gradients in the images, due to each pixel now having a certain probability of belonging to one cluster or another. One can also interpret this value as a measure of how well the spectrum fits to the corresponding cluster. However, the resulting clusters cannot be clustered further as is the case for classical K-means clustering.

5.6 Image Masks and Selective Average Calculation

In order to present the results of a confocal Raman imaging experiment, representative or average spectra found in the sample are typically shown. Extracting individual spectra from the data set is often undesirable, because these measurements typically display signal to noise (S/N) ratios which are unsuitable for presentation.

Therefore, averaging subsets of the data-set is generally employed in order to calculate a smooth average spectrum. The definition of these subsets can be seen as binary images (masks) with the same pixel resolution as the recorded confocal Raman image. In these masks each pixel defines if the spectrum recorded at this position is used for the average calculation or not. This process is sometimes referred to as *selective average calculation*.

The definition of the masks can be performed in various ways:

Manual definition of the pixels:

In order to define areas of interest manually, the user should be able to clearly identify those areas. This can be done through an integral filter and the resulting image. For example, the bright areas in Fig. 5.1 could be marked. The bright areas indicate a high PMMA content in this example and the mask could then be used to calculate the spectrum of PMMA with a good S/N ratio. The user should for this purpose be able to mark any arbitrary area within the image and define it as a mask. While this method is very easy to implement, the major disadvantage is that it is quite subjective and the user can easily mark areas which contain a different spectrum. The average spectrum will then not be representative of the true single component. Additionally, it can be very laborious, if many small domains need to be marked.

Mask definition though calculation:

Not all samples will have clearly defined areas of single components as is the case in the example shown in Fig. 5.1. It can therefore be desirable to use images with mathematical and logical operators in order to define the mask. One simple example is thresholding. In this, each pixel of the image is treated with a "<" or ">" operator in order to generate the mask. It might furthermore be desirable to combine these operations using a calculator style interface. The software needs to enable the user to preview the mask in order to facilitate the calculation. The masks generated in such a way can then be used again for selective average calculation. This method facilitates significantly the marking of regions of interest in comparison to the manual definition described above. If various components show relatively strong intensities, it can become necessary to mathematically link several images in order to find a single component.

Cluster Analysis:

The cluster analysis typically generates binary masks as outputs in addition to the average spectra of the clusters. This method is certainly the most objective to find

the masks. The only disadvantage in this method is that in the case of K-means cluster analysis, small clusters tend to be included in large ones and can be difficult to extract.

5.7 Combination of Single Spectra with Multi-spectral Data Sets

The fundamentals of image generation were described in the previous section. This section describes the generation of images based on the fitting of so-called "basis spectra" to the data set. This procedure produces images with much better contrast than if only a small part of the spectrum is used (as is the case when using a sum filter, for example).

5.7.1 Basis Spectra

Basis spectra can be the spectra of the pure components present in the sample. This is the ideal case. Care must be taken, however, to record the spectra with exactly the same settings as used when the confocal Raman image was recorded. Typically the same integration time and many accumulations are chosen for this in order to obtain basis spectra with a good S/N ratio. An additional point which should be taken into consideration is whether the pure component can be present in the sample or if it might have undergone a chemical reaction to form a new component.

Quite often the pure spectra cannot (easily) be acquired from any arbitrary sample. In this case the basis spectra should be extracted from the scan. The selective averaging described in Sect. 5.6 is one method to perform this. Care must be taken to ensure that the spectra are pure and not mixed themselves. If they are mixed spectra, they need to be de-mixed because the fitting procedure will not work properly otherwise, as described in the following.

5.7.2 Fitting Procedure

The fitting procedure is essentially fitting each of the spectra recorded using the basis spectra. It tries to minimize the fitting error D described by the following equation

$$D = \left(\overrightarrow{[Recorded\ Spectrum]} - a \times \overrightarrow{BS_A} - b \times \overrightarrow{BS_B} - c \times \overrightarrow{BS_C} - \ldots\right)^2 \quad (5.1)$$

by varying the weighting factors $a,\ b,\ c, \ldots$ of the basis spectra $\overrightarrow{BS}$.

In order to improve such a fit, it is not advisable to use the entire recorded spectral range (i.e. from –100 to 3500 rel. cm^{-1}). The Rayleigh peak as well as common parts in the spectra (such as a glass substrate for example) are best excluded from the fit. Additionally, parts of the spectra that do not contain Raman information should not be taken into account as they only contribute noise.

Following the fit of all the tens of thousands of spectra (using (5.1) for each spectrum recorded), the algorithm constructs one image for each basis spectrum showing the factors a, b, c, ... plus one image for the fitting error D.

Care must be taken in order to avoid using mixed spectra as the basis spectra. If such spectra are used the weighting factors can become negative, or if the fit is constrained to weighting factors greater than zero, the fit will not work properly.

Figure 5.9 shows an example of basis analysis. Here a thin layer of a PS-PMMA polymer blend was investigated with very short integration times (4.3 ms). The individual spectra were thus relatively noisy as can be seen from the red and blue spectra in Fig. 5.9c, e.

Using selectively averaged spectra with a good signal to noise ratio (see Fig. 5.9a) one can fit the individual, noisy spectra using the information contained within the entire spectral range. This results in a significant improvement of the S/N ratio and the contrast of the resulting images (see Fig. 5.9b, d).

Variations of this algorithm can also be implemented and, in combination with an automatic determination and averaging of the basis spectra followed by a visually guided de-mixing of the spectra, this dramatically simplifies the usage of this algorithm [17, 18].

5.8 Combination of Various Images

Following the generation of the images from the confocal Raman data, they need to be presented in a suitable way. If only the distribution of a single component or the shift of a Raman line need to be presented, then this is relatively straightforward.

However, if multiple images such as the results of the basis analysis need to be presented, the number of images can quickly become too large. It might be of additional interest to see if certain components are present as pure or mixed phases.

In such cases the combination of images is a good way to illustrate the distribution of components. In Fig. 5.5b the distribution of oil, water and alkane is shown in green, blue and red respectively.

The color scales for each component are first adjusted, so that each component has an individual color scale (Red, Green and Blue (RGB) in this case). The images are then combined. One can combine the images by layering them and making the upper layers transparent depending on the value of each pixel. Another method is to combine the colored pixels in an additive way in order to illustrate the mixing of phases better. The colors are then combined and where, in the example above, water (blue) and Alkane (red) are present, the resulting color is mixed (violet).

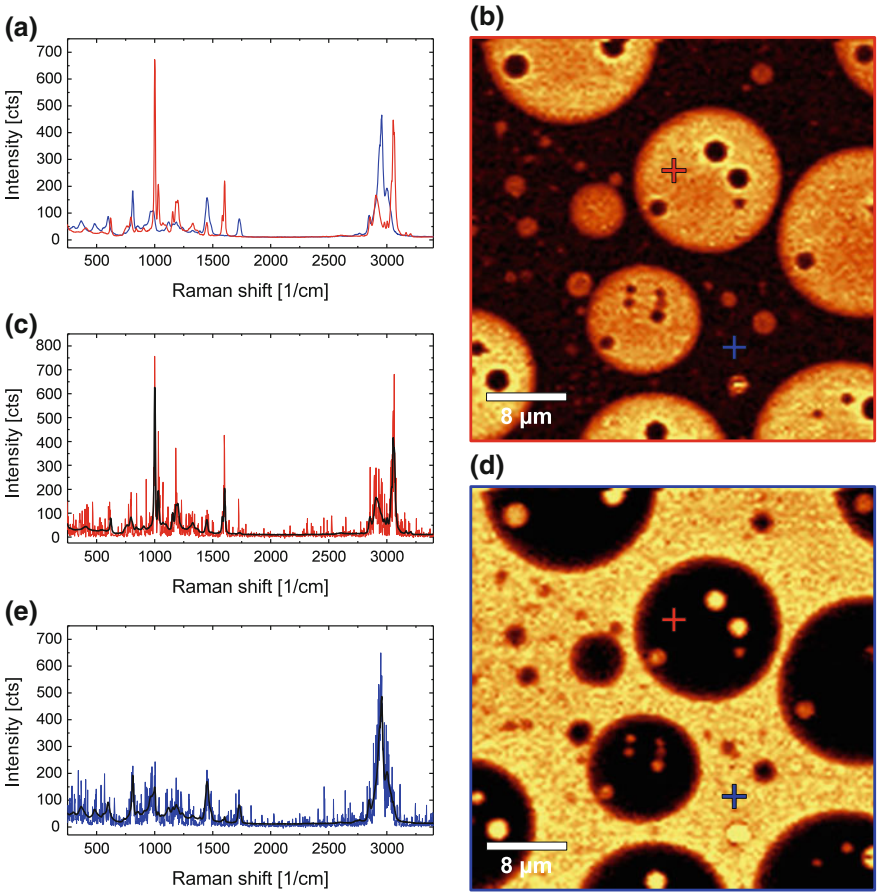

Fig. 5.9 Basis Analysis of a PS-PMMA polymer blend. **a** Average spectra used for the fitting procedure. **c**, **e** Original spectra (red and blue respectively) and fitted spectra (black) for PS (red) and PMMA (blue). The original spectra were recorded at the crosses indicated in the images on the right with the corresponding colors. **b**, **d** Resulting image showing the distribution of PS (**b** red frame) and PMMA (**d** blue frame) following the basis analysis. Brighter colors indicate a higher fitting factor and thus a higher signal intensity of the basis spectrum at the corresponding position

Note that the definition of the range of the color scale bar has a significant influence on the appearance of images and that care must be taken to choose appropriate settings.

5.9 The Law of Numbers

In this section a very noisy example data set is evaluated to illustrate the implementation and capability of the methods described above and show that even though the S/N ratio of the individual spectra is at first glance insufficient, the algorithms used can produce images and spectra of high quality.

The sample investigated was a PET-PMMA polymer blend spin-coated onto a glass slide. The data was acquired in EMCCD mode and Fig. 5.10 shows an example of three of the 22,500 spectra recorded.

The noise level in the spectra is significant and the S/N ratio is only slightly above 1. Even with this noise level, the sum filter applied to the CH-stretching region where PMMA shows a signal, produces some image contrast as can be seen in Fig. 5.10b.

Following cosmic ray removal and a background subtraction, a K-Means cluster analysis was performed on the data set, resulting in three clusters. The average spectra of these clusters as well as the color coded cluster map are shown in Fig. 5.11.

It can be clearly seen that the quality of the spectra as well as the spatial assignment of the pixels and thus the image contrast is dramatically improved. As can be seen from Fig. 5.11a, all spectra still contain the glass background due to the limited depth resolution of the confocal setup and the thickness of the film ($\ll$50 nm). It is additionally noticeable that the glass spectrum still shows a small peak in the CH-stretching region. This is due to edge effects of the clusters as already discussed in Sect. 5.5.2.4.

The spectra can now be de-mixed further by correct subtraction of the spectra from each other, which then results in the spectra shown in Fig. 5.12c.

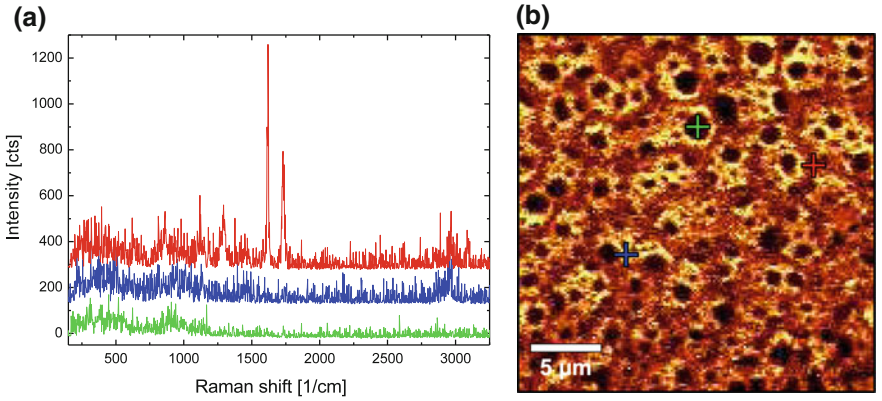

Fig. 5.10 Noisy PET-PMMA Raman image. The spectra (**a**) on the left show the three different components acquired at the positions marked in the image (**b**) with the corresponding colors (green = glass, red = PET, blue = PMMA). The image (**b**) on the right displays the distribution of PMMA in the sample as derived through a simple sum filter

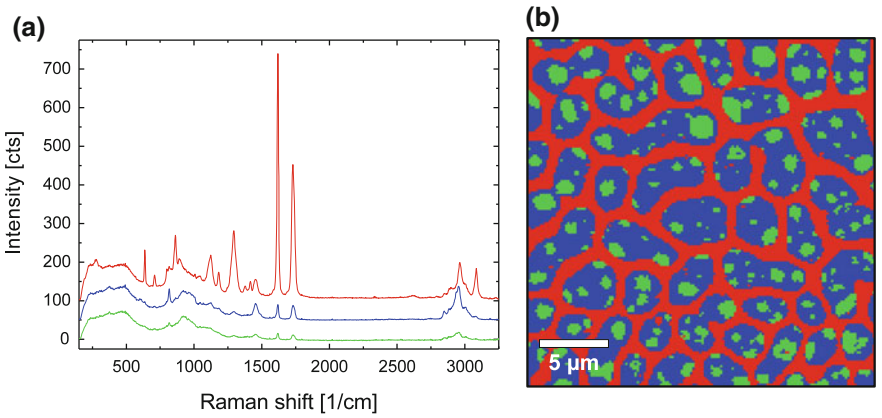

Fig. 5.11 PET-PMMA Raman image and spectra following K-Means cluster analysis. The spectra on the left (**a**) show the average spectra of the three clusters (green = glass, red = PET, blue = PMMA) and the image on the right (**b**) the combined cluster map with the pixels color-coded as the spectra according to their cluster affiliation

These spectra are used for the basis analysis and, after application of an anisotropic filter, the resulting images for PET and PMMA are shown in Fig. 5.12a, b, respectively. The scale bars to the right of image Fig. 5.12a, b indicate the fitting value. The glass background image (not shown here) now shows a homogenous distribution. Figure 5.12d shows the combined image of the three components following basis analysis.

Figure 5.13 illustrates the effect on image contrast for the PMMA phase by simply displaying Figs. 5.10b and 5.12c next to each other. The enhancement in image contrast due to the multivariate data methods and the de-mixing is clearly visible. This is especially apparent in the region where PET is located the contrast is strongly enhanced.

The scale bars on the right hand side of the images are an additional indicator that the sum filter only uses the number of detected electrons[1] in the CH-stretching band, whereas the fitted image uses the photons in the entire spectral range, which is reflected in the higher scale bar values in Fig. 5.13b.

This example demonstrates conclusively, that with a sufficiently large number of spectra (22,500 in this case), it is still possible to obtain a great amount of spectral and spatial information from the data sets by using multivariate methods and advanced data analysis algorithms, even though the individual spectra have a very low signal to noise ratio. However, the signals in the spectra still need to be sufficiently high to allow the cluster analysis to distinguish one cluster from another.

[1] Since this measurement is performed in EMCCD mode, the signal is strongly amplified and thus does not represent the number of photons.

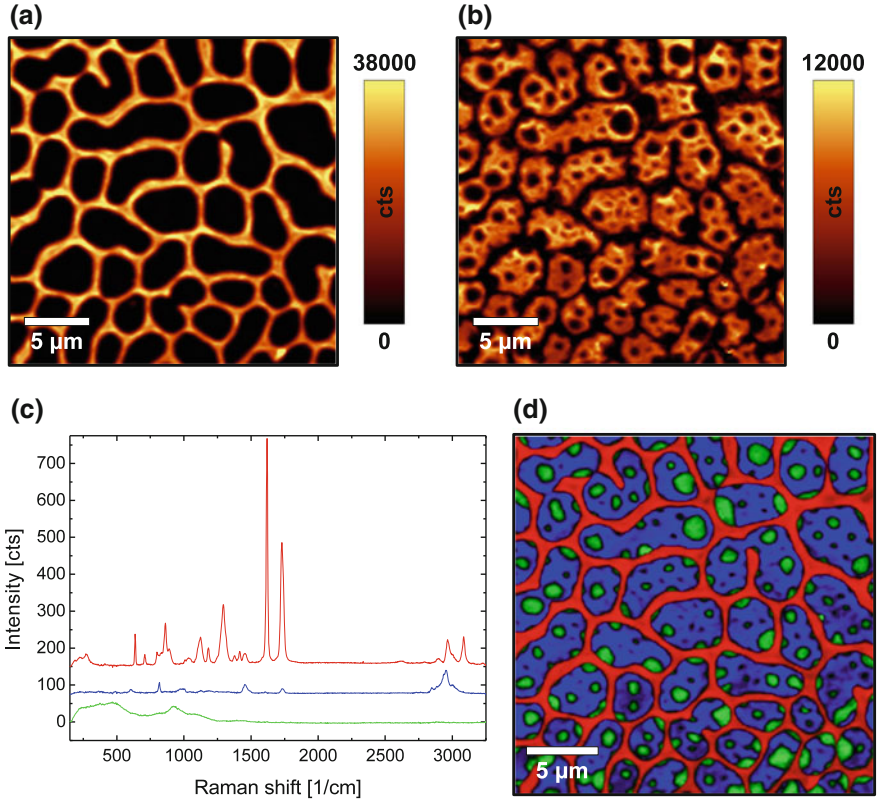

Fig. 5.12 The results of the basis analysis for PET (**a**) and PMMA (**b**), the de-mixed spectra used for the basis analysis (**c**) and the combined image of the three components (green = glass, red = PET, blue = PMMA)

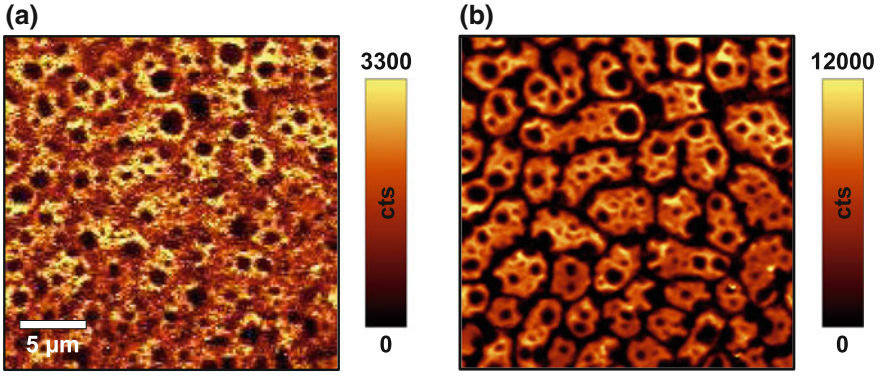

Fig. 5.13 Comparison of the image contrast before and after data evaluation. Image **a** was obtained through the sum filter and image **b** after basis analysis and application of an anisotropic filter

5.10 Materials and Methods

In order to illustrate the data processing of Raman spectra, a few example data sets were utilized throughout this chapter. The samples as well as the acquisition details will be explained in the following.

All data presented were recorded using an alpha300R confocal Raman microscope from WITec GmbH, a frequency-doubled Nd:YAG laser (532 nm) and a spectrometer equipped with a 600 and a 1800 g/mm grating as well as a back-illuminated CCD camera. The samples were:

- A PS-PMMA polymer blend either dropped onto or spin coated onto a glass slide.
- A Si [100] wafer with an indent produced using a nano-indenter.
- An Oil-Alkane-Water (O-A-W) mix which was placed between two cover slips.
- A PET-PMMA polymer blend spin coated on a glass slide.

The objective used was either a 100× air objective with an NA of 0.9 or 0.95 or a 100× oil immersion objective with an NA of 1.25 (Oil-Alkane-Water sample). Further experimental details can be found in Table 5.3.

Table 5.3 Experimental details for the example data sets

Figure number	Sample description	Integration time (s)	Scan size (μm)	Scan resolution	Grating (g/mm)	Layer thickness
1	PS-PMMA	0.062	30 × 30	200 × 200	600	<1 μm
1	PS-PMMA	10 × 0.512	Single spectrum		600	<1 μm
1	PS-PMMA	10 × 1.512	Single spectrum		1800	<1 μm
2	PS-PMMA	5 × 0.512	22.4 (Line Scan)	15	600	<1 μm
3	PS-PMMA	0.062	Single spectrum (extracted)		600	<1 μm
4	PS-PMMA	0.062	Single spectrum (extracted)		600	<1 μm
5	O-A-W	0.017	100 × 100	128 × 128	600	N.A.
6	Si indent	0.069	10 × 10	100 × 100	1800	N.A.
8	O-A-W	0.017	100 × 100	128 × 128	600	N.A.
9	PS-PMMA	0.0043	40 × 40	120 × 120	600	<1 μm
10–13	PET-PMMA	0.050	25 × 25	150 × 150	600	<50 nm

References

1. WITec GmbH, Ultrafast confocal Raman imaging—application examples (2008). http://www.witec.de/en/download/Raman/UltrafastRaman.pdf
2. WITec GmbH, apyron: powerful data acquisition and post-processing (2015). https://youtu.be/vXH8Am8CVl4
3. L. Quintero, S. Hunt, M. Diem, Denoising of Raman spectroscopy signals (2007). Poster presented at the 2007 R2C Multi Spectral Discrimination Methods Conference
4. W.H. Press, S.A. Teukolsky, W.T. Vetterling, B.P. Flannery, *Numerical Recipes in C* (The Press Syndicate of the University of Cambridge, 1999), 2nd edn., Chap. Savitzky-Golay Smoothing Filters, pp. 650–655
5. P. Ramos, I. Ruisánchez, J. Raman Spectrosc. **36**, 848 (2005)
6. G. Gaeta, C. Camerlingo, R. Ricio, G. Moro, M. Lepore, P. Indovina, Proc. SPIE **5687**, 170 (2005)
7. W. Burger, M.J. Burge, *Digitale Bildverarbeitung: Eine Algorithmische Einführung Mit Java* (Springer, Berlin, 2009)
8. D. Tschumperlé, Int. J. Com. Vis. **68**(1), 65 (2006)
9. T. Dieing, O. Hollricher, Vib. Spectro. **48**, 22 (2008)
10. K. Pearson, Phil. Mag. **2**(6), 559 (1901)
11. C. Bishop, *Pattern Recognition and Machine Learning* (Springer, New York, 2007)
12. T. Hastie, R. Tibshirani, J. Friedman, *The Elements of Statistical Learning* (Springer, New York, 2009)
13. S. Wold, K. Esbensen, P. Geladi, Chemometr. Intell. Lab. Syst. **2**(1–3), 37 (1987)
14. H. Lohninger, PCA—loadings und scores (2012). http://www.statistics4u.info/fundstat_germ/cc_pca_loadscore.html
15. Wikipedia.com, Principal component analysis (2017). https://en.wikipedia.org/wiki/Principal_component_analysis
16. A. Hermelink, A. Brauer, P. Lasch, D. Naumann, Analyst **134**(6), 1149 (2009)
17. WITec GmbH, Witec suite five (2017). http://www.witec.de/assets/Literature/Files/WITec-Suite-FIVE-Software-spread-scr.pdf
18. WITec GmbH, Witec suite five. purchasable software (2017)

Chapter 6
Resolution and Performance of 3D Confocal Raman Imaging Systems

Thomas Dieing

Abstract Confocal Raman microscopes are the instruments of choice for chemical characterization in a wide variety of applications including geosciences (Jenniskens et al., in Nature 458(7237): 485, 2009 [1]), (Rotundi et al., in Planet Sci 43(1–2):367, 2008, [2]), (Heim et al., Geobiology in 10(4):280, 2012 [3]), biology (Hild et al., in J Struct Biol 168(3):426, 2009 [4]), (Gierlinger and Schwanninger, in J Spectrosc 21(2):69, 2007 [5]), (Hermelink et al., in Analyst 134(6):1149, 2009 [6]), nanocarbon materials (Xu et al., in ACS nano 5(1):147, 2010 [7]), (You et al., in Appl Phys Lett 93(10):103111, 2008 [8]), (Yu et al., in J Phys Chem C 112(33):12602, 2008 [9]) and pharmaceutics (Matthäus et al., in Mol Pharm 5(2):287, 2008 [10]), (Chernenko et al., in ACS nano 3(11):3552, 2009 [11]) to name but a few. Many pertinent examples can be found within this book. This chapter intends to shed light on the possibilities of confocal Raman systems in general, while briefly reviewing their origins and describing considerations such as spectral and spatial resolution as well as throughput. 3D confocal Raman imaging as well as compensation for surface topography during a confocal Raman image scan will also be outlined.

6.1 Introduction

Evaluating the performance of a confocal Raman microscope can be a tedious undertaking, with varied definitions and interpretations of measurement results making it nearly impossible to objectively compare different instruments. In this chapter several approaches to defining and measuring spectral resolution will be outlined before examples of typical experimental results are shown. The theoretical considerations and varying definitions of lateral as well as depth resolution will then be detailed, with accompanying experimental data. Experimental techniques capable of achieving resolutions beyond the diffraction limit will also be discussed. As the best resolution is only useful if the system simultaneously shows a high throughput, this aspect and experiments to test sensitivity will also be covered.

T. Dieing (✉)
WITec GmbH, Lise-Meitner-Strasse 6, 89081 Ulm, Germany
e-mail: thomas.dieing@witec.de

J. Toporski et al. (eds.), *Confocal Raman Microscopy*, Springer Series in Surface Sciences 66, https://doi.org/10.1007/978-3-319-75380-5_6

If all of the mentioned criteria are fulfilled simultaneously, then high resolution 3D confocal Raman images can be obtained. Examples of how to visualize them will be presented before the concept of following rough or inclined surfaces while maintaining high depth resolution will be described and presented using a suitable example.

In the appendix ideal test samples for all resolution and throughput measurements are presented.

6.2 Resolution of Confocal Raman Microscopes

The resolution of confocal Raman microscopes is one of the key factors that enable truly high performance. In terms of resolution one should differentiate between spatial (the ability to separate two closely spaced sample objects) and spectral resolution (the ability to separate two closely spaced spectral lines). Spectral resolution should be determined purely by the spectrometer and de-coupled from microscope components such as the objective used. With spatial resolution one needs to differentiate between lateral (perpendicular to the optical axis) and depth resolution (parallel to the optical axis). This will be discussed in the following sections but it is important to first consider some basic principles of spectrum and image generation.

6.2.1 Resolution - What Is It that We Measure?

Any measurement performed, whether recording a spectrum or an image in confocal (Raman) microscopy, involves a mathematical convolution between the spectral feature (or object) measured and the "instrument function." The "instrument function" is typically determined by the basic laws of physics, such as the diffraction limit, and the characteristics of the instrument itself. Ideally the influence of the instrument would be negligible, allowing measurements limited only by physical law.

When considering the results as a convolution, two extreme cases can be instructive. While image generation is addressed directly in the comparisons below, this also holds true for spectra and the influence of the spectrometer.

Object $\gg$ "instrument function"
In this case the size as determined by the image is very close to the real dimensions of the object. The influence of the "instrument function" may then be neglected. Mathematically the "instrument function" approaches a delta function in comparison to the object.

Object $\ll$ "instrument function"
In this case the image generated will not display the object, but rather the "instrument function." Mathematically the object approaches a delta function in comparison to the "instrument function."

The latter case can therefore be used in order to determine the resolving power of any system.

Concerning the size of the object relative to the "instrument function" one may consider the convolution of two Gaussian curves, one being the instrument function and the other the object. The convolution result in terms of FWHM is:

$$FWHM_{Result} = \sqrt{FWHM^2_{Object} + FWHM^2_{Instrument}}. \tag{6.1}$$

The deviation of the FWHM of the result from the FWHM of the object will thus be about 3 % if the object is smaller than 25 % of the "instrument function", while the deviation reaches ≈41 % for an object of the same size as the "instrument function." Typically deviations up to 10 % are considered to be acceptable and thus the test objects should be smaller than ≈45 % of the "instrument function."

6.2.2 *Spectral Resolution*

Any confocal Raman system has a spectral resolution which is determined primarily by the following factors:

- Focal length of the spectrometer
  (the longer the focal length, the higher the spectral resolution).
- Grating
  (the higher the groove density, the higher the spectral resolution).
- Pixel size on the CCD camera
  (the smaller the pixels, the higher the spectral resolution).
- Entrance slit or pinhole
  (the smaller the slit/pinhole the higher the spectral resolution).
- Magnification within the spectrometer
  (as this will alter the size of the image of the entrance pinhole on the CCD camera).
- Imaging quality of the spectrometer.

In some cases a single parameter can limit the spectral resolution. If for example the projection of the pinhole onto the CCD is already large compared to the pixel size of the CCD camera, then a further reduction of pixel size will not increase the spectral resolution.

Microscope components such as the objective used for collection of the signal do not influence the spectral resolution if the entrance slit/pinhole is the limiting element. This is preferred with confocal Raman microscopes.

The determination of the spectral resolution is often a point of debate. To begin, one should separate the spectral resolution from the capability of the system to detect shifts of individual peaks. Relative peak shifts can be detected with a much higher accuracy using fitting algorithms. In the histogram in Fig. 6.1 the fitted position of the A_{1g} mode of 1000 consecutive measurements of the same position within a diamond

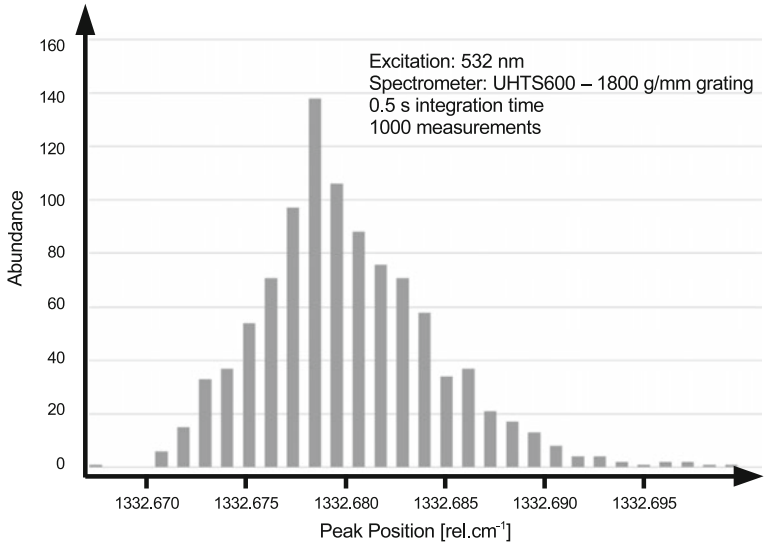

Fig. 6.1 Reproducibility of the position of a diamond Raman line

is shown. The standard deviation of this measurement is $<0.005\,\mathrm{cm}^{-1}$. Considering that the natural line width of most Raman lines is $>3\,\mathrm{cm}^{-1}$ this represents an accuracy of better than 1/500 of the line width. Please note that the maximum achievable fit accuracy depends on the number of detected photons and the width of the peak fitted. Such a shift analysis is especially relevant for examining stress within a sample, but may not be taken as a measurement of the spectral resolution and clearly has to be distinguished from it.

The spectral resolution, which determines how the system can measure i.e. a FWHM of a narrow peak or how well overlapping peaks can be differentiated, needs to be addressed separately from the peak shift sensitivity. There are several ways to state the spectral resolution and some of the most common ones are outlined below:

Pixel Resolution:
The pixel resolution (also known as the technical resolution) is the difference in wavenumbers when moving from one pixel on the CCD camera to the next and is independent from factors such as slit width or peak width of the detected peak. This can only be seen as the true resolution if the pixel size and not the size of the entrance slit/pinhole and/or the imaging quality of the spectrometer is the limiting factor. The physical size of the pixel thus always has to be compared to the dispersion of the spectrometer. As wavenumbers are measured in reciprocal space it should also be noted that the pixel resolution will change with wavelength depending on the spectral position at which it is determined. The resolution close to the Rayleigh line can in this way differ by almost a factor of two from the pixel resolution near 3500 rel. cm^{-1} in the case of 532 nm excitation.

Two Pixel Criterion:
For this criterion the pixel resolution is multiplied by two. The logic behind this is, that in order to discriminate two neighboring peaks one needs to have one pixel on one peak, one in the minimum between the peaks and a third one on the next peak. This criterion is the Nyquist theorem in signal processing. The same limitations as outlined for the pixel resolution criterion apply in this case.
Full Width at Half Maximum (FWHM) of Atomic Emission Lines:
Atomic emission lines are typically much narrower than any Raman line. Their sharpness makes them useful in determining the resolution (see also Sect. 6.2.1). Figure 6.2 shows an atomic emission line of mercury near 546.07 nm which is right in the Raman range for 532 nm excitation. The spectrum was recorded using a mercury/argon calibration lamp coupled via broadband single mode fiber to a UHTS600 spectrograph equipped with both 300 and 2400 g/mm gratings and a CCD camera with a pixel size of 16 µm. The FWHM measured is a good reflection of the resolution ($\approx$0.2 cm^{-1} for the 2400 g/mm grating).
This method is considered to be the most reliable one, since in this case the atomic emission line can be seen as a delta function and thus the "pure" transmission function of the spectrometer is measured.
Resolution Measured on Reference Samples:
There are a few samples which are established standards for demonstrating spectral resolution. The most prevalent is probably CCl_4. Figure 6.3 shows two spectra of CCl_4 recorded with different spectral resolutions. It can be seen that the peaks are nicely separated in the case of the 2400 g/mm grating while being indistinguishable in the case of the 300 g/mm grating. The spectra are offset for clarity. The peak splitting occurs due to the presence of Cl isotopes and their modes can be assigned as follows:

- 450.0 rel. cm^{-1}: $\nu_{1e}(A_1) : C\ ^{37}Cl_4$
- 453.3 rel. cm^{-1}: $\nu_{1d}(A_1) : C\ ^{37}Cl_3\ ^{35}Cl$
- 456.3 rel. cm^{-1}: $\nu_{1c}(A_1) : C\ ^{37}Cl_2\ ^{35}Cl_2$
- 459.5 rel. cm^{-1}: $\nu_{1b}(A_1) : C\ ^{37}Cl\ ^{35}Cl_3$
- 462.3 rel. cm^{-1}: $\nu_{1a}(A_1) : C\ ^{35}Cl_4$

Spectral resolution can therefore be defined in many different ways and it is advisable to specify exactly how it was or should be determined. Comparing measurement results obtained under identical measurement conditions is certainly one of the best ways to illustrate this. It should also be noted that the natural line widths of Raman lines are typically larger than 3 cm^{-1} at room temperature. Taking the Nyquist criterion into account, a spectral resolution of approximately 1 cm^{-1} is sufficient for most samples.

This is especially important when considering that a higher spectral resolution means the same number of photons within one Raman peak are spread over a larger number of pixels on the CCD camera. This therefore reduces the signal-to-noise ratio at each pixel. For limited integration times a balance between the highest spectral resolution and the lowest acceptable signal-to-noise ratio is of great importance.

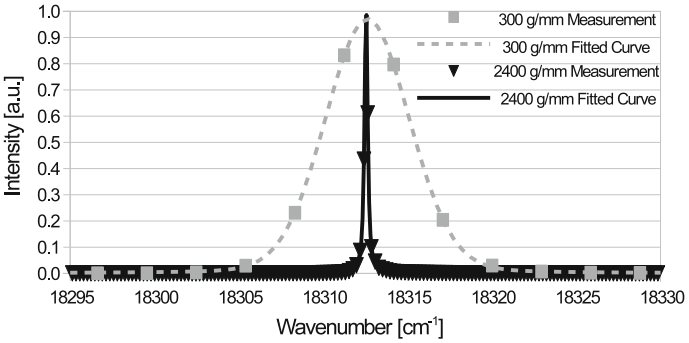

Fig. 6.2 Spectra of the mercury atomic emission line at 546.07 nm plotted as a function of wavenumber assuming a 532.00 nm excitation. The lines are the fitted curves (pseudo-Voigt function) while the squares and triangles represent the measured data points for the 300 and 2400 g/mm gratings, respectively

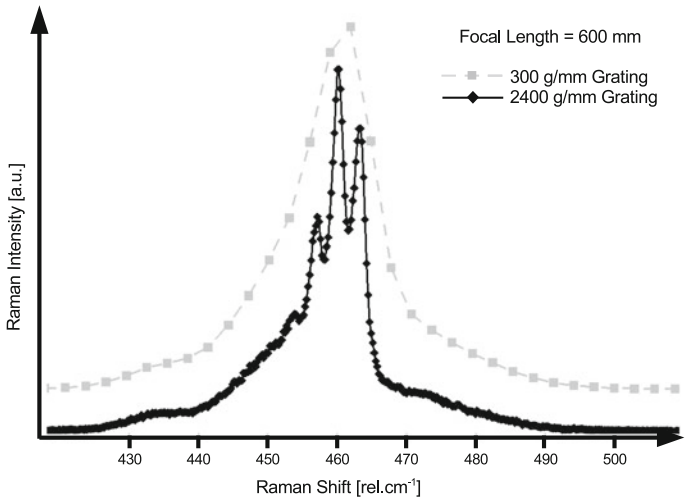

Fig. 6.3 Raman spectrum of CCl_4 recorded using 532 nm excitation and a 600 mm spectrometer, once with a 300 g/mm and once with a 2400 g/mm grating

6.2.3 Spatial Resolution

When considering the spatial resolution of a confocal Raman microscope one may distinguish between the lateral (X & Y) and the depth (Z) resolution. It is, however, possible in either case that limitations will arise due to one of the following points:

- Basic physics (i.e. diffraction limit)
- Limited positioning accuracy of the mechanical components used

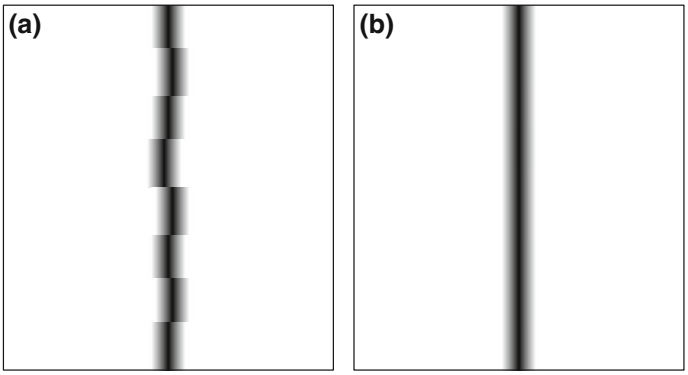

Fig. 6.4 A straight line imaged with insufficient positioning reproducibility (**a**) compared to sufficient positioning reproducibility (**b**)

- Limitations of the optical components in the beam path (resulting in i.e. beam distortion)
- Pixel resolution of the image acquired

In terms of the positioning system it is important to differentiate the single step width of a stepper motor, the positioning reproducibility and the linearity. Reproducibility and linearity are key factors for an imaging system as they allow line-by-line imaging. If a straight line is imaged, for example, it can only reflect the accuracy of the positioning reproducibility though the step size might be much smaller. Figure 6.4 illustrates this effect with Fig. 6.4a showing insufficient positioning reproducibility and Fig. 6.4b with sufficiently high positioning reproducibility.

Even using positioning encoders on a positioning stage does not necessarily improve positioning reproducibility. Positioning in a stage containing encoders requires a positioning feedback. If the feedback is not properly set up, this will show a "hunting" behavior. Even with a proper feedback the positioning device has to stop if the stage is within a certain "window" around the desired position. Therefore a stage equipped with 100 nm encoder resolution might only achieve 500 nm positioning reproducibility, which is significantly larger than the diffraction limit as well as significantly larger than what can be achieved by an accurate stepper motor system without encoders.

Using high quality optical components and positioning systems along with sufficient pixel resolution should allow imaging at the limits of physics.

6.2.3.1 Lateral Resolution

Based on the diffraction theory of Ernst Karl Abbe (∗23.01.1840; †14.01.1905), Lord Rayleigh defined the diffraction limit in 1896 [12]. He thereby quantified the minimum distance at which two point light sources can be discerned. In this case

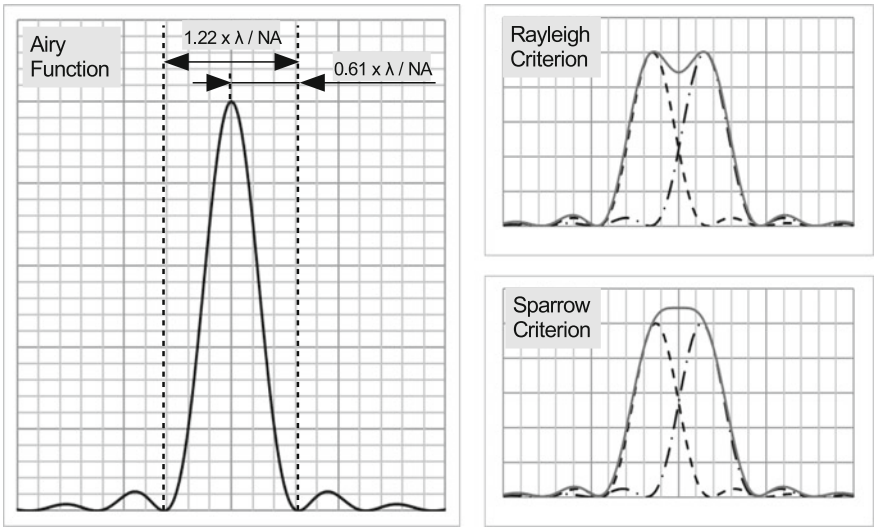

Fig. 6.5 Resolution determination using the Airy function: Diameter of the Airy disk versus the Rayleigh and Sparrow criteria, where two Airy functions are overlap at different distances from each other

one of the sources is located at exactly the position of the first minimum of the Airy function (point spread function) of the other one. This distance (d_{lim}) can be expressed as a function of the wavelength emitted (λ) and the numerical aperture (NA) of the objective used as:

$$d_{lim} = 0.61 \times \frac{\lambda}{NA} \tag{6.2}$$

In literature one can often find the equation $1.22 \times \frac{\lambda}{NA}$ which describes the distance between the first two minima of the Airy function (see Fig. 6.5), often also referred to as the diameter of the Airy disc.

The resolution however is given by, for example, the Rayleigh criterion. Using the definition of the Airy function the resolution can be easily derived from how much the intensity between the two emitting points must decrease according to the Rayleigh criterion ($0.61 \times \frac{\lambda}{NA}$). Please note that the distance is different for other criteria of diffraction such as the Abbe criterion ($0.50 \times \frac{\lambda}{NA}$) or the Sparrow criterion ($0.47 \times \frac{\lambda}{NA}$; see Fig. 6.5).

The highest generally achievable resolution can be further enhanced by up to a factor of $\sqrt{2}$ if a very small pinhole is used (see Chap. 2), but in confocal Raman microscopy this is mostly irrelevant due to the severe loss of signal intensity if this resolution is approached.

In order to establish the resolution of a microscope using either of those criteria it would be necessary to have an array of very small, strongly scattering objects

(small compared to the size of the Airy disk; for example individual TiO_2 particles) at varying distances. Following high resolution Raman imaging one would then analyze the signal intensities and based on the detectable distances between the spots, derive the resolution.

The measurement of regular structures has at times been used in an attempt to determine resolution. While apparently astonishing results can be achieved in this manner they do not describe the true resolving power of a system. An example of such measurements and the potential pitfalls in resolution determination will be outlined in the following before an accurate method for resolution determination is shown.

Pitfalls in Lateral Resolution Determination: Regular Structures

For this measurement a regular structure consisting of square, SiN-coated Ge pillars of 200 nm edge length and 200 nm distance from each other was used (details see [13, 14]). The measurements were performed using a 100× NA 0.9 objective, a 532 nm laser for excitation (FWHM of the Airy function is thus 301 nm) and a pinhole with a 100 nm projected pinhole size (see Sect. 6.2.3.2). A 2 µm × 1 µm confocal Raman image was acquired from this structure with a resolution of 50 × 25 pixels. In Fig. 6.6a the peak position of the SiN Raman peak near 300 rel. cm^{-1} can be seen and in Fig. 6.6b its intensity. The extracted cross sections along the white lines can be seen in Fig. 6.6c.

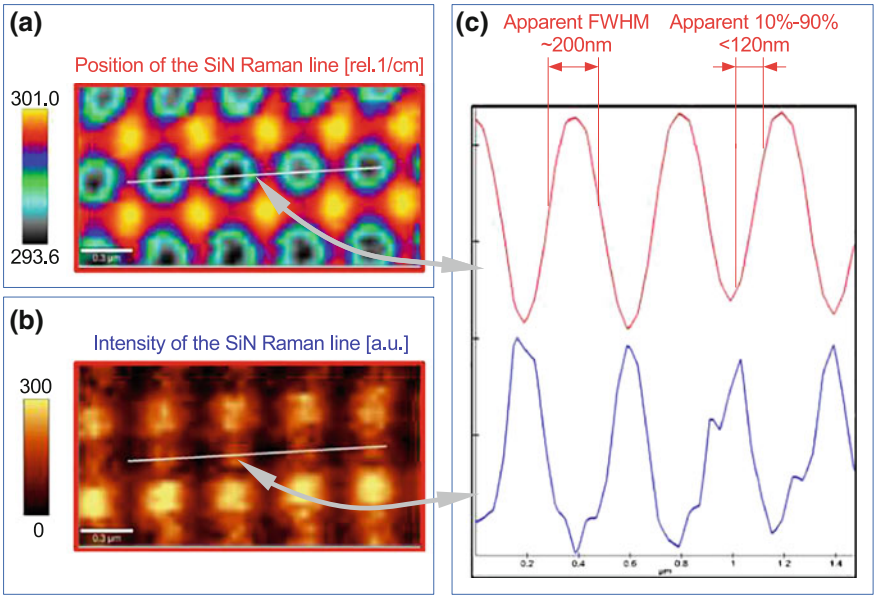

Fig. 6.6 Confocal Raman image of a regular structure of SiN-coated Ge pillars showing the position (**a**) of the main SiN Raman line and its intensity (**b**). The cross sections (**c**) allow the determination of the apparent FWHM and the 10–90% values

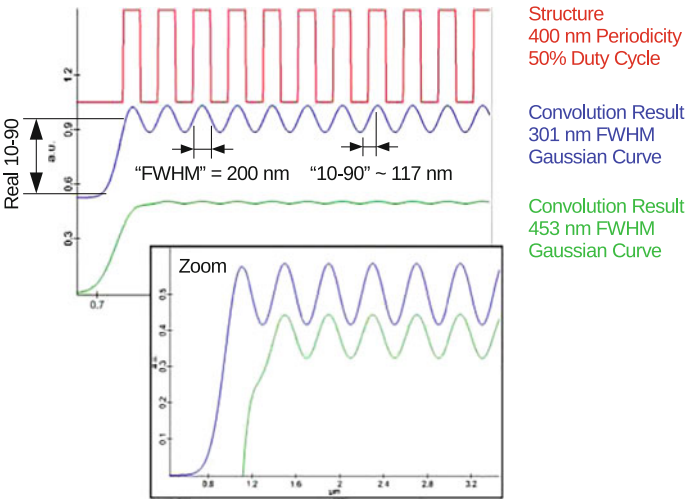

Fig. 6.7 Convolution results of a regular structure with Gaussian curves of different FWHM. The zoom window shows the same curves scaled differently

From the cross sections in Fig. 6.6c the apparent FWHM and 10–90% measurement can be extracted. This is, however, not the actual resolving power of the system.

As outlined, the resulting image is always a convolution of the object and the resolving power of the system. In order to illustrate the effect of a regular structure on the resulting cross section, two Gaussian functions with different FWHM values (301 and 453 nm) were convoluted with a regular structure of 400 nm periodicity and 50% duty cycle. In Fig. 6.7 the structure is shown in red and the convolution results in blue and green, respectively.

Apparent FWHM and apparent 10–90% values similar to the experiment can be deduced from the convoluted result. The zoomed view shows the same results but scaled differently where the green curve is zoomed in more. From this view it can be seen that even with such a wide Gaussian beam the same apparent resolution could potentially be extracted.

As the Gaussian curves represent the instrument function, it is obvious that regular structures are not appropriate for determination of the instrument function as the achievable resolution determined in the middle of the structure would be identical and independent of the width of the instrument function. A statement about the achievable resolution of a system can only be made if the "edge" of the structure is also displayed (see zoom-in Fig. 6.7). A fit of a Gaussian function onto the rising flank could, for example, give an approximation of the achievable resolution.

Accurate Determination of the Lateral Resolution: δ-Function-Like Structures

A correct way to determine the lateral resolving power of a system is to use the full width at half maximum (FWHM) of the image of small objects. Based on the Airy function, the relation between the FWHM of the light emitted from an object and the diffraction-limited distance (d_{lim}) is:

$$FWHM \approx 0.85 \times d_{lim} = 0.51 \times \frac{\lambda}{NA} \tag{6.3}$$

As the measured signal is always a convolution of the object size, the emission characteristics and the system function, objects measured in such experiments should also be small compared to the Airy disk. Mathematically speaking, the objects' size should approach a delta function for the convolution. Such small objects naturally have only limited material for scattering and thus one can expect small Raman signals to be emitted by them. Carbon nanotubes (CNTs) on the contrary show a large Raman signal while being very small in diameter (typically ranging from less than one to several nanometers) and comparatively long (up to a few µm typically). These samples are ideal tools for the determination of the lateral resolution of a confocal Raman microscope. For a 532 nm excitation laser and an objective with an NA of 0.9, one should therefore be able to obtain a FWHM from CNTs of approximately 300 nm.

Figure 6.8a shows the AFM image of a multi-walled CNT on a Si substrate with the cross section illustrated in (b). From this the approximate diameter of the CNT can be established as ~55 nm as determined from the measured height. The width in Fig. 6.8b is wider due to the convolution with the AFM cantilever tip. Figure 6.8c

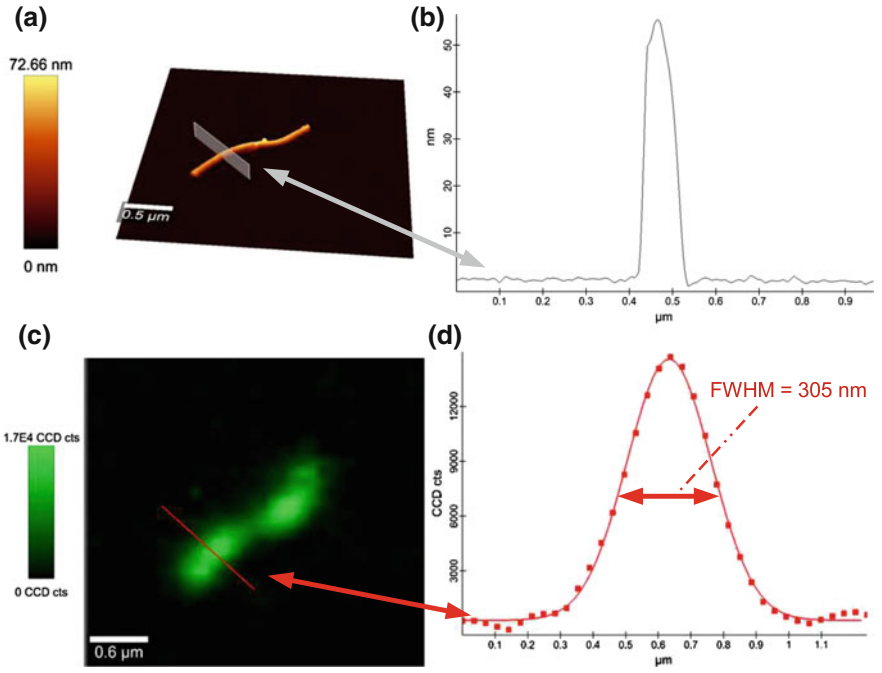

Fig. 6.8 AFM image of a multi-walled CNT (**a**) with the cross section illustrating its diameter (**b**). Confocal Raman image of the G-Band intensity of the same CNT (**c**) with the cross section illustrating the diameter determined (**d**)

shows the integrated intensity of the G-Band of the CNT. The scan range was 4 µm × 4 µm with an integration time of 100 ms per point. An alpha300 R (WITec GmbH) was used for the measurement in combination with a fiber-coupled, frequency-doubled Nd:YAG laser (532 nm emission) and a Zeiss 100× NA 0.9 objective.

An alternative to a δ-function-like structure is one which approaches a mathematical unit step-function (H). The FWHM of the derivative of the recorded cross section perpendicular to the edge (CS) then represents the FWHM of the "instrument function" (IS). Mathematically, the derivative of a convolution result is equivalent to the derivative of one convolution partner with the original second partner. As the derivative of the unit step function is the δ-function, the result is again the "instrument function."

$$\begin{aligned}\frac{d}{dx}CS &= \frac{d}{dx}[IS(x) * H(x)]\\ \frac{d}{dx}CS &= IS(x) * \frac{d}{dx}[H(x)]\\ \frac{d}{dx}CS &= IS(x) * \delta(x)\\ \frac{d}{dx}CS &= IS(x)\end{aligned}$$

6.2.3.2 Vertical or Depth Resolution

The depth resolution is the best indicator of the confocality of a system. Instrument design has great influence on the achievable resolution, but the pinhole/slit as well as the way the sample is illuminated also play essential roles in establishing the depth resolution.

Pinhole/Slit

The size of the detection pinhole plays a crucial role in the depth resolution of a confocal microscope. However, the physical size of the pinhole ($P_{physical}$) cannot be easily compared between different instruments. In image generation using two simple lenses, the focal length of both lenses contribute to the ratio between the object and the image size. This of course also holds true for a microscope. Here we have the magnification of the objective ($M_{objective}$) which is calculated for a certain focal length of the tube/telan lens ($f_{tube,objective}$). This focal length ranges for commercial microscopes from 164.5 mm for Zeiss objectives up to 200 mm for i.e. Leica or Nikon objectives. The magnification printed on the objective is only correct if the objective is designed for the tube focal length of the microscope. In order to have a comparable value for the pinhole size one should therefore calculate the projected pinhole size (P_{proj}) as follows:

$$P_{proj} = \frac{P_{physical}}{M_{eff}} = \frac{P_{physical}}{M_{objective}\frac{f_{tube,objective}}{f_{tube,real}}} \tag{6.4}$$

The same calculation also applies if a slit is used as a pinhole. For the following considerations we will use the projected pinhole size instead of the physical pinhole size. The full theory for confocality including the definition of optical coordinates,

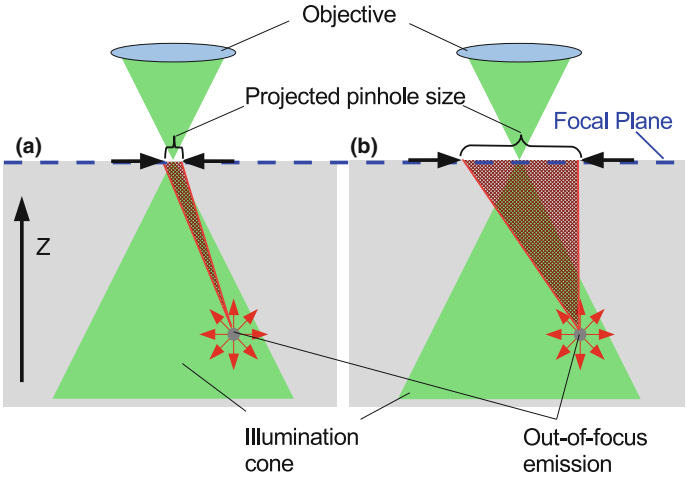

Fig. 6.9 The light collected from an out-of-focus emitter through the projected pinhole and thus the physical pinhole for the case of a small pinhole (**a**) and a large pinhole/slit (**b**)

which allows a comparison independent of wavelength and objective used, can be found in Chap. 2.

The influence of the projected pinhole size is illustrated in Fig. 6.9. Here a point illumination of a small area with an objective with a high NA is assumed. The collection diameter of the objective is assumed to be larger than the shown area and therefore not the limiting factor.

If the sample is sufficiently transparent, light will propagate further through the sample as shown by the illumination cone in Fig. 6.9.

This light excites out-of-focus molecules which then emit light (Rayleigh, fluorescence, Raman,...) in turn. This emission is mainly isotropic, so part of the light will find its way through the position of the projected pinhole in the focal plane and also through the physical pinhole. When comparing Fig. 6.9a, b it is apparent that a large pinhole allows a much larger amount of out-of-focus light to be detected (doubling the pinhole size will typically quadruple the amount of light passing through). Therefore a larger pinhole or slit can never achieve the same out-of-focus light suppression as a small pinhole.

Sample Illumination

In the last section it was shown that part of the emission from out-of-focus material will pass through the pinhole and that its contribution to the detected signal is highly dependent on the pinhole size. The intensity of the excitation light at such an out-of-focus position is directly proportional to the emitted light. This intensity decreases with increasing distance of the point from the focal plane. The strength of this decrease however is heavily dependent on the way the sample is illuminated and can best be compared by taking the power density (power/area) into account.

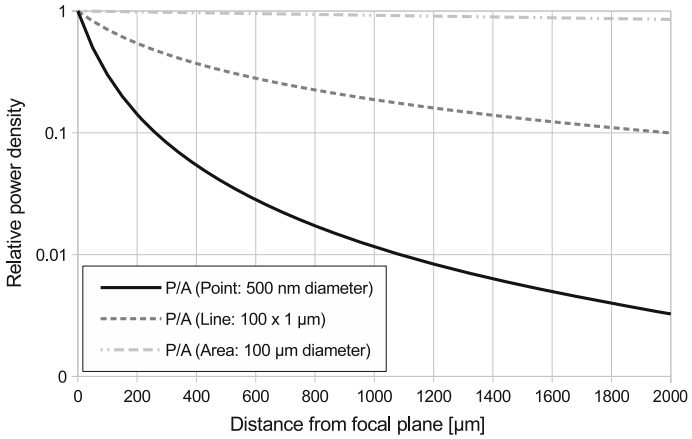

Fig. 6.10 Relative laser power density as a function of distance from the focal plane

Given a fixed illumination power density in the focus one can simply take the increase in the illuminated area as a function of depth into consideration. The numerical aperture of the objective is essential in this context. The higher the NA, the greater the increase of the area as a function of depth and thus the greater the decrease of the power density as a function of depth. In addition to the NA, the way the sample is illuminated plays a key role. Global illumination shows the smallest decrease as a function of depth. Line illumination shows a greater decrease and point illumination gives the strongest decrease of laser power density as a function of depth (see Fig. 6.10).

For the example shown, a point focus of 0.5 µm diameter was used, a line focus of 1 µm × 100 µm and a global illumination of 100 µm. The NA used for the calculations was 0.9. For this approximation a truncated cone was used as the geometry of the point and global illumination and a truncated pyramid for the line illumination.

Theory and Measurement of Depth Resolution

For the prediction of the possible depth resolution in confocal Raman microscopy one commonly uses the theory applicable for small numerical apertures (see for example Chap. 2). This theory predicts a minimum achievable FWHM in the Z-direction (at the minimum pinhole diameter) of about 940 for a 532 nm laser and a 0.9 NA objective.

In order to verify depth resolution the ideal sample would be a very thin, free standing layer of a strongly Raman scattering material.

Graphene or ultrathin graphite (i.e. 5–10 atomic layers) suspended over holes in Si could serve as an ideal sample to illustrate this. Similar to the CNTs for lateral resolution, graphene or ultrathin graphite have a very strong Raman signal and can act as an approximation of a delta function for the convolution of the sample geometry with the system function. In order to compare the achievable results on Si and ultrathin graphite the depth profiles of the suspended ultrathin graphite and the Si were

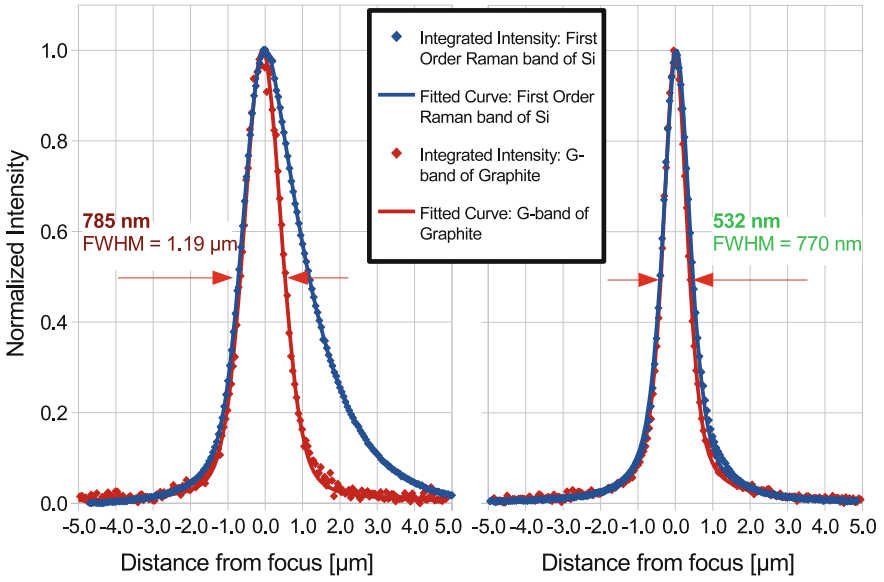

Fig. 6.11 Depth profiles of suspended ultrathin graphite and Si using 785 nm excitation (left) and 532 nm excitation (right). The FWHM given is extracted from a pseudo-Voigt fit applied to the ultrathin graphite data

recorded consecutively, once using 532 nm (very low penetration depth into Si) and once using 785 nm excitation (high penetration depth into Si). Optimized pinholes for both wavelengths were used and all experimental parameters were maintained for both measurements.

Figure 6.11 shows depth profiles of the integrated intensity of the 1st order Si peak (blue) and the integrated intensity of the G-band recorded on suspended ultrathin graphite (red). The system used was an alpha300 R (WITec GmbH) with a 100× NA 0.9 Zeiss objective and a UHTS300 spectrometer with a 600 g/mm grating.

The integration time per point was 0.5 s and the step size was 50 nm. The Z-position was set by an interferometrically-calibrated piezoelectric positioning table. The FWHM given were derived from the pseudo-Voigt fit of the data obtained from the suspended ultrathin graphite. A pseudo-Voigt curve was used due to the fact that an Airy-function does not have a purely Lorentzian nor purely Gaussian character.

It can be seen that the curves of Si and of the ultrathin graphite overlap well on the rising flank above the surface (negative Z-values in this depiction indicate distance above the surface) and that the deviation mainly occurs on the falling flank. There the influence of the penetration depth of the light into the Si can be clearly observed. Silicon shows a very small penetration depth for 532 nm excitation (~0.8 µm as derived from the absorption coefficient [15]).

Ultrathin suspended graphite is a specialized sample and not easily available, but the data shown in Fig. 6.11 illustrate that the depth resolution of a system can be

determined in a good approximation by using the width of the Si peak for wavelengths below 600 nm. This was tested on a variety of systems in different laboratories and can therefore be regarded as a valid method even though this is in contrast to some reference papers [16].

Above 600 nm the penetration depth starts to have a significant impact on the measured FWHM. The rising flank above the surface may still enable a good approximation for the depth resolution of a system by using i.e. the 10–90% criterion (∼1.21 µm in the 785 nm example in Fig. 6.11).

The presented measurements thus clearly indicate that Si is a suitable test sample for determining the depth resolution of any confocal Raman system.

Comparing these results to the theory for low NAs indicates that it cannot be valid for high NAs. Converting this theory to match the high NA case is not trivial, but an approximation can be given following the work by Mack [17]. Based on this, the ratio between the low and high NA results can be calculated as:

$$\frac{low\ NA\ result}{high\ NA\ result} = \frac{4\sin^2(\frac{\Theta}{2})}{\sin^2(\Theta)} \tag{6.5}$$

where Θ is half of the opening angle of the objective. For an NA of 0.9 this results in a correction factor of 1.38. Thus the best depth resolution achievable according to this approximation should be about 682 nm for a 100× NA 0.9 objective using 532 nm excitation.

The work by Wilhelm et al. [18] on confocal laser scanning microscopy can also be followed for this purpose. From this we find an axial optical resolution dependent on the projected pinhole size. For projected pinhole sizes larger than one "Airy unit" ($1.22 \times \lambda/NA$) the following equation applies:

$$FWHM_{axial} = \sqrt{\left[\frac{0.88 \cdot \lambda_{em}}{\left(n - \sqrt{n^2 - NA^2}\right)}\right]^2 + \left[\frac{\sqrt{2} \cdot n \cdot P_{proj}}{NA}\right]^2} \tag{6.6}$$

where λ_{em} refers to the emitted wavelength. Using the experimental parameters shown above with λ_{em} = 580.7 nm, this results in an axial FWHM of 920 nm for a 100× NA 0.9 objective using 532 nm excitation. It should be noted however, that the projected pinhole size is significantly smaller than the Airy unit in the presented data. For this case the work by Wilhelm et al. [18] suggests a different equation as follows:

$$FWHM_{axial} = \frac{0.64 \cdot \overline{\lambda}}{\left(n - \sqrt{n^2 - NA^2}\right)} \quad \text{with} \quad \overline{\lambda} = \sqrt{2}\frac{\lambda_{em} \cdot \lambda_{exc}}{\sqrt{\lambda_{em}^2 + \lambda_{exc}^2}} \tag{6.7}$$

With this the calculated result is approximately 630 nm FWHM.

These theories do not result in the same axial resolution which clearly indicates that there are some inconsistencies [between (6.7) and (6.5)]. The theories also do not take into account a few additional, important factors:

- The intensity distribution of the excitation beam into the back of the objective (Gaussian or flat)
- The different transmission properties of the materials and coatings used in the objective and the detection beam path
- Polarization effects

Given the rather complicated theory and several unknowns it is not surprising that theory and experiment do not fully match. It is nevertheless apparent both from theory as well as experimentally, that depth resolution well below 1 μm is possible in the visible and below 1.5 μm in the NIR. For air objectives with smaller NAs, one can approximate the expectable depth resolution by multiplying the values achieved with a 0.9 NA by $\left(\frac{0.9}{NA}\right)^2$.

6.2.3.3 Layer Thickness Determination Using Confocal Raman Microscopy

The discussion in the previous sections gave clear indications of the achievable depth resolution using a confocal Raman microscope. For surface (XY) scans and depth (XZ) scans close to the sample surface this resolution has been shown in many experiments.

When measuring a buried layer, interpretation of the data becomes more difficult. Especially when using metallurgic air objectives one has to take the change in refractive index into consideration. Due to this change the measured thickness of a buried layer will be significantly thinner than its physical extent. In addition, an increasing focus distortion can be expected as a function of depth. This distortion causes the depth resolution to become consecutively worse as a function of the depth position inside the sample and in addition the signal quality significantly decreases as a function of depth. The use of an oil immersion objective overcomes these limitations to some extent. N. Everall discussed these effects in detail in [19–21], while also outlining the impact of the use of a metallurgic objective on the shape determination of buried objects.

This effect obviously needs to be taken into consideration when performing depth profiles or 3D confocal Raman imaging. If possible, the use of an immersion objective is the preferred way to perform the experiments in order to minimize the jump in refractive index. If this is not possible, then the adverse effect on the measured thickness of sample structures needs to be taken into account. The following example outlines the differences in values obtained using an oil immersion and a metallurgic objective.

A symmetric multi-layer sample consisting of a polyethylene and polypropylene structure of the following nominal thicknesses PE (15 μm)-PP (10 μm)-PE (50 μm)-

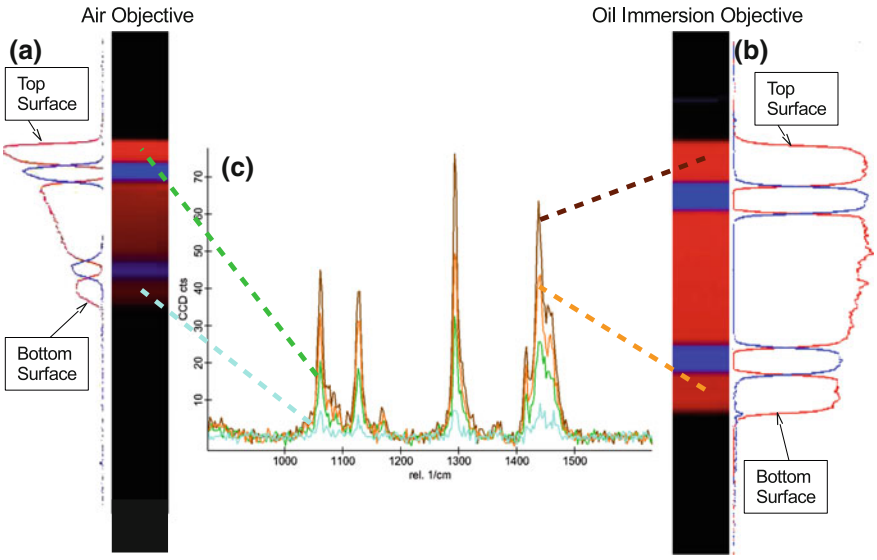

Fig. 6.12 Depth profiles obtained using a metallurgic air objective (**a**) as well as using an oil immersion objective (**b**). The color-coded images show the PP layers in red and the PE layers in blue. In (**c**) the spectra extracted from the indicated positions are shown

PP (10 µm)-PE (15 µm) was used in this example[1] (Fig. 6.12). On these structures two scans with identical parameters were performed: Once using an metallurgic air objective (100×, NA 0.9) and once using an oil immersion objective (100× NA 1.25; 0.17 mm cover glass correction). For the latter case some immersion oil was placed onto the sample followed by a microscope cover slip (0.17 mm nominal thickness). The same immersion oil was then dropped onto the cover glass into which the oil immersion objective was dipped.

The scans were performed using a 532 nm laser with ≈40 mW before the objective. The signal was detected using a UHTS 600 spectrometer, a 300 g/mm grating and an EMCCD camera operated in conventional mode. The depth scans were performed on a width of 10 µm and a depth of 200 µm with 20 × 400 points and an integration time of 34 ms per spectrum recorded. The data was analyzed using the basis analysis tool within the WITec Suite FOUR software package to generate one image per phase for each scan. These images were then combined into false-color images and displayed in Fig. 6.12a for the metallurgic air objective and in (b) for the oil immersion objective. To the left and right of the images, the depth profiles of the two phases can be seen and in Fig. 6.12c the spectra extracted from the background-subtracted data are shown (36 ms exposure time).

The results clearly indicate that the thickness obtained with the air objective is significantly thinner than the real extent, whereas the results obtained using the oil

[1] Sample curtesy José M.F. Swart, AkzoNobel Chemicals bv, Deventer, The Netherlands.

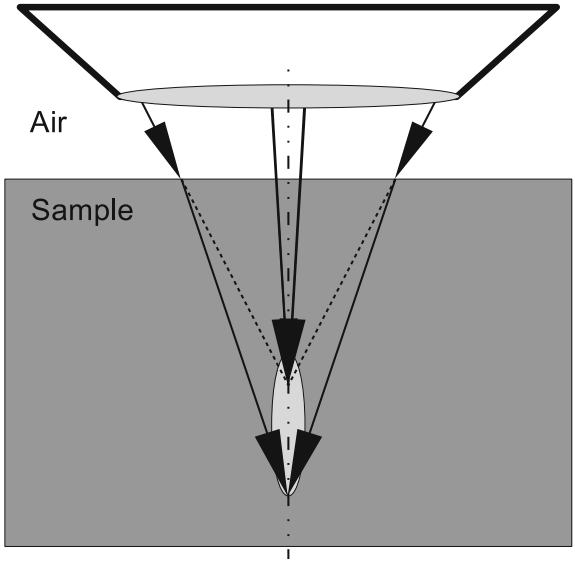

Fig. 6.13 Focus distortion due to spherical aberration. The rays almost parallel to the optical axis hardly change their direction due to the jump in refractive index, but rays hitting the surface under larger angles are diffracted more strongly and therefore cause a focus elongation along the Z-axis

immersion objective are close to the nominal structure thickness. For the second PP layer it is particularly obvious that the profile is smeared out much more for the results obtained using the metallurgic objective than is the case for the oil immersion objective.

Looking at Fig. 6.12c one can additionally see the clear advantage of the oil immersion objective in its collection efficiency. The spectra on top of the structure (dark brown and green) show a difference in intensity because of the index matching and difference in numerical aperture between the objectives, but near the base of the structure the difference becomes much more dramatic (light brown versus turquoise spectrum). This can be attributed to the focus distortion occurring in the case of the metallurgic objective due to spherical aberration (see Fig. 6.13).

For samples located directly underneath a glass slide, a cover glass corrected objective can minimize or even eliminate the effect of spherical aberration. The signal obtained by the oil immersion objective also somewhat decreases, but since the light travelled through a total thickness of about 200 µm for the excitation and again 200 µm for the collection some loss of signal is to be expected. More important contributors to the loss are probably, however, scattering centers within the foil. As the foil is not completely transparent such centers are likely to exist and to scatter part of the light.

In conclusion, care should be taken when interpreting depth profiles obtained using metallurgic air objectives. The use of an oil immersion objective greatly simplifies the interpretation of depth profiles. For samples such as polymers or oil based samples, oil immersion objectives are the ideal choice since the refractive index of the immersion oil (∼1.45) is very close to that of the sample. For samples in a water environment

(i.e. biological cells) the use of a water immersion or water dipping objective is the better choice.

There are, however, situations when a jump in refractive index cannot be avoided. Measuring for example a diamond sample in order to observe an inclusion therein confronts us with a sample exhibiting a refractive index of about 2.4. Also, some samples will not allow the use of immersion liquids since they would i.e. deteriorate the sample. In these cases, one can -as a very rough approximation- multiply the observed Z-axis values (i.e. the layer thicknesses) by the ratio of the refractive index of the sample divided by the refractive index of the immersion liquid (or air if a metallurgic objective is used).

Additional care has to be taken if the sample is not planar and especially if the sample contains many small inclusions which can act as diffracting points or distort the wavefront by other means. In such cases an absolutely correct interpretation of the data can only be achieved using i.e. ray-tracing algorithms in combination with substantial computation power for the necessary simulations. As the detailed structure of the sample would be needed for exact simulations and since this is often unknown or is indeed exactly the feature one wishes to investigate, a level of uncertainty often remains.

Nevertheless, the high level of confocality available with some commercial instruments allows detailed 3D Raman observations, which can shed light on sample properties which otherwise might remain hidden.

6.2.3.4 The Effect of Chromatic Aberration on Depth Profiling and 3D Confocal Raman Imaging

Chromatic aberration in an objective can cause an additional challenge in the interpretation of depth profiles or 3D confocal Raman images. Chromatic aberration is the effect that causes the focus position for a given objective to change with the wavelength, as shown schematically in Fig. 6.14.

The extent to which this effect will occur mainly depends on the objective and an *Epiplan Neofluar* objective will for example show this effect much less than i.e. an *Achromat*. The difference in focal position within the Raman detection range can vary from less than 50 nm for very good objectives to more than 600 nm for less well-corrected objectives [22].

Whether this difference can be detected at all -and thus plays a role in the interpretation of the collected data- heavily depends on the depth resolution of the system used as indicated with the orange and turquoise ellipses in Fig. 6.14. In a system not capable of resolving small differences in depth (orange ellipse), the chromatic aberration will likely not even be detectable, but using a highly confocal system, which is capable of detecting and differentiating even thin layers (turquoise ellipse), this effect should be taken into account. Lasch et al. [22] showed how such aberration can also be corrected for within one dataset in order to obtain an aberration-free 3D representation of the measured sample.

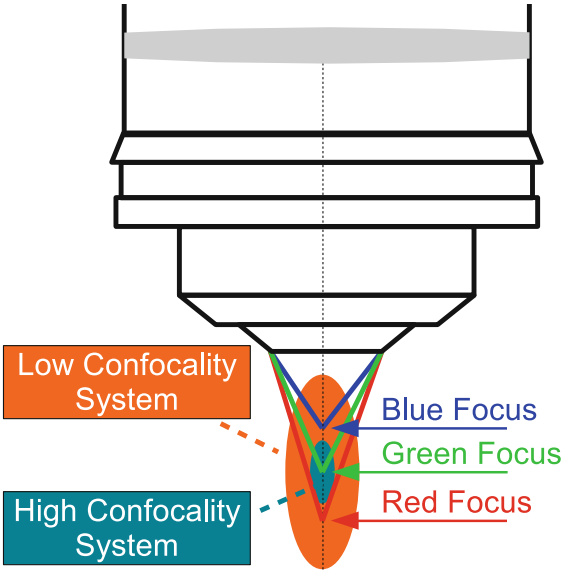

Fig. 6.14 Chromatic aberration of an objective. The effect on the position of the focus for different wavelengths can be seen as well as the difference in effect using a low confocality and a high confocality system

6.2.3.5 Summary of Depth Resolution

Given all the information provided in the sections before, it is apparent that the design parameters for a high resolution confocal Raman microscope are:

- Diffraction-limited illumination and circular pinholes will deliver better depth resolution than line illumination and/or slits for detection.
- The optimum (projected) pinhole diameter should be slightly smaller than the Airy disc size.
- Using a smaller pinhole enhances the depth resolution only slightly but comes at a high price in terms of throughput (sensitivity of the system).
- Using a larger pinhole strongly reduces the depth resolution (and therefore the confocality) which leads to a strong increase in the background signal.
- Spherical and potentially also chromatic aberration need to be taken into account for layer thickness determination. Both can be minimized by the use of an appropriate, high quality objective.

6.3 Throughput and Detection Sensitivity

In establishing the throughput of a confocal Raman system it is worthwhile to evaluate the spectrometer and microscope separately. In either case it should be noted that every passive optical element will decrease the throughput of the system. This means

that an elaborate setup with many mirrors suffers from significant losses. A good overview of suitable components can be found in Chap. 4.

When considering a measurement representative of the throughput and detection sensitivity of a system it is important to note that some equipment, CCD cameras in particular, can be optimized for short integration times while others (i.e. due to lower dark current) might be optimized for long integration times. Using a back-illuminated CCD camera with higher dark noise than a front-illuminated CCD will yield the best results for short integration times (i.e. <10 s per spectrum). With typical dark currents of 0.02 electrons per pixel per second the dark noise of back-illuminated CCD cameras is however already remarkably low while using only fans and Peltier-cooling. Additional (water) cooling of these cameras can further reduce their dark noise and make them the superior choice for measuring weak scattering samples (i.e. gases at low pressures) with which integration times of up to 20 min and more are relevant.

Silicon (Si) is a readily available sample that can be measured without specialized preparation and is often used to demonstrate the sensitivity of a system. While Si is a very good scatterer, the fourth order emission near 1950 rel. cm^{-1} is very weak. For this reason the measurement of the 4th order is often used to show the sensitivity of a system. If, however, the integration time is not given and compared for the measurement, then it in reality can only be seen as a proof that given a long enough integration time, the signal of the 4th order Si peak will eventually become larger than the noise originating from the CCD. From these measurements the level of confocality can, however, be estimated by paying special attention to the often visible N_2 and O_2 Raman lines.

In order to properly compare the results obtained by different systems one should take several points into consideration:

Laser Power
The laser power is directly proportional to the intensity of the measured signal.

Excitation Wavelength
The intensity of the emitted Raman signal is proportional to the excitation wavelength to the power of four.

Objective
The objective is a key element in estimating the lateral resolving power of the system (not shown by the 4th order measurement itself). As the objective can also have a strong influence on the throughput and amount of signal collected this should be taken into account.

Dispersion of the Spectrometer
The dispersion of the spectrometer depends on the focal length, the grating, the entrance slit/pinhole and the pixel size on the CCD. If the signal is dispersed over more pixels on the CCD, then the signal-to-noise will be lower than if the signal only hits a few pixels.

Integration Time
The longer the integration time the better the signal-to-noise ratio.

Confocality

The confocality of the system is of lesser concern during the measurement of the 4th order of Si. It is, however, important for many other measurements and one should ensure that the sensitivity is determined at a high confocality. This can be simply checked if wavelengths in the blue and green region of the spectrum are used for excitation. In these cases the penetration depth of the light into the Si is small (see Fig. 6.11). The volume of the sample investigated is thus limited in the Z-direction by this penetration depth. Part of the collection volume, however, lies above the sample and consists of normal air in a typical experiment. The size of this air volume will depend heavily on the confocality of the system used. The intensity of the N_2 and the O_2 peaks are therefore an indication of how big the sampled air volume was. The lower those peaks relative to the 4th order Si peak, the better the confocality was during the measurement.

An example of measurements of the 4th order of Si with different integration times is shown in Fig. 6.15. The spectra are offset for clarity. The excitation laser used emitted at 532 nm and was set to 5 mW before the objective. A 100× air objective with an NA of 0.9 was used and the dispersion at the position of the 4th order Si peak was $\sim 2.4 \frac{\text{rel. cm}^{-1}}{\text{pixel}}$. The cosmic rays were removed from the signal but no background subtraction or smoothing was applied. The O_2 peak can hardly be recognized unless the integration time is very long and the N_2 peak is about the same height as the 4th order Si peak. The measurements were performed using a standard back-illuminated CCD camera without additional cooling. Even with this camera it is clear that the signal-to-noise ratio improves significantly with a longer integration time and that the intrinsic noise of the CCD does not seem to be the limiting factor.

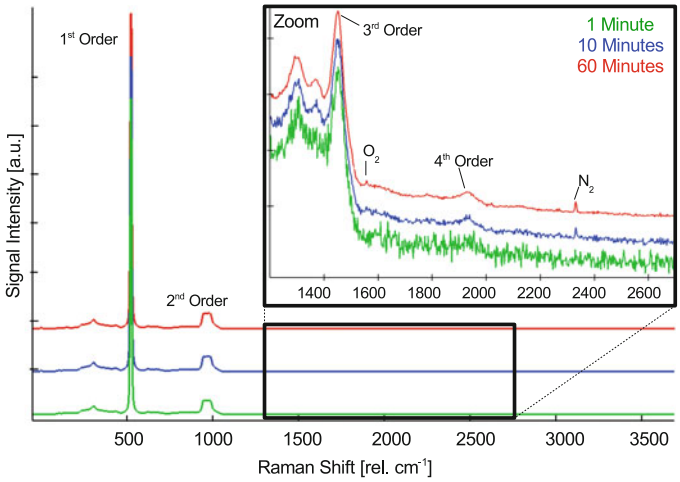

Fig. 6.15 Measurements of the 4th order Si emission line using different integration times

6.4 3D Confocal Raman Imaging

Given that the throughput and resolution discussed in the previous sections are achieved simultaneously, high resolution 3D confocal Raman imaging can be performed. For this, the samples need to be sufficiently transparent for the excitation and detection wavelengths. The sample can be recorded layer by layer into an image stack. This stack can then be evaluated in a similar way as a single layer would be (see Chap. 5) and from the resulting images 3D representations can be generated.

As discussed in Sect. 6.2.3.3, the intensity of the scattered light decreases with increasing depth into the sample - even when using perfectly corrected objectives - and it may be advantageous to compensate for this decrease via software. In order to achieve this, an area where the molecular structure of the sample does not change as a function of depth should be included in the 3D image scan. This could, for example, be the host mineral when measuring an inclusion or the buffer solution when measuring a biological cell. From the spectra of this material an image i.e. of the integrated intensity of a dominant peak can then be calculated for each layer. It is recommended to then average a certain area to minimize fluctuations and errors. Based on the decrease of this averaged integrated intensity, an intensity correction factor can be calculated and applied to the spectral data sets of each layer. Some 3D rendering softwares also offer normalization tools such as a "stack normalizer", which can also work.

For the 3D representation of confocal Raman microscopy data one can largely follow the methods established for i.e. confocal laser scanning microscopy (CLSM) data or scanning electron microscopy (SEM) data sets. There are four commonly used ways to represent the data:

Layer collage
In this representation method all layers are plotted next to each other to form an overview image. The layers are then typically visible as squares. Figure 21.6 in Chap. 21 shows an example of this.

3D Cross sections
For this, a cross section in a freely definable angle is calculated from the stack of images showing, for example, an XZ cross section (see Fig. 21.7b in Chap. 21).

Semitransparent 3D volume representation
In this method the stack is displayed in a 3D representation while the level of transparency of the objects can be controlled in order to also show objects within or behind.

Isoplanar 3D representation
In contrast to the semitransparent representation, this method calculates the surfaces of identical intensity of a phase and then represents this as an object. The above-mentioned correction for the loss of intensity as a function of depth should be applied to the datasets for this representation. An advantage of this method is that the illumination direction and light color as well as the reflectivity of the generated surfaces can also be controlled.

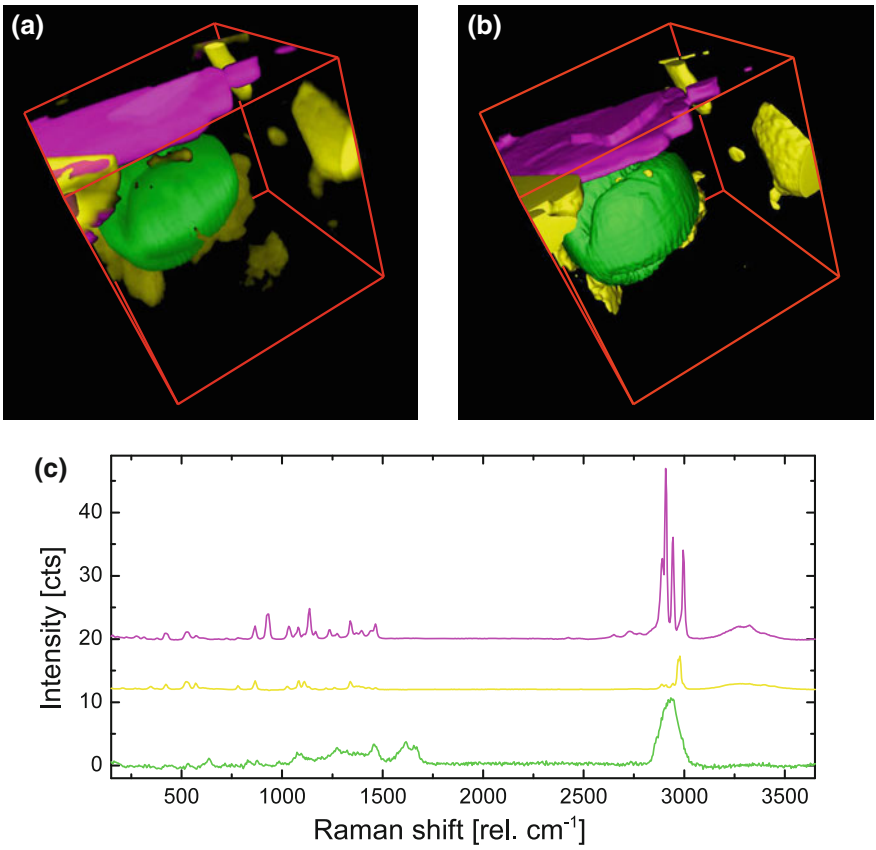

Fig. 6.16 Different 3D representations of a confocal Raman scan of honey: **a** Semitransparent volume view and **b** isoplanar view of the honey sample. Displayed is a pollen in the honey (green) as well as two phases of crystalline sugar (purple and yellow). The corresponding spectra can be seen in (**c**)

Figure 6.16a shows an example of the semitransparent volume view representation and Fig. 6.16b shows an isoplanar representation of the same confocal Raman dataset both produced using the ImageJ[2] software. The sample was honey and the objects plotted are pollen in the honey (green) as well as two phases of the crystalline sugar (purple and yellow) of which in Fig. 6.16c the spectra in the corresponding colors can be seen.

[2]https://imagej.nih.gov/ij/.

The dataset was recorded using an alpha300 R system (WITec GmbH) with an oil immersion objective, 488 nm excitation and a UHTS 300 spectrometer. The integration time per spectrum was 12.2 ms and 150 × 150 × 50 spectra were recorded in a volume of 50 × 50 × 50 µm. The sample was prepared between two cover slips and allowed to settle before measurement.

6.5 Confocal Raman Microscopy on Rough or Inclined Surfaces

The last section outlined how three-dimensional confocal Raman data-sets can be obtained and how they can be displayed for the best visualization. Apart from such 3D measurements, it is also often interesting to measure along the surface of inclined or rough samples. If the sample tilt or its roughness exceed the depth resolution of the system (see Sect. 6.2.3.2), then the sample will be for part of the measurement out of focus. The stronger the inclination or the roughness is, the bigger the portion of the scanned area which is out of focus will be, if a flat scan in i.e. the XY plane is performed.

In order to overcome this problem, different strategies are commonly followed. They can be categorized in:

- Two-pass techniques, in which the surface of the sample is first recorded before, in a second step, the confocal Raman image is recorded while changing the X, Y and Z coordinates for every point in order to follow the previously recorded surface.
- Single-pass techniques, in which the surface is kept in permanent focus using a closed-loop feedback technique. In this way the confocal Raman image along an irregularly shaped surface can be recorded in one pass. This technique has the advantage that it is faster than the two-pass technique and that modifications such as swelling or shrinking of the sample can be compensated for.

Irrespective of the technique used, it is important that the dimensionality of the topography recording matches that of the confocal Raman measurement. It thus does not make sense to use a line focus for confocal Raman measurements in combination with a point focus in the topography feedback, as in such an arrangement only one spot on the line would be kept in focus. The technique of course only works if the depth resolution achieved by the topography compensating component is significantly higher than the depth resolution achievable by the confocal Raman system (see Sect. 6.2.3.2).

TrueSurface microscopy employs such a compensation technique. It was originally a two pass technique, but was in 2017 upgraded to a single-pass topography compensation technique [23]. Figure 6.17 shows a TrueSurface scan of a painkiller tablet containing various ingredients such as paracetamol, aspirin and caffeine.

It can be seen that the total topography that had to be compensated for was more than 800 µm. Since a 50× NA 0.8 objective was used, the depth resolution of the

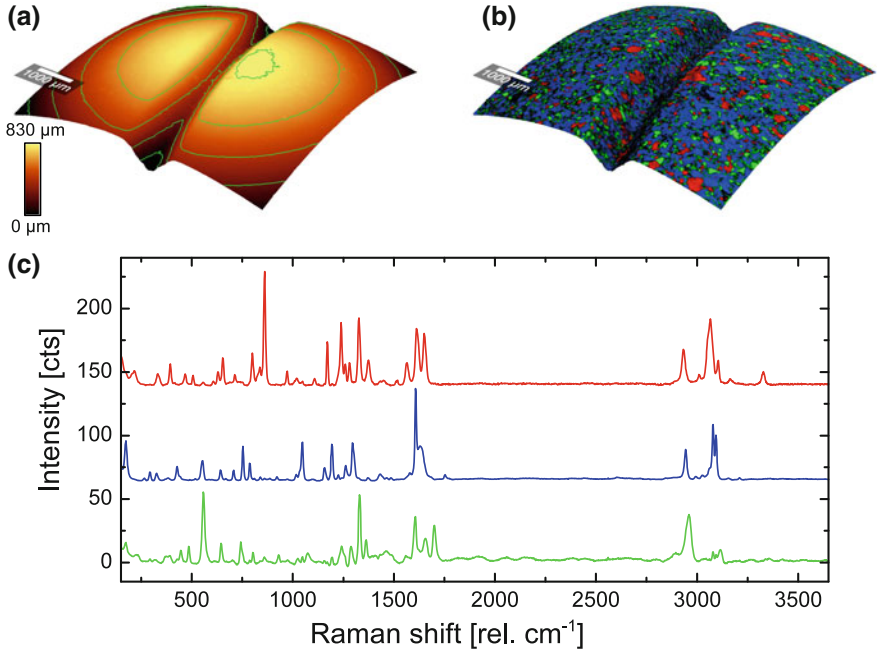

Fig. 6.17 TrueSurface confocal Raman image of a painkiller tablet: **a** Topography of the tablet with contour lines of equal height plotted in green. **b** TrueSurface confocal Raman image of the tablet. **c** Spectra of the components: Red = paracetamol; Blue = aspirin; Green = caffeine. The colors of the spectra correspond to the colors in the confocal Raman image in (**b**)

system was $<1.2\,\mu m$ and it is therefore clear that such a measurement would not have been possible without proper compensation of the topography.

The dataset was recorded using an *apyron* confocal Raman microscope (WITec GmbH) using 532 nm excitation at 15 mW and a UHTS 300 spectrometer. The integration time per spectrum was 140 ms and 600×600 spectra were recorded in an area of $7000 \times 7000\,\mu m$.

6.6 Beyond the Diffraction Limit

In Sect. 6.2 the resolving power achievable with confocal Raman microscopes was outlined. With high quality microscopes this performance is generally achievable in everyday measurements. For certain samples a resolution beyond the diffraction limit is desirable.

On the 8th of October 2014, the Nobel Prize in Chemistry was awarded for "super-resolution-microscopy" to Eric Betzig, W.E. Moerner and Stefan Hell. Some techniques typically described in the context of "super-resolution-microscopy" are:

- STimulated Emission Depletion microscopy (STED)
- STochastic Optical Resolution Microscopy (STORM)
- PhotoActivated Localization Microscopy (PALM)

as well as variations thereof. These techniques, however, rely on the sample being labelled with a fluorescent dye and the localization of the fluorescence emission with high resolution. As this requirement is not fulfilled in confocal Raman microscopy, these techniques do not provide a means of achieving resolution beyond the diffraction limit. Through slight variations of the techniques, however, some impressive results were achieved with a combination of STORM and surface enhanced Raman spectroscopy (SERS) [24]. Also somewhat related to STORM is the approach demonstrated by Roider et al. in which a bundle of fibers was used for detection in order to enhance the achievable lateral resolution [25].

Apart from these super-resolution techniques, two other methods have recently become established as high resolution variations of confocal Raman imaging. They are Tip Enhanced Raman Spectroscopy (TERS) and the lesser-known aperture-based Scanning Nearfield Optical Microscopy (SNOM) and Raman combination. Both techniques will be briefly described in the following. Common to both techniques is that the setup and experimental realization is significantly more involved than for standard confocal Raman imaging and so the challenges posed by the experiment can quickly take precedence over the challenges posed by the sample itself.

6.6.1 Tip Enhanced Raman Spectroscopy (TERS)

The principle of TERS is that a functionalized tip enhances the Raman signal with a very strong localization around the tip [26–28]. TERS has the advantage that for a successfully prepared tip, the Raman signal is amplified and thus made detectable while at the same time the sampling volume is kept very small. There have been many publications on the principles of TERS (i.e. [26, 29]) including some comprehensive reviews [30] as well as numerous publications describing measurements performed (i.e. [31–33]). As it is beyond the scope of this chapter to go deeper into TERS measurements, the reader is referred to the above mentioned literature for further reading on the topic. The biggest challenge of TERS, which remains unsolved, is the stability of the tip during scanning and the accumulation of “debris” on the tip which prevents stable imaging.

6.6.2 Scanning Nearfield Optical Microscopy (SNOM) and Raman

The combination of aperture-based SNOM with Raman has the advantage of using tips that are easier to manufacture and more durable when in contact with a sample.

The downside is that in contrast to TERS, no enhancement is generated at the tip and that the throughput of light through small apertures is obviously low, which can make the detection of the generated Raman signal more difficult.

Aperture SNOM tips are available as fiber-based or cantilever-based sensors. For cantilever-based sensors the light is focused into the backside of a hollow pyramid. The hollow pyramid consists of a thin layer of SiO_2, coated with an aluminium layer. The pyramid has a less-than 50–100 nm small hole that forms the nanoscopic light source aperture.

Although these cantilever SNOM tips have the highest transmission of all aperture SNOM sensors, the transmission is still only in the range of 10^{-4} and the power they can withstand is about 10–20 mW. For fiber-based SNOM tips this value is typically considerably lower. Thus the power at the aperture with maximum input is in the range of 1–2 µW. The signal reduction by four orders of magnitude means that in order to achieve the same signal to noise ratio from a sample the integration time

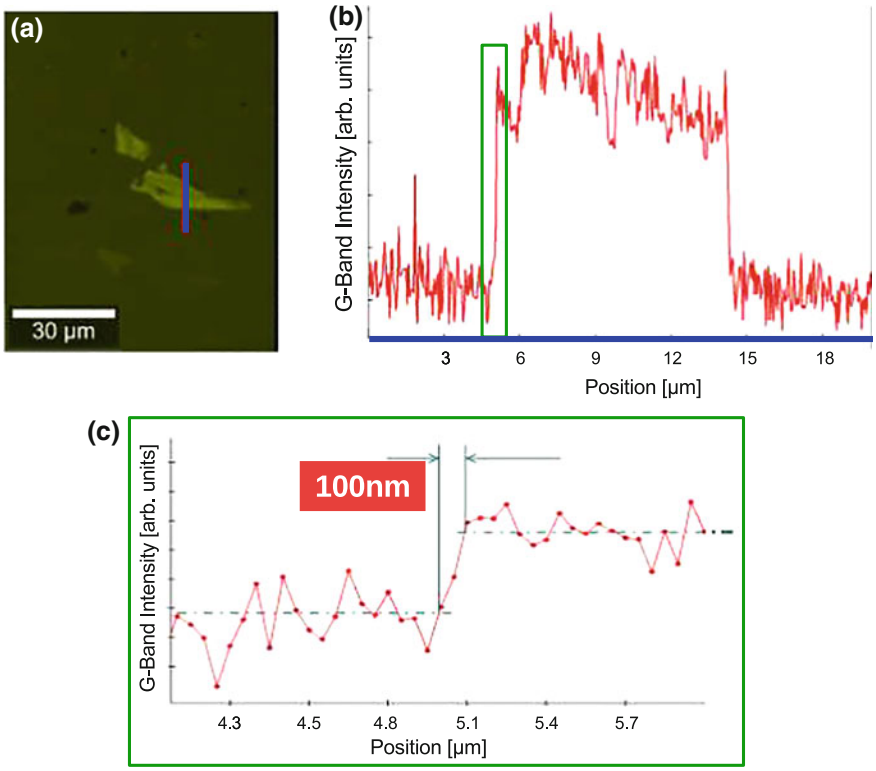

Fig. 6.18 SNOM-Raman measurement on a piece of ultrathin graphite. The blue line in the video image **a** shows the location of the measurement. In **b** the integrated intensity of the G-band along the entire line is shown and in **c** a zoom onto the edge of the ultrathin graphite. The integration time per spectrum was 1 s

has to be 10,000 times longer. When considering the reduced scattering volume due to the small spot size this factor becomes even larger. Therefore only very good Raman scattering samples are within reach of this technique. Nevertheless Fig. 6.18 shows a SNOM-Raman measurement of an ultrathin graphite flake on glass. The measurement has been taken in transmission to increase the collection efficiency and demonstrates a lateral resolution of $<100\,\text{nm}$, a factor of three smaller than the diffraction limit.

6.7 Conclusion

Confocal Raman microscopy measurements carried out at high resolution with reasonable integration times are only possible with systems of sufficient performance. The key factors are spatial and spectral resolution as well as throughput at high confocality. Using readily available standard samples these qualities can be determined and compared between different systems.

It is of critical importance that the different elements in an instrument perform at a high level simultaneously. If, for example, a thin layer is to be measured on a strongly scattering substrate, the system must then maintain a high level of sensitivity (to allow detection of the layer) concurrent with a very high level of confocality (in order to suppress the out-of-focus light originating from the substrate). High lateral resolution is essential for Raman imaging and the throughput determines whether the measurements, which may consist of hundreds of thousands of spectra, can be performed in a practical amount of time. Finally, if a virtual cut into the sample (X-Z scans) or 3D confocal Raman imaging is required, then lateral and depth resolution as well throughput must be optimized in unison. For rough or inclined samples, topography correction techniques allow their measurement while still profiting from the same high depth resolution as is the case for flat samples.

Spectral resolution should be independent of spatial resolution and determined only by the design of the spectrometer. It is the crucial element when evaluating exact peak positions and/or shifts as well as for the differentiation of closely-spaced peaks.

Research-grade confocal Raman microscopes should necessarily offer high throughput at the same time as high spectral and spatial resolution. The ideal system should therefore not require the user to have to choose between high throughput and high resolution solution.

Acknowledgements Proofreading by Olaf Hollricher and Damon Strom is gratefully acknowledged. Wolfram Ibach performed the measurements and prepared the images for Figs. 6.16 and 6.17 and was of immense help in many discussions.

A. Appendix

A.1 Ideal Performance Test Samples

Based on the methods and theories described in this chapter, ideal samples for performance determination are outlined in the following. An ideal system can achieve optimal results for each of the categories in the same configuration.

A.1.1 Lateral Resolution

Ideal sample: **Isolated Single- or Multi-walled Carbon Nano-Tubes (CNTs)**

- Recommended maximum diameter: 75 nm
- Recommended minimum length: 1 µm
- Recommended substrate: Si or glass (required for resolution determination using immersion objectives)

A.1.2 Depth Resolution and Confocality

Ideal sample: **Suspended Graphene or Ultrathin Graphite or Si when using only the rising flank of the depth profile**

- Recommended maximum sample thickness (for suspended samples): 50 nm
- Recommended minimum hole diameter (for the suspended part): 5–10 µm
- Recommended substrate: Si

A.1.3 Spectral Resolution

Ideal sample: **Atomic Emission Lines**
The emission should be guided along exactly the same beam path as the scattered Raman light.

- Recommended emission lines: Within the Raman detection range.

532 nm: Hg @ 546.0735 nm [34]
785 nm: Ar @ 912.2967 nm [35]

A.1.4 Throughput

Ideal sample: **Si**
Crucial parameters for possible comparison:

- Laser power
- Laser wavelength
- Objective
- Spectral dispersion @ $\approx$1950 rel. cm^{-1}
- Integration time
- Confocality (measured by comparison of the peak height of the 4th order Si peak relative to the intensity of the O_2 and N_2 emission lines - see Fig. 6.15).

References

1. P. Jenniskens, M. Shaddad, D. Numan, S. Elsir, A. Kudoda, M. Zolensky, L. Le, G. Robinson, J. Friedrich, D. Rumble et al., Nature **458**(7237), 485 (2009)
2. A. Rotundi, G. Baratta, J. Borg, J. Brucato, H. Busemann, L. Colangeli, L. d'Hendecourt, Z. Djouadi, G. Ferrini, I. Franchi et al., Meteorit. Planet. Sci. **43**(1–2), 367 (2008)
3. C. Heim, J. Lausmaa, P. Sjövall, J. Toporski, T. Dieing, K. Simon, B. Hansen, A. Kronz, G. Arp, J. Reitner et al., Geobiology **10**(4), 280 (2012)
4. S. Hild, F. Neues, N. Žnidaršič, J. Štrus, M. Epple, O. Marti, A. Ziegler, J. Struct. Biol. **168**(3), 426 (2009)
5. N. Gierlinger, M. Schwanninger, J. Spectrosc. **21**(2), 69 (2007)
6. A. Hermelink, A. Brauer, P. Lasch, D. Naumann, Analyst **134**(6), 1149 (2009)
7. Y.N. Xu, D. Zhan, L. Liu, H. Suo, Z.H. Ni, T.T. Nguyen, C. Zhao, Z.X. Shen, ACS Nano **5**(1), 147 (2010)
8. Y. You, T. Yu, J. Kasim, H. Song, X. Fan, Z. Ni, L. Cao, H. Jiang, D. Shen, J. Kuo et al., Appl. Phys. Lett. **93**(10), 103111 (2008)
9. T. Yu, Z. Ni, C. Du, Y. You, Y. Wang, Z. Shen, J. Phys. Chem. C **112**(33), 12602 (2008)
10. C. Matthäus, A. Kale, T. Chernenko, V. Torchilin, M. Diem, Mol. Pharm. **5**(2), 287 (2008)
11. T. Chernenko, C. Matthäus, L. Milane, L. Quintero, M. Amiji, M. Diem, ACS Nano **3**(11), 3552 (2009)
12. L. Rayleigh, Lond. Edinburgh Dublin Phil. Mag. J. Sci. **42**(255), 167 (1896)
13. R. Millar, K. Gallacher, A. Samarelli, J. Frigerio, D. Chrastina, T. Dieing, G. Isella, D. Paul, Thin Solid Films (2015)
14. R. Millar, K. Gallacher, A. Samarelli, J. Frigerio, D. Chrastina, G. Isella, T. Dieing, D. Paul, Opt. Express (2015)
15. M. Shur, *Physics of Semiconductor Devices* (Prentice-Hall, Inc., Englewood Cliffs, NJ, 1990)
16. F. Adar, (2010). http://www.spectroscopyonline.com/depth-resolution-raman-microscope-optical-limitations-and-sample-characteristics
17. C.A. Mack, Microlith. World **13**(1), 14 (2004)
18. S. Wilhelm, B. Gröbler, M. Gluch, H. Heinz, Jena, Germany: Carl Zeiss Advanced Imaging Microscopy p. 258 (2003). http://zeiss-campus.magnet.fsu.edu/referencelibrary/pdfs/ZeissConfocalPrinciples.pdf
19. N. Everall, Spectrosc.-Springfield Eugene Duluth- **19**, 22 (2004)
20. N. Everall, Spectrosc.-Springfield Eugene Duluth- **19**, 16 (2004)
21. N. Everall, J. Raman Spectrosc. **45**(1), 133 (2014)
22. P. Lasch, A. Hermelink, D. Naumann, Analyst **134**(6), 1162 (2009)
23. WITec GmbH. True surface microscopy (2017). http://www.witec.de/products/accessories/truesurface/
24. S. Ayas, G. Cinar, A.D. Ozkan, Z. Soran, O. Ekiz, D. Kocaay, A. Tomak, P. Toren, Y. Kaya, I. Tunc, et al., Sci. Rep. **3** (2013)
25. C. Roider, M. Ritsch-Marte, A. Jesacher, Opt. Lett. **41**(16), 3825 (2016)
26. R.M. Stöckle, Y.D. Suh, V. Deckert, R. Zenobi, Chem. Phys. Lett. **318**(1), 131 (2000)

27. N. Hayazawa, Y. Inouye, Z. Sekkat, S. Kawata, Opt. Commun. **183**(1), 333 (2000)
28. M.S. Anderson, Appl. Phys. Lett. **76**(21), 3130 (2000)
29. E. Bailo, V. Deckert, Chem. Soc. Rev. **37**(5), 921 (2008)
30. T. Schmid, L. Opilik, C. Blum, R. Zenobi, Angew. Chem. Int. Ed. **52**(23), 5940 (2013)
31. A. Weber-Bargioni, A. Schwartzberg, M. Cornaglia, A. Ismach, J.J. Urban, Y. Pang, R. Gordon, J. Bokor, M.B. Salmeron, D.F. Ogletree et al., Nano Lett. **11**(3), 1201 (2011)
32. G. Rusciano, G. Zito, R. Isticato, T. Sirec, E. Ricca, E. Bailo, A. Sasso, ACS Nano **8**(12), 12300 (2014)
33. G. Zito, G. Rusciano, A. Vecchione, G. Pesce, R. Di Girolamo, A. Malafronte, A. Sasso, Sci. Rep. **6** (2016)
34. K. Burns, K.B. Adams, J. Longwell, JOSA **40**(6), 339 (1950)
35. G. Norlén, Physica Scripta **8**(6), 249 (1973)

Part III
New Materials

Chapter 7
Nano-spectroscopy of Individual Carbon Nanotubes and Isolated Graphene Sheets

Alain Jungen

Abstract The following chapter will review the resonant Raman active modes of single-walled carbon nanotubes emphasizing the diameter-dependence of the radial breathing mode and selectivity of the optical transition energies (resonance). Thermal studies of individual freestanding single-walled carbon nanotubes showed a pronounced phonon softening. The second part of the chapter is devoted to Raman imaging of graphene. This particular type of carbon nanophase has become available only recently. The first Raman signatures of few-layer to single-layer graphene flakes could be obtained and compared with scanning probe microscopy. The effect of electrical charging (doping) on the Raman features is also demonstrated.

7.1 Introduction

Carbon is a unique element showing a variety of stable forms based on three different hybridizations of its atomic orbitals. Some of these forms are shown in Fig. 7.1.

Under ambient conditions, the layered structure of sp^2 hybridized graphite is the ground state phase for bulk carbon [1]. In addition to the diamond and graphite bulk phases, the discovery of fullerene triggered much of the recent interest in nanoscale phases of carbon [2].

Graphene is an atomically thin single sheet of sp^2 bonded carbon. It is the basic structural element of all other graphitic materials including graphite, carbon nanotubes and fullerenes. Intrinsic graphene is a semi-metal and features a linear dispersion relation near the six corners of the 2D hexagonal Brillouin zone. This means that electrons and holes near these corners behave like relativistic particles [3].

A single-walled carbon nanotube (SWNT) can be conceptually considered as a seamless cylinder rolling up graphene with a size of a few nanometers in diameter and a length ranging from tens of nanometers to millimeters. For nanotubes there

A. Jungen (✉)
Micro and Nanosystems, ETH Zurich, Zurich, Switzerland
e-mail: ajungen@ethz.ch; ajungen@nicronex.com

A. Jungen
Nicronex Ltd., Luxembourg, Luxembourg

J. Toporski et al. (eds.), *Confocal Raman Microscopy*, Springer Series in Surface Sciences 66, https://doi.org/10.1007/978-3-319-75380-5_7

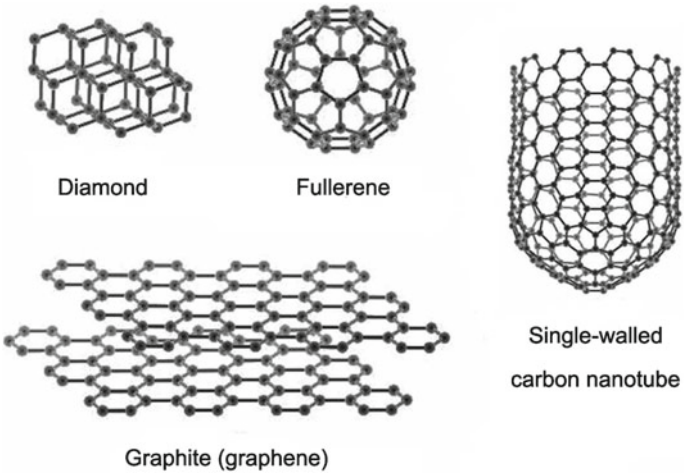

Fig. 7.1 Different carbon allotropes with nanometer-scale phases ranging from 0D C60 fullerenes, 1D carbon nanotubes, 2D graphene to 3D diamond and graphite

are many different types depending on the rolling direction of a sheet into a cylinder which then exhibits different diameters and properties [4, 5].

Single-walled nanotubes show different properties, depending on their diameter and rolling direction. They are characterized by their chiral vector with indices n and m (see Fig. 7.2). This chiral vector determines whether a nanotube is semiconducting or metallic. If $n = m$, the nanotube is metallic, if $n - m$ is a multiple of three, the nanotube is semiconducting with a small bandgap. Otherwise it has semiconducting properties with larger bandgaps.

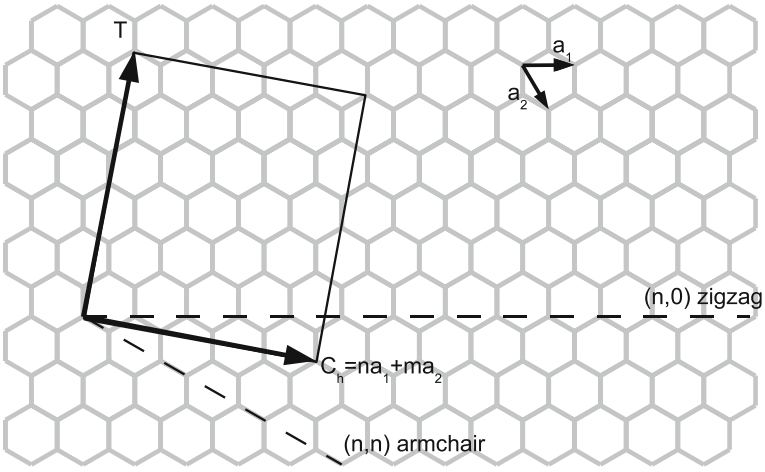

Fig. 7.2 The vector C_h describes, how a sheet of graphene is rolled up to create a carbon nanotube [6]

7.2 Individual Carbon Nanotubes

7.2.1 Phonons

Single-walled carbon nanotubes have several Raman active vibrational modes; the exact number depends on the symmetry of the tube but is independent of its diameter. However, only four to five Raman bands are strongly resonance enhanced. Three of them are located around 1600 rel. cm^{-1} and correspond to the characteristic G+, G– and D modes of the graphene sheet. As they are related to graphite they appear at similar frequencies in nanotubes.

The radial breathing mode (RBM), however, is specific to nanotubes and arises from a radial expansion and contraction of the entire tube. The phonon dispersion can be found theoretically by zone folding the graphene Brillouin zone. However, this approach has some shortcomings, most notably for the acoustic modes. For example, the out-of-plane translation, an acoustic mode in graphene, transforms into the RBM in carbon nanotubes with non-zero frequency at the Γ-point.

A typical Raman spectrum of a single-walled carbon nanotube excited at $E_l = 2.33$ eV is shown in Fig. 7.3. The low-frequency range of the RBM is between 80 and 350 rel. cm^{-1}, the intermediate range with the defect-induced vibration (D-mode), which involves phonons from the graphene K-point, lies between 1200 and 1400 rel. cm^{-1}, and the high-energy range from 1500 to 1600 rel. cm^{-1} belongs to the tangential mode (TM). A fifth feature at twice the dispersive D-mode frequency, often

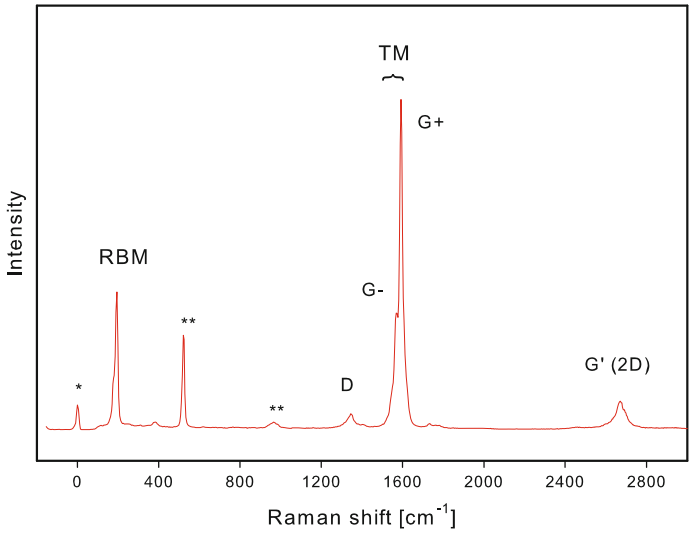

Fig. 7.3 Typical Raman spectrum of an individual single-walled carbon nanotube recorded with a confocal micro-Raman spectroscope using a green 532 nm laser. The feature marked '*' is the attenuated elastically scattered Rayleigh line. Features marked '**' come from the Si support

referred to as the G′-mode, is being considered recently. It is not a defect-induced overtone of the D-mode but a double-resonant process crossing the Γ-point twice. In graphene its shape was found to depend on the number of individual graphene layers.

7.2.1.1 Radial Breathing Mode

In the RBM all carbon atoms move in phase in the radial direction creating a breathing-like vibration of the entire tube (see Fig. 7.4a). The force needed for a radial deformation of a nanotube increases as the diameter (and hence the circumference) decreases.

The expected dependence of the radial breathing mode frequency on diameter is

$$\omega_{\mathrm{RBM}} = \frac{c_1}{d_t} + c_2 \tag{7.1}$$

with c_i being constants. Equation (7.1) was first introduced by Jishi et al. [7] and confirmed by many authors, each with slightly different c_i's [8–11]. The range of proposed values differ by a few percent and translate into a similar uncertainty for d_t. For isolated SWNTs, a quick and good diameter estimate can be made by considering $c_2 = 0$ and $c_1 = 229\ \mathrm{nm \cdot cm^{-1}}$ as reported by Popov et al. [12].

Various authors have measured their conversion parameters for example by fitting their data after having assigned the electronic transition energies (see Sect. 7.3.1).

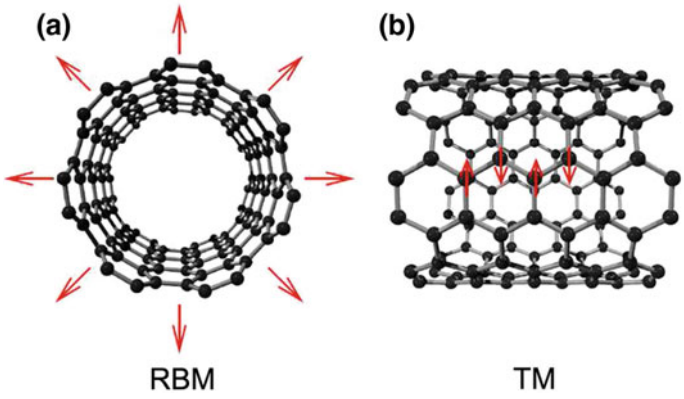

Fig. 7.4 Raman-active vibrational modes of carbon nanotubes. **a** The so-called radial breathing mode (RBM) is a prominent feature of the tubular nanostructure, and not present in planar graphite. The Raman shift of the RBM is approximatively inversely proportional to the tube diameter. **b** is an example of a tangential mode (TM). In analogy to graphitic Raman modes it is often also called G-mode, or high-energy mode (HEM)

7.2.1.2 Defect Mode

In order to understand a defect enabled mode one has to consider the problem with visible Raman spectroscopy. As photons carry very little momentum, only scattering at the Γ-point ($\boldsymbol{q} = 0$) is allowed. If the process involves a non-Γ-point phonon, it takes a defect to elastically scatter back to Γ to compensate the gained momentum in a double resonant process. This mechanism was explained by Thomsen et al. [13].

The D-mode in graphite is found at 1350 rel. cm^{-1} and is induced by disorder or defects. It is also described as a double Raman scattering in graphite. The intensity of the D-mode increases linearly with decreasing graphite crystallite size.

In carbon nanotubes, a Raman mode related to the graphite D-mode is also observed as shown in Fig. 7.3. The mechanism responsible for the laser-energy dependence is defect-induced, double resonant Raman scattering. This mode is known to be dispersive $\omega = \omega(E_l)$ and peaks at 1345 rel. cm^{-1} when excited by a 532 nm green laser.

7.2.1.3 Tangential Mode

The high-energy vibrations in carbon nanotubes correspond to the graphene optical mode at 1580 rel. cm^{-1}. In contrast to the radial breathing mode, the carbon atoms vibrate tangentially to the tube wall as depicted in Fig. 7.4b. A single Γ-point vibration of graphene transforms into a number of modes in carbon nanotubes due to the confinement of wave vectors along the circumference. The curvature of the tube wall introduces a small softening of the in-plane force constants and makes the phonon frequencies slightly diameter dependent [14]. To a first approximation, however, rolling up the graphene sheet does not markedly soften the carbon bonds [15].

The Raman spectrum of the TM is, just like the RBM, specific to single-walled carbon nanotubes which allows their identification in a tube sample. Three to four close-by peaks appear with two dominant features at 1570 and 1593 rel. cm^{-1} and do not have a Lorentzian line-shape. The 1582 rel. cm^{-1} position in SWNT corresponds often to a local minimum, allowing for a quick determination of the single-walled tube signature. Additionally, metallic SWNTs show a strong phonon softening of the longitudinal mode which is due to quantum confinement [16].

7.2.2 Theory

When the incident or scattered photons in the Raman process are in resonance with an electronic transition between the valance and conduction bands of the energy E_{ii}, the signal becomes very large as a result of the strong coupling between the electrons and phonons of the nanotube. This resonance enhancement allows the characterization of individual SWNTs with respect to electronic state, chirality, diameter and conducting properties. As the RBM is characteristic for SWNTs, it can be used to determine

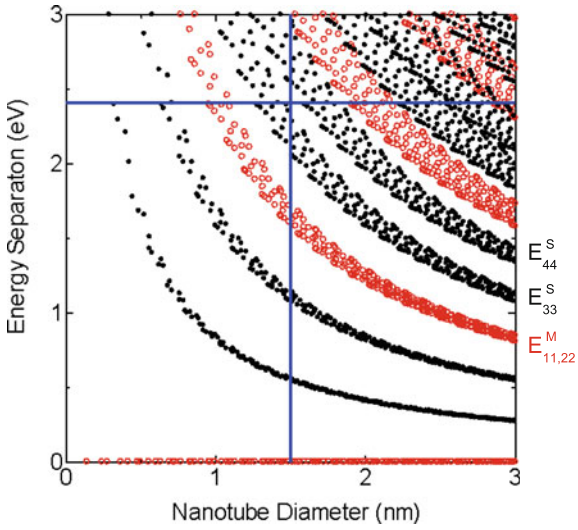

Fig. 7.5 Kataura plot

their properties. The RBM integrated intensity $I(E_{RBM})$ is a function of the laser excitation energy E_L and can be evaluated from the joint density of states according to the theory for incoherent light scattering

$$I(E_{RMB}) = \int \left| D(E) \frac{M_s M_{ep} M_i}{(E_L - E_{ii} - i\Gamma)(E_L - E_{ph} - E_{ii} - i\Gamma)} \right|^2 dE \qquad (7.2)$$

where Γ is the scattering process lifetime, E_{ph} the phonon energy and M matrix elements for the scattering process. M_i, M_s are the matrix elements for the electron-radiation interaction for the incoming and scattered respectively and M_{ep} is the electron-phonon interaction. The first and second factor in the denominator describes the resonance effect with incident and scattered light.

Figure 7.5 shows a so-called Kataura plot [17] relating the electrical transitions E_{ii} to the nanotube diameter. Branches shown in red refer to metallic tubes, whereas the semiconducting tubes' branches are shown in black. It can be seen that the electronic nature of 1.5 nm tubes probed by resonant Raman scattering using the 2.33 eV (532 nm) excitation is semiconducting. Both bands E^S_{33} and E^S_{44} are thus preferentially excited.

7.2.3 Experiment

Recent non-orthogonal tight binding calculations extended the Kataura plot in the sense that maximum Raman intensities I_{ii} were calculated for every optical transition E_{ii} [12]. However the intensity matching with measured data has been an experi-

mental challenge. The Raman intensity, as well as the tube-dependent scattering efficiency, is dependent on the number of tubes under laser exposure. Furthermore, the orientation of the tubes with respect to the direction of the light polarization affects the Raman intensity [18]. Finally, their length and defects together with interactions with neighboring tubes can also affect the measured Raman intensity [19, 20]. This makes the tube-dependent Raman intensity measurement extremely difficult.

A statistical method is proposed for chirality assignment of a nanotube sample using a single laser line E_L. Room temperature Raman spectra were recorded using a WITec CRM200 Confocal Raman Microscope using a frequency-doubled Nd:YAG green laser line (532 nm) delivered through a single mode fiber. This type of fiber supports only an single transversal mode which can be focussed to a diffraction-limited spot of about 400 nm (100× objective, NA = 0.8). The backscattered light passed through a super-notch filter and focussed into a 50 µm pinhole. The 300 mm spectrometer was equipped with a Peltier-cooled, back-illuminated charge coupled device (CCD) camera. Precise positioning of the sample under the laser spot was achieved with piezoelectric actuators with a travel range of $200 \times 200 \times 20\,\mu m^3$ in x, y and z respectively. 9600 spectra were obtained in six planar scans each collecting 40×40 spectra with an inter-spot distance of 1 mm at a rate of 2 Hz. Sample preparation is described elsewhere [21, 22].

Figure 7.6 shows the raw data from the collected Raman spectra. RBM features were resolved by fitting each spectrum with Lorentzian lines in the range from 80 to 350 rel. cm^{-1}. The intensities of the RBM modes were normalized with respect to the integrated intensities from the silicon support (Lo phonon at 520 rel. cm^{-1}). From this large amount of data a distinct picture of the Raman intensity distribution of the observed RBMs was obtained. This distribution was used to establish a histogram. The collected data was then compared to calculated optical transitions E_{ii} and maximum Raman intensities I_{ii}.

Figure 7.7a shows the optical transition energies as a function of the tube diameter (a close up of the Kataura plot from Fig. 7.5) as obtained from a non-orthogonal tight binding model [24]. The tube diameter was calculated using (7.1) with c_1 = 214 cm^{-1} and c_2 = 19 cm^{-1}. The position of the dots is indicated with respect to the excitation line of 2.33 eV (532 nm). The red dots correspond to SWNTs that have sufficient Raman efficiency at E_L. Tubes lying close to the laser line but still shown in grey have a very weak intrinsic Raman intensity. They are omitted in Fig. 7.7b to avoid figure overloading.

Figure 7.7b shows the calculated I_{ii} and attenuated Raman intensities $\alpha\ I_{ii}$ of the selected SWNTs. The open dots are calculated maximum intensities. The filled dots were multiplied with a normal distribution function to model the distance (in eV) to the laser line. The numbers in parenthesis indicate tube families (2n + m = constant).

Figure 7.7c shows the converted histogram from Fig. 7.6. The measured data (open circles) were corrected for sample population independence (filled circles). The intensity distribution shows a strong correlation with the attenuated data from Fig. 7.7b. The pattern match is only valid for the attenuated data which emphasizes the importance of performing such an excitation-dependent correction.

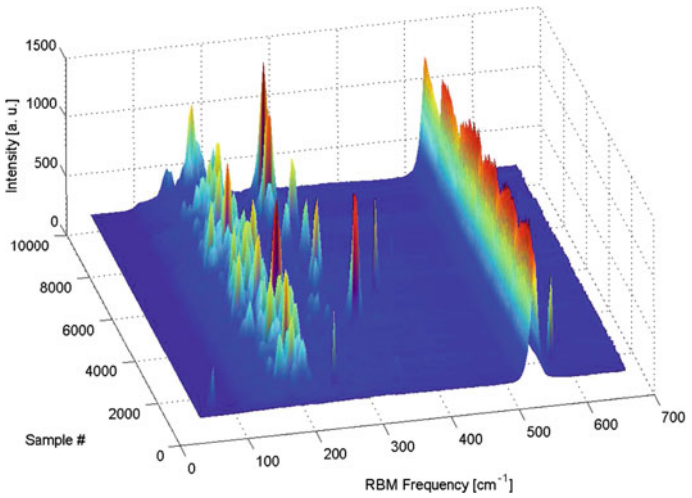

Fig. 7.6 Cascaded collected Raman spectra. The RBM is visible from 80 to 350 rel. cm^{-1} while the LO phonon of the Si support appears at 520 rel. cm^{-1}

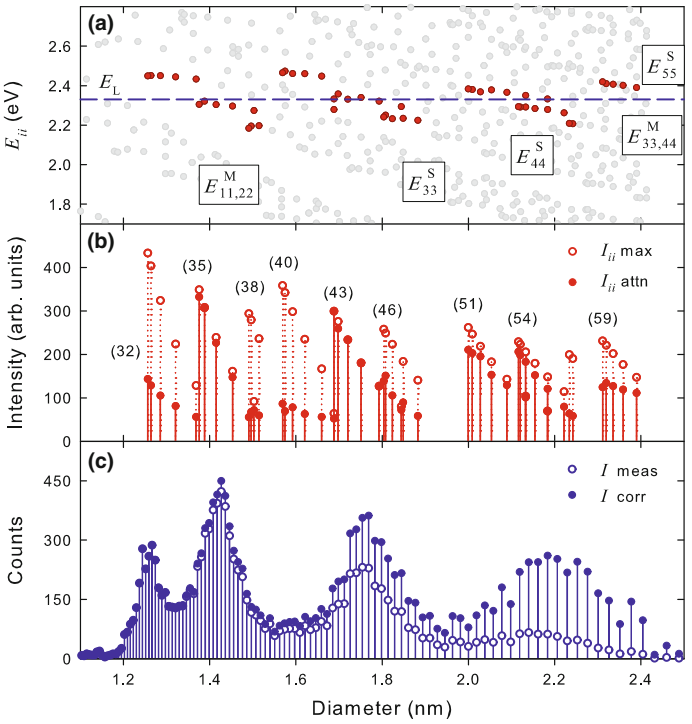

Fig. 7.7 **a** Optical transitions E_{ii} as a function of the tube diameter. **b** Calculated Raman intensities corresponding to the selected dots in (**a**). Numbers in parenthesis indicate tube families $(2n + m)$. **c** Converted measured histogram. After [23]

7.2.4 Microscopy

This section describes the possibility to localize individual SWNTs grown between a support structure. SWNT bridges were synthesized by catalytic thermal CVD in a low pressure furnace which can be operated down to a base pressure of 10^{-5} mbar. Prior to CVD growth, microchips were fabricated by surface micromachining of releasable 1.5 μm thick poly-crystalline silicon (poly-Si) layers. After their release, the poly-Si layers were uniformly coated with a bimetallic thin film of 8 nm Al and 1 nm Ni.The film thickness was measured in situ by a quartz crystal microbalance. The chips were transferred in air and subjected to a hydrogen pre-treatment at 200 mbar and 850 °C for 10 min to allow the reduction of nickel oxides and the formation of Ni islands. The latter serve as catalytic seeds for the growth of SWNTs under methane and hydrogen (3:1) at 200 mbar and 850 °C during 15 min. Heating and cooling were performed under vacuum and the chamber was only opened after cooling to at least 250 °C.

The samples were characterized by scanning electron microscopy (SEM, Zeiss Ultra 55 operated at 5 kV) and transmission electron microscopy (TEM, Philips CM200 microscope operated at 120 kV). Electron diffraction (ED) patterns were recorded on a Zeiss 912 Ω microscope at 60 kV. Raman spectra were recorded on a WITec CRM200. The details of the setup were already described in Sect. 7.2.3.

Figure 7.8 shows three suspended SWNTs across a trench defined by a tip pair at the technological limit for standard (surface micromachining) lithography.

The shape features alternating gap sizes between 12 and 2 μm (Fig. 7.8b to force SWNT growth only between the small gaps without the need of masking the catalyst [25]. Figure 7.8c1 shows a Raman image of the suspended SWNTs. The image was obtained by integrating the SWNT-specific Raman signatures, i.e. the radial breathing mode in the range from 80 to 350 rel. cm^{-1} and the tangential (G) mode around 1592 rel. cm^{-1} as shown in Fig. 7.8d.

Raman scattering is resonant and at a fixed excitation energy of 2.33 eV only two of the three crossing SWNTs could be seen at regular experimental conditions. Equation (7.1) was used to determine the diameter of one of the tubes to 1.43 μm, while for the other tube no RBM could be found. No defect-induced D-band signal at 1350 rel. cm^{-1} was observed, which is indicative for a good SWNT with high crystallinity. The Raman image in Fig. 7.8c2 has been obtained by integrating over the longitudinal optical phonon mode of the poly-Si material. Both images can be overlayed as they picture the same structure. There is no doubt about the origin of the Raman features as the freestanding sample geometry does not suffer from any background signal.

7.2.5 Thermography

SWNTS have been proposed for applications in integrated circuits as transistors or interconnects [26, 27]. In other cases they were proposed as active elements in sensing

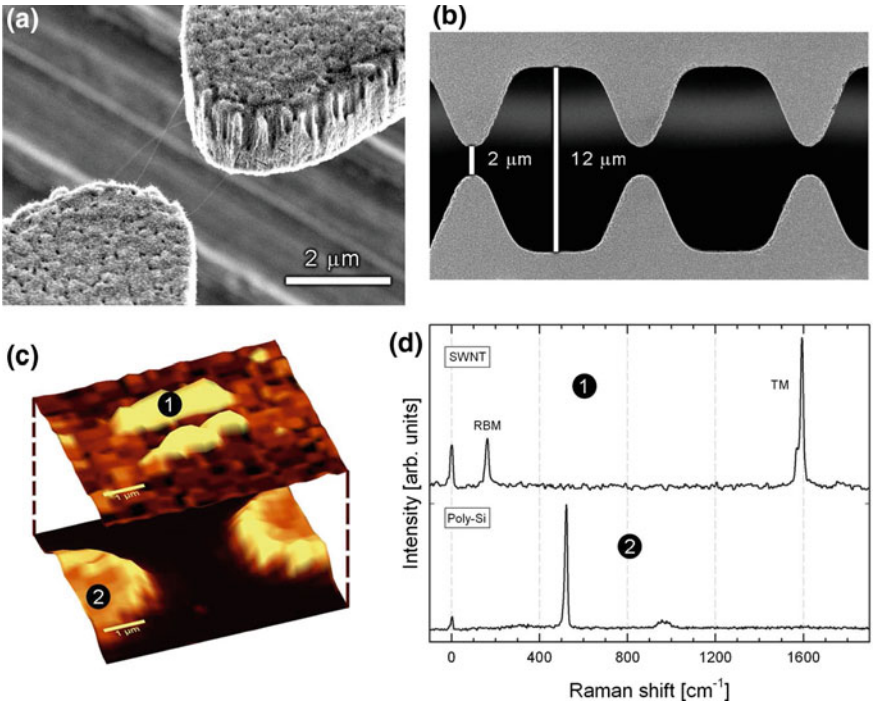

Fig. 7.8 **a** SEM image of three spanned SWNTs between a pair of closely spaced poly-Si tips. **b** Demagnified SEM from (**a**) to show the tip definition. **c** Raman image of the same tip-pair as shown in (**a**). **d** Representative snapshots showing SWNT and poly-Si specific phonon modes in the Raman shift. After [25]

applications based on their unique strain-dependent transport characteristics [28]. In all cases, knowledge about the influence of temperature onto their electro-mechanical properties is important to understand their overall behavior. Although several theoretical studies exist on the thermal properties of individual SWNTs [29], only few experimental investigations below room temperature are currently available.

Figure 7.9a shows a spatially resolved thermal image of a suspended SWNT. The figure shows that the freestanding nanotube is strongly influenced (heated) by the laser spot as a heat source. Laser intensities were varied from 0.5 to 7 mW corresponding to power densities of about 1.5–21 mW/µm^2 [30]. Figure 7.9b shows the thermal profile of the nanotube cross section resolved by its phonon frequency which was characterized beforehand. It shows that for high laser intensities, the phonon softening is pronounced. A Gaussian intensity profile is observed along the cross sectional direction (Y) of the tube indicating a correlation between the (Gaussian) profile of the laser spot and the SWNT as a point scatterer (considered of negligible width).

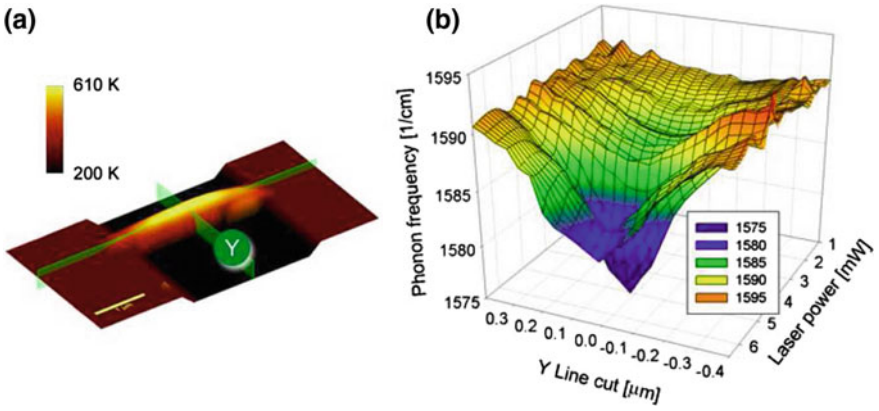

Fig. 7.9 **a** Raman thermal image of a single SWNT suspended between Si posts. **b** Phonon frequency of G-mode as a function of laser intensity scanned across the SWNT

7.3 Isolated Graphene Sheets

7.3.1 Theory

The energy dispersion for 2D graphene can be calculated using a tight binding energy model. For a detailed calculation, the reader is referred to [4, 31]. The result is,

$$E^{\pm}_{g2D}(\boldsymbol{k}) = \frac{\epsilon_{2p} \pm \gamma_0 w(\boldsymbol{k})}{1 \mp s w(\boldsymbol{k})} \tag{7.3}$$

where E_{g2D} is the 2D energy dispersion of graphite, ϵ_{2p} the site energy of the 2p atomic orbital, γ_0 the nearest-neighbor carbon-carbon interaction energy and s the tight binding overlap integral which is associated with the asymmetry between the valence and conduction bands in 2D graphite. E^+ and E^- correspond to the valence π and conduction $\pi*$ energy bands, respectively. The function $w(\boldsymbol{k})$ in (7.3) is given by

$$w(\boldsymbol{k}) = \sqrt{1 + 4\cos\left(\frac{\sqrt{3}k_x a}{2}\right)\cos\left(\frac{k_y a}{2}\right) + 4\cos^2\left(\frac{k_y a}{2}\right)} \tag{7.4}$$

where a is the length of unit vector of graphene and k the wave vector. Equations (7.3) and (7.4) describe the energy dispersion of graphene which corresponds to the electronic properties of SWNTs. In Fig. 7.10 the electronic energy dispersion for 2D graphite is shown as a function of k in the hexagonal Brillouin zone.

The asymmetry of the conduction and valence bands is not important for the calculation of the energy difference of conduction and valence bands. Thus with $s = 0$ and $\epsilon_{2p} = 0$ the dispersion relation simplifies to

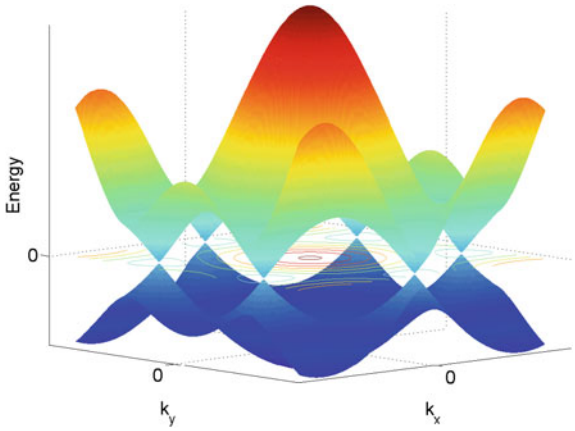

Fig. 7.10 Energy dispersion of π and $\pi*$ bands of graphene. The Fermi level is at $E = 0$. Bands cross at the K-points. Data was computed using (7.3) and (7.4) and parameter values $s = 0.129$, $\gamma_0 = 2.9$ eV

$$E^{\pm}_{g2D} = \pm\gamma_0\, w(\boldsymbol{k}) \tag{7.5}$$

Note that a simple way to get to the electronic properties of single-walled carbon nanotubes consists in starting from the graphene dispersion relation and applying a zone folding approximation between graphene π and $\pi*$ electronic states to calculate the band structure of tubes for any diameter and chirality [5]. Note also that the common π-orbital approach involves the assumption that the tight-binding approximation includes only the interaction of first-neighbor atom (nearest neighboring atom) [4].

7.3.2 Experiment

Only recently, single- and few-layer graphene have been successfully transferred onto a substrate [32].

Transport measurements revealed a highly tunable two-dimensional electron-hole gas with a linear energy dispersion around the Fermi energy embedded in a solid-state environment [33, 34]. Going to few-layer graphene, however, disturbs this unique system in such a way that the usual parabolic energy dispersion is recovered. The large structural anisotropy makes few-layer graphene therefore a promising candidate to study the rich physics at the crossover from bulk to purely two-dimensional systems. Turning on the weak interlayer coupling while stacking a second layer onto a graphene sheet leads to a branching of the electronic bands and the phonon dispersion at the K-point. Double-resonant Raman scattering [13] which depends on electronic and vibrational properties, turns out to be an ingenious tool to probe the lifting of that specific degeneracy.

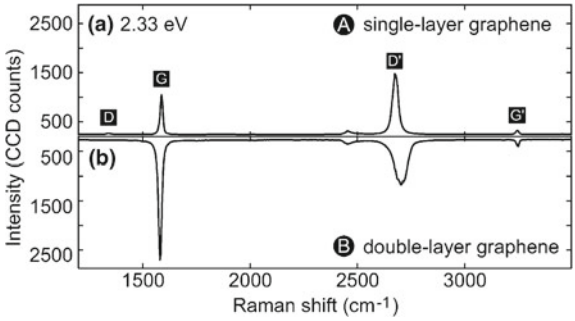

Fig. 7.11 Raman spectra of **a** single- and **b** double-layer graphene (collected at spots A and B, see Fig. 7.13b)

The graphite films were prepared by mechanical exfoliation of highly oriented pyrolytic graphite (HOPG) and subsequent transfer to a highly doped Si wafer with a 300 nm SiO_2 (atomic oxidation process) cap layer.

The experimental setup for the confocal Raman measurement was identical to the one described in Sect. 7.2.3. With a very low incident power of 4–7 μW, heating effects can be neglected.

The Raman spectrum of graphite has four prominent peaks (Fig. 7.11).

The peak around 1582 rel. cm^{-1}, commonly called the G-line, is caused by the Raman active E_{2g} phonon (in-plane optical mode), close to the Γ-point. The D-line around 1350 rel. cm^{-1} exhibits two remarkable features: its position shifts to higher frequencies with increasing incident laser excitation energies [35] and its relative signal strength (compared to the G-line) depends strongly on the amount of disorder in the graphitic material [35, 36]. The associated overtone D′ around 2700 rel. cm^{-1} is pronounced even in the absence of a D-signal. Finally, the overtone of the G-line, the G′-line, is located at 3248 rel. cm^{-1}, which is more than twice the energy of the G- line. The different experimental findings related to the dispersive D- and D′-bands could be explained by Thomsen and Reich within the framework of double resonant Raman scattering [13]. The electronic and vibrational properties of graphite are dominated by the sp^2 nature of the strong intraplane covalent bonds. Raman spectra for multiple graphene layers can be compared qualitatively and quantitatively while investigating flakes with sections of various thicknesses. In Fig. 7.12a, the scanning force microscopy (SFM) micrographof a graphite flake with different layers is presented: the bare SiO_2 (indicated by "0") is surrounded by single-layer sections with steps of up to two, four, and six layers. The different step heights are clearly depicted in Fig. 7.12b, where a cross section of Fig. 7.12a (see white dashed arrow) is shown. By scanning the flake and collecting the complete Raman spectrum at every spot, we can subsequently filter specific spectral data for a spatially resolved data point and construct false-color 2D plots. In Fig. 7.12c, the intensity of the G peak is integrated from 1537 to 1622 rel. cm^{-1}. We find a remarkable correlation with the SFM graph: brighter regions correspond to thicker sections.

The cross section in Fig. 7.12d shows a steplike behavior, perfectly correlated with the topographical changes shown in Fig. 7.12b. In Fig. 7.12e, we plot the FWHM

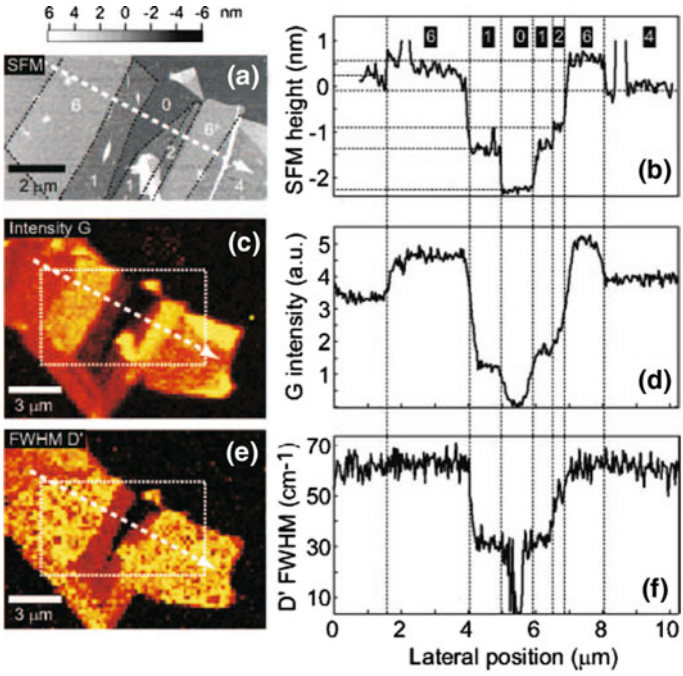

Fig. 7.12 **a**, **b** SFM micrograph and cross-sectional plot (indicated with the white dashed arrow; lateral average over 400 nm) of a few-layer graphene flake with central sections down to a single layer. Raman maps (dashed square corresponding to the SFM image in **a**) showing **c** the integrated intensity of the G-line and **e** the FWHM of the D′-line. The related cross sections **d, f** are aligned (vertical dashed lines) with the height trace

(full width at half-maximum) of the D′-line. It shows the narrowing at the transition to a single layer (see, e.g., Fig. 7.11) and gives an evident contrast between single- and few-layer graphene sections. The two discrete levels in the FWHM of the D′-line shown in Fig. 7.12f related to a single layer ($\approx 30\,\mathrm{cm}^{-1}$) and two and more layers ($\approx 60\,\mathrm{cm}^{-1}$) suggest that the width of the D′-line can be used as an indicator for single-layer graphene. Raman spectroscopy can therefore be used to count the layers of a thin graphite stack and to discriminate between single and double layers. Combined with the double-resonant Raman scattering mechanism, an optical setup using light in the visible range turns out to be an alternative to scanning force microscopy, which requires stacking folds as height references.

Transport measurements show that the quality of the finite graphitic flakes on the silicon oxide matrix obtained with the technique explained above is remarkable: electronic mobilities up to $15{,}000\,\mathrm{cm}^2\,(\mathrm{Vs})^{-1}$ were estimated from transport experiments. We also point out that Raman spectroscopy reveals quasi-defect-free graphitic sheets via the absence of a D-band signal. The appearance of the D-band can be related to the occurrence of defects and disorder. With confocal Raman imaging the spatial origin of the defects can be localized, which can have important consequences for the

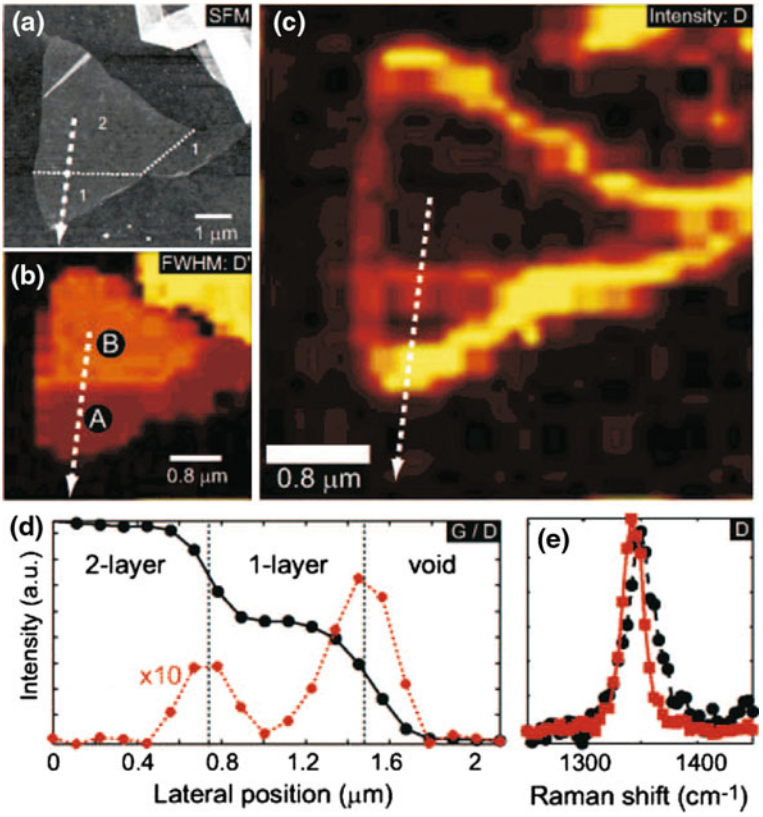

Fig. 7.13 **a** SFM micrograph of a graphitic flake consisting of one double- and two single-layer sections (white dashed line along the boundaries), highlighted in the Raman map **b** showing the FWHM of the D′-line. **c** Raman mapping of the integrated intensity of the D-line: A strong signal is detected along the edge of the flake and at the steps from double- to single-layer sections. **d** Raman cross section (white dashed arrow in **c**): staircase behavior of the integrated intensity of the G-peak (solid line) and pronounced peaks at the steps for the integrated intensity of the D-line (dashed line). **e** Spatially averaged D-peak for the crossover from double to single layer (black) and from single layer to the SiO_2 substrate (red)

electronic properties [37]. By comparing the SFM micrograph in Fig. 7.13a with the Raman image of the integrated D-line (1300–1383 rel. cm^{-1}) intensity in Fig. 7.13c, it is obvious that the edges of the flake and also the borderline between sections of different heights contribute to the D-band signal, whereas the inner parts of the flakes do not. This is somewhat surprising because, for thinner flakes, the influence of a nearby substrate on the structural quality should be increasingly important.

In the cross-section in Fig. 7.13d, one can clearly see that the D-line intensity is maximal at the section boundaries, which can be assigned to translational symmetry breaking or to defects. However, it should be emphasized that the D-line is still 1 order of magnitude smaller than the G-line. In Fig. 7.13e, spatially averaged D mode

spectra from the two steps shown in Fig. 7.13d are presented. The frequency fits well into the linear dispersion relation of peak-shift and excitation energy found in earlier experiments [35]. In addition, it is found that the peak is narrower and downshifted at the edge of the single layer, while it is somewhat broader and displays a shoulder at the crossover from the double to the single layer. In parts (a) and (b) of Fig. 7.11, the Raman spectra of the double- and single-layer graphene shown in Fig. 7.13b are compared and labeled A and B.

The Raman signal is significantly altered when peeling off the penultimate layer: the G peak decreases strongly in intensity and shifts toward higher wavenumbers. In connection with Fig. 7.12b, we already stated that the integrated G-line signal is monotonically increasing with increasing flake thickness.

7.3.3 Charge Distributions

Electron-hole puddles in graphene have been predicted to be responsible for the finite conductance at vanishing average charge carrier density [38] and have recently been observed using a scanning single electron transistor [39]. Thus the identification of different doping domains might be desirable to investigate graphene devices.

Figure 7.14a, b show Raman data for varying back gate voltages V_g, which by utilizing a simple capacitor model can be substituted by the electron/hole concentration $n = \alpha(V_g - V_g^D)$. Here, $\alpha \approx 7.2 \times 10^{10}\,\mathrm{cm}^{-2}/V$ and $V_g^D \approx 2.5$ V mark the charge neutrality point, which has been determined by transport measurements.

Figure 7.14c shows a significant difference between the G and 2D-linewidth (FWHM). The G-phonon shows a rather strong change as a function of carrier density [41, 42] which is due to the fact that the Pauli exclusion principle prevents the phonon from decaying into an electron-hole pair for $|E_F| > \hbar\omega_G/2$, as illustrated in Fig. 7.14d [42]. The decay of the dispersive D phonon with large wave vector q_D is unaffected by the Pauli exclusion principle for low doping Fig. 7.14e. It is expected that the 2D-linewidth stays constant up to a charging that corresponds to a Fermi level shift as large as the exciting laser energy $E_F \approx E_L$. This has a practical implication: Since the peak width of the 2D-line, which has been recognized as the most striking feature to distinguish single layer from few-layer graphene, is insensitive to doping, it is a reliable-doping-independent measure for identifying single-layer graphene.

Raman microscopy sensing the doping-dependent G- and 2D-line shifts provides an interesting tool to investigate charge fluctuations and doping domains in graphene. Figure 7.15 shows the G- and 2D-peak positions and widths, their fluctuations and cross correlations of a graphene flake on a SiO_2 substrate. The RMS fluctuation of the G-peak is $3.3\,\mathrm{cm}^{-1}$explaining the wide spread range of numbers reported in the literature [43–45].

The 2D-line is centered around 2679.4 rel. cm^{-1} and fluctuates about $0.9\,\mathrm{cm}^{-1}$. The ratio of the fluctuations of the G- and 2D-line agrees well with the ratio of the

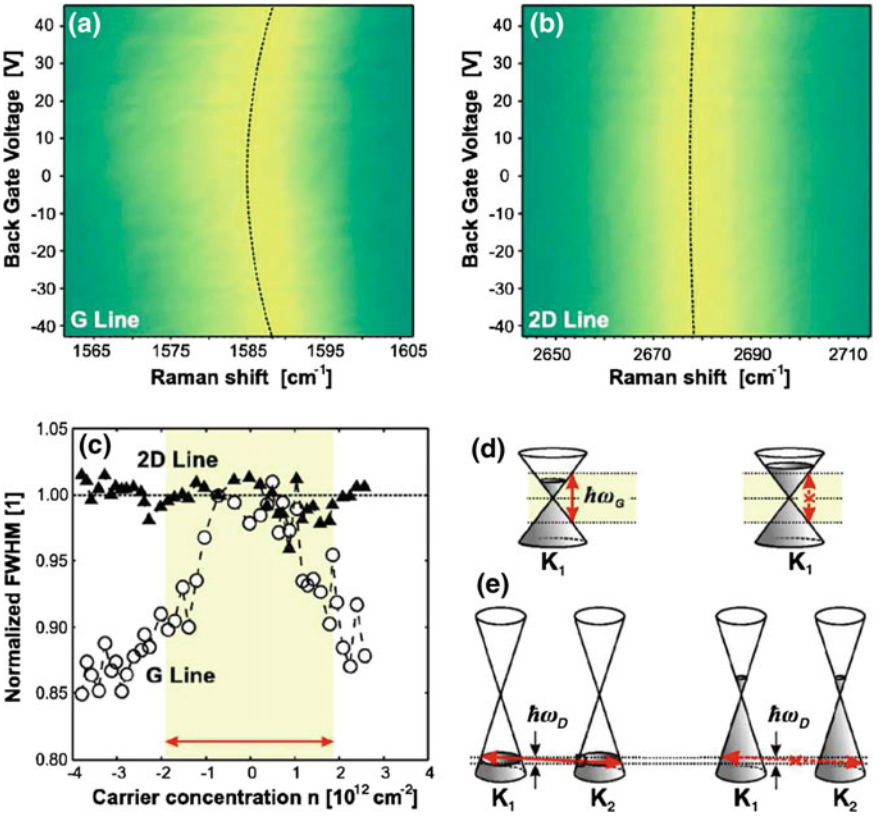

Fig. 7.14 **a**, **b** show maps of the G- and 2D-lines, respectively, as function of applied back gate voltages. **c** shows the normalizeD-bandwidth (FWHM) of G and 2D as function of doping. **d**, **e** show illustrations of the presence and absence of a phonon decay into an electron-hole pair. After [40]

doping-dependent G and 2D stiffening. Doped regions on the imaged flake can be observed. In the upper part of Fig. 7.15c, d one sees that toward the edges of the graphene sample charging is suppressed, whereas in the entire inner area significant charging is present. If one focuses on a quite uniform area it is found that the G fluctuations are approximately $0.6\,\mathrm{cm}^{-1}$, which corresponds to $n = 2.4 \times 10^{11}\,\mathrm{cm}^{-2}$.

Raman shifts of the G- and 2D-lines for charged graphene and spatial variations in the G and 2D peak positions can be attributed to different doping domains. In the low doping regime no clear distinction between electron and hole doping could be made since for both G- and 2D-lines, stiffening is observed. However, absolute doping fluctuations could be estimated.

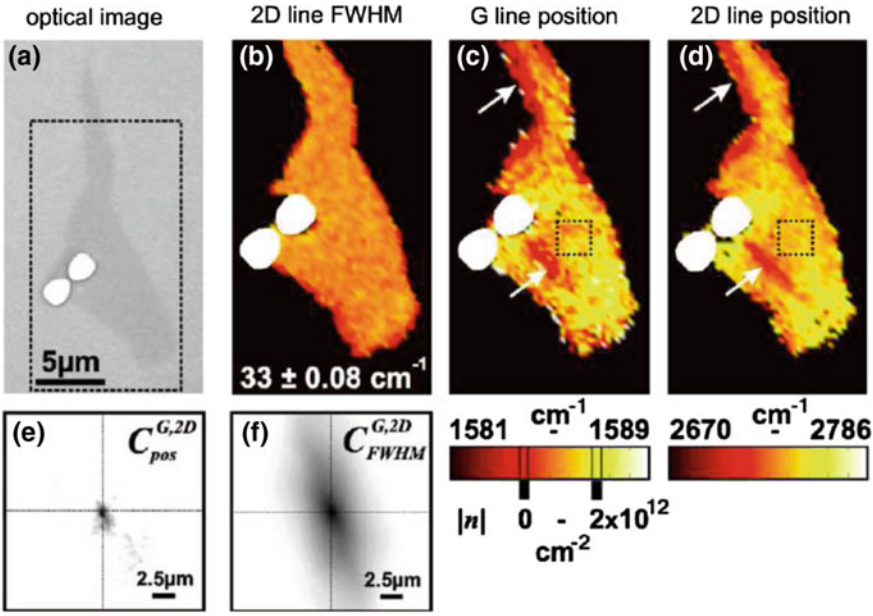

Fig. 7.15 **a** Green-filtered optical image (the two white dots are metal markers). **b** FWHM of the 2D-line. **c**, **d** show regions defined by the G and 2D peak positions, respectively. The white arrows mark correlated low doping areas, whereas the dotted box highlights a region with low charging fluctuations. **e**, **f** Two-dimensional cross correlation (adjusted) of the fluctuations of the G- and 2D-line positions (widths). After [40]

7.4 Conclusion

Raman microscopy is a powerful tool with a very high sensitivity that allows the investigation of single-wall carbon nanotubes (SWNTs) as well as single sheets of graphene with sub-micrometer lateral resolution. With this technique it is easily possible to distinguish SWNTs from MWNTs, as well as to determine their diameter by analyzing the position of the radial breathing mode (RBM). It was demonstrated, that due to the strong resonance enhancement of CNTs, even a single, free standing SWNT could be imaged and its properties could be analyzed. By measuring the intensity and diameter of a large number of nanotubes that were excited with a single excitation wavelength, the phonon scattering cross section as a function of tube diameter could be derived.

Single graphene layers could be easily distinguished from two or more layer graphene, because of their different Raman signature. In addition, the number of layers in a stack of graphene sheets have been correlated with the shape of a dispersive phonon mode enabling layer counting from Raman spectroscopy.

Raman microscopy could be even used to show that the edges of single graphene layers show different spectra than the layers themselves, which is most prominent in the defect (D-) band.

Finally, charging effects on doped graphene sheets could be visualized using Raman microscopy.

Acknowledgements The author wishes to thank in particular Dr. Christoph Stampfer and Prof. Christofer Hierold. Many of the results summarized in the present chapter have been achieved with the support and collaboration of numerous people. They are (in alphabetic order) Lukas Durer, Prof. Klaus Ensslin, Dr. Davy Graf, Thomas Helbling, Dr. Stephan Hofmann, Francoise Molitor, Matthias Muoth, Dr. Jannik Meyer, Simone Pisana, Prof. Valentin Popov, Dr. Stephan Stoll and Dr. Ludger Wirtz. Samples featuring individual nanotubes have been provided in collaboration with Nicronex Ltd., Luxembourg (www.nicronex.com).

References

1. J.D. Bernal, Proc. Roy. Soc. A **106**, 749 (1924)
2. H.W. Kroto, J.R. Heath, S.C. O'Brien, R.F. Curl, R.E. Smalley, Nature **318**, 162 (1985)
3. P. Avouris, Z. Chen, V. Perebeinos, Nat. Nano. **2**, 605 (2007)
4. S. Reich, C. Thomsen, J. Maultsch, *Carbon Nanotubes: Basic Concepts and Physical Properties* (Wiley-VCH Verlag GmbH, Weinheim, 2004)
5. M.S. Dresselhaus, G. Dresselhaus, P. Avouris, *Carbon Nanotubes: Synthesis, Structure, Properties and Applications* (Springer, Berlin, 2001)
6. Adapted from http://en.wikipedia.org/wiki/Image:Types_of_Carbon_Nanotubes.png (2007)
7. R.A. Jishi, L. Venkattaraman, M.S. Dresselhaus, G. Dresselhaus, Chem. Phys. Lett. **209**, 77 (1993)
8. S. Bandow, S. Asaka, Y. Saito, A.M. Rao, L. Grigorian, E. Richter, P.C. Eklund, Phys. Rev. Lett. **80**, 3779 (1998)
9. J. Kuerti, G. Kresse, H. Kuzmany, Phys. Rev. B **85**, 8869 (1998)
10. V.N. Popov, V.E.V. Doren, M. Balkanski, Phys. Rev. B **59**, 8355 (1999)
11. L. Henrard, E. Hernandez, P. Bernier, A. Rubio, Phys. Rev. B **60**, 8521 (1999)
12. V.N. Popov, L. Henrard, P. Lambin, Phys. Rev. B **72**(3), 035436 (2005)
13. C. Thomsen, S. Reich, Phys. Rev. Lett. **85**, 5214 (2000)
14. O. Dubay, G. Kresse, Phys. Rev. B **67**, 035401 (2003)
15. B. Vigolo, A. Pénicaud, C. Coulon, C. Sauder, R. Pailler, C. Journet, P. Bernier, P. Poulin, Science **290**, 1331 (2001)
16. O. Dubay, G. Kresse, H. Kuzmany, Phys. Rev. Lett. **88**, 235506 (2002)
17. H. Kataura, Y. Kumazawa, Y. Maniwa, I. Umezu, S. Suzuki, Y. Ohtsuka, Y. Achiba, Synth. Met. **103**, 2555 (1999)
18. G.S. Duesberg, I. Loa, M. Burghard, K. Syassen, S. Roth, Phys. Rev. Lett. **85**, 5436 (2000)
19. C. Fantini, A. Jorio, M. Souza, M.S. Strano, M.S. Dresselhaus, M.A. Pimenta, Phys. Rev. Lett. **93**, 147406 (2004)
20. A. Jorio, J.H. Hafner, C.M. Lieber, M. Hunter, T. McClure, G. Dresselhaus, M.S. Dresselhaus, Phys. Rev. Lett. **86**, 1118 (2001)
21. A. Jungen, C. Stampfer, J. Hoetzel, V. Bright, C. Hierold, Sens. Actuators, A-Phys. **130–131**, 588 (2006)
22. J. Kong, H.T. Soh, A.M. Cassell, C.F. Quate, H.J. Dai, Nature **395**, 878 (1998)
23. A. Jungen, V.N. Popov, C. Stampfer, L. Durrer, S. Stoll, C. Hierold, Phys. Rev. B **75**, 041405 (2007)
24. V.N. Popov, L. Henrard, P. Lambin, Phys. Rev. B **70**(11), 115407 (2004)

25. A. Jungen, S. Hofmann, J.C. Meyer, C. Stampfer, S. Roth, J. Robertson, C. Hierold, J. Micromech. Microeng. **17**, 603 (2007)
26. P. Avouris, J. Appenzeller, R. Martel, S.J. Wind, Proc. IEEE **91**, 1772 (2003)
27. A.P. Graham, G.S. Duesberg, R.V. Seidel, M. Liebau, E. Unger, W. Pamler, F. Kreupl, W. Hoenlein, Small **1**, 382 (2005)
28. C. Stampfer, T. Helbling, D. Obergfell, B. Schoeberle, M.K. Tripp, A. Jungen, S. Roth, V.M. Bright, C. Hierold, Nano Lett. **6**, 233 (2006)
29. D. Mann, Y.K. Kato, A. Kinkhabwala, E. Pop, J. Cao, X.R. Wang, L. Zhang, Q. Wang, J. Guo, H.J. Dai, Nat. Nano. **2**, 33 (2007)
30. A. Jungen, J. Gauckler, C. Stampfer, L. Durrer, T. Helbling, C. Hierold, in *IEEE MEMS 08* (AZ, USA, Tucson, 2008), p. 733
31. R. Saito, G. Dresselhaus, M.S. Dresselhaus, Phys. Rev. B **61**, 2981 (2000)
32. K.S. Novoselov, A.K. Geim, S.V. Morozov, D. Jiang, Y. Zhang, S.V. Dubonos, I.V. Grigorieva, A.A. Firsov, Science **306**, 666 (2004)
33. K.S. Novoselov, A.K. Geim, S.V. Morozov, D. Jiang, M.I. Katsnelson, I.V. Grigorieva, S.V. Dubonos, A.A. Firsov, Science **438**, 197 (2005)
34. Y. Zhang, Y.W. Tan, H.L. Stormer, P. Kim, Science **438**, 201 (2005)
35. R. Vidano, D. Fischbach, L. Willis, T. Loehr, Solid State Commun. **39**, 341 (1981)
36. F. Tuinstra, J.L. Koenig, J. Chem. Phys. **53**, 1126 (1970)
37. N. Peres, F. Guinea, A.C. Neto, Phys. Rev. B **73**, 125411 (2006)
38. E.H. Hwang, S. Adam, S.D. Sarma, Phys. Rev. Lett. **98**, 186806 (2007)
39. J. Martin, N. Akerman, G. Ulbricht, T. Lohmann, J.H. Smet, K. von Klitzing, A. Yacoby, Nat. Phys. **4**, 144 (2008)
40. C. Stampfer, F. Molitor, D. Graf, K. Ensslin, A. Jungen, C. Hierold, L. Wirtz, Appl. Phys. Lett. **91**, 187401 (2007)
41. S. Pisana, M. Lazzeri, C. Casiraghi, K.S. Novoselov, A.K. Geim, A.C. Ferrari, F. Mauri, Nat. Mater. **6**, 198 (2007)
42. J. Yan, Y. Zhang, P. Kim, A. Pinczuk, Phys. Rev. Lett. **98**, 166802 (2007)
43. A.C. Ferrari, J.C. Meyer, V. Scardaci, C. Casiraghi, M. Lazzeri, F. Mauri, S. Piscanec, D. Jiang, K.S. Novoselov, S. Roth, A.K. Geim, Phys. Rev. Lett. **97**, 187401 (2006)
44. D. Graf, F. Molitor, K. Ensslin, C. Stampfer, A. Jungen, C. Hierold, L. Wirtz, Nano Lett. **7**, 238 (2007)
45. A. Gupta, G. Chen, P. Joshi, S. Tadigadapa, P.C. Eklund, Nano Lett. **6**, 2667 (2006)

Chapter 8
Characterization of Graphene by Confocal Raman Spectroscopy

Christoph Neumann and Christoph Stampfer

Abstract Confocal Raman spectroscopy has emerged as a key characterization technique in graphene research, as with this technique important material characteristics can be obtained locally and noninvasively. In this chapter, the fundamentals of the Raman spectrum of graphene are reviewed and the utilization of Raman spectroscopy for graphene characterization is demonstrated. In this regard, we show how crucial properties of graphene samples, i.e. doping, strain, defect-density and layer-number can be extracted from the Raman spectrum. Accessing these quantities is highly relevant for monitoring, understanding and improving graphene synthesis processes and device fabrication techniques for research and emerging industrial applications.

8.1 Introduction

In 2004, the first mono-atomic layer of carbon atoms, called graphene, was intentionally isolated from a bulk graphite crystal [1]. From this point on, graphene has attracted overwhelming interest in fundamental and applied research in a variety of fields, such as solid state physics, electronics, mechanics, and optics [2]. As a consequence of the discovery of graphene, also other two-dimensional (2d) materials like transition metal dichalcogenides, hexagonal boron nitride and black phosphorous were successfully fabricated [3]. In particular, the possibility of assembling layers of 2d materials on top of each other with any desired stacking order and relative lattice orientation has been shown to be a completely new way of making electronic and opto-electronic devices, like tunneling-transistors [4] or light-emitting diodes [5, 6]. To pave the way for graphene from fundamental research to industrial applications,

C. Neumann (✉)
JARA-FIT and 2nd Institute of Physics, RWTH Aachen University,
52074 Aachen, Germany
e-mail: cneumann@physik.rwth-aachen.de

C. Stampfer
Peter Grünberg Institute (PGI-9), Forschungszentrum Jülich,
52425 Jülich, Germany
e-mail: stampfer@physik.rwth-aachen.de

J. Toporski et al. (eds.), *Confocal Raman Microscopy*, Springer Series
in Surface Sciences 66, https://doi.org/10.1007/978-3-319-75380-5_8

reliable and reproducible fabrication processes and rapid, noninvasive characterization techniques to analyze material parameters are an important prerequisite. In this respect, confocal Raman spectroscopy is of great interest. Although the Raman spectrum of graphene shows only few characteristic lines (see also Sect. 8.4), many crucial parameters, such as the number of graphene layers, doping, strain, and the density of lattice defects can be extracted from the intensity, shape, energy (i.e. frequency) and broadening of the prominent Raman lines. In this chapter, the key aspects of the Raman spectrum of graphene as well as dependences of the Raman lines on various material properties are discussed.

8.2 Electronic Band Structure of Graphene

Graphene consists of a monolayer of carbon atoms, arranged in a hexagonal crystal with strong, in-plane sp^2 bonds between the neighboring carbon atoms. A schematic illustration of the graphene crystal structure with the unit cell spanned by the vectors $\mathbf{a_1}$ and $\mathbf{a_2}$ is shown in Fig. 8.1a. The unit cell of graphene (see hatched area in Fig. 8.1a) consists of two carbon atoms with a carbon-carbon atom distance of $\approx$0.142 nm [7].

The corresponding first Brillouin zone of graphene with the high symmetry points Γ, M, K and K′ is shown in Fig. 8.1b. For a refined understanding of the Raman spectrum of graphene, a closer look into the electron and phonon band structure is required. Electronic transport and opto-electronic coupling in graphene is dominated by the out-of-plane p_z orbitals of the carbon atoms. They give rise to the low-energy π bands of graphene (Fig. 8.2a). At the edges of the Brillouin zone, i.e. around the so-called K and K′ points, the bands can be regarded as linear with an energy-momentum dispersion relation of $E = \hbar v_F |\mathbf{k}|$, where v_F is the Fermi velocity an k the electron wave vector, resembling the dispersion relation of massles Dirac fermions (Fig. 8.2b). This linear approximation holds only true at low energies, e.g. for typical

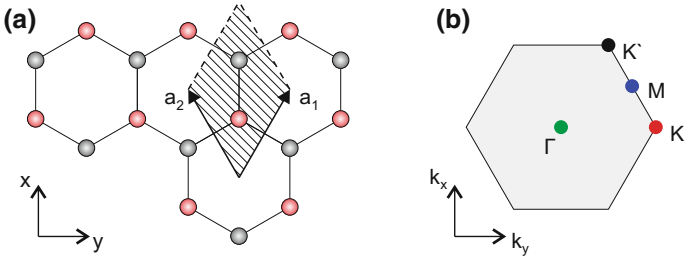

Fig. 8.1 **a** Schematic illustration of the graphene lattice. The two different sublattices are shown in red and black. The unit cell is spanned by the vectors $\mathbf{a_1}$ and $\mathbf{a_2}$. **b** Corresponding first Brillouin zone. The high symmetry points Γ, K, K′, and M are highlighted

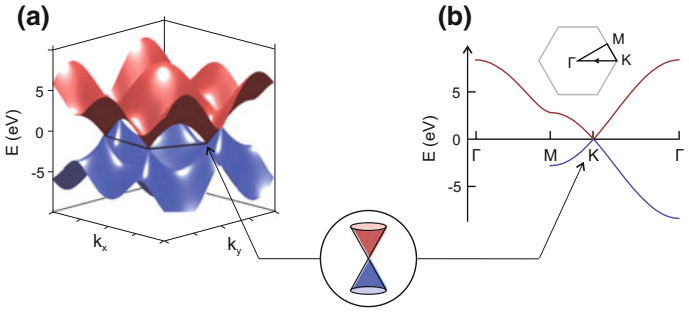

Fig. 8.2 **a** Electronic band structure of graphene. The valence band (π) is shown in blue and the conduction band (π^*) in red. The linear dispersion relation around the K and K′ points is highlighted in the inset. **b** Cut of the electronic band structure through the first Brillouin zone along the high symmetry points Γ-M-K-Γ

Fermi energies in electronic transport. In contrast, for optical processes, it is often required to take into account deviations from this linear relation due to "trigonal warping" that distorts the conic band structure around K and K′ [8].

8.3 Phonon Band Structure of Graphene

As the unit cell of graphene consists of two carbon atoms (compare Fig. 8.1a), there are six phonon branches, three acoustic and three optical ones. The phonon dispersion along a path connecting the high symmetry points in the first Brillouin zone is shown in Fig. 8.3. In this chapter, we will focus on the optical phonon modes that give rise to the most prominent features in the Raman spectrum of graphene (more detailed information on the phonon dispersion relation of graphene can be found in references [9, 10]). For an unperturbed graphene lattice, the longitudinal and transverse (in-plane) optical phonons (LO and TO) at the center of the Brillouin zone (at the Γ point) are degenerate and transform in the E_{2g} representation of the point group. These phonons correspond to a vibration of the two sub-lattices of graphene against each other (Fig. 8.4a, b). At finite momentum the degeneracy is lifted. The third optical phonon branch is an out-of-plane mode with B_{2g} representation and is considerably softer than the in-plane modes. Furthermore, only the E_{2g} modes are Raman-active, while the B_{2g} mode is neither Raman- nor infrared-active [11]. Another important phonon mode stems from the TO branch around the K point with A_{1g} representation. Exactly at the K point, the phonon mode corresponds to a radial breathing of a hexagonal ring of carbon atoms (Fig. 8.4c).

Around specific high symmetry points (Γ and K) a strong renormalization of individual optical phonon branches due to an increased coupling to the electronic system is present (Kohn anomalies), resulting in sharp dips in the phonon dispersion relation [9, 15, 16] (Fig. 8.3). These Kohn anomalies occur, because phonons in the

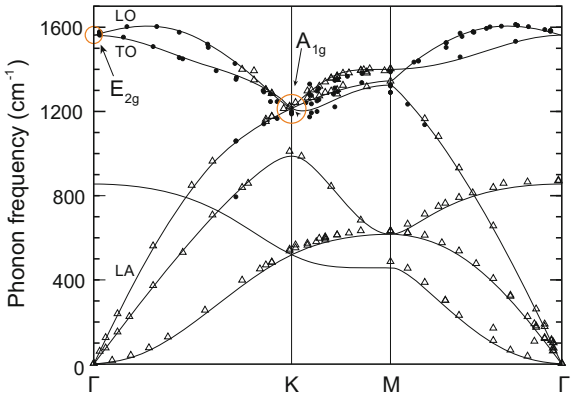

Fig. 8.3 The phonon dispersion of graphene as obtained from DFT-GW (density functional theory supplemented by GW) calculations by Venezuela et al. [10]. The phonon modes Γ and K that are most relevant for the Raman spectrum of graphene are highlighted by orange circles. The dips of the optical phonon branches around K and Γ stem from the strong coupling to the electronic system (Kohn anomalies). The data points come from inelastic X-ray scattering measurements (triangles [12], filled dots [13], open dots [14]). The figure is adapted from Venezuela et al. [10]

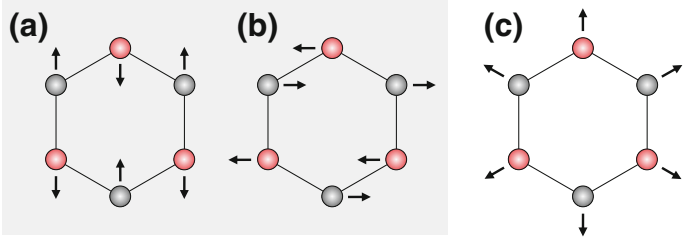

Fig. 8.4 Raman active phonon modes in graphene. **a**, **b** degenerate optical phonon modes at the Γ point with E_{2g} representation. **c** Breathing mode at the K point with A_{1g} representation

vicinity of the Γ point can connect electronic states from the K and K′ valleys to states in the same valley, respectively. On the other hand, phonons at the K point can connect electronic states from the valley around K to the valley around K′ (or the other way around).

8.4 Raman Spectra of Pristine Graphene

The Raman spectrum of graphene is composed of two main and several smaller peaks [11]. The first main Raman line, the so-called Raman G line (Fig. 8.5a), originates from the highest optical phonons at Γ and is observed at around 1580 rel. cm^{-1}. The oscillation pattern of these phonons are illustrated in Fig. 8.4a, b. The 2D line

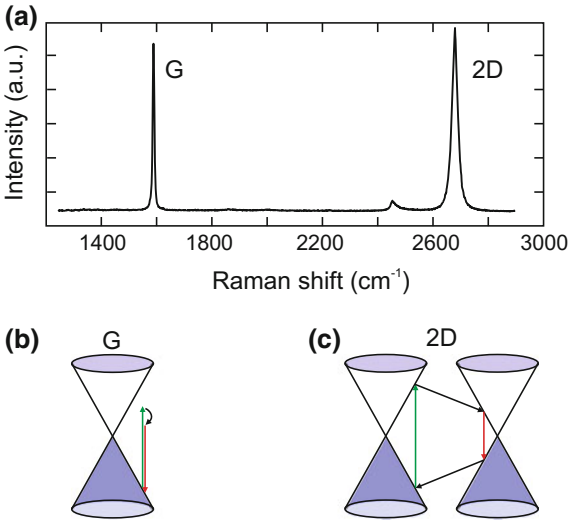

Fig. 8.5 **a** Raman spectrum of pristine graphene **b** Raman processes that lead to the G line are off-resonant. The incident excitation of electrons is represented by green arrows, the relaxation processes by red arrows. Solid black arrows represent phonons. **c** Raman process that contributes to the 2D line. The figure is inspired by Ferrari et al. [11]

(Fig. 8.5a) at around 2680 rel. cm^{-1} originates from the breathing mode of the TO branch around the K point shown in Fig. 8.4c. The associated phonon modes connect electronic states from the K to the K′ valley and consequently have high momentum. For a complete Raman process, the electron or hole that is scattered from the K to the K′ valley (or vice versa), needs to return to its original valley (Fig. 8.5c). For this momentum transfer a second phonon with opposing momentum is needed to guarantee momentum conversation in the Raman process [17].

The exact Raman processes that lead to the 2D mode and its exact line shape have been subject to numerous studies [8, 10, 13, 17–20]. The scattering processes of the 2D line are commonly separated into inner and outer processes, where the phonons taking part in the inner processes come from the area in the Brillouin zone between K and Γ and the outer processes involve phonons from the area between M and K [21, 22]. Despite reported asymmetries in the line shape that are attributed to the exact scattering probabilities of inner and outer processes [20], the 2D line is commonly fitted with a single Lorentzian [23–25]. The 2D line is highly dispersive with laser energy, as the exact phonon wave vector connecting the excited electron state from the K valley to the state in the K′ valley depends on the energy of the excited electron. Thanks to this interplay between the electron and phonon dispersion relation, the 2D line can be effectively used to probe the phonon dispersion relation of the TO branch around the K points [17, 20].

In the remainder of this chapter the frequencies of the G and 2D lines are denoted by ω_G and ω_{2D}, and the full-width at half maximum (FWHM) of the peaks by Γ_G and Γ_{2D}, respectively.

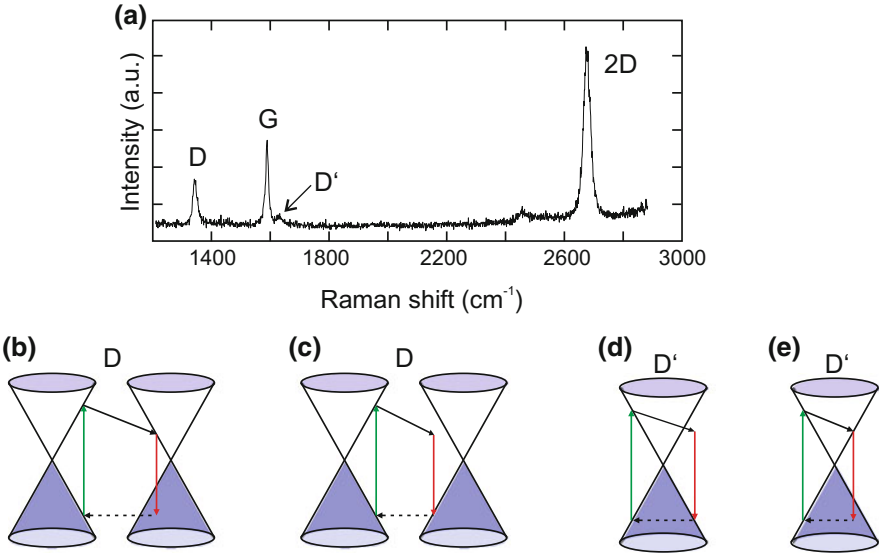

Fig. 8.6 **a** Raman spectrum of defective graphene. Additionally to the G and 2D lines, the defect related D and D′ lines are visible. **b**, **c** Main processes that contribute to the D line. The incident excitation of electrons is represented by green arrows, the relaxation processes by red arrows. Solid black arrows represent phonons and dashed black arrows scattering on defects. **d**, **e** Main processes that contribute to the D′ line. The figure is inspired by Ferrari et al. [11]

8.5 Raman Spectra of Defective Graphene

If there are defects in a graphene lattice (e.g. missing carbon atoms) that alter the sp^2 hybridization locally, additional Raman lines appear (Fig. 8.6a). The strongest defect related Raman line is the so-called D line.[1] The D line is closely related to the 2D line, but only involves one phonon. Instead of the second phonon, a short range scattering center (e.g. a lattice defect) takes part in the Raman process ensuring momentum conservation (Fig. 8.6b, c). While the phonons responsible for the D line connect electronic states in opposing valleys, the phonons of the second defect related Raman line, the D′ line (Fig. 8.6d, e), connect opposing sides within one valley. The D′ line involves phonons of the LO branch close to the Γ point. As for the D line, a defect is needed to ensure momentum conservation in the Raman process.

Since the D and D′ lines only appear in the presence of defects, Raman spectroscopy is a powerful tool to analyze the defect density in graphene sheets. Indeed, if taking into account the excitation energy of the laser, detailed estimations on the defect density can be made by analyzing the intensity ratio of the D and G lines, I(D)/I(G) [26, 27]. For Raman active defects the dependence of I(D)/I(G) on the average distance between two lattice defects, L_D, can be described by [26],

[1] The ‘D’ here indeed stands for defect.

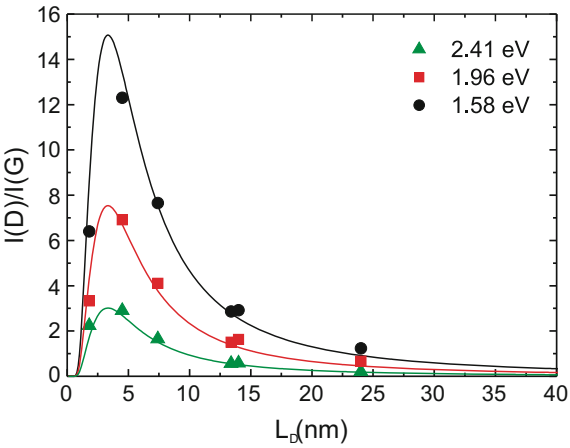

Fig. 8.7 Evolution of the intensity ratio of the D and G lines [I(D)/I(G)] with the average distance between lattice defects L_D for three different laser energies. The figure is adapted with permission from Cancado et al. [26]. Copyright 2011 American Chemical Society

$$\frac{I_D}{I_G} = C_A \frac{(r_A^2 - r_S^2)}{(r_A^2 - 2r_S^2)} \left(e^{-\pi r_S^2/L_D^2} - e^{-\pi (r_A^2 - r_S^2)/L_D^2} \right). \tag{8.1}$$

Here r_S is the radius that corresponds to the area around a defect where the lattice is disordered, r_A is the radius of the area around a defect where a D line process can occur, and C_A gives the maximum I(D)/I(G) ratio, if the D line would be activated along the entire sample. In particular, C_A strongly depends on the laser energy. The solid lines in Fig. 8.7 are fits to (8.1) for the laser energies specified in the inset to the corresponding data from Cancado et al. [26]. They find $r_s = 1$ nm, $r_a = 3.1$ nm and $C_A = (160 \pm 48) E_L^{-4}$, where E_L is the laser energy. As long as the distance between two defects is smaller than the average distance an electron-hole pair travels before scattering with a phonon ($\approx$3 nm [26]), I(D)/I(G) increases linearly with the defect density. This leads to I(D)/I(G) $\propto 1/L_D^2$ as shown in Fig. 8.7. For even higher defect densities, the scattering probabilities with defects do not add up independently anymore and a saturation of I(D)/I(G) is reached. From this point on, the amount of intact carbon hexagons that are required for the phonons of the D line process become less and less and I(D)/I(G) decreases [26].

8.6 Raman Spectra of Doped Graphene

Raman spectroscopy also yields important information on the doping of a graphene sample. In particular, the G line is very sensitive to changes of the charge carrier density [28–31]. In Fig. 8.8a the doping dependence, i.e. charge carrier density dependence of ω_G and Γ_G measured by Froehlicher et al. [30] are shown. With increasing charge carrier density, n, the G line stiffens. At the same time $\Delta\Gamma_G$ decreases. In principle, the change in the frequency of the G line with doping originates from two different contributions, $\Delta\omega_G(n) = \Delta\omega_{G,A} + \Delta\omega_{G,NA}$. Here, $\Delta\omega_{G,A}$ is the adiabatic

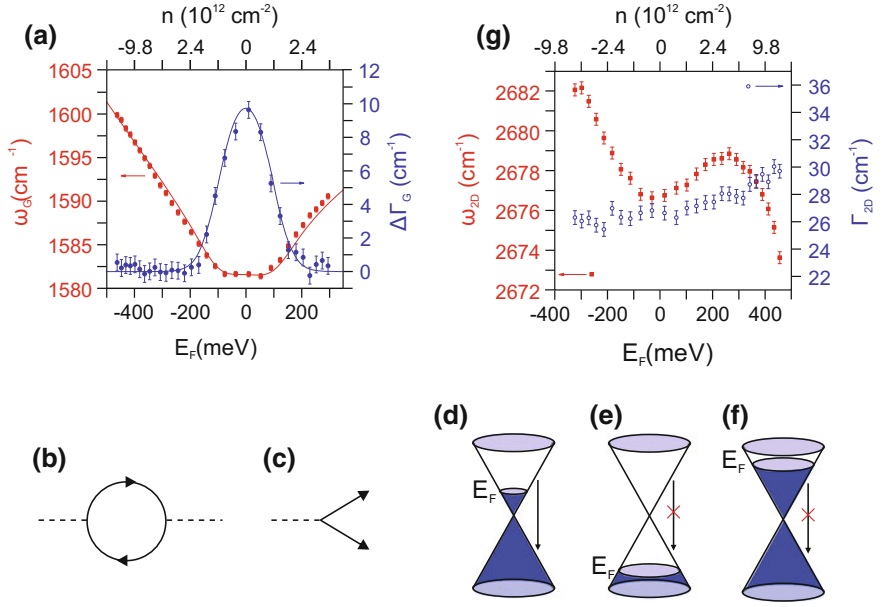

Fig. 8.8 Landau damping of the G line. **a** Dependence of ω_G (red squares) and $\Delta\Gamma_G$ (blue circles) on the Fermi energy measured by Froehlicher et al. [30]. The solid lines are obtained using (8.2) (red) and (8.3) (blue), where the adiabatic contributions calculated by Lazzeri et al. [32] were included for ω_G [30]. **b** Feynman diagram highlighting the coupling of the phonon (dashed line) to virtual electron-hole pairs (solid line) which give a contribution to the self energy of the G line. **c** Feynman diagram describing the decay of the phonon into an electron-hole pair, which broadens the G line. **d** The Fermi energy is near the chage neutrality point. As a consequence, phonons responsible for the G line can decay into electron-hole pairs. **e**, **f** The Fermi energy is below half of the phonon energy (e) or above half of the phonon energy (f) and the phonon decay is blocked due to the Pauli principle. In these cases the phonon cannot decay into electron-hole pairs and the G line becomes narrower. **g** Dependence of ω_{2D} and Γ_{2D} on the Fermi energy. Panels **a** and **g** are taken from Froehlicher et al. [30]

contribution [32] that comes from the change of the lattice parameter, if holes or electrons are induced. The second contribution, $\Delta\omega_{G,NA}$, is the non-adiabatic shift and comes from the coupling of the involved phonon mode to (virtual) electron-hole pairs as highlighted in Fig. 8.8b. By following [32, 33] the non-adiabatic shift can be computed by considering the real part of the self energy of the phonon mode

$$\Delta\omega_{G,NA} = \frac{\lambda}{2\pi\hbar} P \int_{-\infty}^{+\infty} \frac{|f(E-E_F) - f(E)|E^2 sgn(E)}{E^2 - (\hbar\omega_{G,0})^2/4} dE, \qquad (8.2)$$

where λ is the dimensionless electron-phonon coupling constant, P is the Cauchy principle value, $\omega_{G,0}$ is the frequency of the G line at $E_F = 0$, and $f(E)$ is the Fermi-Dirac distribution [30]. Detailed calculations reveal that the non-adiabatic contributions to the shift of ω_G are dominant and the adiabatic contributions only

give a small correction for relevant Fermi energies of $|E_F| < 1$ eV [30, 32]. Also for the linewidth of the G line, Γ_G, non-adiabatic contributions play the most important role. The broadening of the G line due to non-adiabatic effects $\Delta\Gamma_G$ can be computed via the imaginary part of the self energy leading to

$$\Delta\Gamma_G = \Gamma_G - \Gamma_{G,0} = \frac{\lambda}{4}\omega_{G,0}\left[f\left(-\hbar\frac{\omega_{G,0}}{2} - E_F\right) - f\left(\hbar\frac{\omega_{G,0}}{2} - E_F\right)\right], \quad (8.3)$$

where $\Gamma_{G,0}$ includes all other contributions to the broadening, e.g. disorder, and anharmonic coupling [30]. The non-adiabatic broadening is caused by the decay of the phonon into an electron-hole pair (Fig. 8.8c). The strength of this broadening mechanism strongly depends on the value of the Fermi energy, E_F. If the Fermi energy is near the charge neutrality point of graphene, the initial states in the valence band are occupied and the states in the conduction band are empty, allowing the creation of electron-hole pairs (Fig. 8.8d). In contrast, if the Fermi energy is increased to more than half of the phonon energy ($\hbar\omega_G \approx 196$ meV), the final states in the conduction band become occupied and the phonon decay is blocked due to the Pauli principle (Fig. 8.8f).

Effectively, this leads to an increase of the phonon lifetime and reduces the broadening of the G line. The same holds true for hole doping. If the Fermi energy is below –98 meV, the initial states in the valence band are not occupied and the phonon cannot decay into an electron-hole pair (Fig. 8.8e). Consequently, Γ_G is a good measure for the doping, in case the Fermi energy is below half of the phonon energy. However, once the relevant states in the conduction band are fully occupied (or the states in the valence band are fully emptied), no strong changes in Γ_G can be observed. In real measurements, the effect is smeared out by temperature, which is included in (8.2) and (8.3) via the Fermi-Dirac distribution, and spatial variations of the Fermi energy within the laser spot. Taking both effects into account, Froehlicher et al. [30] found excellent agreement between the theoretical curves obtained from (8.2) and (8.3) for ω_G and $\Delta\Gamma_G$ (solid lines in Fig. 8.8a) and their data.

The 2D line, on the other hand, behaves very differently with doping as non-adiabatic effects do not play an important role [28, 30, 31]. As a consequence, the FWHM of the 2D line is only weakly affected upon changing the Fermi energy (Fig. 8.8g). The frequency of the 2D line, however, shows clear changes due to adiabatic effects (Fig. 8.8g). Remarkably the changes for electron and hole doping differ significantly, such that a comparison of ω_G and ω_{2D} may be used to distinguish between hole and electron doping.

8.7 Raman Spectra of Strained Graphene

The phonon mode that gives rise to the G line is doubly degenerate (compare Fig. 8.4a, b). However, any mechanism that breaks the symmetry of the honeycomb lattices also breaks the degeneracy of the two phonon modes. This is the case, if a graphene sheet is

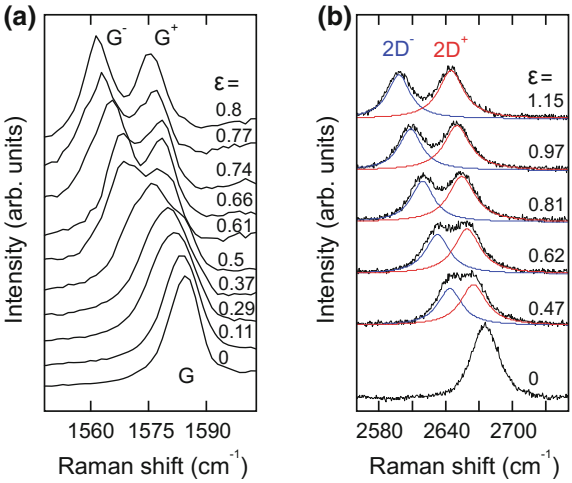

Fig. 8.9 **a** Dependence of the G line on uniaxial strain. A splitting into two sub-peaks G^- and G^+ is observed. **b** Dependence of the 2D line on uniaxial strain in zig-zag direction. A splitting into two sub-peaks $2D^-$ (blue) and $2D^+$ (red) is observed. Panel **a** is taken from Mohiuddin et al. [34] and panel **b** is taken from Yoon et al. [37]

subject to strain ε. In particular, uniaxial strain (applied only in one specific direction of the graphene lattice) lifts the degeneracy at the Γ point as the restoring forces between neighbouring carbon atoms change differently parallel and perpendicular to the direction of the applied strain. In this case, the G-line splits into two components denoted by G^+ and G^- [34, 35], which is nicely visible in the measurements of Mohiuddin et al. [34] shown in Fig. 8.9a. In their study Mohiuddin et al. [34] found shifts of $\delta\omega_{G,+}/\delta\varepsilon \approx -10.8\,\mathrm{cm}^{-1}/\%$ and $\delta\omega_{G,-}/\delta\varepsilon \approx -31.7\,\mathrm{cm}^{-1}/\%$ for the two sub-peaks of the G line. Biaxial strain, by contrast, changes the spring constants equally for both degenerate phonon modes. In this case the Raman line shifts as well, but does not show a splitting. Zabel et al. [36] reported a shift of $\delta\omega_G/\delta\varepsilon \approx -57\,\mathrm{cm}^{-1}/\%$ and Mohiuddin et al. [34] found $\delta\omega_G/\delta\varepsilon \approx -63\,\mathrm{cm}^{-1}/\%$.

The 2D line is also strongly affected by strain. For the 2D line, it is not only important that strain changes the spring constants of the C–C bonds. An additional effect originates from the change of the size and shape of the Brillouin zone if strain is applied. This effect shifts the 2D line, as the momentum needed to connect the K and K′ valleys depends on the exact size and shape of the Brillouin zone [19, 34, 38, 39]. In the case of uniaxial strain, the 2D line can also split into two sub-peaks with frequencies denoted by ω_{2D}^+ and ω_{2D}^- [37, 39] (Fig. 8.9b). According to Huang et al. [39], the splitting is attributed to the deformation of the Brillouin zone that leads to inequivalent energy changes for inner and outer processes along different paths connecting K and K′ [19, 39]. For uniaxial strain applied in armchair direction, Yoon et al. [37] reported $\delta\omega_{2D}^+/\delta\varepsilon \approx -44\,\mathrm{cm}^{-1}/\%$ and $\delta\omega_{2D}^-/\delta\varepsilon \approx -63\,\mathrm{cm}^{-1}/\%$ and for uniaxial strain in zig-zag direction $\delta\omega_{2D}^+/\delta\varepsilon \approx -26\,\mathrm{cm}^{-1}/\%$ and $\delta\omega_{2D}^-/\delta\varepsilon \approx -68\,\mathrm{cm}^{-1}/\%$ for the two sub-peaks, respectively. The intensity of the two sub-peaks depends strongly on the laser polarization with respect to the lattice orientation [37]. For biaxial strain the shift of the 2D line was found to be $\delta\omega_{2D}/\delta\varepsilon \approx -191\mathrm{cm}^{-1}/\%$ by Mohiuddin et al. [34] and $\delta\omega_{2D}/\delta\varepsilon \approx -140\mathrm{cm}^{-1}/\%$ by Zabel et al. [36].

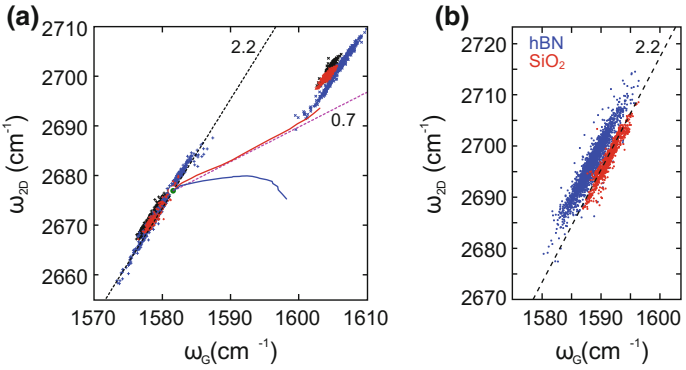

Fig. 8.10 **a** Scatter plot of the frequencies of the 2D and G lines obtained with a laser wavelength of 514.5 nm. The dashed, black line indicates the expected relative shifts for strain. The blue (red) solid lines are the expected shifts for electron (hole) doping. The pink dashed line is a linear approximation of the expected shift for hole doping. It has a slope of 0.7. The green dot is the expected position for undoped and unstrained (pristine) graphene. The different colors of the data points correspond to several different samples. The data clouds on the right side correspond to the same samples as the data on the left side after the samples were thermally annealed [40]. **b** ω_{2D} against ω_G for graphene encapsulated in hBN (blue) and hBN-graphene-SiO_2 (red) measured with a laser wavelength of 532 nm. The dashed, black line shows the expected shifts induced by strain with a slope of 2.2. Panel **a** is taken from Lee et al. [40]. Panel **b** is taken from Neumann et al. [25]

Finally, we take a look at the relative shifts of both Raman modes with strain. It has been shown in a variety of studies that strain in graphene samples, often induced unintentionally during the fabrication process, shifts the G-and 2D-line by a fixed ratio of $\Delta\omega_{2D}/\Delta\omega_G \approx 2.2$ [25, 40–42] (dashed, black lines in Fig. 8.10a, b). Likely, the strain induced in these samples is of biaxial nature as commonly no peak splitting of the Raman lines is observed [25, 40]. Additionally, such built-in strains are usually far below 1%, which would hinders possible peak splitting in the case of uniaxial strain [25, 42, 43].

8.8 Separating Strain and Doping Signatures in the Raman Spectra of Graphene

Taking into account the characteristic relative shifts of the G and 2D peaks for strain and doping discussed in the previous sections, it is possible to separate both contributions in a two-dimensional representation of ω_{2D} versus ω_G first reported by Lee et al. [40]. In Fig. 8.10a, the expected shifts for strain (dashed black line) and charge carrier doping (solid, blue line for electron doping and solid, red line for hole doping) are shown. For high doping regimes (several 10^{12} cm^{-2}) the hole doping can be approximated by a linear relative shift of both Raman peaks with a slope of 0.7 (dashed purple line). The different data clouds in Fig. 8.10a originate from different

samples and different thermal annealing cycles of individual samples. It is evident that for all samples built-in strain distributions are present as the data clouds scatter around the dashed, black line with a slope of 2.2. Between different samples and annealing steps the charge carrier doping can change and the data clouds move along the red, blue and purple lines (see right upper corner in Fig. 8.10a). An exemplary analysis of a graphene sheet partly encapsulated in hexagonal boron nitride (hBN) (blue data) and partly supported by SiO_2 (red data) is shown in Fig. 8.10b. From this representation, in is apparent that the SiO_2 substrate induces more doping in the graphene sheet as compared to hBN, since the red data points are shifted to higher values of ω_G. Note that the offset between the red and blue data points is not necessarily caused by differences in the doping exclusively. Another contribution might stem from differences in the dielectric screening by the substrate material [44]. Furthermore, on both substrates, a strong variation of strain along the graphene sheet is found as both data clouds are spread along the dashed, black line with a slope of 2.2. As the doping within one particular substrate is evidently very uniform in this sample, spatial variations of ω_{2D} can be attributed to different local strain conditions. By plotting a Raman map of ω_{2D}, it is therefore possible to monitor the strain distribution along the graphene sample. An example of the sample analyzed in Fig. 8.10b is shown in Fig. 8.11. In Fig. 8.11a an optical image of the graphene flake covered with hBN is shown. The graphene-hBN layer is partly located on top of another hBN flake and partly on top of SiO_2. In Fig. 8.11b a Raman map of ω_{2D} of the area marked by the dashed box in Fig. 8.11a is presented. The different regions with higher or lower local strain most likely originate from the fabrication process of the sample, where mechanical deformations easily occur due to the mono-atomic thickness of graphene and the micromechanical exfoliation process.

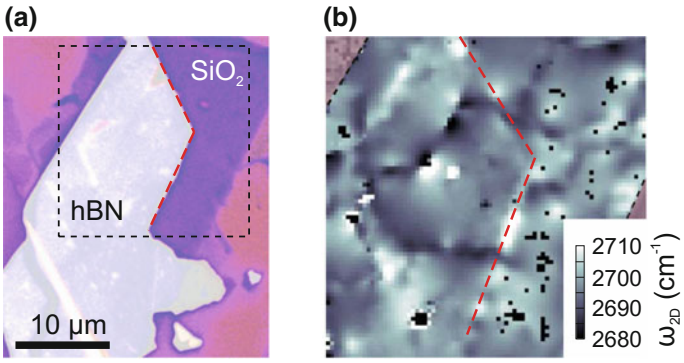

Fig. 8.11 **a** Optical image of a graphene sample covered with hBN. The graphene-hBN layer is partly located on top of SiO_2 and partly on top of another hBN flake (boundary marked by red dashed line). **b** Scanning Raman image of ω_{2D} in the region indicated by the dashed box in panel (**a**). Panel **a** is reprinted from Neumann et al. [25]

8.9 Raman Spectroscopy for Monitoring Nanometer-Scale Strain Variations in Graphene

In the previous section we have seen that scanning confocal Raman spectroscopy is highly useful to examine spatially varying properties in graphene samples such as mechanical strain. In principle, the analysis of the frequencies of the Raman modes restricts the spatial resolution of the probed strain to the dimensions of the employed laser spot. However, the strain in ultra thin membranes like graphene can

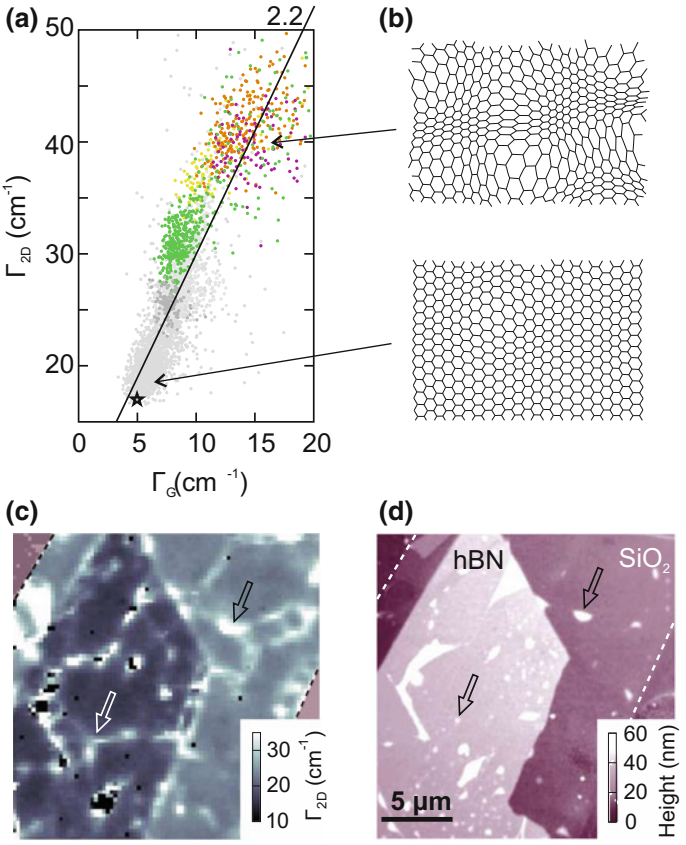

Fig. 8.12 **a** Scatter plot of data obtained on various samples. In all cases the non-adiabatic broadening of the G line was eliminated either by the application of a magnetic field or by high charge carrier doping. Lower values of Γ_{2D} correspond to a low amount of strain variations within the laser spot, while broader Γ_{2D} correspond to larger strain variations as highlighted by the cartoon sketch. **b** Cartoon image of a graphene lattice subject to low strain variations (lower part) and higher strain variations (upper part). **c** Scanning Raman image of the broadening of the 2D line. Folds and bubbles can be seen as regions with increased Γ_{2D}. **d** AFM image of the same area that is shown in panel **c**. The figure is reprinted/adapted from Neumann et al. [25]

substantially change on even smaller length scales, as interactions with the substrate or the formation of folds and bubbles can deform a graphene sheet on nanometer scales [45]. Insights in the strain distribution of a graphene flake on such small length scales can be obtained by analyzing the broadening of the 2D mode. By eliminating the non-adiabatic contributions to the linewidth of the G-line, Neumann et al. [25] could show a linear dependence between Γ_G and Γ_{2D} (Fig. 8.12a). From the slope of the dependence, it was deduced that for defect free graphene this trend is mostly caused by strain inhomogeneities within the laser spot. In particular, Γ_{2D} is strongly influenced by the variation of strain within the laser spot. In fact, a narrow 2D line means that the strain within the laser spot is very uniform, while a broad 2D line indicates substantial changes of the strain (compare Fig. 8.12b). In Fig. 8.12c a confocal Raman image of Γ_{2D} obtained on a hBN-graphene layer partly on top of another hBN crystal and partly SiO_2 (the same sample as shown in Fig. 8.11a) is shown. For comparison, in Fig. 8.12d an atomic force microscopy (AFM) image of the same sample is displayed. Folds and bubbles, measured with the AFM, are also found as regions with increased Γ_{2D} in the Raman map. The strain in the graphene sheet around such lattice distortions changes on length scales below the laser spot size, which broadens the 2D line. These insights are highly useful for the fabrication of high-quality graphene samples for electronic and opto-electronic purposes, because such nm-scale strain variations degrade the charge carrier mobility of graphene [46].

8.10 Characterizing the Thickness of Few-Layer Graphene

So far, only graphene, or more precisely single-layer graphene was discussed. However, Raman spectroscopy can also be used to analyze the thickness, i.e. the layer-number of few layer graphene samples. Most importantly, it allows distinguishing between single-layer graphene (SLG) and bilayer graphene (BLG). The Raman 2D peak originates from resonant processes connecting electronic states around the K and K′ points. As the number of electronic bands and the exact band structure of graphene strongly depend on the number of layers, the 2D line is a good measure for the number of carbon layers. In particular, the 2D line of single-layer graphene (Fig. 8.13a) is usually modeled by a single Lorentzian, while the 2D line of bilayer graphene (Fig. 8.13b) shows contributions from four individual Lorentzians, a direct consequence of the increased number of electronic bands and the related Raman processes (Fig. 8.13c) [21, 23, 24]. Recently, Herziger et al. [21] showed that two of the processes depicted in Fig. 8.13c lead to peaks which lie in very close vicinity to each other and are only seen as one peak in a measurement. The fourth sub-peak of the 2D line of bilayer graphene arises from a strong splitting of the TO-phonon in Γ-K direction. As a consequence, the inner and outer processes connecting the upper valence band to the lower conduction band at K and K′ lead to two distinguishable sub-peaks [21]. A comparison of the 2D line of single-layer and bilayer graphene is

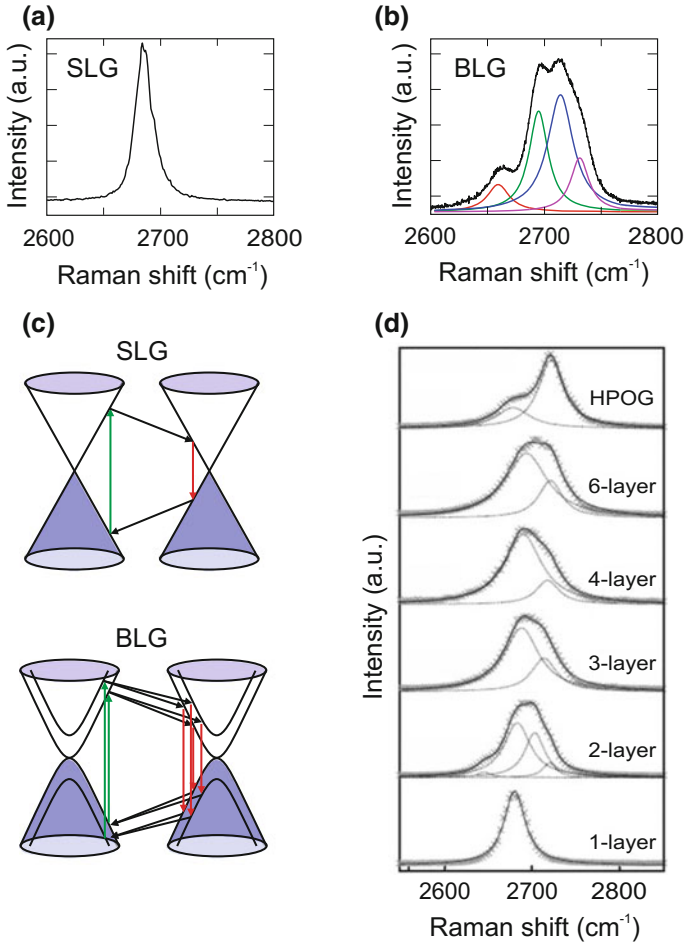

Fig. 8.13 **a** Raman spectrum of single-layer graphene. The 2D line can be approximated by a single Lorentzian. **b** Raman spectrum of bilayer graphene. The 2D line consists of four sub-components as highlighted by the colored Lorentzians. **c** Comparison of relevant processes for the 2D line of single-layer graphene and bilayer graphene. For BLG, four processes that cause three distinguishable sub-peaks of the 2D line of bilayer graphene are shown. The two antisymmetric processes (processes connecting the lower (upper) valence band to the lower (upper) conduction band) are only seen as one peak in the spectrum. The process connecting the upper valence band to the lower conduction band leads to two distinguishable sub-peaks, one originating from the inner and one from the outer process [21]. **d** Evolution of the 2D line for an increasing number of carbon layers from single-layer graphene to bulk graphite. Panels **a**, **b** are taken from Neumann et al. [47]. Panel **c** is inspired by Graf et al. [23] and Herziger et al. [21]. Panel **d** is adapted with permission from Graf et al. [23].

shown in Fig. 8.13c, d. The characteristic line shape of the 2D line of bilayer graphene is highlighted by the four colored Lorentzians that add up to the measured spectrum. With a further increasing number of graphene layers, the number of possible processes and the associated number of sub-peaks increases further and the shape of the 2D line changes (Fig. 8.13d). At the same time, the individual sub-peaks become rather indistinguishable. Consequently, the 2D line of bulk graphite is commonly fitted by two Lorentzians [23, 48, 49].

8.11 Summary

In this chapter the Raman spectrum of graphene was discussed. A particular focus was put on the dependence of relevant material properties on characteristic features of the Raman spectrum, which are summarized in Table 8.1. The plentiful information on a graphene sample that can be obtained from the Raman spectrum makes the technique highly useful for the analysis of device fabrication processes and graphene synthesis techniques in fundamental research and emerging technological applications.

While the qualitative dependencies of the Raman modes on various material properties have been extensively studied in recent years, more precision in the quantitative understanding of the interplay of doping, strain and substrate effects (such as screening, corrugations and short-ranged strain variations) is strongly desired as it will directly improve the usefulness of Raman spectroscopy-based sample characterization.

In this regard, Raman spectroscopy may deliver an important contribution to the commercialization of graphene devices, as features of the Raman spectrum of graphene appear to be very well suited for quality fingerprints and potentially the definition of material standards for graphene samples.

Table 8.1 Summary of the influence of various important material properties on characteristic features of the Raman spectrum of graphene are summarized. ω_{2D} and Γ_{2D} are the frequency and linewidth of the 2D line and ω_g and Γ_G the frequency and linewidth of the G line of graphene. I(D) is the intensity of D line. 'X' marks a strong dependence. 'O' marks less strong dependence and '–' means that the material property only weakly (or not at all) affects the Raman feature

Material characteristics	ω_{2D}	Γ_{2D}	ω_G	Γ_G	$I(D)$
Doping	O [40]	–	X [28, 29, 33, 40]	X [28, 29, 33]	–
Strain	X [19, 34, 37, 39, 40]	X [19]	X [34, 35, 38, 40]	X [34]	–
Strain variations	–	X [25]	–	O [25]	–
Defects	–	O [10]	–	–	X [26, 27]

Acknowledgements The authors wish to thank Sven Reichardt, Marc Drögeler, Luca Banszerus, Michael Schmitz, Donatus Halpaap, Bernat Terrés, Takashi Taniguchi, Kenji Watanabe, Slava V. Rotkin, Francesco Mauri, Pedro Venezuela and Bernd Beschoten, who contributed in different ways to the sample fabrication, measurements and data interpretation shown in this chapter.

References

1. K.S. Novoselov, A.K. Geim, S. Morozov, D. Jiang, Y. Zhang, S. Dubonos, I. Grigorieva, A. Firsov, Science **306**(5696), 666 (2004)
2. A.K. Geim, K.S. Novoselov, Nat. Mater. **6**(3), 183 (2007)
3. A. Geim, I. Grigorieva, Nature **499**(7459), 419 (2013)
4. L. Britnell, R. Gorbachev, R. Jalil, B. Belle, F. Schedin, A. Mishchenko, T. Georgiou, M. Katsnelson, L. Eaves, S. Morozov et al., Science **335**(6071), 947 (2012)
5. B. Hunt, J. Sanchez-Yamagishi, A. Young, M. Yankowitz, B.J. LeRoy, K. Watanabe, T. Taniguchi, P. Moon, M. Koshino, P. Jarillo-Herrero et al., Science **340**(6139), 1427 (2013)
6. B.W. Baugher, H.O. Churchill, Y. Yang, P. Jarillo-Herrero, Nat. Nanotechnol. **9**(4), 262 (2014)
7. R. Saito, M. Fujita, G. Dresselhaus, U.M. Dresselhaus, Appl. Phys. Lett. **60**(18), 2204 (1992)
8. D. Basko, S. Piscanec, A. Ferrari, Phys. Rev. B **80**(16), 165413 (2009)
9. M. Lazzeri, C. Attaccalite, L. Wirtz, F. Mauri, Phys. Rev. B **78**(8), 081406 (2008)
10. P. Venezuela, M. Lazzeri, F. Mauri, Phys. Rev. B **84**(3), 035433 (2011)
11. A.C. Ferrari, D.M. Basko, Nat. Nanotechnol. **8**(4), 235 (2013)
12. M. Mohr, J. Maultzsch, E. Dobardžić, S. Reich, I. Milošević, M. Damnjanović, A. Bosak, M. Krisch, C. Thomsen, Phys. Rev. B **76**(3), 035439 (2007)
13. J. Maultzsch, S. Reich, C. Thomsen, Phys. Rev. B **70**(15), 155403 (2004)
14. A. Grüneis, J. Serrano, A. Bosak, M. Lazzeri, S.L. Molodtsov, L. Wirtz, C. Attaccalite, M. Krisch, A. Rubio, F. Mauri et al., Phys. Rev. B **80**(8), 085423 (2009)
15. S. Piscanec, M. Lazzeri, F. Mauri, A. Ferrari, J. Robertson, Phys. Rev. Lett. **93**(18), 185503 (2004)
16. S. Piscanec, M. Lazzeri, J. Robertson, A.C. Ferrari, F. Mauri, Phys. Rev. B **75**(3), 035427 (2007)
17. C. Thomsen, S. Reich, Phys. Rev. Lett. **85**(24), 5214 (2000)
18. R. Saito, A. Jorio, A. Souza Filho, G. Dresselhaus, M. Dresselhaus, M. Pimenta, Phys. Rev. Lett. **88**(2), 027401 (2001)
19. O. Frank, M. Mohr, J. Maultzsch, C. Thomsen, I. Riaz, R. Jalil, K.S. Novoselov, G. Tsoukleri, J. Parthenios, K. Papagelis et al., ACS Nano **5**(3), 2231 (2011)
20. S. Berciaud, X. Li, H. Htoon, L.E. Brus, S.K. Doorn, T.F. Heinz, Nano Lett. **13**(8), 3517 (2013)
21. F. Herziger, M. Calandra, P. Gava, P. May, M. Lazzeri, F. Mauri, J. Maultzsch, Phys. Rev. Lett. **113**(18), 187401 (2014)
22. M. Mohr, J. Maultzsch, C. Thomsen, Phys. Rev. B **82**(20), 201409 (2010)
23. D. Graf, F. Molitor, K. Ensslin, C. Stampfer, A. Jungen, C. Hierold, L. Wirtz, Nano Lett. **7**(2), 238 (2007)
24. A. Ferrari, J. Meyer, V. Scardaci, C. Casiraghi, M. Lazzeri, F. Mauri, S. Piscanec, D. Jiang, K. Novoselov, S. Roth, A. Geim, Phys. Rev. Lett. **97**(18), 187401 (2006)
25. C. Neumann, S. Reichardt, P. Venezuela, M. Drögeler, L. Banszerus, M. Schmitz, K. Watanabe, T. Taniguchi, F. Mauri, B. Beschoten et al., Nat. Commun. **6**, 8429 (2015)
26. L.G. Cançado, A. Jorio, E.M. Ferreira, F. Stavale, C. Achete, R. Capaz, M. Moutinho, A. Lombardo, T. Kulmala, A. Ferrari, Nano Lett. **11**(8), 3190 (2011)
27. M.M. Lucchese, F. Stavale, E.M. Ferreira, C. Vilani, M. Moutinho, R.B. Capaz, C. Achete, A. Jorio, Carbon **48**(5), 1592 (2010)
28. C. Stampfer, F. Molitor, D. Graf, K. Ensslin, A. Jungen, C. Hierold, L. Wirtz, Appl. Phys. Lett. **91**(24), 241907 (2007)

29. J. Yan, Y. Zhang, P. Kim, A. Pinczuk, Phys. Rev. Lett. **98**(16), 166802 (2007)
30. G. Froehlicher, S. Berciaud, Phys. Rev. B **91**(20), 205413 (2015)
31. A. Das, S. Pisana, B. Chakraborty, S. Piscanec, S. Saha, U. Waghmare, K. Novoselov, H. Krishnamurthy, A. Geim, A. Ferrari et al., Nat. Nanotechnol. **3**(4), 210 (2008)
32. M. Lazzeri, F. Mauri, Phys. Rev. Lett. **97**(26), 266407 (2006)
33. S. Pisana, M. Lazzeri, C. Casiraghi, K.S. Novoselov, A.K. Geim, A.C. Ferrari, F. Mauri, Nat. Mater. **6**(3), 198 (2007)
34. T. Mohiuddin, A. Lombardo, R. Nair, A. Bonetti, G. Savini, R. Jalil, N. Bonini, D. Basko, C. Galiotis, N. Marzari, Phys. Rev. B **79**(20), 205433 (2009)
35. M. Mohr, K. Papagelis, J. Maultzsch, C. Thomsen, Phys. Rev. B **80**(20), 205410 (2009)
36. J. Zabel, R.R. Nair, A. Ott, T. Georgiou, A.K. Geim, K.S. Novoselov, C. Casiraghi, Nano Lett. **12**(2), 617 (2012)
37. D. Yoon, Y.W. Son, H. Cheong, Phys. Rev. Lett. **106**(15), 155502 (2011)
38. G. Tsoukleri, J. Parthenios, K. Papagelis, R. Jalil, A.C. Ferrari, A.K. Geim, K.S. Novoselov, C. Galiotis, Small **5**(21), 2397 (2009)
39. M. Huang, H. Yan, T.F. Heinz, J. Hone, Nano Lett. **10**(10), 4074 (2010)
40. J.E. Lee, G. Ahn, J. Shim, Y.S. Lee, S. Ryu, Nat. Commun. **3**, 1024 (2012)
41. S. Engels, B. Terrés, F. Klein, S. Reichardt, M. Goldsche, S. Kuhlen, K. Watanabe, T. Taniguchi, C. Stampfer, Phys. Status Solidi (b) **251**(12), 2545 (2014)
42. M. Drögeler, F. Volmer, M. Wolter, B. Terrés, K. Watanabe, T. Taniguchi, G. Güntherodt, C. Stampfer, B. Beschoten, Nano Lett. (2014)
43. L. Banszerus, M. Schmitz, S. Engels, J. Dauber, M. Oellers, F. Haupt, K. Watanabe, T. Taniguchi, B. Beschoten, C. Stampfer, Sci. Adv. **1**(6), e1500222 (2015)
44. F. Forster, A. Molina-Sanchez, S. Engels, A. Epping, K. Watanabe, T. Taniguchi, L. Wirtz, C. Stampfer, Phys. Rev. B **88**, 085419 (2013). https://doi.org/10.1103/PhysRevB.88.085419
45. A.V. Kretinin, Y. Cao, J.S. Tu, G. Yu, R. Jalil, K.S. Novoselov, S. Haigh, A. Gholinia, A. Mishchenko, M. Lozada et al., Nano Lett. **14**(6), 3270 (2014)
46. N.J. Couto, D. Costanzo, S. Engels, D.K. Ki, K. Watanabe, T. Taniguchi, C. Stampfer, F. Guinea, A.F. Morpurgo, Phys. Rev. X **4**(4), 041019 (2014)
47. C. Neumann, S. Reichardt, M. Drögeler, B. Terrés, K. Watanabe, T. Taniguchi, B. Beschoten, S.V. Rotkin, C. Stampfer, Nano Lett. **15**(3), 1547 (2015)
48. A.C. Ferrari, Solid State Commun. **143**(1), 47 (2007)
49. S. Reich, C. Thomsen, Philos. Trans. R. Soc. Lond Ser. A: Mat. Phys. Eng. Sci. **362**(1824), 2271 (2004)

Chapter 9
Low Frequency Raman Scattering of Two-Dimensional Materials Beyond Graphene

Hailong Hu, Ze Xiang Shen and Ting Yu

Abstract Two-dimensional (2D) materials beyond graphene are undergoing intense study owing to their remarkable electronic and optical properties. This chapter is mainly devoted to Raman scattering measurements of 2D transition metal dichalcogenides (TMD). The similarities and differences in terms of phonon structure of monolayer and bulk MX_2 are discussed. Layer-dependent Raman characteristics of monolayer and few-layer MoS_2 could be obtained with both high and low frequency detection. The effect of uniaxial strain on the Raman spectrum of monolayer MoS_2 is demonstrated. The stacking order and interlayer van der Waals (vdWs) interaction in few-layer TMD materials could be identified by low frequency (LF) Raman spectrum and imaging ($\sim$10 rel. cm^{-1}).

9.1 Introduction

With the great success of graphene, other two-dimensional (2D) layered crystals with a graphene-like structure have also attracted great attention due to their extraordinary physical and electronic properties [1–6]. So far, a wide spectrum of 2D layered crystals beyond graphene has been successfully prepared by both mechanical/liquid

H. Hu (✉)
WITec GmbH, Beijing Representative Office, # 507, Landmark Tower 1,
8 North Dongsanhua Road, Chaoyang District, Beijing
100004, People's Republic of China
e-mail: hailong.hu@WITec-instruments.com

Z. X. Shen
Division of Physics and Applied Physics, School of Physical and Mathematical Sciences, School of Materials Science and Engineering, Nanyang Technological University, SPMS-PAP-03-01, 21 Nanyang Link, Singapore 637371, Singapore
e-mail: zexiang@ntu.edu.sg

T. Yu
Division of Physics and Applied Physics, School of Physical and Mathematical Sciences, Nanyang Technological University, SPMS-PAP-03-12, 21 Nanyang Link, Singapore 637371, Singapore
e-mail: Yuting@ntu.edu.sg

J. Toporski et al. (eds.), *Confocal Raman Microscopy*, Springer Series in Surface Sciences 66, https://doi.org/10.1007/978-3-319-75380-5_9

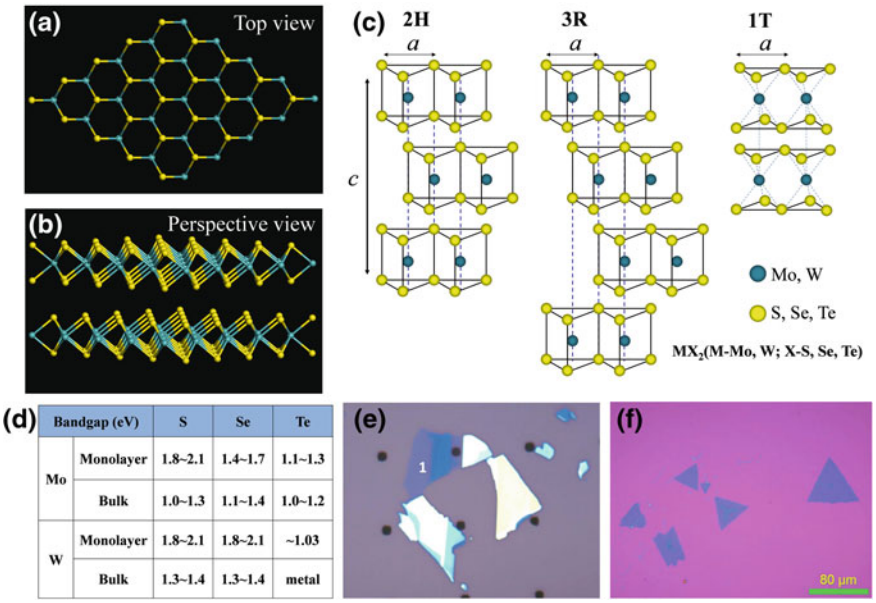

	Bandgap (eV)	S	Se	Te
Mo	Monolayer	1.8~2.1	1.4~1.7	1.1~1.3
	Bulk	1.0~1.3	1.1~1.4	1.0~1.2
W	Monolayer	1.8~2.1	1.8~2.1	~1.03
	Bulk	1.3~1.4	1.3~1.4	metal

Fig. 9.1 Schematic illustration of two-dimensional MX_2 crystals: **a** top view of monolayer MX_2 and **b** perspective view of bilayer MX_2. **c** Schematic diagrams of the three typical structural polytypes of MX_2: 2H, 3R and 1T, where **a** and **c** are the lattice constants. **d** Bandgaps of several monolayer and bulk 2D MX_2 [6, 10, 11]. **e** Optical image of monolayer and few layer MoS_2 on SiO_2/Si substrate prepared by mechanical exfoliation. **f** Optical image of CVD-grown monolayer WS_2

exfoliation [1, 7] and chemical vapor deposition (CVD) [8, 9]. Semiconducting transition metal dichalcogenides with a nonzero bandgap (TMD, e.g., MoS_2, $MoSe_2$, WS_2, WSe_2) are one group of typical 2D crystals that are currently being investigated. All 2D TMD crystals can be represented by a general formula, MX_2, where M is a transition metal atom (M = Mo, W, Ta, etc.) and X is a chalcogen atom (X = Se, S, Te). In contrast to graphene and graphite, every individual layer in all 2D TMD materials has a sandwich structure consisting of one M atom and two X layers [1], as displayed in Fig. 9.1a, b.

There are three typical structural polytypes of multi-layer and bulk MX_2 [10]: 2H (hexagonal symmetry), 3R (rhombohedral symmetry) and 1T (trigonal symmetry) [4], as illustrated in Fig. 9.1c. With reducing dimensionality, monolayer and few-layer 2D MX_2 crystals can exhibit novel electronic characteristics, lattice dynamics and optical properties distinct from their 3D bulk counterparts [3, 6]. For example, a conversion from an indirect bandgap to a direct bandgap occurs from bulk to monolayer MoS_2 [6].

Raman spectroscopy is a rapid, nondestructive and powerful tool for the characterization of graphene [12] and 2D TMD crystals [13]. It can provide much useful structural, optical and electronic information, such as layer thickness [14, 15], strain [16], stacking order [17, 18] and other characteristics. This chapter presents the latest confocal Raman results on 2D TMD materials within both high- and low-frequency ranges, where the latter is also referred to as terahertz (THz) Raman spectroscopy.

9.2 Phonon Structures of Two Dimensional MX_2

To gain a better understanding of Raman scattering of 2D MX_2, it is best to start from the phonon structures of monolayer and bulk MoX_2 calculated by the density functional theory (DFT) method. It has been theoretically and experimentally demonstrated that the general phonon structures of 2D MX_2 are similar [19, 20], although the exact phonon frequencies are different from one another. A typical example is taken from monolayer and bulk MoS_2, which will be detailed in this chapter. The calculated phonon dispersion curves show good agreement with the experimental data acquired by neutron inelastic scattering [21]. For monolayer MoS_2, as shown in Fig. 9.2a, the primitive unit cell includes three atoms with D_{3h} space group symmetry and 9 phonon modes (3 acoustic and 6 optical modes)[20]. The three acoustic branches belong to the in-plane transverse acoustic (TA), longitudinal acoustic (LA) and out-of-plane acoustic (ZA) modes. In addition, the six optical branches are related to two in-plane transverse optical (TO), two in-plane longitudinal optical (LO) and two out-of-plane optical (ZO) phonon modes. In bulk MoS_2, the primitive unit cell enlarges to six atoms with D_{6h} space group symmetry and 18 phonon modes (3 acoustic and 15 optical modes), as illustrated in Fig. 9.2b [20].

When comparing the bulk phonon structures to the monolayer ones, it becomes apparent, that all corresponding modes slightly split into two branches, as a result of the vdWs interlayer interaction. Overall, these two phonon structures are almost identical especially in the high frequency region (>100 rel. cm^{-1}). However, at low frequencies (<100 rel. cm^{-1}), there is a prominent mode splitting around the Γ point, while there are no LF optical modes in monolayer MoS_2. These vibrations are related to the breathing (B1) and shear (S1) vibrational modes between layers, which represent the interlayer vdWs coupling in the multi-layer MoS_2 [14, 22]. The low frequency (LF) Raman vibrations have been used to identify layer number [14, 22] and stacking behavior [17, 18]. They also provide information about both the mechanical and the electrical properties of 2D TMDs.

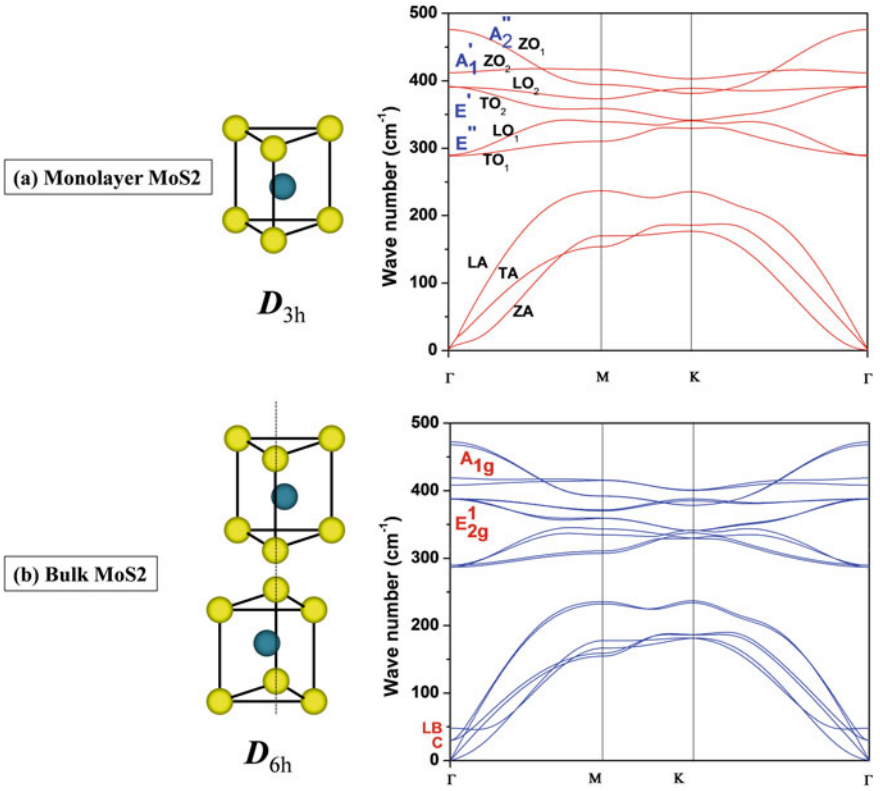

Fig. 9.2 Calculated phonon dispersion curves of **a** monolayer MoS_2 with D_{3h} space group symmetry and **b** bulk MoS_2 with D_{6h} space group symmetry. The general phonon structure of monolayer MoS_2 resembles that of bulk MoS_2, except for the low-frequency acoustic vibrational modes below 100 rel. cm^{-1}

9.3 Raman Scattering of 2D MX_2

9.3.1 High-Frequency Raman Scattering of MX_2 and Layer Identification

From the phonon dispersion curves and Fig. 9.3, it can be seen that there are two distinct Raman-active modes (E^1_{2g} and A_{1g}) for bulk MoS_2 at high frequencies. The in-plane E^1_{2g} mode at ~383 rel. cm^{-1} represents the opposing vibrations of two S atoms with respect to the Mo atom. The A_{1g} mode at ~408 rel. cm^{-1} belongs to the out-of-plane vibrations of only S atoms in opposite directions [13]. The typical Raman spectra of monolayer to bulk MoS_2 are plotted in Fig. 9.3a, where both active modes are observed but with obvious frequency shifts and varying relative intensities. For a monolayer, these two active modes appear at 384 rel. cm^{-1} and 402 rel. cm^{-1},

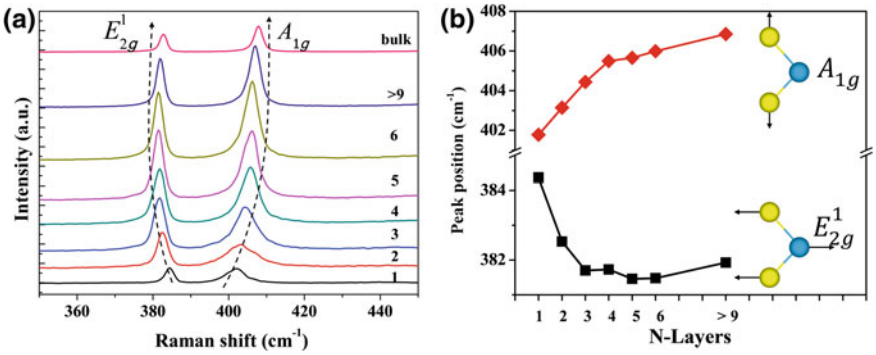

Fig. 9.3 **a** Raman spectra of N layer (N = 1–6 and >9) and bulk MoS_2 on an SiO_2/Si substrate prepared by mechanical exfoliation. The two arrowed dashed lines indicate the evolution of E^1_{2g} and A_{1g} modes with an increasing number of layers. They show red and blue shifts in peak position with respect to the monolayer, respectively, as shown in (**b**)

respectively. With an increase in the number of layers, thickness-dependence of peak positions can be easily observed from both modes. Note that there is an opposite tendency, red shift for the E^1_{2g} mode and blue shift for the A_{1g} mode, as illustrated in Fig. 9.3b. The blue shift of A_{1g} is attributed to the vdWs interlayer coupling, which is analogous to an additional spring on the S atoms [11, 13]. The red shift of the E^1_{2g} mode is the consequence of increasing dielectric screening by long range Coulomb interactions [13, 19]. Similar shift trends in peak positions are found in other 2D MX_2 materials, including: WS_2 [23], WSe_2 [15], and $MoSe_2$ [24]. Frequency shifts with respect to layer number are often utilized for fast thickness identification of MX_2.

9.3.2 *Low Frequency Raman Scattering of MX_2 and Layer Identification*

Low frequency (LF) Raman spectroscopy refers to the chemical vibrational information in the spectral region of <10–100 rel. cm^{-1} [25, 26]. Typical LF Raman features could respond to either the acoustic phonon vibrations in crystals such as graphene [26, 27] or the intramolecular vibrations in substances with heavy atoms and weak bonds such as proteins [28]. The LF Raman spectra and imaging of few-layer MoS_2 were recorded using a WITec alpha300 R confocal Raman microscope with a highly efficient LF RayShield coupler, which is able to acquire LF Raman spectra from as low as 10 rel. cm^{-1}. A frequency-doubled Nd:YAG green laser (532 nm) was focused to a diffraction-limited spot size of 300 nm with a 100×, NA = 0.9 objective. The high throughput of the RayShield coupler allows LF Raman imaging to be performed with short integration times (0.5 s for one spectrum).

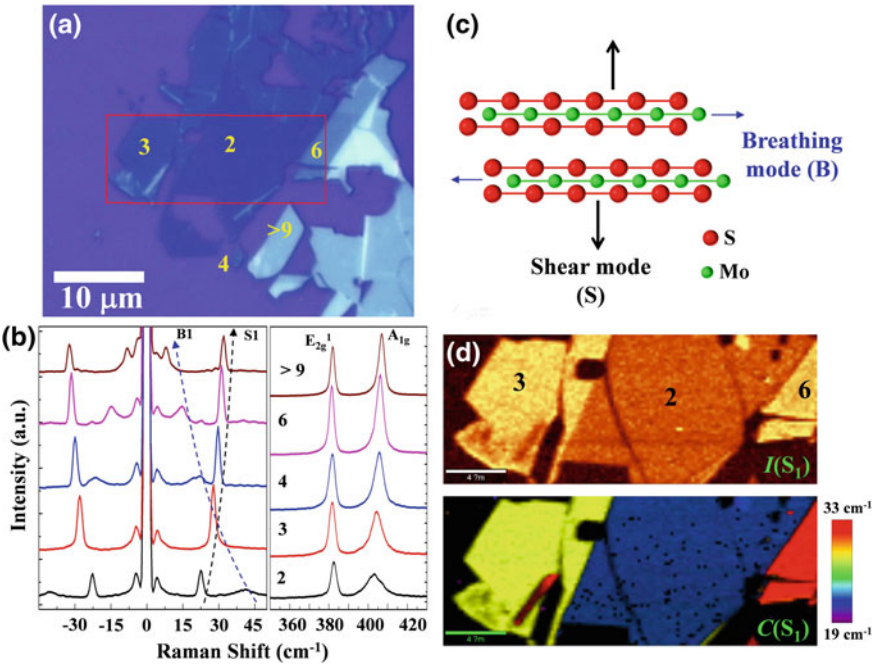

Fig. 9.4 (**a**) Optical image of a few-layer MoS_2 sheet with various layers on an SiO_2/Si substrate, with the number of layers marked: 2–4, 6 and >9. The layer thickness was initially established according to the high-frequency Raman peak position (E^1_{2g} and A_{1g}). (**b**) LF Raman spectra of few-layer MoS_2, exhibiting one interlayer breathing (B1) mode and shear (S1) mode. (**c**) Both vibration modes are related to the interlayer van der Waals forces. (**d**) With increasing layer number, the frequencies of the B1 and S1 modes show prominent blue and red shifts, respectively

Figure 9.4a shows the optical image of a few-layer MoS_2 sheet with various layers on an Si/SiO_2 substrate, which are labelled with the numbers: 2–4, 6 and >9. The layer thickness is determined in accordance with the peak position of two high frequency E^1_{2g} and A_{1g} modes. The corresponding LF Raman spectra are plotted in Fig. 9.4b, which shows peaks belonging to the interlayer breathing mode (B1) and shear mode (S1).

Both modes are related to the weak vdWs interlayer coupling in MoS_2, as illustrated in Fig. 9.4c. For bilayer MoS_2, the B1 and S1 modes appear at 40.3 and 22.6 rel. cm^{-1}, respectively. Both modes are observed to show a strong dependence on increasing layer number: red shift for the B1 mode and blue shift for the S1 mode. This evolution could be better visualized by LF Raman imaging based on the peak position and intensity of S1 mode, as displayed in Fig. 9.4d. This experimental observation also directly indicates a layer-dependent interlayer restoring force. Similar phenomena have been observed in other 2D MX_2 materials, for instance, $MoSe_2$ [22] and WS_2 [14]. Compared to the frequency trend of the E^1_{2g} and A_{1g} modes, it could be more suitable and accurate to probe the layer thickness of 2D MoX_2 based on the

LF breathing and shear modes. Moreover, their mechanical properties such as the force constants of the B1 and S1 vibrations could be also derived from these two vibrational frequencies using a diatomic chain model [14].

LF Raman images extracted from the peak intensity and position of the S1 mode show obvious layer dependencies.

9.4 Application of Raman Spectroscopy in MX_2 Layers

9.4.1 Strain Analysis of Monolayer MoS_2

Strain engineering is an important factor in semiconductor manufacturing to improving device performance [29]. By introducing strain, the optical and mechanical properties of 2D layered materials can be modulated, consequently facilitating the exploration of novel fundamental physics and applications of these materials [16, 30, 31]. For example, by adding uniaxial strain on graphene, a semiconducting graphene with a tunable bandgap has been successfully demonstrated [30]. Phonon vibration is highly affected by strain and Raman spectroscopy is a powerful and nondestructive method for analyzing it [32]. It is very important to understand strain effects on 2D MX_2 materials for both fundamental research and developing more promising applications.

Y. Wang and his coauthors have comprehensively studied the uniaxial strain of monolayer MoS_2 on flexible PET substrates with Raman spectroscopy [16]. MoS_2 samples were fabricated by mechanical exfoliation of bulk crystals and transferred onto PET substrates. The samples were then attached to a strain stage with the desired areas in the middle of the stage gap and could be controllably elongated to apply uniaxial tensile strain.

The inset image in Fig. 9.5b is the optical image of a monolayer MoS_2 on a flexible PET substrate marked by a red dashed rectangle. Figure 9.5b presents in-situ Raman spectra of $E^{'}$ (E^{1}_{2g} in bulk) and $A^{'}_{1}$ (A_{1g} in bulk) modes of monolayer MoS_2 as a function of the uniaxial strain. When increasing strain from 0 to 3.6%, there is no obvious peak shift for the $A^{'}_{1}$ mode but the frequency of the $E^{'}$ mode exhibits a linear red-shift, as plotted in Fig. 9.5c.

It is noted that, with increase of uniaxial strain, the $E^{'}$ mode gradually became asymmetric and splits into two singlet sub-modes, named $E^{('+)}$ and $E^{('-)}$ in terms of their frequencies. As discussed in Sect. 9.3.1, the $E^{'}$ mode refers to the opposing vibrations of two S atoms with respect to the Mo atom in the basal plane and the $A^{'}_{1}$ mode belongs to the out-of-plane vibration of only S atoms in opposite directions [13]. The experimental observations demonstrate that the dominant covalent bonding between S and Mo atoms is rather sensitive to the in-plane uniaxial strain. It could be also concluded that the uniaxial strain could modify the electronic properties of single-layer MoS_2 via changing the projected orbital states of Mo atoms and the coupling between the d orbital of the Mo atom and the p orbital of the S atom.

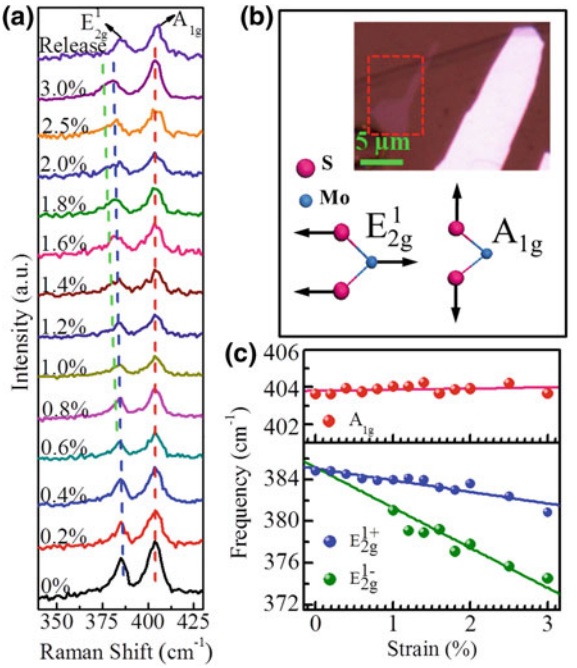

Fig. 9.5 **a** Evolution of the Raman spectra of monolayer MoS_2 under uniaxial strain. The peak positions are indicated by the dashed lines. **b** The schematic representation of the atomic displacements of $E^{'}$ and $A_1^{'}$ modes. The optical image of the single-layer MoS_2 (highlighted by red dashed rectangle) on PET is displayed in the inset. **c** Fitted vibrational frequencies of $E^{'}$ and $A_1^{'}$ modes under increasing uniaxial strain. The solid lines denote the linear fitting. After [16]

9.4.2 Stacking Behavior of Trilayer MX_2 by LF Raman Spectroscopy

There is no doubt that stacking sequences determine the entire structures of crystals and self-assembled molecular materials as well as their physical and chemical properties. In thin-layered crystals, such as graphene and 2D MX_2 materials, layer stacking plays an even more crucial role in the development of their physical and electronic properties [12, 33, 34]. Different stacking configurations could lead to thoroughly different structural symmetries, fundamental properties and potential applications. Therefore, it is important to learn the stacking order of 2D MX_2 materials for both fundamental research and exploring more promising applications.

J. Yan and his coauthors have first studied the stacking of trilayer CVD-grown MoS_2 by using LF Raman spectroscopy [17]. For trilayer MoS_2, there can be four different stacking sequences: ABA, ABB, AAB and AAA following the nomenclature of bilayer systems, as observed from the optical images in Fig. 9.6a. Although this nomenclature here is in terms of the macroscopic geometries from the optical images directly, rather than real atomic stacking, there is an intrinsic correlation between them. Raman intensity mappings of the A_{1g} mode clearly show the layer number of the corresponding samples. The upper panel in Fig. 9.6b shows the LF Raman spectra of trilayer MoS_2 and the corresponding bottom bilayer. For the bottom bilayer, the interlayer S1 and B1 modes occur at ~22 rel. cm^{-1} and ~40 rel.

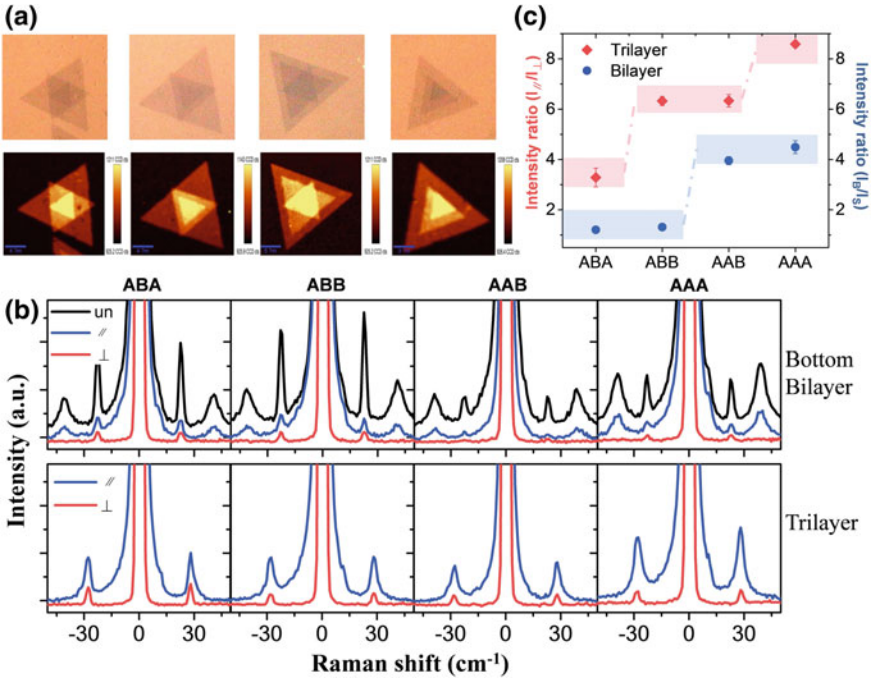

Fig. 9.6 **a** (Upper panel) Optical image of trilayer MoS_2 with four different stacking orders, ABA, ABB, AAB, AAA. The correlated Raman intensity mappings are shown in the lower panel. **b** The LF Raman spectra of the bottom bilayer (upper) and trilayer MoS_2 (lower). **c** The intensity ratio of the interlayer breathing mode and shear mode (blue dots) for bilayer MoS_2, and the $\bar{z}(xx)z$ (∥) and $\bar{z}(xy)z$ (⊥) configuration (red dots) for trilayer MoS_2 with error bars of experimental standard deviation for several samples. After [17]

cm^{-1}, respectively. For AB stacking, the peak intensity of S1 mode is much higher than that of B1 mode, while it reverses for AA stacking. It is noted that the former Raman spectra share strong similarity with that of bilayer MoS_2 prepared by mechanical exfoliation in Fig. 9.4. It demonstrates a two-bilayer stacking periodicity and hexagonal symmetry, namely, 2H crystal structure for AB stacking. The AA stacking refers to the 3R structure. These observations are in good agreement with theoretically-calculated Raman spectra and STM experimental results [17]. Based on the relative intensity ratio between S1 and B1 modes, the stacking in bilayer MoS_2 could be quantitatively determined, ∼1 for 2H AB stacking and ∼4 for 3R AA stacking, as depicted in Fig. 9.6c.

For trilayer MoS_2, the interlayer breathing (B1) mode and shear (S1) mode overlap, as shown in the lower panel in Fig. 9.6b. Similar quantitative determination could also be created in terms of polarized LF Raman scattering. By calculating the total intensity ratio between the parallel and perpendicular components of both shear mode

and breathing mode, a statistical conclusion for trilayer MoS_2 can be reached: ~3 for ABA stacking, ~6 for AAB and ABB stacking and ~8 for AAA stacking, as shown in Fig. 9.6c.

LF Raman spectroscopy has also successfully characterized the stacking in folded graphene with different folding angles [26, 35]. It was found that the shear mode could be enhanced and observed only at certain folding angles. It is also very interesting to study the effect of stacking order on lattice vibrations in folded TMD materials. 3 + 3 folded MoS_2 was naturally created during the mechanical exfoliation process and is investigated with LF Raman imaging. The 3 + 3 folding is confirmed by the correlated atomic force microscopy (AFM). Figure 9.7a, b shows the high-frequency and LF Raman spectra and imaging of 3, 3 + 3 and 6 layer MoS_2. There is a slight shift in the high-frequency A_{1g} mode observed from the 3 + 3 folded sample. It is noted that the twist sample exhibits three Raman peaks at 31.4, 27.8 and 9.5 rel. cm^{-1}. In accordance with the peak positions, the first two peaks may belong to the shear modes in the folded 6 layer areas and individual 3 layer areas. The new peak at 9.5 rel. cm^{-1} may correspond to the interlayer breathing mode (B1) between individual layers in the 3 layer areas. The folded sample area could be clearly visualized by the Raman

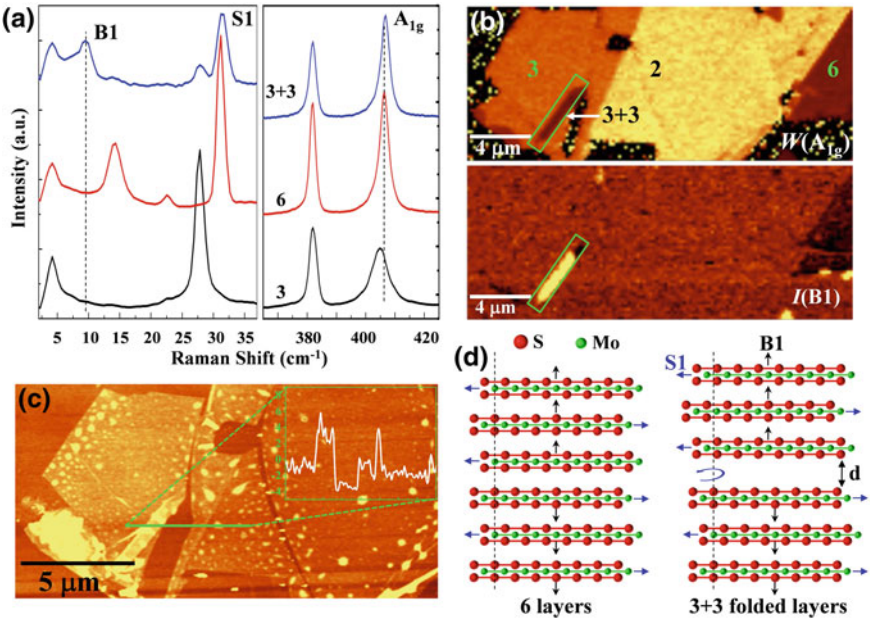

Fig. 9.7 **a** Raman spectra of 3, 6 and 3 + 3 layer MoS_2 acquired from the sample in Fig. 9.3. **b** Raman imaging based on the spectral width of A1g and intensity of interlayer breathing mode (B1), where the area marked with the green frame is 3 + 3 folded MoS_2. The 3 + 3 twist MoS_2 is confirmed by correlated atomic force microscopy (AFM), as shown in (**c**). **d** Schematic illustration of breathing and shear modes in 6 layer and 3 + 3 folded layer MoS_2. The folding angle and interlayer distance between each trilayer may account for the differences in LF Raman spectra

imaging of the peak width of A_{1g} and intensity of B1 mode. This Raman spectral feature in folded MoS_2 is totally distinct from the regularly stacked trilayer MoS_2 above, in which no new vibrational mode occurs. This could be the consequence of different interlayer van de Waals interactions for the folding angle and the elongated interlayer distance with respect to regular closed stacking [26, 35]. This observation shows the capability and potential of LF Raman spectroscopy to verify the interface interaction in heterostructures based on TMDs.

9.5 Conclusion

2D layered TMD crystals have shown phenomenal electronic, optical and spintronic properties. Raman microscopy is a very powerful tool for the characterization of 2D MX2 materials. It was demonstrated that the frequency of E^1_{2g} and A_{1g} modes show obvious layer dependence due to the increasing dielectric screening and interlayer vdWs interaction with increasing layer number. By applying uniaxial strain on monolayer MoS_2, the E^1_{2g} mode was found to be more sensitive than A_{1g} and split into two singlet sub-modes. LF Raman spectra and images revealed that the interlayer breathing and shear modes are significantly dependent upon the number of MoS_2 layers. The effect of stacking order on interlayer coupling in as-grown trilayer and artificially folded MoS_2 was also visualized with LF Raman microscopy. The Raman scattering of 2D MX_2, especially LF Raman scattering, provides an important insight into other 2D layered materials (black phosphorus and perovskite) and heterostructure built from graphene or TMD materials.

Acknowledgements The author wants to thank Dr. Yan Jiaxu, Prof. Cong Chunxiao, Dr. Wang Yanlong Dr. Shang Jinzhi and Xia Juan for their assistance with the schematic diagrams and experimental data. The MoS_2 sample for LF Raman mapping was provided by Dr. Sun Linfeng.

References

1. B. Radisavljevic, A. Radenovic, J. Brivio, V. Giacometti, A. Kis, Nat. Nanotechnol. **6**(3), 147 (2011)
2. A.K. Geim, I.V. Grigorieva, Nature **499**(7459), 419 (2013)
3. M. Eginligil, B. Cao, Z. Wang, X. Shen, C. Cong, J. Shang, C. Soci, T. Yu, Nat. Commun. **6** (2015)
4. G. Eda, H. Yamaguchi, D. Voiry, T. Fujita, M. Chen, M. Chhowalla, Nano Lett. **11**(12), 5111 (2011)
5. H. Nan, Z. Wang, W. Wang, Z. Liang, Y. Lu, Q. Chen, D. He, P. Tan, F. Miao, X. Wang et al., ACS Nano **8**(6), 5738 (2014)
6. A. Splendiani, L. Sun, Y. Zhang, T. Li, J. Kim, C.Y. Chim, G. Galli, F. Wang, Nano Lett. **10**(4), 1271 (2010)
7. J.N. Coleman, M. Lotya, A. O'Neill, S.D. Bergin, P.J. King, U. Khan, K. Young, A. Gaucher, S. De, R.J. Smith et al., Science **331**(6017), 568 (2011)

8. Y.H. Lee, X.Q. Zhang, W. Zhang, M.T. Chang, C.T. Lin, K.D. Chang, Y.C. Yu, J.T.W. Wang, C.S. Chang, L.J. Li et al., Adv. Mater. **24**(17), 2320 (2012)
9. C. Cong, J. Shang, X. Wu, B. Cao, N. Peimyoo, C. Qiu, L. Sun, T. Yu, Adv. Opt. Mater. **2**(2), 131 (2014)
10. Q.H. Wang, K. Kalantar-Zadeh, A. Kis, J.N. Coleman, M.S. Strano, Nat. Nanotechnol. **7**(11), 699 (2012)
11. J. Kang, S. Tongay, J. Zhou, J. Li, J. Wu, Appl. Phys. Lett. **102**(1), 012111 (2013)
12. L. Malard, M. Pimenta, G. Dresselhaus, M. Dresselhaus, Phys. Rep. **473**(5), 51 (2009)
13. C. Lee, H. Yan, L.E. Brus, T.F. Heinz, J. Hone, S. Ryu, ACS Nano **4**(5), 2695 (2010)
14. X. Zhang, W. Han, J. Wu, S. Milana, Y. Lu, Q. Li, A. Ferrari, P. Tan, Phys. Rev. B **87**(11), 115413 (2013)
15. W. Zhao, Z. Ghorannevis, K.K. Amara, J.R. Pang, M. Toh, X. Zhang, C. Kloc, P.H. Tan, G. Eda, Nanoscale **5**(20), 9677 (2013)
16. Y. Wang, C. Cong, C. Qiu, T. Yu, Small **9**(17), 2857 (2013)
17. J. Yan, J. Xia, X. Wang, L. Liu, J.L. Kuo, B.K. Tay, S. Chen, W. Zhou, Z. Liu, Z.X. Shen, Nano Lett. **15**(12), 8155 (2015)
18. X. Lu, M. Utama, J. Lin, X. Luo, Y. Zhao, J. Zhang, S.T. Pantelides, W. Zhou, S.Y. Quek, Q. Xiong, Adv. Mater. **27**(30), 4502 (2015)
19. A. Molina-Sanchez, L. Wirtz, Phys. Rev. B **84**(15), 155413 (2011)
20. C. Ataca, M. Topsakal, E. Akturk, S. Ciraci, The J. Phys. Chem. C **115**(33), 16354 (2011)
21. N. Wakabayashi, H. Smith, R. Nicklow, Phys. Rev. B **12**(2), 659 (1975)
22. Y. Zhao, X. Luo, H. Li, J. Zhang, P.T. Araujo, C.K. Gan, J. Wu, H. Zhang, S.Y. Quek, M.S. Dresselhaus et al., Nano Lett. **13**(3), 1007 (2013)
23. A. Berkdemir, H.R. Gutiérrez, A.R. Botello-Méndez, N. Perea-López, A.L. Elías, C.I. Chia, B. Wang, V.H. Crespi, F. López-Urías, J.C. Charlier, et al., Sci. Rep. **3** (2013)
24. X. Lu, M.I.B. Utama, J. Lin, X. Gong, J. Zhang, Y. Zhao, S.T. Pantelides, J. Wang, Z. Dong, Z. Liu et al., Nano Lett. **14**(5), 2419 (2014)
25. S. Lebedkin, C. Blum, N. Stürzl, F. Hennrich, M.M. Kappes, Rev. Sci. Instrum. **82**(1), 013705 (2011)
26. C. Cong, T. Yu, Nat. Commun. **5** (2014)
27. P. Tan, W. Han, W. Zhao, Z. Wu, K. Chang, H. Wang, Y. Wang, N. Bonini, N. Marzari, N. Pugno et al., Nat. Mater. **11**(4), 294 (2012)
28. K. Brown, S. Erfurth, E. Small, W. Peticolas, Proc. Nat. Acad. Sci. **69**(6), 1467 (1972)
29. C. Maiti, L. Bera, S. Chattopadhyay, Semicond. Sci. Technol. **13**(11), 1225 (1998)
30. Z.H. Ni, T. Yu, Y.H. Lu, Y.Y. Wang, Y.P. Feng, Z.X. Shen, ACS Nano **2**(11), 2301 (2008)
31. C.H. Chang, X. Fan, S.H. Lin, J.L. Kuo, Phys. Rev. B **88**(19), 195420 (2013)
32. T. Mohiuddin, A. Lombardo, R. Nair, A. Bonetti, G. Savini, R. Jalil, N. Bonini, D. Basko, C. Galiotis, N. Marzari et al., Phys. Rev. B **79**(20), 205433 (2009)
33. A.F. Morpurgo, Nat. Phys. **11**(8), 625 (2015)
34. Y. Wang, Z. Ni, L. Liu, Y. Liu, C. Cong, T. Yu, X. Wang, D. Shen, Z. Shen, ACS Nano **4**(7), 4074 (2010)
35. J.B. Wu, Z.X. Hu, X. Zhang, W.P. Han, Y. Lu, W. Shi, X.F. Qiao, M. Ijiäs, S. Milana, W. Ji et al., ACS Nano **9**(7), 7440 (2015)

Part IV
Geosciences

Chapter 10
Raman Spectroscopy and Confocal Raman Imaging in Mineralogy and Petrography

Marc Fries and Andrew Steele

Abstract Confocal Raman Spectroscopy and Microscopy have attained a significant increase in recognition over the past two decades and the method is now well established as another instrument in the geoscientists' toolbox. Here we present and discuss the use and benefit of the method, considering aspects related to sample preparation, effects of the interaction of lasers on specific sample surfaces, as well as instrumental consideration to address these aspects. Further we present examples how confocal Raman microscopy can be applied in mineral phase and phase composition imaging as well as crystallographic orientation imaging in a variety of geological materials, including shocked minerals, carbonaceous materials and fluid inclusions.

10.1 Introduction

Raman spectroscopy is especially well suited for use in mineralogy and petrographic studies, as it provides non-destructive mineral identification very quickly and with excellent specificity. Additionally, it is sensitive to the presence and structure of carbonaceous phases that are difficult to characterize by optical microscopy or electron beam methods. Raman spectroscopy has the capability of revealing the presence of a wide variety of mineral phases in a single spectrum of sub-micrometer resolution, as opposed to, for example, an electron beam technique that performs analyses that sum the contributions of all phases within the excitation volume. The practical result of this is that a Raman spectrum can identify individual mineral phases in fine-grained clusters, while electron probe analyses only produce the bulk composition

M. Fries (✉)
Astromaterials Acquisition and Curation Office, NASA Johnson Space Center, Houston, TX 77058, USA
e-mail: marc.d.fries@nasa.gov

A. Steele
Geophysical Laboratory of the Carnegie Institution of Washington, 5251 Broad Branch Rd. NW, Washington, DC 20015, USA
e-mail: asteele@carnegiescience.edu

J. Toporski et al. (eds.), *Confocal Raman Microscopy*, Springer Series in Surface Sciences 66, https://doi.org/10.1007/978-3-319-75380-5_10

of the intermixed phases. With the relatively recent development of Confocal Raman imaging spectroscopy (sometimes referred to as CRIS), definitive petrography (the study of rocks in thin section) is now possible in fields of view ranging from tens of micrometers to centimeters across. Data gleaned in this way are used in turn for petrology studies (the study of the formation and alteration of rocks primarily through petrographic analysis). An additional benefit of the use of a visible-light excitation laser is the interrogation of features that are not accessible at the sample surface such as opaque and fluid inclusions fully enclosed in the interior of mineral grains. All of this can be done on either prepared thin sections or unprepared mineral surfaces, which places Raman spectroscopic techniques very prominently in a mineralogist's "tool kit" of analytical techniques.

10.2 Raman Spectroscopy and Imaging as a Mineralogy/Petrography Tool

Mineralogy and petrography techniques have traditionally relied heavily on optical microscopy, utilizing reflected, transmitted, and cross-polarized microscopy to identify minerals in thin section and describe their layout. The identities and textures of mineral phases are used to interpret the formation and subsequent alteration history of those minerals and their parent rock formation (Fig. 10.1). From there the investigator can draw conclusions about the history of the entire rock formation and its

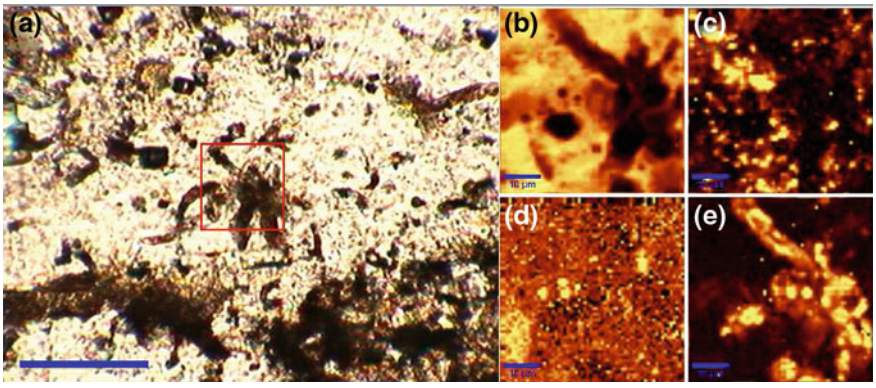

Fig. 10.1 Example of mineral phase mapping using Raman imaging in a thin section of Strelley Pool chert. **a** Transmitted light image showing dark, filamentous features. A Raman image was collected in the red box and the blue scale bar is 80 μm in length. **b** Image of quartz within the red box in **a** showing the mineral matrix. Scale bar is 10 μm long. **c** Image of carbon, which somewhat surprisingly appears as a diffuse blebby phase and is not the primary constituent of the filaments. **d** Small pyrite grains (yellow spots to right and left of the image center). **e** Sulfate minerals that make up the filaments in this image, presumably formed by oxidation of pyrite grains in D. Sample provided by M. Brasier and D. Wacey, of the Dept. of Earth Sciences, Oxford U., UK

relationship to larger geologic units, using observations made under a microscope to draw insights on the creation, alteration, and movement of geological units or even entire continents. In the case of fossilized materials, petrography is used to describe the evolution of life over geologic time as well as to discuss the origin of life itself.

The study of carbonaceous material as a mineral phase in general can be somewhat problematic. Under a microscope, condensed carbonaceous phases simply appear opaque. Electron beam techniques such as SEM or EDX, which are commonly used in mineralogical studies, are less sensitive to carbonaceous materials than phases composed of more massive elements. Some other techniques such as bulk chemical measurements require crushing and extraction, which produces useful information but destroys the fine mineralogical context needed to completely describe the origin and alteration history of the material. Raman spectroscopy is a very useful tool in petrographic analyses like these, as it can be used not only for mineral identification but also for investigation of carbonaceous matter in rocks. Raman spectra are sensitive to the identity and structure of all known condensed carbon phases and are very specific in the identification of other mineral phases (Fig. 10.2). In addition, Raman imaging provides mapping of carbonaceous phases in the mineralogical context of their parent rock. For example, it allows an investigator to discern carbonaceous matter within primary fluid inclusions formed as a rock cooled from its parent melt from other carbonaceous matter found in subsequent alteration veins within the same rock. This distinction is especially important in the study of meteorites, where many features of the rock could be either an original feature of the meteorite, or may be the result of alteration after the meteorite fell to Earth.

The implementation of Raman spectroscopy is very straightforward, as very little sample preparation is necessary for a Raman measurement. Measurements can be performed on whole rocks placed under a microscope in the lab, or on rock formations

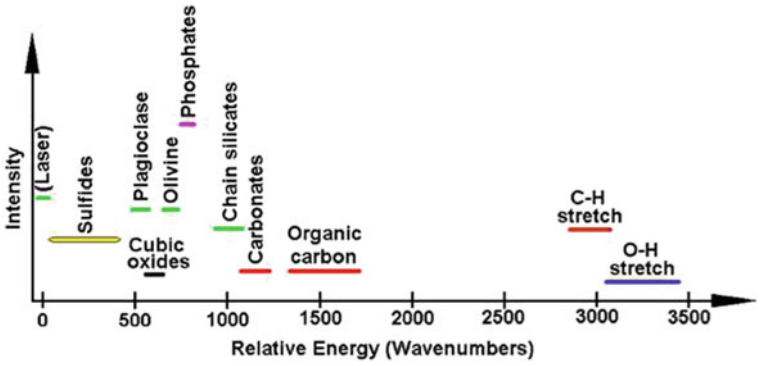

Fig. 10.2 Simplified diagram showing the general positions of prominent Raman peaks for a variety of common rock-forming minerals and compounds. Note that different families of minerals tend to have separate "fingerprint regions", and more importantly that many of these "fingerprint regions" can exist in a single spectrum without substantial overlap. This allows definitive mineral phase identification even in complex mineralogical mixtures

in situ by portable Raman instruments in the field. Samples are usually either ground to produce a flat surface for simple petrographic examination and Raman point measurement (such as in field studies), prepared as thin section for Raman imaging of fine details, or ground to a powder to perform point Raman analysis of a statistically relevant number of grains as a representative analysis of the host rock (but without the contextual information). Practically speaking, however, the most useful mineralogical/petrographic Raman measurements are done using imaging techniques on ground, otherwise smoothed, or polished surfaces both to maximize the signal quality and to remove surface weathering products from the rock. Unless, of course, the goal of the measurement is to examine surface weathering products!

10.2.1 Working with Thin Sections

A typical petrographic thin section consists of a thin wafer of a rock sample that has been polished on both sides until transparent and is thin enough to reveal mineral birefringence in polarized light. The rock slice is affixed to a glass slide on one side, and either sealed with a glass cover slip on the opposing face or left exposed. Confocal Raman spectroscopy is well suited for analysis of thin layers of material (i.e. [1]), as the excitation volume can be constrained in the z-axis to control signal input from polymer and glass layers, as well as from the the x- and y-axes to control and optimize image resolution (see also Chap. 6 in this volume). This allows collection of Raman spectra from selected mineral phases while rejecting spectral contributions from the glass slide, cover slip (if present), or bonding polymer. However, a number of considerations must be accounted for when working with thin sections.
Namely:

1. **Thin section surface irregularities and contamination**:
   Depending on the minerals present in the thin section and the quality of preparation, some surface pits and irregularities may occur in the thin section surface. These commonly occur in anisotropic phases such as pyroxenes and in softer minerals such as clays. Surface roughness within these flaws can scatter the excitation beam somewhat, but the more important consideration is that polishing materials such as diamond paste, abrasive grains, and/or mineral debris from elsewhere in the thin section can become lodged in them (e.g. [2]). When collecting Raman spectra or images from near the surface of the thin section, these contaminants can be misinterpreted as materials native to the thin section rock. To avoid this error, examine the thin section in reflected light before analysis to familiarize yourself with the location and size of flaws. It can also be useful to create an image of the Rayleigh-scattered laser line itself, which serves as a monochromatic reflectivity image at the same resolution and location as Raman images.
2. **Mounting polymer permeation**:
   Since mounting polymer started out as a liquid, expect to find it in every crack in the thin section mineral slab. This is especially true of thin sections made

of friable materials, as these thin sections are often prepared using a vacuum impregnation method. Acquiring a reference spectrum of the polymer used to prepare the thin section under examination is a good idea. This spectrum can be used to differentiate mounting polymer from any organic compounds present in the thin section, usually by identifying spectral features in the C–H stretch mode region which is well removed from Raman modes of rock-forming minerals.

3. **Minor polymer contribution through confocal "leaking"**:
   Confocal spectroscopy constrains light collection to within a narrow band very close to the instrument's focal plane, because light arising from either above or below the focal plane is rejected at the confocal aperture or pinhole(see Chap. 6 in this volume). A small amount of light arising from directly along the long axis of the excitation beam, however, may pass through the confocal aperture regardless of focus. Three conditions must be met for this to occur. One, the Raman signal of the interfering medium must be relatively strong, such as the C–H band stretch region of a thin section mounting polymer. Secondly, the projected confocal aperture[1] is relatively large (depending on the instrument and sample, roughly $\geq$500 nm). Finally, while the excitation laser power density can be relatively high in the focal plane, it decreases dramatically with distance from it. The "leaking" light originates from these out of focus positions and thus the intensity of the interfering Raman signal is intrinsically small. This effect is usually a problem only for spectra collected fairly deep into a thin section such that the excitation volume is close to the lower mounting polymer layer. The result is that a minor C–H stretch mode Raman spectrum can appear in some spectra collected from a thin section, which may lead to the mistaken conclusion that an aliphatic compound is present within the mineral phase.
4. **Focus on the distal mineral surface**:
   When viewing a thin section in transmitted light, it can be possible to focus on the mineral slab surface adjacent to the glass slide instead of the thin section surface, especially if the illumination source is intense. This is a minor problem, but can be rather embarrassing if you happen to be showing off your shiny new Raman spectrometer to a visitor at the time. The easy way around this is to focus on the thin section surface in reflected light when you start your work.
5. **Previous carbon coating**:
   Some thin sections, and especially those prepared from intensely examined samples, are examined with multiple methods in multiple laboratories. If the thin section has been examined using a vacuum electron probe technique such as scanning electron microscopy (SEM) or electron probe analysis, then it has probably been coated with an electrically conductive coating such as Au-Pd or carbon. These coatings can be "removed", but Raman spectroscopy is extraordinarily sensitive to the presence of carbon in particular. Previous Au-Pd coatings will appear as laser-reflective materials in cracks, low spots, and surface imperfections in the thin section. A carbon coating that has been "removed" will show up as an

[1]The projected confocal aperture is the size of the pinhole when projected into the focal plane. It thus includes the influence of all optics of the specific instruments and is thus a comparable value.

opaque or mildly transparent coating in the same surface imperfections but will yield a Raman spectrum consistent with that of glassy carbon. That is, the carbon G and D bands around 1590 and 1350 rel. cm^{-1}, respectively [3], will be broadened to the point that they overlap considerably. The optimal situation is to utilize Raman microscopy before applying techniques that may require elaborate sample preparation.

6. **Surface Alteration of Soft Carbonaceous Phases During Thin Section Preparation**:
   Raman spectroscopy is extraordinarily sensitive to the structure of carbon. The actual interaction volume of the Raman excitation laser is very shallow in opaque phases to the point that it is comparable to the thickness of the surface layer disrupted by mechanical polishing. In other words, a Raman spectrum of a soft, opaque carbonaceous phase in a thin section is very likely only measuring the surface that has been mechanically abraded during polishing. Several researchers have noted this effect (i.e. [4]) and pointed out the importance of taking it into account when describing the structure of carbonaceous phases in thin section. It has been found, however, that the carbon G band is insensitive to polishing and carbonaceous materials analyzed using this Raman feature can produce reliable measurements of crystallite size [5, 6] regardless of polishing. Some researchers [4, 7] state that Raman measurements are best made on the contact between carbonaceous materials and any transparent mineral grain, on a surface that is embedded within the thin section and removed from the actual thin section surface. Another method to avoid polishing effects is to work with fresh, unpolished sample surfaces. Raman images of the thin section can produce in situ maps of carbonaceous material to provide mineralogical context, and multiple spot Raman spectra of the same carbonaceous material on the fractured surface provide a statistically relevant set of spectra for interpretation of bulk microstructure of that same carbonaceous material in order to ascertain the extent of alteration of the carbon measured in thin section.

As long as these considerations are acknowledged and accounted for, none of the above should be a real obstacle to producing high-quality Raman images of samples in thin section.

10.2.2 Control of Laser Power

The signal intensity of Raman scattered photons is commonly quoted to be around one one-millionth of the excitation laser intensity, although in reality this value varies somewhat from mineral to mineral and from one Raman mode to another, as well as whether or not a particular mode undergoes resonant enhancement, etc. It is generally true, however, that the Raman effect is weak relative to the laser power used to observe it, and this leads to the very real possibility that a sample can be damaged by the excitation laser (Figs. 10.3 and 10.4).

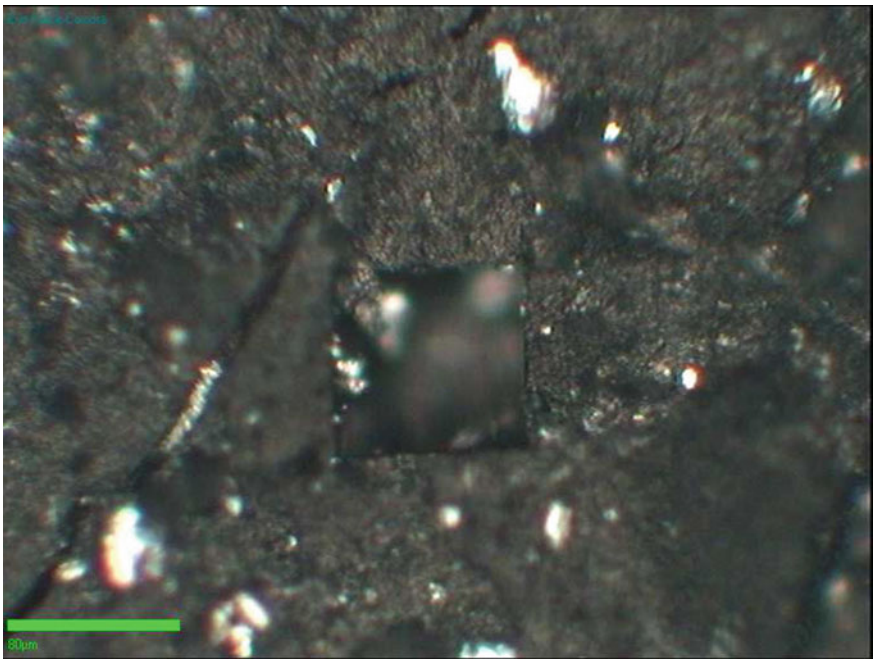

Fig. 10.3 Laser beam damage in a fullerene soot. The square artifact in the center of the image is a hole that perfectly preserves the shape of a Raman image collected with an accidental "overdose" of laser power. A misread dial allowed approximately fifty times as much power as was intended, evaporating the carbonaceous material to leave a square hole and small, surviving silicate contaminants. The scale bar is 80 µm in length

While many early papers described the laser power used in terms of output power at the laser itself, recent literature generally acknowledges the many factors involved and describes power in terms of power density (laser power per unit area) as measured at the laser spot focal plane. This is especially important considering that all Raman instruments feature some variability in total laser throughput due to scattering losses in the focusing optics as well as in the spot size at the focal plane. It is sufficient to describe the power density for a measurement simply by measuring the total laser power at the measurement focus and dividing by the calculated spot area, but there is room for refinement of this method. Laser power distribution at the measurement spot is not uniformly distributed, and there is a need at the time of this writing for establishment of a commonly accepted protocol for reporting laser power values that takes into consideration this and other parameters to include peak laser power for a given measurement spot. Beyond these considerations, for the application of "conventional" Raman spectroscopy (as opposed to resonantly enhanced methods described elsewhere), there are two primary considerations in managing laser power - the nature of the target material and the capabilities of the Raman device used.

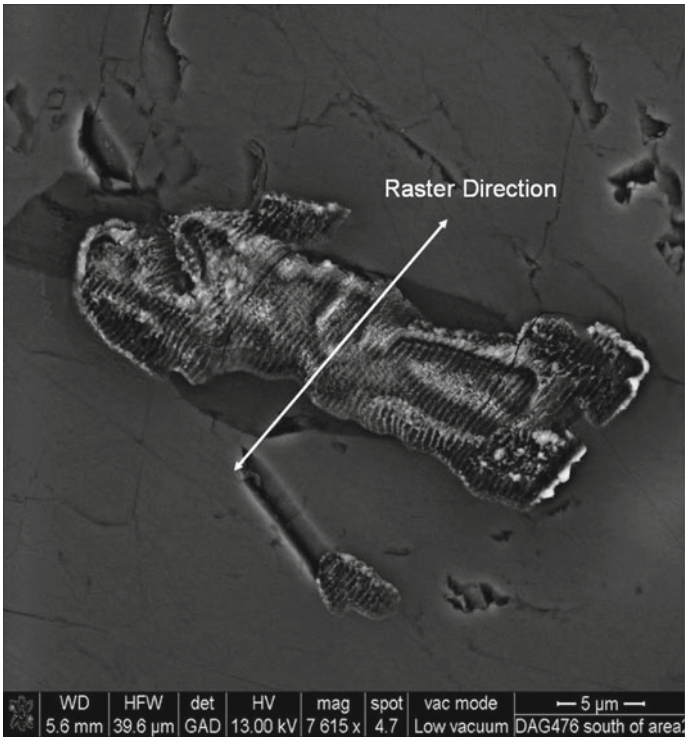

Fig. 10.4 Another one from the "What Not to Do" files, an SEM Image showing laser damage in a chromite grain. A Raman image was collected using excessive laser power density with the raster direction proceeding along the axis indicated by the white arrow. The striation in the chromite grain is the result of damage incurred during repeated, parallel passes by the Raman excitation laser. Note that the opaque chromite grain absorbed sufficient laser power to damage the grain's surface, while the surrounding, transparent olivine was undamaged. This illustrates the dependence of laser power used to collect an image or spectrum on the nature of the material under investigation. Image collected by Dr. Edward Vicenzi, Smithsonian Institution, Washington DC, USA

Due to variation in instrument design and laser spot geometry, it is advisable not to rely on power settings reported in literature but rather to periodically characterize a Raman instrument's laser power output as part of a regular instrument calibration routine.

Nature of the Sample:

Understanding the nature of the sample is an important part of managing laser power. For example, a material that contains fine sulfides that are susceptible to oxidation on heating must be handled more carefully than a sample composed entirely of transparent, high-melting point silicates, for example. A mineral such as quartz or olivine, which exhibits very low absorption in visible light can tolerate very high excitation beam flux without damage. Excitation in such a case occurs over an excitation volume with a size and shape dependent on beam geometry

(see also Chap. 6 in this volume), and thus on the optics of the instrument used. For opaque materials such as chromite and reduced carbon, however, the excitation volume is practically a two-dimensional surface due to strong absorption of the beam at the mineral surface. Power density for such a case can become high, thereby increasing the likelihood of damaging an opaque phase with what would be a benign amount of laser power for transparent grains. Figure 10.4 illustrates this effect, showing small, opaque chromite grains that have been damaged by an excitation beam while surrounding, transparent olivine grains are unaffected.

The message here is that applied power density versus acquisition time per pixel is one of the trade-offs applied to a measurement and that this factor should be applied with an understanding of the nature of the sample. This also serves to reinforce the notion that Raman imaging is best utilized in conjunction with optical petrography techniques, which can provide the general information on sample character needed to select an appropriate amount of excitation laser power.

Other examples of minerals that are especially prone to laser damage include fine-grained minerals, sulfides, or samples embedded in an insulating medium. Fine-grained minerals will include some proportion of porosity and/or poorly-ordered materials in its intergranular volume. Both of these impede thermal conduction, resulting in a material prone to laser heating damage. Many sulfides oxidize readily upon even mild heating, necessitating a sensitive Raman instrument and the use of low laser power density to produce a usable Raman spectrum without inflicting sample damage. A by-product of this fact is that Raman spectral standards of sulfide minerals currently are not as prevalent as spectra of more robust phases, although that situation continues to improve [8].

One example of samples featuring all three of the example features described in the previous paragraph is the suite of cometary samples returned to Earth by the NASA Stardust mission [9]. Most of them are fine-grained, contain fine sulfide grains [10] and in their unprocessed form they are contained in an aerogel insulating medium. Raman measurements of Stardust particles focus on analyses of carbonaceous phases as a result, as these phases typically show strong Raman spectral features and are reasonably resistant to heating damage [11–13], although a limited number of measurements have been performed on other phases [14–16]. These authors determined that fine sulfides fired into aerogel using a light gas gun converted readily to oxides under laser power density of only 33 $\mu W/cm^2$ [17], which made this phase difficult to analyze safely, although not impossible. Stardust samples are generally examined following removal from the aerogel capture medium [18] followed by curatorial processing such as gold foil mounting or ultramicrotoming. The authors also utilized an empirical method for determining the upper threshold of allowable power density for Stardust-like samples using fine, meteoritic sulfide particles. Troilite (FeS) particles were scraped off a slab of the Toluca iron meteorite and pressed onto gold foil just as the Stardust particles were. Sub-micrometer particles were examined over long integration times under increasing laser power to identify the power level where magnetite first started to appear due to heating in air, as seen in the appearance of the strong 670 rel. cm^{-1} Raman peak for magnetite.

Raman Instrument Parameters:

As far as Raman instruments are concerned, there are a few important avenues available for control of sample damage. These are optimizing instrument efficiency/detector sensitivity and the effective control of applied power. For laboratory instruments, modern commercial devices include high-throughput instruments and options for high-sensitivity detectors. Beyond the choice of instrument and detector, the primary factor in instrument design is arguably the choice between fiber-based and fiber-less Raman systems. A system that uses fiber optic cables as the confocal pinhole and for light transmission to the detector is capable of very high resolution imaging with good fluorescence suppression capability, but at the expense of Raman signal throughput due to the small core diameter of the fiber (typically 3–100 μm) (see also Chaps. 2 and 6 in this volume). It is noteworthy, that free beam systems with a pinhole of comparable size would approximate the same level of light throughput (if only limited by the pinhole). The absorption within the fiber itself is measured in dB/km and thus negligible. Conversely, instruments with large pinholes generally allow more light to reach the detector, but at the expense of depth resolution and fluorescence rejection. Differences in signal throughput, sensitivity, excitation beam shape and other variation between instruments demand that a set of trials is done on the actual instrument in use, and that any such measurements done on similar instruments should be used only as broad guidelines.

10.3 "Raman Mineralogy" Using Imaging Raman Techniques

Petrography, at its core, is the study of minerals in thin sections. This means that a petrographer interprets the identity of each mineral in a rock and draws conclusions on the formation and alteration history of the rock and its parent formation from the setting and identity of the suite of minerals present. Imaging Raman spectroscopy is especially well suited to this task, as it not only can be used to identify the minerals but also to map their appearance in a thin section (as in Fig. 10.2). Fine details such as crystallographic orientation, overall water content, presence of aqueous alteration products, compositional variation and others can also be identified and separately mapped (i.e. Fig. 10.5) to highlight and interpret them.

10.3.1 Mineral Phase Imaging

Raman spectroscopy of minerals produces information on the identification of condensed phases with the exceptions of metals and of phases that fluoresce strongly under the excitation beam. A very wide variety of phases produce reasonable Raman

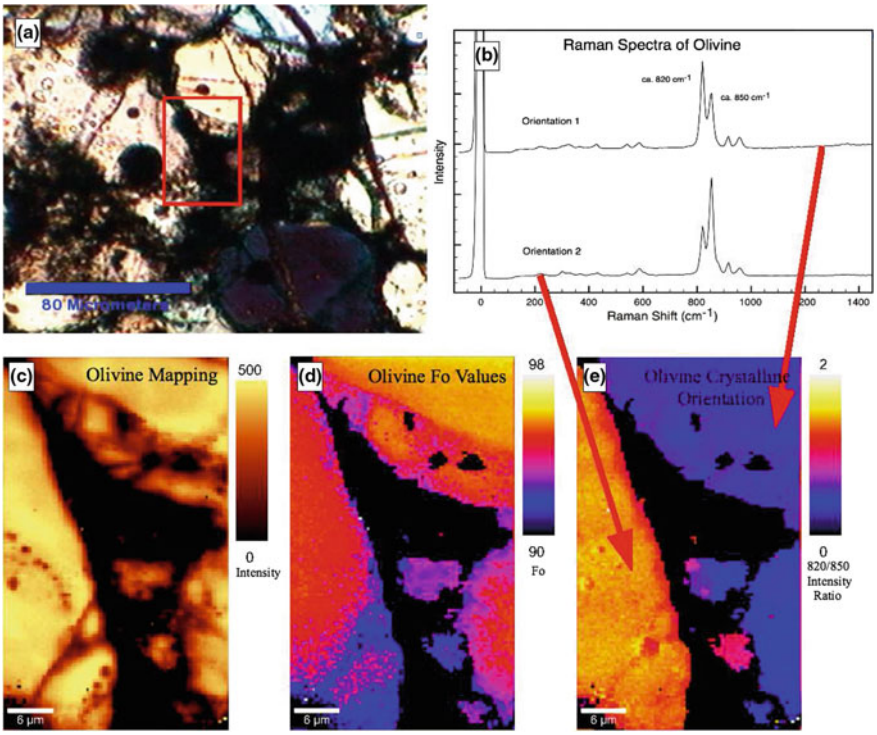

Fig. 10.5 Raman imaging analysis of a portion of the *QUE 94366* carbonaceous chondrite, a meteorite found in Antarctica. **a** Shows a transmitted light microscopy image with the red box highlighting the area examined using Raman imaging. **b** Shows two Raman spectra of olivine within the scan area, showing the variation in peak intensity arising from changes in crystalline orientation relative to the polarization plane of the excitation beam. **c** Is an image of intensity of a Gaussian fit to the ≈850 rel. cm^{-1} Raman peak of olivine, showing the location of olivine within the scan area. **d** This image shows olivine iron content in terms of Fo (Fosterite) number, showing sub-micron variation in iron content in this phase. **e** is an image of the ratio between the ≈820 and ≈850 rel. cm^{-1} Raman peak intensities, indicating crystalline orientation of the various grains. Note that the small grains in the lower center of the image are revealed to be polycrystalline or separate from the larger grains. Also notice that variations in iron content exist within single grains, as shown by comparing (**d**) and (**e**)

spectra, to include transparent, opaque, and metallic phases (including e.g. sulfides). To illustrate the broad range of mineral species that can be identified using Raman spectroscopy, note that the freely available RRUFF online Raman database[2] contains over 2000 distinct mineral spectra [19, 20]. Raman spectra can also contain information on a mineral phase's chemical composition [21, 22], latent strain (see Fig. 10.6) [23, 24], crystalline orientation [22, 25], grain size [26, 27], thermal history in some [28, 29], and are very sensitive to the presence and structure of carbon [3, 30, 31].

[2] http://rruff.info/.

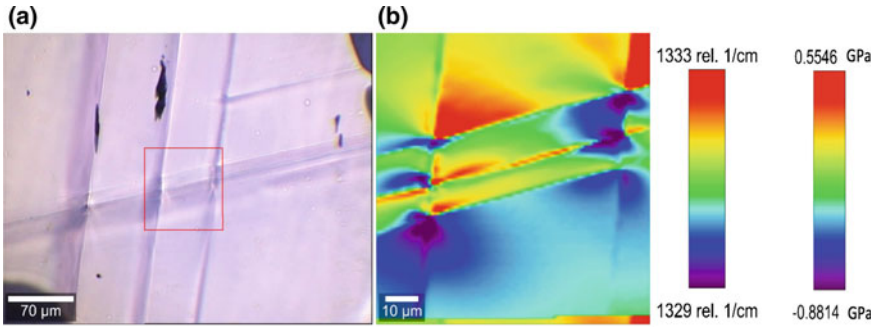

Fig. 10.6 Imaging of strain within a pink diamond. **a** Shows a transmitted light microscopy image of a natural pink diamond (courtesy of E. Gallou). Lamellar fractures can clearly be seen crisscrossing the sample. The red box depicts the area images in **b** which shows the peak center shift (between 1329 and 1333 rel. cm^{-1} and calculated strain in the diamond lattice in GPa. Raman analysis shows the distribution of latent strain throughout the sample due to the fractures, with a complicated pattern of compressive (positive values) and tensile (negative values) strain

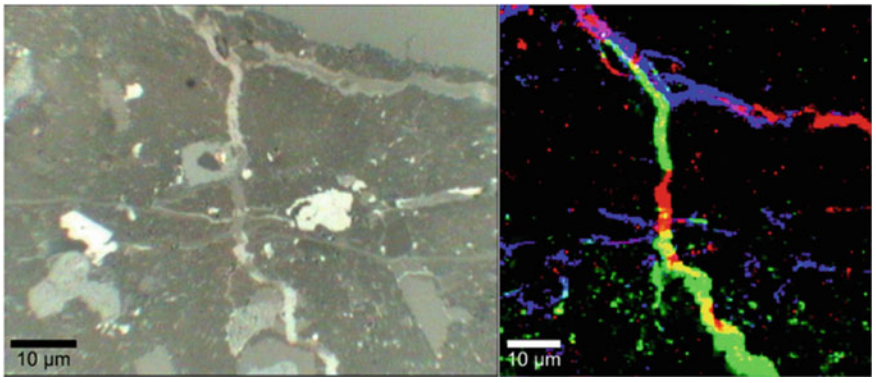

Fig. 10.7 Alteration vein in the *MIL 03346* martian meteorite. Left: Reflected light image of a polished thin section. Right: Raman image with mineral phases highlighted. Red is jarosite ($KFe_3(OH)_6(SO_4)_2$) green is goethite (FeO(OH)), and blue are clay minerals (e.g. the phyllosiliate kaolinite ($Al_2Si_2O_5(OH)_4$). Isotopic analysis of these phases show they are martian in origin, which provides researchers with samples of martian aqueous alteration products for study (from [32])

With the advent of Raman imaging, that information can be expanded from a point measurement to images of petrographic thin sections or even unprepared rock, presented in terms of mineral phase maps or images of mineral properties (Fig. 10.7).

Where electron probe or SEM/EDS imaging produces maps of mineral elemental composition that can identify, for example, an SiO_2 phase, Raman imaging of the same phase can generate maps of quartz, coesite, tridymite, cristobalite, lechatlierite or silicate glass and place that phase in a mineralogic context. Each pixel in such a Raman image can be as small as few hundreds of nanometers across, depending on the instrument, which is a finer resolution than that featured by many analyti-

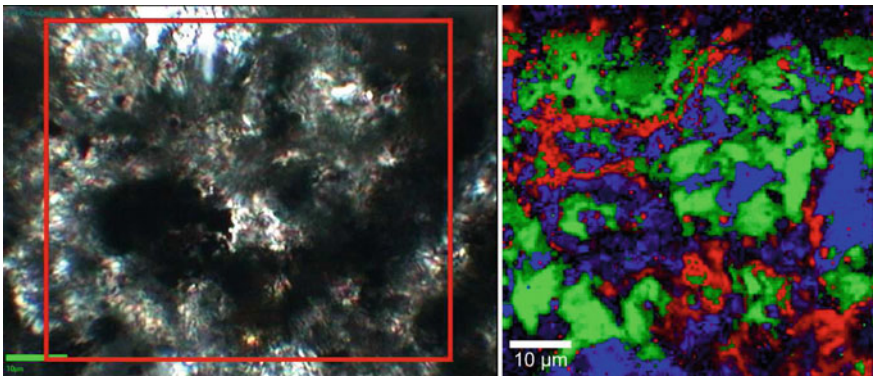

Fig. 10.8 Identification of individual mineral phases in a complex, fine-grained mixture. Left image: Transmitted light microscopy image of the fine-grained rim on a chondrule in the QUE 94366 CV-type carbonaceous chondrite. A Raman image was collected approximately within the red square, and the green scale bar is 10 µm long. Right image: Composite Raman image showing the identity and distribution of macromolecular carbon (Red), olivine (Green), and sulfide minerals (Blue). The petrographic context of these minerals provides insight into the meteorite's formation and alteration history beyond that achievable with optical microscopy alone

cal techniques commonly employed in mineralogy/petrography. Additionally, each Raman spectrum can contain Raman spectral lines of several mineral phases, and by (a happy) coincidence most common rock types generate lines that do not interfere spectrally with those of other phases. For example, have a look at Fig. 10.8.

The mineralogy at the rim of a meteorite chondrule shown there is too fine-grained to completely characterize the minerals present using optical petrography techniques. Raman imaging reveals the various phases present and is used to produce very finely detailed images of each of them, regardless of whether they are transparent silicates or opaque carbonaceous material. This capability allows not only mineralogy by Raman spectroscopy but also petrography by Raman imaging. In other words, a bulk rock can be identified through identification and morphology characterization of its constituent minerals through Raman imaging.

Many modern Raman instruments are capable of producing Raman images in three dimensions. This is done by collecting multiple z-axis stacked layers and assembling them into 3D data sets. Such data add another dimension to the use of Raman imaging to assess the mineral content and petrographic context of samples, such as in Fig. 10.9.

10.3.2 Crystallographic Orientation Imaging

Fundamentally, Raman spectroscopy works by exciting vibrations in the crystal matrix of a target material using an excitation laser. Some of these vibrations propagate along a particular crystallographic direction or directions such that they prop-

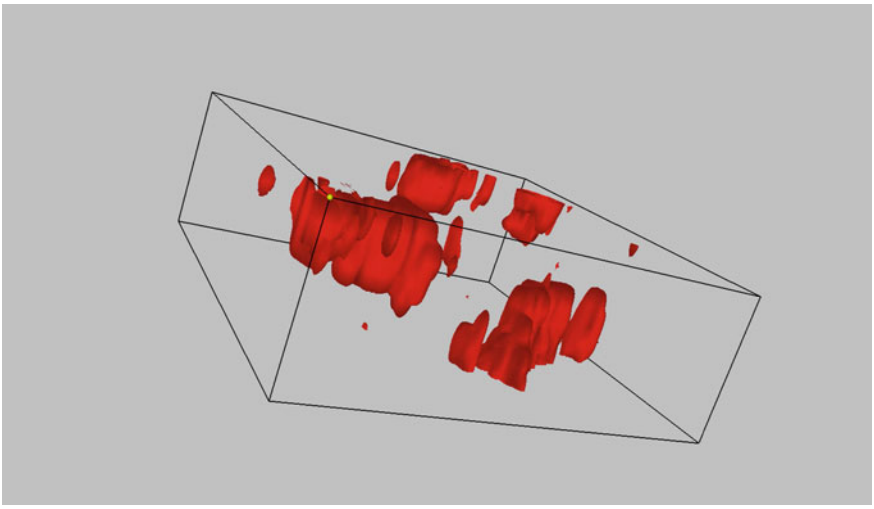

Fig. 10.9 3-D image of the occurrence of MMC in the Tissint meteorite illustrating the advantage of 3-D imaging. This image shows that the MMC is in discrete areas within the sample volume and identifies material is is not in direct contact with the sample surface (top of scan). This information is vital to search for material that has not been contaminated during the sample preparation process

agate asymmetrically through the crystallographic unit cell. In this case, changing the vector of the excitation beam relative to the vibration propagation vector will diminish the likelihood of exciting that particular vibrational mode. The practical effect of this feature is that the same mineral phase in different crystallographic orientations can exhibit a peak or peaks with variable intensity. Raman imaging can reveal the orientation of these grains by generating a calculated image of the ratio of the intensity of an orientation-dependent Raman peak to another peak in the same mineral that is relatively invariant in intensity (Fig. 10.10). This calculation has the added benefit of normalizing the image to remove relative phase spectrum intensity from consideration. The resulting image reveals the orientation of all the grains of a particular phase in a scan field, which allows measurement of grain size as well as providing more detail in the determination of petrographic phase relationships [33].

The example shown in Fig. 10.10 shows quartz grains in the early Devonian Rhynie chert [34] imaged using the ratio of the 128 rel. cm^{-1} peak intensity to that of the 465 cm^{-1} Raman peak. The peak at 128 rel. cm^{-1} is sensitive to crystalline orientation, allowing the calculation of this image. Many minerals exhibit Raman peaks with orientation-sensitive peak intensity and so this technique can be widely applied.

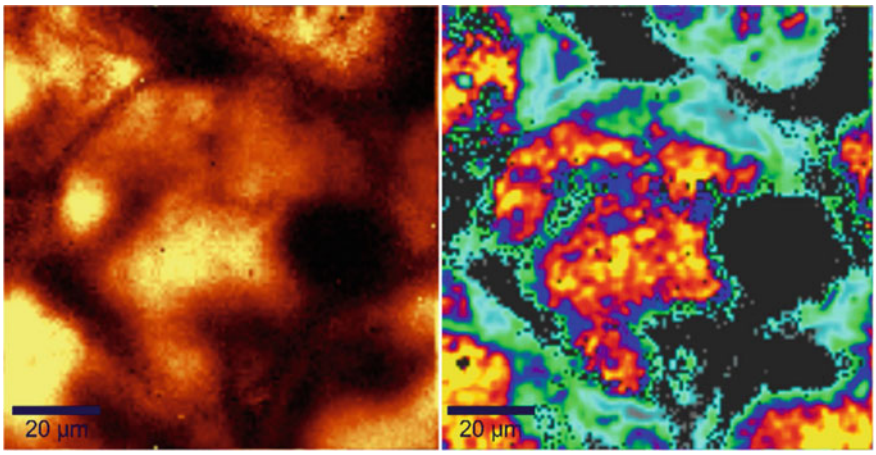

Fig. 10.10 Left image: Image of quartz from a thin section of the Rhynie chert. Right image: Dimensionless quartz grain orientation image assembled by calculating the relative intensity variation of the 132 rel. cm^{-1} quartz peak relative to the 466 rel. cm^{-1} peak. The 132 rel. cm^{-1} peak varies in intensity with change in orientation to the excitation beam but the 466 rel. cm^{-1} does not. Expressing the image as a ratio removes intensity variation due to local quartz abundance and other effects. Sample provided by M. Schweizer, Oxford U., UK

10.3.3 Phase Composition Imaging

Variations in the crystalline unit cell dimensions of a phase are the basis for measurement of phase composition variation, as well as for latent strain. In the case of phase composition, variations in unit cell parameters arise from substitution of one atom for another. A good example of this phenomenon is the replacement of iron with magnesium (or vice versa, depending on the mechanism at work) in the case of the fayalite (Fe_2SiO_4)/forsterite (Mg_2SiO_4) solid solution (Fig. 10.5) [35]. The Raman spectra of these phases are similar and are dominated by symmetric and anti-symmetric SiO_4 tetrahedral vibrational modes, with a continuous shift to higher wavenumbers concurrent with replacement of iron with magnesium (or vice versa, if that's the way you'd prefer to look at it!). This feature is useful for spot Raman analysis, but is especially informative in the form of calculated Raman images of mineral composition. This analysis must be performed with a pair of caveats in place, namely:

(1) latent crystal strain can also produce a Raman peak shift and must be considered, and
(2) Raman peak shift is a function of atomic replacement, but it is not necessarily specific as to which atom is substituted.

As an example of the latter, some olivine grains in extraterrestrial samples are known to feature enhanced manganese up to several weight percent (LIME, or Low-Iron Manganese Enriched olivine [36]). An elemental analysis technique such as

electron probe analysis is necessary to discern this effect from iron/magnesium variation, but in any event the shift of Raman peaks in olivine can be used to produce images of Fe-content variation. In the case of olivine composition, LIME olivines are uncommon and are only known to occur in unequilibrated, ancient meteoritic materials, so are not usually a consideration. And recently, Raman spectroscopy has been demonstrated as a quantitative means of classifying meteorites based on the Fe/Mg content of olivine grains [35]. Other minerals such as the pyroxene family, however, feature cation substitution by a range of elements to include iron, calcium, aluminum, magnesium, chromium, and others and so elemental substitution is much more difficult to deconvolute from Raman spectra alone. Some researchers have addressed this effect, however, and produced systematic trends using natural samples [21, 37].

In the case of latent crystal strain, this effect usually shows a pronounced anisotropy relative to the original shock propagation vector and is revealed in Raman images as a deviation in a single direction across several grains. Compositional changes, in contrast, usually vary radially through individual grains to produce mantle-and-rim microstructure or some other texture, which is clearly tied to grain morphology. Latent strain effects in natural samples are typically rare, as most lithologies which show strain effects (i.e. metamorphic rocks which have experienced plastic flow) are exposed to elevated temperatures at the same time and small-scale strain tends to be reduced or eliminated through annealing. Shocked material such as those associated with terrestrial impact events, however, can exhibit latent strain arising from the impact shock itself, and potentially with associated phase changes, which may or may not revert to low-pressure phases upon post-shock relaxation/annealing.

10.4 Examples of "Raman Petrography" Applications

10.4.1 Raman Analysis of Shocked Minerals

In nature, the most pronounced example of shock processing is seen in impact-altered mineralogy. Examples of shock processing are seen in terrestrial impact craters and materials ejected from craters, meteorites which have experienced impact shock prior to falling to Earth, and terrestrial explosion crater materials such as those found in and around nuclear test pits. The shock in many materials is so intense, such as examples from the ureilite meteorites [38] and terrestrial impact craters such as the Popigai impact structure [39], that graphite or other carbon precursors have been transformed to diamond. Other researchers have noted the presence of a high pressure form of rutile (TiO_2) [40], known as alpha-PbO_2-structured TiO_2 in the Ries crater in Germany [41], the Chesapeake impact structure [42], and in shocked grains associated with the Australasian tektite field [43]. These mineral phases are relatively stable following their shock-induced phase change, as is the SiO_2 polymorph coesite [44–46], and may be signatures of impact processing. Some shock-derived phases, however, are strongly metastable at room temperature and pressure and can revert to an ambient-stable phase upon heating with the excitation laser.

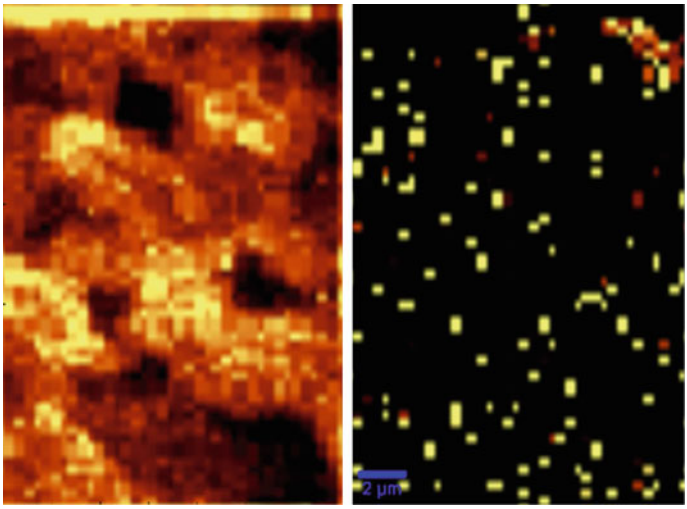

Fig. 10.11 Coesite in impact suevite from the Ries meteorite impact crater, Germany. Left image: Silicate glass. Right image: Small bleb of coesite in the upper right hand corner co-located with "hole" in the glass image on the left. Note the noisy image caused by low excitation power used to preserve this metastable phase combined with the inherent luminescence of shocked materials. Even with this limitation, however, both the placement and identity of coesite are identifiable

Collecting Raman images of shocked samples is difficult and requires careful characterization of the power output of the instrument. Even then, the signal/noise ratio of data in the resulting images is often quite low out of necessity, to prevent damaging the sample with excessive laser power. Even so, images of the petrography of shock-formed phases can be useful, such as that of coesite from the Ries crater breccia shown in Fig. 10.11. In addition Shock-processed samples tend to luminesce under the excitation beam, as they typically contain a high defect density. Nonetheless, the spectra in Fig. 10.11 are sufficient to identify coesite and the image is of sufficient quality to characterize its morphology.

10.4.2 Contextual Imaging of Carbonaceous Materials

Raman spectroscopy of condensed carbon phases such as diamond, kerogen, polymers and macromolecular carbon (MMC, i.e. condensed, reduced carbon spanning a wide range of crystalline order) in general is a topic of special interest when working with minerals. For one thing, the spectrum of all of these phases is particularly intense compared to silicates, allowing for the detection of very small amounts of material. Additionally, other analytical methods commonly used in mineralogy and petrography, such as X-ray diffraction (XRD), are not especially sensitive to poorly ordered carbonaceous materials such as kerogen and macromolecular carbon. Raman imag-

ing allows placement of these phases in a mineralogical context, which is a unique analytical capability. Furthermore, Raman spectra of carbonaceous phases are very sensitive to their degree of crystallographic order, which allows conclusions to be drawn on the thermal history and formation conditions of these phases [28, 47, 48].

The Raman spectrum of MMC exhibits three principal features, namely the "disordered" or D band around 1350 rel. cm^{-1}, the "graphitic" or G band around 1580 rel. cm^{-1} [3, 49, 50], and a series of second-order Raman modes found in the vicinity of 2700 rel. cm^{-1} [51] (Fig. 10.12).

Figure 10.12a shows a typical thin section mounting polymer, with its prominent C–H bands revealing the aliphatic nature of this compound. Note that this spectrum is immediately distinct from the reduced carbon phases here, which allows for definitive discrimination between mounting polymer and native carbon species in a thin section. In Fig. 10.12b a Single-crystal diamond spectrum is displayed showing the distinct, very intense and sharp 1332 rel. cm^{-1} Raman peak whereas in Fig. 10.12c Graphite from the Toluca iron meteorite as an example of highly crystalline, graphitic carbon is shown. As visible in this figure, the primary Raman modes of high-aromaticity condensed carbon are labeled - the D ("disordered") band, the G ("graphitic") band, and the various additive and multiplicative second-order bands. Crystalline graphite can be devoid of a D band, but this example has been polished (see text). Figure 10.12d shows Carbon from a chondrule in the *QUE 94366* CV-type carbonaceous chondrite. This example has been processed at high temperature but apparently not for as long as the Toluca example. The peaks are narrow, which indicates relatively small distribution of graphitic crystallite sizes, but the D band is intense relative to the G band, indicating an overall disordered structure. Minor grossite ($CaAl_4O_7$, Gr) is present in this spectrum. In Fig. 10.12e an example of kerogenous material from the Gunflint microfossil is displayed. The G band is relatively narrow and intense indicating growth of a small size distribution of graphitic domains under thermal metamorphism, and the complex shape of the D band may indicate a wide range of disordered conformations arising from heteroatom enrichment. Finally Fig. 10.12f shows the sub-bituminous type-C coal DECS 1 from the US Department of Energy (DOE) Coal Sample (DECS) Bank and Database, an example of a poorly ordered coal. Broad D and G bands indicate a poorly ordered structure overall.

In some earlier literature, the G band is referred to as the "ordered" or O band. Tuinstra and Koenig [3] were the first to point out that the mean crystalline domain size is proportional to the D/G band intensity ratio, with refinement by Knight and White [52], followed by Matthews et al. [53] that accounts for variation due to laser excitation wavelength. Raman spectra of carbon phases are unusual in two aspects. For one, there is a measurable shift in the D band Raman mode peak position with excitation wavelength [53, 54]. This shift is highly unusual, as Raman modes are essentially energy loss from an incident photon due to crystalline vibrational modes of specific energy and so typically occur at the same Raman shift regardless of excitation wavelength. For the other aspect, the second-order Raman modes commonly seen in condensed carbon are unusual in that most mineral species exhibit first-order modes only.

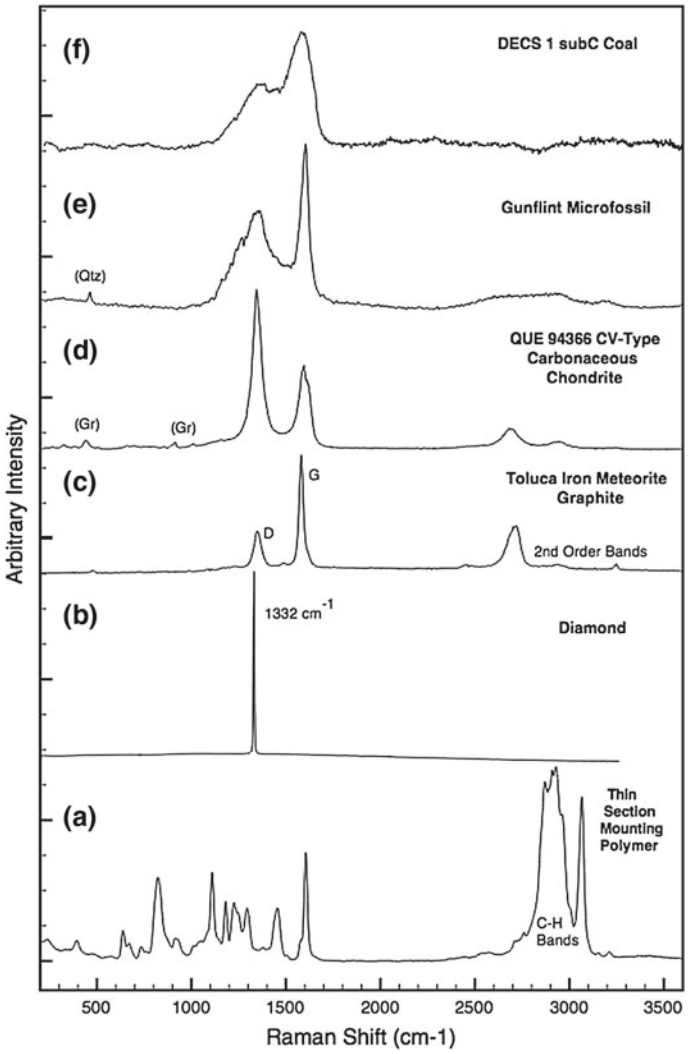

Fig. 10.12 Comparison of the Raman spectra of a few carbon phases. **a** A typical thin section mounting polymer. **b** Single-crystal diamond spectrum. **c** Graphite from the Toluca iron meteorite. **d** Carbon from a chondrule in the *QUE 94366* CV-type carbonaceous chondrite. **e** Kerogenous material from the Gunflint microfossil. **f** Subbituminous (C) coal DECS 1 from the US DOE Coal Sample Bank and Database

As a mineralogical phase, condensed carbon covers a range of structures from diamond with its sp^3-hybridized molecular orbitals and face-centered cubic structure [30] to graphite, which is composed entirely of sp^2-hybridized carbon arranged in a hexagonal lattice. Between these end members (and, arguably, a third end member composed of crystalline aliphatic polymer), condensed carbon spans an infinitely variable degree of crystalline order, ranging from amorphous soot to poorly-ordered kerogens and mildly heated condensed carbon, through a continuum of crystalline ordering up to single-crystal graphite. Much of the naturally-occurring carbon found as a mineralogical phase appears somewhere along this continuum. Generally speaking, MMC found in rocks either precipitates from hydrothermal systems [55], precipitates from mantle-derived fluids and in some pegmatites [56, 57], or it accumulates from organic matter (many references, e.g. [58]), then undergoes metamorphism along with its parent rock. Steele et al. [56] notes an abiogenic MMC formation mechanism from condensation of mantle-derived volatiles in both terrestrial and martian rocks, implying that this is a common process in rocky bodies large enough to support both carbon-containing volatiles at depth as well as intrusive vulcanism. The MMC becomes systematically more crystalline under heat and pressure while losing volatiles (which is why coal seams can contain pockets of methane and/or carbon dioxide), reaching a fully graphitized form above 400 °C according to [59] and at eclogite facies (500 °C and 20 kbar) according to [60]. Extensive graphitization is also noted in carbonaceous materials metamorphosed to granulite [61] and greenschist facies [62]. During metamorphism, trends are seen in both G and D band peak center position (i.e. [60]), G and D band width [61], as well as D/G intensity and area ratios [62]. Wopenka and Pasteris report trends in the intensity of the first overtone of the D band as well, which they define as the "S" peak [61]. Trends are also seen with respect to the L_a (i.e. crystallite length in the a direction parallel to the graphite basal plane) grain size measurement defined by Tuinstra and Koenig [3] as well, where greater thermal treatment generally leads to larger La grain size. Generally speaking, increasing thermal metamorphism leads to greater crystallization (graphitization), which drives the G band center towards ≈1582 rel. cm^{-1}, G band width towards an instrument-limited low value, the D band towards a value that depends on the excitation wavelength [53], and the D/G intensity and area ratios towards zero. Unfortunately, deconvolution of the D band can produce large fitting errors without resorting to fitting the band to multiple peaks, especially for relatively amorphous materials thus complicating the use of D band features as a function of carbon metamorphism. By contrast, use of the G band is relatively straightforward as long as the D' band at 1610 rel. cm^{-1} is deconvolved when that band is prominent. Much of the information to be found in a Raman spectrum of carbon can be expressed with a G band position versus G band width (FWHM) graph, which reveals a trend of graphitization grade as well as a distinct portion of the graph around 1582 and ≈20 cm^{-1} FWHM, respectively, that indicates material featuring graphitic domains that are large with respect to the excitation beam.

The relationship between carbon microstructure as seen in Raman spectra and the thermal history of its parent rock is well established (e.g. [63]). This parameter has

been used to determine the thermal processing history of carbonaceous chondrites of the CV [64] and CO types [65].

One form of poorly ordered carbon, "glassy carbon" [66, 67], exhibits little or no long-range crystallographic ordering but, according to the nomenclature committee of the International Union of Pure and Applied Chemistry (IUPAC), is not truly amorphous, as it exhibits consistent short-range ordering and contains few or no dangling bonds [68]. Glassy carbon was recently noted as a rare phase in cometary materials returned to Earth by the NASA Stardust mission, as well as in a carbonaceous chondrite meteorite (REFS - Stroud, as well as Fries). While glassy carbon is best known as a synthetic phase, it is worthy of mention in a mineralogical context because other studies [69] show that any carbonaceous material arising from organic compounds can show resistance to graphitization even at high temperature. The mechanism at work is the same in both synthetic and naturally occurring phases. Apparently, graphitization is impeded by the presence of a significant atomic percent of heteroatoms such as O, N, and possibly S, leading to a chemically heterogenous, carbonaceous phase which resists metamorphism. This problematic twist means that heteroatom content complicates the analysis of the metamorphic history of MMC. It may be possible to tightly constrain the age and thermal history of a carbonaceous phase if both the crystalline structure and heteroatom content are known, and this topic is ripe for further scientific investigation.

10.4.3 Fluid Inclusions

Fluid inclusions are exactly what they sound like - small pockets of fluid within a mineral grain. They hold special importance in the study of minerals because they represent samples of volatile compounds in the formation environment and subsequent metamorphism (see also Chap. 11 in this volume). The study of volatiles in deeply emplaced rocks such as peridotites, for example, provides information about the melting points and physical behavior of rocks in the deeper parts of the Earth's crust or even the mantle (review by Anderson [70]). Fluid inclusions include two general types - primary and secondary inclusions.

Primary inclusions are essentially trapped pockets of fluid within grains that date to the original crystallization of the host phase. They commonly contain multiple phases, including glass, and are concentrated in elements that feature poor solubility in the parent mineral. Basically, primary fluid inclusions are formed as the surrounding grain solidifies and rejects incompatible elements, which concentrate as droplets and are frozen in place. These inclusions tend to have 'fluid-like' shapes with droplet-like morphology or possibly reverse-crystal morphology that mirrors the crystal shape of the surrounding mineral, and tend to occur alone or in small groups removed from the edges of their parent grain (i.e. [71]). Sometimes, primary fluid inclusions in minerals that form at high temperature and pressure will contain vapor bubbles in them caused by shrinkage of the parent mineral during cooling.

These vapor bubbles can sometimes contain a relative vacuum due to this shrinkage, as improbably as that may seem.

Secondary fluid inclusions are often found lying in a plane or along a line within a mineral grain. These inclusions form when the parent grain cracks while still at relatively high pressure and/or temperature in the presence of volatiles. The volatiles percolate into the crack and form pockets while the parent grain "heals" itself through grain regrowth. The resulting trains of inclusions include material present after the rock has already crystallized from its parent melt, and their contents provide insight into the metamorphic history of the parent rock. There is extensive literature on the analysis and interpretation of fluid inclusions (e.g. [71, 72], Chap. 11 in this volume) and for the purposes of this chapter it is sufficient to simply point this out and comment that Raman spectroscopy and confocal Raman imaging is especially well suited to fluid inclusion analysis (see [73] for a review). A visible-light Raman excitation beam can probe the contents of fluid inclusions within transparent grains such as olivine, pyroxenes and quartz without exposing the inclusion at the thin section surface [74]. This allows for direct measurement of the content of the fluid phase, and virtually eliminates the possibility of contamination if the sample preparation and Raman analysis are done carefully.

Raman analysis of fluid inclusions has been performed on meteorites in one chrondritic setting. To date, two chondrites- the Monahans and Zag ordinary chondrites - have been found to contain halite/sylvite grains with trapped brine inclusions. The parent salt grains are often a brilliant purple color due to irradiation, indicating that these grains are very old [75, 76]. This is a remarkable find, as up to this point no fluid-filled inclusions had been conclusively proven in any type of meteorite. The existence of fluid inclusions in Monahans and Zag showed that liquids could exist at least for a short time on smaller asteroidal bodies.

10.4.4 Ancient Terrestrial Carbonaceous Materials

The topic of Raman imaging of ancient carbonaceous materials, either fossiliferous or just purportedly so, is an expansive topic that can warrant its own chapter. Much of the study of ancient carbonaceous materials has fixated on assigning an age to the earliest life on Earth, perhaps to the detriment of studies of the actual environmental conditions present when these formations - and perhaps life itself - came into being. Nonetheless, much research into ancient carbonaceous materials features Raman spectroscopy and Raman mapping or imaging. Some researchers have made the claim that some particular carbonaceous material is biogenic based on Raman spectra [77] while others have claimed otherwise [78] and even demonstrated that this is not tenable due to lack of sufficient differentiability between biogenic and abiogenic carbonaceous materials, especially for ancient materials that have experienced extensive metamorphism [55, 79]. Uncertainties arise in the interpretation of this information both in how it pertains to the genesis of the carbonaceous material and in the petrologic history of its host formation. This uncertainty is magnified with

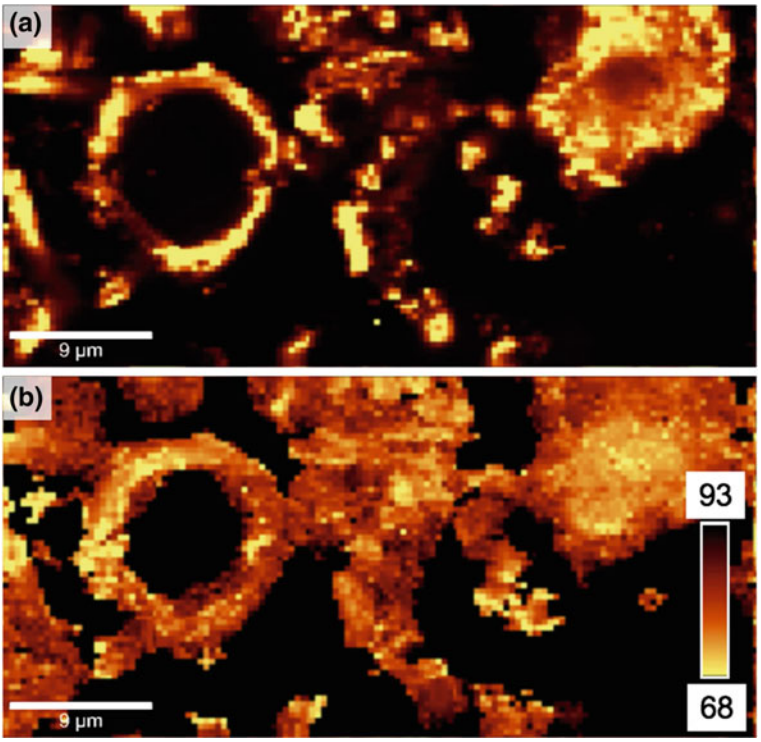

Fig. 10.13 Raman image of kerogenous material from the Precambrian Gunflint chert. **a** Is made from the intensity of a Gaussian fit to the G band of carbonaceous material in the chert. The matrix (not shown here) is quartz, as is befitting a chert. **b** Is calculated to show the graphitic domain size in the *a* crystallographic direction, or L_a [53], regardless of G band intensity. The scale bar shows L_a in angstroms, and the lighter colored areas of the image represent relatively fine-grained carbonaceous material. This effectively reveals sub-micron variation in kerogen structure, which most likely represents metamorphosed remnants of structure from the organic matter precursor. Sample provided by M. Schweizer, Oxford U., UK

increasing age of the material, as both chemical degradation and thermal metamorphism add ambiguity to both the origins of the carbonaceous material and its host rock. There is no doubt that considerable information can be gleaned on the structure of carbonaceous materials using Raman spectroscopy, and that such information tied with spatial context through Raman imaging gives a tremendous amount of information about the nature of a given carbonaceous material and its microenvironment (Fig. 10.13).

Some work has been done in describing fossil carbonaceous material relative to coal, which is fairly well understood, with the result that Nestler et al. [80] described Permian fossilized tree fern materials as having reached anthracite rank during metamorphism.

10.5 Raman Mineralogy in Field Geology Studies

With the development of small, reasonably sensitive spectrograph/detector combinations, miniature solid-state lasers, and field-ruggedized computers, portable Raman spectroscopy devices are now commercially available. Several of these instruments are hand-held, allowing the user to analyze the mineralogy and biological status of outcrops and other samples under their native environmental conditions [81]. Most instruments are even specially designed for performing field mineralogy, and many allow the user to match spectra with any database to include mineral spectral libraries. Some of the pioneers in this application brought full-sized Raman instruments designed for laboratory use into remote field locations [82] for both mineralogy and astrobiological studies. Modern field Raman instruments are capable of identifying most mineral species, but currently available models typically cannot query C–H and O–H stretch modes at high Raman shift, and are limited to interrogating relatively robust mineral species due to their intense laser flux. The high laser power density required for field Raman is a consequence of the uncooled, relatively insensitive detectors that are required for small, battery powered instruments. Future technology improvements in the areas of battery efficiency and/or detector sensitivity may allow for low power density laser sources that will expand the range of mineral phases identifiable using hand-held Raman instruments. At present, the capability to easily collect Raman spectra in a field environment is a powerful mineralogy tool. In the future, instruments will undoubtedly improve on this capability, perhaps to include Raman imaging capabilities.

10.5.1 Extraterrestrial Exploration

At the time of this writing, no Raman spectrometer has flown on a space exploration mission. While Raman is obviously of very little utility for flyby or orbiter missions (a laser powerful enough to produce a Raman signal observable from orbit would produce an impressive network of glassy sidewalks as a by-product!), small Raman spectrometers would be extraordinarily useful for both manned and unmanned landed missions [83, 84]. In pursuit of this, a miniature Raman instrument is currently under development for the European Space Agency's (ESA) ExoMars rover mission [85]. The goal of this mission is to search for life and/or evidence of past life on the martian surface using a variety of instruments. Such an instrument would have to be sufficiently sensitive to collect spectra at low laser power density values in order to detect organic compounds, and both the instrumental parameters and final instrument manifest for the mission are undecided at present. A Raman instrument called the Mars Multibeam Raman Spectrometer (MMRS); [86–88] was also one of the instruments developed for use on NASA's MER rovers (Mars Exploration Rovers, "Spirit" and "Opportunity") that are actively exploring the martian surface

at the time of this writing. Ultimately, however, the MMRS was passed over for other instruments.

A Raman device in general, utilized on a robotic rover/lander or as a hand tool for astronauts, has the advantages of producing very fast identification of mineralogy as well as the potential to directly identify the presence of some organic compounds, or at least point out the presence of a wide variety of carbonaceous phases that may be consistent with evidence of extinct life. As such, Raman spectroscopy is particularly well suited to science priorities identified for exploration of Mars [83]. Rapid mineralogy investigations possible using Raman spectroscopy methods are of particular interest in exploration of the Moon, asteroids, and possibly comets as well. What about using a Raman instrument on Venus, however? Since any venusian mission would be sharply constrained in mission duration (due to the destructively high temperature), sample handling and other factors, some researchers point to the speed and relative simplicity of Raman analysis as advantages for mineralogy studies on our sister planet. Significant obstacles exist in the form of atmospheric scatter and absorption in both the excitation beam and Raman signal, the difficulty of collecting a signal through hot optics, and other problems associated with operating in the ≈92 MPa pressure and ≈460 °C conditions on the venusian surface [89]). Raman spectroscopy may be especially well suited to this environment, however, as its rapid acquisition speed should allow the analysis of a large number of samples, and work has been done on analyzing Venus-specific mineralogy in particular [90]. Work with pulsed Raman systems at a distance through a simulated venusian atmosphere have also produced usable spectra [91]. While this application is intriguing, significant technical challenges must be overcome to make it practical.

10.6 Conclusion

For future applications it is reasonable to expect that technological advancements will deliver improvements in detector sensitivity, power supply efficiency, computing power, more compact lasers and who knows what all else as time passes. Future generations of hand-held Raman systems can conceivably include hand-held instruments for astronauts' use on the lunar, Martian or other planetary surfaces. Such an instrument could provide a rapid mineralogical assessment of rocks and outcrops and could serve as a first-pass tool for astrobiological analysis. Rock targets identified as interesting by a quick, hand-held Raman analysis would conceivably be returned to a laboratory for in-depth study, perhaps to include Raman imaging for petrographic and petrologic analysis. Given present capabilities and future possibilities, it is easy to envision a not-so-distant future where field scientists wield small, powerful Raman instruments as a matter of course both on this planet and others.

References

1. A. Macdonald, A. Vaughan, P. Wyeth, J. Raman Spectrosc. **36**, 185 (2005)
2. L. Dobrzhinetskaya, R. Wirth, H. Green, Earth Planet. Sci. Lett. **387**, 212 (2014)
3. F. Tuinstra, J. Koenig, J. Chem. Phys. **53**, 1126 (1970)
4. J. Pasteris, Appl. Spectrosc. **43**, 567–570 (1989)
5. M. Ammar, J.N. Rouzaud, J. Raman Spectrosc. **43**(2), 207 (2012)
6. O. Maslova, M. Ammar, G. Guimbretière, J.N. Rouzaud, P. Simon, Phys. Rev. B **86**(13), 134205 (2012)
7. A. El Goresy, P. Gillet, S. Mostefaoui, M. Chen, V. Masaitis, *Lunar and Planetary Science XXXIII* (2002), p. 1031
8. C. Avril, V. Malavergne, R. Caracas, B. Zanda, B. Reynard, E. Charon, E. Bobocioiu, F. Brunet, S. Borensztajn, S. Pont et al., Meteorit. Planet. Sci. **48**(8), 1415 (2013)
9. D. Brownlee, Annu. Rev. Earth Planet. Sci. **42**, 179 (2014)
10. M. Zolensky et al., Science **314**, 1735 (2006)
11. D. Fischbach, Carbon **3**, 342 (1965)
12. H. Murty, D. Biederman, E. Heintz, Carbon **7**, 667 (1969)
13. H. Murty, D. Biederman, E. Heintz, Carbon **7**, 683 (1969)
14. S.A. Sandford, J. Aléon, C.M. Alexander, T. Araki, S. Bajt, G.A. Baratta, J. Borg, J.P. Bradley, D.E. Brownlee, J.R. Brucato et al., Science **314**(5806), 1720 (2006)
15. B. Wopenka, G. Matrajt, S. Bajt, *Lunar and Planetary Science XXXIX* (2008), p. 1827
16. B. Wopenka, Meteorit. Planet. Sci. **47**(4), 565 (2012)
17. M. Fries, M. Burchell, A. Kearsley, A. Steele, Meteorit. Planet. Sci. **31**(10), 1465 (2009)
18. D. Brownlee et al., Science **314**, 1711 (2006)
19. R. Downs, Program and Abstracts of the 19th General Meeting of the International Mineralogical Association in Kobe **003**, 13 (2006)
20. B. Lafuente, R. Downs, H. Yang, N. Stone, *The Power of Databases: The RRUFF Project* (W. De Gruyter Berlin, Germany, 2015), pp. 1–30
21. A. Wang, B. Jolliff, L. Haskin, K. Kuebler, K. Viskupic, Am. Mineral. **86**, 790 (2001)
22. M. Fries, A. Steele, *Lunar and Planetary Science XXXVIII* (2007), p. 2195
23. S. Prawer, K. Nugent, Diam. Relat. Mater. **7**, 215 (1998)
24. L. Wong, C. Wong, J. Liu, D. Sohn, L. Chan, L. Hsia, H. Zang, Z. Ni, Z. Shen, Jpn. J. Appl. Phys. **44**, 7922 (2005)
25. H. Ishibashi, M. Arakawa, S. Ohi, J. Yamamoto, A. Miyake, H. Kagi, J. Raman Spectrosc. **39**, 1653 (2008)
26. A. Wang, *Lunar and Planetary Science Conference XXX* (1999), p. 1644
27. M. Salis, P. Ricci, A. Anedda, J. Raman Spectrosc. **40**, 64 (2009)
28. O. Beyssac, L. Bollinger, J. Avouac, B. Goffé, Earth Planet. Sci. Lett. **225**, 233 (2004)
29. G. Cody, C. Alexander, H. Yabuta, A. Kilcoyne, T. Araki, H. Ade, P. Dera, M. Fogel, B. Militzer, B. Mysen, Earth Planet. Sci. Lett. **272**, 446 (2008)
30. S. Solin, A. Ramdas, Phys. Rev. B **1**, 1687 (1970)
31. J. Koenig, Appl. Spectrosc. Rev. **4**, 233 (1971)
32. E. Vicenzi, M. Fries, A. Fahey, D. Rost, J. Greenwood, A. Steele, *Lunar and Planetary Science Conference XXXVIII* (2007), p. 2335
33. D. Bower, A. Steele, M. Fries, L. Kater, Astrobiology **13**(1), 103 (2013)
34. C. Rice, N. Trewin, L. Anderson, J. Geol. Soc. **159**(2), 203 (2002)
35. K.E. Kuebler, B.L. Jolliff, A. Wang, L.A. Haskin, Geochim. Cosmochim. Acta **70**(24), 6201 (2006)
36. W. Klöck, K.L. Thomas, D.S. McKay, H. Palme, Nature **339**, 126–128 (1989)
37. A. Wang, L. Haskin, B. Jolliff, K. Kuebler, *Lunar and Planetary Science Conference XXXI* (2000)
38. C. Goodrich, Meteoritics **27**, 327 (1992)
39. V. Masaitis, M. Mikhailov, T. Selivanovskaya, Meteoritics **7**, 39 (1972)

40. L. Gerward, J. Olsen, J. Appl. Cryst. **30**, 259 (1997)
41. A. El Goresy, M. Chen, P. Gillet, L. Dubrovinsky, G. Graup, R. Ahuja, Earth Planet. Sci. Lett. **192**, 485 (2001)
42. J. Jackson, J. Horton, I. Chou, H. Belkin, Am. Mineral. **91**, 604 (2006)
43. B. Glass, M. Fries, Meteorit. Planet. Sci. **43**, 1487 (2008)
44. L. Coes, Science **118**, 131 (1953)
45. H. Boyer, D. Smith, C. Chopin, B. Lasnier, Phys. Chem. Miner. **12**, 45 (1985)
46. V. Stähle, R. Altherr, M. Koch, L. Nasdala, Contrib. Mineral. Petrogr. **155**, 457 (2007)
47. J. Pasteris, B. Wopenka, Can. Mineral. **29**, 1 (1991)
48. T. Yui, E. Huang, J. Xu, J. Metamorph. Geol. **14**, 115 (1996)
49. C. Castiglioni, C. Mapelli, F. Negri, G. Zerbi, J. Chem. Phys. **114**, 963 (2001)
50. S. Reich, C. Thomsen, Phil. Trans. R. Soc. Lond. A **362**, 2271 (2004)
51. R. Nemanich, S. Solin, Phys. Rev. B **20**, 392 (1979)
52. D. Knight, W. White, J. Mater. Res. **4**, 385 (1989)
53. M. Matthews, M. Pimenta, G. Dresselhaus, M. Dresselhaus, M. Endo, Phys. Rev. B **59**, R6585 (1999)
54. A. Sood, R. Gupta, S. Asher, J. Appl. Phys. **90**, 4494 (2001)
55. J. Pasteris, B. Wopenka, Astrobiology **3**, 727 (2003)
56. A. Steele, M. Fries, H. Amundsen, B. Mysen, M. Fogel, M. Schweizer, N. Boctor, Meteorit. Planet. Sci. **42**, 1549 (2007)
57. M. Tsunogae, T.and Santosh, J. Dubessy, Y. Osanai, M. Owada, T. Hokada, T. Toyoshima, Geol. Soc. London, Special Publications **308**, 317 (2008)
58. W. Francis, *Coal: its Formation and Composition* (Edward Arnold (Ed.) Ltd., London, 1954)
59. C. Landis, Contrib. Mineral. Petrol. **30**, 34 (1971)
60. O. Beyssac, J.N. Rouzaud, B. Goffe, F. Brunet, C. Chopin, Contrib. Mineral. Petrol. **143**, 19 (2002)
61. B. Wopenka, J. Pasteris, Am. Mineral. **78**, 533 (1993)
62. M. Tice, B. Bostick, D. Lowe, Geology **32**, 37 (2004)
63. E. Quirico, G. Montagnac, J.N. Rouzaud, L. Bonal, M. Bourot-Denise, S. Duber, B. Reynard, Earth Planet. Sci. Lett. **287**(1), 185 (2009)
64. L. Bonal, E. Quirico, M. Bourot-Denise, G. Montagnac, Geochim. Cosmochim. Acta **70**(7), 1849 (2006)
65. L. Bonal, M. Bourot-Denise, E. Quirico, G. Montagnac, E. Lewin, Geochim. Cosmochim. Acta **71**(6), 1605 (2007)
66. R. Franklin, Proc. R. Soc. Lond. A **209**, 196 (1951)
67. P. Harris, Phil. Mag. **84**(29), 3159 (2004)
68. E. Fitzer, K.H. Kochling, H. Boehm, H. Marsh, Pure Appl. Chem. **67**, 473 (1995)
69. O. Beyssac, F. Brunet, J.P. Petitet, B. Goffe, J.N. Rouzaud, Eur. J. Mineral. **15**, 937–951 (2003)
70. T. Anderson, E.R. Neumann, Lithos **55**, 1 (2001)
71. E. Roedder, in *Fluid Inclusions*, ed. by P.H. Ribbe, vol. 12 (P. E, Reviews in Mineralogy, 1984)
72. L. Diamond, Lithos **55**, 69 (2001)
73. E. Burke, Lithos **55**, 139 (2001)
74. J. Dubessey, B. Poty, C. Ramboz, Eur. J. Mineral. **1**, 517 (1989)
75. M. Zolensky, R. Bodnar, D. Bogard, D. Garrison, E. Gibson, L. Nyquist, Y. Reese, C.Y. Shih, H. Wiesmann, Science **285**, 1377 (1999)
76. A. Rubin, M. Zolensky, R. Bodnar, Meteorit. Planet. Sci. **37**, 125 (2002)
77. W. Schopf, A. Kudryavtsev, D. Agresti, T. Wdowiak, A. Czaja, Nature **416**, 73 (2002)
78. M. Brasier, O. Green, A. Jephcoat, A. Kleppe, M. van Kranendonk, J. Lindsay, A. Steele, N. Grassineau, Nature **416**, 76 (2002)
79. J. Pasteris, B. Wopenka, Nature **420**, 476 (2002)
80. K. Nester, D. Dietrich, K. Witke, R. Rößler, G. Marx, J. Mol. Struct. **661–662**, 357–362 (2003)
81. J. Jehlička, P. V*í*tek, H. Edwards, M. Heagraves, T. Capoun, Spectrochim. Acta A (2008)
82. D. Wynn-Willams, H. Edwards, Icarus **144**, 486 (2000)
83. A. Ellery, D. Wynn-Williams, Astrobiology **3**, 565 (2003)

84. N. Tarcea, T. Frosch, P. Rösch, M. Hilchenbach, T. Stuffler, S. Hofer, H. Thiele, R. Hochenleitner, J. Popp, Space Sci. Rev. **135**, 281 (2008)
85. I. Escudero-Sanz, B. Ahlers, G. Courreges-Lacoste, Opt. Eng. **47**, 033001 (2008)
86. A. Wang, L. Haskin, A. Lane, T. Wdowiak, S. Squyres, R. Wilson, L. Hovland, K. Manatt, N. Raouf, C. Smith, J. Geophys. Res. Planet. **108**, 5.1 (2003)
87. A. Wang, K. Kuebler, B. Jolliff, L. Haskin, J. Raman Spectrosc. **35**, 504 (2004)
88. S. Sharma, A. Wang, L. Haskin, *Lunar and Planetary Science Conference XXXVI* (2005)
89. K. Lodders, B. Fegley Jr., *The Planetary Scientist's Companion* (Oxford University Press, Oxford, 1998)
90. A. Wang. Planetary Raman Spectroscopic Study for Understanding Venus Evolution History. Venus Geochemistry: Progress, Prospects, and New Missions (2009). Abstract No. 2003
91. S. Clegg, J. Barefield, R. Wiens, C. Quick, S. Sharma, A. Misra, M. Dyar, M. McCanta, L. Elkins-Tanton, Venus Geochemical Analysis by Remote Raman-laser Induced Breakdown Spectroscopy (Raman-LIBS). Venus Geochemistry: Progress, Prospects, and New Missions (2009). Abstract No. 2013

Chapter 11
Application of Raman Imaging in UHPM Research

Andrey V. Korsakov

Abstract Crustal-derived rocks can be subducted to mantle depth and metamorphosed at ultra-high pressure conditions (>2.6 GPa and 600 °C), which are defined by the presence of coesite. Findings of diamond in metamorphic rocks further extended the upper pressure limit for crustal rocks (>4.0 GPa and 900–1000 °C). Almost all ultra-high pressure mineral-indicators occur as small relics and Raman spectroscopy is a very powerful tool for the identification of these relics. Despite the significant progress in Raman imaging, this technique remains underestimated in ultra-high pressure research. In this chapter several examples of Raman imaging applied in ultra-high pressure petrology are summarised and discussed.

11.1 Introduction

Ultra-high pressure metamorphism of crustal materials was recognised not so long time ago, 1984, when coesite was identified in two localities: Norway [1] and Dora Maira [2]. However, the microdiamonds associated with metamorphic complexes were identified much earlier [3], but these findings remain not very well known within the international community. Later, Sobolev and Shatsky [4] reported the findings of microdiamond inclusions in zircon, garnet and clinopyroxene. Since that time the P-T conditions of crustal materials were extended up to 4.0–6.0 GPa, which corresponds to ~120–150 km in depth. Thus it was shown that continental crustal materials can be subducted to mantle depths [5–10]. Today, many coesite-bearing localities were identified worldwide (Fig. 11.1), while the diamond-bearing localities remain rather scarce [11–13]. Raman spectroscopic and microscopic studies play an important role in the discovery of UHPM relics. Improvement of the spatial resolution of modern Raman systems lead to findings of a number of new UPHM diamond-bearing localities [14–18]. However, diamond-bearing materials (e.g. diamond saw,

A.V. Korsakov (✉)
Sobolev Institute of Geology and Mineralogy, Siberian Branch,
Russian Academy of Sciences, 3, Ac. Koptyuga ave., Novosibirsk
630090, Russian Federation
e-mail: korsakov@igm.nsc.ru

J. Toporski et al. (eds.), *Confocal Raman Microscopy*, Springer Series
in Surface Sciences 66, https://doi.org/10.1007/978-3-319-75380-5_11

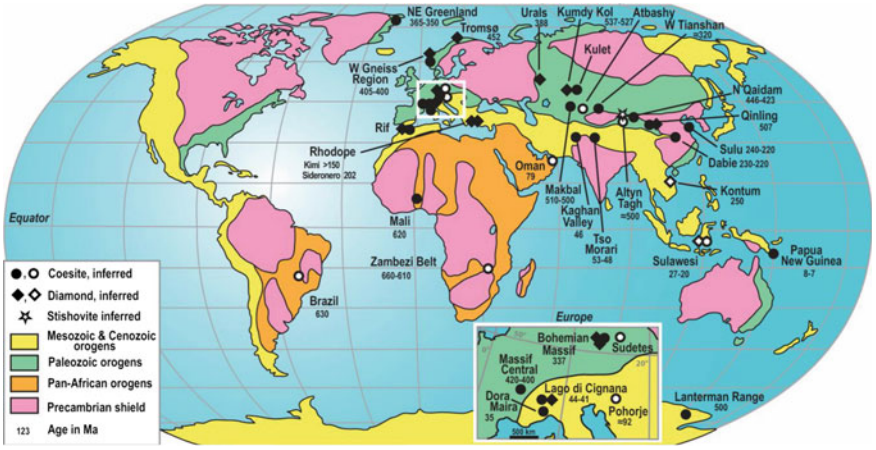

Fig. 11.1 Map of worldwide ultrahigh-pressure (UHP) terrane from [19]. Solid symbols indicate confirmed coesite or diamond. Open symbols show localities where UHP metamorphism is inferred from pseudomorphs or calculated P-T conditions, or cases where index minerals have been published in abstract form but are not documented (e.g. Brazil, Sulawesi, Kontum). Only Lago di Cignana, Zambezi, and Tianshan are oceanic UHP terrane

grinding and polishing paste) frequently used for sample preparation, often bear the risk of contamination of the thin sections and may lead to erroneous conclusions.

Recently the grain scale pressure variation became a new paradigm for the explanation of UHP conditions [20–26], but reliable examples of contribution of these grain scale pressure variation remain highly debatable [27]. Independently from the model of realisation of UHP conditions the coesite, diamond, aragonite, supersilic titanite, K-bearing clinopyroxene are the most common mineral-indicators for the existence of extreme conditions in crustal-derived metamorphic rocks [7, 28]. As outlined before, diamond polishing and cutting may result in misleading contamination in these samples and should thus be avoided. Perraki et al. [29] summarised the mineralogical and spectroscopical criteria to discriminate the "metamorphic" diamonds from contaminants. Several examples of application of Raman imaging for UHPM study are presented in this chapter.

11.2 Application of Raman Imaging for Identification of UHPM Relics

11.2.1 Metamorphic Diamond

For almost 30 years the *Kokchetav massif* (Northern Kazakhstan) remained a unique UHPM diamond-bearing complex. Later, diamonds were identified in the *Erzgebirge*

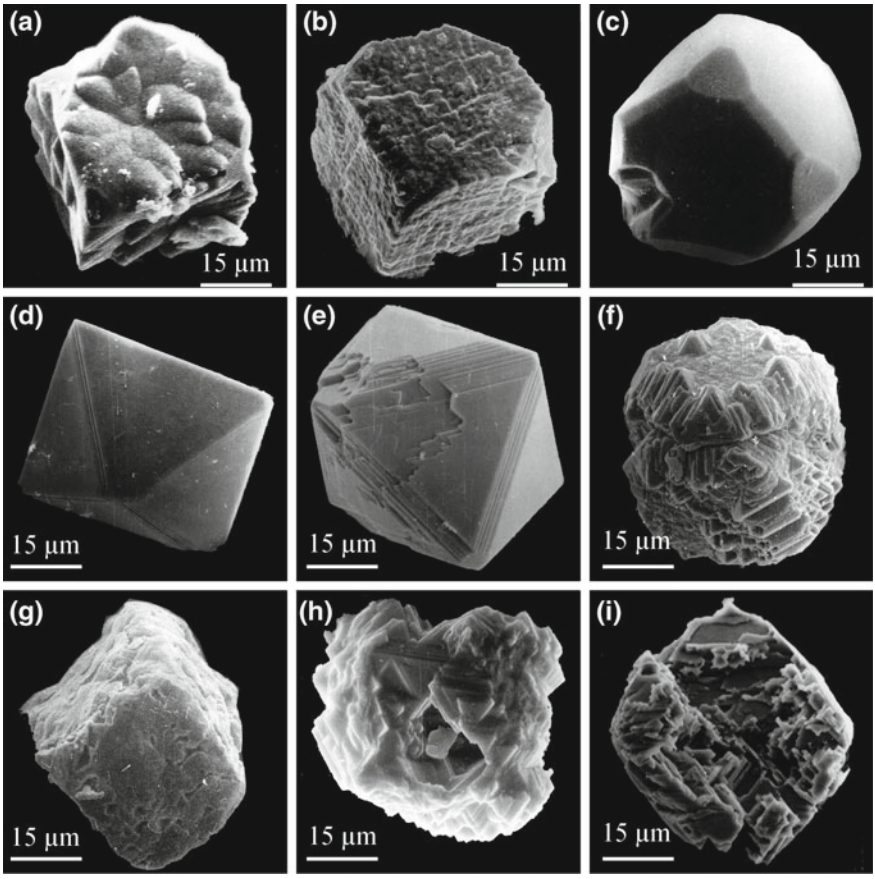

Fig. 11.2 Diversity of diamond morphologies from different lithologies from the Kokchetav massif (after [34]). **a–c** Diamond cuboids extracted from garnet-biotite gneisses; **d–f** octahedral and cuboid diamond crystals extracted from garnet-clinozoisite-biotite gneisses; **g–i** cuboids and skeletal diamond crystals extracted from calc-silicate rocks (marble and Grt-Cpx rocks)

(Germany) [11] and the *Rhodope massif* (Bulgaria and Greece) [12, 13]. The number of localities, where metamorphic diamonds were identified, grow like a tsunami wave [14–18, 30].

Cuboids are the predominant shape of metamorphic diamonds (Fig. 11.2), yet euhedral octahedral crystals (Fig. 11.3) are also common for other lithologies [31–33].

While different aspects of point Raman spectra of metamorphic diamonds have been discussed in number of studies [29, 34–37], Raman mapping or imaging of metamorphic diamonds remains rather scarce [38–40]. Detailed Raman imaging, with spatial resolution down to 200 nm (Fig. 11.4) provides unparalleled opportunities to study growth zoning and strain patterns for diamond inclusions and host

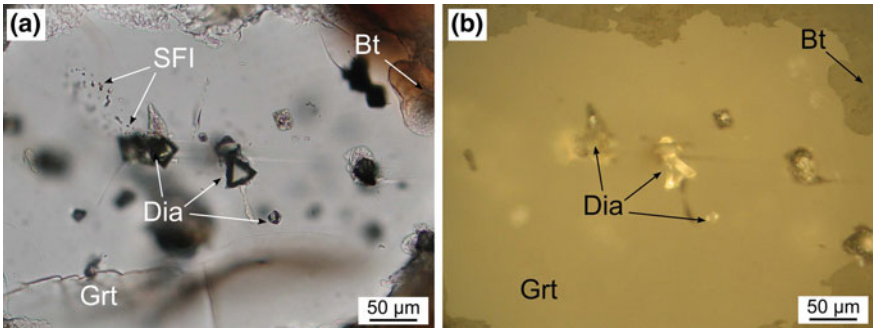

Fig. 11.3 The transmitted **a** and reflected light video images of octahedral diamond crystals from clinozoisite gneisses. The high refraction index of diamond produce the thick dark rim along diamond-garnet interface in plane polarised light (**a**) and it causes the light refraction from the diamond crystal faces in reflected light (**b**). These two features are very useful for microscopic identification of metamorphic diamond. Dia = diamond, Grt = host garnet, Bt = biotite, SFI = secondary fluid inclusions

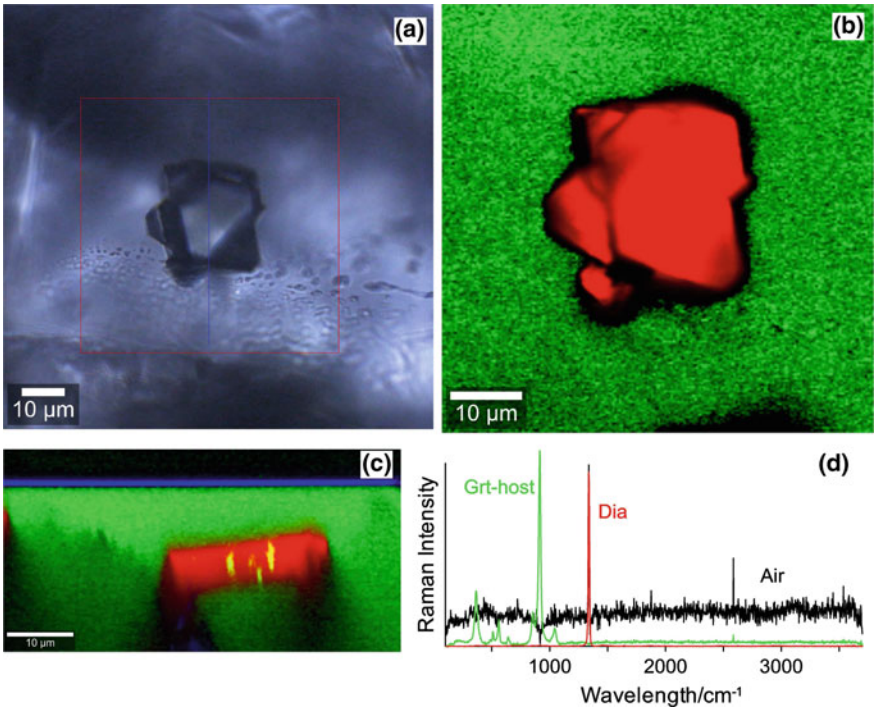

Fig. 11.4 The video image **a** shows the diamond inclusion in garnet from a garnet-clinozoisite gneiss as recorded with the integrated white light microscope. An XY-scan **b** was performed in the area marked in red in the image. The depth (XZ) scan **c** was performed along the blue line in (**a**). **d** The representative Raman spectra of diamond inclusion (red), garnet-host (green) and air above the thin section (black)

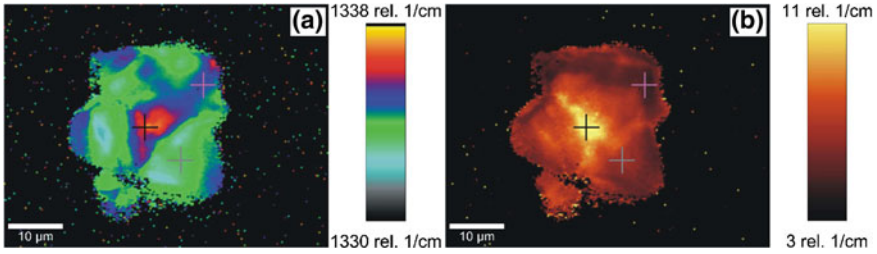

Fig. 11.5 A high resolution XY scan allowed the clear distinction of the position of the diamond line as well as its width and intensity. A Lorenzian curve was fitted to each spectrum of the data set and from each of the spectra the exact position and the width could be calculated. The results of these fits are displayed in the images with the position (**a**) and the width (**b**)

minerals (Fig. 11.5), as well as to discriminate the diamond *in situ* from contaminating diamond crystals.

The surface of the thin section can be easily recognised (Fig. 11.4c) blue and black colour). The diamond twin appears to be subparallel to the thin section surface and located about 8.5 µm below the surface.[1] Such XZ-depth scans, in addition to mineralogical (Fig. 11.3) and spectroscopical criteria listed by Perraki et al. [29], are prerequisite to justify the origin of metamorphic diamonds. Confocal 2D Raman imaging of the same diamond crystal with 1800 groove/mm grating displays the complex internal morphology (Fig. 11.5).

Surprisingly, octahedral diamond crystals have an upshifted and very broad Raman band (shift up to 1338 rel. cm^{-1} and FWHM up to 11 cm^{-1}) in their core (Fig. 11.5). On the other hand, the Raman band from the rim is narrow (down to 3 cm^{-1}) and almost unshifted (1332–1333 rel. cm^{-1}). Upshifts of diamond Raman band associating with broadening are in general assigned to compressive residual pressure (>2 GPa based on calibrations found in [41–43]). Recently, broadening of diamond bands was reported for diamond inclusions in zircons [38, 39] and interpreted as a metamictisation effect. However, in that case the Raman bands of diamond were downshifted. Therefore, the effect of metamictisation is considered not to be significant in the described samples.

According to numerical modelling [27], residual pressure inside cubic-shaped diamond inclusion tends to be homogeneous (see [27] Fig. 9). The deviation observed for hydrostatic pressure occurs along the inclusion-host mineral boundary and particularly at the cube apex. Korsakov et al. [44] as well as Zhukov and Korsakov [27] modelled the behaviour of diamond inclusions in garnet and found that pressure would be concentrated along the diamond-garnet interface, contrary to what was observed in our Raman imaging in Fig. 11.5. Furthermore, numerical modelling predicts "negative" residual pressure values for diamond inclusions in garnet captured at 6 GPa and 1000 °C and subsequently brought to the Earth surface [27, 45–47].

[1] The measured depth in this image is about 5 µm and this needs to be multiplied with the refractive index of Garnet to obtain the approximate correct value.

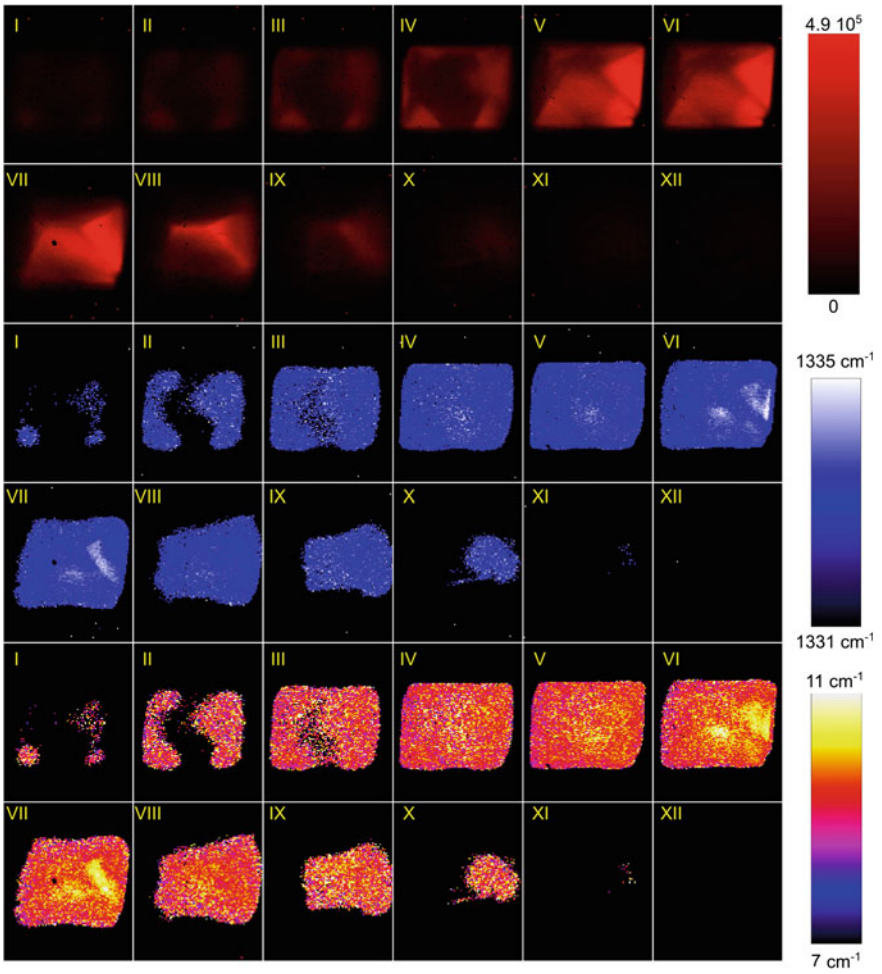

Fig. 11.6 2D Raman images collected at different depth levels for an octahedral diamond crystal in quartz from metasomatic quartz-tourmaline rocks. Red colour = relative intensity; Blue colour = Position of diamond band (1332 rel. cm^{-1}); Multicolour = FWHM of diamond band. I–XII numbers of layer

3D Raman images potentially can provide even more information about microdiamond (Fig. 11.6). However, the high refractive index of diamond crystal compared with other minerals also cause additional difficulties. For example the 3D reconstruction of diamond crystal occurring in quartz matrix of metasomatic quartz-tourmaline rocks (sample G36) significantly differ from optical microscopy image (Fig. 11.7).

It is worth noting that in addition to the diamond Raman band, this 3D imaging of a diamond crystal helps to observe several Raman bands in the Raman dataset collected at the Z-position of layer VI in Fig. 11.6 and shown in Fig. 11.8. Comparison of

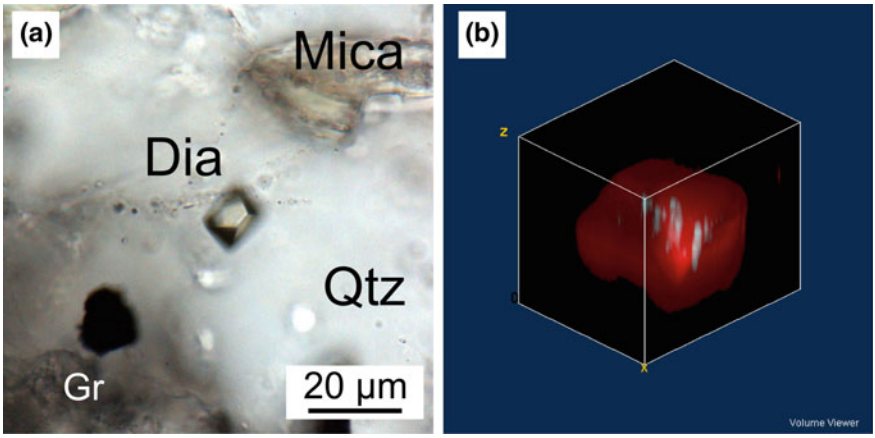

Fig. 11.7 The video image **a** shows the diamond quartz-mica matrix as recorded with a white light microscope. In the 3D reconstruction of the diamond crystal **b** the octahedral shape can be hardly recognised, while in each XY scans in Fig. 11.6 the octahedral is perfectly observable. Animations of the 3D reconstructions facilitate the recognition of the octahedral shape

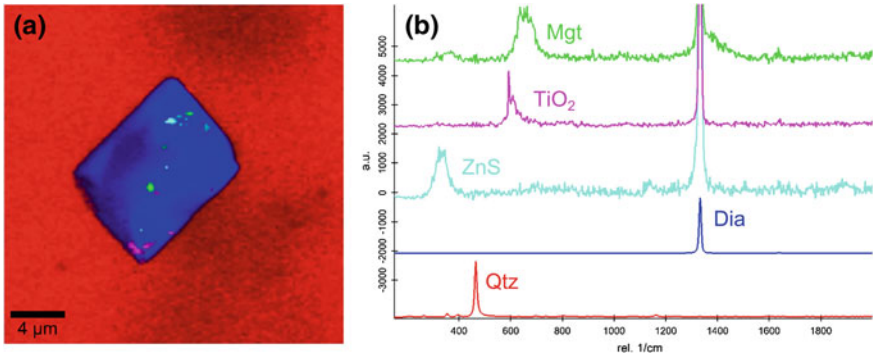

Fig. 11.8 2D Raman image **a** collected at depth level VI of Fig. 11.6 for octahedral diamond crystal in quartz from metasomatic quartz-tourmaline rocks. **b** Individual Raman spectra on the specimen identified as inclusions in diamond

the Raman spectra with RRUFF Raman database (http://rruff.info), allows tentative assignment of these spectra (Fig. 11.8) to magnetite (Mgt – $FeFe_2O_4$), sphalerite (ZnS) and rutile (TiO_2).

Several TEM studies of diamonds and diamond-bearing "melt" inclusions in garnet from the *Kokchetav* and *Erzgebirge* revealed the presence of sulphides and TiO_2 [48, 49], but no magnetite has been reported so far. This finding would indicate relatively oxidising conditions during diamond growth. This observation is in a good agreement with a recent experimental study on diamond synthesis in nonmetallic systems ([50] and references therein). However, it should be noted that magnetite was identified only by one Raman band at ~650 rel. cm^{-1}, while other weaker

Raman bands, which are typical for a Raman spectrum of magnetite (http://rruff.info/R080025) were not present, probably due to very small size of the inclusions and very short acquisition time.

11.2.2 Coesite and Quartz

Coesite (Fig. 11.9a) is one of the most reliable UHPM mineral-indicators [1, 2], used to define the UHPM conditions [51].

Contrary to diamond-to-graphite the coesite-to-quartz as well as quartz-to-coesite transformations are rapid processes, which preclude the formation of metastable SiO_2-polymorphs [52]. However the presence of monocrystalline quartz inclusions in garnet from diamond-grade eclogite xenoliths from kimberlite pipes raise the question about their origin (Fig. 11.10).

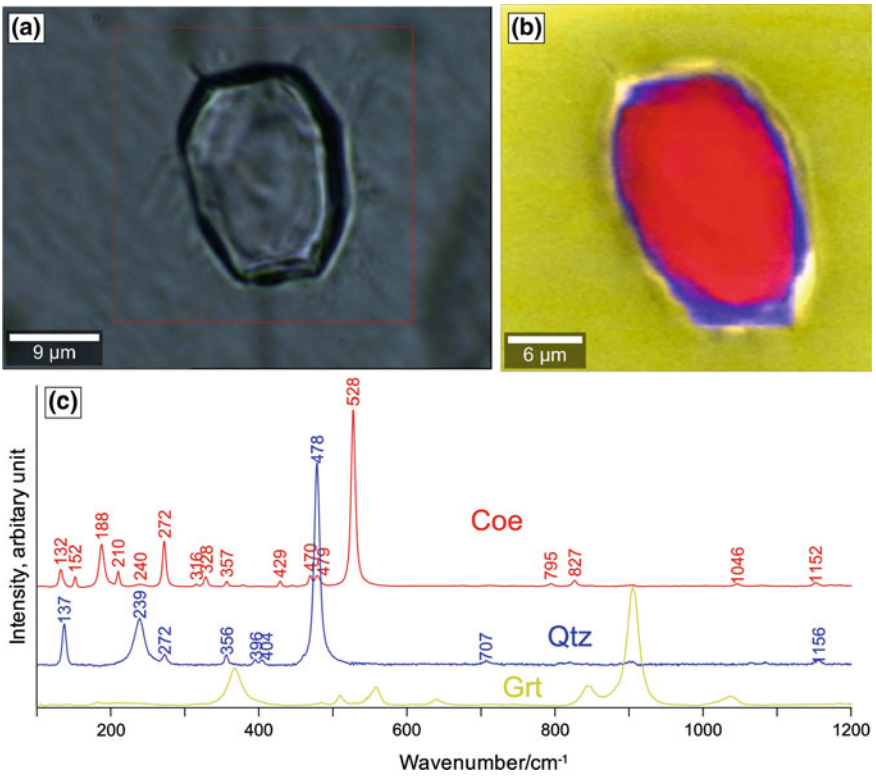

Fig. 11.9 Photomicrograph of euhedral "monocrystalline" coesite inclusion in garnet **a** from garnet-clinozoisite gneiss, Raman image **b** of phase distribution coesite (red), quartz (blue) and garnet (yellow), corresponding Raman spectra **c** of these minerals are coded in the same colours

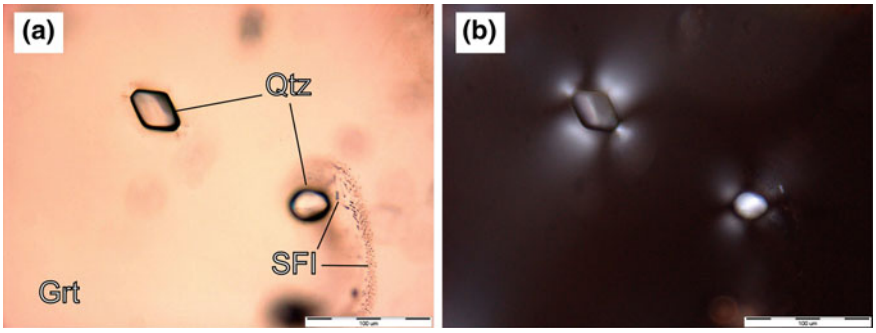

Fig. 11.10 Photomicrographs of euhedral monocrystalline quartz inclusions surrounded by very intense optical birefringent halo from eclogite xenolith

Raman spectroscopic studies of the quartz inclusions in garnet from the eclogite xenolith revealed that they exhibit a very high upshift of the main quartz band up to 474 rel. cm^{-1} (464 rel. cm^{-1} at ambient conditions) (Fig. 11.11). This is the absolute maximum upshift reported so far for monocrystalline quartz inclusions in garnet [27, 53]. On the other hand quartz is not a stable phase in the diamond stability field. Thus it is likely that originally the monocrystalline quartz inclusions were represented by coesite and transformation of high pressure polymorphs occurred during uplift the xenoliths [54].

Coesite-to-quartz transformation is accomplished with significant volume changes; very high residual pressures can be preserved in "monomineralic" (following the definition of [55]) coesite inclusions, as well as in partly transformed coesite [56–59]. The Raman shift of quartz was recently tested on natural samples in order to estimate the effect of peak metamorphic pressure on residual pressure within the quartz inclusions [60]. For different UHPM complexes the maximum upshift of the main Raman quartz bands (477 rel. cm^{-1}) was documented for partly transformed coesite inclusions [59], corresponding to residual pressures of up to 1.6 GPa, (using the calibration found in [61]). This can be explained by the fact that most UHPM complexes underwent near isothermal decompression during the initial stage(s) of exhumation; therefore plastic deformation of the host garnet at $T \sim 800$–900 °C is quite possible [62–65]. Optical undetectable quartz "shell" was identified by Raman imaging (Fig. 11.9).

Raman imaging also can reveal the orientation of the sub-grains, if they exist, by generating a calculated image of the ratio of the intensity of an orientation-dependent Raman peak to another peak in the same mineral that is relatively invariant to orientation (Fig. 11.12). The result, imaged using the ratio of the 132 rel. cm^{-1} peak intensity to that of the 477 rel. cm^{-1} Raman peak, is shown in Fig. 11.12 and displays no distinguishable quartz sub-grains within the newly formed quartz shell. The peak at 132 rel. cm^{-1} (located at ambient conditions at 128 rel. cm^{-1}) is sensitive to crystalline orientation [66], allowing the calculation of this image.

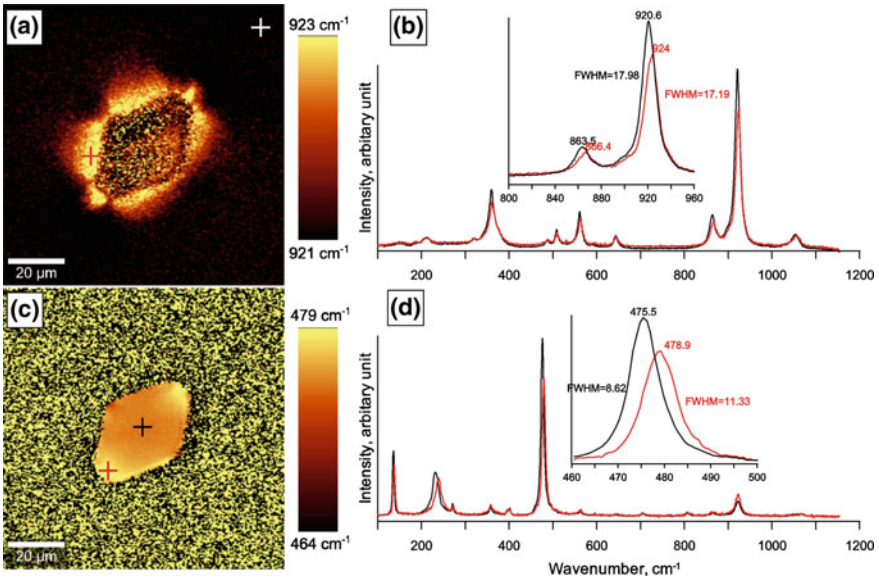

Fig. 11.11 Raman images of euhedral monocrystalline quartz inclusions surrounded by very intense optical birefringent halo as shown in Fig. 11.10b. **a** Raman image of peak position of main Raman band of the garnet-host and **c** of the monocrystalline quartz inclusion, **b**, **d** show representative Raman spectra of the garnet-host and the quartz inclusion. The colours of the crosses correspond to the colours of the spectra

Quartz inclusions in garnets from the eclogite xenolith preserved the highest values of residual pressure (~1.5 GPa) and caused a shift of the main quartz Raman bands by up to 12 rel. cm^{-1}. This is probably related to the very fast uplift of the eclogite xenolith by kimberlite melts compared to the exhumation rate of UHPM complexes [67–69]. Mineral assemblages of this sample formed in the diamond stability field [47, 70] at T = 1100–1200 °C and P > 5 GPa; therefore the degree of transformation of coesite-to-quartz should not be significant. Kinetics of the coesite-to-quartz transformation are very fast at temperatures above 400 °C [71, 72] but the absence of dense radial crack patterns makes this transition unlikely during uplift. The exact P-T conditions of the coesite-to-quartz transformation in the eclogite xenolith remain unknown.

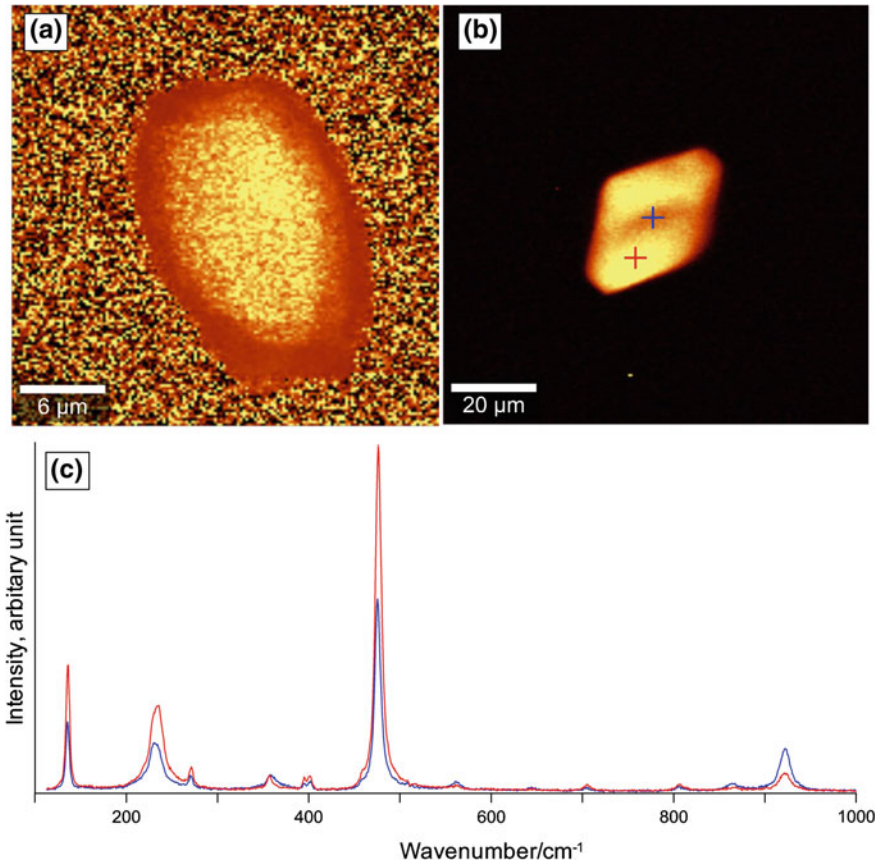

Fig. 11.12 Raman images of the quartz "shell" around the coesite inclusions in garnet (**a**) and monocrystalline quartz inclusion in garnet from an eclogite xenolith (**b**) obtained using the ratio of the 128 rel. cm^{-1} peak intensity to that of the 464 rel. cm^{-1} Raman peak. **c** Raman spectra of quartz collected at different points of the inclusion: red and blue cross, respectively. There are no significant changes in peak ratio within the quartz "shell" allowing to suggest its polycrystalline nature, which is commonly observed in case of higher degree of coesite-to-quartz transformation [7]

11.2.3 K-Bearing Clinopyroxene and Polymorphs of $KAlSi_3O_8$

K-bearing clinopyroxene is one of the important UHPM mineral-indicators, because the potassium was detected in clinopyroxene synthesised only at pressures above 3.0 GPa [73]. Clinopyroxene with K_2O up to 1.5 wt% were obtained exclusively in experimental runs in equilibrium with ultrapotassic liquid at $P > 5$ GPa (for details see review [74]). In natural samples the K_2O contents decreases from the core towards rim zone of the K-bearing clinopyroxene. Such zoning pattern is interpreted in favour of

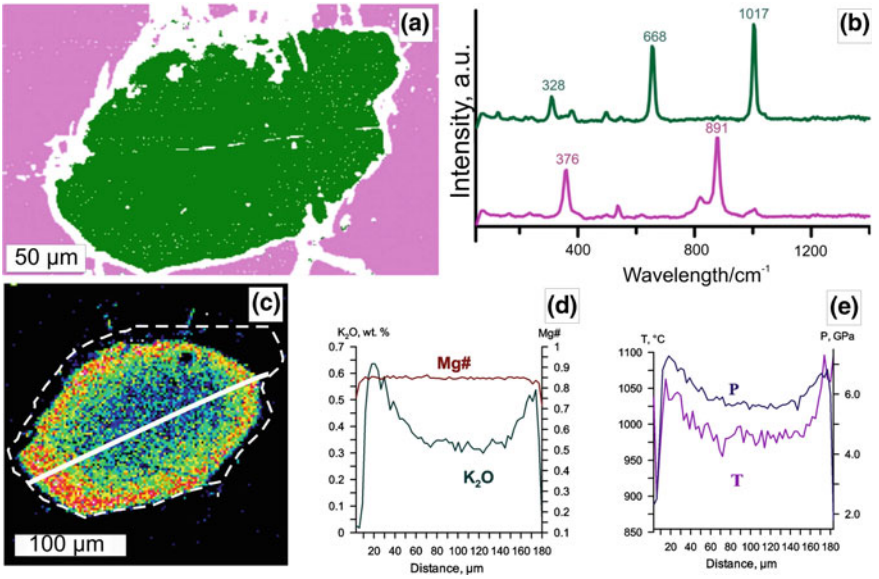

Fig. 11.13 **a** Raman image of the K-bearing clinopyroxene inclusion in garnet from diamond-grade garnet-clinopyroxene rock. **b** Representative Raman spectra of K-bearing clinopyroxene (green) and host-garnet (pink). **c** EDS image of K_2O content and **d** K_2O and Mg# profiles in the clinopyroxene inclusions in garnet. **e** P-T estimates obtained by geothermobarometry for this inclusion [9]

crystallisation of K-bearing clinopyroxene during pressure and temperature decrease (retrograde stage) [6, 74, 75]. Based on this type of zoning pattern, a mantle origin was proposed for K-bearing clinopyroxene [74]. Only recently, a clinopyroxene with prograde zoning pattern was found in UHPM rocks from the *Kokchetav* [9, 76]. These findings are extremely important because they testify for an origin of K-bearing clinopyroxene in situ in UHP metamorphic rocks. Enrichment of the external zone of the clinopyroxene could possibly be explained by partial amphibolisation of the clinopyroxene, because in contrast to pyroxene, amphibole from the same lithologies contains up to 4 wt% of K_2O. Raman imaging was performed for one of such clinopyroxene inclusions with prograde zonation (Fig. 11.13). No traces of amphibolisation were found, implying that either an increase of potassium activity or an increase in pressure and temperature is the origin of such clinopyroxene [9, 76].

A TEM study of K-bearing clinopyroxene with exsolution lamellae of $KAlSi_3O_8$ reveals that in addition to K-feldspar the new mineral – kokchetavite (hexagonal polymorphs of $KAlSi_3O_8$) – is an important phase in calc-silicate UHPM rocks [77]. Theoretical calculation of the physical properties (e.g. density) for the kokchetavite lead to the conclusions that kokchetavite is a high temperature, rather than high pressure phase [77]. In addition to kokchetavite lamellae, this mineral was found as inclusions in polyphase inclusions, which are interpreted as being a result of crystallisation former melts [48, 78]. Thus the metastable crystallisation of kokchetavite from UHPM melt was proposed by Hwang et al. [77].

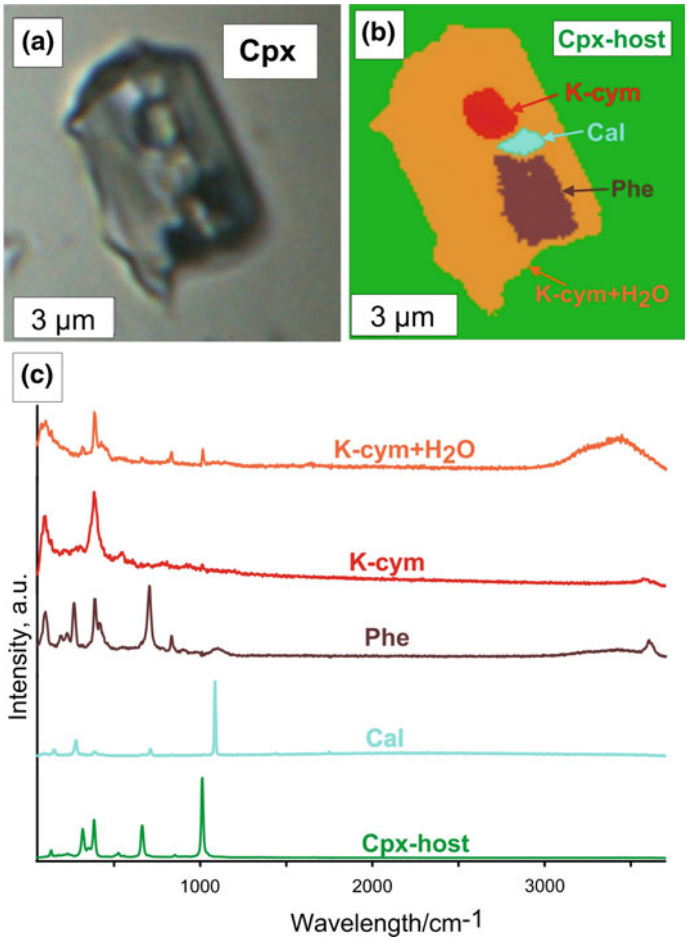

Fig. 11.14 The video image **a** shows a polyphase inclusion in K-bearing clinopyroxene from calc-silicate rocks as recorded with a white light microscope. Results of K-means-cluster analyses of the Raman dataset (**b**). **c** Corresponding, color-coded Raman spectra of the daughter-phases occurring in the inclusion: K-cymrite+H_2O (orange), K-cymrite (red), phengite (brown), calcite (light blue) and K-bearing clinopyroxene-host (green)

Raman imaging of similar polyphase inclusions in K-bearing clinopyroxene (Fig. 11.14) allowed the identification of K-cymrite for the first time for natural samples [79].

The Raman images of the studied polyphase mineral inclusions are presented in Fig. 11.14b. In these inclusions the presence of various phases are confirmed:

- K-cymrite
  - 383–387 rel. cm^{-1}

  - 833–834 rel. cm^{-1}
  - OH-stretching vibrations at 3575 and 3635 rel. cm^{-1}
- Lollingite
  - 198 rel. cm^{-1}
  - 250 rel. cm^{-1}
- Kokchetavite[2]
  - 110 rel. cm^{-1}
  - 393 rel. cm^{-1}
  - 837 rel. cm^{-1}
- Calcite
  - 280 rel. cm^{-1}
  - 713 rel. cm^{-1}
  - 1086 rel. cm^{-1}
- α-cristobalite
  - 112–114 rel. cm^{-1}
  - 230 rel. cm^{-1}
  - 414 rel. cm^{-1}
- Phengite
  - 265–268 rel. cm^{-1}
  - 705–710 rel. cm^{-1}
  - OH-band at 3610 rel. cm^{-1}

The Raman spectra of these minerals can be found in RUFF-databases (http://rruff.info/). The distribution of these minerals is shown colour-coded in the Raman images in Fig. 11.14b.

OH-stretching vibrations in Raman spectra acquired from different zones of K-cymrite in polyphase inclusion vary in peak shape and position (Fig. 11.14c). Thus, the OH-bands at 3575 and 3635 rel. cm^{-1} of the red spectrum (Fig. 11.14c) correspond to the structural H_2O of K-cymrite, whereas shape and position of OH-band at 3450 rel. cm^{-1} (the same figure, orange spectrum) can be associated with liquid water [80]. Changes of the OH-stretching band in inclusions results in an apparent K-cymrite zonation (Fig. 11.14b) are probably due to different contributions of liquid water and K-cymrite to the bulk Raman spectra.

Coexistence of K-cymrite with kokchetavite within the same clinopyroxene porphyroblast leads to the conclusion that kokchetavite is likely to be a dehydration product of K-cymrite, which occurred during exhumation of UHPM rocks [79]. Findings of K-cymrite in UHPM rocks indicate that at peak metamorphic conditions

[2]Mg#: The magnesium number (Mg/(Mg+Fe)) is commonly used in petrology for the calculation of the temperature. The calculation itself can be quite complicated, while Mg# can be considered as “raw” data.

the subducted rocks were H_2O-rich, because K-cymrite was synthesised only if H_2O is nearly equimolar in $KAlSi_3O_8$ [81]. The presence of fluid inclusions in the same rocks further supports this conclusion.

11.2.4 Fluid Inclusions

Fluid inclusions in UHPM rocks are another important target for Raman imaging, because the dimensions of such inclusions are quite small (typically a few m to 10 s of m) and they are located below the sample surface, hence the application of classical surface analytical techniques is impossible. Fluid inclusions in minerals stable at UHPM conditions are relatively well studied for coesite-grade metamorphic rocks [82–84], while for diamond-grade metamorphic rocks the UHPM fluid inclusions are much more rare [9, 30, 85, 86]. Fluid inclusions in metamorphic diamonds are optically invisible and were thus far studied exclusively by TEM [87–89]. Bulk analyses of fluid and mineral inclusions was done by FTIR spectroscopy [90, 91], but these methods only provide qualitative information. TEM studies [87–89] were also unable to identify the "liquid" phase, thus providing information only about "dry" residual.

Confocal Raman imaging of fluid inclusions in garnet (Fig. 11.15) and clinopyroxene (Fig. 11.16) porphyroblasts from diamond-grade metamorphic calc-silicate rocks from the Kumdy-Kol microdiamond deposit (*Kokchetav Massif*, Northern Kazakhstan) reveals that these fluid inclusions consist of almost pure water with different step-daughter phases (e.g. calcite, mica and rarely quartz) [10, 79, 86].

These fluid inclusions are characterised by negative crystal shape of the host mineral and they exclusively occur within the core of garnet or clinopyroxene porphyroblasts. These observations are consistent with their primary origin, since the K_2O content in clinopyroxene testifies for their formation at ultrahigh-pressure (UHP) metamorphic conditions. The euhedral, newly formed garnet, different in colour and composition, was found to be associated with these fluid inclusions (Figs. 11.15 and 11.18). The same feature was observed for fluid inclusions in clinopyroxene (Figs. 11.16 and 11.17). It is proposed that newly formed garnet and water fluid inclusions appear by reaction between the hydrous fluid and the garnet host, while in clinopyroxene this reaction may occur due to partial decripation of fluid inclusion. These fluid inclusions provide an unequivocal record of almost pure H_2O fluids, indicating water-saturated conditions within subducted continental crust during prograde stage and/or ultrahigh-P metamorphism.

Results of 3D Raman imaging are presented in Figs. 11.18 and 11.19. These results are very important for interpretation of the origin of the solid phases occurring inside the fluid inclusions. The high solubility of the major elements at UHPM conditions [92] may cause the formation of high density fluids, which can crystallise either on the

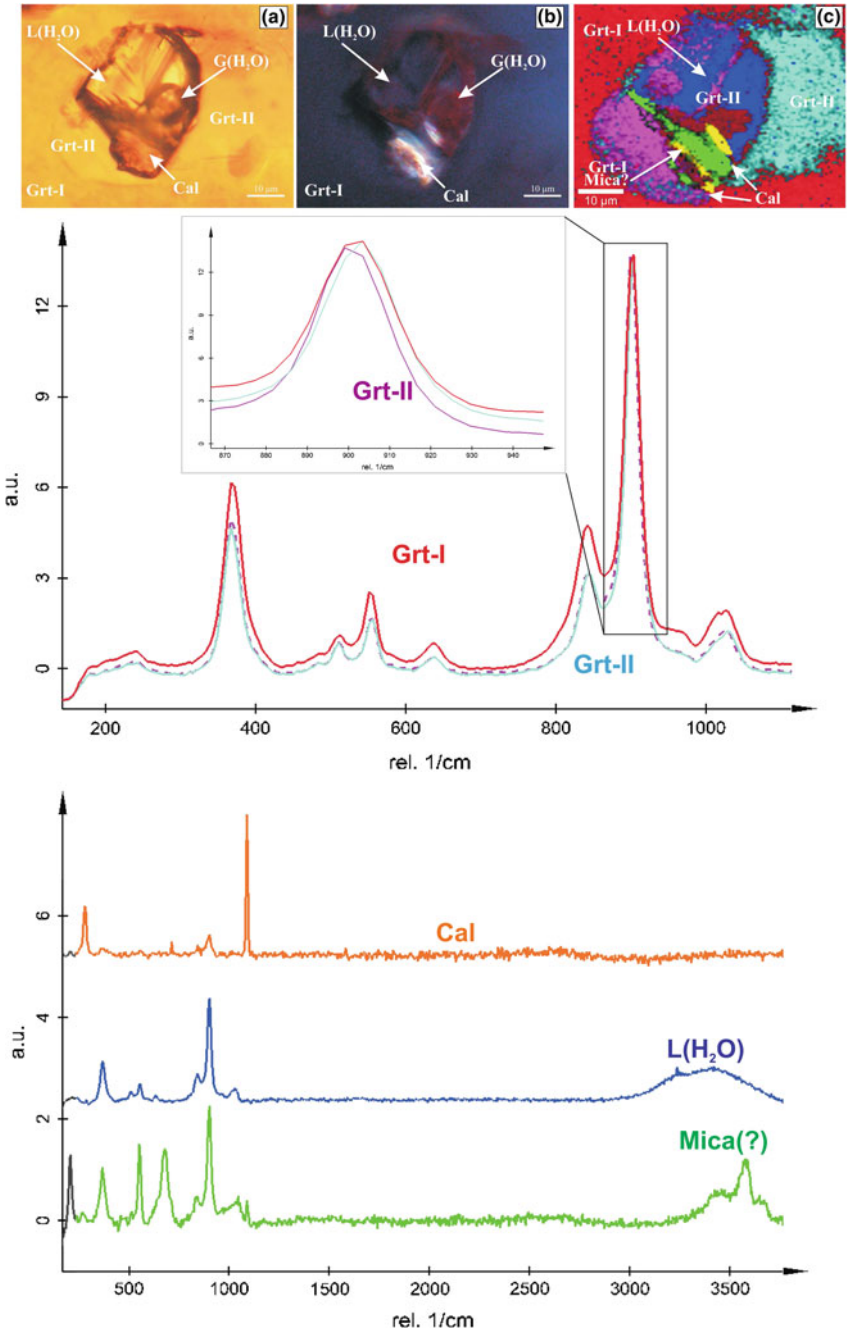

Fig. 11.15 Plane polarized video image **a** and cross polarized video image **b** of a fluid inclusions in garnet. 2D Raman image of the fluid inclusion **c** and individual spectra of the host-mineral and step-daughter phases. Grt-I = garnet-host; Grt-II = newly formed garnet; Cal = calcite; Mica = trioctahedral mica; $L(H_2O)$ = liquid water; Further details can be found [86]

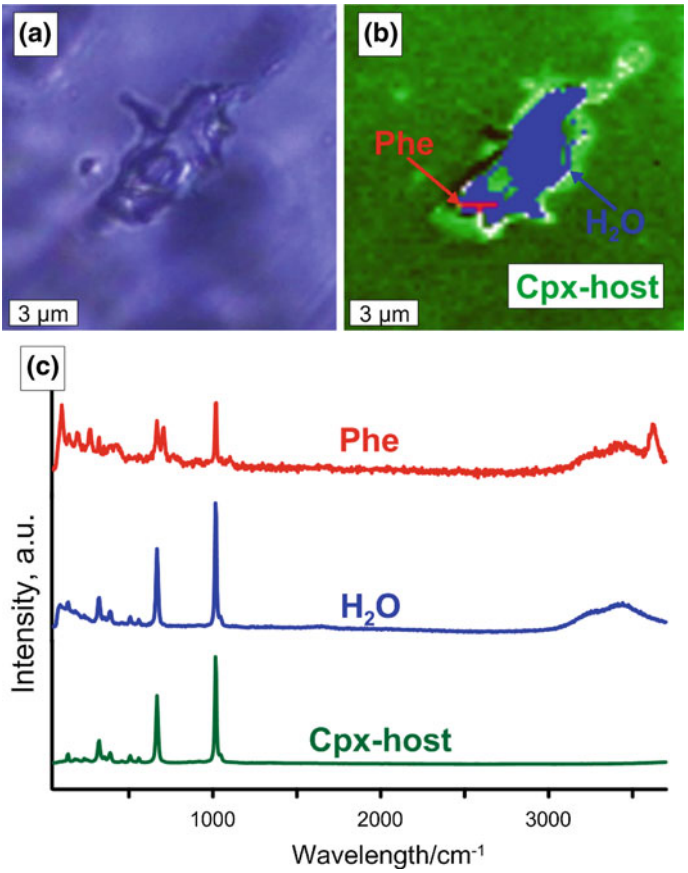

Fig. 11.16 Video image of a fluid inclusion in K-bearing clinopyroxene (**a**), 2D Raman image of the fluid inclusion and individual spectra of the host-mineral and step-daughter phases (**c**). Light green color **b** traces the clinopyroxene around the fluid inclusion, which could form most likely due to partial decripation of the fluid inclusion. Phe = phengite; H_2O = liquid water; Cpx-host = clinopyroxene host

wall of fluid inclusions or as daughter phases. Unfortunately, important information such as volume fraction of each phase can not yet be quantified very precisely, but this problem is related not directly with Raman imaging. Accurate 3D reconstruction algorithms taking for example the differences and jumps in the reflective indices into consideration would, however, help to overcome these limitations.

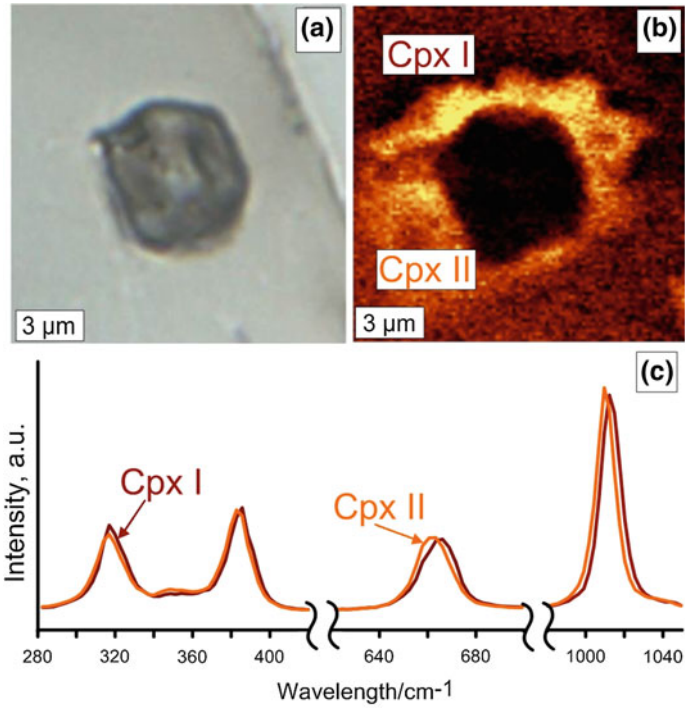

Fig. 11.17 Video image of polyphase inclusion in K-bearing clinopyroxene (**a**), 2D Raman image of the host clinopyroxene (integrated intensity of the peak near 1010 rel. cm^{-1}) around polyphase inclusion (**b**), and individual spectra of the clinopyroxene-host (Cpx-I) and newly formed clinopyroxene (Cpx-II) (**c**)

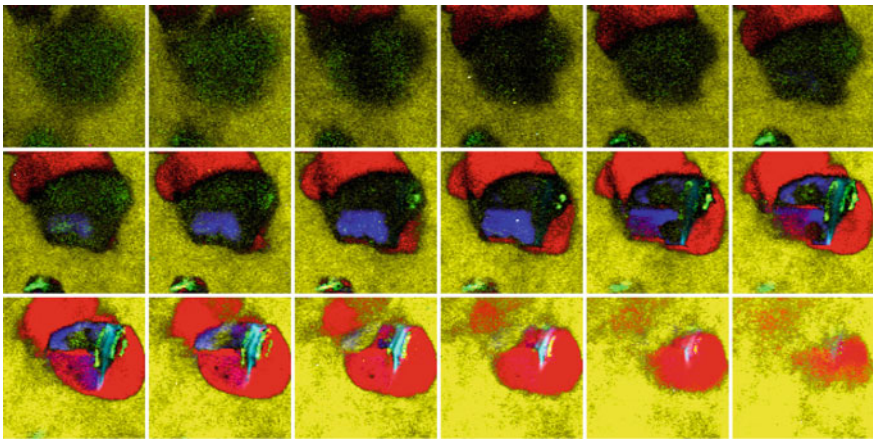

Fig. 11.18 Raman images of a fluid inclusion in garnet (same as in Fig. 11.15), recorded at different depth levels. The corresponding Raman spectra are presented in Fig. 11.19 in the same colours

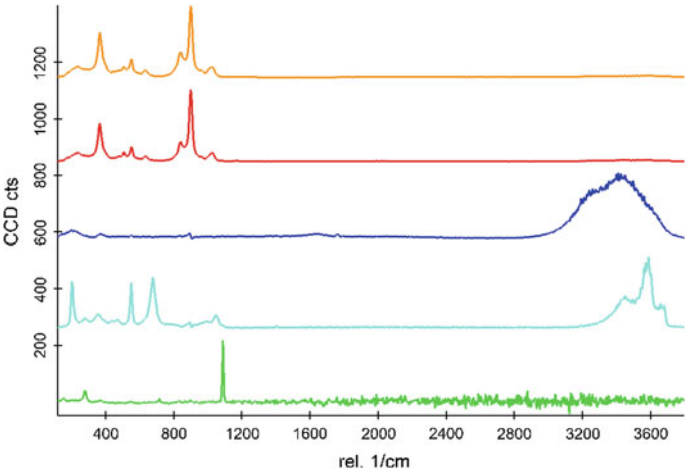

Fig. 11.19 Raman spectra of the phases which were identified by 3D Raman imaging of the fluid inclusion in garnet (Fig. 11.18). Grt-I = garnet-host, Grt-II = garnet domain associated with fluid inclusion, L(H_2O) = Liquid water, Mica = trioctahedral mica, Cal = calcite

11.3 Concluding Remarks

In this chapter several applications of 2D and 3D Raman imaging in UHPM research were presented and discussed. All presented examples, where significant residual "overpressures" are documented, were formed at UHPM conditions, and the "overpressure" appeared during the retrograde stage (exhumation) due to differences in rheological properties of the host-minerals and the inclusions. It is unlikely that the grain-scale pressure variation during the prograde stage of metamorphism can be responsible for origin of the "overpressures". Raman imaging is a very fast and non-destructive technique, if the laser energy is not too high, and it can be used for identification of:

- the chemical composition heterogeneities of the minerals
- the residual stress/strain analyses for inclusion – host-mineral systems
- the crystallographic orientation of grains or sub-grains throughout the sample
- characterization of different fluids as well as daughter phases in fluid inclusion studies
- characterization of the dimensions of objects or the distribution of a certain minerals throughout the sample

The application of confocal Raman imaging for UHPM rocks and minerals may provide significant new and additional information about samples, which may contribute to the understanding of their origin, generation, preservation and exhumation.

Acknowledgements This study was supported by a grant from the Russian Science Foundation (RSF 15-17-30012).

References

1. D.C. Smith, Nature **310**, 641 (1984)
2. C. Chopin, Contrib. Miner. Petrol. **86**, 107 (1984)
3. O. Rozen, Y.M. Zorin, A. Zayachkovsky, Dokl. Akad. Nauk SSSR **203**, 674 (1972)
4. N.V. Sobolev, V.S. Shatsky, Nature **343**, 742 (1990)
5. N.L. Dobretsov, N.V. Sobolev, V.S. Shatsky, R.G. Coleman, W.G. Ernst, I. Arc **4**, 267 (1995)
6. V.S. Shatsky, N.V. Sobolev, M.A. Vavilov, *Diamond-Bearing Metamorphic Rocks of the Kokchetav Massif (Northern Kazakhstan)* (Cambridge University Press, Cambridge, 1995), pp. 427–455
7. C. Chopin, Earth Planet. Sci. Lett. **212**, 1 (2003)
8. J. Hermann, C. Spandler, A. Hack, A.V. Korsakov, Lithos **92**, 399 (2006)
9. A.O. Mikhno, A.V. Korsakov, Gondwana Res. **23**(3), 920 (2013)
10. A. Mikhno, A. Korsakov, Russ. Geol. Geophys. **56**(1), 81 (2015)
11. H.J. Massonne, in *Proceedings of 7th International Kimberlite Conference*, vol 2 (1999), pp. 533–539
12. E.D. Mposkos, D.K. Kostopoulos, Earth Planet. Sci. Lett. **192**, 497 (2001)
13. M. Perraki, A. Proyer, E. Mposkos, R. Kaindl, G. Hoinkes, Earth Planet. Sci. Lett. **241**, 672 (2006)
14. J. Kotková, P.J. O'Brien, M.A. Ziemann, Geology **39**(7), 667 (2011)
15. M. Perraki, S.W. Faryad, Lithos **202–203**, 157 (2014)
16. M. Janak, E. Krogh Ravna, K. Kullerud, K. Yoshida, R. Milovskỳ, T. Hirajima, J. Metamorph. Geol. **31**(6), 691 (2013)
17. M. Janák, N. Froitzheim, K. Yoshida, V. Sasinková, M. Nosko, T. Kobayashi, T. Hirajima, M. Vrabec, J. Metamorph. Geol. (2015)
18. V. Thiéry, P. Rolin, M. Dubois, M.C. Caumon, Gondwana Res. **28**(3), 954 (2015)
19. J.A. Gilotti, Elements **9**(4), 255 (2013)
20. L. Tajčmanová, Y. Podladchikov, R. Powell, E. Moulas, J. Vrijmoed, J. Connolly, J. Metamorph. Geol. **32**(2), 195 (2014)
21. L. Tajčmanová, J. Vrijmoed, E. Moulas, Lithos **216–217**, 338 (2015)
22. M. Dabrowski, R. Powell, Y. Podladchikov, J. Metamorph. Geol. **33**(8), 859 (2015)
23. R. Angel, P. Nimis, M. Mazzucchelli, M. Alvaro, F. Nestola, J. Metamorph. Geol. **33**, 801 (2015)
24. T. Gerya, J. Metamorph. Geol. **33**(8), 785 (2015)
25. E. Moulas, L. Tajčmanová, J. Vrijmoed, Y. Podladchikov, J. Metamorph. Geol. **33**(8), 849 (2015)
26. F. Schenker, S. Schmalholz, E. Moulas, J. Pleuger, L. Baumgartner, Y. Podladchikov, J. Vrijmoed, N. Buchs, O. Müntener, J. Metamorph. Geol. **33**(8), 869 (2015)
27. V. Zhukov, A. Korsakov, J. Metamorph. Geol. **33**(8), 815 (2015)
28. C. Chopin, N.V. Sobolev, *Principal Mineralogical Indicators of Ultra High Pressure in Crustal Rocks* (Cambridge University Press, Cambridge, 1995), pp. 96–131
29. M. Perraki, A.V. Korsakov, D.C. Smith, E. Mposkos, Am. Mineral. **94**, 546 (2009)
30. M.L. Frezzotti, J.M. Huizenga, R. Compagnoni, J. Selverstone, Geochim. Cosmochim. Acta **143**, 68 (2014)
31. V.S. Shatsky, G.M. Rylov, E.S. Efimova, K.D. Corte, N.V. Sobolev, Geol. Geofiz. **39**, 942 (1998)
32. L.D. Lavrova, V.A. Pechnikov, M.A. Pleshakov, E.D. Nadajdina, Y.A. Shukolyukov, *A New Genetic Type of Diamond Deposit* (Scientific World, Moscow, 1999)
33. A.V. Korsakov, V.S. Shatsky, N.V. Sobolev, A.A. Zayachkovsky, Eur. J. Mineral. **14**, 915 (2002)
34. A.V. Korsakov, P. Vandenabeele, K. Theunissen, Spectrochim. Acta Part A **61**, 2378 (2005)
35. L. Nasdala, H.J. Massonne, Eur. J. Mineral. **12**, 495 (2000)
36. N. Yoshioka, A. Muko, Y. Ogasawara, *Extended Abstracts of UHP Workshop 2001 at Waseda University* (2001), pp. 51–55

37. H. Ishida, Y. Ogasawara, K. Ohsumi, A. Saito, J. Metamorph. Geol. **21**, 515 (2003)
38. D.C. Smith, L.F. Dobrzhinetskaya, G. Godard, H.W. Green, *Ultrahigh-Pressure Metamorphism: 25 Years After The Discovery Of Coesite and Diamond* (Elsevier, Amsterdam, 2011), chap. Diamond–lonsdaleite–graphite relations examined by Raman mapping of carbon microinclusions inside zircon at Kumdy Kol, Kokchetav, Kazakhstan: evidence of the metamictization of diamond, pp. 43–75
39. R. Shimizu, Y. Ogasawara, Lithos **206–207**, 201 (2014)
40. A.V. Korsakov, J.Toporski, T. Dieing, J. Yang, P. Zelenovskiy, J. Raman Spectrosc. https://doi.org/10.1002/jrs.4738 (2015)
41. M.H. Grimsditch, E. Anastassakis, M. Cardona, Phys. Rev. B **18**, 901 (1978)
42. S.K. Sharma, H.K. Mao, P.M. Bell, J.A. Xu, J. Raman Spectrosc. **16**, 350 (1985)
43. L. Nasdala, W. Hofmeister, J.W. Harris, J. Glinnemann, Am. Mineral. **90**, 745 (2005)
44. A.V. Korsakov, V.P. Zhukov, P. Vandenabeele, Anal. Bioanal. Chem. **397**(7), 2739 (2010)
45. Y. Zhang, Earth Planet. Sci. Lett. **157**, 209 (1998)
46. L.M. Barron, Can. Mineral. **43**(1), 203 (2005)
47. A.V. Korsakov, M. Perraki, V.P. Zhukov, K. De Gussem, P. Vandenabeelee, A.A. Tomilenko, Eur. J. Mineral. **21**, 1313 (2009)
48. S.L. Hwang, P. Shen, H.T. Chu, T.F. Yui, C.C. Lin, Earth Planet. Sci. Lett. **188**, 9 (2001)
49. S.L. Hwang, P. Shen, T.F. Yui, H. Chu, Eur. J. Mineral. **15**, 503 (2003)
50. A.G. Sokol, G.A. Palyanova, Y.N. Palyanov, A.A. Tomilenko, V.N. Melenevsky, Geochim. Cosmochim. Acta **73**(19), 5820 (2009)
51. J. Liou, R.Y. Zhang, W.G. Ernst, D. Rumble III, S. Maruyama, Rev. Mineral. **37**, 33 (1998)
52. A.V. Korsakov, K. Theunissen, L.V. Smirnova, Terra Nova **16**, 146 (2004)
53. A.V. Korsakov, A.V. Travin, D.S. Yudin, H.R. Marschall, Dokl. Earth Sci. **424**(1), 168 (2009)
54. T. Alifirova, L. Pokhilenko, A. Korsakov, Lithos **226**, 31 (2015)
55. C.D. Parkinson, Lithos **52**, 215 (2000)
56. C.D. Parkinson, I. Katayama, Geology **27**, 979 (1999)
57. N.V. Sobolev, B.A. Fursenko, S.V. Goryainov, J.F. Shu, R.J. Hemley, H.K. Mao, F.R. Boyd, Proc. Nat. Acad. Sci. U.S.A. **97**(22), 11875 (2000)
58. K. Ye, J.B. Liou, B. Cong, S. Maruyama, Am. Mineral. **86**, 1151 (2001)
59. A.V. Korsakov, D. Hutsebaut, K. Theunissen, P. Vandenabeele, A.S. Stepanov, Spectrochim. Acta Part A Mol. Biomol. Spectrosc. **68**, 1046 (2007)
60. M. Enami, T. Nishiyama, T. Mouri, Am. Mineral. **92**, 1303 (2007)
61. R.J. Hemley, *Pressure Dependence of Raman Spectra of SiO_2 Polymorphs: α-Quartz, Coesite, And Stishovite* (Tokyo-AGU, Washington, DC, Terrapub, 1987), pp. 347–359
62. S.I. Karato, Z. Wang, B. Liu, K. Fujino, Earth Planet. Sci. Lett. **130**, 13 (1995)
63. J. Chen, Q. Wang, M. Zhai, K. Ye, Sci. China D **39**(1), 18 (1995)
64. R. Kleinschrodt, J.P. Duyster, J. Struct. Geol. **24**, 1829 (2002)
65. I. Katayama, S.I. Karato, Phys. Earth Planet. Inter. **166**, 57 (2008)
66. M. Fries, A. Steele, *Confocal Raman Microscopy* (Springer, Berlin, 2010), pp. 111–135
67. D. Canil, Y. Fedortchouk, Earth Planet. Sci. Lett. **167**, 227 (1999)
68. M. Grégoire, M. Rabinowicz, A. Janse, J. Petrol. **47**, 631 (2006)
69. S.P. Kelley, J.A. Wartho, Science **289**, 609 (2000)
70. A.A. Tomilenko, S.V. Kovyazin, N.P. Pokhilenko, *ECROFI XVIII. European Current Research on Fluid Inclusions*, Siena, Italy, July 6–9, 2005 (2005)
71. J.L. Mosenfelder, S.R. Bohlen, Earth Planet. Sci. Lett. **153**, 133 (1997)
72. J.P. Perrillat, I. Daniel, J.M. Lardeux, H. Cardon, J. Petrol. **44**, 773 (2003)
73. A. Erlank, I. Kushiro, Carnegie Inst. Wash. Yearb. **68**, 267 (1970)
74. L.L. Perchuk, O.G. Safonov, V.O. Yapaskurt, J.M. Barton Jr., Lithos **60**, 89 (2002)
75. O.G. Safonov, L.L. Perchuk, Y.A. Litvin, Russ. Geol. Geophys. **46**, 1318 (2005)
76. A. Mikhno, A. Korsakov, Dokl. Earth Sci. **447**(2), 1333 (2012)
77. S.L. Hwang, P. Shen, H.T. Chu, T.F. Yui, J.G. Liou, N.V. Sobolev, R.Y. Zhang, V.S. Shatsky, A. Zayachkovsky, Contrib. Mineral. Petrol. **148**, 380 (2004)
78. M. Frezzotti, S. Ferrando, Periodico Mineral. **76**, 113 (2007)

79. A.O. Mikhno, U. Schmidt, A.V. Korsakov, Eur. J. Mineral. **25**(5), 807 (2013)
80. J. Dubessy, T. Lhomme, M.C. Boiron, F. Rull, Appl. Spectrosc. **56**(1), 99 (2002)
81. G.E. Harlow, R. Davies, Lithos **77**, 647 (2004)
82. P. Philippot, P. Chevallier, C. Chopin, J. Dubessy, Contrib. Mineral. Petrol. **121**(1), 29 (1995)
83. M. Scambelluri, P. Philippot, Lithos **55**(1), 213 (2001)
84. B. Fu, J. Touret, Y.F. Zheng, J. Metamorph. Geol. **19**, 529 (2001)
85. A.V. Korsakov, A.V. Golovin, T. Dieing, J. Toporsky, Dokl. Earth Sci. **437**(2), 473 (2011)
86. A.V. Korsakov, T. Dieing, A.V. Golovin, J. Toporski, Spectrochim. Acta Part A Mol. Biomol. Spectrosc. **80**(1), 88 (2011)
87. S.L. Hwang, P. Shen, H.T. Chu, T.F. Yui, J.G. Liou, N.V. Sobolev, V.S. Shatsky, Earth Planet. Sci. Lett. **231**, 295–306 (2005)
88. S.L. Hwang, H.T. Chu, T.F. Yui, P. Shen, H.P. Schertl, J.G. Liou, N.V. Sobolev, Earth Planet. Sci. Lett. **243**, 94 (2006)
89. L.F. Dobrzhinetskaya, R. Wirth, H.W. Green II, Terra Nova **17**, 472 (2005)
90. K. De Corte, P. Cartigny, V.S. Shatsky, N.V. Sobolev, M. Javoy, Geochim. Cosmochim. Acta **62**, 3765 (1998)
91. K. De Corte, A. Korsakov, W.R. Taylor, P. Cartigny, M. Ader, P. De Paepe, I. Arc **9**, 284 (2000)
92. J. Hermann, Y.F. Zheng, D. Rubatto, Elements **9**(4), 281 (2013)

Chapter 12
Multiscale Chemical Imaging of Complex Biological and Archaeological Materials

James C. Weaver and Admir Masic

Abstract Raman chemical imaging provides powerful and general means to chemically characterize biological and synthetic materials under complex experimental conditions. For biological materials, we describe several techniques for investigating in-vivo processes spanning size ranges from single cells to complex multicellular organisms. Because these experimental approaches are non-invasive, Raman chemical imaging allows monitoring of dynamic processes in living systems including, for example, the study of the early stages of bone formation. We also describe large-scale Raman-based imaging techniques, including approaches for analyzing samples exhibiting complex shapes and irregular heterogeneous surface topographies. We further demonstrate how correlative Raman-SEM/EDS approaches can be applied to collect complementary information from complex biological and archaeological samples regarding structural complexity, elemental composition, and short-range chemical bonding parameters.

12.1 Introduction

In this chapter, we discuss three applications of chemical imaging: (1) large-area characterization, (2) methods for monitoring in-vivo processes without sample preparation, and (3) applications for the characterization of samples exhibiting heterogeneous and irregular surface topographies.

A wide range of experimental approaches have been applied to explore complex hierarchical synthetic materials and biological tissues. These include X-ray spectroscopy and X-ray diffraction [1, 2], AFM [3, 4], NMR [5, 6], TEM [7], Raman

J. C. Weaver (✉)
Wyss Institute for Biologically Inspired Engineering, Harvard University, Cambridge, MA, USA
e-mail: James.Weaver@Wyss.Harvard.edu

A. Masic
Department of Civil and Environmental Engineering, MIT, 77 Massachusetts Avenue, Cambridge, MA 02139, USA
e-mail: masic@mit.edu

J. Toporski et al. (eds.), *Confocal Raman Microscopy*, Springer Series in Surface Sciences 66, https://doi.org/10.1007/978-3-319-75380-5_12

[8, 9] and IR spectroscopy [10, 11]. Raman spectroscopy has long been employed as a spectroscopic tool for the characterization of biological materials. Because of its non-invasive and non-destructive nature it is effective for both identification of a material's constituent phases and for in situ damage assessment and monitoring. Potentially damaging sample preparation requirements and frequent autofluorescence associated with age-related degradation products, however, have historically limited the extraction of useful Raman information from a sample of interest. In this paper we present techniques to help overcome some of these challenges.

We address the need to avoid sample trimming and resulting damage by applying a large-area imaging approach in conjunction with state-of-the-art surface profilometry measurements. This method was developed to automatically scan large and structurally complex objects exhibiting topographical variability, while maintaining confocality during the acquisition of surface chemical images.

While sample fluorescence -be this autofluorescence or fluorescence due to labelling- often poses challenges for Raman spectroscopy, it can also contain a wealth of information about the sample itself. As described here, through the introduction of fluorescent labels into living biological specimens, and by expanding the confocal Raman microscope and adding a fluorescence detector, we combine spectral and biological structural information in a correlative manner [12, 13]. To complement this approach, the Raman signal can be further enhanced using surface-enhanced Raman spectroscopy (SERS)-based plasmonic nanoprobes that permit the single molecule detection of biomarkers by intensifying the Raman signals to the point where they can even be detected in the presence of intrinsic sample fluorescence. To illustrate this effect, we describe a SERS platform based on silica probes coated with single wall carbon nanotubes (SWCNT) and gold nanoparticle aggregates for sensing biomolecules inside living cells [14, 15].

12.2 In-Vivo Raman Imaging

Understanding fundamental biological processes relies on the accurate probing of intra- and extracellular environments in living cells and tissues, and the real-time detection and imaging of chemical markers and biomolecules. Confocal Raman spectroscopic imaging is becoming increasingly popular for the label-free chemical imaging of cells due to fact that most biomolecules are Raman active. However, its applicability is often challenging due to the weakness of the detected signals and the high laser intensity required to obtain reliable information, potentially causing beam damage and thus complicating live cell studies [16]. One solution to this problem is through surface enhanced Raman scattering, SERS [17–19], which provides effective means for signal amplification. This approach has been previously employed for molecular detection with high sensitivity recognition of analytes [20], as well as for single molecule detection with up to 10^8 signal amplification over conventional Raman-based techniques [21, 22].

As described in the following section, the application of low laser power in combination with the characteristic and reliable SWCNT Raman spectral signal shows the potential for real-time localization and identification of chemical probes in living cells and tissues. Figure 12.1a presents the Raman image of a living cell with incorporated SERS active probes. Color coding for the cytosol and nucleus was obtained from the typically weak, but chemically specific, non-resonant Raman signals shown in Fig. 12.1b. The of 0.1 mW at 532 nm further guaranties that the measurements do not affect the health and viability of the living cells.

Very strong SERS signals were acquired from the surface of the probe Fig. 12.1c with each spectrum exhibiting either lipid or nucleic acid specific signatures [23]. The biggest advantage of this approach is that it can be applied to any cell type, while not disrupting cell behavior and metabolism.

In addition to microscopic cellular processes, the techniques described here can also be scaled for investigating macroscopic living organisms. Typically, informa-

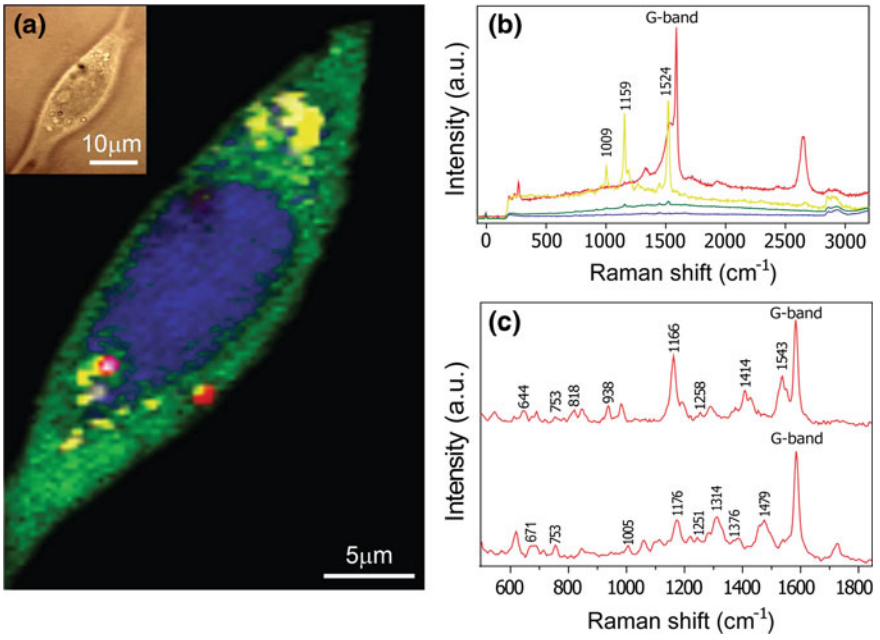

Fig. 12.1 Raman spectroscopic imaging of a living fibroblast cell with incorporated colloidal nanoprobes. The color map in **a** reflects the differences found in the Raman data and is a linear combination of the averaged single spectra (reported in **b**); The spectra in **b** are characteristic for each cellular component (green-cytoplasm, blue-nucleus, yellow-carotenoids) and gold-nanoparticle-SWCNT functionalized colloidal probes (red). The inset in **a** shows the optical micrograph of the same cell. **c** Intracellular SERS signal recorded at the surface of the probe. The two different Raman spectra shown in **c** were recorded from the probe incorporated into different regions of the cell (upper: proteins and lipids, lower: proteins and nucleic acids). Raman images were acquired using an integration time of 0.1 s and with a laser operating at 532 nm (Reproduced from [14])

tion about molecules in cellular environments is obtained by fluorescence microscopy [24]. While it is a powerful imaging tool for localizing and imaging samples, fluorescence microscopy requires the use of molecule-specific fluorescent labels and markers and thus lacks the capabilities for broad quantitative chemical mapping in complex systems. While, in contrast, confocal Raman spectroscopic imaging is an excellent tool for label-free chemical detection [23, 25], it cannot produce real-time, high-resolution imaging of larger regions of interest in complex biological tissues. To help resolve these issues, we recently developed a correlative Raman and fluorescence imaging approach. This method combines the strengths and compensates for the shortcomings of both Raman (small sample area) and fluorescence imaging modalities (probes are typically molecule-specific), thereby permitting the study of in-vivo processes in whole animal models such as zebrafish larvae. The technique was demonstrated to be effective for investigating the different mineral phases involved in early skeletal formation of zebrafish and sea urchin larvae [12, 13, 26]. Figure 12.2a shows a schematic representation of the experimental setup adapted to a commercially available Raman microscope body for simultaneously performing confocal Raman spectroscopy and wide-field fluorescence imaging.

Figure 12.2b shows fluorescence images of an entire zebrafish larva that were acquired with a correlative Raman and fluorescence imaging setup. Larvae of transgenic zebrafish "nacre" mutants (albino fish) expressing enhanced green fluorescent protein (EGFP) in the endothelial cells were used in this study. The newly forming bones were stained by incubating the live embryo in the calcium marker calcein blue, which was subsequently excited at 400 nm. It should be noted that in addition to the labeling of the sites of mineral formation, fluorescence is also detected in the gut of the fish where the calcein enters the digestive tract (Fig. 12.2b, upper). At 490 nm, endothelial cells that line blood vessels expressing EGFP are excited (Fig. 12.2b, lower). Because EGFP and calcein blue have significantly different excitation and emissions spectra, dual staining with calcein blue (as a mineral marker) and EGFP (as an endothelial marker) permits fast-switching dual-wavelength fluorescence imaging. Furthermore, because the absorption maximum of the calcium markers and EGFP are below that of the Raman laser wavelength, these fluorophores are appropriate candidates for experiments requiring simultaneous Raman and fluorescence imaging. This dual-excitation approach offers the ability to simultaneously map several tissues in a single experiment at a high rate. This technique could thus, in principle, be used to probe different parameters of the tissue microenvironment (e.g., pH [27], temperature [28], viscosity [29], calcium concentration [30]) using wavelength-ratiometric fluorescence imaging, which in correlation with confocal Raman spectroscopy, could open new strategies in studies of the micro-environmental properties of living tissues.

The fin rays of zebrafish represent a simple model system for investigating the early stages of bone formation, in which the fins are gradually mineralized within spatially resolved regions [31]. Raman spectra (Fig. 12.2) of progressively mineralized bone tissue were acquired within representative regions exhibiting characteristic bands of organic protein extracellular matrix (collagen), the mature mineral (carbonated hydroxyapatite), and intermediate (octacalcium phospate) mineral phases.

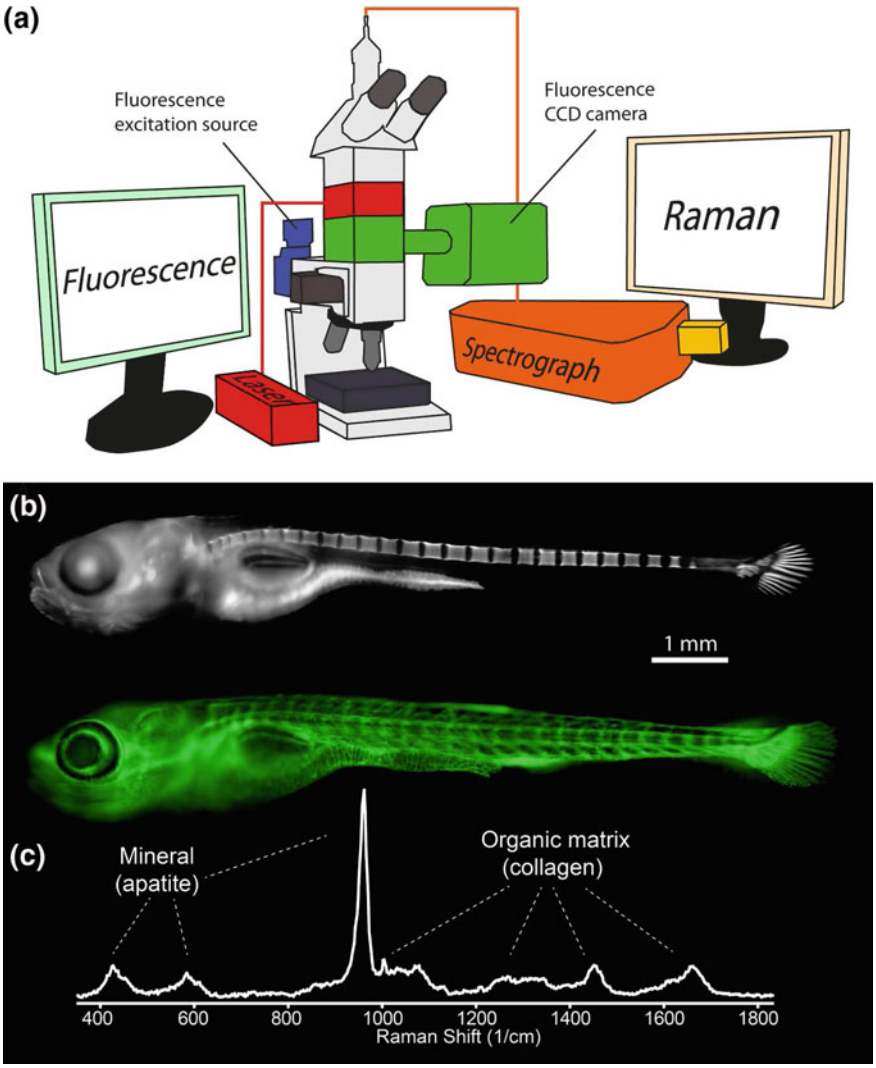

Fig. 12.2 Simultaneous fluorescence-Raman imaging of early bone mineralization in living zebrafish larvae. **a** Schematic drawing of the experimental setup showing how the different modules are assembled onto the microscope for the simultaneous use of confocal Raman spectroscopy and fluorescence imaging. **b** Fluorescence image of calcium-containing tissues and body fluids (including gut contents) stained with calcein blue and excited at 400 nm (top). EGFP-labeled endothelial cells of transgenic zebrafish excited at 490 nm (bottom). **c** Raman spectrum of newly forming bone tissue (Reproduced from [12])

This simultaneous fluorescence-Raman approach permits the unprecedented chemical characterization of fluorescently-labeled biological tissues in-vivo and opens significant opportunities in molecular imaging of metabolic activities, intracellular sensing and molecular trafficking, as well as in-vivo exploration of cell-tissue interfaces.

12.3 Large-Area Topographic Chemical Imaging

Vibrational spectroscopies, specifically Raman and infrared (IR) spectroscopy, have been demonstrated to be excellent characterization tools for extracting spatially localized, short range chemical information from crystalline and amorphous mineral phases in biological systems [32–34]. In contrast to IR-based approaches, however, which are highly sensitive to the presence of water, Raman spectroscopy permits the examination of biological materials in their native state and under physiologically relevant conditions, thus significantly reducing sample preparation time and eliminating the potential for dehydration-induced artifacts (see Sect. 12.2) [35, 36]. In addition to the use of vibrational spectroscopy techniques for the characterization of biological materials, scanning electron microscopy-based imaging techniques such as 16-bit backscattered electron (BSE) imaging and multi-channel (multi-detector) energy dispersive spectroscopy (EDS) can also be employed for investigating differences in either electron density or elemental composition. Since 16-bit BSE imaging results in the generation of 65,536 distinct grayscale intensity levels, it permits the detailed examination of extremely subtle differences in average electron density in heterogeneous samples. In addition, the simultaneous employment of multiple silicon drift detectors [37] for the collection of elemental mapping data permits the high signal to noise identification of small local differences in elemental distributions. Compared to traditional Si (Li) detector technology, silicon drift detectors can operate at much shorter process times while offering similar resolution. As a result, the count rate throughput and the relative peak intensity at an equivalent dead time is much greater, permitting higher signal-to-noise maps, shorter acquisition times, and higher spatial resolution. In addition, simultaneous collection of X-rays from multiple detectors can further increase the map signal-to-noise ratio during the same collection time frame.

Traditionally, EDS and Raman imaging techniques have been designed for use with sectioned and polished samples. However, it is often desirable to examine non-planar samples with complex topographies in their native state, and here we highlight a specific set of methodologies that can help make these goals a reality. Confocal Raman microscopy is a desirable molecular imaging tool due to its suppression of out-of-focus scattered light. The high level of confocality results in a limited depth of field, which can present serious limitations when it comes to analyzing large samples with complex shapes and/or rough surfaces. This issue can be resolved, by applying a large-area imaging approach that is z-indexed at every spectrum acquisition point from 3D profilometry data. Using such an approach, dimensionally large and

topographically complex objects can be automatically scanned and Raman chemical images acquired in a high-throughput manner. This methodology, known as *TrueSurface* microscopy (see Sect. 6.5 in this volume) exploits the principle of chromatic aberration. A white light point source is focused onto the sample surface with a hyperchromatic lens assembly, where every color corresponds to a different focal distance. The light reflected from the sample is then collected and focused through a pinhole onto a spectrometer. Since only one wavelength is in focus at the sample surface, only this specific wavelength will pass through the confocal pinhole and therefore, the detected wavelength will be strictly related to the local surface height. Scanning the sample in the XY plane reveals a topographic map that can be followed with a subsequent Raman imaging scan so that the Raman laser is always kept in focus relative to the sample surface while maintaining the high lateral and depth resolution. Using this approach, irregularly shaped biological samples can be routinely examined without compromising the confocality of the system.

Recently, three material characterization techniques (high dynamic range 16 bit BS-SEM, high throughput multi-detector EDS, and diffraction-limited Raman spectroscopy) were repurposed with the emphasis on large area chemical mapping for the characterization of a structurally complex and compositionally heterogeneous mineralized biological model system, the teeth from the red urchin, *Strongylocentrotus franciscanus* (Fig. 12.3a) [38]. Optical profilometry was used to generate a topographic map of the sample surface near the tooth tip over an area of ca. 6.5 mm^2 and a z-height change of ca. 1.5 mm (Fig. 12.3b), the positional information from which provided the XYZ coordinates for each subsequently acquired Raman spectrum. Figure 12.3c shows the resulting *TrueSurface* confocal Raman image alongside

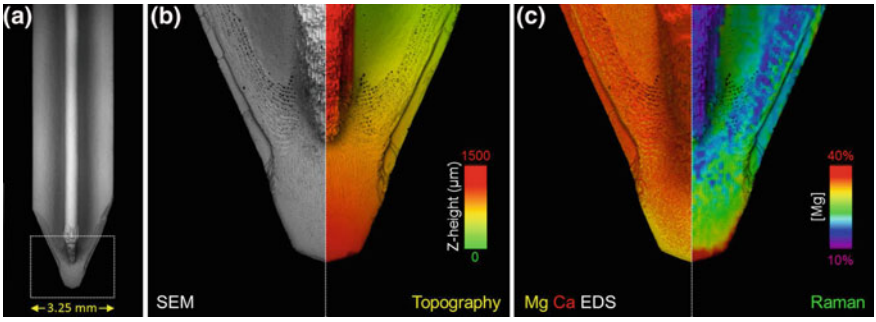

Fig. 12.3 Large area chemical imaging of one of the topographically complex teeth from *S. franciscanus*. BS-SEM image of the distal 50% of the tooth **a** and a detailed view of the substrate contact region (**b**, left). Topographical map of the contact region as recorded by optical profilometry (*TrueSurface*), revealing the highly variable axial profile of the sample surface (**b**, right). Large area multi-channel EDS (**c**, left) along the entire length of the contact region showing the significant increase in Mg concentration towards the tooth tip and *TrueSurface* Raman imaging (**c**, right) confirms this highly localized Mg enrichment. The colored mapping data in **b** and **c** were superimposed on the underlying BS-SEM images in order to better illustrate the underlying topography (Reproduced from [38])

an EDS elemental map obtained from the opposite side of the same tooth. Taking advantage of the diametrically opposed EDS detector geometry, we were able to acquire a nearly shadow-free elemental map which clearly illustrates the local variability in Mg distribution (deducted from the carbonate ν_1 peak position) throughout the tooth tip.

12.4 Large-Area Chemical Imaging of Precious Archaeological Samples

In archeological research, various specimens such as paintings, mummies, antique objects, and fabrics are regularly investigated. These samples are often unique and require special care when handled and studied. Raman chemical imaging has long been employed as a non-destructive spectroscopic tool for materials characterization in the field of cultural heritage [39–42] and the recent instrumental developments described in the previous sections are also enabling remarkable new applications in this field of study. For example, *TrueSurface* Raman chemical imaging permits the non-invasive and non-destructive analysis of large areas of ancient objects with irregular surfaces, and is thus a breakthrough in the field of cultural heritage research. It further allows investigation of extremely precious samples in situ without the need for any destructive sampling or sample preparation. When sub-sampling is possible, the sub-micron resolution, large area imaging of a cross section further improves the quality of the analytical output and allows detailed characterization of primary material constituents at the micron scale.

In the representative archaeological sample shown in Fig. 12.4a, the region of interest exhibits high topographical variability and therefore cannot be successfully analyzed taking a conventional confocal Raman microscopy approach. Following recording of the 3D surface topography, a large area confocal Raman image was obtained using the topographic information to trace the z-position for each acquired spectrum. The scanned area in Raman imaging mode was $5\,\text{mm} \times 10\,\text{mm}$ with 150×300 Raman spectra recorded at an integration time per spectrum of 1 s. Processing the entire data set generated a color-coded image, which could then be overlaid onto the 3D surface reconstruction as shown in Fig. 12.4b.

Through the analysis of material-specific Raman spectral features, the component layers of the painted surface can be identified (plaster, white chalk, carbon black, and cinnabar). Cinnabar (HgS) is a precious red pigment characteristic of the Roman period and Minium, a ground version of cinnabar, was considered the Romans' most valuable pigment. Used in many ambitious works, including several Pompeiian masterpieces, it demonstrated great wealth. In fact, the price of *Spanish Minium* used in Pompeii was capped by law at 150 sesterces per kilogram (ca. $500 per kilogram in todays value) [43]. The location at which cinnabar was detected by confocal Raman imaging is overlaid in red onto the white light image in Fig. 12.4a. By comparing the location of the cinnabar with the red areas shown in Fig. 12.4c,

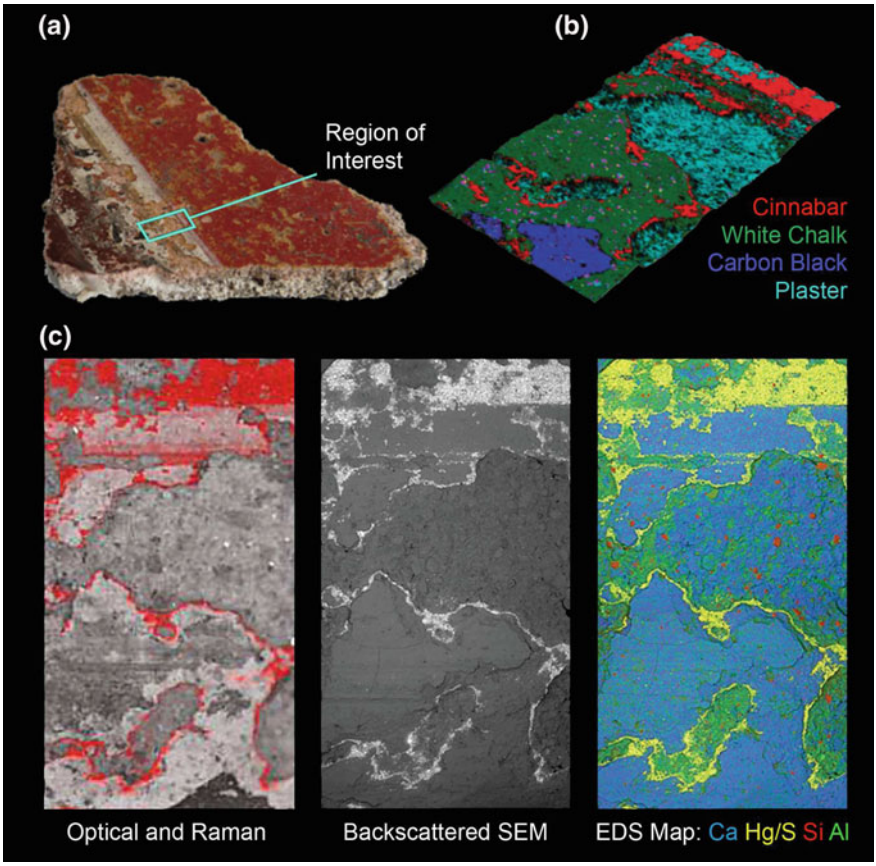

Fig. 12.4 Large area correlative Raman/SEM/EDS imaging of a fragment from a Roman wall painting. **a** Photograph of the Roman wall painting sample with the area of interest indicated by the arrow. **b** Color-coded Raman Image overlaid onto the topography of the area of interest. **c** White light and Raman image of the locations of cinnabar red pigment compared with the Backscattered SEM and EDS maps of the same region of interest

it can be clearly seen that the distribution of cinnabar is closely correlated with the bright regions in the Backscattered SEM image acquired from the same region of interest. The presence of mercury revealed through large area EDS mapping confirms the presence of cinnabar at the edges of the layers, indicating that a cinnabar-based preparation had been applied, highlighting the cultural importance and richness of the analyzed fragment. The correlative Raman/SEM/EDS characterization approach described here thus demonstrates a new set of high throughput, multi-spectral, high resolution methods for the large scale characterization of precious archaeological samples. In addition, the hardware and data collection protocols can be adjusted such that the information is derived from irregularly shaped samples with complex surface topographies and without the need for any sample preparation.

12.5 Conclusion

In this chapter, we have presented several practical examples where confocal Raman microscopy provides an effective and general method for surface chemical characterization. We showed that the non-invasive nature of microscopic Raman imaging makes it equally effective for monitoring dynamic processes in both single cells (fribroblasts) and entire multicellular organisms (zebrafish larvae). Due to the complex hierarchical and irregular structure of biological and archaeological samples, the ability to simultaneously document compositional variability across length scales spanning more than 4 orders of magnitude (from μm to cm) presents many technical challenges. Large area *TrueSurface* Raman chemical imaging provides solutions to this problem, and when integrated with EDS-based elemental mapping data, permits the acquisition of information-rich large-area data sets on compositionally variable samples with complex topographies.

In relation to the available portfolio of analytical techniques, Raman imaging is emerging as an effective method capable of delivering sub-micron chemical maps under physiologically relevant conditions, thus paving the way for additional structure-function investigations in other mineralized and non-mineralized biological materials. The correlative Raman/SEM/EDS approach described here shows remarkable potential for characterizing complex biological tissues, allowing the collection of complementary information regarding structural complexity, elemental composition, and short range chemical bonding information. An "all-in-one" Raman-SEM experimental setup could thus make this approach the method of choice for the high-throughput, economical, laboratory-based characterization of biological and archaeological materials as outlined in Chap. 23.

Acknowledgements We thank Prof. Lia Addadi, Prof. Steve Weiner, Dr. Damien Faivre, Dr. Mathieu Bennet, and Prof. Peter Fratzl for fruitful discussions. We thank Dr. Thomas Dieing for helping with *TrueSurface* data acquisition and processing and Dr. Karl Brommer for helpful suggestions. Part of this research was supported by a German Research Foundation (DFG) grant, within the framework of the SPP 1420.

References

1. O. Paris, B. Aichmayer, A. Al-Sawalmih, C. Li, S. Siegel, P. Fratzl, Adv. Eng. Mater. **13**(8), 784 (2011)
2. C. Riekel, F. Vollrath, Int. J. Biol. Macromol. **29**(3), 203 (2001)
3. M.P. Wenger, L. Bozec, M.A. Horton, P. Mesquida, Biophys. J. **93**(4), 1255 (2007)
4. D. Mahoney, D. Vezie, R. Eby, W.W. Adams, D. Kaplan, in *ACS Symposium Series (USA)* (1994)
5. G. Melacini, A.M. Bonvin, M. Goodman, R. Boelens, R. Kaptein, J. Mol. Biol. **300**(5), 1041 (2000)
6. G. Otting, Prog. Nucl. Magn. Reson. Spectrosc. **31**(2), 259 (1997)
7. W.J. Landis, K.J. Hodgens, M.J. Song, J. Arena, S. Kiyonaga, M. Marko, C. Owen, B.F. McEwen, J. Struct. Biol. **117**(1), 24 (1996)

8. M. Kazanci, H. Wagner, N. Manjubala, H. Gupta, E. Paschalis, P. Roschger, P. Fratzl, Bone **41**(3), 456 (2007)
9. T. Lefèvre, M.E. Rousseau, M. Pézolet, Biophys. J. **92**(8), 2885 (2007)
10. C. Pellerin, M.E. Rousseau, M. Côté, M. Pézolet, Macromol. Symp. (Wiley Online. Library) **220**, 85–98 (2005)
11. E.P. Paschalis, R. Mendelsohn, A.L. Boskey, Clin. Orthop. Relat. Res.® **469**(8), 2170 (2011)
12. M. Bennet, A. Akiva, D. Faivre, G. Malkinson, K. Yaniv, S. Abdelilah-Seyfried, P. Fratzl, A. Masic, Biophys. J. **106**(4), L17 (2014)
13. A. Akiva, G. Malkinson, A. Masic, M. Kerschnitzki, M. Bennet, P. Fratzl, L. Addadi, S. Weiner, K. Yaniv, Bone **75**, 192 (2015)
14. A. Yashchenok, A. Masic, D. Gorin, B.S. Shim, N.A. Kotov, P. Fratzl, H. Möhwald, A. Skirtach, Small **9**(3), 351 (2013)
15. D. Radziuk, R. Schuetz, A. Masic, H. Moehwald, Phys. Chem. Chem. Phys. **16**(44), 24621 (2014)
16. A. Zoladek, F. Pascut, P. Patel, I. Notingher, J. Spectro. **24**(1–2), 131 (2010)
17. M. Moskovits, Rev. Mod. Phys. **57**(3), 783 (1985)
18. J. Kneipp, H. Kneipp, K. Kneipp, Chem. Soc. Rev. **37**(5), 1052 (2008)
19. C.R. Yonzon, O. Lyandres, N.C. Shah, J.A. Dieringer, R.P. Van Duyne, *Surface-Enhanced Raman Scattering* (Springer, Berlin, 2006), pp. 367–379
20. S. Nie, S.R. Emory, Science **275**(5303), 1102 (1997)
21. D.K. Lim, K.S. Jeon, H.M. Kim, J.M. Nam, Y.D. Suh, Nat. Mater. **9**(1), 60 (2010)
22. D.K. Lim, K.S. Jeon, J.H. Hwang, H. Kim, S. Kwon, Y.D. Suh, J.M. Nam, Nat. Nanotechnol. **6**(7), 452 (2011)
23. C. Matthäus, T. Chernenko, J.A. Newmark, C.M. Warner, M. Diem, Biophys. J. **93**(2), 668 (2007)
24. J.R. Lakowicz, *Principles of Fluorescence Spectroscopy* (Springer, New York, 2006)
25. K. Klein, A.M. Gigler, T. Aschenbrenner, R. Monetti, W. Bunk, F. Jamitzky, G. Morfill, R.W. Stark, J. Schlegel, Biophys. J. **102**(2), 360 (2012)
26. N. Vidavsky, A. Masic, A. Schertel, S. Weiner, L. Addadi, J. Struct. Biol. **192**(3), 358 (2015)
27. A.P. Rodó, L. Váchová, Z. Palková, PLoS ONE **7**(3), e33229 (2012)
28. T. Barilero, T. Le Saux, C. Gosse, L. Jullien, Anal. Chem. **81**(19), 7988 (2009)
29. K. Luby-Phelps, S. Mujumdar, R. Mujumdar, L. Ernst, W. Galbraith, A. Waggoner, Biophys. J. **65**(1), 236 (1993)
30. E. Neher, G. Augustine, J. Phys. **450**, 273 (1992)
31. J. Becerra, G. Montes, S. Bexiga, L. Junqueira, Cell Tissue Res. **230**(1), 127 (1983)
32. S. Bentov, P. Zaslansky, A. Al-Sawalmih, A. Masic, P. Fratzl, A. Sagi, A. Berman, B. Aichmayer, Nat. Commun. **3**, 839 (2012)
33. X. Long, M.J. Nasse, Y. Ma, L. Qi, Phys. Chem. Chem. Phys. **14**(7), 2255 (2012)
34. S. Amini, A. Masic, L. Bertinetti, J.S. Teguh, J.S. Herrin, X. Zhu, H. Su, A. Miserez, Nat. Commun. **5** (2014)
35. M.D. Morris, G.S. Mandair, Clin. Orthop. Relat. Res.® **469**(8), 2160 (2011)
36. N. Gierlinger, T. Keplinger, M. Harrington, Nat. Protoc. **7**(9), 1694 (2012)
37. J. Berlin, T. Salge, M. Falke, D. Goran, in *Recent Advances in EDS and EBSD Technology*, 42nd Lunar and Planetary Science Conference (2011)
38. A. Masic, J.C. Weaver, J. Struct. Biol. **189**(3), 269 (2015)
39. F. Casadio, R.P. Van Duyne, Analyst **138**(24), 7276 (2013)
40. F. Pozzi, M. Leona, J. Raman Spectrosc. **47**(1), 67 (2016)
41. R.J. Clark, *Handbook of Vibrational Spectroscopy* (2002)
42. M. Aceto, A. Agostino, G. Fenoglio, P. Baraldi, P. Zannini, C. Hofmann, E. Gamillscheg, Spectrochim. Acta Part A Mol. Biomol. Spectrosc. **95**, 235 (2012)
43. N. Eastaugh, V. Walsh, R. Chaplin, T. Siddall, *The Pigment Compendium CD-ROM* (Elsevier, Amsterdam, 2004)

Part V
Life Sciences and Pharmaceutics

Chapter 13
Raman Micro-spectral Imaging of Cells and Intracellular Drug Delivery Using Nanocarrier Systems

Christian Matthäus, Tatyana Chernenko, Clara Stiebing, Luis Quintero, Miloš Miljković, Lara Milane, Amit Kale, Mansoor Amiji, Stefan Lorkowski, Vladimir Torchilin, Jürgen Popp and Max Diem

Abstract Raman microscopic imaging of eukaryotic cells has become a well-established technique to address various biochemical questions related to cell biology. The combination of Raman spectroscopy with optical microscopy offers the possibility to study the composition of cells and alterations associated with metabolistic activity induced by internal or external factors. Because of the associated spectral information obtained, Raman microscopy can be utilized without the need for fluorescent dyes or laborious sample preparation. In order to contrast the cellular compartments within the cytosol, imaging algorithms based on multivariate data analysis are commonly employed. Apart from imaging the intracellular organelles and structures of eukaryotes based on their intrinsic biochemical composition, it is possible to

C. Matthäus (✉) · T. Chernenko · M. Miljković · M. Diem
Department of Chemistry and Chemical Biology,
Northeastern University, Boston, MA 02115, USA
e-mail: c.matthaeus@yahoo.de
URL: http://www.northeastern.edu

L. Quintero
College of Engineering, University of Puerto Rico,
Mayagües, PR 00680, USA

L. Milane · A. Kale · M. Amiji · V. Torchilin
Department of Pharmaceutical Sciences and Center for Pharmaceutical Biotechnology and Nanomedicine, Northeastern University,
Boston, MA 02115, USA

C. Matthäus · C. Stiebing · J. Popp
Leibniz Institute of Photonic Technology (Leibniz-IPHT),
Albert -Einstein -Straße 9, 07745 Jena, Germany
e-mail: christian.mattaeus@ipht-jena.de

C. Matthäus · C. Stiebing · J. Popp
Institute of Physical Chemistry and Abbe Center of Photonics,
Friedrich Schiller University Jena, Helmholtzweg 4, 07743 Jena, Germany

S. Lorkowski
Institute of Nutrition and Abbe Center of Photonics, Friedrich Schiller University Jena, Dornburger Straße 25, 07743 Jena, Germany

J. Toporski et al. (eds.), *Confocal Raman Microscopy*, Springer Series in Surface Sciences 66, https://doi.org/10.1007/978-3-319-75380-5_13

follow the uptake of various substances. Externally administered molecules can be labeled with stable isotopes, such as deuterium. The unique spectroscopic features of isotopically labeled compounds provide high specificity and sensitivity without changing the chemical properties of the molecules of interest. The concept of isotopic labeling is illustrated for the uptake of lipids into macrophages, as well as for liposomal drug delivery systems.

13.1 Introduction

Microscopic imaging of cells and their substructures by various optical techniques is extensively applied within cellular biology. Apart from conventional optical microscopy, there are numerous imaging techniques based on light absorption, emission and scattering effects. Most prominent are fluorescence imaging techniques, such as epifluorescence and confocal fluorescence microscopy. It is very common to employ lasers as an illumination or excitation source - especially in the case of nonlinear optical techniques including two photon microscopy (TPM), second and third generation imaging (SHIM, THIM) or fluorescence lifetime, fluorescence correlation and fluorescence resonance energy transfer microscopy (FLIM, FCM, FRET) [1–5].

Raman microscopy is a non-invasive imaging technique that combines vibrational spectroscopy with high resolution optical imaging. It has the intrinsic advantage of directly investigating molecular compositions and structures without introducing any external labels or dyes. Fluorescence techniques, based on autofluorescence or fluorescent labels introduced either chemically, genetically (such as green fluorescence protein labeling) or through antibodies, often suffer from rapid photobleaching, and the associated protocols are often rather invasive. The interference of relatively bulky fluorophores with the biological activity of a labeled substance is also a generally debated issue. With the development of Raman microscopes, it is now possible to image cells with subcellular resolution based on differences in chemical composition or protein conformation, which are reflected in the spectral features of the various cellular components. Early studies based on single point spectra have demonstrated that Raman microscopy can be utilized to observe the metabolic activity of single living cells - such as NADPH oxidase activity inside granulocytes, which is important for the initiation of the immune response [6, 7], lipid body accumulation around phagosomes in leukocytes [8], and hemoglobin oxidation/heme aggregation in erythrocytes [9]. The degeneration of proteins during necrosis may be monitored by changes in the appearance of the Raman spectra [10]. There also have been efforts to introduce Raman labels, i.e. molecules that have a high Raman scattering cross section, to detect cellular enzymes and receptors [11].

In terms of imaging cellular components, two main approaches have been pursued. In several cases the distribution of a molecular species can be monitored directly, meaning that the species of interest has characteristic Raman bands, which are sufficiently different from the spectroscopic features of the general protein/lipid environ-

ment of a cell. Reasonable contrast can be achieved by plotting DNA band intensities to image chromatin or the nucleus [12–14]. Sometimes it is possible to observe resonance Raman effects if the system of interest and the employed laser frequency allow for such excitation. For example, resonance Raman effects in cells have been reported for certain cytochromes [15], hemozoin formation in red blood cells infected with malaria [9, 16], and photodynamic agents that are being explored for use in tumor therapy [17, 18]. Resonance Raman signals usually dominate over the spectra from cell proteins. Plotting peak intensities and peak positions can be referred to as univariate imaging.

Raman spectra reflect the biochemical composition within the focal volume, which is determined by the diffraction limit of the applied laser light. As a result, the observed Raman spectra are the superposition of band intensities and shapes, originating from different biochemical components. However, due to the interactions of the components, the observed spectra are never a pure superposition of component spectra. In order to extract the relevant spectroscopic information, several multivariate methods may be applied. Two complementary approaches can be roughly distinguished as clustering and spectral unmixing methods. Clustering algorithms group the spectra by their similarity, whereas spectral unmixing routines divide the dataset according to their dissimilarity. A common clustering method employed for spectral imaging is hierarchical cluster analysis (HCA) [19, 20]. In principle, the algorithm searches for the most similar spectra within a dataset by calculating the vector product for each individual spectrum with every other spectrum in the dataset. The most similar spectra are then grouped together into separate clusters. In contrast to the clustering approach, spectral unmixing algorithms search for the most dissimilar spectra in a given dataset. This can be performed by for example expressing all spectra as a deviation from the mean by a linear combination of the spectral differences as in principle component analysis (PCA). Also commonly employed are vector component analyses (VCA) [21–24]. Both approaches will be described in more detail in the method section. In the following discussion, the concept of Raman imaging in combination with multivariate data analysis will be introduced for several types of common cell lines.

Apart from imaging subcellular features, Raman microscopy may provide an opportunity to follow the uptake of molecules by cultured cells. Controlled by diffusion, endocytosis, and various transport mechanisms, a range of molecules such as polypeptides and carbohydrates may pass the membrane. This uptake may be facilitated by “active transport”, where molecules are pumped in and out of a cell in an energy-dependent manor, or by “passive transport”, which relies on gradient-driven diffusion. Provided that the uptake is sufficiently large, it may be possible to observe optical signals of the targeted molecules. One major advantage of Raman imaging is the high spectral information content. This allows interpretation of the chemical integrity (modification) and physical integrity (conformational change) of a molecule. Many substances are metabolized inside the cell such that the structure of the product differs from that of the original compound. Often, these chemicals

are either activated or deactivated due to metabolic transformation. Raman spectra provide important experimental evidence about the extent and type of metabolic transformations that a compound encounters after cellular internalization. Also of interest are conformational changes of active compounds, such as the conformational change of a peptide at a receptor binding site. Numerous spectroscopic data of solution studies can be found in the literature. Raman microscopy allows the comparison of data measured on isolated structures in solution to data acquired from dynamic experiments conducted inside a living cell. The concept of label free spectroscopic imaging by Raman microscopy has meanwhile become a widespread methodology for single cell analysis [25]. The possibility to observe the intracellular uptake of defined chemical species has been demonstrated for several cases, although direct imaging of individual substances is limited particularly by the applied concentrations and incubation conditions. The important criterion is that the uptake of the molecules of interest is above the detection limit of the Raman scattering. Several spectroscopic features can increase the detection limit and sensitivity. One option is to utilize the intrinsic property of resonance Raman effects of molecules that exhibit conjugated π-bonds and fulfill the required symmetry conditions. Examples of molecular structures that give rise to resonance Raman effects are carotenoids and porphyrins. Also favorable molecular structures are species that have a high Raman scattering cross section as for instance lipids. Lipids play an important role in many intracellular processes, for instance as structural components in membranes, as energy storage in the form of triglycerides and as precursors for signaling molecules. In order to distinguish the lipids of interest from the intracellular lipids, hydrogens of the applied molecules can be replaced by deuterium, which alters the spectral characteristics dramatically, but preserves the chemical properties. The intracellular uptake of lipids is particularly interesting in the context of atherosclerosis, as the metabolism of lipids within plaque formations are regulated by macrophages, a type of white blood cells.

Increasingly popular in pharmaceutical sciences is the concept of active drug delivery systems that can encapsulate and release a payload within the intracellular environment of target (disease) cells with minimal accumulation in non-target (healthy) cells [26]. Many pharmacologically active compounds have low solubility, and thus low bioavailability within diseased tissue. If a compound is fairly soluble in water, it often cannot pass through the cell membrane due to low lipophilicity. Many bioactive compounds do not have amphiphilic properties, meaning that they are both sufficiently hydrophilic as well as lipophilic, which would allow passage through the membrane barrier by diffusion. In order to bypass this problem, small particle based drug delivery systems have been introduced. Currently there are various types of delivery systems under investigation. However, in principle these systems are nanoscale structures that can encapsulate or protect the bioactive species of interest. Again, to distinguish the species of interest from their cellular environment, the carrier particles or the drug load itself may be labeled with deuterium.

13.2 Method

13.2.1 Data Acquisition

Raman spectra were acquired using a CRM200 and alpha300 Confocal Raman Microscope (WITec GmbH, Ulm, Germany). Excitation (ca. 30–100mW each at 488, 514.5, 632.8 and 785nm) is provided by an air-cooled Ar ion, HeNe or solid state diode laser (Melles Griot, Rochester, NY, USA; Toptica, Munich, Germany). Exciting laser radiation is coupled into the microscope through a wavelength-specific single mode optical fiber. The incident laser beam is collimated via an achromatic lens and passes a holographic band pass filter or a dichroic mirror, before it is focused onto the sample through the microscope objective. A Nikon Fluor (60x/1.00 NA, WD = 2.0mm) water immersion objective was used in the studies reported here. Most images presented were recorded at a resolution or step size of 0.5µm with 250–500ms exposure time using either the 488 or 785nm excitation lines, with a 600 or 300gr/mm grating.

Fluorescence measurements were performed on the same instrument, using the 488nm excitation. For a comparison of mitochondrial distribution observed through Raman and fluorescence imaging, the cells were first scanned to collect the Raman spectra. Subsequently, Mitotracker$^{(R)}$ stain was carefully added and the fluorescence emission of the cell was rescanned at significantly lower laser power with a dwell time of 100ms per data point.

13.2.2 Introduction to Data Processing Methods

A number of mathematical methods have been introduced to exploit hyperspectral datasets for imaging applications. Very common are cluster analysis techniques, which sort the spectra of a dataset into different groups or subsets according to their similarity. There are partial clustering algorithms, such as k-means and fuzzy c-means clustering and hierarchical clustering methods. Especially hierarchical clustering has found widespread applications to image Raman datasets of various biological and medicinal samples such as tissue biopsies [27–29].

Another possible approach to analyze data cubes that consist of a large number of spectra is hyperspectral unmixing [21]. In spectral unmixing the spectra from individual pixels are decomposed into several constituent spectra and fractions that indicate to what extent each constituent spectrum contributes to the spectrum in each pixel. By plotting the fractions of the constituent spectra, also called endmembers, the abundances of each endmember can be imaged. Several decomposition algorithms, for example orthogonal subspace projection and vertex component analysis have been developed [22, 30]. So far, hyperspectral unmixing has mainly been employed to datasets of remote sensing techniques in geology, agriculture and ecology.

Spectral data hypercubes, produced by raster-scanning the sample through the focal point of the Raman microscope, were analyzed using software written in-house in the MATLAB(R) (TheMathWorks, Natick, MA) environment. Before analysis, the raw data cubes were processed to remove cosmic ray artifacts, and to present each spectrum of the data set as a vector with linear wavenumber increments.

13.2.2.1 Data Pre-processing

Raman data collected using CCD detectors are frequently contaminated by sharp spikes generally attributed to cosmic rays impinging on the detector array. Depending on their angle of incidence, they produce large spurious intensities (often larger than 100,000 counts) at a few adjacent detector diodes. We have used a combination of spatial and frequency filtering methods to remove these spikes in the raw datasets. Spatial filtering, i.e., comparing the spectrum of a given pixel to the spectra of eight adjacent pixels, is particularly useful, since it is very unlikely that the eight surrounding pixels exhibit a spike at the same wavenumber, since the surrounding pixels were acquired at very different points in time. Contaminated spectral intensity points were corrected using the average of the eight surrounding intensities at the same wavenumber.

Most multivariate methods of data analysis require that each spectrum is represented as a linear vector of equidistant data points. However, in a Czerny-Turner monochromator, the dispersion $d\lambda/d\beta$ in the exit plane changes with the cosine of the diffracted angle β, and therefore, varies over the dimension of the CCD detector. For 488nm excitation and a 600gr/mm grating, the spectral bandpass varies from about 5.5cm^{-1}/pixel at about 200 rel. cm^{-1} to about 3.3cm^{-1}/pixel at 4500 rel. cm^{-1}. Thus, it is necessary to linearize the data before further analysis. The cosmic ray corrected data cubes were linearized as follows. A vector was created with a fixed, preset wavenumber interval, typically 2 or 4cm^{-1}. The MATLAB interpolation function was then used to interpolate the intensities at the non-equidistant wavenumber points to those at the fixed integer increments. At this point, the data cube was stored as a three-dimensional matrix in MATLAB 8-byte floating-point format. However, the length of each spectral vector after linearization is no longer 1024 points, but is given by the difference of the highest and lowest wavenumber point on the array, divided by the wavenumber increment selected (2 or 4cm^{-1}). The number of points in each vector is henceforth referred to as N.

13.2.2.2 Multivariate Data Analysis

In this section, we discuss cluster analysis and spectral unmixing as two different approaches of multivariate data analyses that are commonly used for graphic reconstruction. The algorithms originate from statistical data processing and can be used to visualize the spectral information of a given dataset. The methods are complementary to each other, in a sense that the datasets are divided according to either similarity or

dissimilarity. One of the most widely used clustering algorithms is HCA, which is an unsupervised method that sorts data by similarity. To this end, spectral distances are calculated and spectra are assigned to clusters based on these distances. Unmixing algorithms such as PCA or VCA, on the other hand, are methods that express all spectra in a dataset as linear combinations of the most dissimilar spectra. Both methods have distinct advantages and disadvantages, and may be used to determine different features in a data set.

Hierarchical Cluster Analysis (HCA):

HCA is a powerful method for data segmentation based on local decision criteria. These criteria are based on finding the smallest "distances" between items such as spectra, where the term "distances"' may imply Euclidean or Mahalanobis distances, or correlation coefficients (vide infra). HCA is, per se, not an imaging method, but can be used to construct pseudo-color maps from hyperspectral data sets derived from cells or tissue sections. Later in this chapter, high spatial resolution maps of individual cells will be presented that are based on hierarchical clustering.

HCA starts by computation of the spectral correlation matrix, C according to:

$$C = S^T S \tag{13.1}$$

or

$$C_{ij} = \sum S^i(\nu_N) S^j(\nu_N),\ N = 1..n \tag{13.2}$$

The C matrix is a $(n \cdot n)$ matrix (n is the number of spectra in the data set) in which the off-diagonal terms C_{ij} are the correlation between spectra i and j, summed over all data points of the spectral vector $S(\nu_N)$.

The correlation matrix is subsequently searched for the two most similar spectra coefficients, i.e., two spectra i and j for which the correlation coefficient C_{ij} is closest to unity. Hereafter, these two spectra are merged into a new object, and the correlation coefficient of this new object and all other spectra is recalculated. In this process, the dimensionality of the correlation matrix is reduced by one.

The process of merging is repeated, but the items to be merged may be spectra, or spectra and merged objects. In the merging process, a membership list is kept that accounts for all individual spectra that are eventually merged into a cluster. We have used Ward's algorithm for the process of merging of spectra, and the repeated calculation of the correlation matrix. Once all spectra are merged into a few clusters, color codes are assigned to each cluster. The coordinates from which a spectrum was collected are indicated in this color. In this way, pseudo-color maps are obtained that are based entirely on spectral similarities. Mean cluster spectra may be calculated that represent the chemical composition of all spectra in a cluster.

In HCA cluster memberships are assigned on a yes/no basis: a spectrum is either a member of a cluster, or it is not. This assignment is based strictly on similarity, and requires no fitting to any reference spectra. HCA has been used to produce pseudo-color maps of human cells imaged by confocal Raman microscopy with a spatial resolution of better than 500nm. The algorithm was able to distinguish

cellular regions that were associated with the cytoplasm, mitochondria, nucleus and nucleolus. The spectral differences observed between these subcellular organelles are miniscule; yet HCA was able to group the spectra by small, recurring differences. Subsequent inspection of the mean cluster spectra can often shed light on the spectral differences between the clusters.

The disadvantage of HCA is that the correlation matrix C is of dimension n^2; thus, if a 100 × 100 point map is collected, C is of dimension 10,000 × 10,000. Thus, the memory requirements, and the time necessary for searching this matrix are enormous. Typical execution times for a 100 × 100 pixel map are about 3 h, using fast 64 bit processors running under Windows XP64, and 8 Gbyte of RAM.

Vertex Component Analysis (VCA):

Unmixing algorithms, such as VCA use a completely different approach to reduce the dimensionality of data. Each spectrum is represented as a vector in N-dimensional space, where N, as defined before, is the number of color elements in each vector. This representation may not be too obvious to spectroscopists; thus, it will be elaborated upon in some detail. Imagine that a spectrum is recorded at two frequencies, or channels, $\nu 1$ and $\nu 2$ only. Thus, each spectrum can be decomposed into intensities along the two channels $\nu 1$ and $\nu 2$ as shown in Fig. 13.1a. If two spectra are identical, they will have two identical vectors; two spectra having the same "composition" but different total intensities will have parallel vectors. Figure 13.1b, shows different spectra in two-channel space; their vectors fall on a line as indicated.

For spectra composed of three channels or frequencies, a quiver of vectors is obtained whose endpoints lie on a triangle, as shown in Fig. 13.1c. For four-dimensional spectra, the endpoints of the vectors lie in a tetrahedron. In general, the progression from point to line to triangle to tetrahedron etc. is known in geometry as a simplex. A simplex describes a p-dimensional hull, or polytope that possesses p+1 corners.

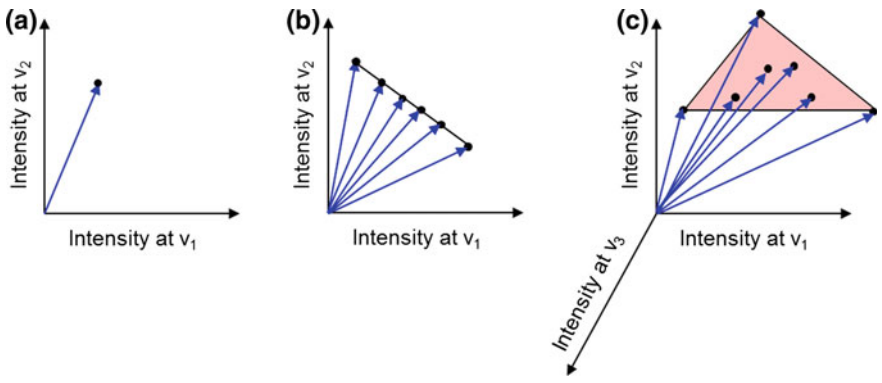

Fig. 13.1 Schematic presentation of a simplex: **a** Represents the resulting vector for a spectrum recorded at two frequencies. **b** Shows different spectra in two-channel space; all vectors fall on a line. **c** Illustrates the vector space for three channels, the vector endpoints lie in a triangle

The principle behind VCA is the assumption that the most extreme vectors in the original representation are "pure component spectra", or endmembers. These endmembers are indicated in Fig. 13.1b and c as the heavy vectors pointing to the ends of the line, or the corners of the triangle, respectively. The algorithm proceeds from the original dimensionality (in our case $N \approx 1000$, the number of color points in each Raman spectrum) and reduces the dimensionality step-by-step by a process known as "orthogonal subspace projection". In each of these steps, the problem is reduced from a p-simplex to a (p-1)-simplex. The process is terminated when the number of endmembers reaches a pre-determined level. This "spectral unmixing" described so far does not necessarily find the true spectral basis sets. For example, in a map of a human cell, VCA will not necessarily produce a pure spectrum of DNA, since no pixel in the sample is due to pure DNA (DNA is always associated with histone proteins). Thus, the best one can do with VCA is the decomposition of the spectra into a few basis spectra, or endmembers, which represent the degree to which spectra can be unmixed. We found that for cells contained in an aqueous environment, one endmember spectrum is always that of pure water (which is truly an endmember). Other endmembers will contain the most significant spectral features of the remainder of the cell. In the examples to be discussed below, the features of water plus protein and the features of phospholipids are found prominently in the endmember spectra. Resulting images of the VCA analysis are reconstructed by coding up to three abundance matrices for each pixel point as RGB maps, and superimposing these maps. Similar to VCA, an alternative algorithm termed N-FINDR also tries to find endmembers corresponding to pure spectra. The N-FINDR algorithm was proposed by Winter [31] to map minerals in geological images. The approach differs as it maximizes the volume of the n-simplex spanned by the spectra. The algorithm also constrains the matrix diagonalization to all positive contributions, which results in endmembers that reflect the spectral information not as a deviation from a mean, but as most dissimilar spectra of the dataset [24].

13.2.3 Experimental

13.2.3.1 Cell Culture Protocols

Human HeLa and MCF-7 cells (cell line CCL-2, and HTB-22, ATCC, Manassas, VA) were grown in 75cm^3 culture flasks (Fisher Scientific, Loughborough, Leicestershire, UK) with 15mL of Eagle's Minimum Essentials Medium (MEM, ATCC) and 10% fetal bovine serum (ATCC) at 37 °C and 5% CO_2. Cells were seeded onto and allowed to attach to polished CaF_2 substrates (Wilmad LabGlass, Buena, NJ), which were chosen to avoid background scattering that is observed from regular glass windows. The CaF_2 substrates were removed from the culture medium after 12–24h, and the cells were fixed in a 10% phosphate buffered formalin solution (Sigma-Aldrich, St. Louis, MO) and washed in phosphate buffered saline (PBS). For Raman and

fluorescence measurements, the CaF_2 windows with the attached and fixed HeLa cells were submerged in buffer solution during the measurement.

Fluorescence staining for mitochondrial distribution was carried out by adding Mitotracker(R) Green FM (Invitrogen, Carlsbad, CA) to a final concentration of 200nM. Fluorescence images were collected 20min after the stain was added.

THP-1 monocytes (DSMZ, Braunschweig, Germany) have been cultured in RPMI 1640 medium (Sigma-Aldrich, St. Louis, MO) containing 10% fetal bovine serum superior (Biochrom, Berlin) and 1% penicillin/streptomycin/L-glutamin (Sigma-Aldrich) in an atmosphere of 5% CO_2 at 37 °C. Monocytes have been differentiated into macrophages using RPMI 1640 medium supplemented with 100ng/mL phorbol-12-myristate-13-acetate and 50µm β-mercaptoethanol for 96 h as previously described [32, 33]. After differentiation, mature THP-1 macrophages were incubated for up to 30 h. Supplemented RPMI 1640 medium without serum was used with either 400µm d_{31}-palmitic acid, d_{33}-oleic acid, d_8-arachidonic acid or a mixture of 400µm d_8-arachidonic acid and d_{31}-palmitic acid (Sigma-Aldrich). Prior to incubation, the fatty acids were complexed to fatty acid free bovine serum albumin (Sigma-Aldrich) at a molar ratio of 4:1 in Krebs-Ringer bicarbonate buffer. After incubation, cells were washed with PBS and fixed with 4% paraformaldehyde in PBS for 20 min at room temperature.

13.2.3.2 Nanoparticle Preparation

Liposomes:

1,2-Distearoyl-d_{70}-*sn*-glycero-3-phosphocholine (DSPC-d_{70}) was obtained from Avanti Polar Lipids, Inc. (Alabaster, AL). Plain liposomes were prepared from DSPC-d_{70} by the lipid film hydration method [34, 35]. The dried lipid film prepared from the chloroform solution of DSPC-d_{70} was hydrated and vortexed with HEPES buffered saline (HBS), pH 7.4, at DSPC-d_{70} concentration of 1.6mM. The resulting liposomes were sized through doublestacked 200nm pore size polycarbonate membranes (Nucleopore) using a hand-held extruder (Avanti Polar Lipids). The liposome size was monitored by using a Coulter N4 MD Sub-micron Particle Size Analyzer (Coulter Electronics, Krefeld, Germany).

TATp-liposomes:

Purified TATp was received from Tufts University Core Facility (Boston, MA). For preparing TATp-liposomes, TATp-PEG_{3400}-PE was added to the lipid film. The hydration and sizing of TATp-liposomes were done as described above. TATp-PEG_{3400}-PE was prepared by reacting TATp with *p*-nitrophenyl carbonyl-PEG_{3400}-DOPE (pNP-PEG-PE) [36].

PEO-PCL-particles:

PCL/Pluronic(R) F 108 blend nanoparticles were prepared using solvent displacement in an acetone/water system as previously described [37]. The nanoparticles were loaded with ceramide at 20% w/w. The deuterated ceramide N-palmitoyl-(d_{31})-D-erythro-sphigosine was provided by Avanti Polar Lipids.

13.3 Results and Discussion

13.3.1 Cell Imaging

A eukaryotic cell consists of 60–70% water and roughly 30% of bioorganic molecules such as proteins, DNA, RNA or nucleic acids, polysaccharides, lipids and some inorganic salts and other small molecules. Most of the dried cell mass consists of proteins (60%) and nucleic acids (25%) [38]. Figure 13.2 shows the Raman spectra of individual cellular components. The spectra A and B are examples of a typical

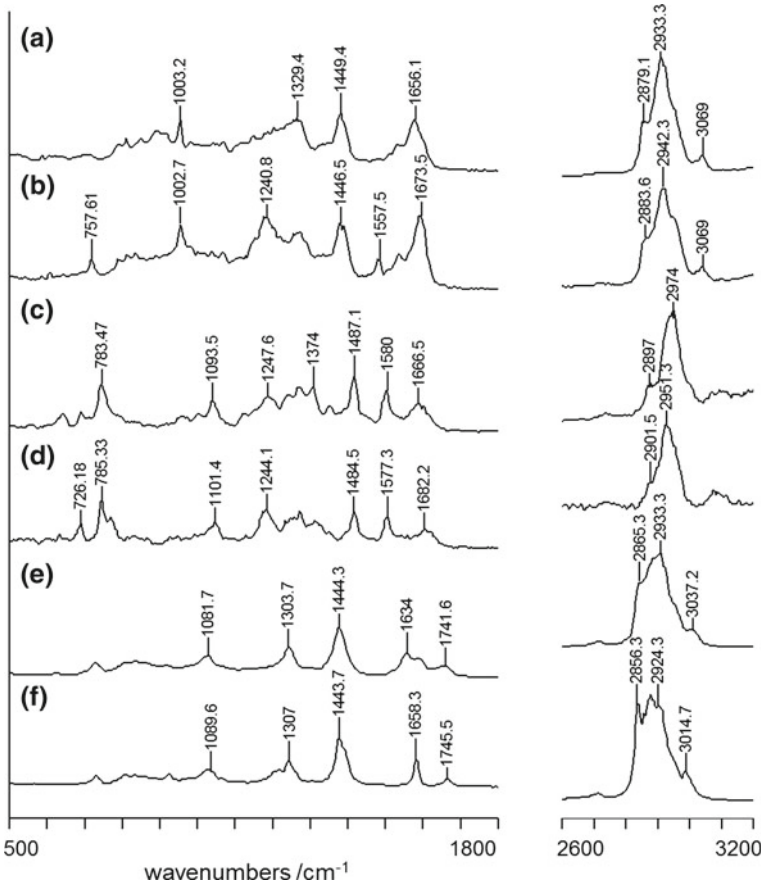

Fig. 13.2 Raman spectra of cellular components: **a** Is a spectrum of albumin, a typical α-helical protein **b** is a spectrum of γ-globulin, a protein rich in β-sheet structure. **c** and **d** are Raman spectra of DNA and RNA respectively. **e** and **f** show the spectra of a phospholipid (phosphatidylethanolamine) and a typical lipid (1,2-dioleoyl-3-trimethylammonium-propane (chloride salt)). All spectra were acquired using a 514.5nm excitation

Table 13.1 Assignment of predominant bands in the Raman spectra of cellular components

Vibrational mode	Frequency rel. cm^{-1}	Description
C–H stretching	2800–3020	C–H stretching mode
C=O stretching	1745	C=O stretching, ester group of lipids and phospholipids
Amide I	1655	C=O stretching mode, peptide linkage
DNA/RNA	1570–1580	C=C stretching, purine bases
CH_2 and CH_3	1425–1475	Anti-symmetric methyl and methylene deformations, peptide side chains, phospholipids, lipids
Amide III	1260–1350	Coupled C–H, N–H deformation modes, peptide backbone
PO_{2^-}	1095	Symmetric stretching mode of phosphate esters, DNA, RNA, phospholipids
Phenylalanine	1002	Symmetric stretching (ring breathing) mode of phenyl group
DNA/RNA	785	Pyrimidine ring breathing

α-helical and β-sheet protein, C and D show the spectra of DNA and RNA, and E and F are spectra of common phospholipids and lipids.

All spectra have very pronounced intensities in the C–H stretching region from 2800 to 3100 rel. cm^{-1} and from 750 to 1800 rel. cm^{-1} often referred to as the fingerprint region. The characteristics of the Raman spectra of cellular components have been well described [38–41] and the main assignments are listed in Table 13.1.

Fig. 13.3a is a microscopic picture of a HeLa cell, an epithelial adenocarcinoma cell obtained from a cervical cancer cell line. Figure 13.3b is a univariate Raman image of that cell constructed from the scattering intensities of the C–H stretching vibrations. The image reflects different protein densities or water content within the cell. Figure 13.3c, d shows the results of the data processing algorithms based on hierarchical cluster and vertex component analysis respectively. Easily discerned is the nucleus as well as different cellular structures within the cytoplasm. Figure 13.3e is a fluorescence image of the cell after adding a rhodamine derivative dye (Mitotracker Green$^{(R)}$) that accumulates inside mitochondria showing their distribution. Mitochondrial aggregation is highest in the perinuclear region and adopts tubular structures in the outer regions of the cytoplasm. It is well known that mitochondria are morphologically heterogeneous within cells [42]. The fluorescence image correlates very well with the outcome of the HCA and VCA, whereas the VCA algorithm seems to result in better spatial resolution. The correlation of mitochondria specific stains and images generated from HCA and VCA was found to be highly reproducible and may be reliable without counterstaining for every experiment [20, 43].

The Raman spectra associated with the pseudo-color images Fig. 13.3c, d are plotted in Fig. 13.4. Graph Fig. 13.4a shows the mean cluster spectra resulting from the HCA and Fig. 13.4b the endmember spectra of the VCA algorithm. The colors of

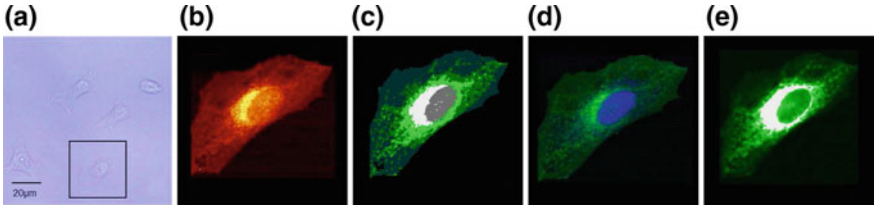

Fig. 13.3 Raman images of a HeLa cell: **a** Is a microscopic picture. **b** Shows a Raman image based on C–H stretching intensities. **c** Is a false color representation of an HCA calculation. **d** Is an abundance map generated by a VCA algorithm and **e** Shows a fluorescence image after adding a mitochondria specific rhodamine dye (Mitotracker Green$^{(R)}$). Both mathematical algorithms reveal the location of the nucleus as well as the distribution of the mitochondria and are consistent with the fluorescence image. The spatial resolution was approximately 300nm

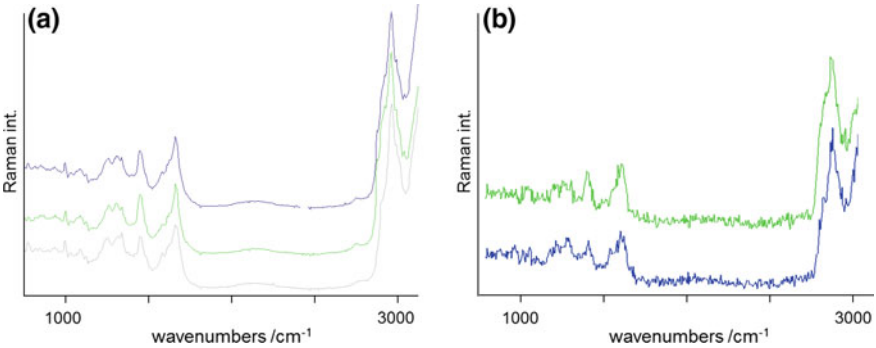

Fig. 13.4 **a** Mean cluster average spectra from the HCA results shown in Fig. 13.3c. Grey trace: nuclear region; light green: mitochondria rich region; blue: cytoplasm. **b** Raman endmember spectra from the VCA image in Fig. 13.3d. Blue trace: nuclear spectrum; light green trace: mitochondria distribution in the cytoplasm

the individual spectra correspond to the colors in the images. The greatest contrast between the spectra is apparent within the C–H stretching region from 2800 rel. cm^{-1} to 3100 rel. cm^{-1}. The C–H band of the mean cluster spectrum from the nucleus is more narrow compared with the bands from the cytoplasm and has a distinct shoulder at around 2880 rel. cm^{-1}, whereas the slope of the spectra from the cytoplasm has more, but less distinct features. There are also many noticeable differences in the fingerprint region of the spectra below 1800 rel. cm^{-1}. For HCA, minute differences are highly reproducible when results from several cells are compared [20]. The signal-to-noise ratio of the mean cluster spectra is, of course, very high given the large number of individual spectra averaged over (ranging from several hundreds to several thousands). The endmember spectra of the VCA have the quality of single point spectra, where spectral differences can easily be recognized.

Figures 13.5 and 13.7 shows examples of Raman intensity, HCA- and VCA-generated images for two other cell types. Figure 13.5b, c, d are images of a MCF-7 cell, an epithelial cell from a breast cancer cell line. Figure 13.7b, c, d show a germ-

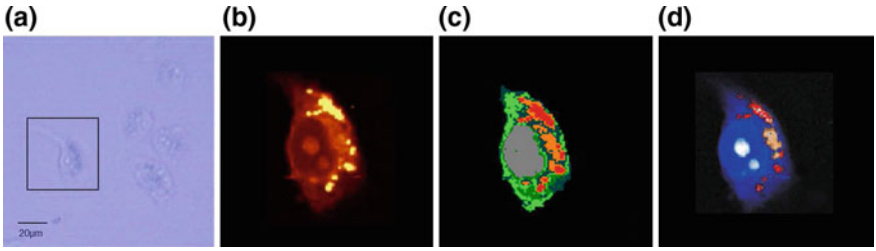

Fig. 13.5 Raman images of an MCF-7 cell: **a** Is a microscopic picture, **b** Raman map reconstructed from the scattering intensities of the C–H stretching vibrations. **c** and **d** Show the results of multivariate data analysis algorithms HCA and VCA respectively. The HCA algorithm depicts the nucleus and differentiates regions in the cytoplasm. The VCA calculation resulted in discrimination between the cell body and lipid rich regions in the cytoplasm

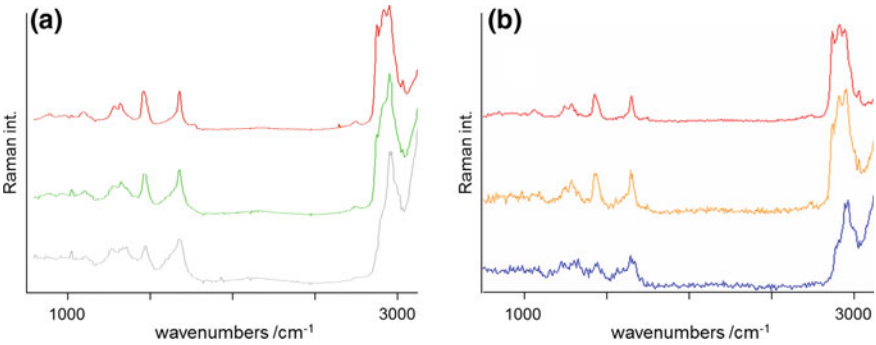

Fig. 13.6 **a** Mean cluster spectra from the HCA results shown in Fig. 13.5. Grey trace: nuclear region; light green: mitochondria rich region; blue: cytoplasm. **b** Raman endmember spectra from the VCA image in Fig. 13.5d. Blue trace: nuclear spectrum; orange and red trace: lipid or phospholipid rich region in the cytoplasm

line cell from a mouse. The morphology of the MCF-7 cells is different from that of the HeLa cells although the nuclei and the cytoplasm are similar in size. Here, the cell has two large nucleoli, which are also typical for HeLa cells. However, MCF-7 cells appear to have relatively large vesicle-like inclusions, which can be noticed as dark spots in the optical image (Fig. 13.5a) and very bright areas in the Raman image (Fig. 13.5b).

The HCA algorithm again easily distinguishes the nucleus and several regions in the cytoplasm including the above mentioned very bright spots of high Raman intensity. The associated Raman spectra are plotted in Fig. 13.6a. The mean cluster spectra of the nucleus and from the cytoplasm are again very similar to the mean cluster spectra from nucleus and cytoplasm of the HeLa cell. The light green and green regions are again likely to be associated with the distribution of mitochondria.

Very different spectral features can be noticed for the spectra from the red and orange regions that correlate very well with the areas that show the vesicle-like

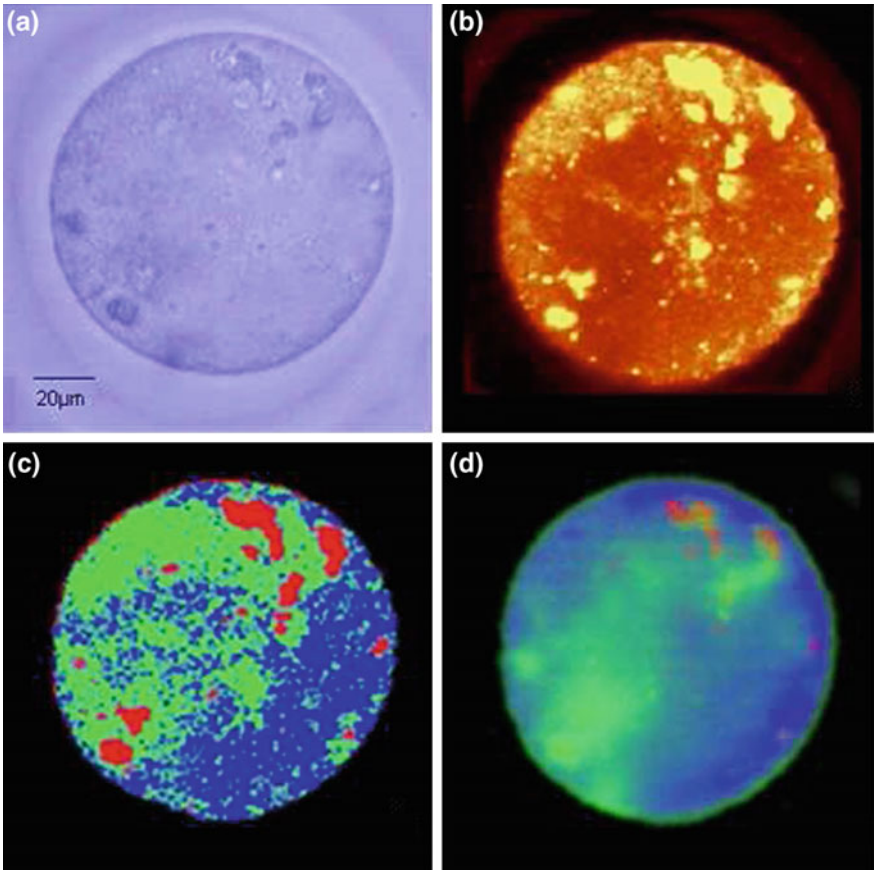

Fig. 13.7 Raman images of a mouse oocyte cell: **a** Is a microscopic picture, **b** Was reconstructed from the scattering intensities of the C–H stretching vibrations. **c** and **d** Show the results of multivariate data analysis algorithms HCA and VCA respectively. The algorithms discriminate between lipid rich regions shown in red, likely to be associated with smooth-surfaced endoplasmic reticulum, and different protein compositions in the cytoplasm

inclusions with high scattering intensities. Comparing these spectra with the lipid and phospholipid spectra from Fig. 13.2 it is obvious that the regions are of high lipid or phospholipid content. It is most likely that these vesicle-like inclusions represent a combination of endosomes, lysosomes, transport vesicles, and metabolic intermediates.

Applying the VCA algorithm to the data set of the MCF-7 cell resulted in three distinct endmembers, which are plotted in Fig. 13.6b. The blue endmember is again a typical protein spectrum. The red endmember shows lipid features and the orange endmember appears as a superposition of spectral characteristics proteins and lipids. The abundances of the endmembers are shown in Fig. 13.5d. The images recon-

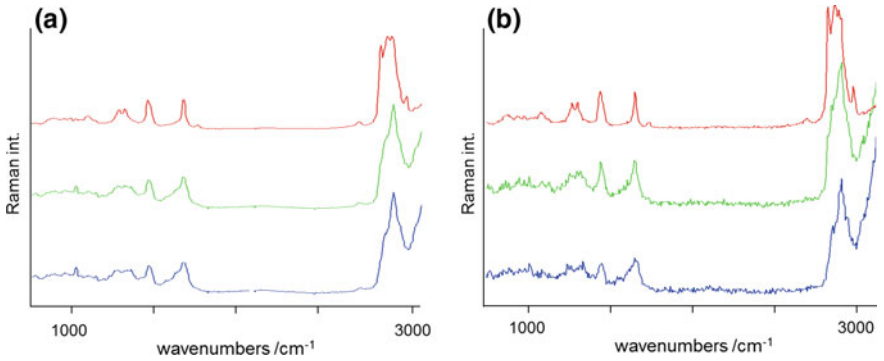

Fig. 13.8 **a** Mean cluster average spectra from the HCA results shown in Fig. 13.7c. Blue trace: cytoplasm; light green: cytoplasm; red: lipid rich regions. **b** Raman endmember spectra from the VCA image in Fig. 13.7d. Blue trace: cytoplasm; green trace: cytoplasm; red trace: lipid or phospholipid rich regions

structed from both algorithms are in very good agreement. Interestingly, the algorithm did not discriminate the regions with high mitochondria concentration. This was found to be typical for datasets from this particular cell type and is perhaps due to the high lipid content in these cells. The distinct spectral features of the alkane side chains may obscure the spectral contrast between the regions of high and low mitochondria concentration.

Figure 13.7a shows the picture of a mouse oocyte. Oocytes are germ-line cells (egg cells) at a specific developmental stage within the reproductive track. Oocytes undergo several stages of maturation before being ready for fertilization. Their morphology is very different from the morphology of any somatic cell. The chromatin is arranged in a germinal vesicle and the cytoplasm is very proliferative and rich in nourishing proteins. Mouse oocytes are usually 80–100μm in diameter, which can be a time challenging size for Raman data acquisition with good signal to noise ratio at the best possible spatial resolution. The HCA and VCA algorithms again readily find three different kinds of spectra, which are plotted in Fig. 13.8a and b. The associated cluster and abundance maps are displayed in Fig. 13.7c and d in the accustomed fashion. The overall protein matrix is shown in blue. Spectra with significant lipid or phospholipid contributions are in red and reveal most likely complexes of smooth-surfaced endoplasmic reticulum (SER) as commonly found in these cells [44]. The green regions and spectra are presumably again related to the distribution of mitochondria that are very abundant to support nourishing processes. The distribution patterns of the green areas agree very well with distribution patterns of mitochondria found in oocytes [45]. Mitochondrial distribution is known to be related to oocyte health and is an indicator for pre-implantation viability [45].

In general, the imaging results for the three cell types presented here are very satisfying. The images based simply on the Raman intensities show great resolution (Fig. 13.7b) and can certainly rival optical images from light microscopy. Very

interesting is the quality of the images generated from the multivariate data analysis algorithms. For the distribution of mitochondria for example, we were able to demonstrate that it is possible to correlate the outcome of these algorithms with organelle specific stains. Imaging the mitochondrial distribution can provide crucial information in experiments monitoring drug response to compounds that trigger apoptosis. For the cell types shown here, the HCA and VCA algorithms delivered similar insight about the cell morphologies, whereas the VCA apparently resulted in slightly better spatial resolution.

13.3.2 Intracellular Uptake of Lipids

The intracellular metabolism of lipids is a widely studied field since dysfunction or overload is associated with diseases such as atherosclerosis or can have a dramatic impact on the function of various organs. Lipids are a family of naturally occurring hydrophobic molecules that are important for energy storage, signaling or as structural components in membranes. Within the body lipids are distributed in the form of high-density and low-density lipoproteins (HDL and LDL, respectively), which facilitates transportation through the circulatory system. Aging- or stress-related processes can lead to inflammation of the inner walls of blood vessels, which then become susceptible to these lipid particles. An inflammation within the vessel walls is usually accompanied by an immigration of monocytes, white blood cells that differentiate into macrophages, which first internalize the lipid excess and subsequentially release them for reverse transportation to the liver. Several processes, as for instance oxidative modification of the lipoproteins, can disturb the processing and transport of lipids. Continuous uptake of the lipids within the oxidatively modified lipoproteins into macrophages, however, is toxic to the cells and the remaining debris of necrotic or apoptotic cells can trigger inflammation and can hence contribute to plaque formation. A high concentration of macrophages is often associated with plaque vulnerability that can lead to plaque rupture and can be the cause of a myocardial infarction or stroke. Although many aspects of the biochemistry behind the uptake and intracellular metabolism of lipids in macrophages are well understood, direct experimental evidence on the cellular level is difficult to access. There are only a few staining protocols available that can visualize lipids with rather low specificity. Fluorescence labels change the chemical properties of lipids largely. By introducing deuterium labels instead, individual species of lipids can be monitored, whereby the chemical integrity of the molecules is maintained. In order to better understand the uptake of lipids at the single cell level different fatty acids have been investigated.

To distinguish the individual fatty acids from those naturally occurring inside the cell, the hydrogen atoms of the alkyl side chains were replaced by deuterium. As long as the deuterium is covalently bound to the molecule of interest, its chemical properties remain unaltered. This approach may generally serve as a non-invasive labeling technique to study the uptake and intracellular fate of biologically active compounds.

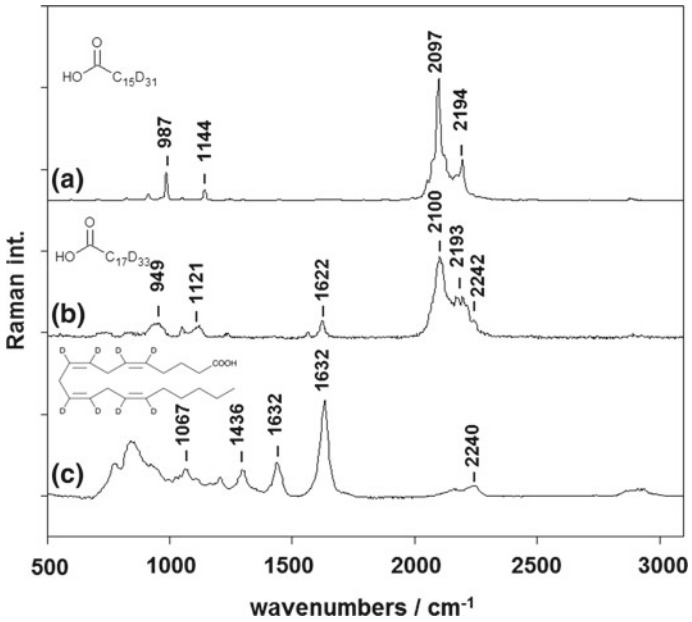

Fig. 13.9 Raman spectra of d_{31}-palmitdic acid (**a**), d_{33}-oleic acid (**b**) and d_8-arachidonic acid (**c**). The Raman bands of the CD stretching vibrations are between 2050 and 2250 rel. cm^{-1} in a region where organic molecules usually do not exhibit any Raman features

The scattering intensities of C-D vibrations are usually very pronounced and shifted away from the C–H intensities by around 800 rel. cm^{-1} into a spectral region where neither proteins nor nucleic acids have any spectral features, thus providing high sensitivity because of the absence of spectral overlap.

In Fig. 13.9 the Raman spectra of deuterated palmitic, oleic and arachidonic acid are plotted. The Raman spectra of d_{31}-palmitic acid and d_{33}-oleic acid are dominated by the Raman intensities of the CD-stretching vibrations between 2050 and 2250 rel. cm^{-1} with maximum band intensities around 2100 and 2195 rel. cm^{-1}. The spectrum of oleic acid exhibits an additional maximum of lower intensity at 2242 rel. cm^{-1}, which is associated with the CD stretches at the position of the CC double bonds. The Raman intensities of the sp^2-hybridized carbons are generally not as pronounced as the CD intensities of sp^3-hybrids. The Raman spectrum of d8-arachidonic acid exhibits lower CD intensities, because all deuterium labels are at CC double bond positions. Furthermore, there are less deuterium atoms in the molecule. The maximum is observed at 2243 rel. cm^{-1}. All other Raman bands of the spectra can be assigned to various vibrations of the aliphatic chain of the fatty acids.

Palmitic acid is a saturated fatty acid, which does not contribute to biochemical pathways and is considered as biologically inactive. Oleic acid and arachidonic acid are unsaturated fatty acids and are biologically active, meaning that both are not only converted into triglycerides to serve as a storage of energy, but are part

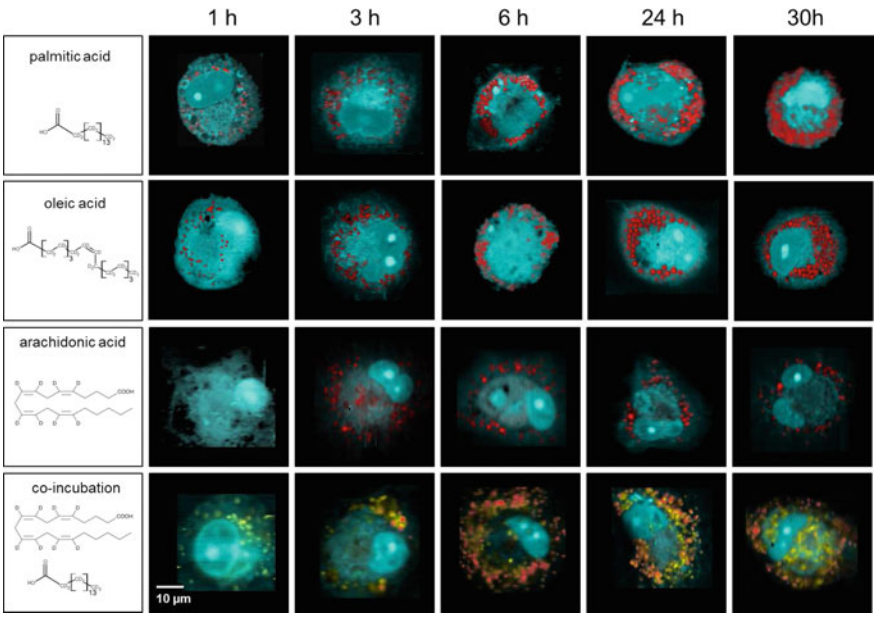

Fig. 13.10 Raman images of macrophages incubated with 400µm of deuterated fatty acids for different incubation times. For palmitic acid and oleic acid, the macrophages develop the typical foamy appearance for the long incubation times. The images where generated by using the N-FINDR spectral unmixing algorithm. The distributions of the different fatty acids are shown in red. For the co-cultivation of d8-arachidonic acid and d_{31}-palmitic acid the distributions are depicted in red and yellow, respectively

of other metabolic pathways. Oleic acid is one of the major constituents of vegetable fats and oils and its effect on health are relatively unknown. Arachidonic acid is present in membranes in the form of phospholipids and is involved in cellular signaling. Figure 13.10 shows Raman images of individual macrophages incubated with palmitic, oleic and arachidonic acid, as well as a co-incubation of palmitic and arachidonic acid over a time interval of up to 30 h. For the in vitro incubation, 400µm of deuterated serum albumin complexed fatty acids was added to an otherwise lipid free medium. After around 1 hour of incubation, the first intracellular incorporation was evident by the detection of the deuterium bands of the fatty acids. The Raman images were reconstructed using the N-FINDR spectral unmixing algorithm. The distributions of the deuterated fatty acids are plotted in red, whereas the cell bodies are depicted in light blue.

For palmitic and oleic acid the molecules aggregate very clearly in small lipid droplet organelles that are about 1µm on average, where fatty acids are usually stored in the form of triglycerides. For the early incubation times with arachidonic acid no significant uptake was detected. Also for the co-incubation only palmitic acid was detected. It should be noted that the CD stretching vibrations of the sp^2-hybridized carbons of the double bounds generally result in lower sensitivities compared to the

sp^3-hybridized CD bonds. After 3 h, the amount of fatty acid derivative-containing lipid droplet organelles steadily increases. In the case of palmitic and oleic acid, as well as for the co-incubation of palmitic and arachidonic acid, the macrophages apparently develop into foam cells, as can be noticed by the overwhelming amount of droplet formation after 24 and 30 h of incubation. The incubation with arachidonic acid alone does not lead to foam cell formation.

For quantification of the deuterated fatty acid molecules that are taken up by the macrophages it is possible to evaluate the intensities of the bands of the CD stretching vibrations. The continuous increase of the deuterated fatty acids becomes clearly obvious by plotting the endmembers of the N-FINDR algorithm associated with the images shown in Fig. 13.10. As an example, the endmembers for the different incubation times with palmitic acid are plotted in Fig. 13.11a.

Between 3 and 6 h, the intensities of the CD vibrations already exceed the CH intensities associated with the proteins and endogenously occurring lipids and other organic molecules in the cell. By plotting the ratios of the CD versus the CH intensities, the relative amount of fatty acids can be evaluated. The graph in Fig. 13.11b shows the increase over the time of the experiment, which can be fitted to $C(t) = C_\infty - (C_\infty - C_0)e^{-t/\tau}$, where C_∞ is the maximum or plateau value, which can be reached depending on the incubation conditions, C_0 is the initial CD/CH value, and τ the time point at which half of the plateau value is reached. For the incubation with d_{31}-palmitic acid the following values were calculated: $C_\infty = 2.107 \pm 0.072$ and $C_0 = 21 \pm 2$h. The initial CD/CH ratio is of course zero. After about 13 h CD scattering intensities of the d_{31}-palmitic acid residues start to exceed CH scattering intensities of the molecules the cell consists of. The plateau or saturation of the cells is reached after about 36 h.

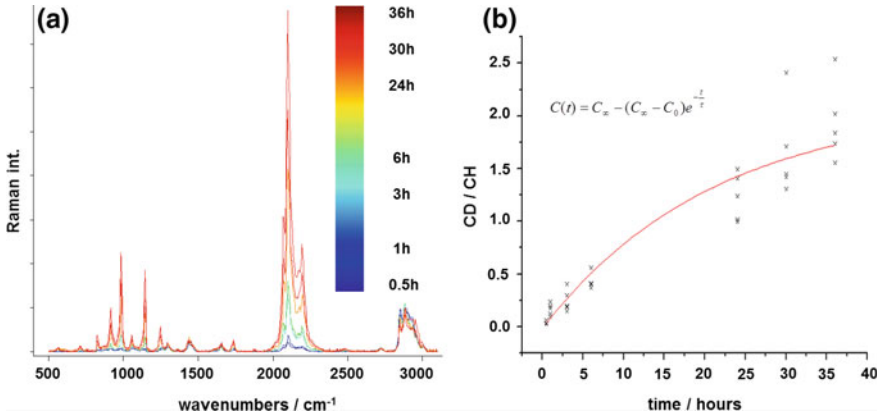

Fig. 13.11 **a** Raman endmember spectra of macrophages incubated with d_{31}-palmitic acid for different time intervals. The CD stretching vibrations steadily increase over time. The ratios of the integrated area of the Raman scattering intensities of the CD versus the CH vibrations are plotted in (**b**). The exponential increase can be fitted to an exponential curve as shown and as described in the text

Quantification of the oleic acid resulted in a very similar plot. Arachidonic acid on the contrary showed a level of saturation after only 8 h. Over time, the content of d8-arachidonic acid in lipid droplets is increasing. However, no foam cell formation is visible due to apparently no excessive formation and accumulation of lipid droplets inside the cells cytoplasm. This is in contrast to the incubation with saturated palmitic and monounsaturated oleic acid. The storage of arachidonic acid in lipid droplets is therefore less efficient. Our findings indicate that this fatty acid is not only stored in lipid droplets but may also be metabolized or subjected to other cellular compartments, for example, in form of phospholipids. The co-supplementation studies also showed clear foam cell formation for long incubation times and a non-homogenous storage pattern in lipid droplets is obvious. In contrast to palmitic acid, arachidonic acid is not stored homogenously in all lipid droplets [46, 47].

13.3.3 Drug Delivery Systems

Many biologically active compounds that may have the potential to be used as therapeutic agents exhibit low efficiency in in vivo experiments due to low bio-availability at the site of action [48, 49]. Apart from physiological reasons, such as metabolic changes before the compound reaches its target organ or tissue, physical properties (for instance solubility, hydrophobicity, or the pK_a value) may hinder the desired activity of a drug. In many treatments, especially in cancer therapy, the active compound has to pass through the cellular membrane to reach its site of action inside the cells of the diseased/target tissue. Furthermore, once inside the cell a compound may be recognized as foreign and be degraded by lysosomal pathways. To overcome these problems, it would be beneficial to deliver the active compound to the actual site of action, not only to the target tissue, but also to the cellular organelles where bioactivity/effect is greatest [26]. Possible intracellular targets are the nucleus for gene therapy [48, 50–52], mitochondria for pro-apoptotic therapy [51, 53], or lysosomes for the therapy of lysosomal storage diseases. Cellular and subcelluar targeting could increase the efficiency of a drug while decreasing the magnitude and occurrence of side effects.

Such considerations have led to the development of so-called drug delivery systems. Extensive research exploring possible chemical structures of drug delivery systems has been performed. Many of these structures are small self-assembling systems that form nano-scale vesicles. These nanoparticles can enclose various compounds and can be designed such that release does not take place before the delivery system has reached its target site. Among the most popular self-assembling nanocarriers are lipid bilayer structures or liposomes, amphiphilic molecules that form micelles and particles composed of biodegradable polymers. To support cell membrane penetration, organelle specificity, or to bypass lysosomal degradation, the surface of these particles may be modified with antibodies, cell-penetrating peptides, or the particles may be constructed from molecules that are pH sensitive and thus release their drug load after entering a low pH environment, such as that of a cancer cell.

So far, the most common approach to image nanoparticle uptake and subcellular distribution is to add a small percentage of a fluorophore to the particles [26, 49]. In principle, this method provides important insight and information about cellular uptake and distribution patterns. However, if the fluorescent labels are not covalently bound to the nanoparticle constituents, the fluorophore may diffuse out of the particles and subsequently show a different distribution that does not correlate with the distribution of the nanocarriers. Although fluorescent labels are widely used in biological applications, fluorophores are generally bulky compounds and the extent of fluorophore interference with the innate activity of drug is a topic surrounded by much contention. If the fluorophore is covalently attached to the nanoparticles' component molecules, it may alter the chemical properties and biological behavior of the core material. Alternative techniques for cellular imaging and trafficking would be invaluable in verifying the results of fluorescent imaging and to compensate for the aforementioned pitfalls of common fluorescent labeling. In the following sections, we are introducing the results of intracellular uptake and trafficking kinetics of drug delivery systems using the spectral information of Raman image acquisition.

13.3.3.1 Liposomes

As mentioned before, one of the promising delivery systems are liposome-based structures. Liposomes are constructed from self-assembling phospholipid molecules that consist of hydrophobic alkane chains and a hydrophilic head group. The molecules form a membrane-like bilayer where the hydrophobic parts point towards each other. The size of these spherical bilayers can vary from around 50nm up to a micron. The feasibility of liposomes as drug delivery systems has been repeatedly demonstrated [54–56]. Although important information regarding the uptake kinetics of liposomes by cells as well as their intracellular distribution and degradation is obtained by applying various techniques, such as small-angle X-ray spectroscopy [56], fluorescence microscopy [49], flow cytometry and spectral bio-imaging [57], many issues related to the fine mechanisms of the liposome/cell interaction remain unresolved.

Again, the phospholipids of the liposomes where labeled with deuterium. Figure 13.12 shows a Raman spectrum of liposomes composed of deuterated 1, 2-distearoyl-d_{70}-sn-glycero-3-phosphocholine (DSPC-d_{70}) in an aqueous environment. The spectrum is clearly dominated by the scattering intensities of the C-D vibrations of the aliphatic side chains between 2000 and 2310 rel. cm^{-1}. All other peaks in the region between 650 and 1800 rel. cm^{-1} are of lower intensity. The CH stretches of the un-deuterated bonds of the phophoester residue appear between 2800 and 3020 rel. cm^{-1}. Spectra of pure vesicles in water were acquired as single position spectra at 2s exposure.

Figure 13.13 shows Raman images of MCF-7 cells incubated with DSPC-d_{70} liposomes for 12 h at a concentration of 2mg/ml. Figure 13.13a1–a3 were constructed from the abundances of the three most dissimilar spectra or end-members found by the VCA algorithm. The endmember spectra are shown in Fig. 13.13c1–c3. The blue

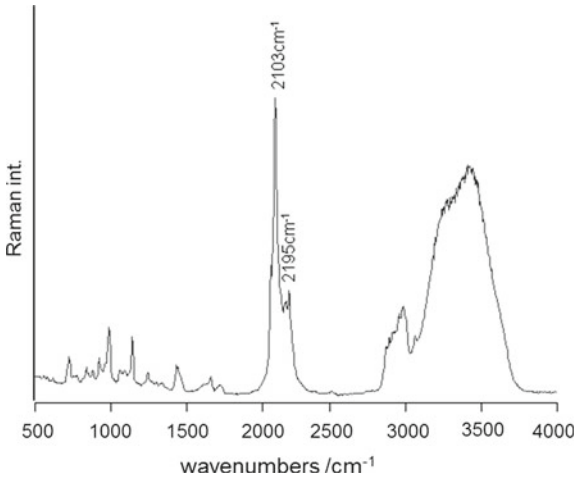

Fig. 13.12 Raman spectrum of DSPC-d_{70} based liposomes in aqueous environment

endmembers show the typical protein features as discussed in the previous section. By plotting the abundances, the cell bodies can be depicted. The green endmembers show very typical features of lipids or phospholipids, which show the distribution of the small vesicles. The red endmembers are very similar to the spectra of the deuterated liposomes and therefore reveal the distribution of the liposomes inside the cells.

It can be seen that after 12 h of incubation a significant amount of liposomes have entered the cells. It appears that they aggregate as small droplet-like inclusions (probable endosomes), which can be found all over the cell body. The size of these aggregates is about 1 to 2μm or smaller. It is known that liposomal nanoparticles enter the cell via macropinocytosis [26, 58], which can be followed by secondary endocytosis and could lead to aggregation on the micrometer scale. However, Rayleigh scattering of very small particles can lead to spots of apparent size larger than the effective one. Thus, some of the observed spots may in reality be smaller than the theoretical spatial resolution. Twelve hours of incubation were needed in order to reproducibly detect liposomal inclusions in most of the cells. After 6 h, very few cells showed inclusions. It is reasonable to assume that between 6 and 12 h the amount of uptake increases linearly before it reaches a plateau. Interestingly, longer incubation times up to 24 h did not result in significantly more inclusions. However, the longer the incubation time, the more inclusions were found in the perinuclear region rather than around the cell peripheries [59]. For every incubation time approximately ten cells were imaged.

In order to enhance the uptake, liposomes were modified with a cell-penetrating peptide, derived from a trans-activating transcriptional activator peptide (TAT-p) from HIV. Carrier systems modified with the TAT peptide are currently considered very promising for drug delivery systems. Figure 13.14 shows the VCA images of MCF-7 cells that were incubated with TAT-p modified DSPC-d_{70} liposomes for 3, 6 and 9 h.

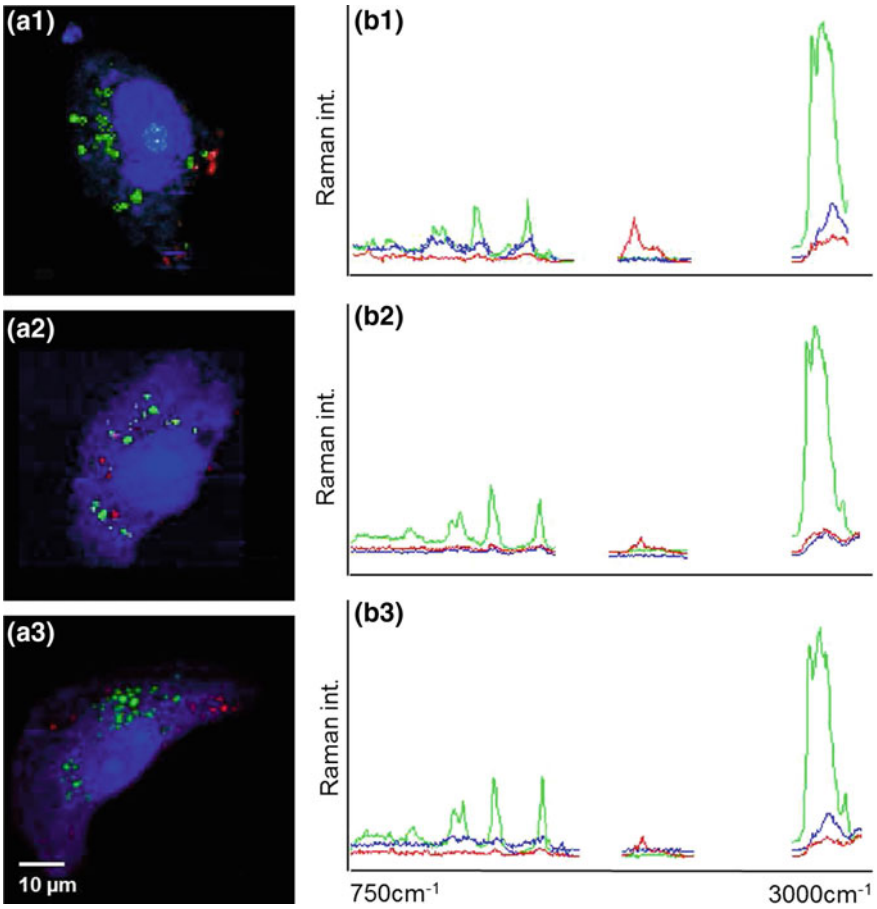

Fig. 13.13 VCA results of MCF-7 cells incubated with DSPC-d_{70} liposomes for 12 h: **a** images were generated using the VCA algorithm for the spectral regions from 750 to 1800 rel. cm^{-1}, 2000 to 2300 rel. cm^{-1} and 2800 to 3100 rel. cm^{-1}. **b** shows the corresponding endmember spectra. The abundances plotted in red show the distribution of the liposomes, green are lipid rich regions, blue depicts proteins

As in the previous images, the protein distribution is plotted in blue; regions rich in lipids or phospholipids are plotted in green and the localization of the liposomes are depicted in red. Very obvious is the tremendous enhancement of the uptake efficiency. Not only is the amount of liposomes that penetrate the membranes increased, but also the necessary incubation times are significantly reduced. After 3 h, large aggregates can be seen around the edges of the cells. Another 3 h of incubation lead to the penetration of the whole cell body, and after 9 h the liposome concentration appears to be largest in the perinuclear region. Due to the enhancement in uptake, the translocation of the liposomes inside the cell bodies can be clearly followed.

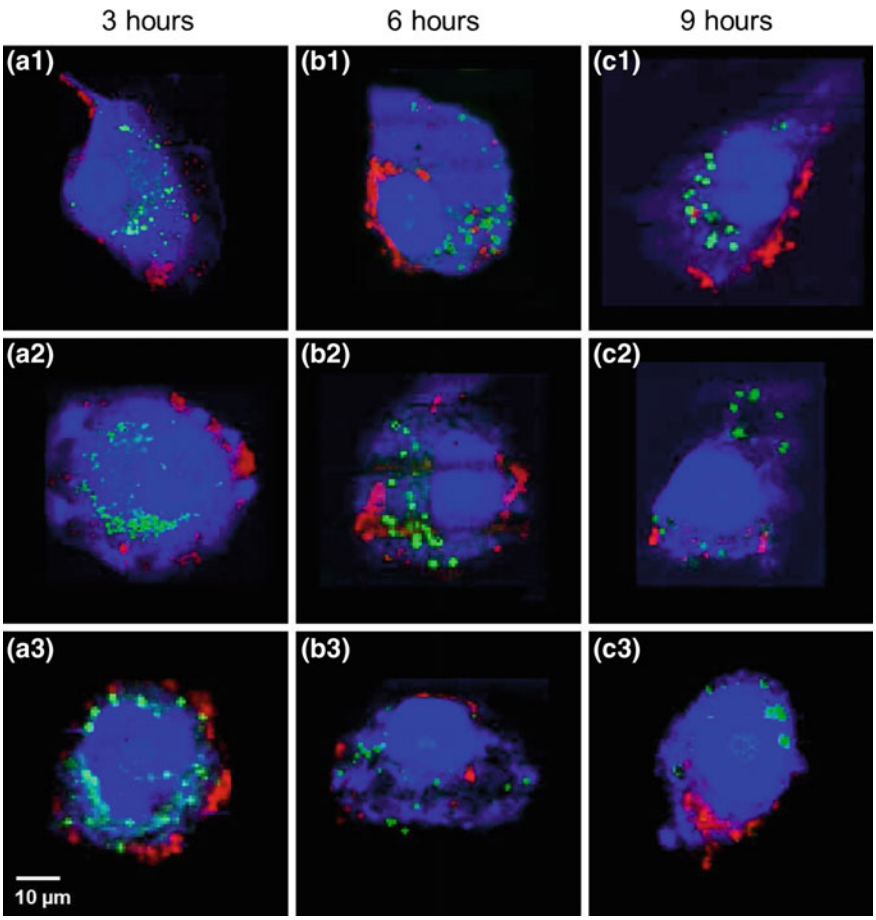

Fig. 13.14 VCA generated images of MCF-7 cells incubated with TAT-p modified DSPC-d_{70} liposomes for 3, 6 and 9 h (color-coding as in Fig. 13.13). The abundances of the modified liposomes are shown in red. The corresponding endmember spectra are shown in Fig. 13.15

Comparing the endmembers associated with the individual incubation times shown in Fig. 13.15, it should be pointed out that the endmembers from the cells incubated for 3 h show the distinct features of the protein, lipid, and liposome components, whereas the blue endmember spectra associated with the lipid-rich regions for the 6 and 9 hour incubations show significant contributions from the C-D vibrations of the liposome phospholipids. Currently, it is not known what the long-term fate of the phospholipids introduced by the uptake of liposome structures is. Even though active intracellular fusion processes of lipids from nanoparticles are entropically un-favored, model studies have shown that lipid transfer between membrane vesicles is generally possible [60–62]. It is conceivable that over time phospholipids from liposomes become incorporated into intracellular membranes.

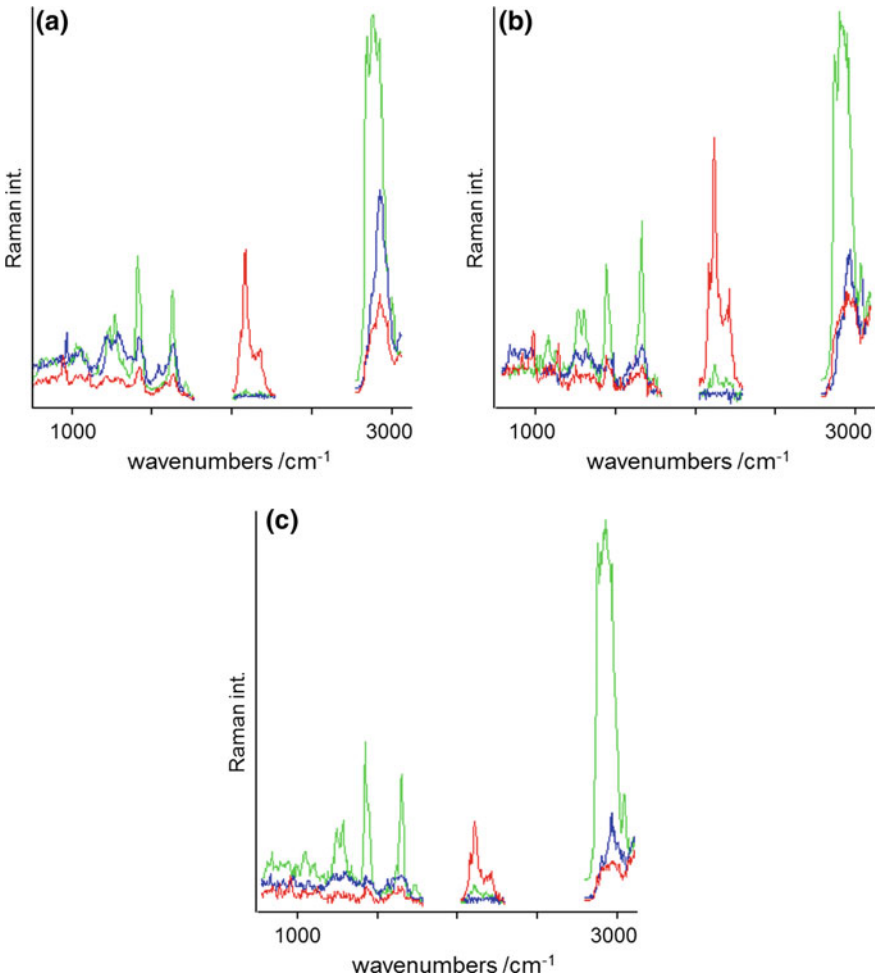

Fig. 13.15 Typical VCA endmember spectra from cells incubated with TAT-p modified DSPC-d_{70} liposomes for **a** 3, **b** 6 and **c** 9 h. The corresponding abundances are shown in Fig. 13.14

13.3.3.2 Biodegradable Polymeric Nanocarriers

Under physiological conditions a number of polymers get degraded, usually by hydrolysis, and therefore offer a variety of biomedical applications. Several biodegradable polymers have been tested as platforms for nano-sized carrier systems. Apart from applications as nanocarriers, biodegradable polymers may serve as coatings for cardiovascular stent implants or as aerosol particles for intrapulmonary drug delivery [63–65]. Among the most popular polymers, which have been approved by the American Food and Drug Administration (FDA) for therapeutic devices, are particles based on poly(ethylene glycol) (PEG) also called poly(ethylene oxide), (PEO),

poly(D,L-lactic-glycolic acid) (PLGA), and poly(ε-caprolactone) (PCL). Employing solvent displacement methods in an organic solvent / water system, the polymers assemble into nano-sized particles, which can subsequently be loaded with smaller molecules.

The particles used in the studies described here were composed of a PEO-PCL polymer blend. To further test the capability of Raman microscopy to follow the uptake of deuterated species, a set of experiments was performed in which the actual payload of the carrier system was deuterated. As a biologically active species, a compound of the ceramide family was selected. Ceramides are known to act as second messenger signaling molecules involved in differentiation, proliferation and apoptosis [66]. Endogenous ceramide (synthesized by sphingomyelin hydrolysis or by de novo synthesis) elicits a response to extracellular stimuli such as irradiation and chemotherapeutic agents [66, 67]. Ceramides contribute to the apoptotic pathway through the activation of apoptotic inducers, the creation of protein permeable channels in the mitochondria outer membrane and the clustering of CD95 (death receptor) in cell membranes [66, 68]. The molecule chosen here was N-palmitoyl-d_{31}-D-erythro-sphingosine (C16-d_{31} ceramide), in which the fatty acid side-chain was fully deuterated.

Figure 13.16 shows the Raman spectra of the plain PEO-PCL nanoparticles, the C16-d_{31} ceramide and the particles loaded with 20% w/w ceramide. All spectra are dominated by the C–H stretching intensities between 2800 and 3100 rel. cm^{-1}. The C-D stretching vibrations of the deuterated alkyl side chain are shifted to 2030 and 2230 rel. cm^{-1}. The spectrum of the loaded particles can be seen as a superposition of the ceramide and the PEO-PCL spectrum.

Figure 13.17 shows the VCA images of HeLa cells treated with C16-d_{31} ceramide loaded PEO-PCL nanoparticles for 7 and 14 h. Again, the abundances of the three most dissimilar endmembers were used to reconstruct the images. The distribution of the endmembers resembling protein spectra are plotted in blue, the endmembers that contain the C-D intensities from the deuterated alkyl chains of the ceramide are in red. The third endmembers are plotted in green and are likely to correlate with the regions where a high concentration of mitochondria is expected. Similar to the liposomes, the PEO-PCL particles appear as small aggregates, which are present within the cytoplasm after 7 h of incubation. Apart from the bright red spots, one can notice areas of a darker red color that seem less dense. Spectra from both regions along with an enhanced image of cell C are shown in Fig. 13.18. The spectrum from the bright red aggregates still exhibits spectral features associated with the PEO-PCL particles, since the shape of the C–H stretching band is very similar and the peak of the ester linkage of the PCL is obviously present. The spectra from the dark red regions, on the other hand, do not show these features. The ceramide molecules are still associated with the nanoparticles in the bright regions and have dissociated from the nanocarrier in the dark red regions. The C-D intensities of the dark red regions rather overlay with spectral features from proteins. Thus, either the ceramide diffused out of the particles or the particles/polymers have already been transformed through cellular metabolism. Little is known about the life time of these particles inside the cytoplasm. However, one can notice a very fine distribution of the ceramide, within

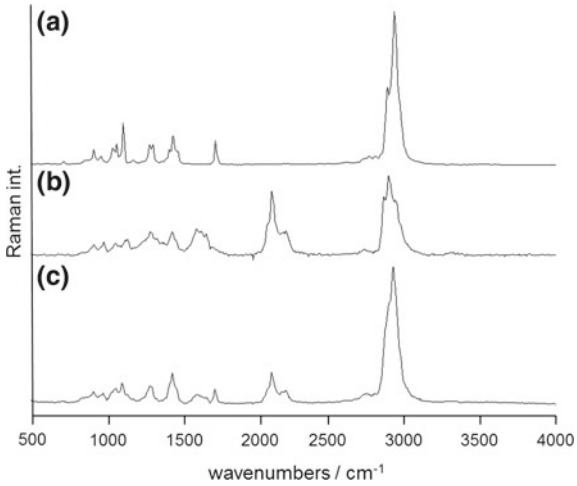

Fig. 13.16 Raman spectra of the plain poly(ethylene oxide)-modified poly(epsilon-caprolactone) (PEO-PCL) nanoparticles (**a**), the C16-d_{31} ceramide (**b**) and the particles loaded with 20% of the ceramide (**c**)

the cytoplasm. It is unlikely that the molecules originate from the aggregates shown in bright red.

Consistent with the liposome experiments, incubation times were selected such that most of the cells had incorporated significant amounts of nanoparticles, which was apparent after 7 h. Incubation for another 7 h did not result in significant additional uptake. Images for 14 h of incubation are shown in the second row in Fig. 13.17. Similar to the results for 7 h, the C-D intensities are either associated with spectral features from the nanoparticles or with spectral features from proteins. It is possible that the upper limit of the uptake processes is regulated by how much each individual cell is able to tolerate. It is not possible to say at this point, whether the limitation is set by the amount of nanoparticles, the amount of ceramide, or by other factors such as particle size or shape. With respect to the amount of uptake, the results from the experiments with the PEO-PCL nanoparticles are similar to the results from the liposome study. In both cases, a certain level or limit was reached after approximately 7 h for the PEO-PCL particles and 12 h for the liposomes. Although it is difficult to quantify the amount of particles that are taken up, it seems that fewer of the PEO-PCL particles get into the cell, but they tend to form larger aggregates. The period of 7 h was apparently sufficient for the cells to metabolize some of the polymeric nanoparticles, whereas the liposomes were stable and showed only translation to the perinuclear region. The experiments with the TAT-p modified liposomes indicated clearly that the phospholipids from the liposomes fuse with intracellular membranes. Perhaps very long incubation times with the non-modified liposomes would show the same result. Thus, the fate of the delivery systems based on liposomes and polymeric nanoparticles is completely different. By comparing the incubation times needed to

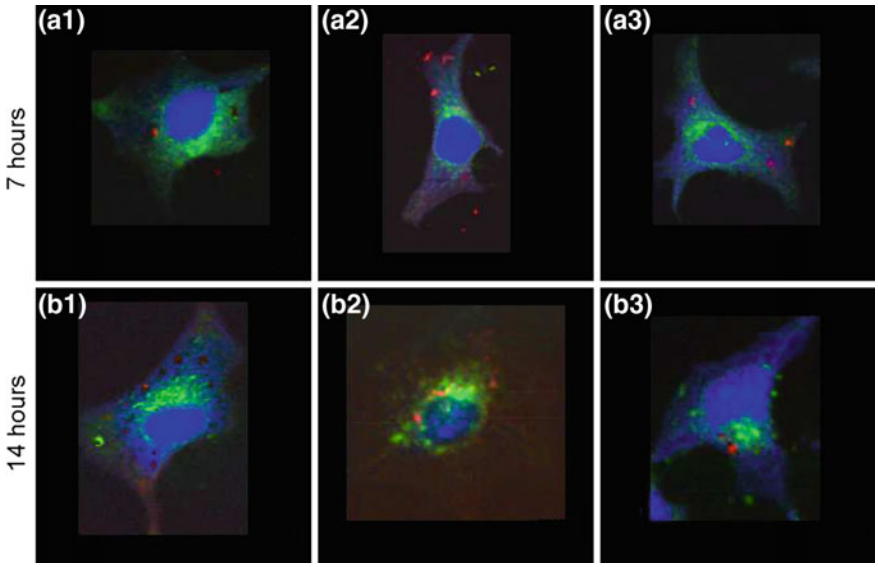

Fig. 13.17 VCA images of HeLa cells treated with C16-d_{31} ceramide loaded poly(ethylene oxide)-modified poly(epsilon-caprolactone) (PEO-PCL) nanoparticles for 7 and 14 h. The distribution of the deuterated ceramide is shown in red

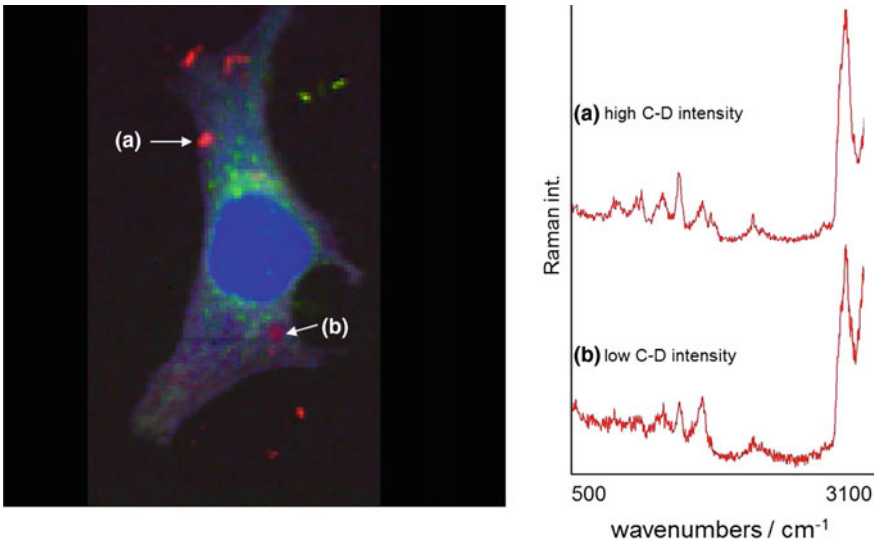

Fig. 13.18 VCA image of a HeLa cell incubated with C16-d_{70} ceramide loaded poly(ethylene oxide)-modified poly(epsilon-caprolactone) (PEO-PCL) particles and Raman spectra with high and low C-D stretching intensities. The spectra from the bright red regions (**a**) still show spectral features of the PEO-PCL particles, whereas the spectra from the dark red regions (**b**) have typical protein features indicating a dissociation of the deuterated ceramide from the nanoparticles

reach a level of saturation, it is possible to conclude that the PEO-PCL particles are taken up faster, by about a factor 2, than the non-modified liposomes.

13.4 Conclusion

The results presented here show the great potential of Raman microscopy for cell imaging applications. In terms of spatial resolution, the images can clearly rival conventional optical microscopy yet with the benefit of adding compositional information. Perhaps the greatest advantage of the technique is that main cellular features or organelles, such as the nucleus, nucleoli, mitochondria or lipid-rich regions can be visualized without any external labels. Although fluorescence staining protocols are widespread and well-established in biology, they are often laborious and difficult to reproduce. Multiple staining procedures may be needed to image more than one feature. As demonstrated here, confocal Raman microscopy in combination with multivariate data analysis offers an interesting alternative for label free non-invasive imaging. The employed methods have, by no means, been exhausted. Different spectral regions may be more sensitive to different types of organelles, and different algorithms may extract different spectral information. To correlate the outcome of multivariate data analysis with well-established staining techniques is an ongoing effort in our research.

The results of the HCA and VCA algorithms are highly intriguing. Both algorithms recognize main morphological features in all cell types presented here. As mentioned before, HCA leads to very good signal-to-noise ratios of the mean cluster spectra. Although HCA is computationally expensive, for very noisy datasets the method may be preferable over the VCA algorithm. VCA, on the other hand, is faster and results in better image contrast because the algorithm does not average over neighboring pixels. Depending on the nature of the dataset, one or the other method may be favorable.

The concept of deuterium labels for Raman microscopic imaging as an alternative for fluorescence microscopy has been demonstrated for the intracellular uptake of lipids as well as for liposome nanocarriers. The fact that labeling with stable isotopes does not change the chemical features of the molecules of interest is of great advantage over other labeling techniques. Furthermore, because of the absence of photobleaching, a quantification of Raman imaging data sets is more reliable compared to fluorescence imaging.

The outcomes of the uptake experiments are very encouraging. The main emphasis of the model studies presented here was to show that Raman microscopy may serve as a new imaging modality to follow the uptake and intracellular fate of biologically interesting compounds. The experiments show that the technique certainly has enough sensitivity. It was possible to image the uptake of liposome-based systems as well as drug-loaded polymeric nanocarriers. For the latter, the dissociation of the active compound was monitored successfully. Especially the concept of deuterium labeling is very promising. In principle, any organic molecule may be labeled with

deuterium. If a sufficient amount of the substance of interest is incorporated into the cell body, Raman microscopy may offer plenty of possibilities to non-invasively study uptake mechanisms, efficiencies, and metabolic transformations of various compounds on cells grown in in vitro cell cultures.

Acknowledgements We would like to thank Judy Newmark and Carol Warner for their inspirations and help with the oocyte images. Partial support for this research was provided by the NIH (Grant No. CA 090346 to M.D.). Funding from the IGERT nanomedicine education program (to T.C. and L.M.) is gratefully acknowledged. We gratefully acknowledge the financial support by the Carl Zeiss Stiftung and the "Jenaer Biochip Initative 2.0" (JBCI 2.0). The project "JBCI 2.0" (03IPT513Y) within the framework "InnoProfile-Transfer -Unternehmen Region" is supported by the Federal Ministry of Education and Research (BMBF), Germany.

References

1. A. García-Sáez, P. Schwille, Appl. Microbiol. Biotechnol. **76**(2), 257 (2007)
2. C. Lim, B. Cho, BMB. Rep. **46**(4), 188 (2013)
3. C. Grienberger, A. Konnerth, Neuron **73**(5), 862 (2012)
4. C. Hsieh, S. Chen, Y. Lee, Y. Yang, C. Sun, Opt. Express **16**(15), 11574 (2008)
5. F. Festy, S. Ameer-Beg, T. Ng, K. Suhling, Mol. Biosyst. **3**(6), 381 (2007)
6. N. Sijtsema, A. Tibbe, I. Segers-Nolten, A. Verhoeven, R. Weening, J. Greve, C. Otto, Biophys. J. **78**(5), 2606 (2000). http://www.biophysj.org/cgi/content/abstract/78/5/2606
7. C. Otto, N. Sijtsema, J. Greve, Eur. Biophys. J. **27**(6), 582 (1998)
8. H.J. van Manen, Y. Kraan, D. Roos, C. Otto, Proc. Natl. Acad. Sci. USA **102**(29), 10159 (2005). https://doi.org/10.1073/pnas.0502746102. http://www.pnas.org/cgi/content/abstract/102/29/10159
9. B. Wood, L. Hammer, L. Davis, D. McNaughton, J. Biomed. Opt. **10**(1), 014005 (2005). http://link.aip.org/link/?JBO/10/014005/1
10. S. Verrier, I. Notingher, J. Polak, H.L.L., Biopolymers **74**(1–2), 157 (2004). https://doi.org/10.1002/bip.20063
11. K. Nithipatikom, M.J. McCoy, S. Hawi, K. Nakamoto, F. Adar, W. Campbell, Anal. Biochem. **322**, 198 (2003). http://www.ingentaconnect.com/content/els/00032697/2003/00000322/00000002/art00521. https://doi.org/10.1016/.ab.2003.07.020
12. N. Uzunbajakava, A. Lenferink, Y. Kraan, E. Volokhina, G. Vrensen, J. Greve, C. Otto, Biophys. J. **84**(6), 3968 (2003). http://www.biophysj.org/cgi/content/abstract/84/6/3968
13. N. Uzunbajakava, C. Otto, Opt. Lett. **28**(21), 2073 (2003)
14. C. Matthäus, S. Boydston-White, M. Miljković, M. Romeo, M. Diem, Appl. Spectrosc. **60**(1), 1 (2006)
15. N.M. Sijtsema, C. Otto, G. Segers-Nolten, A. Verhoeven, G.J., Biophys. J. 74(6), 3250 (1998). http://www.biophysj.org/cgi/content/abstract/74/6/3250
16. B. Wood, D. McNaughton, Expert. Rev. Proteomics. **3**, 525 (2006). http://www.ingentaconnect.com/content/ftd/epr/2006/00000003/00000005/art00008. https://doi.org/10.1586/14789450.3.5.525
17. A. Feofanov, A. Grinchine, L. Shitova, T. Karmakova, R. Yakubovskaya, M. Egret-Charlier, P. Vigny, Biophys. J. **78**(1), 499 (2000)
18. S. Arzhantsev, A. Chikishev, N. Koroteev, J. Greeve, C. Otto, N. Sijtsema, J. Raman Spectrosc. **30**, 205 (1999)
19. C. Krafft, T. Knetschke, R. Funk, R. Salzer, Anal. Chem. **78**(13), 4424 (2006). http://pubs3.acs.org/acs/journals/doilookup?in_doi=10.1021/ac060205b

20. C. Matthäus, T. Chernenko, J. Newmark, C. Warner, M. Diem, Biophys. J. **93**(2), 668 (2007). https://doi.org/10.1529/biophysj.106.102061. http://www.biophysj.org/cgi/content/abstract/biophysj.106.102061v1
21. N. Keshava, Lincoln. Lab. J. **14**(1), 55 (2003)
22. J. Nascimento, J. Bioucas Dias, IEEE Trans. Geosci. Remote. Sens. **43**(4), 898 (2005). 0196–2892
23. M. Miljković, T. Chernenko, M. Romeo, B. Bird, C. Matthäus, M. Diem, Analyst **135**(8), 2002 (2010)
24. M. Hedegaard, C. Matthäus, S. Hassing, C. Krafft, M. Diem, J. Popp, Theor. Chem. Acc. **130**, 1249 (2011)
25. B. Kann, H. Offerhaus, M. Windbergs, C. Otto, Adv. Drug. Deliv. Rev. **15**(89), 71 (2015)
26. V. Torchilin, Annu. Rev. Biomed. Eng. **8**, 343 (2006)
27. C. Krafft, M. Kirsch, C. Beleites, G. Schackert, R. Salzer, Anal. Bioanal. Chem. **389**(4), 1133 (2007)
28. B. de Jong, T. Schut, K. Maquelin, T. van der Kwast, C. Bangma, D. Kok, G. Puppels, Anal. Chem. **78**(22), 7761 (2006)
29. C. Krishna, G. Sockalingum, R. Bhat, L. Venteo, P. Kushtagi, M. Pluot, M. Manfait, Anal. Bioanal. Chem. **387**(5), 1649 (2007)
30. C. Chang, IEEE Trans. Geosci. Remote Sens. **43**(3), 502 (2005)
31. M. Winter, Proc. SPIE **3753**, 266 (1999)
32. M. Schnoor, P. Cullen, J. Lorkowski, K. Stolle, H. Robenek, D. Troyer, J. Rauterberg, S. Lorkowski, J. Immunol. **180**, 5707 (2008)
33. M. Schnoor, I. Buers, A. Sietmann, M. Brodde, O. Hofnagel, H. Robenek, S. Lorkowski, J. Immunol. Methods **344**, 190 (2009)
34. S. Dipali, S. Kulkarni, G. Betageri, J. Pharm. Pharmacol. **48**(11), 1112 (1996)
35. W. Liang, T. Levchenko, V. Torchilin, J. Microencapsul. **21**, 151 (2004)
36. V. Torchilin, T. Levchenko, A. Lukyanov, B. Kwah, A. Klibanov, R. Rammohan, G. Samokhin, K. Whiteman, Biochim. Biophys. Acta. **1511**, 397 (2001)
37. D. Shenoy, M. Amiji, Int. J. Pharm. **293**(1–2), 261 (2005)
38. D. Naumann, Appl. Spectrosc. Rev. **36**(2–3), 239 (2001)
39. T.G. Spiro, Biological Applications of Raman Spectroscopy, vol. 1 (Wiley, 1987)
40. C. Yu, E. Gestl, K. Eckert, D. Allara, J. Irudayaraj, Cancer. Detect. Prev. **30**(6), 515 (2006). http://www.sciencedirect.com/science/article/B6X28-4MCW9N6-4/1/f1be1eb8a2bd6bcbd84c3bc8a20ed470
41. K. Short, S. Carpenter, J. Freyer, J. Mourant, Biophys. J. **88**(6), 4274 (2005). https://doi.org/10.1529/biophysj.103.038604. http://www.biophysj.org/cgi/content/abstract/88/6/4274
42. T. Collins, M. Bootman, J. Exp. Biol. **206**(12), 1993 (2003). https://doi.org/10.1242/jeb.00244. http://jeb.biologists.org/cgi/content/abstract/206/12/1993
43. C. Matthäus, T. Chernenko, L. Quintero, L. Milan, A. Kale, M. Amiji, V. Torchilin, M. Diem, in *Biophotonics: Photonic Solutions for Better Health Care*, vol. 6991 (SPIE, 2008), vol. 6991, pp. 699,106–108. http://link.aip.org/link/?PSI/6991/699106/1
44. J. van Blerkom, Reproduction **128**, 269 (2004)
45. C. Warner, J. Newmark, M. Comiskey, S. De Fazio, D. O'Malley, M. Rajadhyaksha, D. Townsend, S. McKnight, B. Roysam, P. Dwyer, C. DiMarzio, Reprod. Fertil. Dev. **16**, 729 (2004)
46. C. Stiebing, C. Matthäus, C. Krafft, A. Keller, K. Weber, S. Lorkowski, J. Popp, Anal. Bioanal. Chem. **406**(27), 7037 (2014)
47. C. Matthäus, C. Krafft, B. Dietzek, B. Brehm, S. Lorkowski, J. Popp, Anal. Chem. **84**(20), 8549 (2012)
48. V. Torchilin, Eur. J. Pharm. Sci. **11**(Supplement 2), S81 (2000). http://www.sciencedirect.com/science/article/B6T25-41KPF70-9/1/5e8f6c99b36e1d549dcab7bb408d2213
49. V. Torchilin, Adv. Drug. Deliv. Rev. **57**(1), 95 (2005)
50. C. Plank, W. Zauner, E. Wagner, Adv. Drug. Deliv. Rev. **34**(1), 21 (1998)
51. G. Kaul, M. Amiji, Pharm. Res. **22**(6), 951 (2005)

52. J. Panyam, V. Labhasetwar, Adv. Drug. Deliv. Rev. **55**(3), 329 (2003)
53. J. Chawla, M. Amiji, Int. J. Pharm. **249**(1–2), 127 (2002)
54. V. Torchilin, Nat. Rev. Drug. Discov. **4**, 145 (2005)
55. L. Serpe, M. Guido, R. Canaparo, E. Muntoni, R. Cavalli, P. Panzanelli, C. Della Pepal, A. Bargoni, A. Mauro, M. Gasco, M. Eandi, G. Zara, J. Nanosci. Nanotechnol. **6**(9–10), 3062 (2006)
56. N. Rao, V. Gopal, Biosci. Rep. **26**(4), 301 (2006)
57. U. Huth, R. Schubert, R. Peschka-Süss, J. Control Release **110**(3), 490 (2006)
58. J. Wadia, R. Stan, S. Dowdy, Nat. Med. **10**(3), 310 (2004)
59. C. Matthäus, A. Kale, T. Chernenko, V. Torchilin, M. Diem, Mol. Pharm. **5**(2), 287 (2008)
60. J. Kristl, B. Volk, P. Ahlin, K. Gombac, M. Sentjurc, Int. J. Pharm. **256**, 133 (2003)
61. J. Wojewodzka, G. Pazdzior, M. Langner, Chem. Phys. Lipids **135**(2), 181 (2005)
62. C. Palmerini, C. Cametti, S. Sennato, D. Gaudino, E. Carlini, F. Bordi, G. Arienti, J. Membr. Biol. **211**, 185 (2006)
63. E. Kang, J. Robinson, K. Park, J. Cheng, J. Control Release **122**(3), 261 (2007)
64. A. Belu, C. Mahoney, K. Wormuth, J. Control Release **126**(2), 111 (2008)
65. D. Edwards, J. Hanes, G. Caponetti, J. Hrkach, A. Ben-Jebria, M. Eskew, J. Mintzes, D. Deaver, N. Lotan, R. Langer, Science **276**(5320), 1868 (1997)
66. L. Siskind, J. Bioenerg. Biomembr. **37**(3), 143 (2005)
67. A. Struckhoff, R. Bittman, M. Burow, S. Clejan, S. Elliott, T. Hammond, Y. Tang, B. Beckman, J. Pharmacol. Exp. Ther. **309**(2), 523 (2004)
68. E. Gulbins, H. Grassmé, Biochim. Biophys. Acta. **1585**(2–3), 139 (2002)

Chapter 14
Raman Imaging of Biomedical Samples

Agnieszka Kaczor, Katarzyna M. Marzec, Katarzyna Majzner, Kamila Kochan, Marta Z. Pacia and Malgorzata Baranska

Abstract Fluorescence microscopy, a gold standard in the tissue or cell imaging, has several drawbacks, with a severe one being its disability to elucidate the chemical characteristics of the sample. Confocal Raman microscopy is a tempting label free alternative to fluorescence and a prospective future method of medical diagnostics. Raman measurements of tissues can provide information about their chemical composition, i.e. main components but also specific compounds, and their changes upon the development of patholog or its treatment. The analysis is based on characteristic marker bands, provided they can be identified in the spectra, or by more common approach using chemometrics. Moreover, Raman microscopy can be used to detect small biochemical alterations and their respective distribution in a single cell or even at sub-cellular level. The impact of various factors, including the uptake of drugs, bioactive compounds or non-chemical stressors can be observed using such investigations of cells.

14.1 Introduction

In this chapter the reader can find several examples of tissues (PART I; Sect. 14.2) and cells (PART II; Sect. 14.3) imaging using Raman spectroscopy and microscopy combined with other complementary or reference methods. Each part begins with an *Experimental* section, where details on the sample preparation,

A. Kaczor · K. Majzner · K. Kochan · M. Z. Pacia · M. Baranska (✉)
Faculty of Chemistry, Jagiellonian University, Ingardena 3,
30-060 Krakow, Poland
e-mail: baranska@chemia.uj.edu.pl

A. Kaczor · K. M. Marzec · K. Majzner · K. Kochan · M. Z. Pacia
M. Baranska
Jagiellonian Centre for Experimental Therapeutics, Jagiellonian University,
Bobrzynskiego 14, 30-348 Krakow, Poland

K. M. Marzec
Center for Medical Genomics (OMICRON), Jagiellonian University
Medical College, Kopernika 7C, 31-034 Krakow, Poland

J. Toporski et al. (eds.), *Confocal Raman Microscopy*, Springer Series
in Surface Sciences 66, https://doi.org/10.1007/978-3-319-75380-5_14

data acquisition and data analysis are provided. That is followed by a *Results and Discussion* section, where biochemical analysis of various tissues or cells is discussed in the context of diagnosis and treatment of some modern lifestyle diseases.

In PART I (Sect. 14.2), various approaches for imaging the tissues from murine models of diseases of affluence are shown. Hypertension, atherosclerosis or diabetes are related to alterations in the vessel wall and, particularly, in the endothelium, the innermost layer (*tunica intima*) of the vessel wall separating the *tunica media* (smooth muscle cells with elastin and collagenous components) from the lumen of the blood vessel. Since the endothelial dysfunction is an early feature of such pathologies, the implementation of Raman imaging to study diseases of affluence is, therefore, aimed at identifying subtle differences in chemical and structural composition and in distribution of components in the endothelium.

The key issue in studying thin tissue layers, such as endothelium, is the clear assignment of their signal. Conventional cross-section preparation yields information about the whole vessel wall. However, sometimes this is not practical, as extraction of the signal from the endothelial layer of the thickness of about 1μm is complicated (practically the information has to be read out from 1–2 voxels). The additional problem is the fact, that a delicate endothelial layer, intrinsically uneven, can be even more perturbed due to microtome section cutting. Therefore, as an alternative, we adopted so-called *en face* preparation, previously used in scanning electron microscopy (SEM) [1–3] and atomic force microscopy (AFM) [4, 5] studies, in which the accessible surface of the endothelium is large and easy to image. In our developed methodology, *en face* tissue, in which the vessel wall is resected and split open, was submitted to combined Raman and AFM imaging [6]. Additionally, application of depth profiling combined with the independent analysis of subsequent layers enabled to define changes in the endothelium and *tunica media*, separately [7]. So, depending on the scientific aim, either cross-section or *en face* preparation was applied.

The verification of applicability of the combined Raman-AFM approach to study vessel walls and to recognize key cellular compartments was done based on the comparison with fluorescence imaging (Fig. 14.1) [8].

Figure 14.1 demonstrates that confocal Raman distribution images are in perfect agreement with the images of the immunochemically stained tissue, clearly visualizing distribution of key cellular components and compartments. Additionally, AFM data complement Raman images with information about the tissue topography and compressibility.

In PART II (Sect. 14.3), the potential of Raman imaging of single cells is discussed. With Raman microscopy we can detect small biochemical changes and their distribution at the sub-cellular level [9]. Investigations of cells allow tracking of changes under the impact of various factors, e.g. monitoring the uptake of drugs, nanoparticles and bioactive compounds, as well as non-chemical stressors [10–14]. Raman measurements with spatial resolution ~300nm (limited by Rayleigh criterion) allow for detection and characterization of such small structures as nucleolus, nucleoli, mitochondria, lipid droplets (LDs; or lipid bodies) or introduced nanoparticles [15–18].

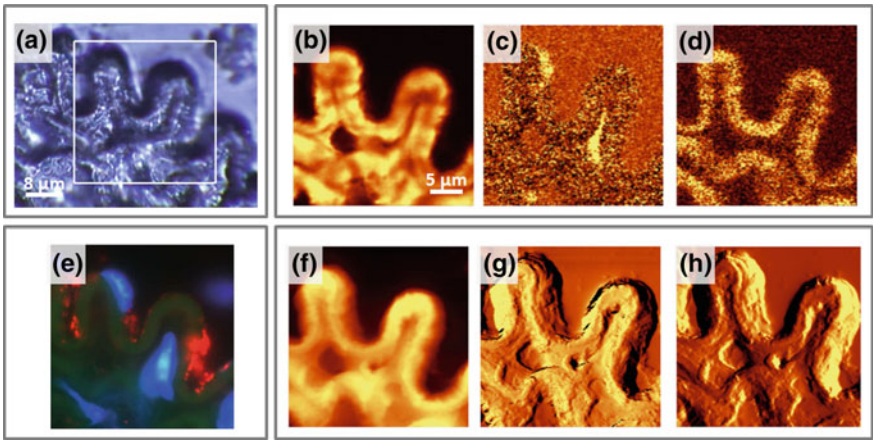

Fig. 14.1 Comparison of Raman-AFM combined imaging with fluorescence imaging of a vessel wall cross-section: The visual image [×100, (**a**)], Raman images showing distribution of organic matter (**b**), cell nuclei (**c**) and elastin fibres (**d**), fluorescence images of immunochemically stained tissue (**e**), red, blue and green denote endothelium, nuclei and elastin fibres, respectively), topography image (**f**), phase image (**g**) and amplitude image (**h**)

In cell biology most commonly used methods are electron microscopy and fluorescence microscopy. Each of these techniques requires a specific sample preparation, thus modifying sample composition and changing its physiological conditions. With Raman microscopy, changes in the cells during the cell cycle, cell death, drug-cell interactions, proliferation and differentiation can be successfully studied avoiding the above mentioned modifications [19, 20].

14.2 Part I

14.2.1 Experimental

14.2.1.1 Sample Preparation

For diabetes, hypertension and cancer metastasis, the samples were resected from a thoracic fragment of the murine aorta.[1] Two types of sample preparation were used: cross-section of aorta and aorta *en face* (split open, Fig. 14.2).

For the cross-section preparation, the samples were fixed for 10 min in 4% buffered formalin (Merck), embedded in optimal cutting temperature (OCT) medium

[1] All procedures involving animals were conducted in accordance with the Guidelines for Animal Care and Treatment of the European Union and were approved by the 1st Local Animal Ethics Commission in Krakow (decision no. 51/2009).

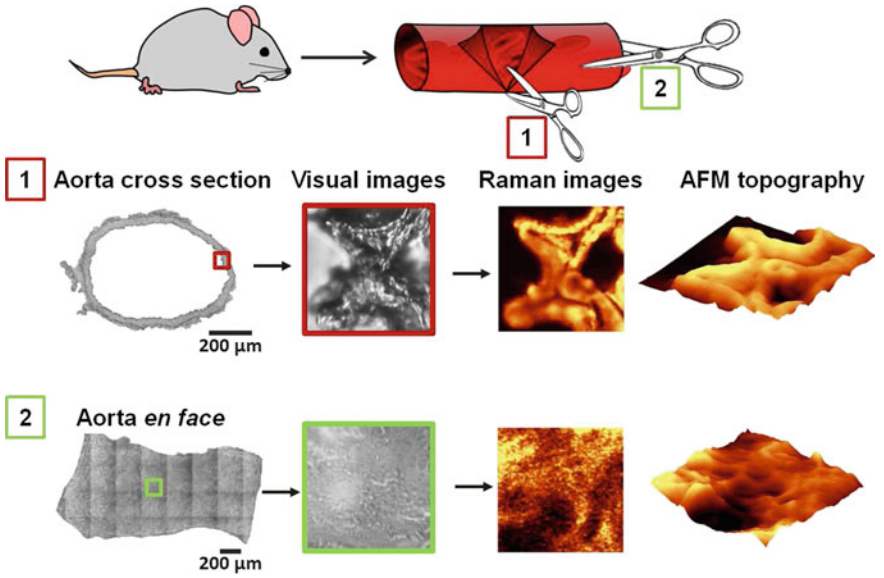

Fig. 14.2 Schematic illustration of methodology of sample preparation and measurement: Cross-sections of aorta (1) or resected and split-open aorta fragments (2) were mounted on CaF_2 slides. For cross-section samples, the area of the sample was chosen in a way to allow imaging of the inner-most (endothelium) part. Samples were submitted to Raman imaging and (in selected cases) subsequent AFM imaging

(Thermo) and frozen at −80 °C. Cross-sections of 5µm thickness were cut with the microtome and mounted onto cell-Tak®-coated calcium fluoride slides. For *en face* preparation, the resected and split-open fragments of arteries were tightly glued to the cell-Tak®-coated calcium fluoride slides. Then tissues were preserved by a 10 min soak in 4% buffered formalin (Merck) and rinsed twice with distilled water.

For fluorescent detection of endothelial caveolin-1 (murine model of diabetes type 2) the tissue sections, prepared by blocking reagent and pre-incubation, were incubated with polyclonal rabbit anti-caveolin-1 antibody (Sigma) and cholera toxin B subunit (Sigma). Nuclei were stained using a Hoechst 33258 solution (Sigma).

For the examples of atherosclerosis plaque studies presented here, the cross-sections of brachiocephalic arteries (BCA) with visible lesions were taken from ApoE/LDLR$^{-/-}$ mice of different ages or with different types of diets (chow, AIN-93G, LCHP). As the same cross-sections were used for co-localized IR, Raman, AFM and staining, a routine methodology was defined in the following way. The isolated BCA were fixed for 6 h in 4% buffered formalin. After fixation, BCA were mounted for further 6 h in a tissue freezing medium (Leica, Germany) with distilled water (1:1) and finally embedded in the OCT medium and frozen at −80 °C. The 5mm thick cross-section slides were put on CaF_2 slides. OCT was washed out before measurements.

For liver tissue sections the following procedure of sample preparation was used: immediately after collection, livers were embedded in OCT medium and frozen at −80 °C. Immediately prior to the measurements, livers were cut into sections of 10μm thickness in a cryostat chamber (−23°C) and placed on CaF_2 slides. Tissues were preserved using 4% buffered formalin solution (10 min). The remainder of the fixative and OCT were washed out with distilled water (2 × 5 min).

Tissue sections were measured directly after preparation. If necessary, they were stored no longer than 48 h, ensuring conditions of zerolight exposure, as it is known that light and time strongly affect the unsaturation degree of lipids [21].

14.2.1.2 Data Acquisition

Raman imaging was done using the WITec alpha300 Raman microscope, which was equipped with an air cooled solid-state laser operating at 532 nm and a CCD detector (cooled to −65 °C). The laser was coupled to the microscope via a polarization maintaining, single mode optical fibre. A 100× air objective (Olympus, MPlan FL, NA = 0.9) was used. The scattered radiation was focused onto a multi-mode fibre (50μm diameter) and a single monochromator (focal length of 300mm and aperture ratio equal to f/4). The integration time for a single spectrum varied from 0.2–0.3s, and the spectral resolution was equal to $3cm^{-1}$ (600grooves/mm grating used). The spectrometer was calibrated using the spectrum of a Mercury/Argon atomic emission lamp (WITec). Additionally, standard alignment procedures (single point calibration) were performed before each measurement with the use of the Raman scattering line produced by a silicon sample (520.5 rel. cm^{-1}). The sampling density of the results presented here varied from 0.2 to 1.7μm, while the laser power on the sample was in the range of 5–10mW (intensity in the focus spot). Such power allowed for tissues measurements without photo-damage of any of the measured cells. In selected cases 3D confocal Raman imaging of the tissues was performed by imaging repeatedly the same area at several heights of the sample moving in steps of 0.5μm up until a considerable decrease in the signal was observed. The central layer was chosen at the Z-position of the maximal intensity of the Raman signal (see for example Fig. 14.4).

Usually, subsequent to Raman measurements, AFM and IR (sometimes before Raman) measurements were performed for selected samples in the diabetes, cancer metastasis and atherosclerosis models. AFM imaging was done in the AC (equivalent to tapping) mode or PFM (Pulsed Force Mode) with force modulation AFM probes (k = 2.8N/m, WITec) and a step resolution of 0.1μm. Fluorescence imaging was acquired with an Al-Si Nikon confocal laser scanning system built onto a Nikon inverted microscope Ti-E using a Plan Apo 100×/1.4 oil DIC objective. The images were acquired at a resolution of 1024 × 1024pixels. Specimens were excited with 405, 488 and 561nm diode lasers.

Histochemical staining of liver tissue sections was performed with Oil Red O (Sigma-Aldrich, St. Louis, MO, USA) according to the following scheme: deionized

water (3 min), 60% isopropanol alcohol (2 min), Oil Red O (30 min) and deionized water (1 min). After the application of listed solutions tissue sections were covered with glycerol gel.

14.2.1.3 Data Processing

Raman data analysis was performed with Opus™ and WITec Project Plus™ 2.10 software. Raman images were generated based on the integrated intensity of marker bands and were calculated without pre-processing. Cluster analysis was carried out after cosmic ray removal and background subtraction (using a polynomial or auto-polynomial function). K-Means Clustering (KMC) results were obtained using the Manhattan method for distance calculation. The number of clusters was determined in order to obtain the best recognition between the clusters. This number depended on the size of the imaged area, sampling density and complexity of the sample. The averaged single spectra extracted from the obtained clusters follow the spectral profile of the assigned components.

For statistical analysis, t-Test or ANOVA were applied using commercial computer software (Origin Pro 9.1, OriginLab). Results are presented as means±SEM (standard error of mean). A difference between means was considered significant if $p < 0.05$.

The ImageJ processing program [22] was used to calculate the size of lipid raft aggregates (diabetes) and the elastin fibre area (hypertension).

14.2.2 Results and Discussions

14.2.2.1 Type 2 Diabetes Mellitus (T2DM)

Long standing diabetes leads to structural and functional changes in both the micro- and the macro vasculature system, particularly in the endothelium. To investigate these changes, a multiparameter approach based on the combination of Raman confocal 3D imaging with AFM was applied to analyze alterations in the endothelium in the murine model of diabetes (Fig. 14.3). Leptin-receptor deficient mice (db/db) [23] were used as a model for type 2 diabetes, while heterozygotic db+ mice established the control group. Simultaneous application of Raman and AFM imaging to the same area of the sample enabled obtaining information about both the chemical composition and physical properties of studied tissue fragments in the *en face* preparation [24].

The apparent differences observed in the images of the endothelium of the db/db and db+ mice were related to the presence of the lipid-rich structures at the very top of the studied tissue, i.e. at the uppermost layer of the endothelium. The combination of Raman imaging and AFM was a key point in characterization of these structures, which formed upon the pathology progress. Obviously, these structures

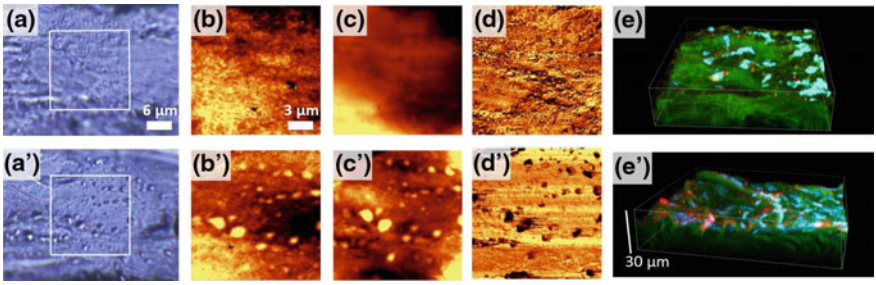

Fig. 14.3 Combined Raman and AFM imaging of *en face* aorta in db/db [diabetic, (**a**–**e**)] and db+ [control, (**a**′–**e**′)] mice: Visual images (**a**, **a**′), Raman distribution images obtained by integration of the range 2800–3100 rel. cm^{-1} (**b**, **b**′), AFM topography images (**c**, **c**′), AFM phase images (**d**, **d**′) and confocal fluorescence images [(**e**, **e**′); endothelial caveolin-1, cell nuclei and elastin fibers visualized in red, blue and green channels] for db+ (**a**–**e**) and db/db (**a**′–**e**′) samples. Figure adapted upon Creative Commons Attribution License from [24]

had an increased lipid content as shown by the enhanced intensity of the band due to the C-H stretching vibrations (2800–3100 rel. cm^{-1} range) in the Raman images of samples from mice with developed diabetes. Topography AFM images indicated that these assemblies were protuberances of the tissue surface, while the phase images demonstrated that they had a considerably different physicochemical character relative to the surroundings. This observation confirmed that these protuberances were localized, above the surface of the tissue and were not deposited below the membrane level. A detailed chemical characterization of the observed lipid-rich structures was undertaken based on the depth profiling of the tissue and subsequent analysis of the recorded spectra with the help of cluster analysis (K-means, Manhattan distance). Figure 14.4 presents the results of the cluster analysis of the single lipid-rich structure [24].

The central part of the structure, extracted as an orange class, exhibited a Raman signature significantly different than the surroundings of the assembly. Generally, the increased intensity of the bands characteristic for lipids (at 1745, 1446–1455, 1300–1315, 1134 and 1075 rel. cm^{-1}) was observed in the average spectrum of this class. In addition, the increase of the intensity of the band at ca. 1099 rel. cm^{-1}, due to the symmetric phosphate stretching mode, and the appearance of two other features: at ca. 780 rel. cm^{-1}, due to the O-P-O bending mode and, particularly, at 725 rel. cm^{-1}, assigned to the symmetric stretching vibrations of the $N^{+}(CH_3)_3$ choline group in sphingolipids [25] was also observed. The chemical characteristic of the lipid-rich assemblies along with the AFM-based information about the localization of theses protuberances on the very top of the endothelium enabled identification of these structures as aggregated lipid rafts. Lipid rafts are nanoscale assemblies that may agglomerate into bigger structures upon certain stimuli as described in [26]. A way of initiation of this process is, among others, cross-linking of lipid raft proteins with the cholera toxin or anti-caveolin-1 antibody, a method enabling fluorescent detection of caveolin-1, the raft characteristic protein [27]. Fluorescence microscopy is the main

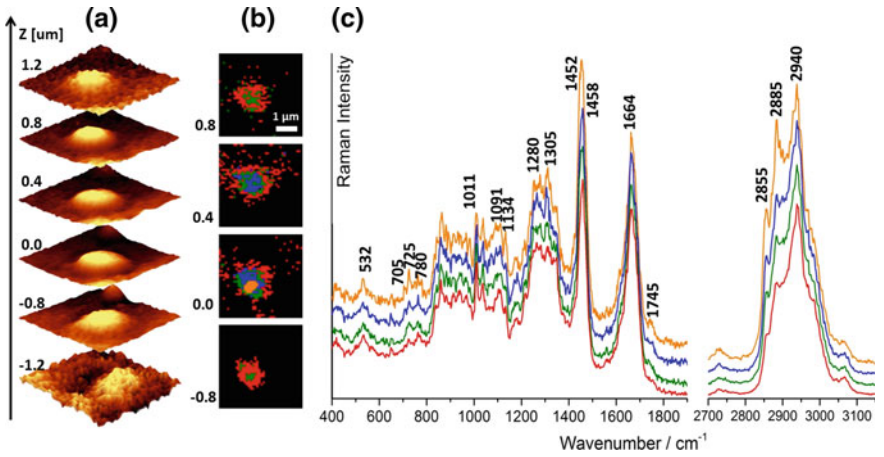

Fig. 14.4 Depth profiling of the aggregated lipid raft: Raman distribution images (integration over the band in the 2800–3100 rel. cm^{-1} range) at different depths [denoted by Z value, the layer marked as Z = 0.0µm was chosen by maximizing the Raman intensity signal, (**a**)], Cluster Analysis of the corresponding images (**b**) with the averaged spectra of the clusters [(**c**), spectra were normalized to the 1011 rel. cm^{-1} band and offset in order to emphasize the differences between them. The Raman intensity in the 2700–3200 rel. cm^{-1} range is 3.5-fold relatively to the fingerprint region]. Figure adapted upon Creative Commons Attribution License from [24]

method used to study lipids rafts and it was used also to confirm the Raman and AFM based observations (Fig. 14.3e, e'). In agreement with the results of Raman-AFM imaging, fluorescence images also demonstrated a significant increase in the number and size of lipid rafts aggregates in the endothelium of the db/db mice compared with the control ones. Nevertheless, fluorescence detection of rafts possesses the inherent problem related to the above-mentioned label-induced aggregation [27]. Therefore, the label-free methodology based on subsequent Raman and AFM imaging, has the advantage of registration of unperturbed and size-conserved lipid rafts assemblies. The benefit of this approach is the possibility of the estimation of the size of formed aggregates. AFM is the method of significantly better spatial resolution relative to confocal Raman microscopy, therefore, obtained AFM topography images were used to calculated the height and the x,y dimensions of lipid rafts aggregates (Fig. 14.5a).

The size of the observed lipid rafts assemblies spanned the range of 300–3000nm in x, y and ca.30–300nm in z. It was also noticed comparing 16- and 20-weeks old mice that with pathology development the size (particularly the height) of lipid raft aggregates increased due to progressive clustering of rafts into bigger platforms [24]. Additionally, interrelation of Raman and AFM-based data enabled to correlate the lipid content in the lipid raft aggregates with their size (Fig. 14.5b). The overall lipid content, measured as the ratio of the integral intensity of the band characteristic for lipids and proteins at ca. 2940 rel. cm^{-1} to the band due to phenylalanine at ~1005 rel. cm^{-1}, increased with the increase of the area of rafts. The increase of the lipid character of lipid rafts with the size (and therefore the disease progression)

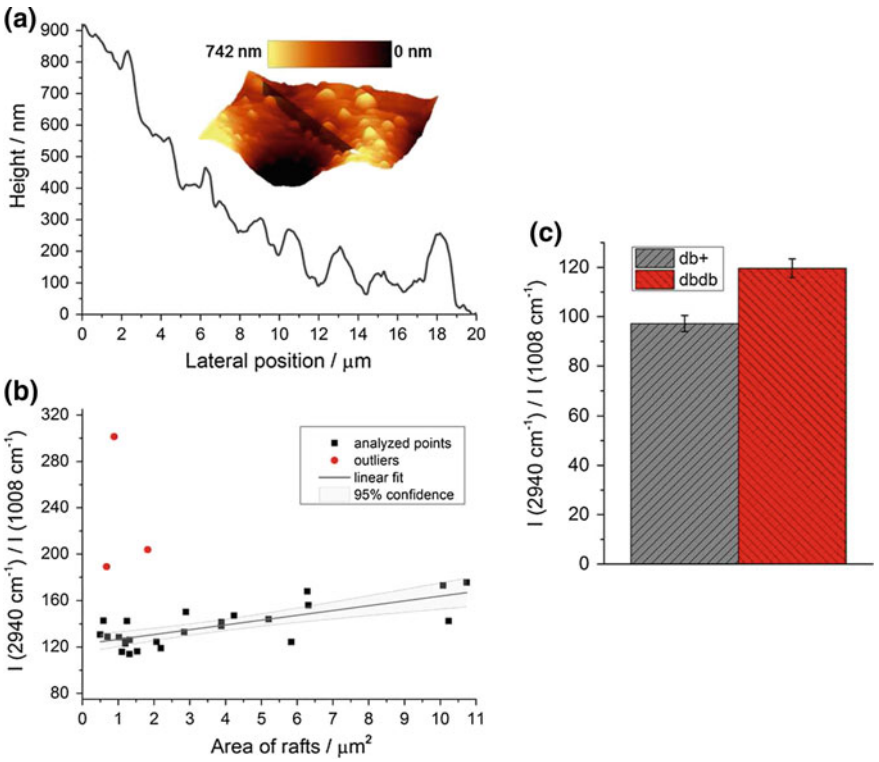

Fig. 14.5 The size and lipid content of lipid raft aggregates in endothelium upon diabetes development: A representative AFM topography image with the cross-section showing the height of lipid aggregates (**a**), correlation of the rafts area and their relative lipid content (**b**) and comparison of the average lipid content in the db+ and db/db tissue (**c**). Figure adapted upon Creative Commons Attribution License from [24]

resulted in one more pattern, i.e. the overall increase of the lipid content in the tissue upon T2DM development, observed in the average Raman spectra of tissue as the increase in the intensity of the band at ca.2940 rel. cm^{-1} to the feature at ~1005 rel. cm^{-1}. The increase of the overall lipid content in the tissue is, therefore, caused by aggregation of lipid rafts in the endothelium resulting in about ten-fold increase of the lipid rafts coverage of endothelium surface.

It is important to underline that elucidation of the pathological mechanism associated with lipid rafts aggregation was possible due to the application of the methodology based on the combined confocal Raman imaging and AFM. Raman data enabled a detailed chemical characteristics of lipid rafts, while AFM topography images demonstrated the localization of these structures. Additionally, phase AFM images served as proof that the observed structures coated the endothelium i.e. they were not covered with the cellular membrane as for example lipid droplets. Additionally, the AFM images enabled determination of the size of lipid rafts aggregates. Interrelation

of Raman and AFM data that resulted in correlation of the size of rafts with their chemical composition showed that lipid character increased with the increased size of the aggregates [24].

14.2.2.2 Hypertension

Hypertension, a condition of elevated blood pressure, is associated with the vascular stiffness, endothelial dysfunction and abnormalities in nitric oxide (NO) production pathway [28, 29]. To evaluate endothelial changes upon hypertension development three groups of animals were studied: control mice (C57BL/6J), animals supplemented with L-nitroarginine methyl ester (L-NAME, 8 weeks treatment; 100mg kg^{-1}) and, to evaluate efficiency of treatment, NO-deficient mice supplemented with nitrate (8 weeks treatment; 100mg kg^{-1} + $NaNO_3$ in a dose of 1mmol kg^{-1}) [30]. Representative Raman images of aorta cross-sections for these three groups of animals are shown in Fig. 14.6a–c.

No apparent differences were observed in the Raman distribution images of vessel wall cross-sections in the three groups of animals studied. Additionally, as the boundary between the *tunica intima* and *media* was not clear, separation of the signal from the endothelium was impossible based on these images. Therefore, multivariate data analysis was applied to extract the endothelial layer observed in Fig. 14.6 (column 4)

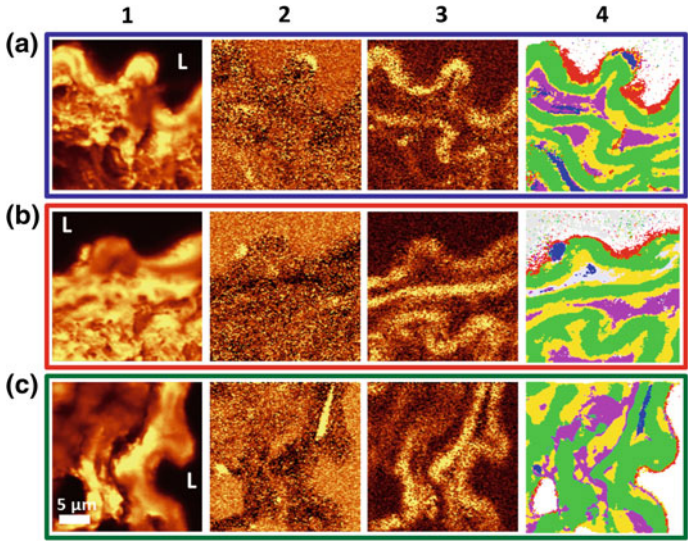

Fig. 14.6 Representative images of aorta cross-sections in control (row **a**), NO-deficient (row **b**) and NO-deficient nitrate-treated (row **c**) mice: Raman images showing distribution of organic matter (column 1, integration in the 3100–2800 rel. cm^{-1} range), cell nuclei (column 2, integration in the 775–800 rel. cm^{-1} range) and elastin fibers (column 3, integration in the 540–560 rel. cm^{-1} range) with cluster analysis images (K-means, Manhattan distance, column 4)

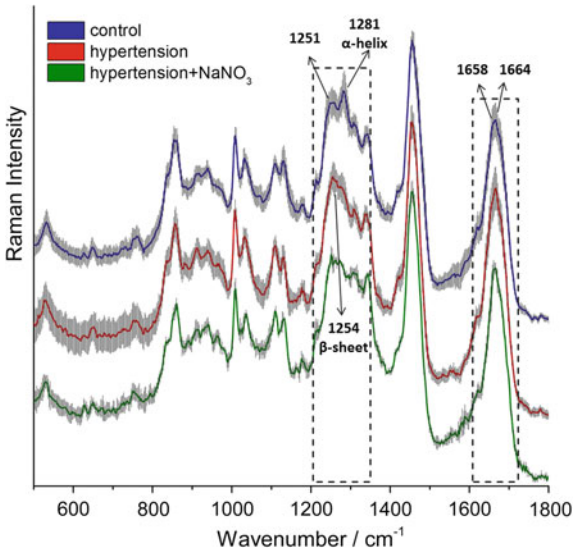

Fig. 14.7 Comparison of the average endothelium spectra in control, NO-deficient and NO-deficient, nitrate-treated mice: The average spectra of the control (blue: 360 spectra, 7 animals), NO-deficient hypertensive (red: 360 spectra, 7 animals) and nitrate-treated (green: 250 spectra, 3 animals) mice taken from the endothelium region with standard deviation on each data point of the spectra. Adapted from [30] with permission from The Royal Society of Chemistry

as the red class. Extraction of the endothelium signal was verified by the localization of the endothelial nuclei and the internal elastic lamina (Fig. 14.6, column 3 and the green cluster in 4). To determine global changes in the endothelium Raman profile upon hypertension development and nitrate treatment, the representative spectra of the endothelium were obtained by averaging of random spectra extracted from Raman measurements of control, NO-deficient and NO-deficient nitrate-treated groups of mice (Fig. 14.7). Overall, 12 Raman measurements were recorded both for the vessel wall of control and NO-deficient hypertensive mice and 5 for the nitrate-treated hypertensive animals, and 360 and 250 spectra in total were averaged for control/NO-deficient and NO-deficient drug-treated hypertensive mice, respectively.

The average spectra demonstrate chemical alterations occurring in the endothelium upon hypertension development and nitrate treatment (Fig. 14.7). The most evident changes were observed in the 1400–1200 rel. cm^{-1} spectral region (i.e. Amide III region) and were related to changes in the secondary structure of endothelial proteins. Particularly, the decrease in the intensity of the band at 1281 rel. cm^{-1}, assigned predominantly to the α-helix protein structure, and the parallel increase of the intensity of the signal at 1254 rel. cm^{-1}, attributed to the β-sheet, observed in the average spectra of mice with hypertension (both treated and untreated) were indicative of the α to β protein structural conversion. Additionally, analogical changes were seen in the Amide I range. The relative abundance of the band at 1656 rel. cm^{-1}, characteristic for the α-helix (and lipids), decreased from 27 to 22% in favour of the β-sheet counterpart at 1668 rel. cm^{-1} that increased from 25 to 30% [30]. Significantly, none of the above-mentioned alterations were reversible upon treatment, as the spectral profiles of hypertensive and hypertensive drug-treated endothelium were quite alike in the Amide I and III ranges. Previously, structural rearrangement of α-helix to

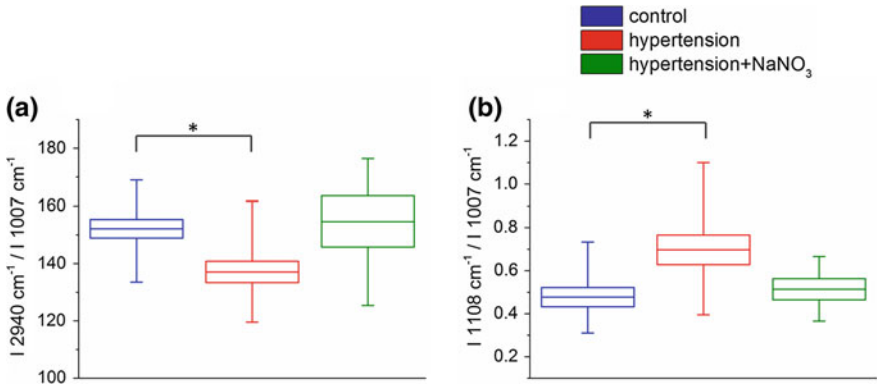

Fig. 14.8 Chemical changes in the murine endothelium upon hypertension and nitrate-treatment. The ratio of the integral intensity of bands at 2940/1005 rel. cm^{-1} (**a**) and 1108/1005 rel. cm^{-1} (**b**) in the endothelium of control (blue box), NO-deficient hypertensive (red box) and NO-deficient drug-treated mice (green box). Boxes, lines and whiskers denote standard error, mean and max/min values, respectively; $*$, $p < 0.05$

the β-sheet have been observed upon melanoma skin cancer [31] and diabetes [32] development.

As the lipid and protein relative content is an important marker of the pathological changes in the tissues, the relative lipid to protein ratio was calculated for the average spectra of the endothelium in three studied groups of mice based on the integral intensity of the band for lipids and proteins centered at 2940 rel. cm^{-1} and the phenylalanine band at ~1005 rel. cm^{-1}. The resulting ratio (Fig. 14.8a) demonstrated that hypertension resulted in the statistically significant increase of the lipid content relatively to the protein content in the endothelium.

This chemical change, contrarily to the previously described rearrangement of the secondary protein structure, was fully reversible upon treatment as the lipid to protein level increased up to the level in control upon nitrate supplementation of the NO-deficient hypertensive animals. Additionally, the change in the relative intensity of the band at 1108 rel. cm^{-1} was observed as shown in Fig. 14.8b. This band is assigned to the twisting vibrations of the NH_2 group [33] and very often assigned to desmosine and isodesmosine [34], amino acids characteristic for elastin structure. The proposed explanation for the increase of the intensity of the band at 1108 rel. cm^{-1} relatively to the band at ~1005 rel. cm^{-1} was the increased production of elastin-forming amino acids (desmosine and isodesmosine) in the endothelium upon pathology development. Alterations related to the band at 1108 rel. cm^{-1} were also reversible upon treatment.

Investigation of cross-sections of aorta enabled determining changes not only in the endothelium, but also in the deeper layers of the tissue sample. Vascular remodeling of the vessel wall, manifested as thickening of the elastin fibers was clearly seen in the Raman images of *tunica media* of animals with hypertension (both treated and untreated, Fig. 14.9), in agreement with previous reports [35].

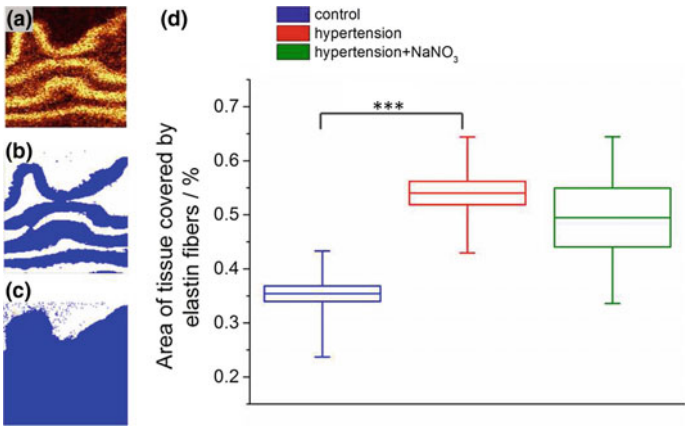

Fig. 14.9 Hypertension-induced changes in *tunica media*: A Raman image of elastin fibers (integration in the 540–560 rel. cm^{-1} range, **a**) in the vessel wall of the control mice and the images showing methodology of calculating the elastin thickness: images showing the area covered by elastin (**b**) versus tissue area (**c**) and the calculated tissue area covered by elastin fibers for control, NO-deficient and NO-deficient nitrate-treated mice (**d**). Boxes, lines and whiskers denote standard error, mean and max/min values, respectively; $***$, $p < 0.005$

Various structural (the relative increase of the β-sheet content versus the α-helix, thickening of elastin fibers in *tunica media*) and chemical (the relative decrease of lipid-to-protein ratio and increase of the content of the elastin-forming amino acids) changes associated with the development of hypertension were characterized in the vessel wall based on Raman imaging. Additionally, the efficacy of the nitrate supplementation on hypertension development in the vessel wall was assessed, showing that chemical, but not structural alterations in the vessel wall can be reversed upon nitrate supplementation.

14.2.2.3 Cancer Metastasis

Molecular specificity in conjunction with chemometric methods of data analysis makes Raman spectroscopy a potent tool to recognize precancerous or early cancerous changes in tissues [36–38], but not too much attention was devoted to study metastasis processes with the help of this technique. It has been recently reported that the endothelium, being a barrier for migrating cancer cells, undergoes significant alterations upon cancer metastasis [39–41]. To investigate these changes, the combined Raman and AFM imaging of the *en face* vessel wall of BALB/c mice (7–8 weeks old females, Charles River Laboratories) orthotopically inoculated with viable 4T1 tumor cells (American Type Culture Collection) and healthy BALB/c mice was performed [7]. In order to extract the signal from the endothelium, Raman imaging was repeated for several layers of the sample, starting from the layer of the maximum signal and going up every 0.5μm up to the layer where the Raman

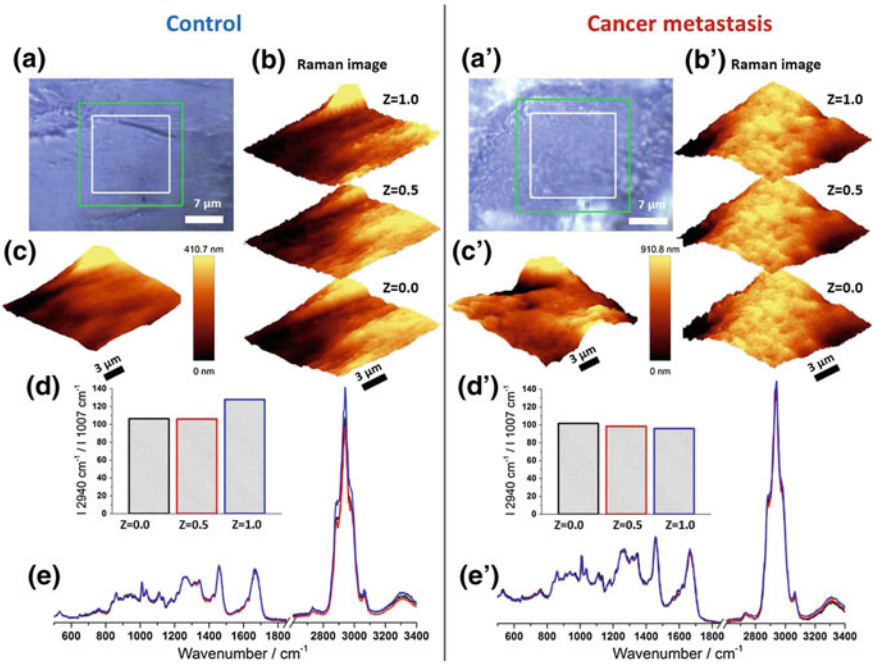

Fig. 14.10 Results of representative measurements of the vessel wall in control (left panel) and upon cancer metastasis (right panel): The areas of Raman and AFM measurements are denoted with white and green rectangles, respectively, in the visual images (**a**, **a**′). Three Raman distribution images at different depths of tissue were obtained by integration of the band in the range of 2800–3100 rel. cm^{-1} (**b**, **b**′) and compared with the AFM topography images (**c**, **c**′). The lipid to protein ratio (**d**, **d**′), defined as the intensity ratio of the band at 2940 rel. cm^{-1} to the band at ~1005 rel. cm^{-1}, was calculated based on the average spectra (**e**, **e**′) of presented Raman images (**b**, **b**′). Figure adapted upon Creative Commons Attribution License from [7]

signal was unmeasurably low. Raman measurements were complemented with the AFM imaging, applied to confirm approximate flatness of the surfaces, necessary for effective separation of the signal from different layers. Finally, Raman spectra recorded for different layers were analyzed separately by averaging of all spectra belonging to a given layer. A representative set of data for control and metastatic tissues (Fig. 14.10) demonstrated that the chemical composition of the endothelium of mice with cancer metastasis was significantly different compared to the endothelium of the control group.

The most prominent differences in the tissues of control and metastatic mice were related to the overall lipid and protein content calculated based on the integral intensity of the signals at ca. 2940 rel. cm^{-1} and ~1005 rel. cm^{-1}, respectively. In particular, the vascular endothelium of the control mice has the higher content of lipids and/or the lower content of the proteins than the deeper layers of the aorta. This effect is not observed for the tissues of metastatic animals, where the lipid to protein

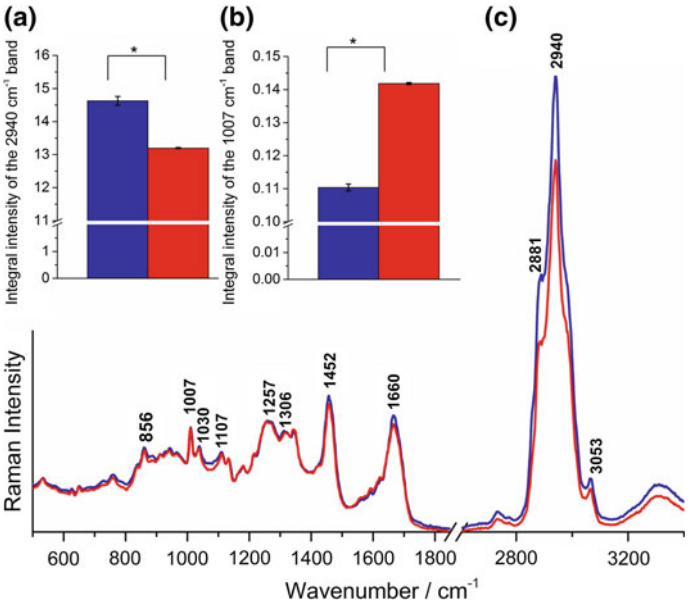

Fig. 14.11 Lipid and protein content in the endothelium of control and metastatic mice: The integral intensity of the lipid (**a**) and protein (**b**) bands and the comparison of the average endothelium spectra (**c**): control (blue), and metastasis-altered (red, spectra were normalized to the phenylalanine band at ~1005 rel. cm^{-1}). Figure adapted upon Creative Commons Attribution License from [7]

ratio is comparable for all measured layers. Moreover, for deeper layers of the tissue, the lipid-to-protein ratio for metastatic and control mice is comparable, showing that the effect of a changed lipid-to-protein ratio is confined to the endothelium. To answer the question which of the components i.e. lipids or proteins change its content upon metastasis, vector normalization of the average spectra (in the 3200–450 rel. cm^{-1} range) and calculations of the integral intensity of the following bands: 2940 rel. cm^{-1} (in the 3030–2825 rel. cm^{-1} range) and ~1005 rel. cm^{-1} (in the 1023–993 rel. cm^{-1} range) were performed (Fig. 14.11).

The results demonstrate that the lipid content significantly (about 6%) decreased for the metastatic mice relatively to the control ($p = 0.013$), while even more striking effect of the metastasis was observed for proteins. The intensity of the band at ~1005 rel. cm^{-1} increased up to 22% ($p = 0.011$) in the endothelium upon metastasis in comparison with the control. The phenotype of "cancer associated" dysfunctional endothelial cells has been previously characterized in vitro showing that these cells were more active, e.g. secreted larger amounts of proteins (mainly pro-inflammatory cytokines) [39]. This finding is in agreement with changes in the protein and lipid content observed in Raman spectra of the endothelium upon metastasis resulting from dysfunctional activation related to cancer and inflammation mediators.

The endothelium-confined chemical changes upon cancer metastasis were detected due to application of the 3D confocal imaging and analysis of the information from

the consecutive layers individually. Metastasis-induced changes in the endothelium are one more example of a critical role of endothelial response to various pathologies related not only topically to the vessel wall, but also via the systemic inflammation [7].

14.2.2.4 Atherosclerotic Plaque

The consequence of the atherosclerosis disease is the formation of the plaque inside arteries. In the advanced stage of atherosclerosis the plaque may contain calcified lesions with inflammatory cells and lipids what hardens and narrows arteries. A detailed review of the research on atherosclerotic plaque with the use of Raman spectroscopy was previously published [42]. It has been also shown that Raman spectroscopy offers high content images (micro and sub-micro resolution) of the morphological structure of the tissue of diagnostic, prognostic and therapeutic significance [43].

The use of Raman imaging in studies of the cross-sections of the atherosclerotic plaques in different murine models allowed us for biochemical analysis and visualization of the most important plaque features. Micro-damages of the fibrous cup, the exact places where the cholesterol crystals are created, the distribution of calcification and many other aspects visualized by Raman microscopy provide additional knowledge compared to just quantitative measurements of an average plaque features in some parts of aorta. This helped us to study the atherosclerosis progression, impact of different diets on plaque formation, its distribution as well as its vulnerability.

Figure 14.12 shows the Raman images of selected areas of the cross-section of plaques from a brachiocephalic artery (BCA). Distribution of the organic matter was obtained by integration of the CH stretching band approx. in the region 2800–3020 rel. cm^{-1}. The use of a 532nm excitation induced not only Raman effect, but also autofluorescence of the sample. Autofluorescence of internal elastic lamina and fibrous cap (called generally "elastin") manifested itself by an increased background. The increased background can be also associated with hemoglobin (Hb), which absorbs a considerable amount of photons [45]. The KMC results show four main clusters of the plaque: lipids, remodelled media, heme and elastin. Taking into account the place of deposition of heme, in both plaques we can observe intraplaque hemorrhages and only in the second example (e') the luminal thrombus. The green cluster corresponds mainly to internal elastic lamina of the artery wall, however in both examples we can also see the fibrous cap. The average spectra of the respective four clusters of the tissue and comparison with IR and AFM results are discussed in [44].

Raman imaging of the selected areas of the plaque was successfully used in combination with IR studies to characterize biochemical content of BCA plaques from ApoE/LDLR$^{-/-}$ mice fed Low Carbohydrate High Protein (LCHP) diet as compared to American Institute of Nutrition (AIN) diet. High resolution Raman imaging enabled the identification of necrotic core/foam cells, lipids (including cholesterol crystals), calcium mineralization and fibrous cap. Raman imaging was particularly

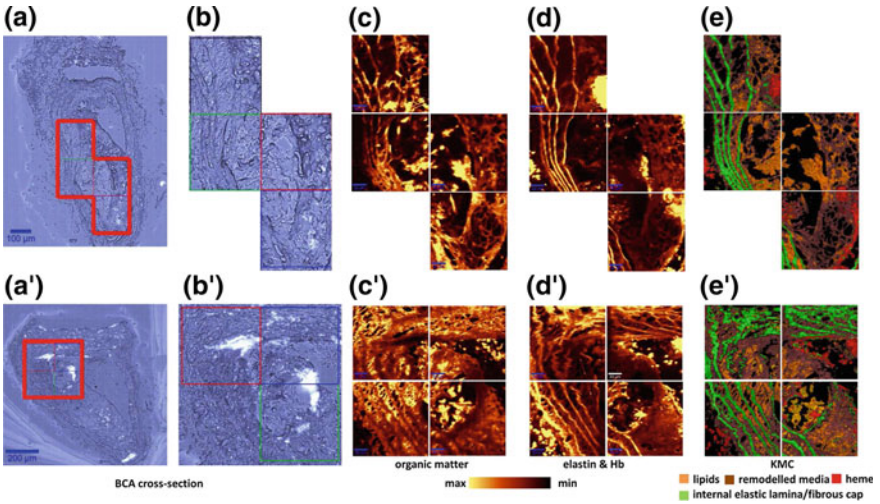

Fig. 14.12 Raman images obtained from the selected areas of the cross-section of atherosclerotic plaques obtained from BCA: (**a**, **a**′) microphotographs of the cross sections of a brachiocephalic artery taken from a 6-month-old ApoE/LDLR$^{-/-}$ mouse fed chow diet with the labelled areas (**b**, **b**′) investigated with the use of Raman; (**c**, **c**′) Raman images obtained by integration of the CH stretching band in the region 2800–3020 rel. cm^{-1}; (**d**, **d**′) Autofluorescence images of samples connected with the presence of elastin features (internal elastic lamina and fibrous cap and hemoglobin); (**e**, **e**′) KMC results with four main clusters which include remodelled media, heme, internal elastic lamina/fibrous cap and lipids. Sampling density was equal to 1.7μm. Adapted with permission from [44].Copyright (2014) WILEY-VCH Verlag GmbH & Co. KGaA

useful to describe the relative thickness of the outer fibrous cap and the presence of buried caps, which are known to be prominent features of the vulnerable plaques [46].

Figure 14.13 shows a high resolution (sampling density equal to 0.33μm) imaging of the luminal part of the calcified plaque. The presence of the fibrous cap, which separates the plaque from the artery lumen, can still be observed. The occurrence of small amounts of heme on top of the fibrous cap corresponds rather to free heme from destroyed red blood cells than to a luminal thrombus. The interior part of the plaque is occupied by calcification and lipids. The average Raman spectra of the elastin-rich cluster (fibrous cap/internal elastic lamina) are characterized by the bands related to proteins in general, i.e. Amide I at 1660 rel. cm^{-1}, Amide III approx. at 1257 rel. cm^{-1} and phenylalanine at ∼1005 rel. cm^{-1} as well as bands specific for desmosine, isodesmosine (1108, 1336 rel. cm^{-1}) and disulphide bridges in elastin (530 rel. cm^{-1}). The use of the 532nm excitation gives the resonance Raman (RR) spectrum of Hb (heme class) with the strongest bands at around 1580, 1130 and 750 rel. cm^{-1}. These bands originate from the ν_{19}, ν_{22} and ν_{15} modes, respectively. The Raman spectrum of calcified lesion is characterized by the intense band at approx. 960 rel. cm^{-1}, which is assigned to the stretching vibrations of $\nu(PO_4)$. Other bands of hydroxyapatite are observed at 440, 590 and 1081 rel. cm^{-1}. Because the Raman

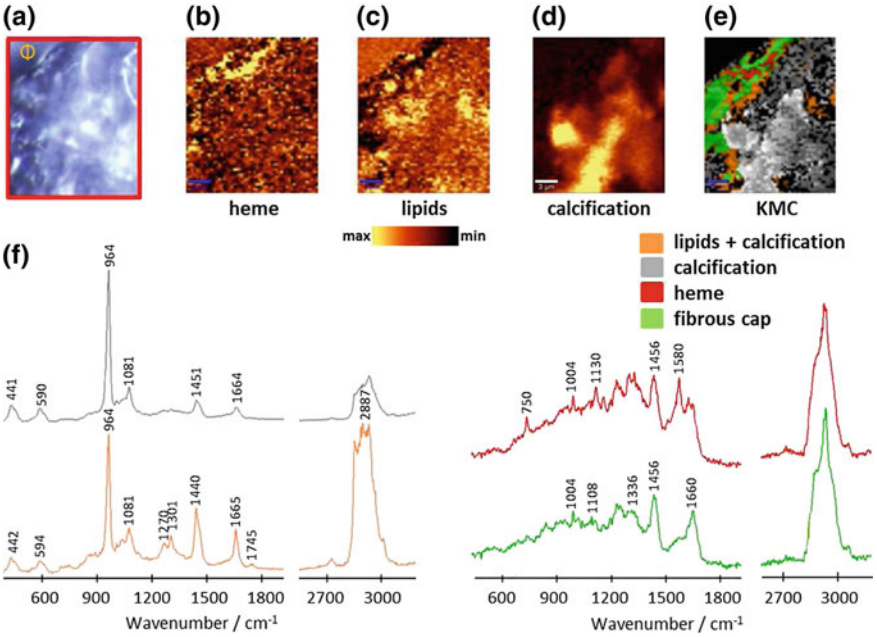

Fig. 14.13 Raman results from the calcified plaque: **a** Microphotograph of the cross section of a brachiocephalic artery taken from a 6-month-old ApoE/LDLR$^{-/-}$ mouse fed chow diet with the labeled area (red) investigated with the use of Raman spectroscopy; Raman distribution images obtained by integration of **b** hemoglobin (heme) band at 1580 rel. cm^{-1}, **c** lipid band at 2887 rel. cm^{-1} and **d** hydroxyapatite band at 964 rel. cm^{-1}; **e** KMC results with the four main clusters, which include heme, fibrous cap, calcification and lipids; **f** The average spectra of heme, fibrous cap, calcification and hydroxyapatite mixed with lipids obtained from whole measured tissue. The Greek letter "Φ" indicates the side of artery lumen

spectrum in Fig. 14.13 corresponds to the lipid cluster mixed with the calcified lesion, we may suspect that this plaque comes from the mice with the advanced stage of atherosclerosis. The bands typical for lipids maybe observed at around 1745 rel. cm^{-1} (C=O stretching mode), 1670 rel. cm^{-1} (C=C stretching mode) and 1440 rel. cm^{-1} (C-H bending mode), however the most intense bands are visible in the higher wavenumber region, and originate from the stretching vibrations of CH groups. Overall, the method enables not only imaging of the total amount of lipids, but sometimes also differentiation of the cholesterol from the cholesteryl esters is also possible (Fig. 14.14).

Differentiation between cholesterol and cholesteryl esters can be made by integration of bands at 1740 or 2887 rel. cm^{-1}, which are characteristic for C=O and C–H stretching vibrations in esters, respectively. Bands observed at lower frequencies, below 700 rel. cm^{-1} are characteristic mainly for cholesterol moiety due to vibration modes of the steroid ring. Single Raman spectra obtained from the cholesterol crystals in the studied plaques may even allow for detection of the specific type of

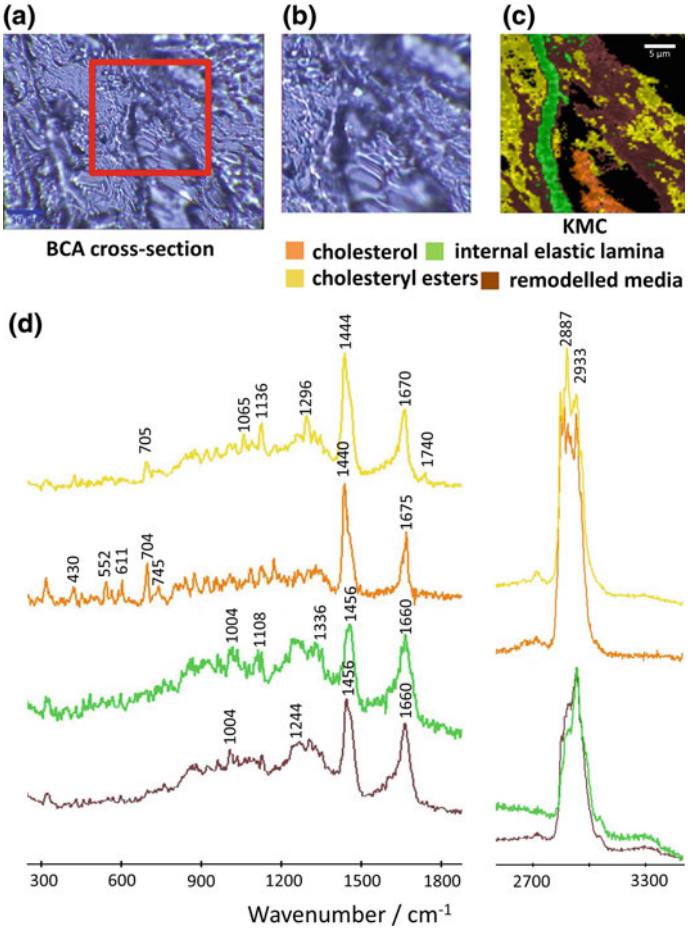

Fig. 14.14 Differentiation between cholesterol and cholesteryl esters inside a plaque: **a** Microphotograph of the cross section of a brachiocephalic artery taken from a 6-month-old ApoE/LDLR$^{-/-}$ mouse fed LCHP diet with the labeled area **b** investigated with the use of Raman spectroscopy; **c** KMC results with four main clusters which include remodelled media, internal elastic lamina and cholesterol esters and cholesterol; **d**. The average spectra of the respective four clusters of the tissue. Sampling density was equal to 0.33μm

crystalline cholesterol [44]. The Raman spectrum of remodelled media, which corresponds to the pathologically altered media tissue, is very similar to elastin features, but this part of plaque does not exhibit autofluorescence when the 532nm excitation is used. To confirm the legitimacy of Raman results, they were compared with the histopathological staining [42, 44].

Additional information about atherosclerotic plaque may be obtained when confocal Raman imaging is combined with IR imaging or AFM. All these methods can be carried out on the same area of the tissue and can be successfully used in

atherosclerotic plaque analysis [44]. Figure 14.15 presents the results obtained by combination of IR and Raman imaging, which allowed [46] for quantitative (IR) and qualitative (Raman) analysis of the vulnerable plaque.

AFM results supported Raman information about the physical properties of the fibrous cap surrounding the atherosclerotic plaque and internal elastic lamina. They were found to be the stiffest parts of the tissue or plaque (besides calcification and cholesterol crystal) and serve as the tissue or plaque framework. As we previously reported with the use of AFM technique and Raman microscopy, it was possible to define the thickness of the murine fibrous caps [44, 46]. AFM allowed also the visualisation of shape and topography profiles of cholesterol crystals and other plaque features (see Fig. 14.16). Additionally, AFM is able to provide the insight into the mechanical properties of the cap.

Presented results indicated that AFM, IR and Raman imaging might be regarded as complementary methods to histological and immunocytochemical staining to study the properties of atherosclerotic plaque. A variety of staining methods specific for individual plaque features is available, however, it is not possible to use them at the same area of the sample. Raman imaging combined with other methods enables detection of all features during one measurement within the specified tissue area and that is, we believe, the main advantage of the multimodal approach presented here.

Chemical analysis of the tissue of organs like liver, brain and lung carried out with Raman imaging and histochemical staining has previously been reported [47, 48]. Moreover, it was also possible to study the primary atherosclerotic changes at the endothelial cell level [49].

14.2.2.5 NAFLD-Affected Liver

Non-Alcoholic Fatty Liver Disease (NAFLD) is a common chronic liver disorder, considered as a manifestation of metabolic syndrome [50, 51]. It can be characterized as an excessive accumulation of lipids in the liver tissue in the form of LDs. The lack of specific symptoms as well as of optimal diagnostic methods makes the detection of this disorder challenging. If left untreated, NAFLD can lead to liver cirrhosis and fibrosis (Non-Alcoholic Steatohepatitis, NASH) and finally - irreversible liver damage.

For the study of fatty liver various animal models were used. The genetic models involve a mutation in a specific gene, resulting in promoting the development of fatty liver (e.g. spontaneous mutation in the leptin gene in db/db mice). Dietary models are based on selected nutrition protocols, which determine the feeding of animals. They can involve e.g. high content of saturated fats (High Fat Diet, HFD) or deficiency of methionine and choline (Methionine-Choline-Deficient diet, MCD). Finally, the combined models use genetically modified animals fed according to a specific manner (e.g. ApoE/LDLR$^{-/-}$ mice fed with Low Carbohydrate High Protein Diet) [52]. The most commonly used dietary model is the HFD, with the fat content of approx. 60% that includes primarily saturated lipids [53].

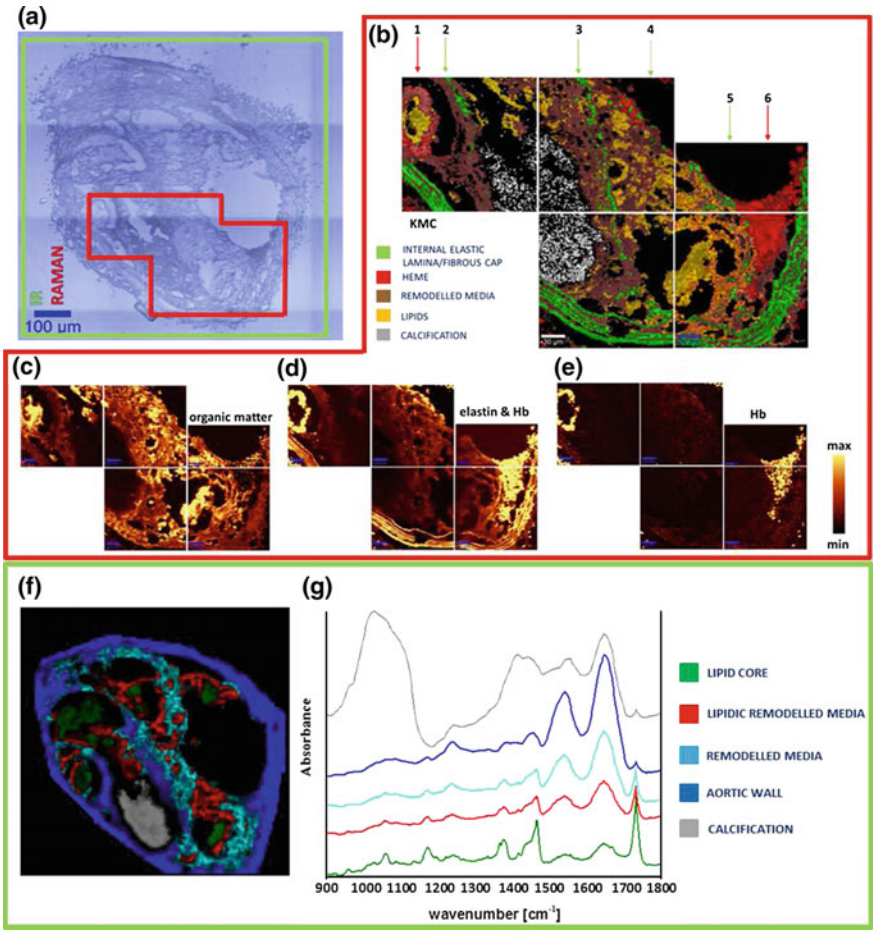

Fig. 14.15 Raman and IR as complementary techniques in plaque studies: **a** Microphotograph of a cross section of a brachiocephalic artery taken from a 6-month-old ApoE/LDLR$^{-/-}$ mouse fed LCHP diet with the labelled regions investigated with the use of IR (green) and Raman (red); **b** KMC results with four main clusters including remodeled media, heme, internal elastic lamina/fibrous cap and lipids; Existence of three buried fibrous caps marked with the green arrows 2, 3 and 5 from the middle to the external part of the plaque, respectively **c** Raman images obtained by integration of the CH stretching band approx. in the 2800–3050 rel. cm^{-1} region; **d** Autofluorescence of the sample connected with the presence of elastin features (internal elastic lamina and fibrous cap) and Hb; **e** Raman images obtained by integration of the band centered at 1130 rel. cm^{-1} or 745 rel. cm^{-1} (Hb); For Raman imaging the sampling density was equal to 1.67μm. Color coding for the clusters is presented in figure; **f** A Fuzzy C-Means (FCM) clustering image of the whole section, based on FT-IR imaging data, with five clusters. **g** The corresponding average spectra from FCM analysis - spectra were offset for clarity. Figure adapted upon Creative Commons Attribution License from [46]

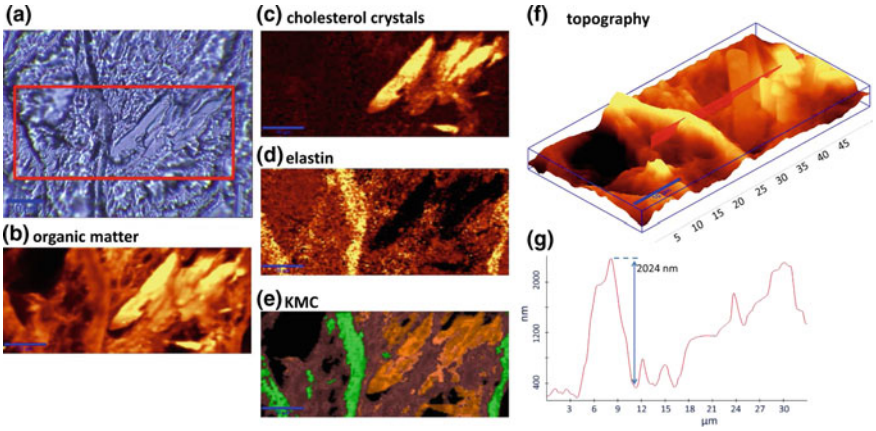

Fig. 14.16 Raman and AFM as complementary techniques in plaque studies: **a** Microphotographs of the cross sections of a brachiocephalic artery taken from a 6-month-old ApoE/LDLR$^{-/-}$ mouse with investigated areas labeled (red). Raman images of: **b** the band due to the CH stretchings approx. in the region 2800–3020 rel. cm^{-1}, **c** cholesterol at 704 rel. cm^{-1}; **d** elastin at 530 rel. cm^{-1}; **e** the KMC results with three main clusters. The clusters include crystalline cholesterol, remodelled media and internal elastic lamina; sampling densities were equal to 500nm; AFM image of: **f** topography of part "a" with the **g** topography cross section according to red line. Adapted with permission from [44]. Copyright (2014) WILEY-VCH Verlag GmbH & Co. KGaA

For the measurements, Raman imaging combined with FT-IR imaging and histochemical staining (considered as a 'gold standard') were applied. By performing the experiments with the use of confocal Raman imaging the chemical information can be linked with the spatial information. The location of changes can indicate the type of the liver cell involved in the disease development. Furthermore, Raman imaging allows obtaining detailed information on the molecular level, including the secondary structure of proteins or lipids composition (free fatty acids, triglycerides, cholesterol esters, etc.) [44], as well as it provides information on the location and the structure (a degree of unsaturation, lipid chain branching, etc.) [45, 47, 54].

One of the most prominent features of NAFLD-affected tissue is the presence of relatively large lipid droplets. A comparison between the lipid distribution in livers of C576BL/6J (control) mice fed with AIN-93G (a standard dietary protocol for early growth and reproduction) and HFD (containing 60% of kcal from saturated fat) after 15 weeks is presented in Fig. 14.17.

A distribution of selected components of liver tissue in the control and NAFLD-affected one (Fig. 14.17) distinctly reveals the most significant feature of fatty liver: the presence of large lipid droplets [45]. This prominent attribute is connected not only to fatty liver itself, but also to any NAFLD-related diseases, such as atherosclerosis or diabetes mellitus type II [47]. Within healthy tissue small lipid accumulations can sometimes also be observed. They are mainly associated with the storage of vitamin A [45]. However, the size and density of LDs in fatty liver increase drastically,

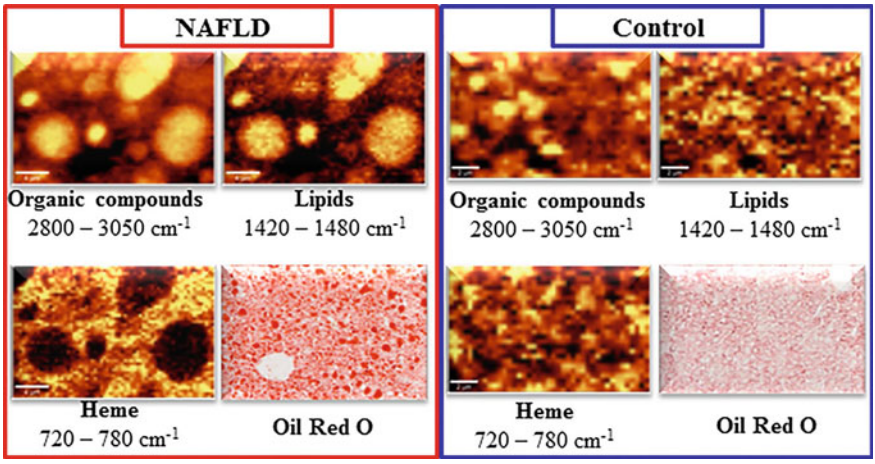

Fig. 14.17 Raman images of liver tissue collected from murine models of NAFLD (red panel) and control (blue panel) along with results of Oil Red O staining: Distribution of organic components (2800–3050 rel. cm^{-1}), lipids (1420–1480 rel. cm^{-1}) and heme (720–780 rel. cm^{-1}). The presence of large lipid droplets within NAFLD-affected tissue can be seen (red panel)

changing the biochemical composition of the tissue entirely and thereby impairing the actions of this organ.

Figure 14.18 shows the results on the composition of LDs. As can be seen the area corresponding to lipid droplets (Fig. 14.18b) is easily identified by KCA due to the significant changes in the collected spectra. However, further analysis of the lipid droplet cluster (Fig. 14.18c) does not reveal any prominent differences. The cluster division is a result of differential intensities of the signals, which decreases from the border of droplet towards its centre. No heterogenic distribution of any lipids in the plane of the droplet can be seen [55]. Confocal Raman imaging allowed additionally investigation of the droplet composition within their volume (Fig. 14.18a), confirming the homogenous distribution of lipids. Interestingly, we were able to observe and to study not only the droplets visible from the surface of the tissue sections but also droplets occurring inside (Fig. 14.18d). Such droplets are exposed to a lesser extent to possible changes in the composition due to preparation or storage of the samples (e.g. changes in the degree of unsaturation due to long exposure to visible light). Their composition is the same as the droplets located on the tissue surface, confirming the proper approach used for the tissue preparation and its storage.

Inspection of the LDs spectra led to the conclusion that the droplets are composed mainly of triglycerides, whereas cholesterol and its esters were not observed. Raman results were confirmed by an assessment of lipid content in the tissue with the use of gas chromatography/mass spectrometry (GC/MS) [56].

A degree of lipid unsaturation can be determined on the basis of the ratio of intensities of bands corresponding to the vibrations of C=C and C–C moieties, respectively. In Raman spectra of lipids three major bands due to C–C vibrations can be iden-

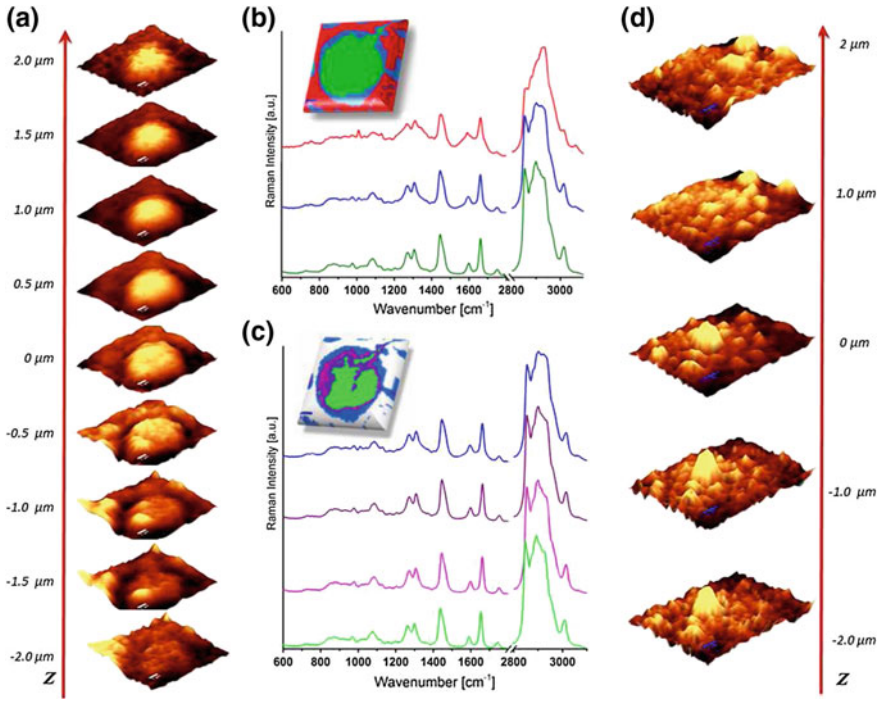

Fig. 14.18 Investigation of LDs composition: **a** A 3D stack representing the distribution of saturated lipids (1420–1480 rel. cm^{-1}) in lipid droplet from NAFLD-affected tissue (droplet visible on the surface); **b** KMC analysis of of LD: the distribution of clusters along with corresponding spectra; **c** KMC detailed analysis of clusters from panel B corresponding to lipid droplet: the distribution of clusters along with corresponding spectra, **d** 3D stack representing the distribution of saturated lipids (1420–1480 rel. cm^{-1}) in lipid droplet from NAFLD-affected tissue: please notice the location of the droplet deep within the tissue

tified: ~1300 rel. cm^{-1} associated with the CH_2 twisting mode, ~1444 rel. cm^{-1} due to the CH_2 deformation mode and ~2855 rel. cm^{-1} originating from the CH_2 stretching vibrations. Presence of lipids with C=C double bonds manifests itself by three major bands: ~1266 rel. cm^{-1} associated with deformation of the =C–H groups, ~1656 rel. cm^{-1} due to the C=C stretching and ~3010 rel. cm^{-1} originating from the =CH stretching vibrations. Therefore, determination of the degree of unsaturation can be performed on the basis of at least three band pairs: I_{3010}/I_{2855}, I_{1656}/I_{1444} and I_{1266}/I_{1301} [55]. The first criterion has, however, a low sensitivity for changes, as the band corresponding to unsaturated bonds is characterized by small intensity compared to the band corresponding to single bond vibrations. Therefore only big changes in the intensity of the band ~3010 rel. cm^{-1} will result in slight changes of the value of I_{3010}/I_{2855}. The criterion of I_{1266}/I_{1301} has been commonly used. However, in terms of biological materials, often characterized by raised baseline and the richness of composition, it is a source of numerous difficulties. The elevated baseline

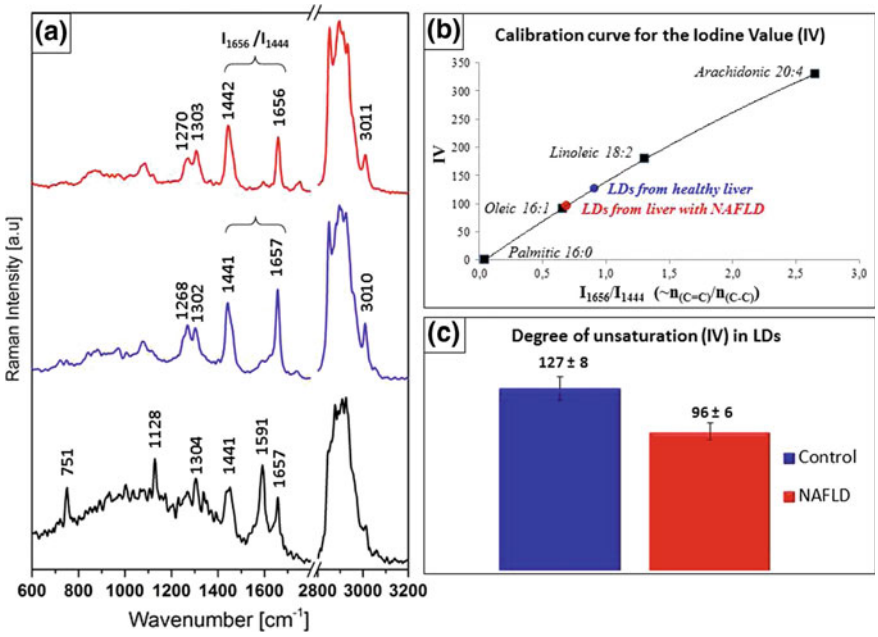

Fig. 14.19 **a** Raman spectra of LDs from NAFLD-affected liver (red), small LDs from control liver (blue) and typical control liver tissue (black); **b** Calibration curve for assessment of iodine value (IV) on the basis of I_{1656}/I_{1444}: red and blue dots mark the values obtained for LDs from control and NAFLD-affected liver; **c** Iodine values (degree of unsaturation) for LDs from control mice and mice with NAFLD. IVs were calculated on the basis of Raman spectra and the calibration curve

is an important problem particularly for the liver tissue, as it is rich in heme. So, the criterion of I_{1656}/I_{1444} seems to be the most suitable for the determination of the degree of unsaturation of LDs in biological materials [54].

A comparison between the degree of unsaturation of lipids from LDs in the liver of control and NAFLD-affected mice indicates a significant difference in their composition (Fig. 14.19).

By the use of standards of free fatty acids it is possible to calibrate the selected criterion (I_{1656}/I_{1444}) and express the degree of unsaturation as iodine value. The value obtained for the sample refers to the lipid mixture building the droplet. As can be seen, the degree of unsaturation decreases considerably for fatty liver droplets. The LDs resulting from pathological disorder induced by high fat diet (containing high amounts of saturated fat) tend to be composed of saturated lipid [45].

The degree of unsaturation is different not only for healthy and diseased tissues but also in the case of pharmacological treatment, based on two reference drugs: metformin, perindopril, and two NO-donors V-PYRRO/NO and V-PROLI/NO. The major change induced by treatment with reference drugs was a clear reduction of the size and number of lipid droplets. This effect has not been observed for any of the NO-donors. In addition to these changes, for the treatment with metformin and perindopril

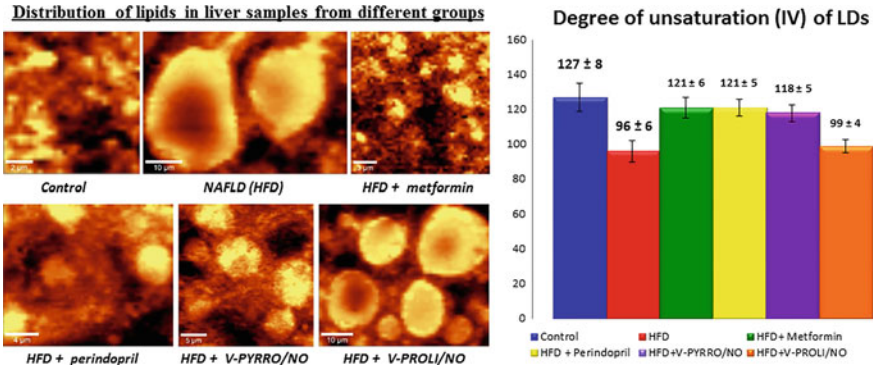

Fig. 14.20 (Left) Distribution of lipids in livers from control, NAFLD (HFD-induced), NAFLD treated with: metformin, perindopril, V-PYRRO/NO and V-PROLI/NO, obtained on the basis of integration of Raman band in the range 1420–1480 rel. cm^{-1}. (Right) Iodine values (degree of unsaturation) for LDs from control mice, mice with NAFLD and mice with NAFLD subjected to treatment. IVs were calculated on the basis of Raman spectra and calibration curve presented in Fig. 14.19b

there was a significant increase in the value of the degree of unsaturation, nearly aligning it with the value determined for control [56]. Therefore, it can be concluded that a successful treatment manifested itself by the change in the composition of LDs and - possibly due to this - the reduction of size and number of LDs.

An interesting observation can be made for the NO-donors (Fig. 14.20). Both of them did not lead to the reduction of the size nor number of LDs. However, an administration of V-PYRRO/NO has resulted in a change of the degree of unsaturation of lipids composing LDs, increasing the iodine value towards the value corresponding to control (similarly as in case of metformin and perindopril). Therefore we can conclude, that the HFD-induced decrease in the ratio of unsaturated (UFA) to saturated fatty acids (SFA) was reversed by treatment with V-PYRRO/NO. GC/MS results confirmed the reduction of the total liver triacylglycerols, diacylglycerols and ceramides fraction. The modification of the composition of LDs (degree of unsaturation) is a change that occurs prior to their size reduction and can indicate the effectiveness of therapy.

The composition of LDs (the ratio of UFA/SFA) depends on many factors, including e.g. diet or type of NAFLD. The dietary model of HFD results in large droplets in the fatty liver. The changes in the degree of unsaturation for the small droplet type model can be tested using ApoE/LDLR$^{-/-}$ mice fed with Low Carbohydrate High Protein diet. However, independently of the size of LDs, the tendency in decreasing the ratio of UFA/SFA due to the development of the disease is preserved [45].

Another marker of livers' condition observed via Raman spectroscopy is vitamin A stored in Hepatic Stellate Cells (HSC). It is commonly known, that during the first stage of liver injury HSCs become activated, the number of LDs increases but the amount of retinyl esters decreases, suggesting a crucial role of vitamin A in injury

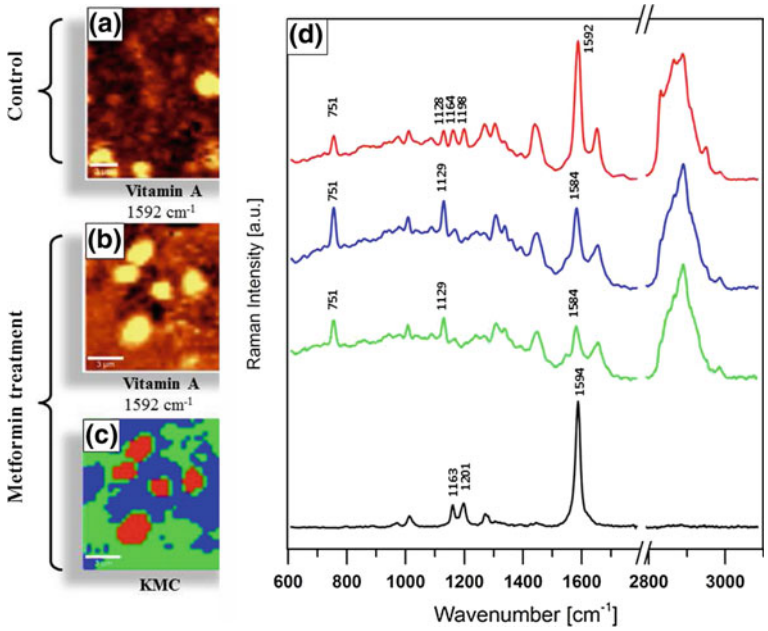

Fig. 14.21 Distribution of vitamin A: Analysis based on a marker band at 1594 rel. cm^{-1} in: **a** control liver and **b** liver from mice with NAFLD, subjected to treatment with metformin. Results of K-means cluster analysis presented in (**c**): KMC clusters along with (**d**) average spectra of clusters (red, blue, green) and spectrum of the standard of all-trans-retionol (black)

and liver repair process [57]. Vitamin A has been observed in samples of healthy liver tissue numerous times [45, 47, 58]. Detailed investigations of vitamin A content in healthy tissues was performed on liver sections obtained from C57BL/6J mice fed with a standard diet (AIN-93G). The presence of vitamin A can be clearly revealed by the marker band located at 1594 rel. cm^{-1} (Fig. 14.21). The position of this band is close to one of three marker bands of heme (~751, 1130, 1585 rel. cm^{-1}), often observed in liver tissue spectra. However, the intensity of vitamin A signals greatly exceeds the intensity of any other components of liver tissue.

In addition, the spectrum of vitamin A exhibits two additional marker bands of lower intensity, at 1163 and 1201 rel. cm^{-1} (Fig. 14.21). The majority of vitamin A in HSCs of healthy liver is in the form of all-trans-retinol [45]. In accordance with the above stated facts, vitamin A was not found in any of liver injury models. However, its presence was observed in liver samples from mice with the HFD-induced NAFLD, subjected to treatment with metformin. As discussed previously, metformin (a reference drug) therapy was proven to be effective. Small lipid accumulations, with characteristic signals from vitamin A were observed in metformin treated samples. The signals from vitamin A were of lower intensity than in control samples, suggesting a lower content of vitamin A. However, their reappearance in metformin treated samples indicate the rebuilding of vitamin A storage occurring as a result of the effective therapy.

14.3 Part II

14.3.1 Experimental

14.3.1.1 Cell Culture Protocols

EA.hy 926 cells, immortalized hybrids, were derived by fusion of Human Umbilical Vein Endothelial Cells (HUVEC) with human lung carcinoma cells line A549 [18]. EA.hy 926 cells were cultured in Dulbecco's modified Eagle's medium (DMEM, Lonza) supplemented with 10% fetal bovine serum (FBS), 1% penicillin-streptomycin, 2mM L-glutamine (Invitrogen) and 2% HAT medium supplement. Primary human aortic endothelial cells (HAoEC) were purchased from Gibco and cultured in supplemented endothelial cell growth medium (EGM-2 MV from Lonza). The cells were grown in 75 cm^3 culture flasks (BD Falcon) and were incubated in a 37 °C, 5% CO_2/95% air, humidified cell culture incubator. For Raman measurements cells were directly grown on calcium fluoride slides (CaF_2, 25 × 2mm, Pike Technologies, U.S.) and after 24 h were fixed for 4 min with 4% paraformaldehyde or 2.5% glutaraldehyde and stored in isotonic phosphate buffer, pH = 7 at 4 °C until data acquisition. For Raman measurements the CaF_2 slides with cells were submerged in PBS.

14.3.1.2 Preparation of Blood Smears and Functional Erythrocytes

Capillary blood samples were obtained from healthy volunteers. 20μL of fresh blood was transferred to an 80 mm diameter glass Petri dish filled with 10 mL of cold saline solution (around 5 °C). The Petri dish was pre-coated with gold and poly-L-lysine as previously described [59]. The cells were settled for around 10 min until a thin monolayer of blood cells was observed. Thin smears of whole blood were prepared by pinprick. The blood was smeared on the ethanol cleaned and dried CaF_2 windows to obtain a monolayer of blood cells. Such prepared blood smears were air-dried and selected areas were measured using Raman, AFM and scanning near-field optical microscopy (SNOM) (RBCs, leucocytes and blood plasma) [60].

14.3.1.3 Data Acquisition

Confocal Raman imaging was done using an alpha 300 Confocal Raman Imaging system (WITec GmbH, Ulm, Germany) as described in Sect. 14.2.1.2, with the application of a 60× water immersion objective (Nikon Fluor, NA = 1) or for dried blood smears a 100× air objective (Olympus, MPlan FL, NA = 0.9). Data acquisition was controlled by the WitecControl data acquisition software package.

14.3.1.4 Endothelial Cells

Raman spectra from endothelial cells were recorded using 488nm solid state laser (laser power of ca.15mW at the sample). Raman imaging of cells was performed by collecting spectra with 0.5 s exposure time and moving the sample in increments of 0.6μm (65 × 40μm^2, 108 × 66 points). The depth of cell profiling was 9μm (volume of 13 × 28 × 9μm^3) measured as nine layers in a stack every 1.0μm in the z-direction from top to bottom. Each voxel of obtained 3D image represents a full Raman spectrum which was collected using 0.4 s exposure time and sampling density of 0.6μm (13 × 28 × 9μm^3, 21 × 46 × 9 points). The total exposure time was ca.2 h [1 h per Raman image of the entire cell and additional 1 h for depth profiling of the selected area (7 min per layer)]. Cells were submerged in PBS during the measurement.

14.3.1.5 Red Blood Cells

Results for functional RBCs as well as air-dried smears were obtained using 488 and 532nm laser excitations. The integration time for a single spectrum was 0.3s and the spectral resolution was equal to 1 or 3 rel. cm^{-1} (depending on the grating used, 1800grooves/mm or 600grooves/mm, respectively). The laser power used varied from 9μW to 5mW. The AFM measurements were performed in the AC mode using standard force modulation probes (WITec, Ulm, Germany) with a nominal spring constant of 2.8N/m and the resolution 256 × 256 points per 20 × 20μm. The SNOM measurements were carried out using cantilever SNOM sensors (WITec) with a <100nm aperture diameter, an excitation laser wavelength of 488nm and with a resolution of 256 × 256 points per 10 × 10μm.

14.3.1.6 Data Processing

Raman, AFM and SNOM data analysis were performed using WITecProject Plus software package (Version 2.10). All spectra were baseline corrected using a 2nd order polynomial (for liver cells) or 3rd order polynomial (for endothelial cells) and the routine procedure for cosmic rays removal was applied. Raman distribution images of selected compounds or groups of compounds were obtained based on integration of corresponding marker bands. Cluster analysis was performed using the K-means method with Manhattan distance. The Image J processing program was used to obtain 3D pictures of cells [22]. For calculations of the area occupied by cells and cell nuclei, the Matlab software was used.

14.3.2 Results and Discussions

14.3.2.1 3D Raman Imaging of Single Endothelial Cells

3D-approach for cell analysis is a novel trend in analytical spectroscopy, which allows determination of the biochemical composition at the subcellular level with a high spatial (both lateral and depth) resolution [61].

Taking into account the small size of endothelial cells and their heterogeneous biochemical composition, significant spectral changes along few microns of depth profiling were expected within a cell (Fig. 14.22). Two-dimensional spectral images calculated by integrating the intensity of the C–H stretching vibrations in the 2800–3020 rel. cm^{-1} range were acquired (Fig. 14.22b). Bright and dark regions are related mainly to differences in protein and lipid density, water content and sample thickness. For Fig. 14.22d, e the same colour scaling was provided to allow the reader to judge the overall relative concentration of selected compounds. Raman spectra obtained from the same point of each imaged layer of the cell is presented in Fig. 14.22f (500–1800 rel. cm^{-1} range). Spectra were selected from the nucleoli area in the xy-plane. Based on extracted spectra (Fig. 14.22f) and Raman images obtained by integration of the 1630–1690 rel. cm^{-1} spectral range (Fig. 14.22e), the variation in the intensity of the registered spectra was observed between layers.

Most information about the chemical composition of biological samples can be found in the fingerprint range (400–1800 rel. cm^{-1}). The presence of proteins manifests itself in the Raman spectra by two characteristic bands, Amide I and Amide III, which are sensitive to the secondary structure of proteins. Generally, information on the content and structure of proteins in the cells can be obtained by the analysis of position and intensity of the following bands: approx. 1660 rel. cm^{-1} (Amid I), 1450 rel. cm^{-1} (CH_2 bending), 1100–1375 rel. cm^{-1} (Amid III) and ~1005 rel. cm^{-1} (phenylalanine). The lipid composition of cells can be determined based on the bands: 1740 rel. cm^{-1} (C=O); 1656 rel. cm^{-1} (cis C=C); 1441 rel. cm^{-1} (CH_2 bending) and 1304 rel. cm^{-1} (CH_2 twisting). An informative spectral observation is also the density of the investigated area of the sample, e.g. cytoplasm can be recognised in the spectra by the noticeably lower signal to noise ratio (especially in the fingerprint range).

The high wavenumber range (2800–3030 rel. cm^{-1}) provides information on the protein-lipid composition. The intensity of bands at 3005–3015 rel. cm^{-1} (stretching vibrations of the =C–H bonds) can be correlated with the amount of double bonds in the molecules of lipids/fatty acids. The spectral difference associated with lipids can be tracked by analyzing the bands in the range of 2850–2900 rel. cm^{-1}, that is more useful for the areas of the cytoplasm around the nucleus (endoplasmic reticulum and mitochondria).

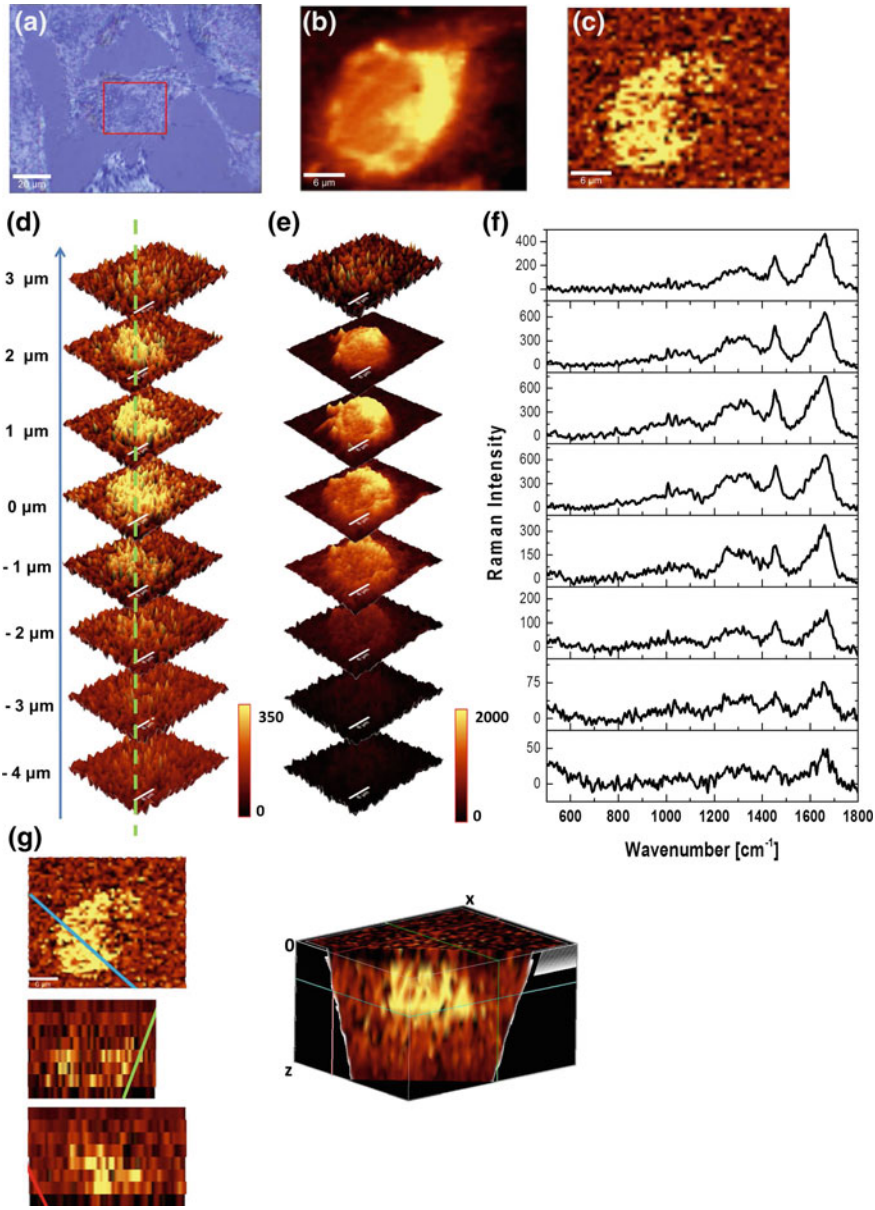

Fig. 14.22 Confocal Raman imaging-stack of an endothelial cell (33 × 27µm, 55 × 45 points). The visual image (×60, **a**), integration images of the third layer (**b**, **c**) obtained by integration of the ν_{C-H} and ring breathing modes in the DNA/RNA bases bands (2800–3020 and 760–805 rel. cm^{-1} range, respectively), an imaging-stack of the endothelial cell covering $33 \times 27 \times 8\,\mu m^3$ of the cell (integration images in the 760–805 (**d**) and 1630–1690 rel. cm^{-1} (**e**) range), single spectra (**f**) extracted from the same point of the images (green dotted line in **d**), a reconstructed 3D image - a cross-section of the reconstructed 3D image (volumes within a 3D-(xyz)-space) with intersection in xy-, zy- and xz-planes (**g**). Scale bars: 20µm for (**a**), 6µm for (**b**–**f**)

The reconstructed three dimensional cell image is presented in Fig. 14.22g as a volume within a xyz-coordination system. By using the volume viewer option and rendering with intersection in xy-, zy- and xz-plane it was possible to obtain cross-sections of the cell together with selected subcellular structures [61]. These results show that by using confocal Raman imaging it was possible to define the size, volume, shape and biochemical composition of selected cellular components inside a single cell without the need for special sample preparation.

14.3.2.2 Confocal Raman Imaging of Lipid Droplets Formed in Endothelium

We have shown that endothelial cells are able to take up exogenous polyunsaturated fatty acids (PUFAs) and to form lipid droplets (LDs) [55, 62]. Moreover, 1-methylnicotinamide (MNA) facilitates this process and increases the number of endothelial LDs [62].

LDs can be identified using Raman spectroscopy by characteristic bands (Fig. 14.23f), at 1660 rel. cm^{-1} and ~3015 rel. cm^{-1} due to the stretching mode of the C=C bonds and =C-H bonds associated with the C=C double bonds [55]. In Fig. 14.23 two-dimensional spectral images calculated by integrating the intensity of the C-H stretching vibrations of aliphatic molecules in the 2800–3020 rel. cm^{-1} range (Fig. 14.23b), cytosine ring breathing vibrations of DNA in 775–790 rel. cm^{-1} range (Fig. 14.23c) and =CH-stretching vibrations in 3000–3030 rel. cm^{-1} range (Fig. 14.23d) are shown. Additionally, confocal Raman imaging was used as

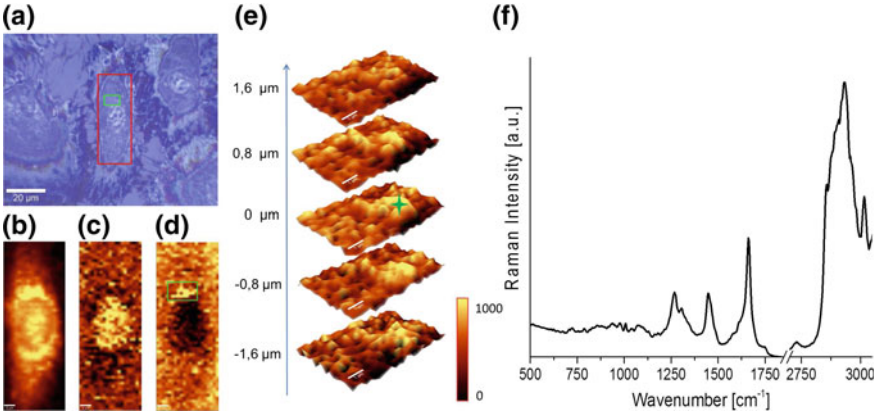

Fig. 14.23 Confocal Raman imaging of the HAoEC cell with LDs. The full area of the cell [(**a**), red square] with the zoomed area (marked in green), images obtained by integration of the 3000–3030 rel. cm^{-1} (**b**), 760–805 rel. cm^{-1} (**c**) and 3000–3030 rel. cm^{-1} (**d**) ranges, imaging-stack of LDs (**e**) covering $8 \times 5 \times 4.2 \mu m^3$ of cell (green square in (**a**); images obtained by integration of the 1630–1690 rel. cm^{-1} range), single Raman spectrum of a LD (**f**). Scale bars: 20µm for (**a**), 3µm for (**b**–**d**) and 1µm for (**f**). The same colour scaling (min - 0, max - 450) was provided to help to judge the overall concentration of lipids

a non-invasive tool to illustrate the 3D distribution of LDs in the single endothelial cell (Fig. 14.23e). Comparison of the LDs' average spectrum (Fig. 14.23f) with standards of selected unsaturated fatty acids [63] allows an approximation of biochemical composition of these lipidic structures. The bands at 1447, 1658, 1736, 2855 and 3015 rel. cm^{-1} have been assigned to PUFAs and detailed analysis of LDs average spectrum suggests that the main component of LDs is arachidonic acid [62].

Lipid droplets formation upon the unsaturated fatty acid uptake was studied in the context of their structure and content. In the literature investigation of LDs formation in various cells using Raman spectroscopy, including also more involved techniques such as coherent anti-stokes Raman scattering (CARS) microscopy, has been reported [64–68]. It has also been demonstrated that stimulation of endothelial cells using arachidonic acid (a precursor of prostacyclin (PGI_2) and other prostaglandins) and 1-methylnicotinamide leads to formation of LDs in high amount [62]. A similar cell response was observed for eicosapentaneoic acid (EPA). Altogether it has been shown that Raman spectroscopy is applicable to study LDs in situ, that helped to demonstrate a novel biological context of LD formation in the endothelium, of potential physiological significance.

14.3.2.3 Single Endothelial Cells Exposed on Anthracycline

Raman imaging represents a new methodological approach in pharmacology, since it provides information on the biochemical changes occurring in endothelial cells at the subcellular level following their exposure to anthracyclines antibiotics. Raman spectra of investigated anthracyclines (doxorubicin (DOX), daunorubicin (DNR), epidoxorubicin (EDOX), epidaunorubicin (EDNR)) are shown in Fig. 14.24.

By using the excitation in the 400–550nm range, the resonance Raman spectra of anthracyclines can be recorded [69, 70]. However, these compounds exhibit strong fluorescence, which can be observed in Raman spectra as an increased background in the high wavenumber range (maximum at approx. 3800–4200 rel. cm^{-1}).

To study an impact of anthracyclines on endothelium, the cells (EA.hy 926 line) were incubated for 24 h with DOX, DNR, EDOX and EDNR, at the concentrations in the range of 100nM–1μm. It is known that the cytostatic function of anthracyclines is related to the formation of a stable complex with the DNA helix, which prevents further division and leads to cell death, so the analysis of changes in the cell nucleus was carried out. Since the spectral range of the maximum anthracycline fluorescence coincides with the raised background of anthracycline-stimulated cells (3800–4200 rel. cm^{-1}), it seems to be the best spectral marker of the presence of anthracyclines in the cell. Therefore, the integration of this spectral range allowed for studying the distribution of anthracyclines in the cells. Figure 14.25 shows the results of integration of the marker range (3820–4200 rel. cm^{-1}) for cells stimulated with anthracyclines at the concentrations of 100nM–1μm.

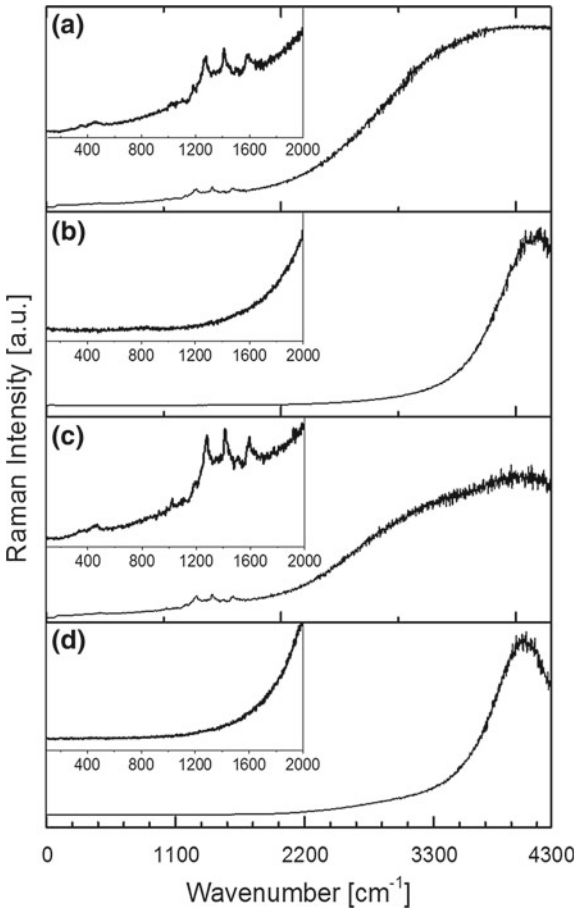

Fig. 14.24 Raman spectra of studied anthracyclines: **a** daunorubicin (DNR), **b** doxorubicin (DOX), **c** epidaunorubicin (EDNR) and **d** epidoksorubicin (EDOX) in full spectral range and magnification of the 100–2000 rel. cm^{-1} range. Spectra of anthracyclines (powder) recorded using the 488nm laser line

Integration of the marker spectral range of anthracyclines showed that DNR and EDOX accumulates in the nucleus beginning from a concentration of 300nM. The presence of EDNR in a cell can be observed at higher doses, i.e. 500nM, therefore the epimer of toxic DNR seems to be an interesting candidate as a chemotherapeutic agent from the point of view of low accumulation in endothelium. Additionally, accumulation of anthracyclines overlapped the nucleus area (DNA distribution) [71, 72].

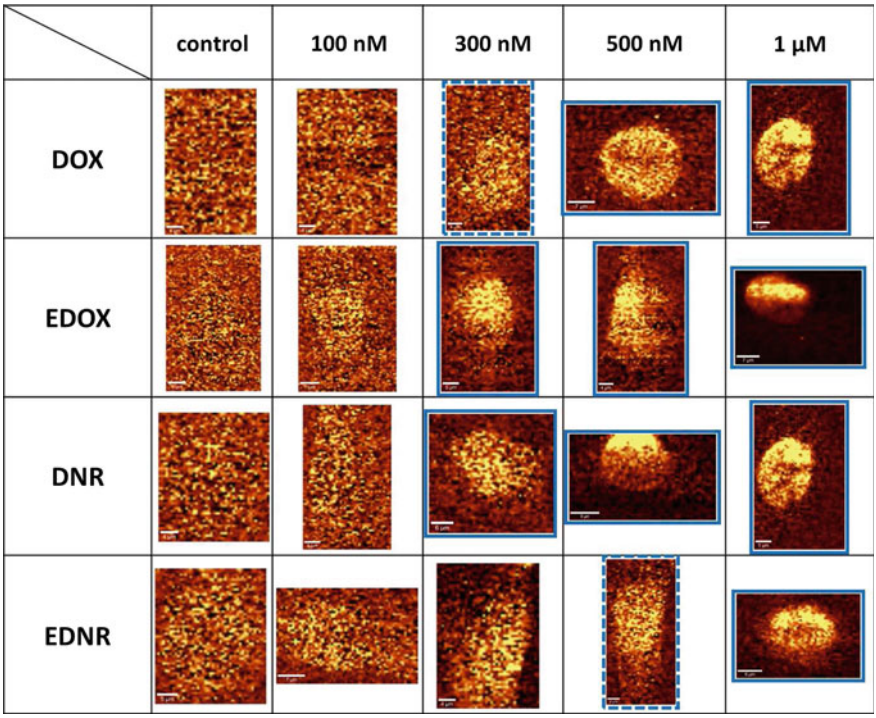

Fig. 14.25 Representative images obtained by integration of the 3820–4245 rel. cm^{-1} range (spectral range of anthracycline maximum fluorescence). "Threshold concentrations" (the lowest concentration for which the accumulation of anthracyclines in the nucleus was observed) are marked with a blue square (dashed line indicates these concentrations of the drugs for which part of the cells exhibit slight and ambiguous background increasing due to antibiotic fluorescence)

14.3.2.4 Raman Spectroscopy and Complementary Techniques in Red Blood Cells Analysis

Raman spectroscopy was successfully used for studies of standard hematoporphyrin as well as for imaging of heme, both in cells and tissues [73]. Functional as well as air-dried RBCs can be investigated by that method. The resonance Raman spectrum of hemoglobin (Hb) is observed when this compound is irradiated with the laser line, which corresponds to the wavelength of an electronic transition of Hb (488 and 532nm). Moreover, it has been previously suggested that the highly aligned structural arrangement of Hb inside functional RBCs causes a significant increase in the non-fundamental modes of the Raman spectra when excitation line is in close proximity to the vibronic band Qv (observed for 514.5 and 532nm excitation laser lines). It was reported that bands associated with oxyHb in malaria-infected RBCs can be identified more readily in the non-fundamental region [74].

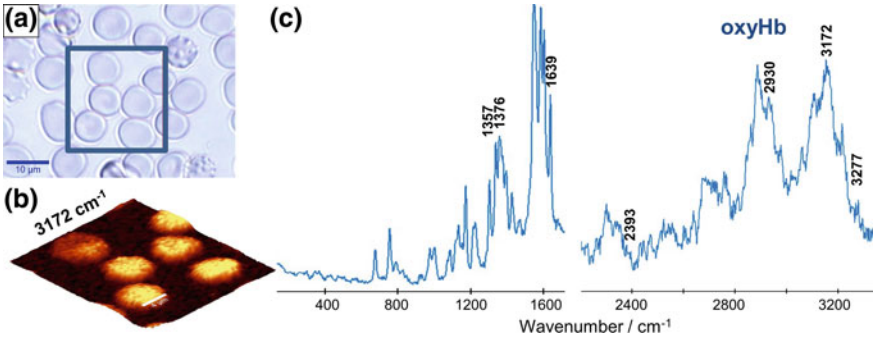

Fig. 14.26 Raman imaging of oxyHb in functional RBCs with the use of the overtone region band: **a** A photomicrograph of the live RBCs with the investigated area outlined (blue); **b** A Raman image obtained by integration of the oxyHb band in the overtone region at 3172 rel. cm^{-1} (ν_4); **c** the average resonant Raman spectra of oxyHb inside RBC obtained with the excitation of 532nm. Figure adapted with permission from [74]. Copyright (2014) John Wiley & Sons, Inc.

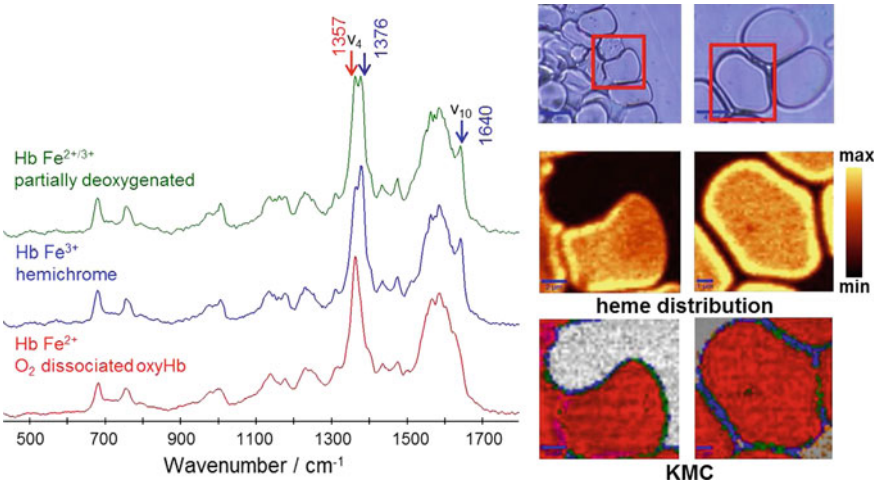

Fig. 14.27 High-resolution Raman imaging reveals spatial location of heme oxidation sites in single red blood cells of dried smears. A photomicrographs of the selected area of the air-dried human RBCs (whole blood, smear on the CaF_2 slide) with the labelled (red) investigated area; Raman images obtained by integration of the Hb's band in the spectral region of around 1350–1380 rel. cm^{-1} (ν_4); KMC results with three main clusters for RBCs. The clusters include hemichrome Hb Fe^{3+} (blue), laser-induced O_2 dissociated oxyHb, Hb Fe^{2+} (red) and partially deoxygenated Hb $Fe^{2+/3+}$ (green). The grey cluster observed between RBC's corresponds to substrate signal and is removed as an outlier. The representative spectra of the obtained clusters of RBCs obtained from the K-means Clustering (KMC). Figure adapted with permission from [60]. Copyright (2014) John Wiley & Sons, Inc.

The use of both, fundamental and overtone Raman regions improved the diagnostic capability of the Raman technique for malaria disease [74]. Figure 14.26 presents the Raman image obtained by integration of the overtone at 3172 rel. cm^{-1} of oxyHb of functional RBCs.

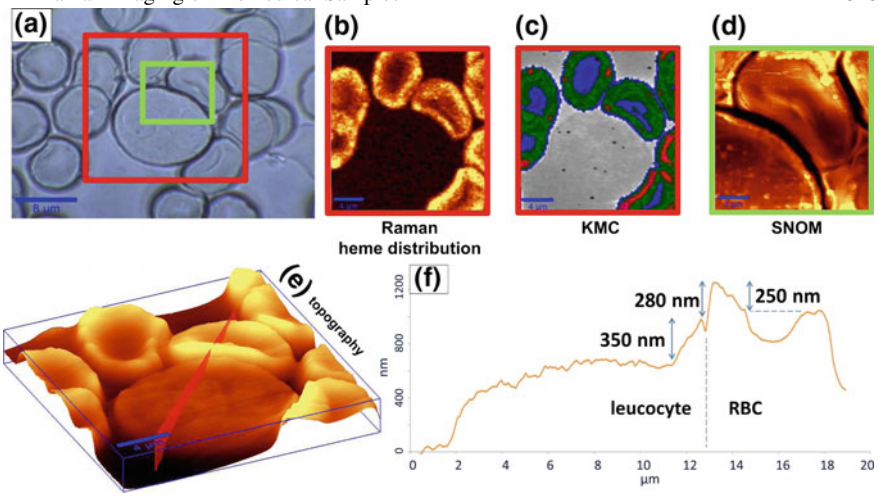

Fig. 14.28 Raman, AFM and SNOM as complementary techniques: **a** A photomicrograph of the air-dried human RBCs around a single leucocyte with the investigated area by Raman and AFM (red) as well as SNOM (green); **b** A Raman image obtained by integration of the Hb band in the spectral region around 1350–1380 rel. cm^{-1} (ν_4); **c** A KMC image of Fe^{2+} and Fe^{3+} distribution - colour coding as in Fig. 14.27; **d** SNOM results; **e** AFM topography image; **f** Topography cross section according to the red line presented in (**e**). Figure adapted with permission from [60]. Copyright (2014) John Wiley & Sons, Inc.

In analogy to functional RBCs, also for dried RBCs, which are measured in ambient conditions, the majority of the hemoglobin (Hb) exists in the oxyHb state. However, the studies of the thin smears of whole blood with the use of high-resolution Raman imaging shows also the hemichrome in the thin outer layer of RBCs [60]. To image the presence of the different heme type inside RBCs, 488nm excitation and laser-induced photo/thermal-dissociation of O_2 from oxyHb was used. The laser induced dissociation of oxyHb (Fe^{3+}, low spin) produces deoxyHb (Fe^{2+}, high spin). The observed hemichrome is a bishistidine complex, which does not contain the O_2 molecule, so no change to Fe^{2+} is observed in the regions where hemichrome is present [60].

The resonance Raman spectra allowed for observation of the oxidation state marker band (ν_4 mode), which changes from 1376 to 1357 rel. cm^{-1} for Fe^{3+} and Fe^{2+} Hb, respectively [75]. Figure 14.27 presents the visualization of the hemichrome inside air-dried RBCs with the representative Raman spectra.

The visualization of distribution of $Fe^{2+/3+}$ heme was studied also for RBCs in direct contact with some leucocytes (Fig. 14.28). This studies were supported with the AFM and SNOM techniques. AFM enabled the measurement of the RBCs-leucocyte topography that was very useful for the determination of the necessary size of the Raman imaging stack. SNOM results provided the information about the existence of the fluorophore compound in the area of the contact between RBC and leucocyte.

14.4 Summary and Outlook

Modern confocal Raman microscopy becomes an increasingly important tool in biological and medical sciences, due to the lateral resolution close to the Rayleigh limit and a high throughput. Raman imaging of cells and tissues yields a plethora of information about the distribution of biocomponents, their molecular structures and interactions between them. Therefore, Raman imaging is a suitable tool to study mechanisms of pathology development in model systems, such as cell cultures in vitro or tissues ex vivo.

This chapter summarizes our recent research focusing on application of Raman imaging to study murine models of lifestyle diseases, i.e. type 2 diabetes mellitus, hypertension, metastatic cancer, atherosclerosis, and non-alcoholic fatty liver disease. Moreover, the suitability of Raman microscopy for the characterization of biocomponents as well as processes of biomolecules and drugs uptake in single cells is also demonstrated. Several examples of successful combinations of Raman imaging with other complementary methods such as AFM or SNOM as well as applications of 3D imaging are also presented.

Raman microscopy is a unique probe to study cellular processes and chemical alterations in tissues due to pathology. It is expected that this technique, at the moment used mostly as a research tool in model systems, in the future may become a routine method of medical diagnostics, for example in cytopathology or a non-invasive investigation of disease margins.

Acknowledgements The financial support by National Science Centre (DEC-2013/08/A/ST4/00308) and by the European Union under the European Regional Development Fund (grant coordinated by JCET-UJ, POIG.01.01.02-00-069/09) is acknowledged.

References

1. J. Peloquin, J. Huynh, R.M. Williams, C.A. Reinhart-King, J. biomechanics **44**(5), 815 (2011)
2. J. Clark, S. Glagov, Br. J. Exp. Pathol. **57**(1), 129 (1976)
3. U. Smith, J.W. Ryan, D.D. Michie, D.S. Smith, Science **173**(4000), 925 (1971)
4. K. Kusche-Vihrog, K. Urbanova, A. Blanqué, M. Wilhelmi, H. Schillers, K. Kliche, H. Pavenstädt, E. Brand, H. Oberleithner, Hypertension **57**(2), 231 (2011)
5. H. Oberleithner, W. Peters, K. Kusche-Vihrog, S. Korte, H. Schillers, K. Kliche, K. Oberleithner, Pflügers Arch.-Eur. J. Physiol. **462**(4), 519 (2011)
6. M. Pilarczyk, A. Rygula, A. Kaczor, L. Mateuszuk, E. Maślak, S. Chlopicki, M. Baranska, Vib. Spectrosc. **75**, 39 (2014)
7. M.Z. Pacia, E. Buczek, A. Blazejczyk, A. Gregorius, J. Wietrzyk, S. Chlopicki, M. Baranska, A. Kaczor, Anal. Bioanalytical Chem. **408**(13), 3381 (2016)
8. M. Pilarczyk, A. Rygula, L. Mateuszuk, S. Chlopicki, M. Baranska, A. Kaczor, Biomed. Spectrosc. Imaging **2**(3), 191 (2013)
9. K.W. Short, S. Carpenter, J.P. Freyer, J.R. Mourant, Biophys. J. **88**(6), 4274 (2005)
10. C. Krafft, T. Knetschke, R.H. Funk, R. Salzer, Anal. Chem. **78**(13), 4424 (2006)
11. B.R. Wood, B. Tait, D. McNaughton, Biochimica et Biophysica Acta (BBA)-Molecular. Cell Res. **1539**(1), 58 (2001)
12. K. Meister, J. Niesel, U. Schatzschneider, N. Metzler-Nolte, D.A. Schmidt, M. Havenith, Angew. Chem. Int. Ed. **49**(19), 3310 (2010)

13. H.J. van Manen, C. Otto, Nano lett. **7**(6), 1631 (2007)
14. M. Davoren, E. Herzog, A. Casey, B. Cottineau, G. Chambers, H.J. Byrne, F.M. Lyng, Toxicol. In Vitro **21**(3), 438 (2007)
15. P. Candeloro, L. Tirinato, N. Malara, A. Fregola, E. Casals, V. Puntes, G. Perozziello, F. Gentile, M.L. Coluccio, G. Das et al., Analyst **136**(21), 4402 (2011)
16. C. Scalfi-Happ, M. Udart, C. Hauser, A. Rück, Med. Laser Appl. **26**(4), 152 (2011)
17. T. Chernenko, C. Matthäus, L. Milane, L. Quintero, M. Amiji, M. Diem, ACS Nano **3**(11), 3552 (2009)
18. C. Matthäus, T. Chernenko, J.A. Newmark, C.M. Warner, M. Diem, Biophys. J. **93**(2), 668 (2007)
19. H. Yao, Z. Tao, M. Ai, L. Peng, G. Wang, B. He, Y.Q. Li, Vib. Spectrosc. **50**(2), 193 (2009)
20. Z. Liu, K. Chen, C. Davis, S. Sherlock, Q. Cao, X. Chen, H. Dai, Cancer Res. **68**(16), 6652 (2008)
21. D.M. Stitt, M.Z. Kastyak-Ibrahim, C.R. Liao, J. Morrison, B.C. Albensi, K.M. Gough, Vib. Spectrosc. **60**, 16 (2012)
22. W. Rasband, http://rsb.info.nih.gov/ij pp. 1997–2007 (1997)
23. H. Chen, O. Charlat, L.A. Tartaglia, E.A. Woolf, X. Weng, S.J. Ellis, N.D. Lakey, J. Culpepper, K.J. More, R.E. Breitbart et al., Cell **84**(3), 491 (1996)
24. M. Pilarczyk, L. Mateuszuk, A. Rygula, M. Kepczynski, S. Chlopicki, M. Baranska, A. Kaczor, PLoS ONE; e106065. **9**(8) (2014). https://doi.org/10.1371/journal.pone.0106065
25. C. Krafft, L. Neudert, T. Simat, R. Salzer, Spectrochim. Acta Part A: Mol. Biomol. Spectrosc. **61**(7), 1529 (2005)
26. K. Simons, D. Toomre, Nat. Rev. Mol. Cell Biol. **2**(3), 216 (2001)
27. K. Simons, M.J. Gerl, Nat. Rev. Mol. Cell Biol. **11**(10), 688 (2010)
28. H. Cai, D.G. Harrison, Circ. Res. **87**(10), 840 (2000)
29. H.D. Intengan, E.L. Schiffrin, Hypertension **38**(3), 581 (2001)
30. M.Z. Pacia, L. Mateuszuk, S. Chlopicki, M. Baranska, A. Kaczor, Analyst **140**(7), 2178 (2015)
31. M. Gniadecka, P.A. Philipsen, S. Sigurdsson, S. Wessel, O.F. Nielsen, D.H. Christensen, J. Hercogova, K. Rossen, H.K. Thomsen, R. Gniadecki et al., J. Invest. Dermatol. **122**(2), 443 (2004)
32. K. Majzner, T.P. Wrobel, A. Fedorowicz, S. Chlopicki, M. Baranska, Analyst **138**(24), 7400 (2013)
33. J. Suh, M. Moskovits, J. Am. Chem. Soc. **108**(16), 4711 (1986)
34. B.G. Frushour, J.L. Koenig, Biopolymers **14**(2), 379 (1975)
35. M.M. Steed, N. Tyagi, U. Sen, D.A. Schuschke, I.G. Joshua, S.C. Tyagi, Am. J. Physiol.-Lung Cell. Mol. Physiol. **299**(3), L301 (2010)
36. S. Duraipandian, W. Zheng, J. Ng, J.J. Low, A. Ilancheran, Z. Huang, Analyst **136**(20), 4328 (2011)
37. E.M. Kanter, S. Majumder, E. Vargis, A. Robichaux-Viehoever, G.J. Kanter, H. Shappell, H.W. Jones III, A. Mahadevan-Jansen, J. Raman Spectrosc. **40**(2), 205 (2009)
38. A. Robichaux-Viehoever, E. Kanter, H. Shappell, D. Billheimer, H. Jones III, A. Mahadevan-Jansen, Appl. Spectrosc. **61**(9), 986 (2007)
39. J.W. Franses, N.C. Drosu, W.J. Gibson, V.C. Chitalia, E.R. Edelman, Int. J. Cancer **133**(6), 1334 (2013)
40. S. Dalaklioglu, A. Tasatargil, S. Kale, G. Tanriover, S. Dilmac, N. Erin, Vasc. Pharmacol. **59**(3), 103 (2013)
41. E. Buczek, A. Blazejczyk, T. Wojcik, B. Sitek, L. Mateuszuk, A. Jasztal, E. Maslak, A. Fedorowicz, B. Proniewski, R. Gurbiel, J. Wietrzyk, S. Chlopicki, BMC Cancer **in review** (2016)
42. T. Wrobel, A. Fedorowicz, L. Mateuszuk, E. Maslak, A. Jasztal, S. Chlopicki, K. Marzec, *Vibrational Microspectroscopy for Analysis of Atherosclerotic Arteries* (Springer, Dordrecht, 2014), pp. 505–535
43. K.M. Marzec, A. Rygula, M. Gasior-Glogowska, K. Kochan, K. Czamara, K. Bulat, K. Malek, A. Kaczor, M. Baranska, Pharmacol. Rep. (2015)

44. K.M. Marzec, T.P. Wrobel, A. Rygula, E. Maslak, A. Jasztal, A. Fedorowicz, S. Chlopicki, M. Baranska, J. Biophotonics **7**(9), 744 (2014)
45. K. Kochan, K. Marzec, E. Maslak, S. Chlopicki, M. Baranska, Analyst **140**(7), 2074 (2015)
46. T. Wrobel, K. Marzec, S. Chlopicki, E. Maślak, A. Jasztal, M. Franczyk-Żarów, I. Czyżyńska-Cichoń, T. Moszkowski, R. Kostogrys, M. Baranska, Sci. Rep. **5** (2015)
47. K. Kochan, K.M. Marzec, K. Chruszcz-Lipska, A. Jasztal, E. Maslak, H. Musiolik, S. Chłopicki, M. Baranska, Analyst **138**(14), 3885 (2013)
48. K. Marzec, K. Kochan, A. Fedorowicz, A. Jasztal, K. Chruszcz-Lipska, J.C. Dobrowolski, S. Chlopicki, M. Baranska, Analyst **140**(7), 2171 (2015)
49. A. Rygula, M. Pacia, L. Mateuszuk, A. Kaczor, R. Kostogrys, S. Chlopicki, M. Baranska, Analyst **140**(7), 2185 (2015)
50. Y. Takahashi, Y. Soejima, T. Fukusato, World J. Neurogastroenterol: WJG **18**(19), 2300 (2012)
51. A.M. Zivkovic, J.B. German, A.J. Sanyal, Am. J. Clin. Nutr. **86**(2), 285 (2007)
52. G. Kanuri, I. Bergheim, Int. J. Mol. Sci. **14**(6), 11963 (2013)
53. R. Buettner, K. Parhofer, M. Woenckhaus, C. Wrede, L. Kunz-Schughart, J. Schölmerich, L. Bollheimer, J. Mol. Endocrinol. **36**(3), 485 (2006)
54. O. Samek, A. Jonáš, Z. Pilát, P. Zemánek, L. Nedbal, J. Tříska, P. Kotas, M. Trtílek, Sensors **10**(9), 8635 (2010)
55. K. Majzner, K. Kochan, N. Kachamakova-Trojanowska, E. Maslak, S. Chlopicki, M. Baranska, Anal. Chem. **86**(13), 6666 (2014)
56. E. Maslak, P. Zabielski, K. Kochan, K. Kus, A. Jasztal, B. Sitek, B. Proniewski, T. Wojcik, K. Gula, A. Kij et al., Biochem. Pharmacol. **93**(3), 389 (2015)
57. N. Testerink, M. Ajat, M. Houweling, J.F. Brouwers, V.V. Pully, H.J. van Manen, C. Otto, J.B. Helms, A.B. Vaandrager, PloS ONE **7**(4), e34945 (2012)
58. K. Galler, F. Schleser, E. Fröhlich, R.P. Requardt, A. Kortgen, M. Bauer, J. Popp, U. Neugebauer, Integr. Biol. **6**(10), 946 (2014)
59. B.R. Wood, L. Hammer, L. Davis, D. McNaughton, J. Biomed. Opt. **10**(1), 014005 (2005)
60. K.M. Marzec, A. Rygula, B.R. Wood, S. Chlopicki, M. Baranska, J. Raman Spectrosc. **46**(1), 76 (2015)
61. K. Majzner, A. Kaczor, N. Kachamakova-Trojanowska, A. Fedorowicz, S. Chlopicki, M. Baranska, Analyst **138**(2), 603 (2013)
62. K. Majzner, S. Chlopicki, M. Baranska, J. Biophotonics **10**, 1 (2015)
63. K. Czamara, K. Majzner, M. Pacia, K. Kochan, A. Kaczor, M. Baranska, J. Raman Spectrosc. **46**(1), 4 (2015)
64. X. Nan, J.X. Cheng, X.S. Xie, J. Lipid Res. **44**(11), 2202 (2003)
65. C.W. Freudiger, W. Min, B.G. Saar, S. Lu, G.R. Holtom, C. He, J.C. Tsai, J.X. Kang, X.S. Xie, Science **322**(5909), 1857 (2008)
66. T.T. Le, S. Yue, J.X. Cheng, J. Lipid Res. **51**(11), 3091 (2010)
67. C. Nieva, M. Marro, N. Santana-Codina, S. Rao, D. Petrov, A. Sierra, PLoS ONE; e46456. https://doi.org/10.1371/journal.pone.0046456, **7**(10) (2012)
68. M.N. Slipchenko, T.T. Le, H. Chen, J.X. Cheng, J. Phys. Chem. B **113**(21), 7681 (2009)
69. Q. Yan, W. Priebe, J.B. Chaires, R.S. Czernuszewicz, Biospectroscopy **3**(4), 307 (1997)
70. G. Das, A. Nicastri, M.L. Coluccio, F. Gentile, P. Candeloro, G. Cojoc, C. Liberale, F. De Angelis, E. Di Fabrizio, Microsc. Res. Tech. **73**(10), 991 (2010)
71. T. Wojcik, E. Buczek, K. Majzner, A. Kolodziejczyk, J. Miszczyk, P. Kaczara, W. Kwiatek, M. Baranska, M. Szymonski, S. Chlopicki, Toxicol. In Vitro **29**(3), 512 (2015)
72. K. Majzner, T. Wojcik, E. Szafraniec, M. Lukawska, I. Oszczapowicz, S. Chlopicki, M. Baranska, Analyst **140**(7), 2302 (2015)
73. D. McNaughton, B.R. Wood, T.C. Cox, J.C. Drenckhahn, in *Infrared and Raman Spectroscopic Imaging*, ed. by R. Salzer, H.W. Siesler (Wiley-VCH Verlag GmbH & Co. KGaA, 2009), pp. 203–220
74. K.M. Marzec, D. Perez-Guaita, M. De Veij, D. McNaughton, M. Baranska, M.W. Dixon, L. Tilley, B.R. Wood, Chem. Phys. Chem. **15**(18), 3963 (2014)
75. A. Rygula, K. Majzner, K. Marzec, A. Kaczor, M. Pilarczyk, M. Baranska, J. Raman Spectrosc. **44**(8), 1061 (2013)

Chapter 15
ISERS Microscopy for Tissue-Based Cancer Diagnostics with SERS Nanotags

Yuying Zhang and Sebastian Schlücker

Abstract Immuno-SERS (iSERS) microscopy is an emerging imaging technique in tissue-based cancer diagnostics, which is based on antibodies labelled with SERS-active noble metal nanoparticles (NPs) in conjunction with Raman microspectroscopy for localizing target proteins. Advantages of SERS over existing labeling approaches include its high capacity for spectral multiplexing (parallel detection of target molecules), quantification (based on the characteristic SERS signatures), high photostability (no or minimal photobleaching), minimization of autofluorescence from biological specimens (via red to near-infrared excitation), and the technical advantage of using only a single laser excitation line. In this book chapter, we will first give a very brief tutorial on the fundamentals of SERS, followed by an introduction into the concept and current designs of target-specific SERS probes based on noble metal NPs. Next, the fast developing applications of iSERS microscopy for tissue-based cancer diagnostics are highlighted, and finally the challenges and future perspectives of this emerging field are presented.

15.1 Introduction

Cancer is one of the biggest causes of mortality in the world. Effective diagnostic tools for cancer detection are highly desirable in order to provide early intervention by therapy as well as to reduce costs associated with cancer patient management. Detection and localization of prognostic markers in tissues is of central importance for cancer diagnostics. Currently, the most widely used method to detect protein expression in tissue specimens is immunohistochemistry (IHC), a staining method based on antigen-antibody recognition. In order to visualize the antigen-antibody immunoreaction, the antibody must be labelled, usually by enzymes, fluorophores, radioactive compounds or colloidal gold [1]. Multiplexed immunohistochemistry (mIHC), in which two or more antigens are detected simultaneously, is powerful in tumor

Y. Zhang · S. Schlücker (✉)
Department of Chemistry and Center for Nanointegration Duisburg-Essen (CENIDE), University of Duisburg-Essen, Universitätsstr. 5, 45141 Essen, Germany
e-mail: sebastian.schluecker@uni-due.de

J. Toporski et al. (eds.), *Confocal Raman Microscopy*, Springer Series in Surface Sciences 66, https://doi.org/10.1007/978-3-319-75380-5_15

diagnosis and classification as it offers greater insights into, spatial relationships and heterogeneity of protein expression in the same tissue specimen [2]. However, current readout methods for mIHC based on dyes or molecular fluorophores are limited because of spectral overlap due to the broad electronic absorption and emission bands, respectively. The introduction of quantum dots [3–5], semiconductor nanocrystals with size-dependent fluorescence emission, has been a major improvement in the multiplexing capacity of fluorescence-based detection schemes: approx. 3–10 quantum dots may be detected simultaneously because of their narrower emission peaks (peak width ~30 nm compared with molecular fluorophores (typically >50 nm)) [6].

Surface-enhanced Raman scattering (SERS) has experienced significant growth in biomedical research during the past decade [7–9]. Numerous applications have demonstrated the potential of SERS for label-free detection of various analytes, especially in human biological samples such as blood, saliva, cells, and serum [10–12]. More recently, "SERS labels / nanotags" that combine metallic nanoparticles (NPs) and organic Raman reporter molecules have been designed and used for the selective and sensitive detection of proteins and oligonucleotides [13–15]. These SERS-active colloids produce strong, characteristic Raman signals, exhibit optical labeling functions similar to external chromophores like organic dyes, fluorophores, and quantum dots, and additionally, have much narrower emission peaks (<2 nm) [16]. Compared with existing labeling approaches, SERS labels offer advantages such as tremendous spectral multiplexing capabilities for simultaneous target detection (>10 different "colors"), the need of only a single laser excitation wavelength to excite multiple SERS labels simultaneously, no or only minimal photobleaching and improved image contrast by red or near-infrared (NIR) laser excitation [17].

Immuno-SERS (iSERS) microscopy (Fig. 15.1), which employs target-specific colloidal SERS probes in combination with Raman microspectroscopy, is an emerging imaging method in tissue diagnostics [17]. The concept of protein localization in iSERS is the same as in conventional IHC, i.e., the target antigen is recognized by a labelled antibody (Fig. 15.2). Tissues, either frozen or formalin-fixed and paraffin-embedded (FFPE) specimens, are usually prepared as micrometer-thick sections

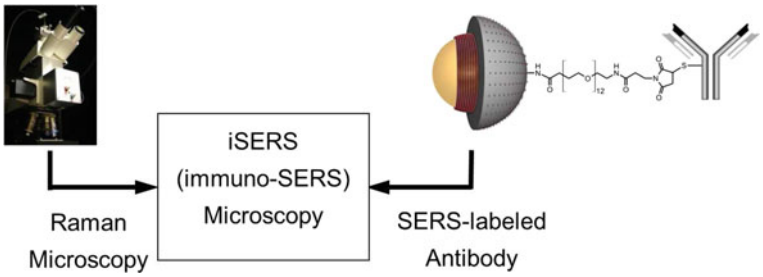

Fig. 15.1 Immuno-SERS (iSERS) microscopy is an emerging imaging method for the selective and sensitive localization of target molecules. Target-specific SERS particles, obtained after the conjugation of SERS labels to target-specific binding molecules, can be localized in cells and tissue and identified by their characteristic signature using Raman microscopy [18]

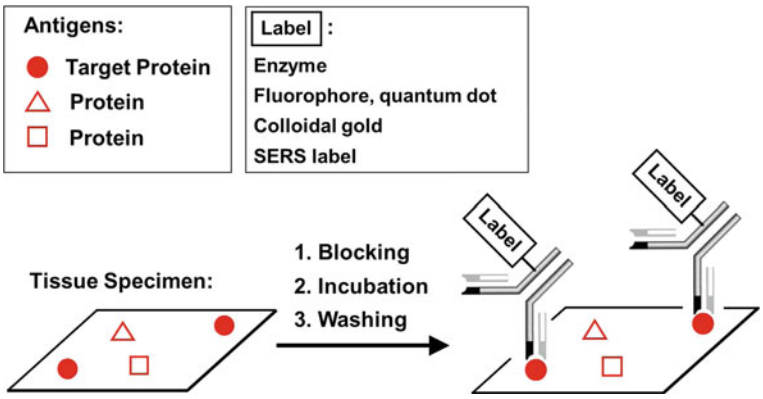

Fig. 15.2 Principle of immunohistochemistry for target protein localization. For minimizing non-specific binding, the tissue specimen is first blocked and then incubated with the labelled antibody as the target-specific probe. The antibody selectively recognizes the antigen via the binding sites and forms the corresponding antigen-antibody complex. Finally, washing removes unbound antibodies. The antigen can be localized by the characteristic SERS spectrum of the SERS label using Raman microspectroscopy [18]

using a microtome. In order to minimize non-specific binding, blocking agents such as goat serum or bovine serum albumin (BSA) may be employed prior to staining. Then the tissue specimen is incubated with antibodies to form corresponding antigen-antibody complexes, and subsequently unbound antibodies are removed by washing. The characteristic signals of the SERS labels indicate target protein localization because the labels are attached to the antibody, which specifically binds to the target protein.

15.2 Brief Tutorial on SERS

In addition to conventional Raman spectroscopy, SERS requires metallic nanostructures that can support localized surface plasmon resonances (the so-called SERS substrate). Figure 15.3 shows for a gold nanoparticle how the oscillating electric field of the incoming laser radiation with angular frequency ω_{inc} and amplitude E_0 drives an oscillation of the conduction electrons of the metal, leading to charge separation (dipole). This type of resonance is termed dipolar localized surface plasmon resonance (LSPR). The sign of the localized induced dipole μ_{ind} changes periodically with the angular frequency ω_{inc} of the electromagnetic wave as the external driving force. Overall, a Hertzian dipole (see electric field lines in Fig. 15.3a) on the nanoscale has been generated. This nanoantenna can then emit radiation at the same frequency ω_{inc} (green color in Fig. 15.3a, b; elastic scattering).

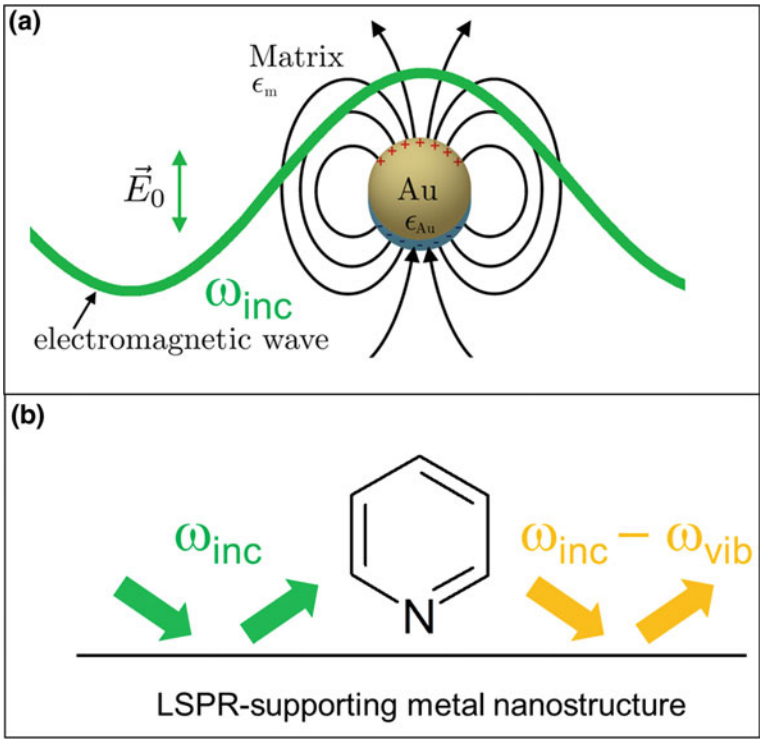

Fig. 15.3 Electromagnetic enhancement in SERS. **a** A gold nanoparticle acts as a nanoantenna by excitation of a dipolar localized surface plasmon resonance (LSPR); **b** Both the "incoming" field (ω_{inc}, green) and the "outgoing" field ($\omega_{inc} - \omega_{vib}$, orange) are enhanced by elastic light scattering off the LSPR-supporting metal nanostructure [19]

The increased local electric field $E_{loc}(\omega_{inc})$ in the vicinity of the metal particle can interact with a molecule nearby the surface of the metal sphere (Fig. 15.3b) and induce a molecular dipole (Rayleigh and Raman scattering). The Stokes-Raman scattering component with $\omega_{inc} - \omega_{vib}$ (left orange arrow in Fig. 15.3b) itself can excite a LSPR of the metal colloid in Fig. 15.3a. Again, elastic light scattering off the metal sphere can take place (right orange arrow in Fig. 15.3b) and the emitted radiation is finally detected in the far field. This physical picture applies to all nanostructures which support LSPRs.

The overall SERS intensity depends on both the "incoming" (ω_{inc}) and the "outgoing" ($\omega_{inc} - \omega_{vib}$) field: $I_{SERS} = I_{inc}(\omega_{inc})I(\omega_{inc} - \omega_{vib}) = |E_{inc}(\omega_{inc})|^2 \cdot |E(\omega_{inc} - \omega_{vib})|^2$. Optimal SERS enhancements therefore require that both the incident radiation at ω_{inc} and the Stokes-Raman-shifted radiation at $\omega_{inc} - \omega_{vib}$ are in resonance with the plasmon peak of the metal nanostructure. For $\omega_{inc} \approx \omega_{inc} - \omega_{vib}$ the widely used $|E|^4$ approximation of the SERS intensity results: $I_{SERS} \approx |E(\omega_{inc})|^4$.

This electromagnetic enhancement is the dominant contribution to SERS since it is responsible for the tremendous signal increase compared to conventional Raman scattering: moderate local field enhancements (E_{loc}) yield huge SERS enhancements ($\sim |E|^4$). SERS is additionally a truly surface-selective effect: only molecules on or nearby such plasmonic nanostructures exhibit huge enhancement due to the SERS distance dependence. The electric field strength of dipolar radiation scales with $E(r) \sim r^{-3}$. The SERS distance dependence is therefore $I_{SERS} \sim r^{-12}$ under the $|E|^4$ approximation, i.e. the SERS intensity drops down drastically with increasing distance r between the molecule and the metal surface. The SERS enhancement factor (EF) is a very central figure in SERS for quantifying the overall signal enhancement. The experimental determination of EFs in SERS requires measurements of the SERS intensity for the adsorbed molecule on the metal surface, relative to the normal Raman intensity of the same, "free" molecule in solution. Both intensities must be normalized to the corresponding number of molecules on the surface (SERS) and in solution (conventional Raman), respectively. Further information on SERS can be retrieved from several review articles [19–23] and monographs [24, 25].

15.3 SERS Nanoparticle Labels

The rational design of SERS nanoparticle labels with defined physicochemical properties is essential for successful applications in bioanalytical assays and cancer diagnostics. For an introduction to the topic of the synthesis and characterization of SERS labels and their application in bioanalysis, recent reviews [13, 14] are recommended. SERS colloids for targeted research contain three basic constituents: a colloidal SERS substrate for signal enhancement, Raman reporter molecules adsorbed onto its surface for identification, and biomolecules attached to the SERS label for target-specific recognition. Figure 15.4a shows an example of a target-specific SERS probe [17, 26], comprising a monolayer of Raman reporter molecules on the surface of a Au/Ag nanoshell, a silica shell, which chemically and mechanically stabilizes the SERS label, and a spacer molecule for bioconjugation of the antibody to the SERS label. The protective encapsulant, such as silica or polymer coatings, is optional but desirable since it enhances the stability and biocompatibility of the colloid. Using a spacer molecule between the antibodies and the SERS label instead of direct conjugation of the antibody to the metal surface introduces conformational flexibility and may be beneficial for proper target recognition via the antigen binding sites.

Figure 15.4b depicts the sequence of chemical modifications by which SERS-labelled antibodies are synthesized from metal colloids. The addition of Raman reporter molecules to the colloid with subsequent encapsulation leads to a stabilized SERS particle. Modification of the shell with spacers and their conjugation to antibodies finally yields SERS-labelled antibodies.

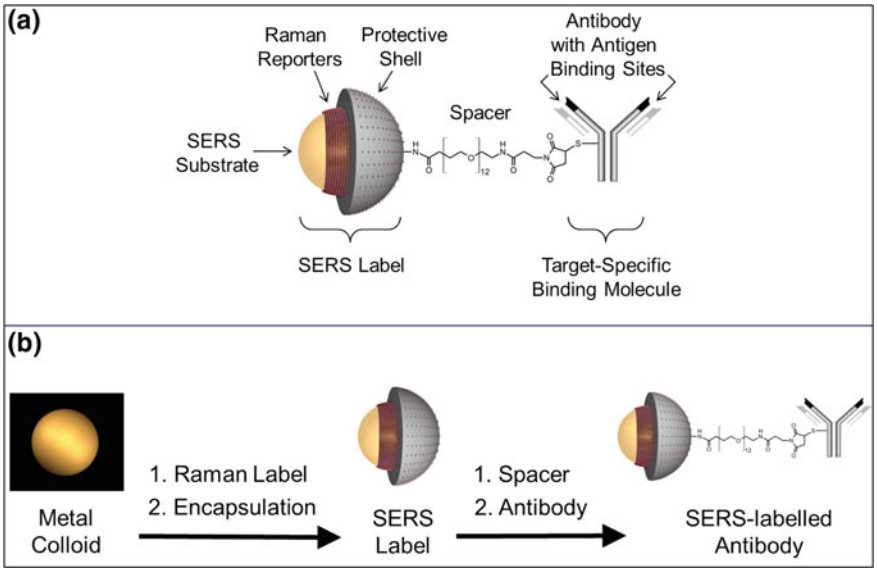

Fig. 15.4 **a** Components of a target-specific SERS probe: Colloidal SERS substrate (Au/Ag nanoshell), Raman reporters adsorbed to its surface (organic monolayer), an optional protective encapsulant (glass shell) and a target-specific binding molecule (antibody) attached to the SERS label via a spacer molecule; **b** Synthesis of SERS-labelled antibodies: The metal colloid is incubated with Raman labels and optionally encapsulated with a protective shell. The resulting encapsulated SERS label is then conjugated to antibodies via spacer units [18]

15.3.1 Choice of Metal Colloids as SERS Substrates

The first step to design a SERS label is to choose and prepare a metal colloid with the desired optical properties, in particular with respect to the position of the LSPR peak and the achievable signal enhancement. Noble metal NPs in the size range 10–100 nm are typically suitable for SERS and in addition to size, other parameters such as shape and chemical composition determine their optical properties. Ideally, the Raman enhancement is so high that single nanoparticles can be detected.

15.3.1.1 Single Nanoparticle-Based SERS Substrates

Optical excitation of localized surface plasmons is achieved by matching the plasmon peak of the metal colloid with a given laser wavelength for resonant excitation. In biomedical applications, SERS substrates with a LSPR peak in the red or NIR region are often favored, because of minimal autofluorescence of biological specimens and improved image contrast [27, 28]. Silver and gold NPs are the most widely used SERS substrates, however, their extinction maximum occurs in the blue to green region, respectively. Au/Ag nanoshells are suitable substrates in biomedical applications

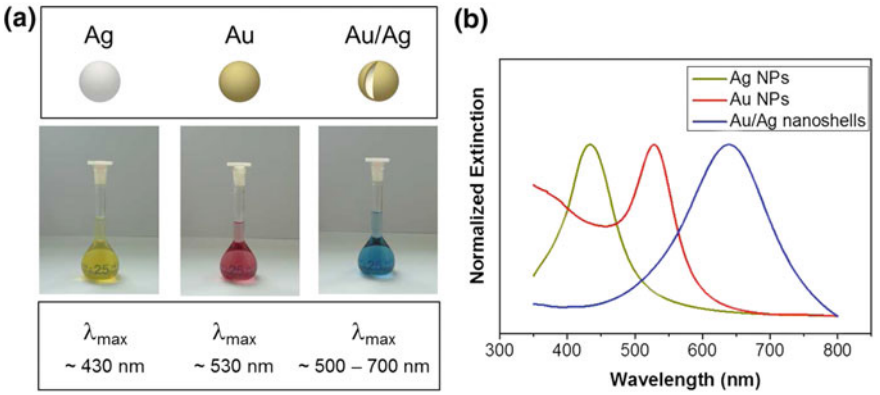

Fig. 15.5 **a** Photographs of different noble metal colloids with a diameter of ~55 nm, together with the approximate wavelength of the plasmon peak in water. In contrast to Ag and Au solid nanospheres, the plasmon resonance of Au/Ag nanoshells occurs in the red to near-infrared region and - in addition to the particle diameter - can be controlled by the shell thickness; **b** Experimental extinction spectra of different noble metal nanoparticles (~60 nm AgNPs, Au NPs and Au/Ag nanoshells) in water [18]

since their LSPR peak is tunable from the red to NIR region (Fig. 15.5a). The optical properties of nanospheres can be calculated by the Lorenz-Mie theory.

Figure 15.6 illustrates the tunable plasmon band of Au/Ag nanoshells [29] with varying shell thickness based on Mie calculations [30, 31]. All particles have a diameter of 55 nm and the shell thickness d decreases from left to right. The position of the LSPR peak depends on a number of parameters, in particular the size of the NPs and the dielectric function of both the metal and the surrounding medium. The experimental extinction spectra of quasi-spherical 60 nm AgNPs, AuNPs and Au/Ag nanoshells in water are shown in Fig. 15.5b: the corresponding LSPR peaks are observed at ~430, ~540 and ~630 nm, respectively. By using red laser (He-Ne laser, 632.8 nm) excitation, it has been shown experimentally that 60 nm Au/Ag nanoshells yield about 8 times higher SERS intensities compared with gold nanospheres of the same size [26]. Besides the nanoshells with a solvent core and a Au/Ag alloy shell discussed here, several kinds of other nanoshell structures, such as SiO_2/Au nanoshells, hollow Au nanoshells, and nanocages, have been developed as SERS substrates [32–35].

A new class of multibranched metal NPs such as nanostars or nanoflowers [36, 37] are of particular interest because minor shape modifications enable manipulation of their optical properties. Similar to the nanoshells, the LSPR peak of nanostars is tunable throughout the visible and NIR spectrum. Furthermore, the increased surface area and roughness allows more Raman reporter molecules to be attached on the nanostars than on spherical NPs with a same size and due to their sharp tips, they exhibit high SERS enhancement factors, enabling single-particle SERS detection [38]. In contrast to nanospheres and nanoshells, which exhibit a single LSPR peak, nanorods [39, 40] have two resonances: a weak transverse plasmon

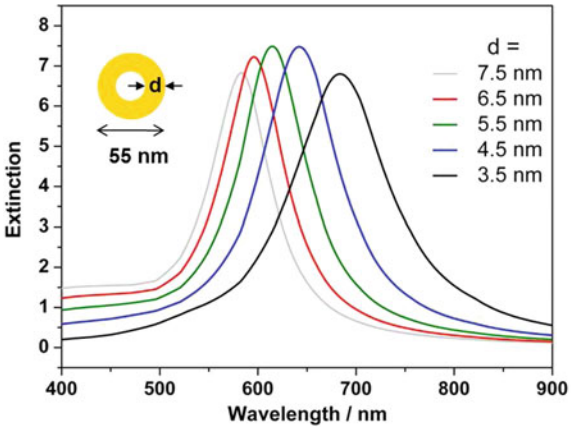

Fig. 15.6 Extinction spectra of single Au/Ag nanoshells with a constant diameter of 55 nm but varying shell thickness, calculated by Lorenz-Mie theory with water as the surrounding medium. The plasmon peak shifts to higher wavelengths as the shell becomes thinner [18]

peak in the visible region and a strong longitudinal plasmon peak in the longer wavelength region. Au nanorods have also attracted much attention because their longitudinal plasmon resonance as well as the Raman enhancement can be tuned by changing their aspect ratio [41].

15.3.1.2 Aggregates and Assemblies of Metal Nanoparticles as SERS Substrates

Aggregation of metal NPs (Fig. 15.7a) exhibit great SERS enhancements at the junctions between the NPs, which are usually called "hot spots".

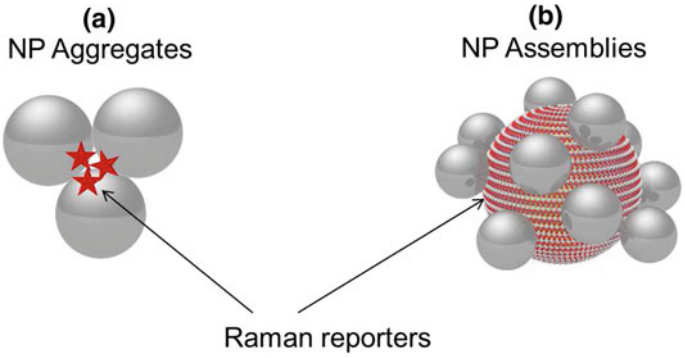

Fig. 15.7 **a** Protein (BSA)-encapsulated aggregates of metal nanoparticles; **b** Well-defined assemblies of metal nanoparticles

The electromagnetic field enhancement at hot spots of up to several orders of magnitude enables even single-molecule detection [42]. Particle aggregation is initiated very easily, for example, simply by changing solvents or adding salts. Control over size and shape of NP aggregates is highly desirable for fabricating uniform SERS labels with reproducible signals on a particle-by-particle basis. The biotechnology research group of Intel Corporation claimed to have established a method of Raman label-induced controlled aggregation of silver NPs, the so called Composite Organic-Inorganic Nanoparticles (COINs) [43]. BSA encapsulation is adopted to stabilize the NPs from further aggregation and introduce surface functional groups for bioconjugation [44]. Alternatively, different methods such as electrophoresis, filtration, size exclusion chromatography and density gradient centrifugation can be used to separate small clusters from larger aggregates in crude colloidal mixtures. For example, Salehi and Steinigeweg et al. have established a method to purify small glass-coated clusters (dimers and trimers) of Au NPs by using continuous density gradient centrifugation. The purified clusters exhibit the desired single-particle SERS brightness, even at acquisition times as short as 30 ms per pixel [45].

In addition to small NP aggregates, well defined NP assemblies, which contain controllable hot spots (Fig. 15.7b), are also developed as bright SERS substrates. Dimers of metal NPs are the smallest possible assemblies, which exhibit a single hot spot between the two NPs upon resonant laser illumination. Geometrical configurations that integrate more than two metal NPs into three dimensions represent the next level of complexity beyond dimers and produce multiple hotspots [46]. Silica particles are commonly used as a template for the assembly of many small metal NPs onto its surface, followed by the adsorption of Raman reporter molecules onto the small satellites. The satellite NPs can be either synthesized in situ by adsorbing metal salts and adding reducing agents [47, 48] or be assembled with as-prepared NPs based on covalent linkage or electrostatic interaction [49]. For example, Jeong and co-workers have introduced fluorescent SERS dots, which consist of silica NPs as a core with Raman reporter-labelled silver NPs on their surface and a fluorescent dye-conjugated outer silica shell. The overall size of the assemblies is ca.240 nm and they have been applied for multiplexed molecular diagnostics [48]. Further, also 3D plasmonic nanoassemblies were successfully synthesized via electrostatic self-assembly by Schlücker's group [46]. Specifically, monodispersed 80 nm gold nanospheres were incubated with Raman reporters and encapsulated with an ultrathin, about 2 to 3 nm thick silica shell and functionalized with amino groups, yielding positively charged glass-encapsulated Au cores. Negatively charged, citrate-stabilized 20 nm AuNPs were then assembled onto the surface of the Au cores via electrostatic attraction. Finite element method (FEM) calculations indicate that the plasmonic coupling between the core and satellite particles as well as between satellites results in large $|E|^4$ values of up to $\sim 2 \times 10^{10}$. In order to avoid the relatively large core-satellite gap (>2 nm) due to the silica shell, which reduces the plasmonic enhancement, recently, the same group presented a new route to core-satellite assemblies based on heterobifunctional Raman reporters which serve as molecular linkers for

electrostatic conjugation [50]. With a small core-satellite gap (1–2 nm), 3D noble metal NP assemblies using both AgNPs and AuNPs as core particles in combination with smaller AgNPs or AuNPs as satellites were fabricated.

15.3.2 Labeling with Raman Reporter Molecules

The second step to construct a SERS label is the choice of Raman reporter molecules. A large variety of molecules may be employed as Raman reporters. Ideal Raman reporter molecules exhibit high differential Raman scattering cross sections for bright SERS signals, a minimal number of Raman bands for multiplexing, strong adsorption to the colloid metal surface for stable binding and low or no photobleaching for signal stability. Generally, Raman reporter molecules must be attached directly on or at least near the surface of SERS substrates to experience significant Raman signal enhancement (SERS distance dependence). Positively charged dyes, such as crystal violet, Nile blue, basic fuchsin and cresyl violet may adsorb to the metal surface by electrostatic interactions and delocalized π-electrons. Sulfur containing molecules such as fluorescein isothiocyanate (FITC) and rhodamine B isothiocyanate (RBITC) are also often used because of their high affinity to silver and gold [14]. Recently, Chang's group reported on the combinatorial synthesis and screening of a triphenylmethane dye library for developing highly sensitive SERS tags, from which they found at least 13 compounds show stronger SERS signal than crystal violet [51]. With a lipoic acid linker, the novel Raman reporters strongly bind to gold NPs and produce strong and stable SERS signals [52]. While most of the commonly used Raman signature molecules are active in the UV/Vis range, endeavors were also made to develop Raman reporters with absorption maxima that are resonant with NIR detection lasers. By synthesizing and screening of an 80-member tricarbocyanine library, Chang and co-workers identified CyNAMLA-381 as a NIR SERS reporter with 12-fold higher sensitivity than the standard 3,3'-diethylthiatricarbocyanine (DTTC), and validated its advantages for the construction of ultrasensitive in vivo SERS probes [53, 54]. More recently, Kircher's group reported the design and synthesis of a class of NIR absorbing 2-thienyl-substituted chalcogenopyrylium dyes tailored to have high affinity for gold [55]. One notable feature of the pyrylium dyes is the ease in which a broad range of absorptivities can be accessed, and consequently be matched with the NIR light source by careful tuning of the dye's optical properties. When adsorbed onto gold NPs, these dyes produce biocompatible SERRS probes with attomolar limits of detection amenable to ultrasensitive in vivo multiplexed tumour and disease marker detection [55].

The SERS intensity correlates with the number of Raman reporter molecules on the metal substrates. Porter and co-workers were among the first to employ self-assembled monolayers (SAM) of Raman reporter molecules on noble metal NPs for SERS in immunoassays [56]. They used arylthiols/disulfides as Raman reporters which form a SAM on the metal surface via stable Au-S bonds [57]. The formation of a SAM provides several significant advantages: the uniform orientation of Raman

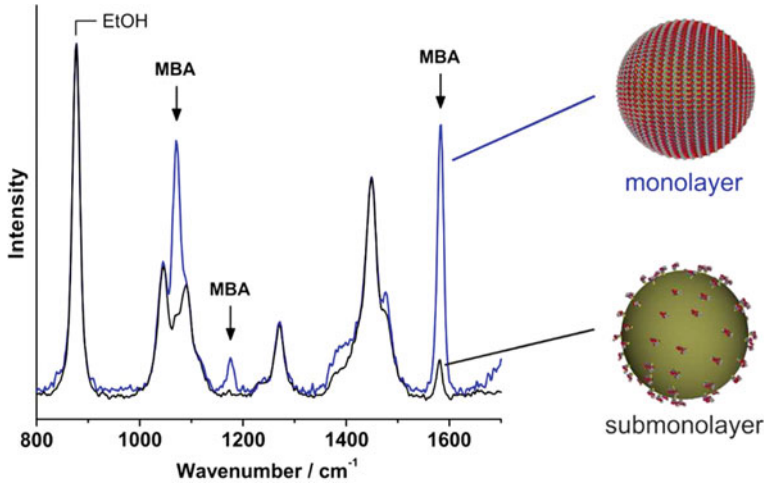

Fig. 15.8 Influence of surface coverage on the brightness of SERS labels: complete SAM compared to submonolayer coverage with Raman labels. The concentration of the colloid with submonolayer coverage is two times larger than in the colloid with monolayer coverage. The increase in signal brightness is 22 ± 5 (n = 3) [26]

reporter molecules leads to reproducible SERS signatures; the dense packing minimizes co-adsorption of other molecules on the particles surface and thereby reduces or excludes unwanted spectral signals; in addition, a SAM maximizes the number of Raman reporter molecules on the metal surface and creates a maximum SERS intensity. For instance, Au/Ag nanoshells covered with a complete SAM yield ca. 22 times more intense signals compared with the sub-monolayer coverage Fig. 15.8 upon red laser excitation (632.8 nm) [26].

15.3.3 Protection and Stabilization

In biomedical applications, further stabilization and protection of the SERS labels is generally a prerequisite. The encapsulation of SERS particles has several benefits. For instance, the resulting chemical and mechanical stability of the colloidal particles allows particle storage and prevents particle aggregation. Furthermore, the desorption of Raman labels from the metal surface as well as the adsorption of spectrally interfering molecules from the environment to the surface can be eliminated. Various encapsulants, including proteins, organic polymers, silica and hydrophilic SAMs, have been applied to improve colloid stability and biocompatibility of SERS labels as well as to provide functional groups for further bioconjugation [27, 44, 45, 58].

15.3.3.1 Stabilization with Proteins or Polymers

BSA and thiolated polyethylene glycol (PEG) are two kinds of commonly used surface-coating molecules. BSA adsorbs on the metal surfaces via electrostatic interactions and produces a protective shell. For instance, in a recent study Ren and co-workers introduced a facile way to prepare BSA-coated SERS-based pH sensors [59]. Modification of the NPs with BSA not only protected the Raman reporter molecules in complex conditions, such as high ionic strength solution or biological systems, which ensures the sensitivity and stability of the sensor, but also prevented further aggregation of the NPs and improved their biocompatibility. Another example is the functionalization of COINs [44] (Fig. 15.9a): BSA and glutaraldehyde were introduced to the COINs to form a ca. 10 nm-thick organic encapsulant around them, and to also provide carboxylic acid groups for subsequent bioconjugation. PEG is a non-toxic and hydrophilic polymer that is commonly used to improve drug compatibility and system circulation. Nie and co-workers have investigated the stability of PEGylated gold NPs (Fig. 15.9b) by measuring their SERS signals under a wide range of conditions. The thiol- PEG -coated NPs were stable in even very harsh conditions including strong acids or bases, concentrated salts, or organic solvents (methanol, ethanol and dimethylsulfoxide) [27].

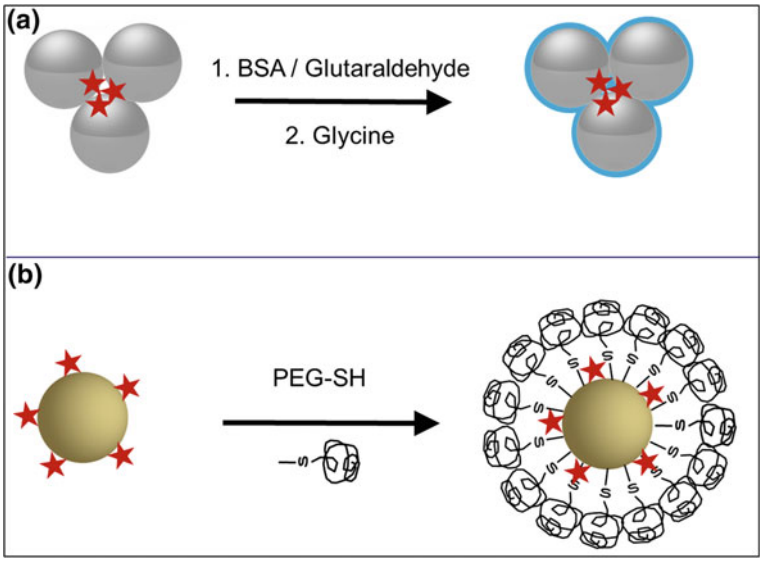

Fig. 15.9 **a** Coating of SERS labels with BSA [44]; **b** Coating of SERS labels with thiol-PEG [27]

15.3.3.2 Silica-Encapsulation

Silica-encapsulated SERS labels are attractive because of their high mechanical stability and the option for long-term storage. The concept of silica encapsulation for SERS labels was first introduced by Natan [60] and Nie [61] in 2003. Co-adsorption of Raman labels and SiO_2 precursors (typically in a 1:20 stoichiometry) leads to formation of a sub-monolayer coverage with Raman reporter molecules onto the metal surface, followed by silica encapsulation with a modified Stöber method [62]. The glass shell provides chemical and physical stability to the SERS label, as well as storage stability and protection against mechanical deformation.

As mentioned in Sect. 15.3.2, in contrast to the sub-monolayer coverage with Raman reporter molecules, a complete SAM with full surface coverage leads to a higher sensitivity. Silica-encapsulated SERS particles comprising a complete SAM combine the chemical stability of a glass shell with the spectroscopic advantages resulting from the maximum and dense surface coverage with Raman reporters in a uniform orientation. Figure 15.10 shows two different synthesis routes towards silica-encapsulated SERS labels comprising a full SAM.

In the first route [26] (Fig. 15.10 left), the addition of Raman labels (Ra) to the SERS substrate produces SAM-coated metal nanospheres (1a). Layer-by-layer adsorption of poly(allylamine hydrochloride) (PAH) and polyvinylpyrrolidone (PVP) onto the SAM leads to the polyelectrolyte-coated SAMs 1b and 1c, respectively. The silica shell in 1d is then formed upon addition, hydrolysis and finally condensation of tetraethoxy orthosilicate (TEOS). This route involves different solvents exchange and multiple centrifugations, it is therefore labor and time intensive. A simpler, faster and generally applicable route to silica-encapsulated SERS labels is achievable via a SAM containing terminal SiO_2-precursors [63] (Fig. 15.10 right): Ra and terminal SiO_2-precursor are covalently bound to each other (Ra-SiO_2), i.e. both functions are merged into a single molecular unit. This strategy is independent of the SAM's surface charge, and is therefore universally applicable. However, it requires an additional synthesis step for the Ra-SiO_2 precursor conjugate. The transmission electron microscopy (TEM) images in Fig. 15.11 demonstrate the monodispersity of the resulting glass-encapsulated SERS NPs [26]. The thickness of the glass shell can be controlled by the amount of TEOS. The 60 nm Au/Ag nanoshells in Fig. 15.11 have a ~10 nm thick (top left) and ~25 nm thick (bottom left, right) silica shell. In addition to Au NPs and Au/Ag nanoshells, the silica encapsulation has also been demonstrated for a variety of other plasmonic NPs, including gold nanostars [64], dimers of gold NPs [65], aggregates [45], and core-satellite assemblies [46, 50], which highlights the potential of this approach.

15.3.3.3 Hydrophilic Stabilization of SAMs

Instead of coating an additional polymer or glass layer on the SERS labels as introduced above, another SERS label design is based on relatively short terminal hydrophilic spacers attached to the SAM [58, 66]. In this rational design of SERS labels depicted in Fig. 15.12, the stabilization of the SAM is achieved by attaching

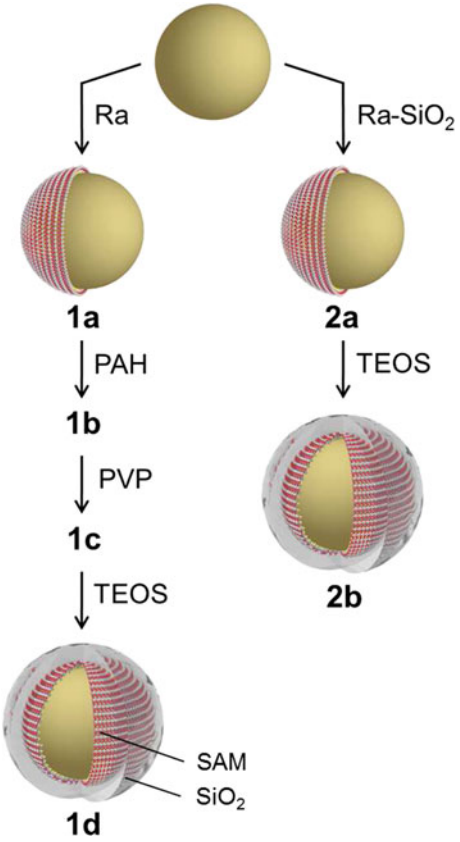

Fig. 15.10 Two different routes to SERS labels with a glass shell as an encapsulant and a self-assembled monolayer (SAM) of Raman reporters on the surface of the metal nanoparticle. Left: Three-step synthesis, starting from a SAM 1a of Raman reporter molecules (Ra) on the surface of Au/Ag nanoshells, subsequent layer-by-layer deposition of the polyelectrolytes PAH (1b) and PVP (1c) and finally the glass encapsulation using tetraethoxyorthosilicate (TEOS) to 1d [26]. Right: One-step approach via a SAM 2a of Raman reporter molecules containing terminal SiO_2 precursors (Ra-SiO_2) and its direct silica encapsulation to 2b using TEOS [63]

hydrophilic monoethylene glycol (MEG) units with terminal OH groups to the Raman reporters. A small portion of Raman reporter molecules is conjugated to longer triethylene glycol (TEG) units with terminal COOH moieties for bioconjugation. Four advantages result from this strategy: (i) the colloidal surface is completely covered exclusively by Raman reporters for maximum sensitivity; (ii) the entire SERS label is hydrophilic and water soluble due to the MEG/TEG units, i.e. independent of a particular Raman reporter molecule; (iii) increased sterical accessibility of the SAM for bioconjugation via the longer TEG spacers with terminal COOH groups, and (iv) the option for controlled bioconjugation by varying the ratio of the two spacer units (TEG-OH : MEG-COOH).

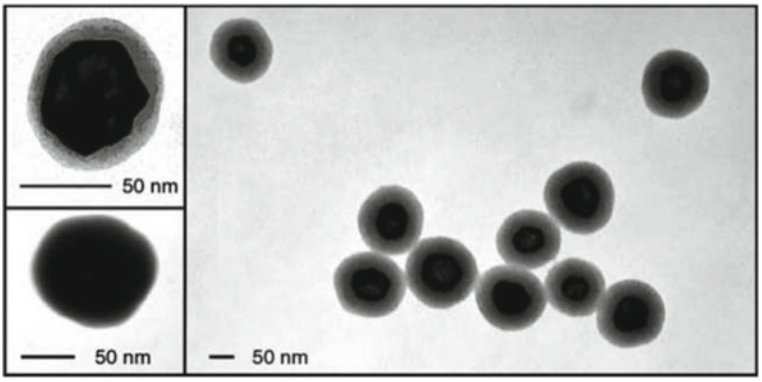

Fig. 15.11 Transmission Electron Microscopy (TEM) images of silica-encapsulated SERS labels with ~10 nm (top left) and ~25 nm (bottom left and right) thick silica shells. The diameter of the gold/silver nanoshell core is ~60 nm [26]

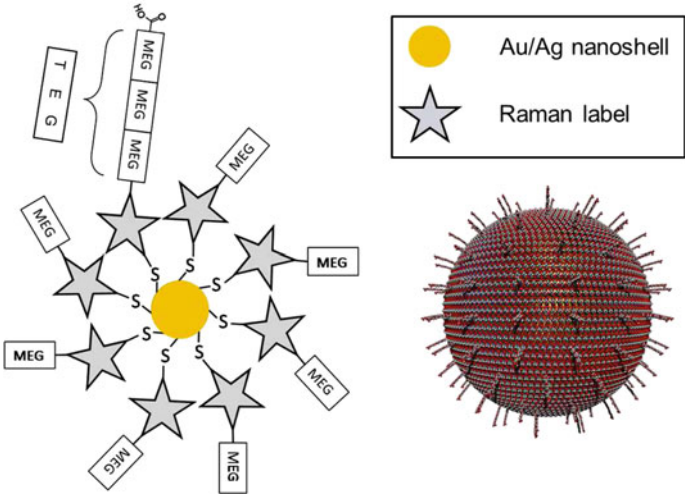

Fig. 15.12 Hydrophilic SERS labels for controlled bioconjugation. A complete SAM of arylthiols as Raman reporters is adsorbed onto the surface of the metal colloid. Hydrophilic mono- and triethylene glycols (MEG and TEG, respectively) are conjugated to the Raman reporters and stabilize the SAM. The water soluble SERS label can be conjugated to biomolecules via the terminal carboxy moieties of the longer TEG spacers [58]

15.3.4 Bioconjugation with Antibodies

For iSERS applications, SERS labels must be conjugated to target-specific ligands such as antibodies for antigen recognition. A comparison of different conjugation protocols is summarized in a recent review [67], including physical adsorption, covalent binding and use of adaptor biomolecules. The antibodies can be attached either

directly to the NP surface, to the Raman labels, or to the encapsulant such as a PEG or silica shell. Different conjugation strategies are discussed in this section.

15.3.4.1 Conjugation of Antibodies to SERS Substrates or to Raman Reporter Molecules

Adsorption of proteins, especially of antibodies to colloidal gold (immunogold) based on electrostatic forces, has been explored for decades. An initial design of SERS labels for immunoassays by Porter and co-workers was based on the co-adsorption of antibodies and Raman labels on the surface of gold NPs [56]. In this approach, Raman reporter molecules (arylthiols) and antibodies are directly co-adsorbed to the surface of Au NPs. By using different labels with little spectral overlap, two different antigenic species can be detected simultaneously. However, this design suffers from non-specific binding and "cross-talk" between different SERS labels [57]. An alternative approach based on covalent binding of the antibodies to the Raman reporter molecules improved particle stability and lowered the detection limit, but the steric accessibility of the COOH moieties reduced due to the densely packed SAM [68]. Recently, the same research group presented an improved design using a mixture of two different thiols: an aromatic thiol for the generation of intense and characteristic Raman signals and an alkylthiol with a terminal functional group (e.g. succinimidyl group) for bioconjugation [57]. Schlücker and co-workers have presented an approach (Sect. 15.3.3.3) to synthesize hydrophilic SERS labels in which the colloidal particle was stabilized by two different ethylene glycols (MEG-OH and TEG-COOH) attached to the SAM. This hydrophilically stabilized SAM design guarantees maximum SERS signal intensity and enables efficient conjugation of antibodies, while the number of antibodies can be controlled via the stoichiometric ratio of the two spacers [58].

15.3.4.2 Conjugation of Antibodies to Protecting Shells

Proteins such as BSA contain a large number of amino and carboxyl groups, which can be used for conjugation with targeting molecules. For example, the functionalization of an encapsulated COIN is based on the activation of the carboxylic acid groups of BSA by N-(3-(dimethylamino)-propyl)-N'-ethylcarbodiimide (EDC); the resulting O-acylisourea intermediates are reacted with amino groups from the antibodies to form amide bonds between the encapsulation layer and the antibodies [69]. Polymer-encapsulated SERS labels usually provide terminal functional groups from the polymer shell. For instance, Nie and co-workers introduced AuNPs coated with thiolated PEG containing terminal carboxyl groups, to which single-chain variable fragments (scFv) were covalently linked [27].

Silica encapsulation provides chemical and physical stability to the SERS labels. Bioconjugation of silica-encapsulated SERS labels usually requires the introduction of functional groups via silane chemistry, e.g. APTMS (NH_2) or MPTMS (SH) [13].

The presence of functional moieties on the silica shell then allows bioconjugation of antibodies by established protocols, i.e. amino groups (via succinimides, isothiocyanates or hydrazines), carboxyl groups (via carbodiimides), thiol groups (via maleimides or acetyl bromides) and azides (via click chemistry) [70].

15.3.4.3 Conjugation of Antibodies by Chimeric Proteins

Molecular recognition of the target antigen by the antigen recognition sites of the antibody is highly important for obtaining molecular specificity and reliable diagnostic results in IHC. However, conventional bioconjugation schemes (Fig. 15.13a) through covalent binding do not provide site-specificity, i.e. there is no control over reaction with a particular amino acid residue: the amino acid residues might be close to the Fc part of the receptor (preferred) or within the antigen recognition sites (non-preferred). Overall, this uncontrolled binding in terms of missing site-specificity may result in a "scrambled" orientation of the antibodies on the surface of the SERS labels. In contrast, the approach (Fig. 15.13b) employed by Salehi et al. avoids this problem by using the chimeric protein A/G, which exhibits multiple bindings to the Fc domain of the antibody [71]. Coating the silica surface of the SERS labels with protein A/G leads to controlled binding and directed orientation of the antibodies

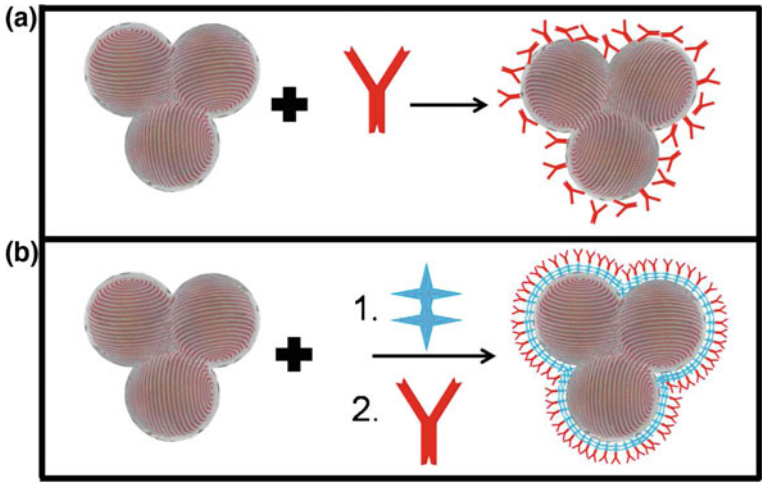

Fig. 15.13 Silica-encapsulated clusters of AuNPs coated with a SAM of Raman reporter molecules (left) are bright SERS labels with single-particle SERS brightness. **a** Uncontrolled binding of the antibody onto the glass surface of the SERS NP clusters. Due to the uncontrolled orientation of the antibodies, antigen binding sites may be blocked. **b** Controlled binding and directed orientation of the antibodies onto the silica surface of the SERS NP cluster via coating with protein A/G (blue), which exhibits multiple binding sites for the Fc fragment of the antibody (red). In this case, all antigen binding sites are accessible [71]

onto the silica surface, and is therefore desirable in iSERS staining since all antigen recognition sites of the antibody are accessible for binding to the antigen.

15.3.5 Single-Particle Brightness and Homogeneity of SERS Labels

iSERS microscopy is a novel imaging technique in tissue diagnostics based on the selective staining of multiple target proteins in tissues. The quality of the IHC staining results strongly depends on the quality of the SERS NPs. Brightness, ideally a detectable SERS signal at the single-particle level, and homogeneity, ideally every SERS particle is equally bright, are the two key issues related to (quantitative) iSERS. The term "single-particle brightness" may be defined in a pragmatic way: a SERS label with single-particle brightness per definitionem exhibits a detectable SERS signal within the defined acquisition time per point (pixel), usually milliseconds [45] or at most 1 s. In a recent study [45], two central questions in iSERS microscopy were addressed: (i) What is the role of SERS labels with single-particle brightness in IHC in terms of false-positive results? and (ii) What are the resulting requirements on the purity of the SERS colloid at the ensemble level?

The role of single-particle brightness in IHC is schematically illustrated in Fig. 15.14. Silica-encapsulated dimers of gold NPs have been demonstrated to exhibit single-particle SERS brightness (1 sec acquisition time) in correlative single-particle AFM/SERS experiments [65]. Figure 15.14a shows the situation of "binding plus detectable SERS signal" when such a dimer, conjugated to the corresponding antibody, binds to the antigen presented on the tissue section. Due to the single-particle SERS brightness of this type of highly active SERS label, a Raman signal is detectable within the defined acquisition time of the Raman mapping experiment. Overall, the presence of the antigen is correctly indicated by the Raman spectrum of the SERS label (positive result). In contrast to dimers, single gold NPs do not exhibit a notable plasmonic enhancement. In previous experiments on single 60 nm gold NPs, no SERS signal could be detected within 1 s acquisiton time [65]. A recent experimental study also demonstrated that 80 nm gold and silver NP monomers were both not SERS-active [72]. Figure 15.14b shows the situation of "binding but no detectable SERS signal" for gold NPs monomers conjugated to antibodies for target recognition. Although the antibody correctly recognizes its antigen, no SERS signal is detectable due to the lack of plasmonic activity of the single gold NP used as a SERS label. Overall, a false-negative result is obtained.

The second question on the role of using homogenous SERS colloids at the ensemble level is directly related to the first one. Again, antibody-monomer conjugates yield false-negative results (Fig. 15.14b) and the corresponding antigen is not accessible anymore for detection by an antibody-dimer conjugate. Therefore, a colloidal mixture containing both NPs with and without single-nanoparticle brightness is not optimal for iSERS microscopic experiments; instead, only highly sensitive SERS

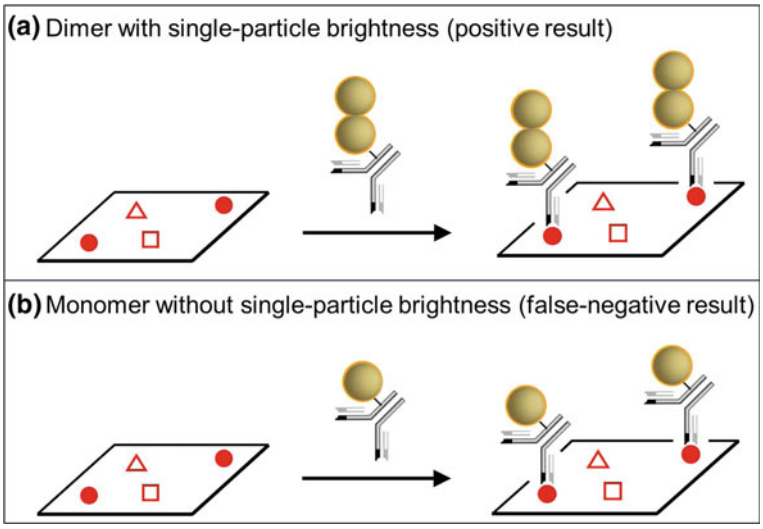

Fig. 15.14 The role of single-particle brightness in IHC via iSERS microscopy. **a** Clusters (dimers and trimers) of gold NPs with single-particle brightness yield positive results, while **b** monomers without single-particle brightness give false negative results [45]

labels with single-particle brightness should be employed. In summary, in a population of SERS labels, every particle exhibits single-particle brightness. Every individual SERS NP that selectively binds to the target should be detectable within the given (short) acquisition time (per pixel). Otherwise, false-negative results may be generated.

Correlative SEM/SERS experiment of single particles provide the most direct and unambiguous way for establishing structure-activity correlations [46]. Determining the structure of a single plasmonic nanostructure as well as its optical activity requires electron and optical microscopic experiments on the same particle. First, it is necessary to ensure that exactly the same particle is characterized by both electron and optical microscopy. Second, this particle must be spatially isolated from other particles in order to avoid disturbing spectral interferences in the optical experiments. Salehi et al. have compared SERS signals from a glass-coated monomer, dimer, and trimer of gold NPs by correlative SEM/SERS experiments [45] Fig. 15.15. Colloids were deposited on a framed silicon waver and high resolution scanning electron microscopy (HR-SEM) was employed to identify single NPs/clusters. With 30 ms integration time, the glass-coated trimer (red) and dimer (blue) yielded detectable SERS signals, while the glass-coated monomer (black) did not. The SERS signal from the single trimer is about two to three times stronger than that from the single dimer. This is presumably due to orientation effects since the dimer response is highly anisotropic while that of the trimer is not. Also, the trimer has a larger number of hot spots than the dimer. Multiple hotspots occurs at the tips of nanostars and at

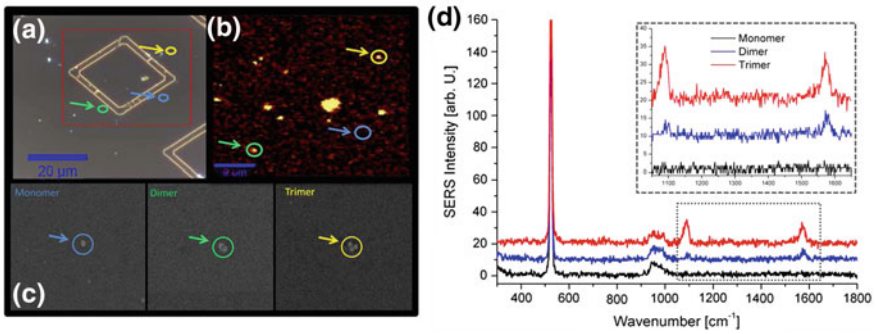

Fig. 15.15 Correlative dark-field/SERS/SEM single-particle experiments on glass-coated monomers and clusters of gold NPs. **a** Dark-field microscopy, **b** SERS microscopy and **c** HR-SEM images. Only the glass-coated gold trimer (yellow arrow) and dimer (green arrow) exhibit single-particle SERS brightness (30 ms integration time), while the glass-coated monomer (blue arrow) does not. **d** Normalized single-particle SERS spectra of the glass-coated monomer, dimer, and trimer from (**b**) [45]

the junctions between two nanospheres in 3D plasmonic superstructures. Thus, they exhibit a quasi polarization-independent SERS response at the single-particle level [38, 46, 50].

15.4 Application of iSERS Microscopy for Tissue-Based Cancer Diagnostics

iSERS microscopy is the combination of target-specific SERS probes and Raman microspectroscopy. Various methodologies in Raman microspectroscopy are available [73]. Mapping approaches with point or line focus illumination, providing full spectral information in combination with a xy-translation stage are most commonly applied.

15.4.1 Localization of Single Proteins by iSERS Microscopy

The proof of principle for iSERS microscopy using a SERS-labelled primary antibody for protein localization in tissue was demonstrated by Schlücker and coworkers in 2006 [74]. Prostate-specific antigen (PSA) was chosen as a target protein because of its high expression levels in prostate tissue and its selective histological abundance in the epithelium of the prostate gland. By using Au/Ag nanoshells as colloidal SERS substrates, aromatic thiols as Raman reporters, the localization of PSA in tissue specimens of biopsies from patients undergoing prostatectomy was achieved with

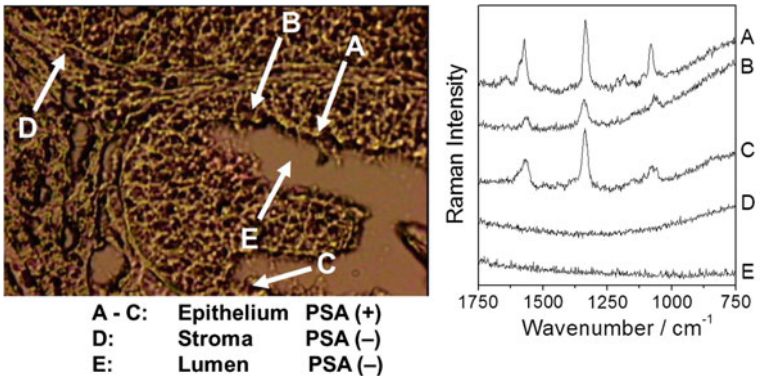

Fig. 15.16 Proof of principle for iSERS microscopy using SERS-labelled primary antibodies for tissue diagnostics. Prostate-specific antigen (PSA) was localized in biopsies from patients with prostate cancer. Left: White light image of the prostate tissue section. Three different histological classes can be observed: epithelium, stroma or connective tissue and lumen, in which PSA is either abundant (+) or not (−). Right: Spectra obtained at the locations (A) to (E) indicated by arrows in the white light image. SERS-labelled anti-PSA antibodies are detected in the PSA-(+) epithelium (locations A-C), exhibiting the characteristic Raman signals of the SERS label. Locations in the PSA-(-) stroma (D) and lumen (E) serve as negative controls where no spectral contributions of the SERS-labelled antibody are detected [74]

SERS-labelled primary anti-PSA antibodies. SERS signals were detected in the PSA-(+) epithelium of the incubated prostate tissue section (Fig. 15.16A–C), while locations in the PSA-(-) stroma and lumen served as negative controls (Fig. 15.16D, E).

Further applications of iSERS microscopy for tissue diagnostics with various types of SERS probes appeared soon after this initial study. For example, Sun and coworkers used BSA-coated aggregated silver clusters (COINs) as SERS NPs for PSA localization in prostate tissue sections [44]. In order to illustrate the multiplexing capabilities of iSERS in tissue staining, a two color-COIN staining against PSA was performed: SERS labels with two distinct Raman signatures were conjugated to anti-PSA antibodies, and simultaneous applied to the tissue. The characteristic Raman signatures from both COINs were detected at almost every location in the epithelium, suggesting that steric hindrance from the SERS probes does not represent a major problem. In a subsequent study, the same group presented a detailed comparison of the staining performance with SERS- and fluorophore-PSA antibody conjugates on adjacent tissue sections [69]. Staining with COIN- and Alexa-fluorophore labelled antibodies yielded similar results, with a lower staining accuracy for COINs, which is attributed to an elevated false negative rate, but signal intensities were comparable for COINs and Alexa-fluorophore, supporting the further development of SERS NP labels for iSERS.

Application of Au/Ag nanoshells with a hydrophilic-spacer SAM on selective imaging of PSA by SERS microscopy is illustrated in Fig. 15.17 [58]. A bright field image is shown in Fig. 15.17a, the region used for Raman point mapping is

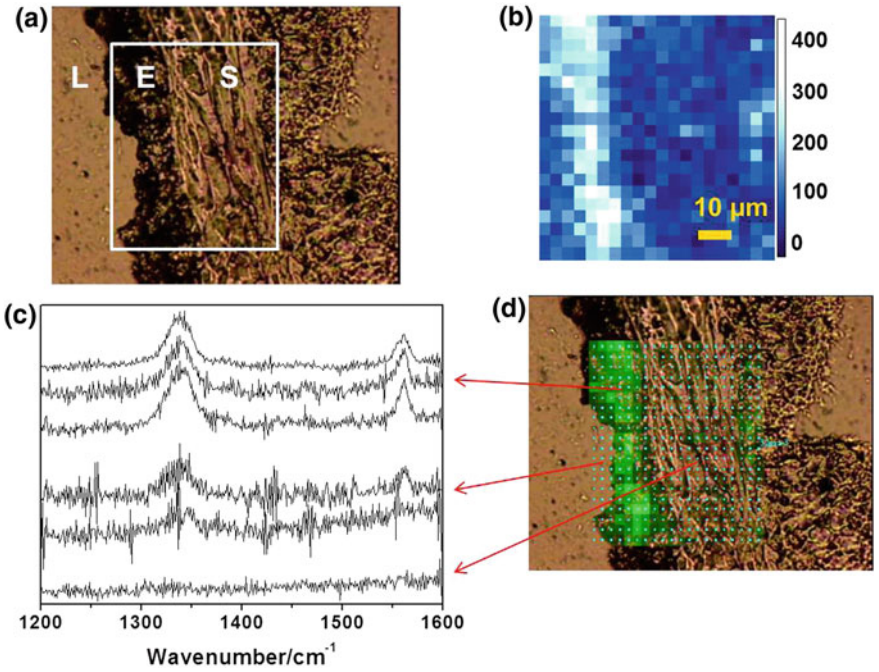

Fig. 15.17 iSERS imaging for tissue diagnostics. **a** Bright field microscope image of a prostate tissue section. Different histological classes are indicated: lumen (L), epithelium (E) and stroma (S). The rectangular box shows the region in which spectra were acquired by point mapping. **b** The false-color SERS image. **c** Representative SERS spectra recorded at selected locations in the (E), (L) and (S). **d** Overlaid bright field image with the false-color SERS image shows that the characteristic signal of the SERS-labelled antibody is observed selectively in the epithelium. Low nonspecific binding is attributed to the hydrophilic ethylene glycols of the SERS probes [58]

indicated with a white box. Three different histological classes can be identified: epithelium (E), stroma (S) and lumen (L). Epithelium is PSA-(+), while (S) and (L) are PSA-(-). The false-color image in Fig. 15.17b is based on the intensity of the Raman marker band at 1336 rel. cm^{-1}, which shows the selective abundance of PSA in the epithelium. Representative SERS spectra recorded at selected locations in the (E), (S) and (L) are shown in Fig. 15.17c. In negative control experiments with either bare SERS labels or SERS labels conjugated to BSA, no binding to the tissue was observed. This additionally confirms the specific recognition capacity of the SERS-labelled anti-PSA antibody in the epithelium.

Localization of the basal cell marker p63 is a clear test whether iSERS microscopy provides the necessary specificity for selectively staining the nuclei of the basal cells. In a recent study [66], hydrophilically stabilized gold nanostars served as SERS labels for imaging of p63 in benign prostate biopsies. The comparison of the SERS false-color image and the white light image in Fig. 15.18a reveals that p63 is only abundant in the basal epithelium of benign prostate tissue, but not in the lumen

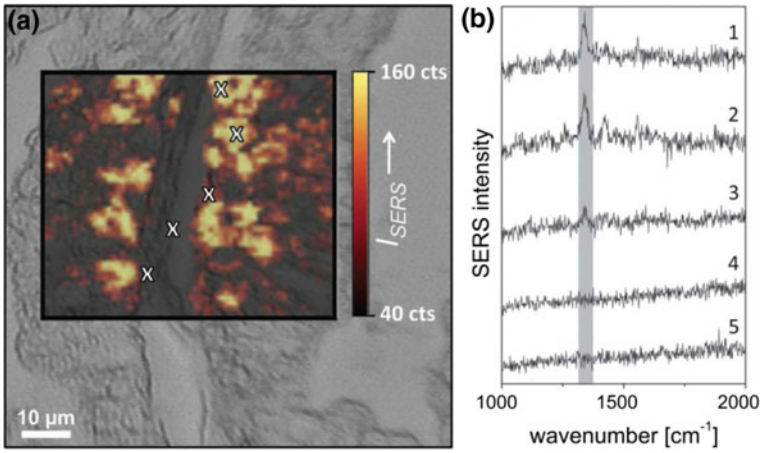

Fig. 15.18 **a** Bright field image of a prostate tissue specimen with an overlaid SERS false-color image based on the intensity of the 1340 rel. cm^{-1} Raman marker band of the SERS label. **b** Five representative SERS spectra from different locations in (**a**), indicated by white crosses in the SERS false-color image (from top to bottom) [66]

or other histological classes and subclasses such as connective tissue (stroma) and secretory epithelium. Five representative SERS spectra from different regions in Fig. 15.18a are displayed in Fig. 15.18b: (1–3) basal epithelium, (4) lumen and (5) stroma. The corresponding locations are marked with white crosses in Fig. 15.18a (1–5: from top to bottom). The SERS mapping experiment clearly demonstrates the specific binding of the SERS-labelled anti-p63 antibody to its target molecule p63 in the basal epithelium. Negative control experiments with SERS-labelled BSA did not exhibit detectable Raman signals.

Epstein-Barr virus (EBV)-encoded latent membrane protein 1 (LMP1) is closely associated with the occurrence and development of nasopharyngeal carcinoma and can be used as a tumor marker in screening for the disease [75]. Chen and coworkers fabricated LMP1-functionalized and 4-mercaptobenzoic acid (4-MBA)-labelled Au/Ag core-shell bimetallic NPs. They applied them for analyzing LMP1 in nasopharyngeal tissue FFPE sections obtained from 34 cancer patients and 20 healthy controls. Data from iSERS microscopy showed that this kind of SERS NP conjugates detected LMP1 in nasopharyngeal tissue sections with high sensitivity and specificity. The results are superior to those of conventional IHC staining for LMP1 and in excellent agreement with those of in situ hybridization for EBV-encoded small RNA [75].

The development of increasingly sensitive SERS NP labels with single-particle brightness enables faster imaging experiments. Earlier reports of iSERS microscopy used integration times of 100 ms [44, 66] or even 1 sec [74]. In a recent study presented by Salehi et al. a proof of concept for rapid iSERS microscopy with 30 ms acquisition time per pixel for selective imaging of p63 in prostate tissue sections

was demonstrated [45]. Purified glass-coated clusters (dimers and trimers) of gold NPs were applied as SERS labels and conjugated to anti-P63 antibodies. With 30 ms acquisition time per pixel, the selective staining of p63 in the basal cells of the epithelium is clearly observable. Negative control experiments (100 ms per pixel) with SERS-labelled BSA indicate no or only minimal non-specific binding. Time efficiency is critically important in particular when large or even very large areas in histopathological studies must be investigated, not necessarily with high spatial resolution, but with a large number of points.

15.4.2 Co-localization of Multiple Proteins by iSERS Microscopy

A central advantage of iSERS is its enormous spectral multiplexing capacity for multi-color IHC. Generally, the term multiplexing refers to the parallel determination of several parameters within a single experiment. In the context of SERS as a labeling strategy for targeted research, multiplexing addresses the issue of simultaneously detecting and identifying the spectral fingerprint of several distinct SERS nanoparticle labels conjugated to different target-specific ligands, i.e. antibodies in the case of IHC.

Fig. 15.19 shows the SERS spectra of two different SERS labels comprising aromatic thiols present as a SAM on the surface of AuNPs [71]. The two Raman reporter molecules are 4-nitrothiobenzoic acid (4-NTB, red solid line) and 4-mercaptobenzoic acid (4-MBA, green solid line), respectively. Since unique and spectrally separated Raman marker bands for both SERS labels are available, a univariate approach based on the integrated Raman intensities of single peaks - here around 1340 rel. cm^{-1} (4-NTB, red) and around 1590 rel. cm^{-1} (4-MBA, green) - is sufficient for spectral

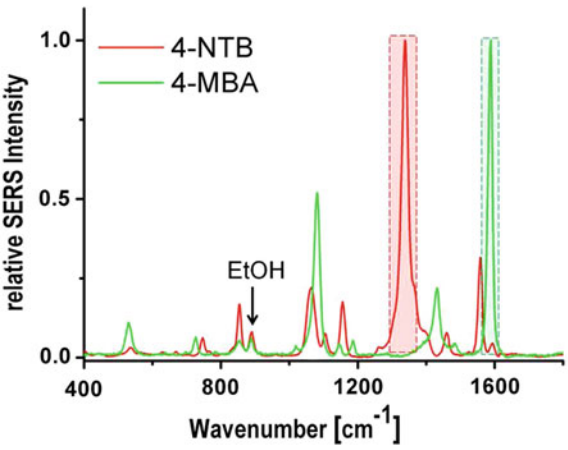

Fig. 15.19 SERS signatures of two different SERS labels comprising two different aromatic thiols present as a SAM on the surface of AuNPs: 4-nitrothiobenzoic acid (4-NTB) and 4-mercaptobenzoic acid (4-MBA). The colloidal SERS particles were dispersed in ethanol [71]

discrimination in a two-color SERS microscopic experiment employing 4-NTB- and 4-MBA-based SERS labels.

Using highly sensitive, silica encapsulated gold nanoparticle clusters as SERS labels, two-color iSERS microscopy for co-localization of PSA and p63 in non-neoplastic prostate tissue FFPE specimens was demonstrated [71]. The tissue sections were incubated with both SERS-labelled PSA antibodies (Raman reporter: 4-NTB) and SERS-labelled p63 antibodies (Raman reporter: 4-MBA). The false-color SERS image in Fig. 15.20 confirms the binding specificity and signal brightness of the two SERS probes: p63 is selectively observed in the nuclei of the basal cells, while PSA is abundant in the entire epithelium, but not in the stroma.

For multi-color (>2) SERS experiments, data analysis based on single Raman peaks is usually not feasible because of spectral overlap. For decomposition of the overlapping spectral contributions of the individual SERS probes, signal processing algorithms must be applied. Knudsen and coworkers reported a multiplex spectral fitting method that exploits the entire fingerprint to separate and quantify individual SERS probe signals [76]. They first tested four COINs conjugated to antibodies in a quadruplex plate binding assay detecting PSA in solution. Figure 15.21a shows the spectral decomposition for one sample. The best-fit spectrum (black) is overlaid on the measured spectrum (gray, largely covered by the black) and contains signatures of all four antibody-COIN conjugates. Isolated peaks arising from a single COIN are indicated by colored arrows, while peaks arising from multiple COINs are indicated by colored boxes. The typical single peak method cannot be used for quantification due to spectral overlap. The spectral fitting method exploits the entire

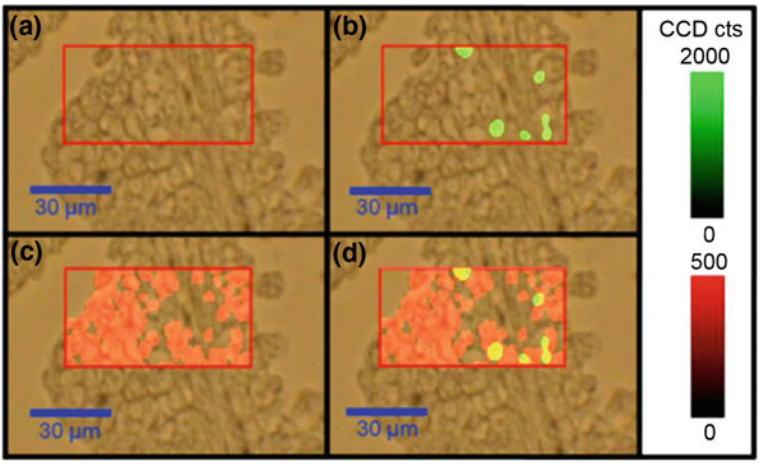

Fig. 15.20 Two-color immuno-SERS microscopy for the co-localization of p63 (green) and PSA (red). **a** White light image of a healthy prostate sample. **b** Overlay with a p63 false-color SERS image; Raman reporter: 4-MBA. **c** Overlay with a PSA false-color SERS image; Raman reporter: 4-NTB. **d** Co-localization by overlay with p63/PSA false-color images. Acquisition time: 100 ms per pixel [71]

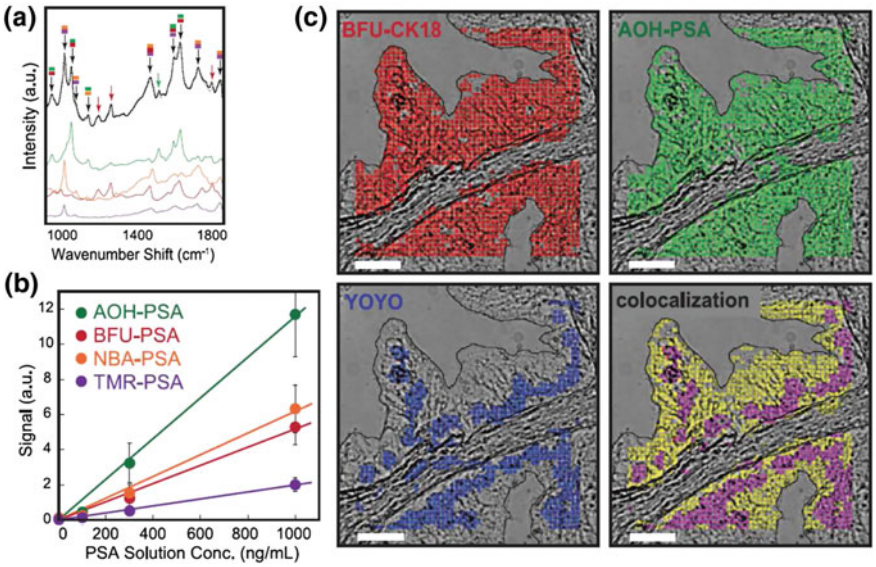

Fig. 15.21 **a** Spectral deconvolution of the quadruplex assay. The upper traces represent the measured spectrum (gray, largely covered by the black spectrum) and best-fit (black) spectrum. The colored lines represent the pure COIN spectra extracted with the spectral deconvolution method. Peaks that primarily arise from a single COIN are shown by colored arrows, and peaks arising from multiple COINs are color-coded by boxes. **b** Dose-response curves for the multiplex plate binding assay using four COIN preparations conjugated to anti-PSA antibody. **c** Spectral deconvolution in a multiplex FFPE tissue assay. BFU-COIN was conjugated to anti-CK18 antibody (BFU-CK18); AOH-COIN was conjugated to anti-PSA antibody (AOH-PSA), and a fluorescent dye targeted DNA (YOYO) [76]

spectral signature to extract individual component spectra (Fig. 15.21a, colored) and quantitative signals for each antibody-COIN conjugate. The calculated intensity of individual antibody-COIN conjugates in Fig. 15.21b is proportional to the coated PSA concentration and comparable to the linear antibody-COIN dose-response in singlet experiments. Then the authors applied the spectral fitting method to image the expression of PSA, cytokeratin-18, and DNA in FFPE prostate tissue sections (Fig. 15.21c). The spectral analysis method effectively removes tissue autofluorescence and other unknown background, allowing accurate and reproducible imaging at subcellular spatial resolution.

15.4.3 Non-specific Binding

Rapid advances in nanotechnology have led to an increasing number of nanomaterials for biomedical applications in the areas of cancer diagnostics and therapeutics. For both in vitro and in vivo applications of NPs conjugated to targeting molecules,

one of the major challenges is the reduced targeting efficiency caused by non-specific binding. The main reasons for non-specific binding using functionalized NPs are: the increased size, weight and surface area of NPs compared to traditional labeling with dyes or molecular fluorophores; conjugation of the targeting molecules onto NPs usually requires the introduction of reactive functional groups on the NPs, while excess or unreacted groups often lead to increased nonspecific protein interaction; aggregation of NPs during the preparation process or in physiological media. Numerous efforts have been made to analyse and reduce non-specific binding of bioconjugated NPs, including: comparing the effect of size and shape of NPs on their targeting efficiency; surface modification of NPs; blocking the surface of NPs with proteins or hydrophilic molecules. A new strategy to minimize the effect of non-specific binding in tissue staining is the simultaneous detection and ratiometric quantification of targeted and non-targeted NPs by staining tissues with an equimolar mixture of targeted NPs and non-targeted NPs that account for nonspecific effects [77].

15.4.3.1 Size and Shape of NPs

Immunogold labeling, in which colloidal gold in the size range from few nm up to 30 nm is attached to antibodies, has been broadly applied for identification and localization of proteins at the ultrastructural level. Colloidal gold particles with different diameters (5 and 20 nm) were compared with respect to non-specific binding. The results indicate that small gold NPs have a greater tendency to non-specific binding although they present higher labeling densities resulting from the greater accessibility to binding sites and lower steric interference [78]. This is probably due to a larger percentage of uncoated surface area with proteins on 5 nm NPs than the larger NPs [79]. Recently, Mitragotri and coworkers reported a surprising finding that particle shape enhances avidity as well as specificity of interactions of antibodies with their targets. Using spherical, rod-, and disk-shaped polystyrene NPs and trastuzumab as the targeting antibody, they studied specific and nonspecific binding and uptake in breast cancer cells. The conclusion is that, rod-shaped NPs exhibit higher specific and lower nonspecific accumulation compared with their quasi-spherical counterparts [80].

15.4.3.2 Surface Modification and Blocking of NPs

Covalent conjugation of target-specific binding molecules to the SERS nanoparticle labels requires the presence of functional groups on the surface of the particles. However, following conjugation, excess active functional groups, which are capable of binding to or reacting with various chemical and biological species, might induce aggregation of NPs or non-specific adsorptions, and lead to false positive/negative results. Therefore, nanoparticle surface design involves an optimum balance of the use of inert and active surface functional groups [81]. Tan and coworkers produced silica NPs with different functional groups, including

carboxylate, amine, amine/phosphonate, poly(ethylene glycol), octadecyl, and carboxylate/octadecyl groups, and compared their non-specific binding behavior using confocal imaging of amine-modified glass slides. The results indicate that silica NPs modified with a combination of carboxylate and octadecyl groups have less agglomeration and non-specific binding to the glass slide as compared to NPs having only carboxylate, octadecyl, or PEG groups on the surface [81]. In another immunoassay performed by Arslanoglu et al., carboxyl-terminated SERS tags show strong Raman signal, specificity for the target protein, robust response in the presence of various inorganic pigments, and reduced aggregation on sample surfaces compared to amino-terminated or commercial SERS tags [82]. An elegant strategy established by Nie's group for modifying SERS labels is to functionalize the NPs with a mixed layer of 85% thiolated PEG (HS-PEG), which ensures minimal non-specific binding and stabilizes the NPs against aggregation, and 15% HS-PEG-COOH containing an additional carboxyl group for conjugation with targeting molecules [27, 83]. The dual-SAM design reported by Schlücker's group is a similar approach to synthesize hydrophilic SERS probes. Two different ethylene glycol spacers are covalently bound to the same type of Raman reporter molecule: a short monoethylene glycol (MEG-OH) and a longer triethylene glycol (TEG-COOH) moiety. The terminal of hydroxyl group of the MEG spacer guarantees water solubility and reduces non-specific interactions, while the terminal carboxyl group of the TEG spacer allows subsequent conjugation to biomolecules such as antibodies. Controlled bioconjugation is possible by varying the stoichiometric ratio of both spacers [58, 66].

An alternative approach to reduce non-specific binding is to block the NPs with proteins like BSA or protein/PEG mixtures [84]. BSA is a blocking agent widely used in enzyme-linked immunosorbent assay (ELISA), western blot and IHC, which blocks potential sites of nonspecific interaction, eliminates background without altering or obscuring the epitope for antibody binding. It has also been reported that BSA-conjugated NPs show improved stability against flocculation and low toxicity, while simultaneously providing functional groups for further bioconjugation [85]. In recent studies on NP-based cell imaging, intracellular sensing or tissue staining, it was found that an additional blocking step with BSA on the NPs effectively reduces non-specific binding and minimizes cross talk [59, 85, 86].

15.4.3.3 Ratiometric Quantification of Specific and Non-specific Binding

In the approaches discussed above, efforts are mainly made to minimize non-specific binding through optimizing the preparation or modification process of the SERS NPs. Recently, the dual-reporter ratiometric detection with multiplexed positive- and negative-control contrast agents has become a valuable new strategy for accurately quantifying specific versus non-specific signals [77, 87]. Distinguishing between specific and non-specific probe accumulation on tissues is critical. Current designs of the negative control to detect non-specific binding are normally performed in two ways: i) staining two adjacent sections with target antibody-modified SERS

NPs and non-targeted isotype control antibody-modified SERS NPs, respectively; ii) compare accumulation of target antibody-modified SERS probes on normal tissue sections and cancerous tissue sections. However, variable tissue optical and mechanical properties (e.g. diffusion, porosity, interstitial pressure), uneven rinse removal of unbound probes, and uneven detection working distance can all lead to non-specific and misleading sources of contrast [88]. For example, Liu and coworkers observed that non-targeted NPs which are topically applied on tissues show higher retention in normal tissues versus xenograft tumors [77]. Instead of using FFPE tissue sections, they stained fresh tissues with an equimolar mixture of targeted NPs and non-targeted NPs. A calibrated ratiometric analysis method was used to investigate the performance of SERS probes under clinically relevant conditions, demonstrating the ability to accurately quantify molecularly specific versus nonspecific NP accumulation on tumor and normal tissues with a spectral integration time of 0.1 s [77]. The authors claimed that, SERS NPs are particularly well-suited for ratiometric detection, not only because of their high multiplexing capability but also due to the ability to excite multiple SERS NP colors with a single laser wavelength, ensuring that all SERS NPs are interrogated identically in terms of illumination intensity, spot size and effective excitation depth [77]. Using a cocktail of many targeted SERS NPs and one non-targeted NP to account for nonspecific effects, this approach will offer increased accuracy for multiplexed-tumor detection in spite of the large degree of molecular heterogeneity amongst tumors [88].

15.5 Summary and Outlook

iSERS microscopy is a novel and promising imaging approach for tissue-based cancer diagnosis, in particular because of its immense multiplexing capacity for simultaneous target localization in combination with quantification (see Fig. 15.22) [17]. First applications of iSERS microscopy in ex-vivo tissue imaging, i.e. the combination of target-specific antibody-SERS NP conjugates in conjunction with Raman microspectroscopy, have been demonstrated within the last 10 years. These studies were mainly performed on prostate tissue, which was also used in the proof of concept experiment as a model, but multiplexed detection of prognostic markers in various kinds of tissues are expected to appear within the next years.

As emerging optical nanodiagnostic probes, SERS NP labels have been developed as an attractive class of biological labeling agents with unique advantages and applications that are not achievable with organic dyes or molecular fluorophores. Advantages include spectral multiplexing, quantitation in combination with high sensitivity and photostability. High quality data, in particular the ability to clearly distinguish the SERS signals from background autofluorescence, is also an important aspect. A disadvantage may be the relatively large size of SERS labels compared with molecular fluorophores and quantum dots. However, in a recent study using SERS NPs with two distinct spectral signatures for staining the same protein in tissue, both

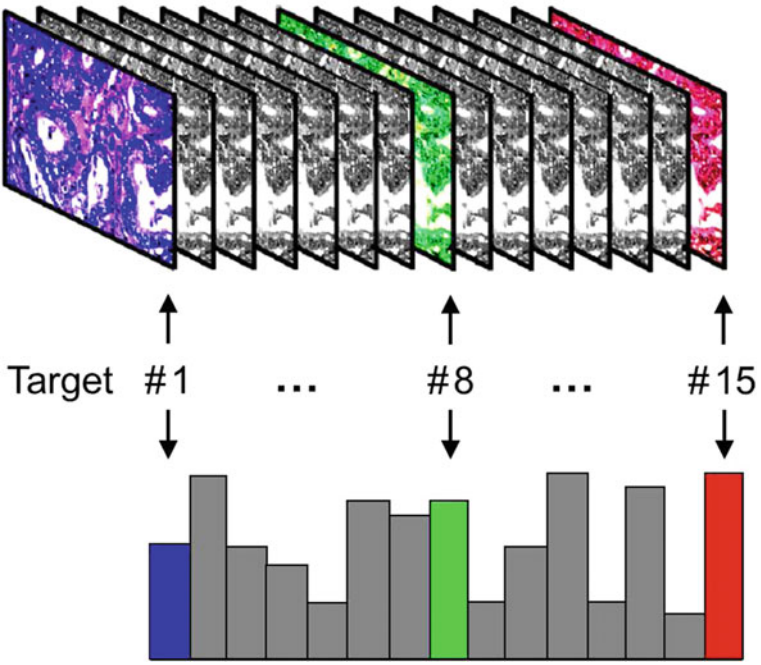

Fig. 15.22 SERS microscopy has the potential for the detection of multiple targets (multiplexing) and their quantification, two important aspects for tissue diagnostics [17]

particles were detected in all spots, suggesting that steric hindrance from the SERS probes does not represent a major problem [44].

Two most essential issues in the preparation of colloidal SERS labels are their brightness, ideally at the single-particle level, and their homogeneity/uniformity at the ensemble level. Several groups worldwide are actively working on improved designs and syntheses of SERS labels with high brightness and reproducible signals. Target-specific binding molecules, including antibodies, peptides, engineered proteins and nucleic acid aptamers, are "smart molecules" which recognize and selectively bind to the corresponding targets. Antibodies are the most widely used targeting molecules in current applications, however, in future studies, smaller targeting molecules like peptides or aptamers may be increasingly used, in particular because of their lower cost.

Advances in laser, filter, spectrometer and detector technology contributed to the fact that Raman including SERS spectroscopy is now a mature analytical technique. Easy to use commercial equipment permits to perform experiments without an in-depth knowledge of optics and lasers. For Raman microscopy, extremely fast Raman systems equipped with motorized xy-stages are commercially available, enabling data acquisition down to only few milliseconds or even sub-milliseconds per pixel.

In order to enable a direct comparison and correlation of Raman images to other optical microscopic images, like fluorescence and dark-field, an integration of different optical techniques on the same microscope setup is favorable.

References

1. D.E. Carvajal-Hausdorf, K.A. Schalper, V.M. Neumeister, D.L. Rimm, Lab. Invest. (2014)
2. E.C. Stack, C. Wang, K.A. Roman, C.C. Hoyt, Methods **70**(1), 46 (2014)
3. J. Liu, S.K. Lau, V.A. Varma, R.A. Moffitt, M. Caldwell, T. Liu, A.N. Young, J.A. Petros, A.O. Osunkoya, T. Krogstad et al., ACS Nano **4**(5), 2755 (2010)
4. L.W. Wang, C.W. Peng, C. Chen, Y. Li, Breast Cancer Res. Treat. **151**(1), 7 (2015)
5. T.Q. Vu, W.Y. Lam, E.W. Hatch, D.S. Lidke, Cell Tissue Res. **360**(1), 71 (2015)
6. J.R. Lankowicz, *Principles of Fluorescence Spectroscopy*, 3rd edn. (Springer, USA, 2006)
7. A. Matschulat, D. Drescher, J. Kneipp, ACS Nano **4**(6), 3259 (2010)
8. M. Vendrell, K.K. Maiti, K. Dhaliwal, Y.T. Chang, Trends Biotechnol. **31**(4), 249 (2013)
9. W. Xie, S. Schlücker, Phys. Chem. Chem. Phy. **15**(15), 5329 (2013)
10. S. Feng, S. Huang, D. Lin, G. Chen, Y. Xu, Y. Li, Z. Huang, J. Pan, R. Chen, H. Zeng, Int. J. Nanomedicine **10**, 537 (2015)
11. S. Feng, D. Lin, J. Lin, B. Li, Z. Huang, G. Chen, W. Zhang, L. Wang, J. Pan, R. Chen et al., Analyst **138**(14), 3967 (2013)
12. K. Kong, C. Kendall, N. Stone, I. Notingher, Adv. Drug Delivery Rev. (2015)
13. Y. Wang, S. Schlücker, Analyst **138**(8), 2224 (2013)
14. Y. Wang, B. Yan, L. Chen, Chem. Rev. **113**(3), 1391 (2012)
15. W.E. Doering, M.E. Piotti, M.J. Natan, R.G. Freeman, Adv. Mater. **19**(20), 3100 (2007)
16. R.L. McCreery, *Raman Spectroscopy for Chemical Analysis*, vol. 225 (Wiley, New York, 2005)
17. S. Schlücker, Chem. Phys. Chem. **10**(9–10), 1344 (2009)
18. S. Schlücker (ed.), *Surface Enhanced Raman Spectroscopy: Analytical, Biophysical and Life Science Applications* (Wiley, New York, 2011)
19. S. Schlücker, Angew. Chem. Int. Ed. **53**(19), 4756 (2014)
20. M. Moskovits, Rev. Mod. Phy. **57**(3), 783 (1985)
21. A. Otto, J. Raman Spectrosc. **22**(12), 743 (1991)
22. A. Campion, P. Kambhampati, Chem. Soc. Rev. **27**(4), 241 (1998)
23. M. Moskovits, J. Raman Spectrosc. **36**(6–7), 485 (2005)
24. P.L. Stiles, J.A. Dieringer, N.C. Shah, R.P. Van Duyne, Annu. Rev. Anal. Chem. **1**, 601 (2008)
25. R. Aroca, *Surface-Enhanced Vibrational Spectroscopy* (Wiley, New York, 2006)
26. B. Küstner, M. Gellner, M. Schütz, F. Schöppler, A. Marx, P. Ströbel, P. Adam, C. Schmuck, S. Schlücker, Angew. Chem. Int. Ed. **48**(11), 1950 (2009)
27. X. Qian, X.H. Peng, D.O. Ansari, Q. Yin-Goen, G.Z. Chen, D.M. Shin, L. Yang, A.N. Young, M.D. Wang, S. Nie, Nat. Biotechnol. **26**(1), 83 (2008)
28. G. von Maltzahn, A. Centrone, J.H. Park, R. Ramanathan, M.J. Sailor, T.A. Hatton, S.N. Bhatia, Adv. Mater. **21**(31), 3175 (2009)
29. M. Gellner, B. Küstner, S. Schlücker, Vib. Spectrosc. **50**(1), 43 (2009)
30. G. Mie, Ann. der Phys. **330**(3), 377 (1908)
31. C.F. Bohren, D.R. Huffman, *Absorption and Scattering of Light by Small Particles* (Wiley, New York, 2008)
32. Y. Cui, B. Ren, J.L. Yao, R.A. Gu, Z.Q. Tian, J. Phys. Chem. B **110**(9), 4002 (2006)
33. C. Sauerbeck, M. Haderlein, B. Schürer, B. Braunschweig, W. Peukert, R.N. KluppTaylor, ACS Nano **8**(3), 3088 (2014)
34. W. Shi, Y. Sahoo, M.T. Swihart, P. Prasad, Langmuir **21**(4), 1610 (2005)
35. M. Rycenga, K.K. Hou, C.M. Cobley, A.G. Schwartz, P.H. Camargo, Y. Xia, Phys. Chem. Chem. Phys. **11**(28), 5903 (2009)

36. A.M. Fales, H. Yuan, T. Vo-Dinh, J. Phys. Chem. C **118**(7), 3708 (2014)
37. Y. Liu, H. Yuan, F.R. Kersey, J.K. Register, M.C. Parrott, T. Vo-Dinh, Sensors **15**(2), 3706 (2015)
38. C. Hrelescu, T.K. Sau, A.L. Rogach, F. Jäckel, J. Feldmann, Appl. Phys. Lett. **94**(15), 153113 (2009)
39. P. Negri, R.A. Dluhy, J. Biophotonics **6**(1), 20 (2013)
40. S.H. Seo, B.M. Kim, A. Joe, H.W. Han, X. Chen, Z. Cheng, E.S. Jang, Biomaterials **35**(10), 3309 (2014)
41. C.J. Orendorff, L. Gearheart, N.R. Jana, C.J. Murphy, Phys. Chem. Chem. Phys. **8**(1), 165 (2006)
42. N.J. Halas, S. Lal, W.S. Chang, S. Link, P. Nordlander, Chem. Rev. **111**(6), 3913 (2011)
43. X. Su, J. Zhang, L. Sun, T.W. Koo, S. Chan, N. Sundararajan, M. Yamakawa, A.A. Berlin, Nano Lett. **5**(1), 49 (2005)
44. L. Sun, K.B. Sung, C. Dentinger, B. Lutz, L. Nguyen, J. Zhang, H. Qin, M. Yamakawa, M. Cao, Y. Lu et al., Nano Lett. **7**(2), 351 (2007)
45. M. Salehi, D. Steinigeweg, P. Ströbel, A. Marx, J. Packeisen, S. Schlücker, J. Biophotonics **6**(10), 785 (2013)
46. M. Gellner, D. Steinigeweg, S. Ichilmann, M. Salehi, M. Schütz, K. Kömpe, M. Haase, S. Schlücker, Small **7**(24), 3445 (2011)
47. J.H. Kim, J.S. Kim, H. Choi, S.M. Lee, B.H. Jun, K.N. Yu, E. Kuk, Y.K. Kim, D.H. Jeong, M.H. Cho et al., Anal. Chem. **78**(19), 6967 (2006)
48. S. Jeong, Y.i. Kim, H. Kang, G. Kim, M.G. Cha, H. Chang, K.O. Jung, Y.H. Kim, B.H. Jun, Y.S. Lee, et al., Sci. Rep. **5** (2015)
49. C. Wang, Y. Chen, T. Wang, Z. Ma, Z. Su, Adv. Funct. Mater. **18**(2), 355 (2008)
50. M. Schütz, S. Schlücker, Phys. Chem. Chem. Phys. **17**(37), 24356 (2015)
51. S.J. Cho, Y.H. Ahn, K.K. Maiti, U. Dinish, C.Y. Fu, P. Thoniyot, M. Olivo, Y.T. Chang, Chem. Commun. **46**(5), 722 (2010)
52. K.K. Maiti, A. Samanta, M. Vendrell, K.S. Soh, M. Olivo, Y.T. Chang, Chem. Commun. **47**(12), 3514 (2011)
53. A. Samanta, K.K. Maiti, K.S. Soh, X. Liao, M. Vendrell, U. Dinish, S.W. Yun, R. Bhuvaneswari, H. Kim, S. Rautela et al., Angew. Chem. Int. Ed. **50**(27), 6089 (2011)
54. K.K. Maiti, U. Dinish, A. Samanta, M. Vendrell, K.S. Soh, S.J. Park, M. Olivo, Y.T. Chang, Nano Today **7**(2), 85 (2012)
55. S. Harmsen, M.A. Bedics, M.A. Wall, R. Huang, M.R. Detty, M.F. Kircher, Nat. Commun. **6** (2015)
56. J. Ni, R.J. Lipert, G.B. Dawson, M.D. Porter, Anal. Chem. **71**(21), 4903 (1999)
57. M.D. Porter, R.J. Lipert, L.M. Siperko, G. Wang, R. Narayanan, Chem. Soc. Rev. **37**(5), 1001 (2008)
58. C. Jehn, B. Küstner, P. Adam, A. Marx, P. Ströbel, C. Schmuck, S. Schlücker, Phys. Chem. Chem. Phys. **11**(34), 7499 (2009)
59. X.S. Zheng, P. Hu, Y. Cui, C. Zong, J.M. Feng, X. Wang, B. Ren, Anal. Chem. **86**(24), 12250 (2014)
60. S.P. Mulvaney, M.D. Musick, C.D. Keating, M.J. Natan, Langmuir **19**(11), 4784 (2003)
61. W.E. Doering, S. Nie, Anal. Chem. **75**(22), 6171 (2003)
62. W. Stöber, A. Fink, E. Bohn, J. Colloid Interface Sci. **26**(1), 62 (1968)
63. M. Schütz, B. Küstner, M. Bauer, C. Schmuck, S. Schlücker, Small **6**(6), 733 (2010)
64. M. Li, J. Zhang, S. Suri, L.J. Sooter, D. Ma, N. Wu, Anal. Chem. **84**(6), 2837 (2012)
65. D. Steinigeweg, M. Schütz, M. Salehi, S. Schlücker, Small **7**(17), 2443 (2011)
66. M. Schütz, D. Steinigeweg, M. Salehi, K. Kömpe, S. Schlücker, Chem. Commun. **47**(14), 4216 (2011)
67. J.M. Montenegro, V. Grazu, A. Sukhanova, S. Agarwal, M. Jesus, I. Nabiev, A. Greiner, W.J. Parak, Adv. Drug Delivery Rev. **65**(5), 677 (2013)
68. D.S. Grubisha, R.J. Lipert, H.Y. Park, J. Driskell, M.D. Porter, Anal. Chem. **75**(21), 5936 (2003)

69. B. Lutz, C. Dentinger, L. Sun, L. Nguyen, J. Zhang, A. Chmura, A. Allen, S. Chan, B. Knudsen, J. Histochem. Cytochem. **56**(4), 371 (2008)
70. G.T. Hermanson, *Bioconjugate Tech*. (Academic Press, Cambridge, 2008)
71. M. Salehi, L. Schneider, P. Ströbel, A. Marx, J. Packeisen, S. Schlücker, Nanoscale **6**(4), 2361 (2014)
72. Y. Zhang, B. Walkenfort, J.H. Yoon, S. Schlücker, W. Xie, Phys. Chem. Chem. Phys. (2015)
73. S. Schlücker, M.D. Schaeberle, S.W. Huffman, I.W. Levin, Anal. Chem. **75**(16), 4312 (2003)
74. S. Schlücker, B. Küstner, A. Punge, R. Bonfig, A. Marx, P. Ströbel, J. Raman Spectrosc. **37**(7), 719 (2006)
75. Y. Chen, X. Zheng, G. Chen, C. He, W. Zhu, S. Feng, G. Xi, R. Chen, F. Lan, H. Zeng, Int. J. Nanomedicine **7**, 73 (2012)
76. B.R. Lutz, C.E. Dentinger, L.N. Nguyen, L. Sun, J. Zhang, A.N. Allen, S. Chan, B.S. Knudsen, ACS Nano **2**(11), 2306 (2008)
77. Y.W. Wang, A. Khan, M. Som, D. Wang, Y. Chen, S.Y. Leigh, D. Meza, P.Z. McVeigh, B.C. Wilson, J.T. Liu, Technology **2**(02), 118 (2014)
78. P. Lackie, R. Hennessy, G. Hacker, J. Polak, Histochemistry **83**(6), 545 (1985)
79. M. Hayat, *Colloidal Gold: Principles, Methods and Applications* (San Diego, 1989)
80. S. Barua, J.W. Yoo, P. Kolhar, A. Wakankar, Y.R. Gokarn, S. Mitragotri, Proc. Natl. Acad. Sci. **110**(9), 3270 (2013)
81. R.P. Bagwe, L.R. Hilliard, W. Tan, Langmuir **22**(9), 4357 (2006)
82. E. Perets, A. Indrasekara, A. Kurmis, N. Atlasevich, L. Fabris, J. Arslanoglu, Analyst **140**(17), 5971 (2015)
83. X. Wang, X. Qian, J.J. Beitler, Z.G. Chen, F.R. Khuri, M.M. Lewis, H.J.C. Shin, S. Nie, D.M. Shin, Cancer Res. **71**(5), 1526 (2011)
84. A. Housni, M. Ahmed, S. Liu, R. Narain, J. Phys. Chem. C **112**(32), 12282 (2008)
85. B. Zhang, X. Wang, F. Liu, Y. Cheng, D. Shi, Langmuir **28**(48), 16605 (2012)
86. H. Xu, J. Xu, X. Wang, D. Wu, Z.G. Chen, A.Y. Wang, ACS Appl. Mater. Interfaces **5**(8), 2901 (2013)
87. K.M. Tichauer, K.S. Samkoe, K.J. Sexton, J.R. Gunn, T. Hasan, B.W. Pogue, J. Biomed. Opt. **17**(6), 0660011 (2012)
88. L. Sinha, Y. Wang, C. Yang, A. Khan, J.G. Brankov, J.T. Liu, K.M. Tichauer, Sci. Rep. **5** (2015)

Chapter 16
Confocal Raman Microscopy in Pharmaceutical Development

Thomas F. Haefele and Kurt Paulus

Abstract There is a wide range of applications of confocal Raman microscopy in pharmaceutical development. It is a powerful tool to probe the distribution of components within a formulation, to characterize homogeneity of pharmaceutical samples, to determine solid state of drug substances and excipients as well as to characterize contaminations and foreign particulates. The information obtained by confocal Raman microscopy is extremely useful, sometimes even crucial, for drug substance design, for the development of solid and liquid formulations, as a tool for process analytics and for patent infringements and counterfeit analysis. In this chapter, those aspects and applications will be presented, focusing on solid drug formulations. This chapter will also reveal the advantages and demonstrate the synergies of Raman mapping as compared to/with similar imaging methods such as SEM/EDX, NIR and MIR imaging.

16.1 Introduction

Pharmaceutical development links research and production. It starts with the takeover of a lead compound (the drug) from research and continues until the final drug product is launched on the market. It comprises all steps necessary to deliver a safe, effective and economic drug to the patient. Until the launch of a pharmaceutical product, extensive efforts are required to explore its toxicology, to develop a vehicle for drug delivery, to generate clinical data on safety and efficacy as well as to invent robust processes to manufacture the drug and the drug product. Everything needs to fulfil regulatory requirements for a successful registration. There is a wide range of applications of chemical imaging (CI) in pharmaceutical development. CI is powerful to probe the distribution of components within a formulation, to characterize homogeneity of pharmaceutical samples, to determine solid state of drug substances and excipients as well as to characterize contaminations and foreign particulates. The information obtained by chemical imaging, in particular by confocal Raman

T. F. Haefele · K. Paulus (✉)
Technical Research and Development, Novartis Pharma AG, 4002 Basel, Switzerland
e-mail: kurt.paulus@novartis.com

J. Toporski et al. (eds.), *Confocal Raman Microscopy*, Springer Series in Surface Sciences 66, https://doi.org/10.1007/978-3-319-75380-5_16

microscopy, is essential, sometimes even crucial, for drug substance design, for the development of solid and liquid formulations, as a tool to assure process quality and for counterfeit analysis. Complex systems from the submicron up to the macroscale can be investigated. Especially in combination, chemical imaging methods exhibit their full potential and the information obtained is very complementary. The more methods employed, the more comprehensively a system is described.

Raman spectroscopy is successfully applied for a manifold of tasks in the whole process of drug discovery and drug development. In this book chapter we will focus on the applications of confocal Raman microscopy for the technical aspects of drug development. Usages of Raman technology to investigate biomedical tissue or cells, either in vivo or ex vivo will not be reviewed. For implementations of Raman spectroscopy in this field we would like to refer to other literature [1, 2].

By far the most commonly employed and most compliant dosage forms today are solid oral dosage forms (e.g. tablets). On the other hand, synthetic chemical molecules of limited molecular weight (typically smaller than 1000 $g \cdot mol^{-1}$) depict the main class of active pharmaceutical ingredients (API). Biological APIs, such as proteins, antibodies, enzymes, etc. are contained only in a minor part of marketed products.

In this article we will describe the application of confocal Raman microscopy to characterize solid dosage forms of small synthetic APIs, not only due to their importance and predominance, but also due to other aspects: When investigated with Raman spectroscopy both, solid materials and small synthetic molecules, yield more information (sharper and stronger signals) and are simpler to investigate compared to liquids and large biological molecules. We elucidate relevant aspects and applications of chemical imaging. Also we will discuss advantages and demonstrate the synergies of complementary imaging methods when applied in combination. The content of this chapter is relating to industrial applications and much of the data and figures presented are from investigations of IP (intellectual property) protected specimens. Comprehensive descriptions and details of samples can thus not be given, structural and spectral features not be presented.

16.1.1 Vibrational Spectroscopy in Pharmaceutical Development

16.1.1.1 Analytical Requirements

When a lead compound is handed over from research to development, often only the molecular structure and a limited number of physical parameters are known (besides, of course, biomedical target and mode of action). In technical development, first an efficient and economic synthesis pathway for the drug substance needs to be discovered or optimized and the reactions required need to be upscaled to production scale. The output of such processes should not only be chemically pure substances,

but also materials possessing optimized physical and physicochemical properties. Particle size, particle shape and most importantly solid state (polymorphism and salt form) need to be optimized according to specific needs. A tailor-made particle design is the base for a stable drug product formulation as well as reproducible pharmacology.

In parallel to drug substance development, drug product development takes place. A route of administration and a suitable dosage form need to be defined and tested, formulation processes need to be optimized and scaled up.

All these steps require substantial analytical support. Especially the release of materials for clinical testing requires extensive analysis. The workhorse for routine analytics is liquid chromatography, but the list of methods to fully characterize a material and prove its safety is very long. Almost every producer of analytical equipment has invented some kind of more or less significant applications of his technology for the (once) sound and solvent cash cow - pharmaceutical industry. Thus any available analytical method is somewhere employed in pharmaceutical development, either in-house or externally.

Apart from release of clinical material the most critical analytical challenge is the characterization of the solid state of the active pharmaceutical ingredients. Polymorphism is the ability of a compound to crystallize as more than one distinct crystal species. This means that different polymorphic forms (or polymorphs) have different arrangements or conformations of the molecules in the crystal lattice. Solvates, also known as pseudopolymorphs, are crystal forms having either stoichiometric or nonstoichiometric amounts of a solvent incorporated in the crystal lattice. If the incorporated solvent is water, the solvate is commonly known as a hydrate. If a solid does not possess a distinguishable crystal lattice and the molecular arrangement of molecules is disordered, it is considered amorphous. The amorphous state is structurally similar to the liquid state [3–5].

Polymorphic forms of a drug substance can have different chemical, physical and physicotechnical properties. Differences can occur e.g. in:

- Packing properties (density, refractive index, conductivity, hygroscopicity)
- Thermodynamic properties (melting point, heat capacity, vapor pressure, solubility)
- Kinetic properties (dissolution rate, stability)
- Surface properties (surface free energy, interfacial tension, shape, morphology)
- Mechanical properties (compactibility, tensile strength).

These properties can have a direct effect on the ability to process and manufacture the drug substance and the drug product. Polymorphism further has pharmacological implications due to altered effectiveness and suitability for a particular formulation. Finally, polymorphism also effects regulatory approval and intellectual property issues. Thus, polymorphism of an active pharmaceutical ingredient (API) can affect the quality, safety, efficacy and developability of a drug product and is therefore of fundamental importance in pharmaceutical industry [6, 7].

In addition to polymorphic modifications a drug substance can be crystallized in different salt forms. Any drug substance can be classified as either an acid or base

because the drug substance possesses the ability to react with other, stronger acids or bases. As such, the drug substance also would possess the ability to exist as an ionic species when dissolved in suitable fluid media. If an API is crystallized together with an appropriate counterion, a salt can be generated. There is a wide range of cationic as well as anionic counterions available. Screening of the best available and crystallizable salt is performed routinely with every novel chemical entity. Similar to polymorphism, salt forms are varying from each other in the degree of solubility and many other physical and chemical factors, as denoted for polymorphs. If the characteristics of the free acid or free base are found to be not acceptable an appropriate salt form might provide improved aqueous solubility, dissolution rate, hygroscopicity, chemical stability, melting point, or mechanical properties of a drug substance. There are a number of methods that can be used to characterize polymorphs and salt forms of a drug substance. X-ray powder diffraction (XRPD) is regarded as the gold standard for solid state analysis. Other methods include thermal analysis (e.g. differential scanning calorimetry (DSC) and thermal gravimetric analysis (TGA)), hot-stage microscopy, solid-state nuclear magnetic resonance spectroscopy (ssNMR) and last but not least vibrational spectroscopy.

16.1.1.2 Infrared Spectroscopy

Vibrational spectroscopy is in any case one of the more significant classes of analytical methods used in pharmaceutical development. Not only solid state analysis but also a wealth of other applications is feasible. Mid infrared (IR) spectroscopy is very commonly employed to prove chemical identity and to characterize solid state. Even though IR spectroscopy is simple to perform and cheap to acquire, it normally yields only limited information and additional analytical methods are required as a backup.

Near infrared (NIR) spectroscopy is gaining much of importance in recent years, mainly driven by the initiative of the International Conference on Harmonization (ICH) for Quality by Design (QbD) [8] and by the US Food and Drug Administration (FDA) Guidance on Process Analytical Technology (PAT) [9]. Scientific process understanding shall support innovation and efficiency in pharmaceutical development, manufacturing, and quality assurance. NIR is thus employed throughout processing and manufacturing to monitor quality as well as performance parameters in production based systems. Not only NIR spectroscopy is employed but also NIR imaging using a microscope-mounted focal plane array (FPA) detector. Both quantitative and qualitative analysis are feasible and NIR can also be deployed in-line of a production line [10].

Terahertz (THz) spectroscopy and Terahertz imaging evolved only very recently. They make use of THz frequencies, which lie in between microwaves and near infrared. Complementary to the other vibrational spectroscopy methods, Terahertz spectroscopy also allows the characterization of solid states [11, 12]. The development

of terahertz chemical imaging is still in its infancy. Due to the intrinsic limitation of chemical information obtained it is mainly employed to investigate tablet integrity as well as coating uniformity and thickness [13]. It is also reported that THz imaging was successfully employed to investigate the spatial distribution of excipients on tablet surfaces [14].

16.1.1.3 Raman Spectroscopy

The applications of Raman spectroscopy in the pharmaceutical environment are discussed more in detail. Raman spectroscopy is applied routinely to resolve a wide range of tasks. Due to the easy or even needless sample preparation, as well as the ability to measure in aqueous environment, it is a very important technology [2]. Its main application is within solid state analysis. Apart from XRPD, DSC and TGA, Raman spectroscopy is the most beneficial tool to characterize polymorphic forms. Vibrations originating from the crystal lattice (phonons) and from the Carbon backbone yield much stronger signals in Raman compared to IR and NIR spectroscopy. In addition, the low wavenumber region, where most of the relevant vibrational information on the solid state is contained, is easily accessible by Raman. Specially designed spectrometers allow the registration of Raman spectra down to 50 rel. cm^{-1}.

Due to the ability of small-volume sampling, speed of data acquisition, fingerprinting capabilities and automated high through-put analysis of multi-well plates, Raman spectroscopy is routinely used for polymorph and salt screening [15, 16].

Due to these high through-put screening (HTS) capabilities, Raman spectroscopy is also implemented to support structure elucidation in combinatorial and parallel-synthesis technologies. Because of the intrinsic lack of structural information it is only complement to backup IR. Asymmetrical functional groups with a large dipole moment do not yield strong signals in Raman spectroscopy in contrast to IR [17].

Market approval of a new drug product requires extensive testing of product stability. Ageing and stressing under defined conditions of temperature and humidity for long time periods are inevitable. Owing to the HTS potential Raman spectroscopy is also routinely employed for stability screening of drug products [18–21].

Raman is also employed as PAT technology. Being insensitive to aqueous solvents Raman spectroscopy is an appropriate tool for reaction monitoring. Glass signals do not interfere and thus direct product analysis in vials and process quality control using fibre probes is feasible [22, 23].

Non-invasive in nature and easy and fast to perform, Raman spectroscopy is also a suitable tool for counterfeit identification. Counterfeits generally either do not contain any API or contain a different API. Raman allows distinguishing between genuine and counterfeit product either by identification of the ingredients or even by investigation of (fake) packaging [24].

16.1.2 Imaging in Pharmaceutical Development

16.1.2.1 Light Microscopy

Microscopes of almost any kind are in use within pharmaceutical development. Depending on the probe or radiation deployed, visual investigations can be performed from the macro scale down to a few nanometres. Often not only surfaces can be visualized but also information can be gained from the inner structure of a specimen. The most commonly employed microscopes are light microscopes. Available in various setups almost only the financial budget limits the resolution and available methods. Simple stereo microscopes are very prominent and abundant tools to get a rough idea of visual appearance of any kind of sample. More advanced light microscopes for material testing are less often encountered in pharmaceutical laboratories. Both, upright stands and inverse systems with optical beam paths for incident and transmitted light are in use. In combination with motorized sample stages and image analysis, automated investigations of large numbers of samples or large sample areas are feasible [25, 26].

Apart from simple bright field microscopy by far the most important illumination technique is polarized light microscopy. It is usually performed with a polarizing element below the sample to produce plane polarized light and an analyzer that is set to give total extinction of the background and thus to detect any birefringence. Polarized light microscopy can distinguish between isotropic and anisotropic materials. Isotropic materials (e.g. gases, liquids, unstressed glasses) demonstrate the same optical properties in all directions. Anisotropic materials, in contrast, have optical properties that vary with the orientation of incident light with the crystallographic axes. They demonstrate a range of refractive indices depending both on the propagation direction of light through the substance and on the vibrational plane coordinates [27, 28].

Polarized light microscopy is very efficient to investigate particle shape, particle size and in combination with image analysis also particle size distribution. But in the latter case, a $\lambda/4$ filter must be used, to change the character of polarization of light from linear to circular and thus to avoid an extinction of particles caused by 90° crossed polarizers. In addition to the ability to detect any birefringence it is very powerful in exploring crystal growth and crystallinity in general. In combination with a hot-stage, temperature dependent phase transformations can be observed. Not only melting points but also eventual solid state transformations can be followed [29, 30].

Contrasting methods commonly employed in biological sciences such as phase contrast or differential interference contrast (DIC) to visualize thin low-contrast structures such as cells are required for creams and ointments to increase the contrast of the border of emulsion droplets. Histological approaches to increase contrast (e.g. staining) are uncommon for investigation of pharmaceutical materials by light microscopy.

Fluorescence microscopy in contrast, another typical tool from biological sciences, is a very valuable tool also in pharmaceutical material sciences. Many APIs

exhibit autofluorescence due to functional groups. Polymeric and inorganic excipients not uncommonly reveal also an intrinsic fluorescence. Even though the emission wavelengths are very unspecific and difficult to assign, valuable information can be obtained on the homogeneity and uniformity of a mixture [31–33].

An interesting approach to further investigate the structure of a dosage form as well as its dissolution behaviour is the substitution of the API with a model fluorescent dye. In this way, distribution of the API in the formulation and the release of the API from the formulation can be simulated [34].

Time dependent disintegration of tablets is a further area, in which light microscopy can be applied. The understanding of such complex dissolution reactions is crucial for method development. This has been shown recently by investigating drug release of osmotic depot systems by stereo light microscopy [35].

16.1.2.2 Electron Microscopy

Electron microscopy is evenly used to probe visual appearance of pharmaceutical samples. Most advantageous is scanning electron microscopy (SEM), which is routinely employed for drug substance analysis. Extremely high resolutions down to a few nanometres and a very flexible field of view make it a very powerful tool. Transmission electron microscopy (TEM) is rarely employed, mainly due to the demanding sample preparation and limited sample contrast. But when highest resolution for investigation of finest nano structures is required, TEM is the most powerful method.

When a material is probed using a focused electron beam various types of radiation are produced. These secondary radiations can be registered using different detectors to gain characteristic information on the specimen under investigation.

Most commonly secondary electrons (SE) are detected leading to a large depth of field, which yields a characteristic 3D appearance useful for understanding the sample's surface structure. SE imaging is used to obtain surface information for a qualitative description of the sample: surface defects, porosity, and the three dimensional structure can be evaluated.

The intensity of back scattered electrons (BSE) is strongly related to the atomic number of the specimen. Thus, BSE images can provide a certain material contrast.

Other resulting types of signals are e.g. X-rays or cathode luminescence, which will be partly discussed later on [36].

An SEM setup does not necessarily need to be bulky in space and fill a whole room. Today, also transportable bench top systems are available, still offering acceptable resolution. This allows on-site inspection of analytes at the production site.

High resolution SEM usually requires high vacuum and coating of the samples surface with a thin carbon or metal film to prevent electric charging of the sample. As a consequence, liquid samples, biological cells and living tissue will be denatured or disintegrated. Recently, new types of detectors, e.g. inlens detectors have evolved. Optimally localized in the gun they require only low voltages and not necessarily a sputtering of the sample to gain reasonable results.

SEM is ideally suited to characterize the morphology and homogeneity of a sample. Particle sizing and determination of particle size distribution are an easy task as well. An experienced operator can deduce a multitude of characteristics of a sample just by obtaining and interpreting meaningful scanning electron micrographs [37–40].

16.1.2.3 Further Microscopic Methods

Atomic Force Microscopy (AFM) is best employed to resolve submicrometer structures. From an atomic force microscopists point of view, a tablet needs thus to be considered a very large body. Lateral dimensions of primary particles of solid dosage forms are typically in a size range of 0.01–0.1 mm. Even after tabletting the surface roughness of pharmaceutical solid samples can be of considerable height differences. The lateral scan range (the field of view) and the vertical range of the cantilever might thus be too limited to investigate 'macroscopic' specimens like a tablet. If the system is adapted to the analyte or vice versa, decent information on surface topography can be obtained. The application of nano-particles is very unusual up to now but is increasing and thus also the need for AFM will be enhanced [41, 42].

Other approaches have been taken to circumvent the hindrance of oversized roughness height. The combination of an AFM with an ultramicrotome has provided very interesting results. Sequential trimming of a specimen surface with an ultramicrotome followed by characterization by an AFM of each section allows insights into the sample. Reassembling the obtained z-stacks and rendering them allows the generation of the specimens 3D structure [43].

AFM is not only applied to characterize topography and surface roughness but also to investigate mechanical properties of surfaces. Recording force-distance curves allows information on adhesion, elasticity or friction [44, 45]. Nanomechanical measurements were successfully applied to quantitatively distinguish amorphous and crystalline domains through local Young's modulus measurements [46].

Further imaging methods popular in conventional materials testing are e.g. X-ray microtomography (XMT) and acoustical imaging. XMT uses X-rays to create cross-sections of a 3D-object, which can be rendered to recreate a 3D model of a body. X-rays can be used to see inside a sample based upon material density differences [47, 48]. Acoustical imaging employs ultra high frequency ultrasound. The transmitted or reflected echo of the ultrasound reflects changes of the impedance due to varying material density [49]. Both methods are non-destructively and penetrate solid materials allowing the visualization of internal features, including defects such as cracks, delaminations and voids. Due to the limited spatial resolution, applications in pharmaceutical development are scarce.

16.1.3 Chemical Imaging in Pharmaceutical Development

Imagine watching a movie without the ability to hear or see. Seeing only screenplay without sound, or vice versa, communicates limited information of the message the director of the film or actors may want to transport. Understanding the seen or heard more than anything will be a matter of interpretation, only the combination of both senses would allow enjoying and comprehending the full experience. Spectroscopic investigations yield chemical and physical information, microscopy on the other hand delivers spatial information. In analogy to the above, the merger of both, spectroscopy with microscopy, must be very powerful. In fact, many methods of microspectroscopy have evolved in the last decades. The approach has either originated from the spectroscopy side by spatially focusing and rastering the exciting radiation (e.g. time-of-flight secondary ion mass spectroscopy, TOF-SIMS), or from the microscopy side by extracting physico-chemical information from secondary signals (e.g. X-ray quanta from SEM). In contrast to fluorescence microscopy no marker needs to be introduced into the system under investigation. Chemical imaging (CI) probes intrinsic properties of a molecule or atom, often in a non-invasive way. Spatially resolved chemical information delivers a wealth of new information, not accessible otherwise. Furthermore, an image can often reveal more information than any table or numerical result. A colour-coded distribution map of a system can be very straightforward to elucidate the complexity of the system. Just like adding additional senses to a living organism, the combination of several types of detectors in one and the same imaging system strongly enhances the analytical capability (e.g. FTIR & Raman in a light microscope). If such a combination in the same system is not feasible, then the sequential investigation of the same area using different chemical imaging methods can be considered an alternative approach. The more complementary methods are applied to investigate an analyte, the more information is obtained and the more comprehensive the analyte is characterized [50–53].

Chemical imaging is new to pharmaceutical development and not yet routinely employed. Sizeable investments and lack of request from health authorities has impeded the wide proliferation of CI technologies in pharmaceutical industry, even though a wealth of applications exist, which allow new insights into old challenges. The assessment of visual appearance as well as chemical and physical nature is feasible in one step. Particle size, particle size distribution (PSD), morphology and particle shape are delivered by microscopy [54]. Combined spectroscopy techniques as described above resolve spatially the chemical identity of ingredients (structure and/or elements) as well as their solid state (polymorphism, crystallinity, etc.). Supplementary information regarding mechanical properties such as adhesion, elasticity and stiffness can also be made available. Possible foreign particulates can easily be detected and identified. Content uniformity, sample homogeneity and spatial distribution of components are important information, required for all pharmaceutical products. The chemical compatibility of actives and excipients after stressing at increased temperature and humidity can be resolved and aging effects detected. The

information obtained by chemical imaging technologies allows improved and accelerated drug product design and can proof novel drug delivery concepts.

There is some controversy as to when to denominate a method "imaging" or "mapping". We will refer to the term imaging whenever a technology yields an image, no matter if the image was produced by point-mapping, line-scanning or global illumination [55].

Of the available CI technologies we would like to introduce the following, relevant to pharmaceutical sciences.

Energy-dispersive X-ray spectroscopy (EDX) is generally performed in conjunction with a scanning electron microscope (SEM). When irradiating a sample in the SEM with an electron beam, several types of secondary radiation are produced. Secondary electrons and backscattered electrons are used for generating SEM images as described above. X-rays are another type of radiation that is generated. When a high energy electron beam hits an atom in its ground state, an electron in an inner shell might be excited and ejected, creating an electron vacancy in the shell. This vacancy is immediately filled by an electron from a higher-energy shell. The resulting potential energy is released as a discrete X-ray quant, characteristic for the potential difference between higher-energy to a lower-energy electron shell. Thus, the X-rays detected are characteristic of the atomic structure of the element from which they were emitted; this allows the elemental composition of the specimen to be measured qualitatively and quantitatively, if the roughness of the sample surface is low. Theoretically, all elements with at least one p-shell electron (starting from ^{5}Boron) are suitable for EDX analysis. Practically, however, reasonable signals are achieved starting from ^{8}Oxygen [56]. Modern SEMs allow a spatial resolution down to a few nanometres. For EDX this resolution can hardly be achieved, mostly due to limited acquisition times. Generally, an EDX map consists of a much lower number of pixels than a typical SEM image. EDX is typically employed for characterization of polished metallic surfaces or minerals, but it can be very useful also for the analysis of drug products [57, 58]. Pharmaceutical samples unfortunately rarely exhibit flat planes or polished surfaces, further limiting resolution and making quantitative analysis difficult. Flat surfaces to improve resolution for EDX mapping can be prepared for example by microtomy. The vast majority of pharmaceutical actives and excipients is of organic nature, thus contains Carbon, Hydrogen and Oxygen atoms. A discrimination of components is difficult because no intrinsic marker, e.g. a more exotic element, is present. EDX mapping thus only allows substantial spatial discrimination of ingredients if at least one component includes a different element, e.g. Sulphur, Phosphorous or Chlorine. If such an element is present in the API or any of the excipients, the distribution within pharmaceutical systems can easily be characterized. SEM generally requires sputtering of the samples surface with a thin conducting layer of typically Carbon, Platinum or Gold. Improper choice of the sputtering material can limit spectral resolution of EDX due to overlapping peaks of the coating material. Thus, the optimal material to improve surface conductivity is a layer of Carbon which does not disturb the emission of the X-ray signals of the analyte.

EDX-mapping is a widely underestimated method and very complementary to vibrational microspectroscopy. Due to the widespread availability in pharmaceutical laboratories, it should be applied much more often [59–61].

A method related to EDX is X-ray fluorescence (XRF). Similar to EDX, electrons from the inner orbitals of an atom are expelled due to bombardment with an irradiation, creating an electron vacancy which is refilled by an electron from higher energy orbitals. Again, the energy released is detected as an X-ray quant characteristic for the electron configuration of the element. In XRF a high-energy X-ray beam is employed as primary irradiation in contrast to an electron beam in EDX. The term fluorescence is applied to phenomena in which the absorption of higher-energy radiation results in the re-emission of lower-energy radiation. Due the incorporation of an X-ray source, the irradiating beam is less focused than an electron beam in SEM. The spatial resolution in XRF is best around 10 μm, about 1000 times worse compared to EDX. Another drawback is that elements can only be detected starting from the third period (Sodium and heavier). On the other hand, a major advantage is that XRF can be operated under atmospheric pressure and is thus less invasive than high-vacuum EDX. It is therefore better suited to investigate virtu, archeological samples and specimens from forensic science. In addition, XRF is also employed for elemental analysis of metals, glasses and ceramics [62–64].

Time-of-Flight Secondary Ion Mass Spectroscopy (TOF-SIMS) is another method which can be employed for chemical imaging. It uses a focused, pulsed primary ion beam (typically Cs, Ga, Au or Bi dimers or trimers, SF_5, or C_{60}) to produce secondary molecular ions from the surface monolayer of a sample. The ejected secondary ions are collected and their mass is determined by measuring the exact time at which they reach the detector. Because it is possible to measure the time-of-flight on a scale of nano-seconds, it is possible to produce a very high mass resolution down to 0.001 atomic mass units (amu) at a range of typically 0–10.000 amu. The limit of detection can be as low as ppb although TOF-SIMS generally does not allow fully quantitative analysis. The ion beam can be scanned over a sample to produce maps at sub-micrometer resolution. TOF-SIMS is a highly surface-sensitive method being able to detect molecules within a depth of a few Ångstrom. The invasive nature of the primary ion beam can be used to generate depth profiles by removal of surface monolayers by sputtering under the ion beam. TOF-SIMS is useful to determine the elemental, isotopic, or molecular composition of the surface [65]. TOF-SIMS is best used to probe flat surfaces. Microscopically rough materials such as pharmaceutical products need to be trimmed first. Due to the high vacuum required in the analytical chamber, only solid samples can be investigated. Charging of non- or poorly conducting samples surfaces due to the irradiating ions may inhibit analysis, even though charge compensation is applied. Even though complex and cost-intensive, TOF-SIMS provides unique information on composition of molecular components up to several thousands of Daltons and is well complementary to other imaging methods. Several successful applications in pharmaceutical sciences have been reported [66–69].

Apart from spatially resolved X-ray spectroscopy to probe elemental configuration and mass spectroscopy to probe molecular composition, vibrational spectroscopy is

most commonly used for chemical imaging. Efficient mid infrared spectral imaging (MIRSI) requires a focal plane array (FPA) detector, single nitrogen-cooled MCT (Mercury-cadmium-telluride) detectors would require immense time spans to generate a map. An FPA detector is a device at the focal plane of the lens consisting of a rectangular array of light-sensing pixels. In contrast to a charge coupled device (CCD) sensitive to visible light, an FPA is sensitive in the infrared spectrum. MIRSI employs attenuated total reflectance (ATR) objectives made from either a germanium or diamond crystal. ATR allows direct examination without further preparation. A beam of infrared light is passed through the ATR crystal in such a way that it reflects at least once off the internal surface in contact with the sample. This reflection forms the evanescent wave, which extends into the sample, typically a few micrometers. The beam is then collected by a detector as it exits the crystal. Transmission mode and diffuse reflection are normally not suitable for MIRSI. The image resolution is actually limited to 64 × 64 or 128 × 128 pixels. Also the field of view (FOV) is inflexible and defined by the ATR lens employed. MIRSI allows fast acquisition of chemical images at spatial resolutions of only a few micrometers. The chemical information obtained is generally very specific and significant [10, 70]. A prerequisite for MIRSI is thus to have a flat surface, i.e. trimming of a sample is often required. Physical contact of the ATR crystal might induce sample damage. Furthermore, the bent shape of the ATR crystal can lead to optical aberrations. Only few applications of MIRSI within pharmaceutical development are reported in literature e.g. [71–76].

More convenient and more commonly employed is near infrared spectral imaging (NIRSI), also employing a FPA detector, enabling thousands of spectra to be acquired simultaneously. NIRSI is operated either in transmission or in diffuse reflection mode. ATR is not required. In diffuse reflection, the primary radiation is scattered by interaction with the sample and the reflected light is recorded by the detector. The NIR radiation can penetrate considerably into the specimens. NIRSI is much easier to perform than MIRSI but the spectra obtained lack specificity. Both NIRSI and MIRSI are generally good for differentiating solvates and pseudo-polymorphs. Because NIRSI primarily probes broadened combination and overtone bands, it lacks specificity to discriminate true polymorphs. Similarly to mid infrared, FOV, pixel resolution and spatial resolution are defined by the lens and the FPA and cannot be changed flexibly. Flat surfaces are advantageous for NIRSI as well, and sample trimming may be required. Except for sample heating NIRSI is fully non destructive. Various NIRSI applications are reported in the literature e.g. [77–79], the recent review of Gendrin et al. provides a comprehensive overview [10].

16.1.4 Confocal Raman Microscopy in Pharmaceutical Development

Theory, device-setup, advantages and limitations of confocal Raman microscopy (CRM) are discussed elsewhere in this book. We will thus only give an overview of the applications of CRM in pharmaceutical development reported in literature.

The first application of CRM to map pharmaceuticals appeared in 1999 [80]. It entails the mapping of a binary solid dispersion (API and polymer) prepared through melt extrusion. Although rather old by now, this publication illustrates well, what CRM is best used for. The goals of this study reflect the main applications of CRM in pharma development today: Physical state of the drug, stability of the formulation as well as content uniformity and homogeneity. Compared to recent instrumentation, the technology that the authors had at hand seems very basic [40]. A map of $45 \times 25\,\mu m^2$ consisting of only 200 measurements is very rough compared to around 10,000 to 100,000 spectra of a today's Raman images. Even though much higher resolution is available, also today the interpretation of chemical images is difficult and can be ambiguous. The authors of the 1999 publication seemed very keen to conclude that the solid dispersion investigated was homogeneously distributed. Nonetheless, this article is extraordinary due to the fact that a semi-solid dosage form is investigated and not a common solid dosage form, such as a tablet, which is in general easier to characterize.

In the same year, a short conference contribution appeared, in which confocal Raman imaging was employed to study the structural ordering and the micron-scaled homogeneity of bio-polymers for pharmaceutical applications. Unfortunately, no experimental details are given [81]. A very fascinating result was reported in another publication, where CRM was applied to generate a three dimensional visualization of a three component salt [82]. Kador et al. (2001) report on the complementarity of various chemical imaging methods. NIRSI and CRM were employed sequentially to describe an entire formulation at exactly the same area. This chemical image fusion approach could remove ambiguity from the data obtained by the two separate techniques. It was also found that CRM is most suitable to detect the active and inorganic constituents whereas NIRSI is best to characterize carbohydrates [83].

By far the most common application of CRM is the imaging of solid dosage forms to prove content uniformity. Tablets generally are ideal to be investigated by CRM. API and excipients often exhibit major spectral differences. Primary particles used for granulation are typically in a size range from 1 to 100 μm. These dimensions are also found as individual component domains in tablets. As described elsewhere in this volume, the resolution of CRM just perfectly fits these requirements. Domains and boundaries can be visualized at full resolution. If the CRM system allows large area mapping, even entire tablets (up to cm) can be characterized regarding content uniformity. Starting from the year 2000 several reports have appeared where the spatial distribution and identification of individual components within a tablet were investigated [84–86]. The complexity of the systems regarding number of components and similarity is varying significantly. Simple two-component systems are investigated, but also systems with up to five different tablet ingredients were discriminated [78, 87]. Concentrations of the API below 1% wt/wt are detectable [88]. Also, discrimination of particulate polymorphic impurities in tablets of only 0.05% wt/wt was described. This is very astounding because this reflects a much better limit of detection (LOD) than e.g. powder XRD (PXRD) [77]. The ability not only to probe content uniformity but also to verify the solid state of the active component makes CRM an extremely powerful tool. Mechanical stress during processing (gran-

ulation and tabletting) similar as ageing at elevated temperatures and/or humidity can affect the solid state of the active, which is, of course, highly undesirable. Surface amorphization e.g. can affect considerably the bioavailability of a dosage form.

Other important dosage forms where CRM can show its full potential are powder inhalation formulations. These formulations normally consist of small API particles below 10 μm dispersed with a carrier excipient. Flight and release properties are often improved by particle design and eventually by addition of lubricants. Of course, agglomeration of API particles or demixing of the dispersion is very undesirable and may strongly affect the efficiency of the formulation. CRM can either be applied to study the original bulk dispersion or also deposits on cascade impactors, which simulate the different regions within the pulmonary tract. Characterization of component distribution and deposition of powder inhalation formulations by CRM has been successfully demonstrated in the literature with various components and inhaler systems [89, 90].

Two out of three compounds in the drug discovery pipelines in pharmaceutical companies have a solubility in water of less than 100 μg/ml and may thus be termed insoluble or practically insoluble. Semi-solid dosage forms for oral or topical administration (application to body surfaces) e.g. solid dispersions or solid microemulsion preconcentrates, may help to overcome this challenge by stabilizing a specific form of an API, which is generally thermodynamically less favourable but more soluble. Semi-solid dosage forms filled into hard gelatine capsules are thus employed in pharmaceutical sciences to improve solubility, leading to an improved bioavailability while decreasing variability and reducing food effect [91]. CRM was successfully applied to probe uniformity and distribution as well as solid state within the formulation. Generally the systems under investigation consist of the API dispersed in one dispersing agent [80, 92]. The preparation method of the dispersions can affect the solid state. Results showed the presence of different polymorphic forms as well as an amorphous form [93]. Recently, the fine structure of solid microemulsion preconcentrates was resolved. It was found that the preconcentrates are two-phase systems, where clusters of crystalline polyethylene glycol form the solid structure and the liquid microemulsion preconcentrate is dispersed in between as a separate phase. The drug remained dissolved in the liquid phase even at increased concentrations. Solid dispersions, in contrast, could stabilize a dissolved state of the API only to a certain concentration. Increasing the amount of API leads to a precipitation of API in a crystalline state [40].

Depot systems for intramuscular application or stents for applications in blood vessels generally consist of a biodegradable polymeric matrix, in which the API is dispersed either in particulate form or molecularly. Upon administration in the body the polymer matrix is slowly hydrated and degraded releasing the active component. Depot systems are optimized for a steady long acting release over weeks and months. Bursts in release are strongly unwanted. Content uniformity, accurate particle size distribution and defined solid states are a prerequisite to achieve this effect. CRM can resolve any of these challenges. Either in original state or after weeks of hydration, coherent results can be generated.

Homogeneity regarding API concentration as well as effect of drug elution on coating morphology was recently investigated with stents. Effects such as appearance of particulate structures, segregation of API to the outer surfaces as well as drug/polymer demixing could be observed by CRM and other chemical imaging methods [66]. Although developed over a decade ago there are still only a limited number of reports discussing the application of CRM in pharmaceutical development. There might be two reasons for this: first, only the major pharmaceutical companies can afford chemical imaging facilities, and second, the pharmaceutical industry is very much restricted due to intellectual property reasons and reports thus are scarce. At least also health authorities have now discovered the value of confocal Raman microscopy and the wealth of information available generated by this technique [94]. A boost of chemical imaging might therefore be expected to happen within pharmaceutical development [95].

16.2 Applications of Confocal Raman Microscopy in Pharmaceutical Development

16.2.1 Practical Considerations

Confocal Raman microscopy is perfectly suited to characterize pharmaceutical specimen. At the same time, pharmaceutical specimens represent ideal samples for maximum performance of a CRM system for several reasons:

Most pharmaceutical samples consist of white powders. Visible light can therefore be applied to probe the specimens without risk of absorption, followed by sample heating and degradation. Visible radiation, e.g. green light, yields good optical resolution, acceptable Raman intensities and normal optics and detectors can be used, fluorescence is rarely a problem.

Synthetic APIs typically weigh less than 1000 g/mol and consist of a distinct Carbon backbone, typically with aromatic and non-saturated functional groups. They yield very strong and very sharp Raman signals, normally of several times higher intensity and less broad than the signals of (polymeric) excipients. Smallest variations in the Carbon backbone and the crystal lattice yield spectral variation. Thus polymorphic forms and solvates can generally easily be discriminated by CRM. Biomolecules and biopolymers, e.g. RNA, oligopeptides and proteins are much more demanding with respect to experimental parameters and yield weaker and broader signals. Fortunately for the analyst, biomolecules still account only for a small part of pharmaceutical API.

Due to regulatory requirements, pharmaceutical substances are of very high purity. In addition, reference material of various polymorphic forms and salt forms are available due to the respective screening programs. Molecular structure, solid state, solvent content, crystallinity and particle size are generally known of every component in the system under investigation. It is thus possible to obtain reference spectra from pure,

clearly defined material at high spectral resolution. These reference spectra are very valuable for multivariate data analysis, e.g. as basis spectra for classical least squares (CLS) algorithms. CLS can improve the LOD and noise levels and it is considered as the most credible data processing algorithm in comparison to principal component analysis, cluster analysis or multivariate curve resolution [86, 96].

As mentioned earlier, the size range of pharmaceutical samples is just right for a modern CRM. Primary particles are usually 1–100 μm, granules are typically a few hundred micrometers whereas a tablet measures millimetres to centimetres. A CRM equipped with a state-of-the-art Piezo-drive scan stage is excellent for imaging at highest spatial sub-micron resolution with FOV of a few hundred micrometers. Attachment of an additional motorized scan stage allows generating large area mappings of entire macro-objects. Thus, overview images of a full body can be generated followed by high-resolution images of areas of interest at a much smaller scale.

16.2.1.1 Critical Parameters

Even though analytes and analytical technology match very well, there are certain restrictions to be considered. Certain critical parameters need to be adjusted carefully.

The irradiating laser wavelength and laser power are the most determining factors and need to be tuned to maximize Raman signal levels yet must exclude absorption by the sample followed by degradation at the same time. A sample can decompose, undergo a phase transition, or simply heat up and emit longer-wavelength radiation when absorbing energy. The sample's electronic absorption spectrum has a strong effect on the probability that the sample will absorb energy. A hot sample emits black-body radiation. Thus, for samples that absorb radiation at the laser wavelength, the operator must be careful when selecting the appropriate laser power to maximize the S/N and minimize black-body radiation caused by sample heating. If the sample absorbs too strongly, a change of laser wavelength is required [97, 98]. Defocusing, change of lens to a lower magnification and N.A. or cooling of the sample using a cryogenic stage decrease the probability of sample degradation additionally [99].

Although mentioned as the issue number one in every text book on Raman spectroscopy [100], to our experience fluorescence noise due to improper choice of laser wavelength is only a minor problem when conducting confocal Raman microscopy of pharmaceuticals. Even when using a green laser at 532 nm, only a very low percentage of pharmaceutical samples exhibit intrinsic fluorescence, mostly originating from celluloses and polymeric excipients; intrinsic fluorescence of APIs is very seldom. Fluorescence can either be removed through photo bleaching or be eliminated by data treatment. Polynomial baseline correction or inclusion of extracted fluorescence signal as additional basis spectra during data processing using classical least squares allows removal of such noise. This offers the advantage that components can be localized also according to their fluorescent trace and not only due to the Raman signal. An elegant and efficient way to remove fluorescence (as well as to improve S/N) is to employ a numerical method based on wavelet transforms to process data. Wavelet transforms can be suitable to suppress non-correlated noise and background

signals. The Raman spectrum is decomposed by wavelet transform into 'frequency components'. The low frequency (fluorescence, background) and the high frequency data sets (noise, spikes and 'cosmic rays') are rejected and the remaining sets are reconstructed to yield an improved Raman spectrum [101–104].

Another decisive component of a CRM is the objective lens. The numerical aperture (NA) of the lens defines the spatial resolution as well as the collection efficiency. Thus, a maximum NA is desirable. High NA means applying an oil immersion objective or objectives with very short working distance. For non-invasive investigation of rough solids, however, a long working distance non-immersed objective is required. Hence, a compromise needs to be made. Of high importance is also the focal depth of a lens, a measurement of the space in which an object can be displayed at acceptable sharpness. If flat polished surfaces are under investigation, this parameter will not be of interest. Should samples exhibit very rough and curved surfaces it will be difficult to get all objects within the FOV in focus. Due to the fact that CRM is performed confocally, all objects not in focus (above or below the focus plane) will not yield Raman signals. If very uneven specimens need to be characterized, objective lenses with a lower magnification and lower NA and a large pinhole are required.

Alternatively, sample preparation to generate flat surfaces is a solution. Tablets e.g. can be treated employing a tablet mill or a microtome equipped with a steel or glass knife. For the investigation of powders and microscopic particles it is recommended to embed the materials in a non-fluorescent resin. The resin blocks with embedded particles can be cut with a glass or diamond knife of a microtome to generate blockfaces with flat surfaces. Embedding and sectioning yields an additional advantage: the inside of a specimen is revealed and can be imaged as cross-section of the sample.

Measurement time is limited in an industrial environment. A maximized cost-benefit ratio thus often defines the quality of results. Modern CRM allow the generation of low resolution maps (e.g. 10,000 pixels per image) with limited information contents within a few minutes. Higher quality images of 50,000–100,000 pixels per image may require measurement time of an hour or more. Already at a pixel number of 40,000, images of acceptable smoothness and graininess are achieved. If acquisition time is not a limiting factor, the number of pixels per image might be limited by the performance of the computer employed for data processing. Data treatment such as noise removal demands considerable computing power.

Even though the spot size of the laser, and thus the optical resolution, is diffraction limited, the image quality can be improved considerably through oversampling. Oversampling means imaging at increments considerably smaller than the "theoretical" optical resolution. If the step size of a scanner is chosen at a value of 5–10 times smaller than the laser spot size, chemical images at very high resolutions can be achieved [105]. This is illustrated with a CRM image and a corresponding SEM image of a two component inhalation particle in Fig. 16.1. The particles' shape was optimized to yield better flight properties and a very low bulk density. The lateral resolution R_L of confocal Raman microscopy is diffraction limited and approximated by the irradiating wavelength multiplied by 0.61 and divided by the numerical aperture NA of the lens. For very small pinholes, the resolution can be further improved by

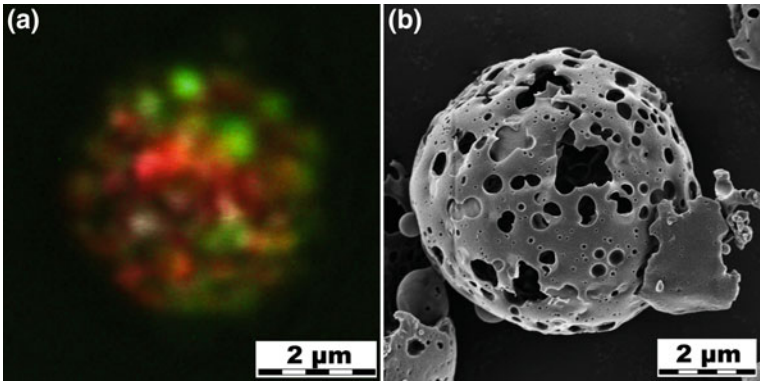

Fig. 16.1 Confocal Raman microscopic image (**a**) and a corresponding yet not colocalized SEM image (**b**) of inhalation particles with optimized flight properties, consisting of two components. Component A is visualized in red whereas component B is represented in green. A submicron resolution is achieved by CRM. SEM further visualizes the nanoscopic morphology. CRM data were obtained using a WITec CRM200 equipped with a 63× lens (NA 0.75) and a Nd:YAG Laser (532 nm at 50 mW) at a pixel number of 62500 and an integration time of 40 ms per pixel

a factor of $1/\sqrt{2}$ [106]. The theoretical lateral resolution of the example in Fig. 16.1 (λ 532 nm, NA 0.75) is thus equal to 284 nm. Oversampling at a step size of 32 nm has resulted in an image where this theoretical spatial resolution has been at least levelled. A nanoscopic non homogeneous distribution of component A (in red) and component B (in green) is visible.

16.2.1.2 Limitations

CRM being a spectroscopic imaging method also entails various limiting aspects innate to spectroscopy or microscopy.

Typical for imaging methods, CRM does not allow bulk analysis of an entire lot. Generally only confined areas are investigated and a finite number of images are acquired. Sampling is thus critical. Areas under investigation need to be representative of the entire sample, which further needs to be representative of the whole lot. The higher the number of images acquired the more significant the results [100].

Also, spatial quantization is difficult. Two dimensional chemical images underestimate the size of spheres and overestimate the size of cubes [87].

Further, the interpretation of microscopic and spectroscopic data and judging of data quality requires substantial expertise and experience on the user side. The representation of microscopic results is often subjective. Reviewers therefore often "blame" (the of course respectable) microscopy to be an "art" rather than science. Quantitative results are difficult to achieve in Raman spectroscopy. Even though Raman intensity is directly proportional to the concentration of the scattering species several effects falsify any attempt to deduce quantitative output. Raman intensity

and thus also LOD are very specific to every kind of substance and may differ greatly. A dissolved plasticizer is much more difficult to detect than any particulate pharmaceutical active. Intensities of Raman bands further depend on the intensity and wavelength of irradiation as well as state of polarization of the irradiating light and of the collection optics [98]. Variation of focus due to topography effects and resulting beam geometry at the sample further affect signal intensity. The Raman spectrum of the sample is also affected by the transmission characteristics of the sample matrix or the sample container [97, 107]. When characterizing solids, varying packing densities (intrinsic for polymorphs!) and particle size strongly affect signal strength [108, 109]. At best semi quantitative output can be generated regarding composition. Only relative assumptions of concentrations are possible. When studying a series of related samples with different relative concentrations, CRM can be used to elucidate trends.

In confocal Raman microscopy, where the irradiating laser spot is often smaller than the particle under investigation, an additional effect can occur. Already in very early publications, C.V. Raman mentioned the polarization of inelastic scattering [110, 111]. The Raman spectrum depends on the orientation of the crystallographic axes with respect to the direction and polarization of both the excitation and the scattered light [112–114]. Intensities of Raman bands may vary dramatically depending on the angle between polarizability tensor of a specific molecular vibration and the exciting source (Fig. 16.2).

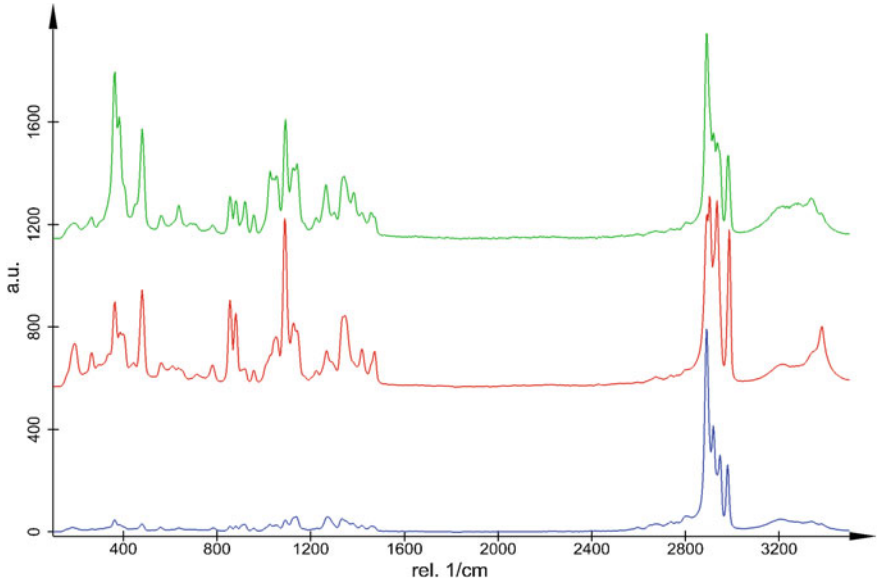

Fig. 16.2 Raman spectra of α-lactose monohydrate with spectral dissimilarities due to different angles between crystallographic axes of underlying single particles and incident light. Throughout the whole spectral range, peak intensities are varying. In addition, certain vibrations are fully annihilated or strongly amplified due to varying spatial orientation of the imaged crystalline particles

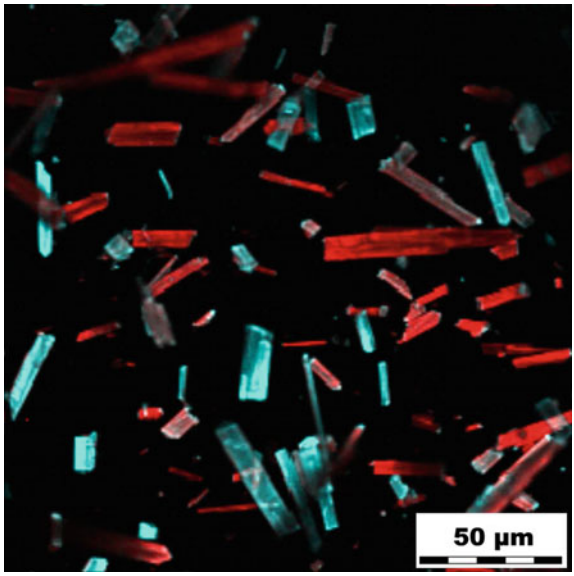

Fig. 16.3 Confocal Raman microscopic image of lath shaped API particles. Particles are all of identical chemical and physical state but can be discriminated according to spatial orientation: Horizontally oriented particles in red, vertically oriented particles in cyan. Data was obtained using a WITec CRM200 equipped with a 40× lens (NA 0.60) and a Nd:YAG Laser (532 nm at 50 mW) at a pixel number of 62500 and an integration time of 20 ms per pixel

In widefield Raman microscopy and FT-Raman spectroscopy this effect is often negligible since the optical resolution of typically several hundreds of micrometers is much larger than the irradiated crystal species and thus averaged spectra are collected. In contrast, confocal Raman microscopy allows a spatial resolution down to the optical limit of diffraction. It is therefore easily feasible to image single particles. Raman spectra obtained with CRM can thus reveal substantial differences in peak intensities due to unequal orientations of single crystals. A discrimination of single particles is possible due to different spatial orientation (Fig. 16.3).

Since a complete extinguishment of certain vibrations is possible, the erroneous conclusion might be drawn that observed spectral differences are due to e.g. polymorphism. Varying band intensities can make it difficult to get qualitative information on polymorphism.

On the other hand, the polarization effects also yield valuable additional information. Reports in the literature show, polarized micro Raman spectroscopy has successfully been employed to study molecular orientation distributions of various materials, including ceramics and inorganics [115, 116], polymer films [117], liquid crystals [118, 119] or biological polymers [81]. Such polarization effects are very pronounced with small synthetic API crystals, containing aromatic structures allowing pi-stacking. Excipients, which are often of polymeric nature (PEG, Cellulose, PVP, etc.) or occur in an amorphous state, exhibit this phenomenon rarely. Data processing of hyperspectral data cubes by classical least squares algorithms using base spectra, which include polarization information can improve the fit quality considerably and can also improve image resolution.

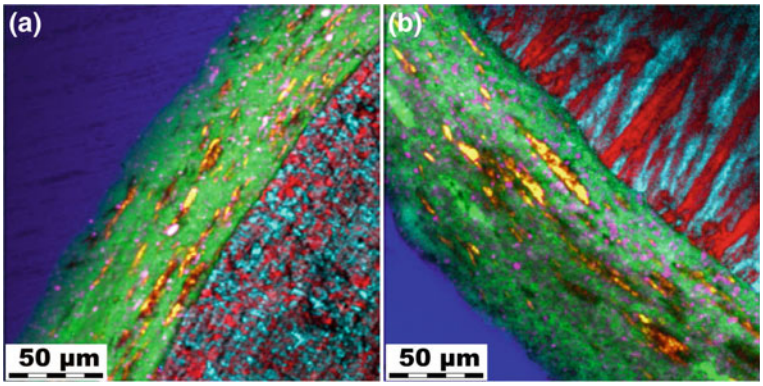

Fig. 16.4 Confocal Raman microscopic images of two types of modified release pellets. The APIs in both pellets were resolved according to spatial orientation of the single crystals (visualized in red and cyan). In image (**a**), the internal structure of the API layer indicates a concentric layered growth of the phase during spray drying. On the other hand, the API in image (**b**) has (re-)crystallized in a perpendicular star-like manner, even though spray dried and thus applied layer by layer. Pellets were embedded in a resin (visualized in blue) and cut equatorially using a microtome. The film coat consists of organic (green) and inorganic components (purple and orange). The internal structure of the coating indicates a concentric onion-like growth. Data was obtained using a WITec CRM200 equipped with a 20× lens (NA 0.40) and a Nd:YAG Laser (532 nm at 50 mW) at a pixel number of 62500 and an integration time of 20 ms per pixel

In a recent study in our laboratories, single pellets for modified release were tested regarding internal structure, long term stability and drug release. Modified release pellets consist of an inert carbohydrate-based core on which an API layer is applied through a spray drying process. Finally, the pellets are coated with a film for sustained release [60, 120]. One interesting aspect was found when inspecting two types of modified release pellets by CRM (Fig. 16.4). Both types were processed and prepared exactly the same way, but two different API were applied. The APIs in both pellets were resolved according to spatial orientation of the single crystals (visualized in red and cyan). The outer coating consists of organic (green) and inorganic components (purple, orange) whereas the resin used for embedding is visualized in blue.

In Fig. 16.4a, the internal structure of the API layer indicates a concentric layered growth of the phase after spray drying, as can be expected. Interestingly, even though spray dried and thus applied layer by layer, the API crystals in the second type of pellets have arranged in a perpendicular, star-like manner. The second API thus appears to have dried and crystallized much slower, allowing rearranging its secondary structure. Possibly, the first solidification of the API has resulted in an amorphous phase, which subsequently has transformed over time in a more stable, crystalline form. This information was only achievable due to the ability to discriminate crystalline species according to their spatial orientation.

16.2.2 Investigation of Solid Dosage Forms by Chemical Imaging

16.2.2.1 Product Homogeneity

Long acting release (LAR) depots generally consist of an API dispersed within a biodegradable matrix. The drug is slowly released as the matrix degrades, primarily through hydrolysis. LAR depot injections maintain all of the clinical and pharmacological characteristics of the immediate-release dosage form, with the added feature of slow release from the site of injection, reducing the need for frequent administration. With its specific pharmacokinetic profile, LAR depots can be administered e.g. once a month instead of three times a day, strongly enhancing patient compliance [121]. Long acting release depot injections have demonstrated their clinical and economic value on the market [122, 123].

Although these systems have achieved a high level of success, some unmet technical challenges remain, amongst others the ease of reconstitution and injection of the depot injections. Surface properties and internal structure can be tailored through preparation methods as well as composition of biodegradable matrix. Analytical methods, however, are required to attest the required structure. A non homogeneous drug distribution can lead to a retarded or accelerated release (e.g. a burst). Many studies have investigated the detailed structure of LAR depots and the relationship to drug release. To achieve this goal, techniques providing spatially resolved information such as scanning electron microscopy or confocal microscopy were used [124]. However, most of the studies were performed with model compounds, such as fluorescent dyes, or were focusing on drug release and burst [125].

CRM and EDX allow the investigation of real samples, e.g. for clinical testing, and are not restricted to model compounds. They allow detailed information of the spatial drug distribution within the depots by making use of the chemical contrast of API and matrix. Both methods are excellent tools which help in optimizing processes to produce ideal LAR depots. Figure 16.5a shows an SEM image of typical LAR depots. Even though surface roughness can be estimated, no information is available on the inner structure. Embedding in a resin followed by trimming with a microtome discloses this information. Several kinds of depots, prepared by different processes, were investigated by EDX and CRM. In Fig. 16.5b, c, two SEM images of blockfaces are overlaid by EDX mappings of the API. The API in this example contains a unique element and can thus be discriminated from the matrix and embedding resin.

CRM further allows the location of biodegradable matrix (green) and the resin used for embedding (blue, Fig. 16.5d, e). The resolution is more than sufficient to clearly visualize the basically homogeneous distribution of the API (colour-coded red), even though primary API particles are smaller than five microns. By interpreting data from both methods, SEM and CRM, additionally a core-shell structure can be assigned to one sort of the depots (Fig. 16.5c, e). They possess a much thicker shell of pure matrix material than the other depots (Fig. 16.5b, d). This information on the

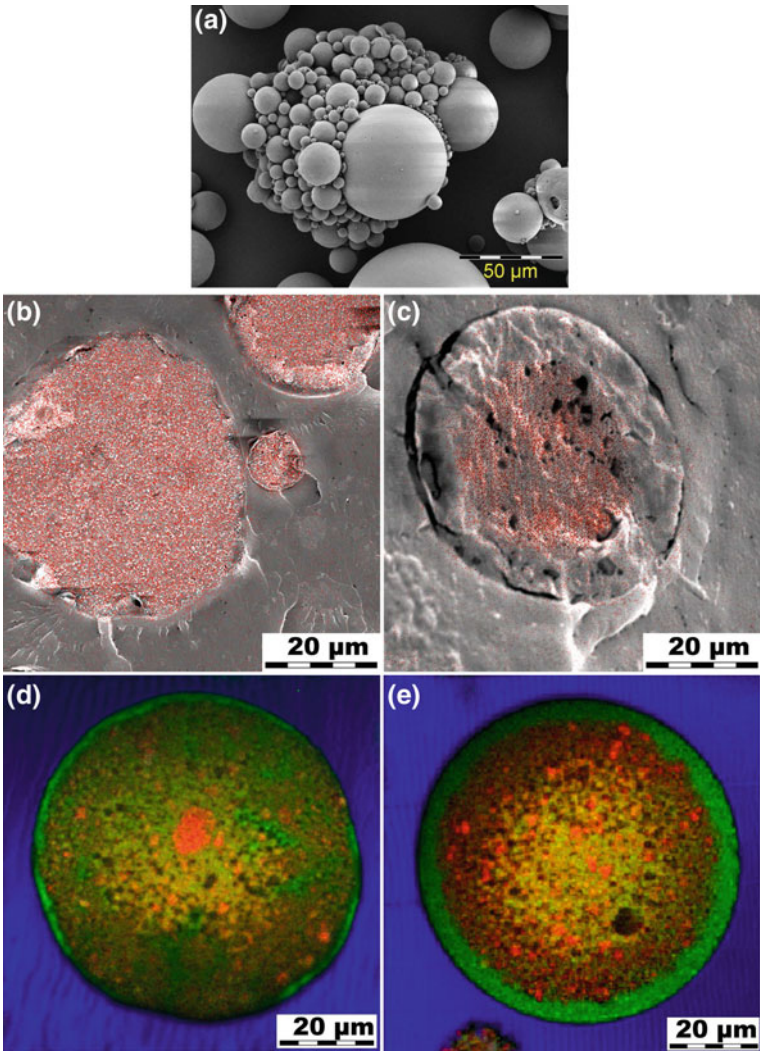

Fig. 16.5 **a** SEM micrograph of typical LAR depots; **b**, **c** SEM images of block faces overlaid by EDX map; **d**, **e** CRM mappings of similar blockfaces of corresponding depots. The API (in red) is homogeneously distributed within the biodegradable matrix (green) but the depots in (**c**, **e**) possess a much thicker shell of pure matrix material than the depots in (**b**, **d**). Depots were embedded in a resin (visualized in blue) and cut equatorially using a microtome. CRM data was obtained using a WITec CRM200 equipped with a 40× lens (NA 0.40) and a Nd:YAG Laser (532 nm at 20 mW) at a pixel number of 62500 (Fig. 16.5d) resp. 40000 (Fig. 16.5e) and an integration time of 100 ms per pixel

internal structure was very important to improve process to obtain LAR depots of optimized release as well as syringeability.

Solid oral dosage forms often feature a coating on top of the tablet core. On one hand this might be motivated by marketing purposes where colour coatings are applied to foster branding and make tablets visually more attractive. On the other hand, coatings may also improve compliance by making a tablet smoother and easier to swallow or to mask an unpleasant taste. Coatings often also have a pharmacological function. Functional coatings are e.g. used to modify the release or to improve the stability of a formulation [126–128]. The solubility of a functional coating can be tailored by variation of the mixture, e.g. hydrophobic agents, hydrophilic agents and plasticizers [129–131].

On an industrial scale, the smallest alteration of a process may have dramatic effects on the output. A change of the quality of an ingredient, exchange of equipment or modification of reaction parameters can affect the product. In many cases the cause of altered product quality cannot be elucidated by simple means. An extensive root-cause analysis might be required to identify the reasons. Chemical imaging can be a powerful tool to fulfil such tasks. Dissolution testing of a tablet lot has revealed a modified release, compared to regular tablet lots. After inspection with various methods, CRM could resolve the cause. The tablet coating, which controls the release, exhibited inhomogeneities (Fig. 16.6).

On a microscopic level, a layering of the three coating components, separated from each other, could be visualized. The root-cause was a coagulation of the coating solution during the spray drying process. Elucidation of the root-cause with any other method than chemical imaging would have been very difficult.

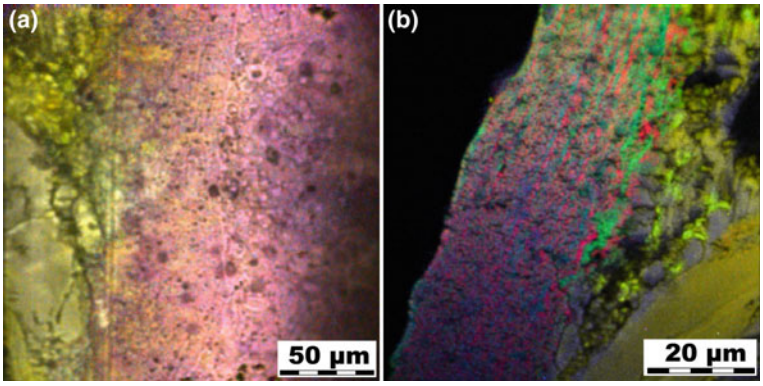

Fig. 16.6 CRM images of tablet coatings. The tablets were cut using a scalpel. The coating consists of a hydrophobic coating agent (red), a hydrophilic coating agent (green) and a plasticizer (blue). Tablet core ingredients are not discriminated but entire core is visualized in yellow. The regular tablet coating in (**a**) appears homogeneous with occasional air bubbles. The coating of the tablet lot showing anomalous dissolution behaviour in (**b**) exhibits a layered, phase separated structure. Data was obtained using a WITec CRM200 equipped with 20× (**a**) and 63× (**b**) lenses (NA 0.40 respectively 0.75) and a Nd:YAG Laser (532 nm at 50 mW) at a pixel number of 62500 and an integration time of 50 ms per pixel

16.2.2.2 Content Uniformity

One alternative to oral dosage forms is administration through the respiratory tract via inhalation. Inhalation provides an excellent delivery route for the treatment of both pulmonary and non-pulmonary conditions. Delivering medications via inhalation generally requires smaller doses, offers a rapid onset of drug action, and reduces adverse effects compared with other routes of administration [132]. Nebulizers, metered dose inhalers (MDI), and dry powder inhalers (DPI) have been competing on the market for many years. DPIs in general are easier to use and cause fewer irritant effects than the pressurized MDIs, in which a drug/propellant mixture is stored in solution in a pressurized canister. DPIs involve micronised powder, often packaged in single dose quantities in packs. Dry powder inhalers have therefore a considerably longer shelf life compared to MDIs containing drug solutions [133].

When the lung is the target for the aerosol (either because the intent is to treat the lung surface or to get the drug into the blood through the capillaries via the alveoli), the inhaled aerosol must consist of particles in a certain size range. The size range, where drug particles can efficiently be adsorbed, ranges from 0.1 to 5 μm. Larger particles tend to simply land in the mouth and throat and do not make it into the lung. Smaller particles tend to get inhaled and may immediately be exhaled.

In many DPIs, much larger carrier particles are used as bulking agent and to aid in powder uptake from the device during inhalation. These carriers are often sugar particles, typically 50–100 μm in diameter. The much smaller drug particles attach to these excipient particles. The increased aerodynamic forces on the carrier/drug agglomerates improve entrainment of the small drug particles upon inhalation. In addition easier filling of small individual powder doses is allowed. Upon inhalation, the powder is broken up into its constituent particles with the aid of turbulence or mechanical devices such as screens or spinning surfaces on which particle agglomerates impact, releasing the small, individual drug powder particles into the air to be inhaled into the lung. The sugar particles are intended to be left behind in the device and in the mouth/throat region.

Sometimes an additional lubricant is included in the DPI formulation. The lubricant is meant to form a film on the other particles' surfaces and is supposed to avoid agglomeration and to ease the release of the API particles from the carriers [134, 135].

One of the main challenges in commercial research and development is the production of such micronised API particles on a large scale. Crystallization of such small API particles is rarely feasible, thus comminution, e.g. by milling is required. Milling may lead to solid state transformations or amorphization of the drug particles. As mentioned before, the solid state of an API is crucial for its bioavailability [136].

Even though the composition of a DPI formulation is rather simple, a homogeneous distribution of the active and the carrier particles is required. Demixing or agglomeration is strongly unfavourable. Micronised API particles should be statistically distributed and sticking to larger carrier particles.

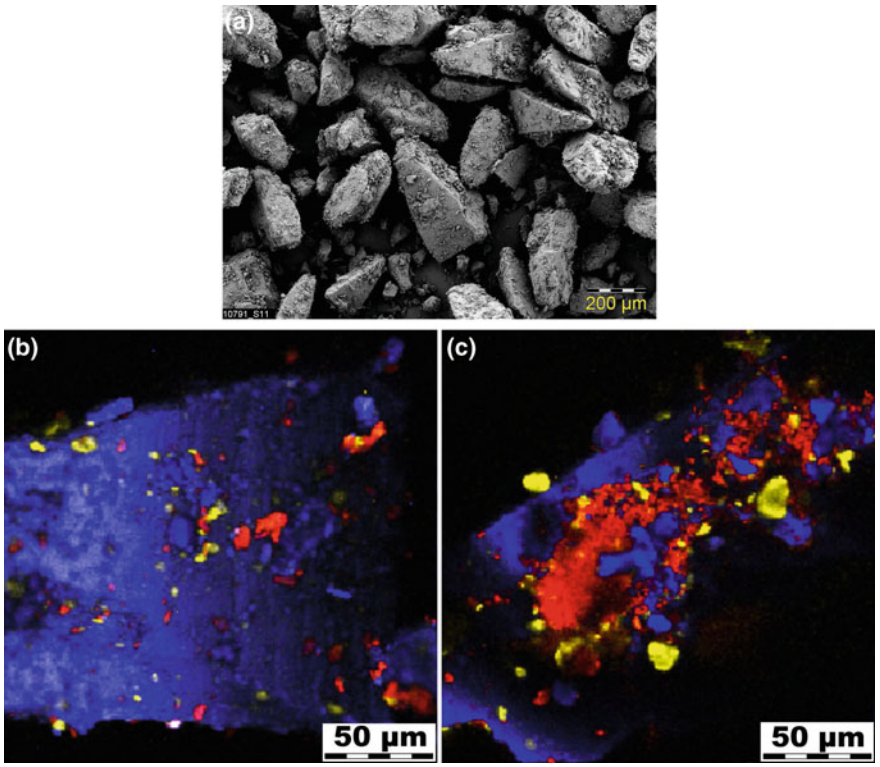

Fig. 16.7 **a** SEM image of a dry powder inhaler formulation consisting of large carrier particles on which micronised API powder is absorbed. **b** and **c** CRM images of similar DPI mixture. API particles are visualized in red, lubricant in yellow and the carrier particles in blue. CRM image (**b**) was obtained using a WITec CRM200 equipped with a 20× lens (NA 0.40) and a Nd:YAG Laser (532 nm at 50 mW) at a pixel number of 40000 and an integration time of 200 ms per pixel. 7c was obtained using a WITec CRM200 equipped with a 63× lens (NA 0.75) and a HeNe-Laser (633 nm at 35 mW) at a pixel number of 40000 and an integration time of 150 ms per pixel

Chemical imaging is well suited to characterize formulation for dry powder inhalers. SEM can quickly resolve morphology, particle size distribution and detect possible agglomerates. CRM in addition is capable of probing solid state and content uniformity, which is illustrated in Fig. 16.7.

SEM was applied to confirm a uniform content and particle size distribution. CRM was further applied to probe several different approaches to prepare DPI mixtures. The powder formulation in (b) appears to consist of homogeneously distributed API (visualized in red) and lubricant particles (in yellow) on carriers (in blue). Micronised particles are not agglomerated. Even the lubricant film on the carrier is detectable. In contrast, the formulation in (c) cannot be denoted optimal. In this formulation, the API tends to be strongly agglomerated. A homogeneous statistical distribution is not the case, such a formulation cannot yield an efficient delivery of the drug. No

unwanted polymorphic forms or other solid state variation could be confirmed in any of the formulations.

Tablets are the most popular dosage form in use today. About two-thirds of all prescriptions are dispensed as solid dosage forms, and half of these are compressed tablets, as they are easy and convenient to apply. A tablet can be formulated to deliver an accurate dosage to a specific site; it is usually taken orally, but can be administered sublingually, rectally or intravaginally.

Some APIs may be tableted as pure substances, although this is rarely the case; most formulations include excipients. These are inert ingredients, which either enhance the therapeutic effect or are necessary to construct the tablet. The filler is a bulking agent, providing a quantity of material which can accurately be formed into a tablet. Binders hold the ingredients together so that they can form a tablet. Lubricants are added to reduce the friction between the tablet and the punches so that the tablet compression and ejection processes are smooth. Disintegrants are used to promote wetting and swelling of the tablet so that it breaks up in the gastrointestinal tract. Additional ingredients may also be added such as colouring agents, flavouring agents, and coating agents.

Crucial in the manufacturing process of tablets is content uniformity. To ensure that the appropriate amount of active ingredient is equal in each tablet, it is a prerequisite that the ingredients are well-mixed. Powders that can be mixed well do not require granulation and can be directly compressed into tablets. If a sufficiently homogenous mix of the components cannot be obtained by simple mixing, the ingredients must be granulated prior to compression to assure an even distribution of the active compound in the final tablet. Two basic techniques are used to prepare powders for granulation into a tablet: wet granulation and dry granulation.

In a wet granulation process, a liquid binder or adhesive is added to the powder mixture. The amount of binder needs to be adjusted properly, over wetting will cause the granules to be too hard whereas under wetting will cause them to be too soft and friable. Once the solvent evaporates the wet mass has formed densely held agglomerates. Finally, the agglomerates are milled, which results in formation of granules.

Dry granulation is employed when the product to be granulated may be sensitive to moisture and heat. The dry mixture is compacted and densified in a press followed by milling. It requires drugs or excipients with cohesive properties. Dry granulation often produces a higher percentage of non-compacted products, which can compromise the quality or create yield problems for the tablet [137–139].

Compressed tablets are exerted to great pressures in order to compact the material. These mechanical stresses can affect the solid state of ingredients. Polymorphic forms of the drug substance can undergo phase conversion when exposed to manufacturing processes, such as compaction, drying and milling. Exposure to environmental conditions such as humidity and temperature can also induce polymorph conversion. Tabletting can also yield amorphization, e.g. at the tablet surface. Any alteration in solid state of course also affects the dissolution behavior and thus the bioavailability of the drug.

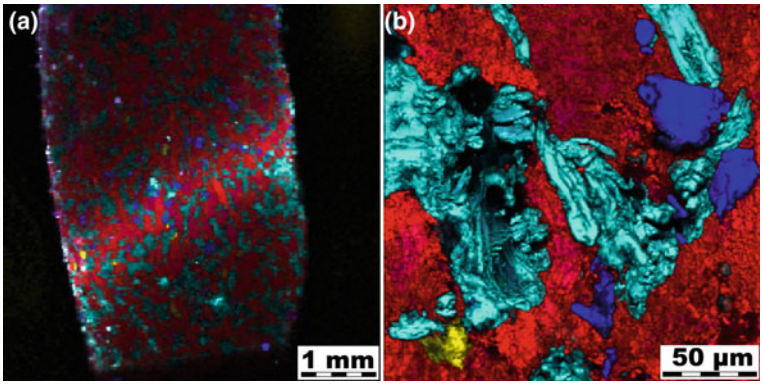

Fig. 16.8 **a** CRM large area imaging of a tablet section. The tablet contains an API (in red), a filler (in cyan), a disintegrant (in blue) and a lubricant (in yellow). A homogeneous distribution and PSD of the components can be confirmed. The sample was partly tilted during acquisition resulting in partly defocused areas. **b** CRM high resolution imaging of a section of the same tablet lot as in (**a**). Data in (**a**) was obtained using a WITec alpha700 equipped with a 40× lens (NA 0.6) and a Nd:YAG Laser (532 nm at 50 mW) at a pixel number of 22500 and an integration time of 30 ms per pixel. Data in (**b**) was obtained using a WITec CRM200 equipped with a 63× lens (NA 0.75) and a Nd:YAG Laser (532 nm at 50 mW) at a pixel number of 122500 and an integration time of 20 ms per pixel

Chemical imaging is suitable to probe both, content uniformity as well as analysis of chemical and physical state. Figure 16.8 shows chemical images of a sectioned tablet. The tablet contains an API (visualized in red), a filler (in cyan), a disintegrant (in blue) and a lubricant (in yellow).

All four tablet components can be identified and discriminated. Large area mapping provides information on content uniformity whereas high resolution images provide details on the fine structure within the tablet. The solid state of the API can be analyzed and confirmed by either method, large area scan or high resolution image. The FOV is too limited to conclude upon content uniformity but the high resolution structure can be elucidated. The tablet was trimmed using a microtome to obtain a flat surface.

Tablets can also be inspected using SEM and EDX. Even though most pharmaceutical ingredients contain C, H and O, it is feasible that components can be identified and discriminated according to exceptional elements. In Fig. 16.9, an SEM image (a) and the corresponding EDX map (b) are presented of the surface of another tablet. Four unique elements are contained within the tablet. The element visualized in red is only present in the API; the element visualized in green belongs to the filler; the element visualized in yellow to the glidant, whereas the element in blue is present in filler as well as in glidant. SEM allows inspecting smallest particles and their morphology. EDX can be used to identify particles and domains according to their elemental fingerprint.

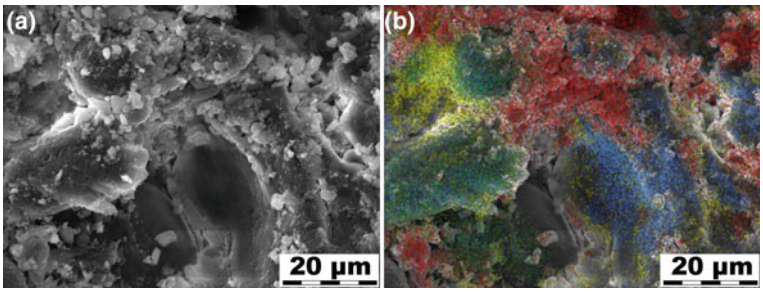

Fig. 16.9 SEM image (**a**) and corresponding EDX mapping (**b**) of a tablet surface. Four unique elements are present within the tablet. The element visualized in red is only present in the API; the element visualized in green belongs to the filler; the element visualized in yellow to the glidant, whereas the element in blue is present in filler as well as in glidant. Identification of particles of interest according to the elemental composition at high spatial resolutions is feasible

16.2.2.3 Solid State Analysis

In the last section we have elucidated the possibility that an API can undergo a solid state conversion during processing, e.g. granulation or tabletting. Mechanical stress, increased humidity or temperature can affect the integrity of dosage forms. CRM is an excellent tool to investigate such solid state transformations. In Fig. 16.10 an image of a tablet surface containing API and four excipients is presented. It was found that the API is present not only in crystalline state, but also amorphous. The crystalline form was detected only as discrete particles on the surface. The remainder of the API presented at the surface had transformed into an amorphous phase during tabletting.

Crystalline API is visualized in red, amorphous API in green, binder in cyan, disintegrant in blue, lubricant in yellow and glidant in purple.

Not only final products can be investigated, also before and after processing steps CRM can be employed to control quality of a product. In Fig. 16.11 an image of a granular after wet granulation is presented. Even though only one specific polymorphic form was deployed in the initial powder blend, a mixture of two polymorphic forms was detected after wet granulation. The initial polymorph (visualized in red) must have partially converted into another polymorphic form (in cyan) due to processing. The filler is visualized in green and the disintegrant in blue.

The stability and shelf life of dosage forms are routinely tested at defined temperatures and humidity for extended periods of time. Chemical incompatibilities of API and ingredients might lead to reactions or degradations. CRM is commonly employed to investigate effects of stressing and ageing. Initial samples are compared with samples from specific intervals. Figure 16.12 depicts a rare case where a solid state reaction has taken place. Only from inspection by stereomicroscopy it was obvious that some transformation must have occurred. The originally smooth surface had transformed and become rough and brittle. Investigation of tablets before and after stressing has resulted in a very interesting conclusion. Initially the API was present

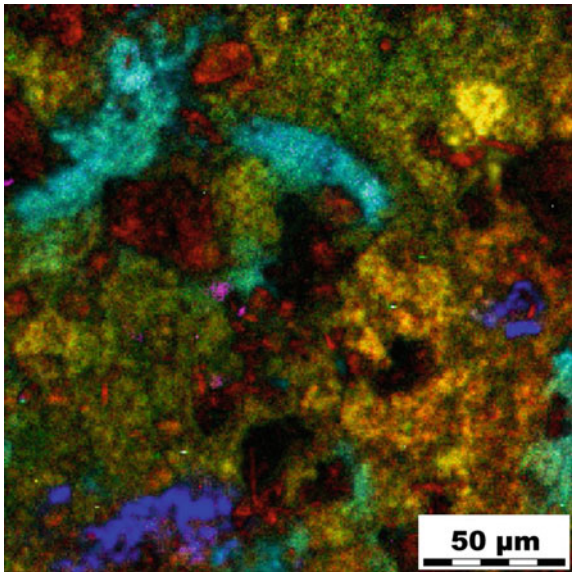

Fig. 16.10 CRM image of a tablet surface. The API was found to be present in crystalline (red) but also in amorphous state (in green). The excipients included are as follows: Binder in cyan, disintegrant in blue, lubricant in yellow and glidant in purple. Data was obtained using a WITec CRM200 equipped with a lens (NA 0.40) and a Nd:YAG Laser (532 nm at 33 mW) at a pixel number of 90000 and an integration time of 100 ms per pixel

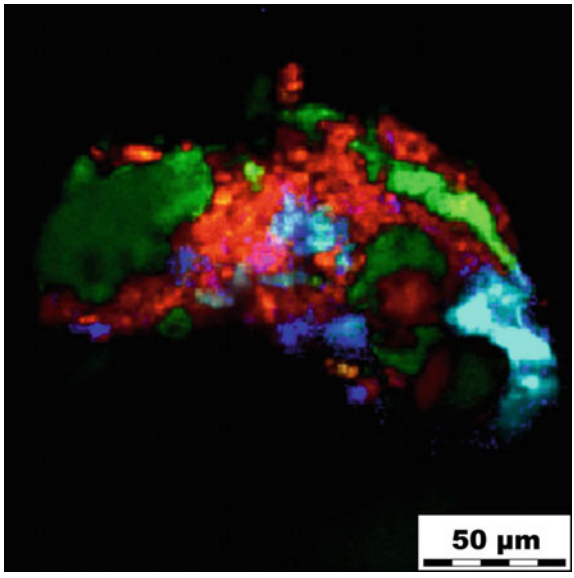

Fig. 16.11 CRM image of a granule after wet granulation. Two polymorphic forms of the API are found. The initial polymorph (in red) has partly transformed into a second polymorphic form (in cyan) during wet granulation. Filler is visualized in green and the disintegrant in blue. Data was obtained using a WITec CRM200 equipped with a 20× lens (NA 0.40) and a Nd:YAG Laser (532 nm at 33 mW) at a pixel number of 40000 and an integration time of 20 ms per pixel

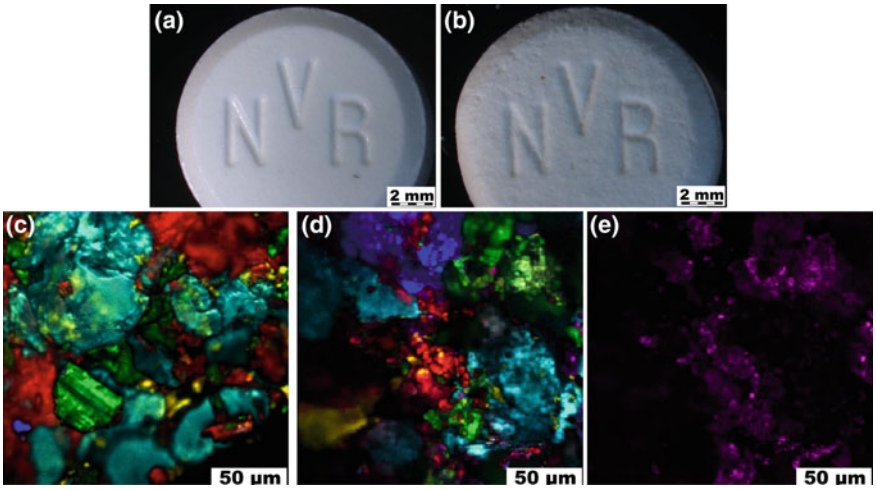

Fig. 16.12 Stereomicroscopic image of a tablet illustrating the initial appearance. Image **b** visualizes the alterations that occurred during stressing at increased temperatures and humidity for a certain point in time. The surface of the tablet has become much rougher and the texture more brittle. **c** CRM image of an initial smooth tablet surface. The API is present as a Calcium salt. The acidulant is visualized in green, the filler in blue, the binder in cyan and the lubricant in yellow. Image **d** represents a CRM image of the rough surface of a stressed tablet. Acidulant, filler, binder and lubricant are still present but the API is now found as free base; no more API-Ca salt is present. In addition a further component was detected which could be identified as the Calcium salt of the acidulant, visualized in purple in (**e**). CRM data was obtained using a WITec CRM200 equipped with a 20× lens (NA 0.40) and a Nd:YAG Laser (532 nm at 50 mW) at a pixel number of **c** 62500 and **d**, **e** 40000 and an integration time of 50 ms per pixel

solely as a Ca salt (visualized in red) together with four excipients: acidulant (in green), filler (in blue), binder (in cyan) and lubricant (in yellow). After stressing the situation had changed: the API was found in the aged tablets only as free base. No more Ca salt was detectable. Astonishingly, an additional component was found in the tablet, which was identified with reference spectra: a Calcium salt of the acidulant (visualized in purple).

This finding has led to the conclusion, that the API must have reacted with the acidulant and a cation transfer must have occurred. The initial Ca salt form of the API was hydrated. During the solid state reaction with the acidulant the crystal water was released and the free water had soaked the tablet, leading to an increased surface roughness. The reaction is denoted as follows:

$$[API][Ca]^{*} \times H_2O + [Acidulant][H]_2 \rightarrow [API][H]_2 + [Acidulant][Ca] + \times H_2O \tag{16.1}$$

Confocal Raman microscopy is extremely powerful in discriminating solid states. Even when substances are chemically identical or very closely related, the Raman

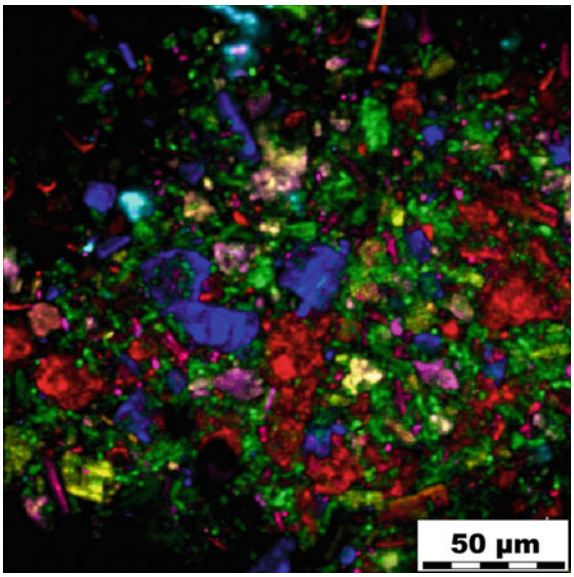

Fig. 16.13 CRM image of a physical mixture of six closely related APIs: a co-complex of two APIs (API1 & API2) in red, a salt form of API1 in blue, the free acid form of API1 in green, a salt form of API2 in purple, the free acid form of API2 in yellow and finally an ester form of API2 in cyan. Even though very close chemical relationships the six compounds can be discriminated by CRM. See main text body. Data was obtained using a WITec CRM200 equipped with a 20× lens (NA 0.40) and a Nd:YAG Laser (532 nm at 50 mW) at a pixel number of 16000 and an integration time of 50 ms per point

spectrum normally shows sufficient spectral dissimilarities due to different solid state to discern them unequivocally. Figure 16.13 represents a CRM image of a physical mixture of six closely related APIs.

This physical mixture was prepared as proof that CRM is suitable to discriminate a co-complex of two APIs (API1 & API2) and the pure non-complexed forms of API1 and API2. Too further complicate things, other solid state forms of API1 and API2 were added. Even though very closely chemically related, the six compounds were easily discriminated by CRM. Co-complex and single API particles showed sufficiently different spectral features to distinguish them.

16.2.2.4 Foreign Particulates

In general, pharmaceutical products are required to be essentially free of visible foreign particles, limits on the number of subvisible particles are allowed. The FDA requires that contamination problems are fully investigated in a timely fashion. Identification of small particle contamination is thus of key importance in the development of pharmaceutical products and formulations for regulatory compliance [140].

There are two general types of contaminants, product-related and foreign material. Ingredients may coagulate or precipitate, thus forming solid particles, or degradation of any component might be the origin of any product-related contaminant. Particles of external origin may be derived from the product container or packaging material. These types of particles include glass, rubber, aluminium, plastics and paper. Contamination can also result from the manufacture of the product; examples of these include charred product, detergents and lubricant oils. Metal and metal corro-

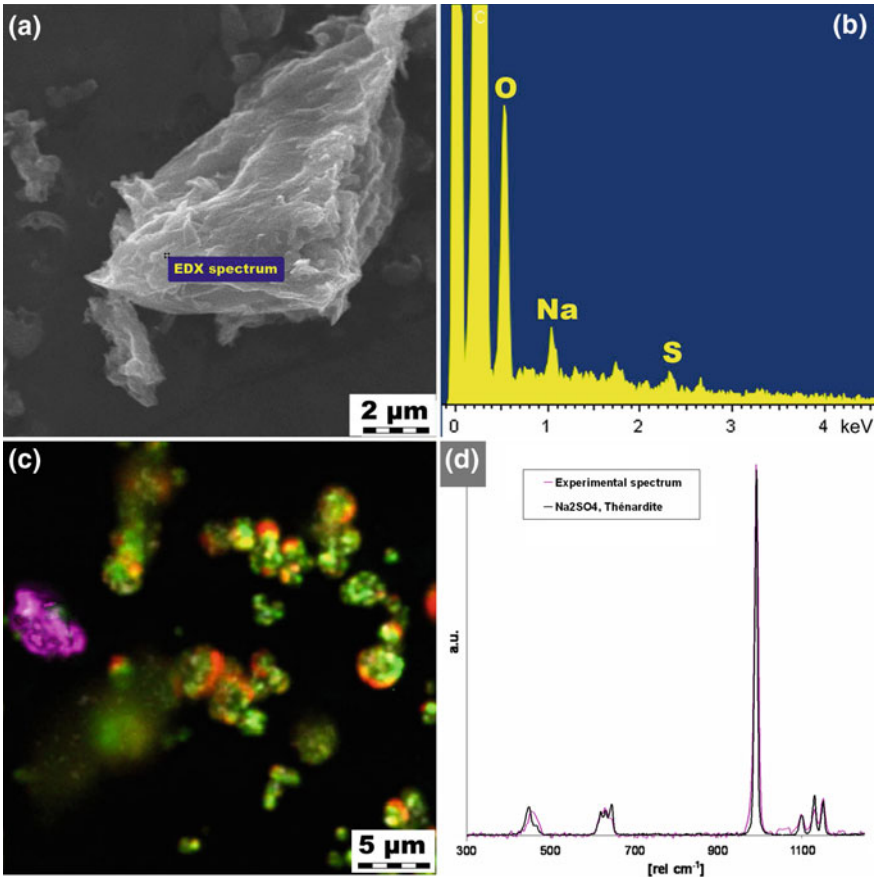

Fig. 16.14 A contaminant, foreign in particle size and shape, was found in a powder mixture as can be seen in the SEM image in (**a**). An EDX spectrum was acquired on one of these particles. Elemental analysis has disclosed the presence of Sodium, Oxygen and Sulphur within the contaminant as presented in (**b**). Further analysis by CRM has similarly resolved such particulates, visualized in pink in (**c**). Comparison of the obtained Raman spectra with reference spectra has led to the solution Sodium sulphate, presented (**d**). CRM data was obtained using a WITec CRM200 equipped with a 63× lens (NA 0.75) and a Nd:YAG Laser (532 nm at 50 mW) at a pixel number of 62500 and an integration time of 50 ms per pixel

sion, Teflon, graphite and rubber particles are indications of tank, filter or equipment failure. Environmental contaminants such as fibers and skin cells are also detected. The most common contaminants in pharmaceuticals are cellulose (cotton and paper) fibres, synthetic fibres, silicone, plastics, rubber, metal particles and corrosion products, glass particles and char particles [141].

Microscopical analysis is particularly well suited to the analysis of particulate contamination because the particles are usually too small to be analyzed using conventional methods. Size, shape and surfaces of a foreign body can be described with simple light microscopy. Often more powerful methods are required, allowing obtaining information on the identity of the material. Chemical imaging is highly suitable to resolve such tasks. EDX is especially valuable in the analysis and comparison of glass and metallic fragments. Vibrational microspectroscopy is similarly powerful for identification of small particles, especially those of an organic nature [142–144].

The potential of chemical imaging is illustrated in Fig. 16.14. Foreign particulates were found within a solid powder mixture. The contaminants were different from the rest of the powder particles in particle size and shape. EDX elemental analysis of one of these particles has disclosed the presence of Sodium, Oxygen and Sulphur within the contaminant. Further analysis of the contaminants by CRM and comparison of the obtained Raman spectra with reference spectra from a database has resolved the identity. The foreign particulates were made from non critical anhydrous Sodium sulphate, a by-product of a preparation process.

16.3 Conclusions

Health authorities are encouraging the pharmaceutical industry to adopt the use of a Quality by Design (QbD) approach, where quality is designed into the product rather than quality is tested in the product. The concept of QbD, which can be applied during development, manufacturing and life cycle management, is based on the idea that processes are understood thoroughly.

One approach towards successful QbD is the implementation of chemical imaging methods within the development cycle. CI, in particular confocal Raman microscopy, provides valuable information on pharmaceutical samples. Various aspects of a product can be characterized by chemical imaging, such as visual appearance (morphology, particle size, particle size distribution, and surface roughness), content uniformity (composition, distribution, and homogeneity), chemical identity (structure, stability) and physical state (solid state, polymorphism, crystallinity, phase transformations). Especially the combination of several CI methods is highly valuable. Due to their complementary nature with different spatial resolution and different types of chemical information provided, intrinsic advantages of every method accumulate, limitations are decreased. Chemical imaging can be applied for product development, product design, process validation, process quality control, life cycle management but also counterfeit and generics analysis. Solid as well as liq-

uid and semi-liquid dosage forms can be probed; single components, e.g. pure drug substance, as well as complex formulations can be investigated from a nanoscopic resolution up to the macroscopic regime.

Several successful applications of confocal Raman microscopy and energy dispersive X-Ray analysis implemented for the characterization of pharmaceutical solid dosage forms were presented in this chapter. Content uniformity, solid state analysis or contaminant analysis are easy tasks for CI, especially if methods are applied in combination. The complementarity of CRM together with EDX is apparent.

16.4 Materials and Methods

Confocal Raman Microscopy was performed using a WITec CRM200 (WITec GmbH, Ulm, Germany) equipped with a Nd:YAG Laser (532 nm at 50 mW) and a HeNe Laser (633 nm at 35 mW). Three LD Plan-Neofluar®lenses were employed, namely 20× (NA 0.40), 40× (NA 0.60) and 63× (NA 0.75, Carl Zeiss MicroImaging GmbH, Jena, Germany).

Alternatively, a WITec Alpha700 (WITec GmbH, Ulm, Germany) equipped with a 40× Plan ELWD lens (NA 0.6, Nikon GmbH, Düsseldorf, Germany) and a Nd:YAG Laser (532 nm at 50 mW) was employed.

SEM investigations were performed using a FESEM Supra 40 microscope from Zeiss (Carl Zeiss NTS GmbH, Oberkochen, Germany).

EDX data was obtained using a INCA 300 detector (Oxford Instruments, Abingdon, UK) attached to a JEOL JSM 6040 LV (JEOL Inc., Peabody, USA). The Si(Li) detector consisted of a 30 mm^2 detecting crystal and was mounted at a take off angle of 35° and at 10 mm working distance. Mappings were registered at a spatial resolution of 256 × 256 spectra and a spectral range of 0–20 keV at frame rates of 26.7 s.

Stereomicroscopy was executed using a SteREO Discovery.V12 with PlanApo S 0.63× objective (both Carl Zeiss MicroImaging GmbH, Göttingen, Germany).

Blockfaces and tablet sections were prepared using glass knifes and/or a histo diamond knife (Diatome AG, Biel, Switzerland) attached to a Leica EM UC6 ultramicrotome (Leica Microsystems GmbH, Wetzlar, Germany).

Acknowledgements We would like to thank Dirk Märtin for his assistance with scanning electron microscopy and energy dispersive X-ray spectroscopy.

References

1. E. Pivonka, J. Chambers, P. Griffiths, *Applications of Vibrational Spectroscopy in Pharmaceutical Research and Development* (Wiley, Chichester, 2007)
2. S. Sasic, *Pharmaceutical Applications of Raman Spectroscopy* (Wiley, Chichester, 2008)

3. R. Hilfiker, F. Blatter, M. von Raumer, *Relevance of Solid-state Properties for Pharmaceutical Products in Polymorphism in the Pharmaceutical Industry* (Wiley, 2006), pp. 1–19
4. W. McCrone, Phys. Chem. Org. Solid State **2**, 725 (1965)
5. D. Giron, Am. Pharm. Rev. **11**, 66 (2008)
6. D. Giron, M. Mutz, S. Garnier, J. Therm. Anal. Cal. **77**, 709 (2004)
7. G. Chawla, A. Bansal, Curr. Res. Inf. Pharm. Sci. **5**, 9 (2004)
8. http://www.ich.org/LOB/media/MEDIA1707.pdf
9. http://www.fda.gov/cder/guidance/6419fnl.pdf
10. C. Gendrin, Y. Roggo, C. Collet, J. Pharm. Biomed. Anal **48**, 533 (2008)
11. J. Zeitler, D. Newnham, P. Taday, T. Threlfall, R. Lancaster, R. Berg, C. Strachan, M. Pepper, K. Gordon, T. Rades, J. Pharm. Sci. **95**, 2486 (2006)
12. P. Taday, Phil. Trans. R. Soc. Lond. A **362**, 351 (2004)
13. J. Spencer, Z. Gao, T. Moore, L. Buhse, P. Taday, D. Newnham, Y. Shen, A. Portieri, A. Husain, J. Pharm. Sci. **97**, 1543 (2008)
14. Y. Shen, P. Taday, D. Newnham, M. Pepper, Semicond. Sci. Technol. **20**, S254 (2005)
15. T. Kojima, S. Onoue, N. Murase, F. Katoh, T. Mano, Y. Matsuda, Pharm. Res. **23**, 806 (2006)
16. C. Anderton, Pharm. Rev. **7**, 42 (2004)
17. S. Moss, R. Bovermann, G. Denay, J. France, C. Guenat, L. Oberer, M. Ponelle, H. Schröder, Chimia **61**, 346 (2007)
18. S. Bell, J. Beattie, J. McGarvey, K. Peters, N. Sirimuthu, S. Speers, J. Raman Spectrosc. **35**, 409 (2004)
19. K. Chan, O. Fleming, S. Kazarian, D. Vassou, G. Chryssikos, V. Gionis, J. Raman Spectrosc. **35**, 353 (2004)
20. L. Taylor, F. Langkilde, J. Pharm. Sci. **89**, 1342 (2000)
21. M. Auer, U. Griesser, J. Sawatzki, J. Mol. Struct. **661–662**, 307 (2003)
22. V. Tumuluri, M. Kemper, I. Lewis, S. Prodduturi, S. Majumdar, B. Avery, M. Repka, Int. J. Pharm. **357**, 77 (2008)
23. G. Walker, S. Bell, M. Vann, D. Jones, G. Andrews, Chem. Eng. Sci. **62**, 3832 (2007)
24. M. de Veji, P. Vandenabeele, K. Alter Hall, F. Fernandez, M. Green, N. White, A. Dondorp, P. Newton, L. Moens, J. Raman Spectrosc. **38**, 181 (2007)
25. K. Sugano, T. Kato, K. Suzuki, K. Keiko, T. Sujaku, T. Mano, J. Pharm. Sci. **95**, 2115 (2006)
26. E. Brewer, A. Ramsland, J. Pharm. Sci. **84**, 499 (1995)
27. J. Heath, *Dictionary of Microscopy* (Wiley, Chichester, 2005)
28. D. Murphy, *Fundamentals of Light Microscopy and Electronic Imaging* (Wiley, Chichester, 2001)
29. I. Vitez, A. Newman, M. Davidovich, C. Kiesnowski, Thermochim. Acta **324**, 187 (1998)
30. D. Berry, C. Seaton, W. Clegg, R. Harrington, S. Coles, P. Horton, M. Hursthouse, R. Storey, W. Jones, T. Friscic, N. Blagden, Cryst. Growth Des. **8**, 1697 (2008)
31. S. Pygall, J. Whetstone, P. Timmins, C. Melia, Adv. Drug Del. Rev. **59**, 1434 (2007)
32. B. Jovice, P. Kamali-Zare, H. Brismar, L. Bergstroem, Langmuir **24**, 11096 (2008)
33. R. Ortiz, J. Au, Z. Lu, Y. Gan, M. Wientjes, AAPS J. **9**, E241 (2007)
34. C. Berkland, K. Kim, D. Pack, Pharm. Res. **20**, 1055 (2003)
35. V. Malaterre, J. Ogorka, R. Gurny, N. Loggia, K. Paulus, Eur. J. Pharm. Biopharm (submitted)
36. G.I. Goldstein, D.E. Newbury, P. Echlin, D.C. Joy, C. Fiori, E. Lifshin, *Scanning Electron Microscopy and X-ray Microanalysis* (Plenum Press, New York, 1981)
37. D. Murphy, F. Rodriguez-Cintron, B. Langevin, R. Kelly, N. Rodriguez-Hornedo, Int. J. Pharm. **246**, 121 (2002)
38. P. Mura, M. Faucci, A. Manderioli, G. Bramanti, L. Ceccarelli, J. Pharm. Biomed. Anal. **18**, 151 (1998)
39. D. Bozic, R. Dreu, F. Vrecer, Int. J. Pharm. **357**, 44 (2008)
40. L. Ping, S. Hynes, T. Haefele, M. Pudipeddi, A. Royce, A. Serajuddin, J. Pharm. Sci. (in print)
41. T. Li, K. Park, Pharm. Res. **15**, 1222 (1998)
42. L. Sipos, A. Som, R. Faust, R. Richard, M. Schwarz, S. Ranade, M. Boden, K. Chan, Biomacromolecules **6**, 2570 (2005)

43. A. Efimov, A. Tonevitsky, M. Dittrich, N. Matsko, J. Microsc. **226**, 207 (2007)
44. L. Harding, M. Reading, D. Craig, J. Pharm. Sci. **97**, 2768 (2008)
45. U. Sindel, I. Zimmermann, Powder Technol. **117**, 247 (2001)
46. S. Ward, M. Perkins, J. Zhang, C. Roberts, C. Madden, S. Luk, N. Patel, S. Ebbens, Pharm. Res. **22**, 1195 (2005)
47. V. Busignies, B. Leclerc, P. Porion, P. Evesque, G. Couarraze, P. Tchoreloff, Eur. J. Pharm. Biopharm. **64**, 38 (2006)
48. C. Wua, B. Hancock, A. Mills, A. Bentham, S. Best, J. Elliott, Powder Technol. **181**, 121 (2008)
49. L. Kessler, *Acoustic Microscopy, Metals Handbook* (International, ASM, 1989), pp. 465–482
50. M. Nelson, C. Zugates, P. Treado, G. Casuccio, D. Exline, S. Schlaegle, Aerosol Sci. Tech. **34**, 108 (2001)
51. A. Apeldoorn, Y. Aksenov, M. Stigter, I. Hofland, J. Bruijn, H. Koerten, C. Otto, J. Greve, C. Blitterswijk, J.R. Soc, Interface **2**, 39 (2005)
52. P. Bergese, I. Alessandri, I. Colombo, N. Coceani, L. Depero, Compos. Part A **36**, 443 (2005)
53. D. Volodkin, A. Petrov, M. Prevot, G. Sukhorukov, Langmuir **20**, 3398 (2004)
54. H. Lange, Chem.-Ing. Tech. **9**, 1091 (1993)
55. D. Clark, M. Henson, F. LaPlant, S. Sasic, L. Zhang, *Pharmaceutical Applications of Chemical Mapping and Imaging, in: Applications of Vibrational Spectroscopy in Pharmaceutical Research and Development* (Wiley, 2007), pp. 309–335
56. A. Garratt-Reed, *Energy Dispersive X-Ray Analysis* (BIOS Scientific Publishers, Oxford, 2003)
57. A. Kenda, O. Eibl, P. Pongratz, Micron **30**, 85 (1999)
58. J. Bovin, Micron Microscopica Acta **23**, 143 (1992)
59. K. Paulus, in *Proceedings of 31st Micro Conference* (DGE, Dresden, 2003)
60. S. Ensslin, K. Moll, K. Paulus, C. Mäder, J. Contr. Rel. **128**, 149 (2008)
61. P. Nevsten, P. Borgquist, A. Axelsson, L. Wallenberg, Int. J. Pharm. **290**, 109 (2005)
62. S. Fitzgerald, Spectrosc. Eur. **17**, 24 (2005)
63. T. Miller, G. Havrilla, Powder diffr. **20**, 15 (2005)
64. B. Beckhoff, B. Kanngiesser, N. Langhoff, R. Wedell, H. Wolff, *Handbook of Practical X-Ray Fluorescence Analysis* (Springer, Berlin, 2006)
65. A. Benninghoven, Angew. Chemie Int. **33**, 1023 (1994)
66. A. Belu, C. Mahoney, K. Wormuth, J. Contr. Rel. **126**, 111 (2008)
67. A. Belu, D. Graham, D. Castner, Biomater. **24**, 3635 (2003)
68. N. Winograd, Appl. Surf. Sci **203–204**, 13 (2003)
69. A. Belu, M. Davies, J. Newton, N. Patel, Anal. Chem. **72**, 5625 (2000)
70. N. Harrick, *Internal Reflection Spectroscopy* (Wiley, Chichester, 1967)
71. K.L.A. Chan, S.V. Hammond, S.G. Kazarian, Anal. Chem. **75**, 2140 (2003)
72. C. Krafft, D. Codrich, G. Pelizzo, V. Sergo, Analyst **133**, 361 (2008)
73. G. Reich, Pharm. Ind. **64**, 870 (2002)
74. Y. Roggo, A. Edmond, P. Chalus, M. Ulmschneider, Anal. Chim. Acta. **535**, 79 (2005)
75. C. Ricci, L. Nyadong, F. Fernandez, P. Newton, S. Kazarian, Anal. Bioanal. Chem. **387**, 551 (2007)
76. C. Ricci, C. Eliasson, N. Macleod, P. Newton, P. Matousek, S. Kazarian, Anal. Bioanal. Chem. **389**, 1525 (2007)
77. M. Henson, L. Zhang, Appl. Spectrosc. **60**, 1247 (2006)
78. S. Sasic, Appl. Spectrosc. **6**, 239 (2007)
79. G. Reich, Adv. Drug Del. Rev. **57**, 1109 (2005)
80. J. Breitenbach, W. Schrof, J. Neumann, Pharm. Res. **16**, 1109 (1999)
81. I. Chourpa, P. Carpentier, P. Maingault, P. Dubois, SPIE **3608**, 48 (1999)
82. L. Kador, T. Schittkowski, M. Bauer, Y. Fan, Appl. Opt. **40**, 4965 (2001)
83. F. Clarke, M. Jamieson, D. Clark, S. Hammond, R. Jee, A. Moffat, Anal. Chem. **73**, 2213 (2001)
84. H. Boyer, J. Oswalt, Analusis **28**, 3 (2000)

85. P. Treado, M. Nelson, Pract. Spectrosc. **28**, 191 (2001)
86. L. Zhang, M. Henson, S. Sekulic, Anal. Chim. Acta **545**, 262 (2005)
87. D. Clark, S. Sasic, Cytometry A **69A**, 815 (2006)
88. S. Sasic, Pharm. Res. **24**, 58 (2007)
89. D. Fraser Steele, P. Young, R. Price, T. Smith, S. Edge, D. Lewis, AAPS J. **6**, Article 32 (2004)
90. A. Theophilus, A. Moore, D. Prima, S. Rossomanno, B. Whitcher, H. Chrystyn, Int. J. Pharmaceut. **313**, 14 (2006)
91. A. Serajuddin, P. Li, T. Haefele, Am. Pharm. Rev. **11**, 34 (2008)
92. A. Docoslis, K. Huszarik, G. Papageorgiou, D. Bikiaris, A. Stergiou, E. Georgarakis, AAPS J. **9**, Article 43, E361 (2007)
93. G. Papageorgiu, D. Bikiaris, E. Karavas, S. Politis, A. Docoslis, Y. Park, A. Stergiou, E. Georgarakis, AAPS J. **8**, Article 71, E623 (2006)
94. W. Doub, W. Adams, J. Spencer, L. Buhse, M. Nelson, P. Treado, Pharm. Res. **24**, 934 (2007)
95. Committee on Revealing Chemistry through Advanced Chemical Imaging, *Visualizing Chemistry: The Progress and Promise of Advanced Chemical Imaging* (National Academies Press, Washington, 2006)
96. H. Martens, T. Naes, *Multivariate Calibration* (Wiley, New York, 1992)
97. B. Bowie, D. Chase, I. Lewis, P. Griffiths, Handb. Vib. Spectrosc. **3**, 2355 (2002)
98. J. Thomas, P. Buzzini, G. Massonnet, B. Reedy, C. Roux, Forensic Sci. Int. **152**, 189 (2005)
99. P. Hendra, Int. J. Vib. Spect. **4**, 2 (2000)
100. C. McGoverin, T. Rades, K. Gordon, J. Pharm. Sci. **97**, 4598 (2008)
101. C. Camerlinge, F. Zenone, G. Gaeta, R. Riccio, M. Lepore, Meas. Sci. Technol. **17**, 298 (2006)
102. P. Ramos, I. Ruisanchez, J. Raman. Spectrosc. **36**, 848 (2005)
103. T. Cai, D. Zhang, D. Ben-Amotz, Appl. Spectrosc. **55**, 1124 (2001)
104. F. Ehrentreich, L. Sümmchen, Anal. Chem. **73**, 4364 (2001)
105. F. Adar, E. Lee, S. Mamedov, A. Whitley, Spectroscopy Supplement: Raman June (2006)
106. http://www.olympusfluoview.com/theory/resolutionintro.html
107. N. Everall, J. Lumsdon, Vib. Spectrosc. **2**, 257 (1991)
108. M. Pellow-Jarmann, P. Hendra, R. Lehnert, Vibrat. Spectrosc. **12**, 257 (1996)
109. T. De Beer, W. Baeyens, J. Vander Heyden, Y.and Remon, C. Vervaet, F. Verpoort, Eur. J. Pharm. Sci. **30**, 229 (2007)
110. C. Raman, K. Krishnan, Nature **121**, 501 (1928)
111. C.V. Raman, K.S. Krishnan, Nature **122**, 169 (1928)
112. R. Snyder, J. Molec. Spectrosc. **37**, 353 (1971)
113. D. Bower, J. Polym. Sci. **10**, 2135 (1972)
114. C. Bremard, P. Dhamelincourt, J. Laureyns, G. Turrell, Appl. Spectrosc. **39**, 1036 (1985)
115. X. Zhang, Y. Liu, S. Chen, J. Raman Spectrosc. **36**, 1101 (2005)
116. M. Bickermann, B. Epelbaum, P. Heimann, Z. Herro, A. Winnacker, Appl. Phys. Lett. **86**, 131904 (2005)
117. M. Tanaka, R. Young, J. Mater. Sci **41**, 963 (2006)
118. W. Jones, D. Thomas, D. Thomas, G. Williams, J. Mol. Struct. **708**, 145 (2004)
119. P. Camorani, M. Fontana, Mol. Cryst. Liq. Cryst. **465**, 143 (2007)
120. S. Ensslin, K. Moll, T. Haefele, C. Mäder, Pharm. Res. (submitted)
121. http://www.sandostatin.com
122. R. Langer, Nature **392**, 5 (1988)
123. M. van de Weert, W. Hennink, W. Jiskoot, Pharm. Res. **17**, 1159 (2000)
124. A. Messaritaki, S. Black, C. van der Walle, S. Rigby, J. Contr. Rel. **108**, 271 (2005)
125. S. Mao, J. Xu, C. Cai, O. Germershaus, A. Schaper, T. Kissel, Int. J. Pharm. **334**, 137 (2007)
126. F. Sadeghi, J. Ford, A. Rubinstein, M.H. Rajabi-Siahboomi, Drug Dev. Ind. Pharm. **27**, 419 (2001)
127. K. Goracinova, L. Klisarova, A. Simov, Drug Dev. Ind. Pharm. **22**, 255 (1996)
128. S. Lin, Curr. Ther. Res. Clin. **41**, 564 (1987)
129. R. Rowe, J. Pharm. Pharmacol. **38**, 214 (1986)
130. M. Saettone, G. Perini, P. Rijli, Int. J. Pharm. **126**, 83 (1995)

131. M. Beck, I. Tomka, Macromolecules **29**, 8759 (1996)
132. J. Rau, Respir. care **50**, 367 (2005)
133. G. Crompton, J. Aerosol Med. **4**, 151 (1991)
134. A. Hickey, *Pharmaceutical Inhalation Aerosol Technology* (Marcel Dekker, New York, 2004)
135. W.H. Finlay, *The Mechanics of Inhaled Pharmaceutical Aerosols: An Introduction* (Academic Press, London, 2001)
136. D. Wieckhusen, Chimia **60**, 598 (2006)
137. L. Augsburger, S. Hoag, *Pharmaceutical Dosage Forms: Tablets* (Informa HealthCare, London, 2008)
138. M. Rubinstein, J. Wells, *Pharmaceutical Technology: Tableting Technology* (Ellis Horwood, Chichester, 1993)
139. D. Parikh, *Handbook of Pharmaceutical Granulation Technology* (Informa HealthCare, London, 2005)
140. K. Steffens, Pharm. Indus. **52**, 1412 (1990)
141. G. Shearer, The microscope **51**, 3 (2003)
142. X. Cao, Z. Wen, A. Vance, G. Torraca, G. Li, W. Jing, P. Masatani, C. Yee, Microsc. Microanal **14**, 1608 (2008)
143. M. Lankers, J. Munhall, O. Valet, Microsc. Microanal. **14**, 1612 (2008)
144. J. Blanchard, J. Coleman, C. D'Abreu Hayling, R. Ghaderi, B. Haeberlin, J. Hart, S. Jensen, R. Malcolmson, S. Mittelman, L. Nagao, S. Sekulic, C. Snodgrass-Pilla, M. Sundahl, G. Thompson, R. Wolff, Pharm. Res. **21**, 2137 (2004)

Chapter 17
Raman Spectroscopy in Skin Research and Dermal Drug Delivery

Nathalie Jung, Branko Vukosavljevic and Maike Windbergs

Abstract Raman spectroscopy represents an upcoming analytical technique in the field of skin research and dermal drug delivery. In the last few decades, significant progress in optical equipment like lasers and detectors as well as in microscopy and software development paved the way for chemically selective three-dimensional Raman imaging with high spatial resolution. Potential applications range from analysis of physiological and pathophysiological skin conditions (e.g. non-destructive cancer detection in clinics) up to surgery guidance. In the field of drug delivery and cosmetics, Raman microscopy is successfully applied for investigating interactions with skin as well as for elucidation of drug penetration kinetics within the different skin tissue layers, thus strongly supporting rational development and improving product safety of novel skin therapeutics. This chapter provides a brief introduction about skin anatomy and dermal drug delivery systems, as well as state-of-the-art analytics in skin research. Furthermore, the potential of Raman spectroscopy for application in skin research, particularly its advantages and limitations in the field, is comprehensively elaborated. Subsequently, an overview about skin research studies applying Raman spectroscopy is given comprising various in vitro as well as in vivo implementations. Finally, employment of Raman spectroscopy for advanced diagnosis and surgery guidance are discussed and a future perspective in the field of skin research is given.

Nathalie Jung and Branko Vukosavljevic are contributed equally to this work.

N. Jung · B. Vukosavljevic · M. Windbergs (✉)
Institute of Pharmaceutical Technology and Buchmann Institute for Molecular Life Sciences, Goethe University, Frankfurt am Main, Germany
e-mail: windbergs@em.uni-frankfurt.de

N. Jung
e-mail: n.jung@em.uni-frankfurt.de

B. Vukosavljevic
e-mail: branko.vukosavljevic@helmholtz-hzi.de

N. Jung · M. Windbergs
Department of Drug Delivery, Helmholtz Centre for Infection Research (HZI) and Helmholtz Institute for Pharmaceutical Research Saarland (HIPS), Saarbruecken, Germany

J. Toporski et al. (eds.), *Confocal Raman Microscopy*, Springer Series in Surface Sciences 66, https://doi.org/10.1007/978-3-319-75380-5_17

17.1 The Human Skin - From a Biological Barrier to a Therapeutic Application Site

17.1.1 Skin Anatomy and Morphology

The skin is one of the largest organs in the human body and constitutes a biological barrier successfully protecting the organism from physical, chemical and thermal influences. Based on a complex layered structure, the human skin serves as a durable protection against external hazards like harmful chemicals and biological pathogens. The skin consists of three main tissue layers and different appendages as depicted in Fig. 17.1.

The lowermost layer of the skin called subcutis mainly consists of fibroblasts, macrophages and adipocytes. Fibrous bands in the tissue anchor upper layers of the skin to deep fascia and bones below. The subcutaneous tissue also contains bigger blood vessels, nerves and fatty tissue with the purpose of energy supply for the upper skin layers and thermal insulation for the organism with a varying thickness depending on the needs and constitution of the individual organism.

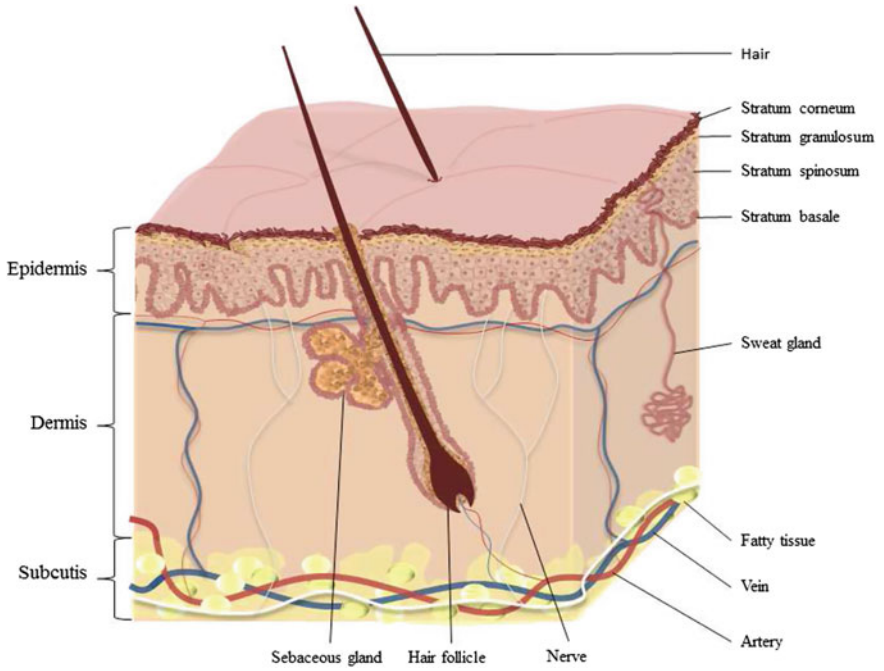

Fig. 17.1 Schematic illustration of the human skin with its three main layers constituted by epidermis, dermis and subcutis

On top of the subcutis lies the dermis, a vascularized, collagen-rich, 0.3–3.0 mm thick layer. It contains sweat and sebaceous glands, nerves, lymph vessels and hair follicles. Smaller blood vessels provide nourishment and waste removal for dermal and epidermal tissue, whilst collagen and other matrix components provide this layer with great mechanical strength and flexibility.

The outermost region of the skin is the epidermis. Depending on the body site the epidermis greatly varies in thickness: ranging from only 0.05 mm at the eye-lids up to 1.5 mm at the palms of hands and feet. The epidermis can be divided into two parts: the viable epidermis which consists of three separate layers (stratum basale, stratum spinosum and stratum granulosum), and the stratum corneum. The viable epidermis is a non-vascularized tissue and the site of keratinocyte proliferation. The bottom layer of the epidermis is the stratum basale. It connects the epidermal to the dermal tissue and consists like the rest of the epidermis mostly of keratinocytes. This layer also contains melanocytes that produce melanin as a protection against the destructive effect of UV radiation. Melanosomes that contain melanin are transferred to adjacent keratinocytes, which proliferate in the stratum basale and differentiate during their migration towards the top layer. These cells migrate through the stratum spinosum and the stratum granulosum until they reach the outermost layer of the skin, the stratum corneum. Here, they become cornified cells in a coherent lipid matrix, resembling a "brick and mortar" structure. The protein-rich, dead corneocytes provide the physical stability, whereas the lipid matrix acts as a binding substrate that inhibits the penetration of water and other dissolved substances into and evaporation of water out of the skin. The presence and arrangement of lipids like cholesterol ester, triglycerides and glycosphingolipids in small quantities play an important role in the integrity of this layer. Together with the slightly acidic pH value of the stratum corneum, they form a permeability barrier that is a major obstacle for all kinds of substances and pathogens to overcome in order to be absorbed.

17.1.2 Drug Delivery to the Human Skin

Skin represents a favored application site for the delivery of drugs as it allows for painless and easy administration associated with good patient compliance. Delivering drugs to the skin can either aim on local therapy for the treatment of skin diseases and defects (e.g. wounds, infections, psoriasis, atopic dermatitis) or use the skin solely as application route to reach the blood circulation for systemic drug delivery. There is a broad variety of different skin therapeutics on the market ranging from semisolids like creams and ointments up to drug-loaded adhesives.

Depending on their physical state, dermal therapeutics aimed for the local therapy can be classified into liquids (e.g. suspensions and emulsions), semisolids (e.g. creams, ointments, gels, and pastes) and solids (e.g. local adhesives and wound dressings). In this context, semisolids represent the largest group comprising a large variety of different dosage forms.

In comparison, dosage forms for systemic drug delivery can, according to the physical state, generally be categorized into semisolid and solid systems. Here, solid systems such as dermal and subdermal patches, microneedles and bioadhesive films for transdermal drug delivery represent the predominant subgroup. However, besides a suitable application system, for controlled or even targeted delivery to the skin, accurate and comprehensive knowledge about absorption mechanisms and transport kinetics in skin tissue is needed.

Due to the complex skin structure, as introduced in the previous section, skin absorption is multifaceted. Most skin absorption processes are driven by passive diffusion controlled by the main barrier which is posed by the stratum corneum, thus upon stratum corneum disruption (e.g. by wounding or diseases like atopic dermatitis) absorption can greatly differ from the healthy state. Depending on the depth of penetration, epidermal and dermal absorption can be differentiated (Fig. 17.2). Further, absorption pathways are provided by hair follicles as well as by eccrine glands. However, as eccrine glands are so profusely active, it is unlikely that molecules can diffuse inwardly against the gland's output. Inside the skin, absorbed substances can also be metabolized in the skin or form localized depots.

With respect to the aforementioned, advanced analytics capable of comprehensive characterization of dermal drug delivery systems, especially their interaction with skin, could help supporting rational development and improve product safety of novel therapeutics for skin application.

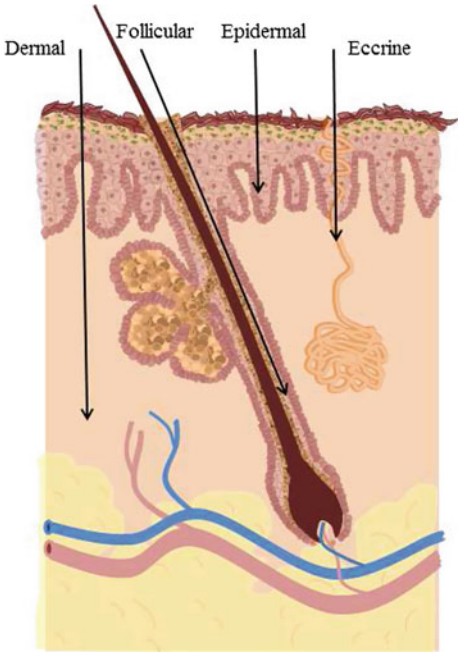

Fig. 17.2 Illustration of different pathways for skin absorption

17.2 Analytics in Skin Research and the Potential for Raman Spectroscopy

17.2.1 State-of-the-Art Analytics for Skin Research

Since skin represents a complex biological tissue and exhibits diverse functions, skin research is focused on a wide range of different aspects. The scientific interest ranges from elucidation of biochemical composition and physiological functions as well as diagnosis of pathological skin states up to the discovery of strategies to influence and manipulate physiological functions and processes in the skin for delivery of actives and cosmetics. In this context, skin absorption processes are the main focus of interest. On the one hand, knowledge about skin absorption is required for testing harmful substances with respect to risk assessment and safety studies; on the other hand, this information is the basis for rational development and testing of cosmetics, protective skin care products and therapeutics.

As controlled or even targeted drug delivery to the human skin requires in-depth knowledge about absorption mechanisms and transport kinetics in skin tissue, suitable analytical techniques are essential prerequisites. Visual inspection of the tissue is the first approach for medical doctors to analyze skin status and to propose a clinical diagnosis. Furthermore, assessment of the physiological status, e.g. water content in the skin tissue or pH value can non-invasively be assessed. For a more detailed analysis of the skin and especially its deeper layers, biopsies and further histological investigations of skin sections represent a valuable methodology.

Besides clinical studies which are performed in the last stage of the development of novel therapeutics, the initial stage of development involves the use of laboratory animals or even excised human skin. In this context, a specific analytical setup for in vitro determination of skin absorption is generally used, the so called Franz diffusion cell (Fig. 17.3). The cell consists of two compartments: a donor and an acceptor compartment, separated by a piece of excised skin. The amount of substance which permeates the skin sample can completely be detected by quantifying the drug in the acceptor compartment, whereas the amount of substance which remained in the skin can subsequently be extracted from the tissue for quantification.

For a detailed analysis of the penetration depth of substances in the skin, the skin sample needs to be sectioned. For this purpose, the stratum corneum as the outermost layer can serially be removed by means of adhesive tapes. This procedure is called tape-stripping. The applied substance can be extracted from the tapes and quantified in a subsequent step [1]. Tape-stripping allows for in vitro and in vivo analysis of the extent and kinetics of skin absorption behavior into the stratum corneum. For investigation of the deeper skin layers, the remaining skin sample after tape stripping is sectioned parallel to the surface with a cryotome and extracted for quantification.

However, all aforementioned techniques are destructive, time consuming and lack accurate spatial resolution. Moreover, the supply of excised human skin is often limited. Consequently, there is a strong need for non-destructive and chemically

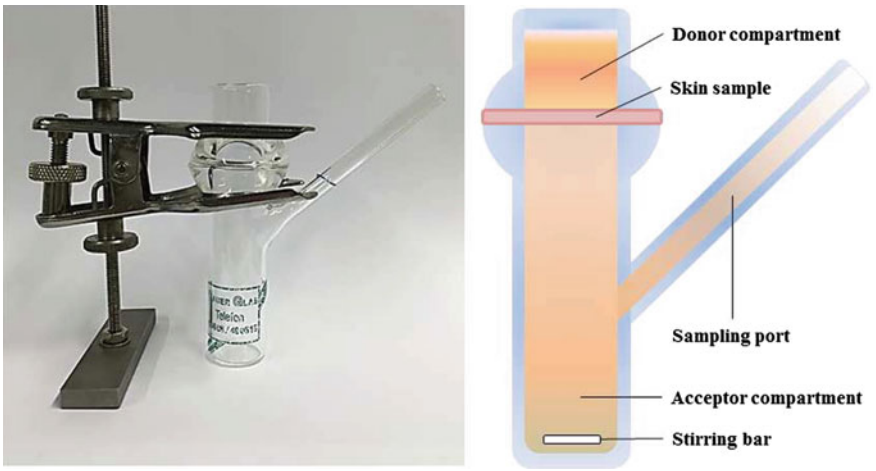

Fig. 17.3 Photograph and schematic illustration of a Franz diffusion cell

selective analytical techniques to reduce sample numbers and size in vitro as well as to allow more comprehensive in vivo analysis. In this context, confocal Raman microscopy (CRM) shows the potential to fill these scientific gaps.

17.2.2 The Potential of Raman Spectroscopy for Skin Analysis

Since Raman spectroscopy is non-invasive and allows for label-free identification of different compounds based on their spectral contrast, there is a multitude of different applications in the field of skin research.

The specific molecular structure even allows for differentiation between the diverse layers of a highly complex biological system like the skin solely based on their Raman spectra as exemplarily depicted for hair, sebum, dermal and epidermal structure in Fig. 17.4a [2]. Based on a false color coding, the individual components can be visualized in a spatially resolved way (Fig. 17.4b).

Furthermore, Raman spectroscopy allows for the assessment of physiological states (like hydration and antioxidative potential) and the evaluation of pathophysiological conditions [3, 4]. In addition, Raman spectroscopy is applied as a diagnostic tool to distinguish between healthy and cancerous tissue without the need for specific markers for labelling of the sample [5, 6]. Depending on the measurement settings and the laser power used for the analysis, the method can be employed as a non-invasive imaging technique for depth profiling, since the laser is able to penetrate into the skin. In combination with a confocal microscope setup, it is even possible to create virtual cross sections of the sample with a high spatial resolution without

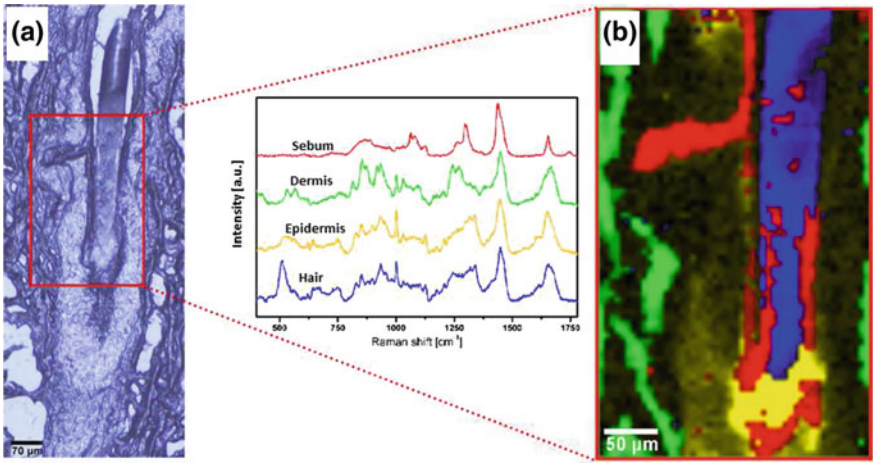

Fig. 17.4 Raman analysis of a porcine hair follicle. **a** Light microscopy image of a histological hair follicle cross-section. **b** False-color Raman image of the area indicated in (**a**). Raman spectra of the individual sample components are depicted in the middle according to the color coding of the Raman image (sebum - red, dermis - green, epidermis - yellow, hair - blue). Adapted from [2] with permission from the publisher

the need of destroying the tissue. These measurements are not limited to in vitro systems, with an adjusted setup Raman spectroscopy can also be used for in vivo studies.

Apart from tracking biological factors of the skin itself, Raman spectroscopy is applied to monitor the interaction of chemicals with the skin. For the development of cosmetics as well as novel skin therapeutics, there is a high potential for monitoring the effect of marketed and newly developed formulations on the skin structure [7, 8]. In this respect, the basic risk assessment of new chemicals for incorporation in cosmetics and pharmaceutics can also be performed by applying Raman to observe any destructive effects the substance might have on the skin [9]. Without the need for cutting and thereby destroying the tissue, the penetration of substances can be monitored rather than being limited to the measurement of permeation like in Franz diffusion cell experiments. Due to the non-invasive nature of a Raman analysis, the technique even allows for complementary combinations with other analytical methods. After performing Raman measurements on a skin sample it is possible to do subsequent histological studies or quantitative measurements by a combination of tape-stripping and high-performance liquid chromatography (HPLC).

Even though Raman spectroscopy is a valuable approach to tackle various questions in the field of skin research, the acquisition and analysis of data sets are quite time consuming. In this context, the application of non-linear Raman techniques like stimulated Raman spectroscopy (SRS) and coherent anti-Stokes Raman spectroscopy (CARS) hold a great potential for future investigation due to the fast data acquisition ability [10, 11].

Despite the challenges of working with Raman spectroscopy on biological tissue, CRM can be applied in numerous ways to investigate processes in the skin and can even answer questions on a cellular level [12].

17.3 Application of Raman Spectroscopy in Skin Research

17.3.1 Analyzing Skin with Raman Spectroscopy

Since skin is a highly complex biological tissue and Raman spectroscopy itself as a method that requires a high level of expertise, the combination of both fields constitutes a particularly demanding task even for experienced scientists. Different factors can greatly influence the Raman analysis, among them are the sample itself and its preparation, as well as the instrumental setup and the measurement parameters.

There is a variety of samples that can be analyzed by Raman spectroscopy. As the acquisition of Raman spectra is generally non-destructive, measurement of cultivated cells and tissue engineered models and even excised skin from mouse, pig or human as well as in vivo do not pose a problem. The most accurate in vitro absorption testing can be performed using excised human skin as a gold standard, as the barrier function of excised skin samples is preserved and similar compared to human skin in vivo.

However, when performing experiments on biological samples, the experimental conditions can have a huge impact on the acquired data. The hydration and temperature of the sample as well as the choice of laser and laser power are crucial factors and should be considered thoroughly before venturing into Raman analysis on tissue samples.

Depending on the nature of the in vitro system used, there are several ways to prepare the sample for Raman spectroscopy. When working with excised skin samples, there is the choice of using fresh skin or tissue that was stored in frozen state. Generally, it is desired to perform measurements as closely to the natural state of the tissue as possible, so during an experiment, there are several factors that should be kept in mind like (over)hydration and movement of the sample. In the case of full-thickness skin, the bottom layer (dermis) should be immersed in a fluid to maintain the hydration of the tissue. Phosphate buffer saline (PBS) is used to mimic the in vivo situation, since the osmolarity and ion concentrations match the parameters found in the human body. However, when providing the skin constantly with fluids, the tissue inevitably swells. The resulting movement in the sample can substantially impede the Raman measurements. To eradicate this undesired effect, it is advised to fixate the sample in some way. Suitable techniques involve clamping, sewing or even gluing the skin to a sample holder. It should also be considered to perform the measurement at 32 °C, the actual skin temperature.

Another way to circumvent the problem of tissue movement is the preservation of the sample by freeze drying. By instantly freezing the tissue in liquid nitrogen and removing the water in the sample completely over several days using a freeze

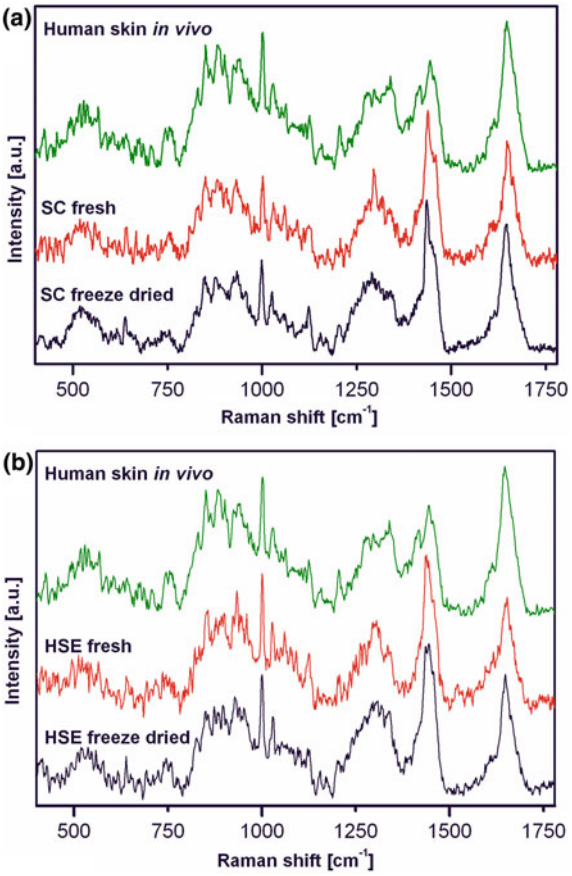

Fig. 17.5 Comparison of Raman spectra acquired from excised human skin samples before and after freeze drying in comparison to Raman spectra acquired in vivo. Isolated stratum corneum (SC) in (**a**) and heat-separated epidermis (HSE) in (**b**). Adapted from [13] with permission from WILEY-VCH Verlag GmbH & Co. KGaA,Weinheim

dryer, the skin is conserved in its original state and also potential microbial growth is prevented. Franzen et al. proved that freeze-drying is a suitable technique for preserving skin tissue [13]. They could successfully show for isolated stratum corneum as well as for heat-separated epidermis, that after freeze-drying the optical and spectral similarity to human skin in vivo is preserved as shown in Fig. 17.5.

When it comes to the choice of laser for an experiment on biological tissue there is one main problem to consider: due to the pigmentation of the skin, fluorescence can emerge in the sample [14]. Depending on the laser, the Raman peaks in the fingerprint region (800–1800 rel. cm^{-1}) can be exceeded by a high fluorescence signal when working with a 532 or 633 nm laser. Since this effect is highly dependent on the laser light source, this problem can be addressed by using lasers with an emission wavelength in the near-infrared region (660 and 785 nm).

In addition, upon penetration of the laser into the skin layers, the scattering of light leads to Raman signals with decreased intensity. Lasers emitting light at 532 and 633 nm experience more severe signal attenuation when penetrating into skin tissue

compared to lasers with a longer wavelength [15]. For penetration studies, the signal attenuation plays an important role, since substances are monitored even in deeper skin layers. In this case, lasers emitting light in the near-infrared range (like 633 and 785 nm) are the better choice. However, when it comes to detection of Raman spectra with lasers of a higher wavelength, the efficiency of detection by the charged coupled device decreases tremendously. Consequently, a 785 nm laser allows for a suitable compromise combining deep penetration into to tissue with a good signal-to-noise ratio.

The choices of laser power and acquisition time are also crucial factors for Raman measurements on skin. It is important to find a compromise based on good signal intensity with no thermal damage of the sample [16]. Due to the low Raman scattering intensity of biological tissue, long acquisition times of about 30 seconds are often required to record a decent Raman spectrum. When working with freeze-dried material shorter acquisition times are usually sufficient [17].

Raman spectroscopy in skin research offers a variety of data acquisition modes depending on the scientific question. The collection of single spectra at any point of the skin sample in all three dimensions and the acquisition of a two-dimensional scan in xy-direction are the most established modes. In addition, depth profiling along a single line in z-direction allows the graphic illustration of Raman peak intensity profiles over depth (Fig. 17.6a). The collection of Raman data in yz-direction in a spatially resolved way creates a virtual cross section and shows in a false-color intensity map the distribution of a specific peak inside the tissue without the need of cutting it (Fig. 17.6b). The same principle can be applied to measurements in xy-direction whilst moving deeper into the tissue along the z axis as shown in Fig. 17.6c. By collecting scans parallel to the surface of the skin and stacking them on top of each other, it is possible to create a three-dimensional reconstruction of the sample, which can give information about drug penetration and distribution inside the skin tissue.

When working with skin samples, one point to consider is the duration of the experiment. As diffusion is proceeding during the experiment, conservation of diffusion state at one time point is a valuable approach. As described above, this can be achieved by freeze-drying.

The analysis and interpretation of Raman spectra of human skin and biological materials in general are challenging tasks. The availability of good reference spectra and efficient software analysis tools are basic prerequisites. Although the application of a laser emitting light in the near infrared region significantly reduces the fluorescence, acquired datasets still require background subtraction. The adjustment of the spectral baseline was investigated by Silveira et al., who showed that discrete wavelet transformation and polynomial fit both are suitable filter methods for discriminating experiments between different cell types [19]. In addition, fluorescence-to-noise removal algorithms and photobleaching as methods to increase spectral information of a dataset are described by several other groups [20–22].

Besides cosmic ray removal and background subtraction, a crucial part in interpreting Raman data - especially when performing depth measurements - is the determination of the skin surface and the understanding of signal attenuation in skin tissue.

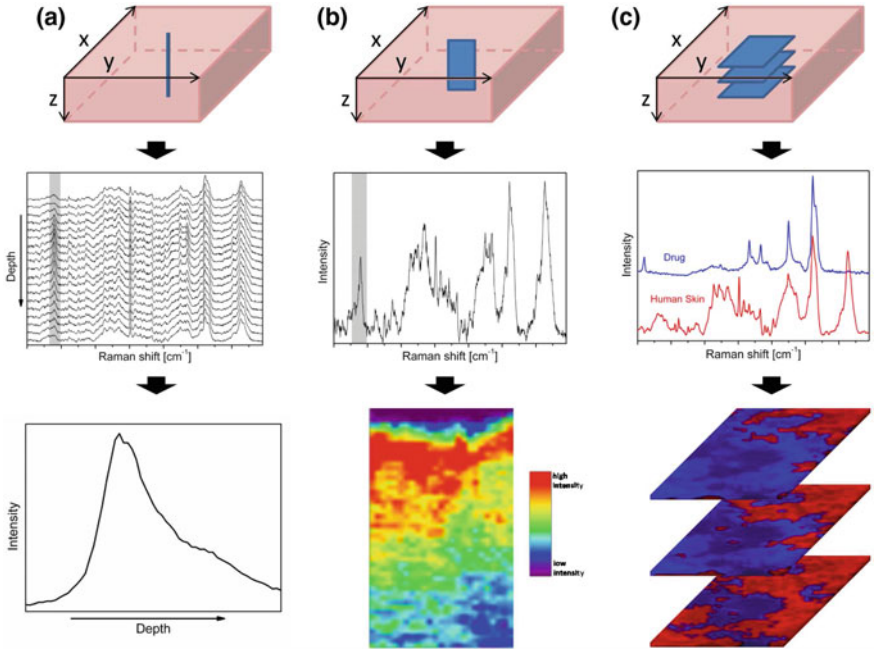

Fig. 17.6 **a** Raman depth profiling: Single spectra are recorded along a line in z-direction; intensities of a single peak are depicted as an intensity profile against depth. **b** Raman intensity mapping: Raman spectra are acquired along a xz-plane to create a virtual cross section. The spectra are presented in a two-dimensional color coded intensity map. **c** z-stack: series of xy false color images are stacked to create a three-dimensional data set, different components are depicted in different colors (skin - red; drug - blue). Reprinted from [18] with permission from Elsevier

Generally, the skin surface is defined as the point where the laser spot entered halfway into the sample. In a Raman intensity depth profile, the skin surface is localized at half of the maximum of the Lorentzian fit of the curve. When the laser crosses the skin surface and moves deeper into the non-transparent skin tissue in z-direction, the laser light intensity as well as the intensity of the detected light decreases. This attenuation effect in the collected Raman spectra is illustrated in Fig. 17.7.

Not only signal attenuation but also the determination of the accurate depth of a measuring point in a skin sample is an important issue. Everall et al. demonstrated the correlation of exact depth determination and technical factors like the numerical aperture of the objective and proposed a mathematical model for correction [23, 24]. Several groups followed that approach and developed their own models for depth correction [25–27]. The influence of the difference of refractive indices of air and skin and also between the different skin layers has also a distorting effect on the depth determination as shown by Xiao et al. [28]. They used multilayered polymer films with refractive indices close to those of human skin and showed that the depth value might even be underestimated by 15–20 % of the measured depth.

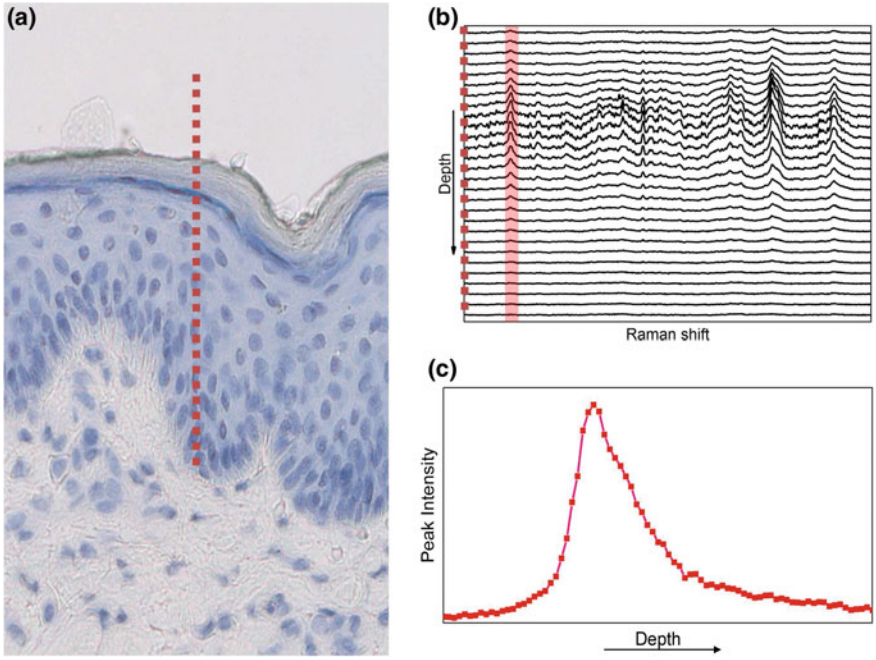

Fig. 17.7 Raman signal attenuation in the skin. **a** Histological cross section of skin and the basic principle of depth profiling indicated by the red dotted line. **b** Recorded Raman spectra associated with the red points in (**a**). **c** Peak intensity profile of the highlighted Raman peak in (**b**). Due to the reduction of collected photons with increasing depth, a decay of the Raman signal can be observed. Reprinted from [18] with permission from Elsevier

Besides analyzing skin samples with Raman spectroscopy, it is also possible to monitor the interaction of the skin with a substance. From application of potentially hazardous substances onto skin for risk assessment studies up to application of topical formulations for monitoring of drug delivery to the skin, Raman spectroscopy and microscopy allows for a wide array of studies in the field of penetration. Given that the penetrating substance provides sufficient spectral contrast to the biological tissue, it can be distinguished from the skin and its effect can be observed in the skin tissue. For penetration experiments, several approaches are described for overcoming this issue. Franzen et al. developed a mathematical model for determination and subsequent correction of signal attenuation by building an artificial skin surrogate with the same optical properties as human skin. Based on the data derived from the surrogate, an algorithm was successfully designed for correction of signal attenuation in human skin [29]. In addition, the drug-associated peak can be related to an endogenous skin-specific peak. However, this implies homogeneous distribution of the compound which is assigned to this peak. Franzen et al. investigated different peaks and their suitability for quantitative depth profiling of drugs in human skin [30].

Despite taking all these factors into consideration and standardizing Raman measurements on skin, results may differ immensely between single experiments. Due to the high variability of biological tissue, it is inevitable to perform a high number of experiments to create convincing and consistent data.

The interpretation of the acquired Raman spectra at a specific point in the sample is also a rather difficult task due to the complexity of biological tissue, which is discussed in the next paragraph.

As already mentioned above, Raman spectroscopy can not only be applied for in vitro experiments. In the 90s the advancements in optical technology allowed for the production of Raman setups for in vivo application. Shim et al. described several modifications in a commonly used Raman setup that enabled to acquire spectra in live tissue without damage [31]. In addition, they presented a study on optical fibers that are designed to suppress confounding signals for fast spectra acquisition in vivo[32]. The group of Caspers et al. also pioneered in the field of in vivo application of CRM. In the late 90s, they conducted studies on human skin in vitro and in vivo and investigated the natural moisturizing factor [33]. In the following years, the same group extended their research in the field of in vivo application of Raman spectroscopy and provided a solid proof-of-concept study with their investigations of molecular concentration profiles of several substances [34, 35]. These studies paved the way for versatile in vivo application of Raman spectroscopy in many fields comprising diagnosis and absorption studies.

17.3.2 Analysis of Human Skin Physiology and Pathological States

Confocal Raman microscopy represents a beneficial method for comprehensive analysis of skin physiology and pathophysiology. Due to the significant spectral contrast of the major skin compounds, such as lipids, amino acids and proteins, it is possible to differentiate between different skin layers like epidermis and dermis, as well as skin's appendages, i.e. follicles and glands. Compared to healthy tissue, pathological processes can also often be detected by changes in the Raman spectral peak patterns.

The first Raman investigations on excised human skin were performed in the early 90s, and compared to IR spectroscopy analysis for evaluation of the skin physiology in vitro. Excised human cadaver skin and isolated stratum corneum were used to prove the applicability of Raman microscopy for skin research [36, 37]. In addition, the individual spectral bands of the acquired Raman spectra were assigned to the corresponding endogenous skin components. Table 17.1 summarizes the most specific bands recognized in Raman spectra obtained from human skin.

There are two major sources for excised human skin: cadaver skin, removed from deceased humans and human skin obtained from plastic surgery. However, the sources for human skin obtained from surgery are rather limited. For cadaver skin, freshness

Table 17.1 Assignment of spectral bands in a representative Raman spectrum of healthy human skin. Reprinted from [18] with permission from Elsevier including data from [37]

Raman shift (rel. cm^{-1})	Assignment
565	ν (SS)
600	ρ (H)
623	ν (CS)
644	ν (CS) amide 4
746	ρ (CH_2) in phase
827	δ (CCH) aliphatic
850	δ (CCH) aromatic
883	δ (Ch_2), ν (CC), ν (CN)
931	ρ (CH_3) terminal, ν (CC) α-helix
956	ρ (CH_3), δ (CCH) alkenic
1002	ν (CC) aromatic ring
1031	ν (CC) skeletal cis
1062	ν (CC) skeletal trans
1082	ν (CC) skeletal random
1126	ν (CC) skeletal trans
1155	ν (CC), δ (COH)
1172	ν (CC)
1244	δ (CH_2) wagging, ν (CN)amide 3 disordered
1274	ν (CN), δ (NH) amide 3 α-helix
1296	δ (CH_2)
1385	δ (CH_3) symmetric
1421	δ (CH_3)
1438	δ (CH_2) scissoring
1552	δ (NH), ν (CN) amide 2
1585	ν (C=C) alkenic
1652	ν (C=O) amide 1 α-helix
1743	ν (C=O) amide 1 lipid
1768	ν (COO)
2723	ν (CH) aliphatic
2852	ν (CH_2) symmetric
2883	ν (CH_2) asymmetric
2931	ν (CH_3) symmetric
2958	ν (CH_3) asymmetric
3050	ν (CH) alkenic
3280	ν (OH) of H_2O

ν = stretch, ρ = rock, δ = deformation

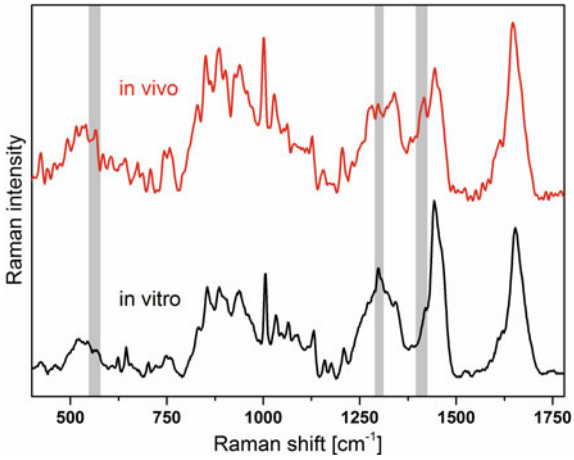

Fig. 17.8 Raman spectra recorded from human skin in vivo (red) compared to excised human skin in vitro (black). Reprinted from [18] with permission from Elsevier

and potential alterations by ongoing decomposition after death confine its suitability. The second source is preferable for research, as differences compared to the viable status are minimal assuring direct usage after excision and storage in frozen state. For illustration, Fig. 17.8 depicts Raman spectra obtained from human skin in vivo, depicted in red and excised human skin in vitro, depicted in black. The spectra were taken from the stratum corneum of a healthy female volunteer in vivo and excised female abdominal skin obtained from plastic surgery. Very little differences between the two spectra are detectable (highlighted in Fig. 17.8), due to lipid residues on the skin surface upon excision.

Besides the analysis of freshly excised or cadaver skin, Raman microscopy has successfully been used to investigate the skin decomposition of the about 5200-year-old iceman, found in Southern Tyrolia [38]. The mummy's skin showed protein degradation, oxidized olefinic bonds but unaltered lipids compared to freshly freeze-dried skin samples. The same group performed a comprehensive analysis of keratotic tissues like skin, callus, hair and nail. In this context, they were able to detect differences in the sulphur content and further structural differences attributable to variations in the amino acid [39].

Recently, the suitability of preparation techniques for human skin tissue sections was investigated [40]. Unprocessed and formalin fixed as well as paraffin-processed and subsequently dewaxed skin samples from human cadaver hand and thigh were compared. It was revealed that the dewaxing procedure also removed most of the stratum corneum lipids, influencing further differentiation between different anatomical sites. Raman spectroscopy was also applied for investigation of the skin hydration status. Isolated stratum corneum was exposed to different humidity conditions [3]. The ratio between bound and unbound water influenced the lipid and protein organization, thus indicating a direct correlation of the skin barrier function and its hydration status.

Furthermore, structural changes of full thickness skin during uniaxial stress obtained from cadaver thighs were tested mechanically and compared to Raman spectroscopy analysis [41]. In another study, externally applied stretching forces were correlated to changes in protein and lipid conformation of isolated stratum corneum [42]. Approximately after 9% deformation skin structure reached the plateau in disorganization.

17.3.2.1 In Vitro Skin Diagnosis

Besides exploring skin physiology, Raman spectroscopy and microscopy has gained a great interest for investigation of skin pathophysiological states and for diagnosis. In this context, a wide range of diagnostic applications of confocal Raman microscopy has been established so far [43]. Biopsies of potentially cancerous human skin have been evaluated by Raman microscopy. Comparison of individual Raman spectra of excised skin with melanoma, pigmented nevi, cell carcinoma, seborrheic keratosis, and normal skin has shown less intensity of amid I and increased lipid Raman bands in diseased skin [44]. In addition, the implementation of neural networks in this study, as an automated discrimination tool, allowed for discrimination between different disease states with 85% sensitivity and 99% specificity.

In the context of diagnosis, a very important challenge to overcome was to discriminate healthy from diseased skin. For example, basal cell carcinoma (BCC) were differentiated from their surrounding tissue [45, 46]. Interestingly, hierarchical cluster analysis allowed for differentiation between dermis and BCC, but not between epidermis and BCC. Furthermore, the reduction of collagen in nodular BCC surrounding dermis was detected. In addition, Raman imaging was compared to the state-of-the-art staining methods. After analyzing a wide range of biopsies, discrimination between the different cancer types, BCC, squamous cell carcinoma (SCC), melanoma and normal skin was successfully shown [47].

Raman microscopy also was evaluated as an upcoming technique for differentiation between normal and diseased excised skin, as well as between different types of skin diseases. In this context, the challenge was to establish and optimize an algorithm for automated data evaluation. Established algorithms allow for their clinical application, which is already a big step forward. Although, for providing an alternative to established histopathologic methods, further improvements in cost effectiveness and simplified handling are necessary.

The presented work proves the versatility of different in vitro applications of Raman microscopy ranging from basic skin analysis performed on excised human skin up to identification of pathological states and diagnosis.

17.3.3 Skin Penetration and Permeation Studies

The penetration and permeation of chemicals and especially pharmaceutics into and through the skin are the focus of many studies in skin research, since Raman spectroscopy allows for non invasive analysis of the tissue. The method also enables differentiation between skin and penetrant, provided that the substance under investigation fulfils the requirement of adequate spectral contrast in comparison to the skin. If the spectra of the penetrant and the skin itself are too similar, it is not possible to follow the penetration of the substance into the tissue. Although mathematical algorithms have been developed for estimation of dermal drug absorption that consider chemical properties of the penetrant and exposure time [48], for the collection of reliable data, the execution of experiments in vivo or in vitro systems is irreplaceable.

Besides the skin itself, the characterization of the substance under investigation is an important part in penetration experiments. Raman spectroscopy has been used for years for drug product development and characterization [49, 50]. The method even allows for the distinction between drug and single excipients of a formulation. Based on these abilities, Raman is used for quality control of drug products and determination of drug content in semi-solid formulations [51]. Since the principle of Raman spectroscopy is based on the molecular structure of a compound, it is possible to detect disintegration of substances due to the dissolution of chemical bonds and the subsequent changes in the corresponding Raman spectra, as well as the discrimination between different polymorphs [52].

In addition, the conversion of a prodrug into an active drug upon interaction with pig skin tissue can also be observed as shown by Zhang et al. [53, 54]. The group monitored the transformation of two prodrugs: they visualized the dephosphorylation of resveratrol triphosphate in skin by imaging the penetration of the substance in steamed and intact pig skin. Upon penetration into the intact skin sample, resveratrol triphosphate was metabolized to its active form by skin enzymes, whereas on the steamed sample the enzymes were inactive. The group also imaged the transformation of a pro-5-fluorouracil (pro-5FU) into 5-fluorouracil. Zhang et al. investigated the penetration of pro-5FU and 5-FU at two different temperatures and showed high concentrations of drug at 12 μm below the stratum corneum (SC) with correspondingly low amounts of the prodrug in this area (Fig. 17.9). Additionally, they showed that pure 5-FU was not able to penetrate as deeply into the tissue as the penetration enhancing prodrug. These studies highlight Raman as an elegant approach to study drug penetration behavior in skin and elucidate the pharmacokinetic profile of a substance.

It has been shown in several studies that surfactants can affect the permeability of the skin barrier by modifying the lipid structure of the tissue by fluidization or polarity alteration [55]. Anigbogu et al. investigated the penetration enhancing effect of dimethyl sulfoxide (DMSO) on human stratum corneum with Fourier-transformed Raman spectroscopy [56]. After one hour of incubation, the keratin in the SC of the skin sample exhibited a change in conformation from α-helical to β-sheet. Anigbogu et al. also observed interactions with lipids and state an altering effect of DMSO on

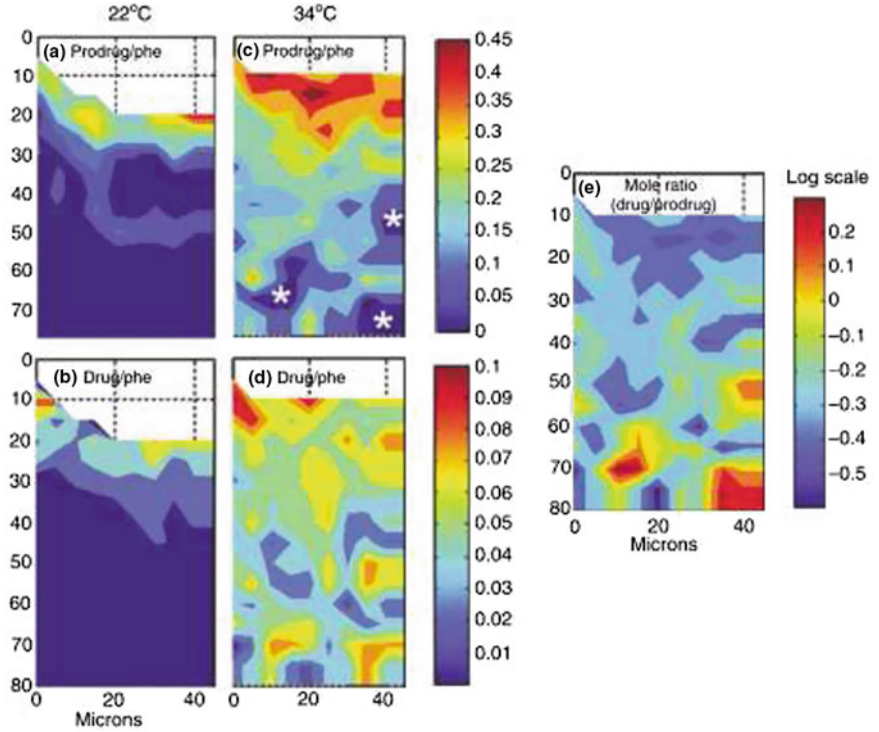

Fig. 17.9 Spatially resolved visualization of 1-ethyloxycarbonyl-5-fluorouracil (prodrug) (**a**, **c**) and of 5-fluoruracil (drug) (**b**, **d**) after penetration at 22 and 34 °C, respectively. Regions in the epidermis with a high concentration of drug (red) correspond to relatively low prodrug concentrations as indicated by asterisks in (**c**). The mole ratio of drug and prodrug is depicted in (**e**). Reprinted by permission from Macmillan Publishers Ltd: Journal of Investigative Dermatology [53], copyright 2007

the SC lipid organization. By changing the natural lipid structure of the skin, the penetration of additional substances into the skin is promoted. Based on these findings, the effect of penetration enhancers on drug delivery to human skin has also been the focus of several studies in vitro and in vivo [57–59]. Tfayli et al. investigated the penetration of metronidazole in excised human skin with CRM [60]. They applied metronidazole with the penetration enhancing 2-(2-ethoxyethoxy) ethanol on the skin and were able to detect the specific Raman bands down to 40 μm within the sample. To verify their results, Tfayli et al. cryosectioned the skin samples and detected the substance at a similar depth in the slices as they did with Raman depth profiling. The same group showed in a subsequent study that temporally resolved tracking of caffeine in excised human skin is possible [61]. Franzen et al. performed quantitative depth profiling of caffeine in excised human skin [17]. After incubating excised human skin with different concentrations of caffeine, the authors performed drug quantification by established tissue segmentation followed by drug extraction

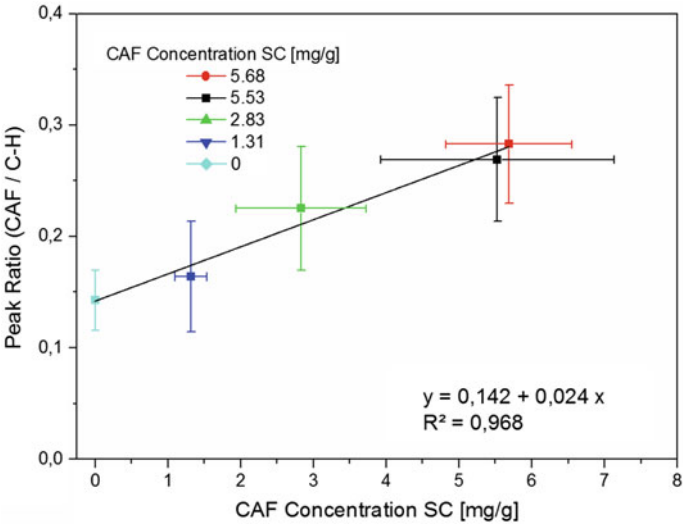

Fig. 17.10 Correlation of caffeine (CAF) quantification within human stratum corneum (SC) performed by destructive extraction/quantification versus Raman microscopy. Adapted from [17] with permission from WILEY-VCH Verlag GmbH & Co. KGaA, Weinheim

and quantification as well as by confocal Raman microscopy. They could successfully quantify caffeine in different depth by applying the peak correlation method. Comparing the two methods resulted on a good correlation ($R^2 = 0.968$) as depicted in Fig. 17.10.

Penetration studies with CRM are also performed in different in vitro systems. In a study on pig skin, Förster et al. investigated the penetration enhancement effect of several PEG solutions and their effect on skin absorption of retinol [8]. They also performed Franz diffusion cell experiments and were able to correlate their findings with the Raman data showing that CRM provides useful additional data in these kinds of investigations.

Besides conventional Raman spectroscopy, non-linear techniques like SRS and CARS are used to evaluate the penetration of substances into skin tissue. Belsey et al. used SRS to study the penetration of ibuprofen and propylene glycol in pig skin to visualize the transport pathway and crystallization of the drug [62].

CRM can also be applied in addition to IR spectroscopy to investigate the penetration behavior of substances. Xiao et al. examined the penetration of dimyristoylphosphatidylcholine and 1,2-dipalmitoylphosphatidylcholine into pig-skin with this approach [63, 64]. While IR spectroscopy provides information about the relative concentration of molecular species like endogenous and exogenous lipids as well as proteins, CRM allows for the chemical examination of the sample with high resolution. The same combination of spectroscopic measurements was applied by another group to monitor and compare the penetration and distribution of sodium dodecyl sulfate (SDS) in human and in pig skin [65]. They found that SDS penetrates

in a time and temperature dependent manner into the skin tissue with a slightly higher permeability through the SC of pig skin.

Comparison of penetration abilities of different oils can also be performed by CRM and was investigated by the group of Choe et al. who did several experiments on pig and human skin [66, 67]. Choe et al. compared several data interpretation methods and showed that the investigated oils do not penetrate deeper than 10 μm into the SC in vivo (human) and in vitro (pig skin).

Since in vivo experiments are regarded as the gold standard of penetration studies, many groups focus on performing investigations on human volunteers. The interaction of penetration enhancers with human skin is also monitored in vivo by several groups. The penetration behavior and distribution of DMSO in the skin tissue were investigated by Caspers et al. [68]. They showed that DMSO passed through the SC within 20 min, but traces were still detected after days in the skin. In addition, they observed changes in the amide I region on the skin surface upon DMSO application.

Pudney et al. compared the penetration of trans-retinol in combination with the penetration enhancer propylene glycol (PG) versus a triglyceride-containing formulation in vivo [58, 59]. They showed that trans-retinol in PG penetrates deeply into the human skin and can be found in the viable epidermis, whereas in combination with the triglyceride, trans-retinol hardly penetrates at all. They also showed that when using oleic acid, which is a lipid fluidizer, a better delivery of trans-retinol in the skin can be observed.

The penetration of ibuprofen in PG solutions was the object of investigation in a study conducted in 2013 by Mateus et al. Here they compared the penetration of the drug in vivo with results previously obtained in vitro by tape stripping and HPLC [69]. Their findings confirmed that in vitro data were similar to measurements in vivo. Recently, niacinamide permeation from a range of vehicles was investigated in vitro by HPLC and compared to in vivo results obtained by CRM [70]. The amount of niacinamide permeated through skin in vitro was linearly proportional to the intensity of the niacinamide signal that was determined in the SC in vivo by CRM.

In the research field of cosmetics, Raman spectroscopy was already successfully used for assessment of the protective capacity of sunscreen. Egawa et al. investigated trans-urocanic acid (UCA) in the stratum corneum of volunteers by CRM [71]. T-UCA converts to cis-UCA upon UV exposure. The concentration of t-UCA in a depth from 0 to 12 μm was calculated in a time interval of one year and it was found that the application of sunscreen in fact hinders the conversion of t-UCA to c-UCA. These findings were confirmed by a later study that combined CRM measurements with HPLC and tape stripping in vivo [72].

17.3.4 In Vitro Skin Models

In the last few decades, scientists were attracted to find suitable alternatives to in vivo animal testing. In this context, the current trend aims for a reduction in the number of

used animals, refinement of testing to reduce animal suffering, as well as replacing animal testing whenever it is possible.

There is a variety of established in vitro skin models ranging from excised human/animal skin, models based on cultivated monolayers of skin cells, or cell co-cultures, up to 3D tissue models depending on the application. Cytotoxicity and immune response assays, as well as penetration and permeation experiments, are only some of the studies performed using diverse in vitro models. In this chapter, different skin models as well as their application in the field of skin research will be evaluated.

17.3.4.1 Snakeskin Models

With its wide availability and the absence of ethical and hazardous restrictions, shed snake skin was in the center of attention as a potential model for the human skin in the beginning of the 90s. The Raman spectra of different snake skins were evaluated and compared to mammalian skin samples [37, 73]. Besides a significant autofluorescence, only little difference were detected between different snake species. Due to less ordered lipids in snakeskin, the variability in permeation is found to be a big disadvantage of the model. In addition to that, Raman microscopy has proved the difference in the predominant secondary protein structure between mammalian (α-helix) and reptilian keratotic materials (β-sheet) [74].

Consequently, due to the significant differences in the composition and the structure between human and reptile skin, reptile skin is rarely used in today's skin research.

17.3.4.2 Porcine Skin Models - In Vitro Physiological Evaluation and Penetration Studies

Porcine (pig) skin is recognized as the closest animal model for human skin. Regarding penetration experiments, porcine skin represents the most frequently used human skin substitute due to its accessibility. Penetration and permeation testing through porcine skin using Raman microscopy have already been described in literature [75, 76]. Comparison of Raman spectral features of excised human and porcine skin visualized some differences, as well as certain comparability, which proved the potential of the porcine skin model [77]. In addition, the physiology of excised pig skin was evaluated using Raman microscopy [78].

Raman is a valuable tool for evaluation of stratum corneum removal by tape stripping, cyanoacrylate biopsies and trypsinization [79]. Acquisition of confocal Raman depth profiles, as a non-invasive method, allow for correlation of the stratum corneum-epidermis border and the water content within the individual skin samples. After the aforementioned procedures, the remaining stratum corneum was detected by Raman microscopy and verified by histological cuts.

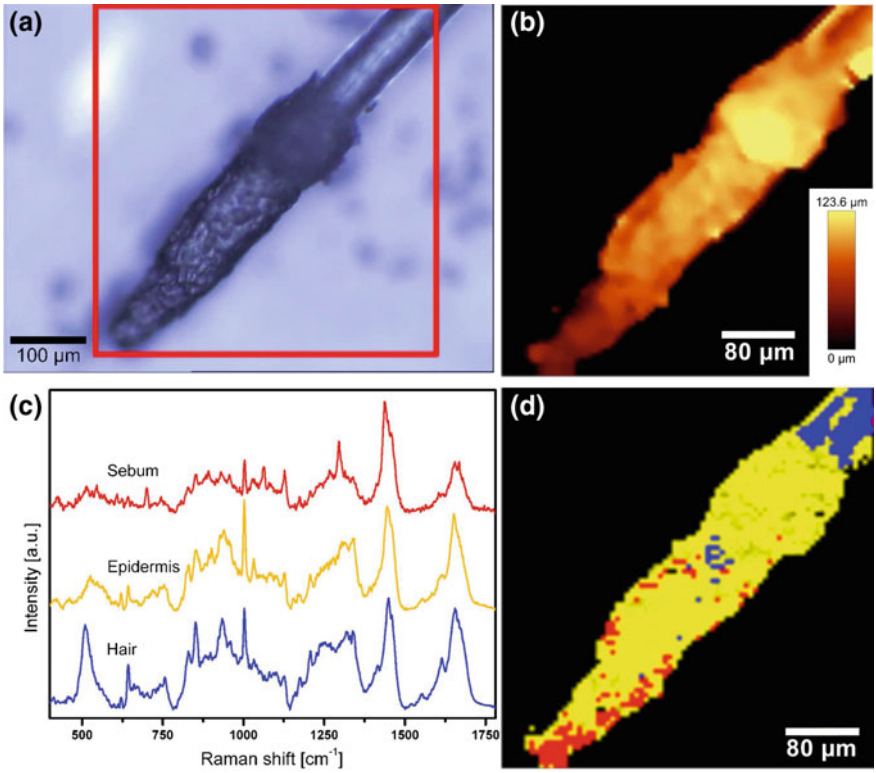

Fig. 17.11 **a** Light microscopy image of an excised hair follicle. **b** Surface topography map of an excised hair follicle. **c** Individual Raman spectra of the chemical components in the hair follicle. **d** False color Raman image displaying the component distribution on the excised hair follicle. Reprinted [2]

Raman imaging was applied for visualization of cross sections of porcine hair follicles as potential application sites for drug delivery [2]. The anatomical composition of the follicle could be illustrated without any markers or dyes and a spectral comparison hinted towards the suitability of porcine hair follicles as models for human hair follicles. Furthermore, cyanoacrylate biopsies were analyzed with confocal Raman microscopy and optical profilometry (TrueSurface^{TM}) to gain three-dimensional information of such structured objects and evaluate whether the follicles remain intact during excision. As Fig. 17.11 depicts, the follicles were covered with a thin epidermal layer, thus proving their intactness after excision.

It has been shown that confocal Raman depth profiling can also be used to determine the quality and thickness of porcine adipose tissue in the food industry in order to determine thickness and composition of the outer and inner fat layer [80].

Confocal Raman microscopy is often combined with infrared (IR) imaging. In one of the studies, these complementary techniques were applied to follow up pen-

etration of liposomes made from different deuterated lipids into excised pig skin [63, 64]. IR imaging was performed on histological skin sections and compared to non-destructive depth profiles obtained by confocal Raman microscopy. Different lipids had different penetration depths ranging from 15 to 35 μm after 24 h. In another study, the penetration of deuterated sodium dodecyl sulfate on human and porcine skin was examined and Raman data were compared to IR data [65]. Histological sections were visualized by Raman and IR microscopy and the peaks representing the carbon-deuterium stretching vibrations, which appear in the silent region, could be detected. A slightly deeper penetration was recognized in hairless pig skin than in human abdominal skin.

In conclusion, the aforementioned studies highlight confocal Raman microscopy as powerful and upcoming technique for formulation development and drug delivery investigations.

17.3.4.3 Tissue Engineered Skin Models

Due to the limited availability and viability of excised human and porcine skin, the cultivation of cells represents a valuable approach for skin research. Human or animal cell lines and even primary cells can be cultivated as monolayers, cell co-cultures or complex 3D tissue models, all of them individually important for a variety of tests, ranging from cytotoxicity and immune response assays up to penetration and permeation experiments.

Replacement of animal tests with non-animal alternatives is strongly encouraged especially in the development of cosmetics and skin care products, whenever this is possible. Therefore, tissue engineered skin reconstructions or lipid-based models are gaining more and more attention. In this context, vibrational spectroscopy techniques were used for comparison of cultured adult human keratinocytes on a collagen substrate and excised human abdominal skin [81]. The engineered skin model contained less carotenoids than the excised human tissue, which was observed by following differences in the C-S bond vibration. Another type of reconstructed human epidermis was used to monitor photo damage during simulated solar radiation [82]. The decrease of the DNA representing Raman spectral feature was observed indicated a reduced viability of the skin model after photo damage.

Skin models based on cultivated cells are commercially available, mostly based on immortalized human epithelial keratinocyte cell lines like the human adult low calcium high temperature keratinocytes (HaCaT). For advanced tissue engineering, different cell types need to be combined for artificial skin constructs. In this context, Raman microscopy was successfully used to discriminate between primary human fibroblasts, keratinocytes and melanocytes, as well as HaCaT cells [83].

An in vitro model for psoriatic skin derived from primary human material was also investigated by Raman microscopy and changes in the secondary structure of proteins were elucidated [84].

Toxicity studies were also already performed using Raman microscopy. In one of the studies, $HgCl_2$ and the pesticide chlorpyriphos were investigated in combi-

nation with skin cells [85, 86]. Raman spectroscopy revealed several structural and biochemical alterations even after application of non-cytotoxic concentrations. In addition, alterations in amid and CH deformation bands could be correlated with a high passage number in HaCaT cells for instance [87]. Since the same alterations appeared in the cancerogenic A5RT3 cell line, an influence on the tumorigenic development is assumed.

Confocal Raman microscopy shows a high potential to be a valuable characterization tool in the field of tissue engineering since it overcomes certain limitations of histopathology and allows for getting deeper insight into complex reconstructed human skin models.

17.3.4.4 Lipid-Based Skin Models

Lipid-coated membranes represent another approach to mimic the barrier function of the human skin and to investigate penetration processes. In this context, Raman mapping was applied to prove the homogeneity of the lipid-coated model membranes [88] and for detection of crystalline structures in lipid mixtures mimicking the lipids of stratum corneum [89].

Raman and Fourier transformed infrared spectroscopy (FTIR) were combined for a three-dimensional evaluation of the penetration of dithranol in artificial acceptor membranes [90]. Lateral drug distribution was visualized by FTIR mapping and confocal Raman microscopy detected the active ingredient down to 49 μm depth in the model membrane.

Using lipid-based skin models, the influence of penetration enhancers on ceramides as the main skin lipid component can be investigated [91]. Changes in specific spectral features of the ceramides like double-bonds upon usage of different penetration enhancers were successfully followed by Raman microscopy.

Raman and IR spectroscopy represent two complementary vibrational techniques used for substance localization, as well as for elucidation of lipid orientation and organization in lipid-based skin models.

17.4 Conclusion and Outlook

Confocal Raman microscopy has already proven its value as a versatile analytical tool for a wide array of studies in the field of skin research, ranging from analysis of physiological and pathophysiological states including diagnosis up to investigations of skin interactions with chemicals and therapeutics. Investigating drug delivery through the skin with non-invasive Raman analysis is currently attracting huge interest in the field of pharmaceutics. However, complex composition of drug delivery systems requires advanced multivariate data analysis for their spectral characterization, especially upon interaction with skin. Well established methods for skin absorption analysis like Franz diffusion cell testing and tape-stripping combined

with HPLC are beneficial, but destructive and limited to quantitative measurements of the substance penetration and permeation through the skin. Raman spectroscopy overcomes these limitations with its ability to monitor the substance interactions with skin using a non-invasive approach.

Physiological investigations with Raman spectroscopy imply examination of skin structure, hydration status, and determination of endogenous compounds like the natural moisturizing factor. Furthermore, Raman is used for monitoring the interaction of chemicals with skin as well as potential damage of the tissue. The method is applied in penetration studies, in the development of pharmaceutics but also for risk assessment of new chemicals.

Raman spectroscopy and CRM allow for non-invasive, spatially resolved, and chemically selective analysis, such as depth profiling. This is of great importance for sample investigation in vitro and even allows the execution of experiments in vivo. Especially for diagnosis of pathological skin conditions as cancer, this aspect is very promising and holds great potential for future advances in the field of dermatology.

Non-linear Raman techniques like coherent anti-Stokes Raman scattering (CARS) and stimulated Raman scattering (SRS) as complementary approaches to spontaneous Raman spectroscopy are currently developing fast and will most likely be more employed in the future to target various questions in the field of dermatology.

In terms of in vivo applications, needle and fiber optics based Raman probes already allow for advanced diagnosis as well as surgery guidance for accurate excision of tumorous tissue. Future technical improvements will pave the way for facilitated data acquisition and use of Raman spectroscopy in clinics on a daily basis.

References

1. K. Myer, H. Maibach, Skin Res. Technol. **19**(3), 213 (2013)
2. L. Franzen, C. Mathes, S. Hansen, M. Windbergs, J. Biomed. Opt. **18**(6), 061210 (2013)
3. R. Vyumvuhore, A. Tfayli, H. Duplan, A. Delalleau, M. Manfait, A. Baillet-Guffroy, Analyst **138**(14), 4103 (2013)
4. M.E. Darvin, J.W. Fluhr, P. Caspers, A. Van Der Pool, H. Richter, A. Patzelt, W. Sterry, J. Lademann, Exp. Dermatol. **18**(12), 1060 (2009)
5. P. Philipsen, L. Knudsen, M. Gniadecka, M. Ravnbak, H. Wulf, Photochem. Photobiol. Sci. **12**(5), 770 (2013)
6. E. Brauchle, S. Noor, E. Holtorf, C. Garbe, K. Schenke-Layland, C. Busch, Clin. Exp. Dermatol. **39**(5), 636 (2014)
7. L. Chrit, P. Bastien, B. Biatry, J.T. Simonnet, A. Potter, A. Minondo, F. Flament, R. Bazin, G. Sockalingum, F. Leroy et al., Biopolymers **85**(4), 359 (2007)
8. M. Förster, M.A. Bolzinger, D. Ach, G. Montagnac, S. Briançon, Pharm. Res. **28**(4), 858 (2011)
9. H.C. Broding, A. van der Pol, J. de Sterke, C. Monsé, M. Fartasch, T. Brüning, JDDG: J. der Deutsch. Dermatol. Ges. **9**(8), 618 (2011)
10. C.W. Freudiger, W. Min, B.G. Saar, S. Lu, G.R. Holtom, C. He, J.C. Tsai, J.X. Kang, X.S. Xie, Science **322**(5909), 1857 (2008)
11. A. Zumbusch, G.R. Holtom, X.S. Xie, Phys. Rev. Lett. **82**(20), 4142 (1999)
12. B. Kann, H.L. Offerhaus, M. Windbergs, C. Otto, Adv. Drug Deliv. Rev. (2015)
13. L. Franzen, L. Vidlářová, K.H. Kostka, U.F. Schaefer, M. Windbergs, Exp. Dermatol. **22**(1), 54 (2013)

14. R. Na, I.M. Stender, M. Henriksen, H.C. Wulf, J. Invest. Dermatol. **116**(4), 536 (2001)
15. S. Tfaili, G. Josse, C. Gobinet, J.F. Angiboust, M. Manfait, O. Piot, Analyst **137**(18), 4241 (2012)
16. T. Dai, B.M. Pikkula, L.V. Wang, B. Anvari, Phys. Med. Biol. **49**(21), 4861 (2004)
17. L. Franzen, J. Anderski, V. Planz, K.H. Kostka, M. Windbergs, Exp. Dermatol. **23**(12), 942 (2014)
18. L. Franzen, M. Windbergs, Adv. Drug Deliv. Rev. (2015)
19. L. Silveira Jr., B. Bodanese, R.A. Zangaro, M.T.T. Pacheco, Instrum Sci. Technol. **38**(4), 268 (2010)
20. M.G. Ramírez-Elías, J. Alda, F.J. Gonzalez, Appl. Spectrosc. **66**(6), 650 (2012)
21. H. Wang, J. Zhao, A.M. Lee, H. Lui, H. Zeng, Photodiagn. Photodyn. Ther. **9**(4), 299 (2012)
22. F. Bonnier, S.M. Ali, P. Knief, H. Lambkin, K. Flynn, V. McDonagh, C. Healy, T. Lee, F.M. Lyng, H.J. Byrne, Vib. Spectrosc. **61**, 124 (2012)
23. N.J. Everall, Spectroscopy **19**, 16 (2004)
24. N.J. Everall, Analyst **135**(10), 2512 (2010)
25. N.J. Everall, Appl. Spectrosc. **54**(10), 1515 (2000)
26. K. Baldwin, D. Batchelder, Appl. Spectrosc. **55**(5), 517 (2001)
27. J. Bruneel, J. Lassegues, C. Sourisseau, J. Raman Spectrosc. **33**(10), 815 (2002)
28. C. Xiao, C.R. Flach, C. Marcott, R. Mendelsohn, Appl. Spectrosc. **58**(4), 382 (2004)
29. L. Franzen, D. Selzer, J.W. Fluhr, U.F. Schaefer, M. Windbergs, Eur. J. Pharm. Biopharm. **84**(2), 437 (2013)
30. L. Franzen, J. Anderski, M. Windbergs, Eur. J. Pharm. Biopharm. (2015)
31. M.G. Shim, B.C. Wilson, J. Raman Spectrosc. **28**(2–3), 131 (1997)
32. M.G. Shim, B.C. Wilson, E. Marple, M. Wach, Appl. Spectrosc. **53**(6), 619 (1999)
33. P. Caspers, G. Lucassen, R. Wolthuis, H. Bruining, G. Puppels, BIOSPECTROSCOPY-NEW YORK- **4**, S31 (1998)
34. P.J. Caspers, G.W. Lucassen, E.A. Carter, H.A. Bruining, G.J. Puppels, J. Invest. Dermatol. **116**(3), 434 (2001)
35. P. Caspers, G. Lucassen, G. Puppels, Biophys. J. **85**(1), 572 (2003)
36. A. Williams, H. Edwards, B. Barry, Int. J. Pharm. **81**(2), R11 (1992)
37. B. Barry, H. Edwards, A. Williams, J. Raman Spectrosc. **23**(11), 641 (1992)
38. A.C. Williams, H.G. Edwards, B.W. Barry, Biochim. Biophys. Acta (BBA)-Protein Struct. Mol. Enzymol. **1246**(1), 98 (1995)
39. A. Williams, H. Edwards, B. Barry, J. Raman Spectrosc. **25**(1), 95 (1994)
40. S.M. Ali, F. Bonnier, A. Tfayli, H. Lambkin, K. Flynn, V. McDonagh, C. Healy, T.C. Lee, F.M. Lyng, H.J. Byrne, J. Biomed. Opt. **18**(6), 061202 (2013)
41. M. Gąsior-Głogowska, M. Komorowska, J. Hanuza, M. Mączka, A. Zając, M. Ptak, R. Będziński, M. Kobielarz, K. Maksymowicz, P. Kuropka et al., J. Mech. Behav. Biomed. Mater. **18**, 240 (2013)
42. R. Vyumvuhore, A. Tfayli, H. Duplan, A. Delalleau, M. Manfait, A. Baillet-Guffroy, J. Raman Spectrosc. **44**(8), 1077 (2013)
43. Q. Tu, C. Chang, Nanomed. Nanotechnol. Biol. Med. **8**(5), 545 (2012)
44. M. Gniadecka, P.A. Philipsen, S. Sigurdsson, S. Wessel, O.F. Nielsen, D.H. Christensen, J. Hercogova, K. Rossen, H.K. Thomsen, R. Gniadecki et al., J. Invest. Dermatol. **122**(2), 443 (2004)
45. A. Nijssen, K. Maquelin, L.F. Santos, P.J. Caspers, T.C.B. Schut, J.C. den Hollander, M.H. Neumann, G.J. Puppels, J. Biomed. Opt. **12**(3), 034004 (2007)
46. A. Nijssen, T.C.B. Schut, F. Heule, P.J. Caspers, D.P. Hayes, M.H. Neumann, G.J. Puppels, J. Invest. Dermatol. **119**(1), 64 (2002)
47. C.A. Lieber, S.K. Majumder, D. Billheimer, D.L. Ellis, A. Mahadevan-Jansen, J. Biomed. Opt. **13**(2), 024013 (2008)
48. R.L. Cleek, A.L. Bunge, Pharm. Res. **10**(4), 497 (1993)
49. C. Wang, T.J. Vickers, C.K. Mann, J. Pharm. Biomed. Anal. **16**(1), 87 (1997)
50. J. Breitenbach, W. Schrof, J. Neumann, Pharm. Res. **16**(7), 1109 (1999)

51. B. Gotter, W. Faubel, S. Heißler, J. Hein, R. Neubert, in *Journal of Physics: Conference Series*, vol. 214 (IOP Publishing, 2010), vol. 214, p. 012129
52. P.J. Larkin, M. Dabros, B. Sarsfield, E. Chan, J.T. Carriere, B.C. Smith, Appl. Spectrosc. **68**(7), 758 (2014)
53. G. Zhang, D.J. Moore, K.B. Sloan, C.R. Flach, R. Mendelsohn, J. Invest. Dermatol. **127**(5), 1205 (2007)
54. G. Zhang, C.R. Flach, R. Mendelsohn, J. Control. Release **123**(2), 141 (2007)
55. A.C. Williams, B.W. Barry, Adv. Drug Deliv. Rev. **64**, 128 (2012)
56. A.N. Anigbogu, A.C. Williams, B.W. Barry, H.G. Edwards, Int. J. Pharm. **125**(2), 265 (1995)
57. A. López, F. Llinares, C. Cortell, M. Herraez, Int. J. Pharm. **202**(1), 133 (2000)
58. M. Mélot, P.D. Pudney, A.M. Williamson, P.J. Caspers, A. Van Der Pol, G.J. Puppels, J. Control. Release **138**(1), 32 (2009)
59. P.D. Pudney, M. Mélot, P.J. Caspers, A. Van Der Pol, G.J. Puppels, Appl. Spectrosc. **61**(8), 804 (2007)
60. A. Tfayli, O. Piot, F. Pitre, M. Manfait, Eur. Biophys. J. **36**(8), 1049 (2007)
61. S. Tfaili, C. Gobinet, G. Josse, J.F. Angiboust, A. Baillet, M. Manfait, O. Piot, Anal. Bioanal. Chem. **405**(4), 1325 (2013)
62. N.A. Belsey, N.L. Garrett, L.R. Contreras-Rojas, A.J. Pickup-Gerlaugh, G.J. Price, J. Moger, R.H. Guy, J. Controlled Release **174**, 37 (2014)
63. C. Xiao, D.J. Moore, C.R. Flach, R. Mendelsohn, Vib. Spectrosc. **38**(1), 151 (2005)
64. C. Xiao, D.J. Moore, M.E. Rerek, C.R. Flach, R. Mendelsohn, J. Invest. Dermatol. **124**(3), 622 (2005)
65. G. Mao, C. Flach, R. Mendelsohn, R. Walters, Pharm. Res. **29**(8), 2189 (2012)
66. C. Choe, J. Lademann, M. Darvin, Skin Pharm. Physiol. **28**(6), 318 (2015)
67. C. Choe, J. Lademann, M.E. Darvin, J. Dermatol. Sci. (2015)
68. P.J. Caspers, A.C. Williams, E.A. Carter, H.G. Edwards, B.W. Barry, H.A. Bruining, G.J. Puppels, Pharm. Res. **19**(10), 1577 (2002)
69. R. Mateus, H. Abdalghafor, G. Oliveira, J. Hadgraft, M. Lane, Int. J. Pharm. **444**(1), 106 (2013)
70. D. Mohammed, P. Matts, J. Hadgraft, M. Lane, Pharm. Res. **31**(2), 394 (2014)
71. M. Egawa, H. Iwaki, Skin Res. Technol. **14**(4), 410 (2008)
72. M. Egawa, J. Nomura, H. Iwaki, Photochem. Photobiol. Sci. **9**(5), 730 (2010)
73. G. Howell et al., Analyst **119**(4), 563 (1994)
74. H. Edwards, D. Hunt, M. Sibley, Spectrochim. Acta Part A Mol. Biomol. Spectrosc. **54**(5), 745 (1998)
75. R.L. Bronaugh, R.F. Stewart, E.R. Congdon, Toxicol. Appl. Pharmacol. **62**(3), 481 (1982)
76. U. Jacobi, M. Kaiser, R. Toll, S. Mangelsdorf, H. Audring, N. Otberg, W. Sterry, J. Lademann, Skin Res. Technol. **13**(1), 19 (2007)
77. S. Tfaili, C. Gobinet, G. Josse, J.F. Angiboust, M. Manfait, O. Piot, Analyst **137**(16), 3673 (2012)
78. J. Wu, T. Polefka, Int. J. Cosmet. Sci. **30**(1), 47 (2008)
79. M. Förster, M. Bolzinger, M. Rovere, O. Damour, G. Montagnac, S. Briançon, Skin Pharmacol. Physiol. **24**(2), 103 (2011)
80. L.B. Lyndgaard, K.M. Sørensen, F. Berg, S.B. Engelsen, J. Raman Spectrosc. **43**(4), 482 (2012)
81. A. Tfayli, O. Piot, F. Draux, F. Pitre, M. Manfait, Biopolymers **87**(4), 261 (2007)
82. S. Ali, F. Bonnier, K. Ptasinski, H. Lambkin, K. Flynn, F. Lyng, H. Byrne, Analyst **138**(14), 3946 (2013)
83. M. Pudlas, S. Koch, C. Bolwien, S. Thude, N. Jenne, T. Hirth, H. Walles, K. Schenke-Layland, Tissue Eng. Part C: Methods **17**(10), 1027 (2011)
84. G. Bernard, M. Auger, J. Soucy, R. Pouliot, Biochim. Biophys. Acta (BBA)-Gen. Subj. **1770**(9), 1317 (2007)
85. G. Perna, M. Lastella, M. Lasalvia, E. Mezzenga, V. Capozzi, J. Mol. Struct. **834**, 182 (2007)
86. G. Perna, M. Lasalvia, P. D'Antonio, N. L'Abbate, V. Capozzi, J. Raman Spectrosc. **42**(4), 603 (2011)

87. P. Donfack, M. Rehders, K. Brix, P. Boukamp, A. Materny, J. Raman Spectrosc. **41**(1), 16 (2010)
88. M. Ochalek, S. Heissler, J. Wohlrab, R. Neubert, Eur. J. Pharm. Biopharm. **81**(1), 113 (2012)
89. A. Percot, M. Lafleur, Biophys. J. **81**(4), 2144 (2001)
90. B. Gotter, W. Faubel, R. Neubert, Eur. J. Pharm. Biopharm. **74**(1), 14 (2010)
91. A. Tfayli, E. Guillard, M. Manfait, A. Baillet-Guffroy, Analyst **137**(21), 5002 (2012)

Chapter 18
Characterization of Therapeutic Coatings on Medical Devices

Klaus Wormuth

Abstract Therapeutic coatings on medical devices such as catheters, guide wires and stents improve biocompatibility by favorably altering the chemical nature of the device/tissue or device/blood interface. Such coatings often minimize tissue damage (reduce friction), decrease chances for blood clot formation (prevent platelet adsorption), and improve the healing response (deliver drugs). Confocal Raman microscopy provides valuable information about biomedical coatings by, for example, facilitating the measurement of the thickness and swelling of friction-reducing hydrogel coatings on catheters, and by determining the distribution of drug within polymer-based a drug eluting coatings on stents. This chapter explores the application of Raman microscopy to the imaging of thin coatings of cross-linked poly(vinyl pyrrolidone) gels, parylene films, mixtures of dexamethasone with various polymethacrylates, and mixtures of rapamycin with hydrolysable (biodegradable) poly(lactide-co-glycolide) polymers. Raman microscopy measures the thickness and swelling of coatings, reveals the degree of mixing of drug and polymer, senses the hydrolysis of biodegradable polymers, and determines the polymorphic forms of drug present within thin therapeutic coatings on medical devices.

18.1 Background

The introduction of synthetic or modified natural materials ("biomaterials") into the human body for the treatment, augmentation, or replacement of tissue or organs presents significant challenges. First, the biomaterial must retain "biofunctionality" in the aggressive chemical, enzymatic and mechanical stress environments within the human body. Secondly, the biomaterial must exhibit "biocompatibility" and thus not induce allergic, toxic or carcinogenic reactions, or create blood clots. Ideal biocompatibility means the body "accepts" the biomaterial: the surface of the implanted material induces the same biochemical reactions induced by tissues in the body [1, 2].

K. Wormuth (✉)
SurModics, Inc., 9924 West 74th St., Eden Prairie, MN 55344, USA
e-mail: kwormuth@surmodics.com
URL: http://www.surmodics.com

J. Toporski et al. (eds.), *Confocal Raman Microscopy*, Springer Series in Surface Sciences 66, https://doi.org/10.1007/978-3-319-75380-5_18

Unfortunately, most implanted materials react non-ideally with the body, inducing a cascade of biochemical processes. Tissues surrounding an implant often react as if an injury or infection had occurred, and inflammation cells attack the implant. In the typical positive scenario, biocompatibility occurs through creation of a thin layer of fibrotic (scar) tissue without inflammation cells which encapsulates the implant and prevents further biochemical reactions [3].

The nature of the outer surface of the biomaterial influences the types of proteins which initially adsorb onto the implant surface, and thus influences cellular responses to the implant. Both surface chemistry (charge, polarity, hydrophilicity) and surface morphology (roughness, mechanical compliance) play a role in cell-biomaterial interactions. In general, hydrophilic surfaces are more biocompatible than hydrophobic surfaces [1]. Surface modification of biomaterials through application of "therapeutic coatings", coatings, which induce beneficial healing effects, is one approach for improving the biocompatibility of medical devices.

Therapeutic coatings for medical devices fall into two categories: passive and active. Upon coating a hydrophobic material with a hydrophilic gel, "passive" therapeutic effects occur as the medical device surface now presents the surrounding tissue with a soft, porous, hydrophilic surface filled with body fluids. In the case of temporary use medical devices such as catheters or guide wires, hydrophilic gels improve the ability to maneuver the device through arteries by providing a slippery low friction and non-thrombogenic surface between the device and the blood vessel walls. In the case of implanted devices, healthy tissue often grows into hydrophilic gels [1].

"Active" therapeutic coatings result from binding biochemically active materials (proteins, biopolymers) onto surfaces, which hopefully induce the biochemical reactions to favor biocompatibility [2]. Another type of active therapeutic coating controls the release of a drug into the tissue surrounding a device with the goal of inducing the proper healing responses in a localized area around the device [4]. Local drug delivery (with controlled release) offers significant advantages over systemic drug delivery (injections or tablets) by maintaining drug dosage within the therapeutic window and reducing toxic side effects (Fig. 18.1). One highly successful example of an active therapeutic coating on a medical device is the "drug-eluting stent" [4].

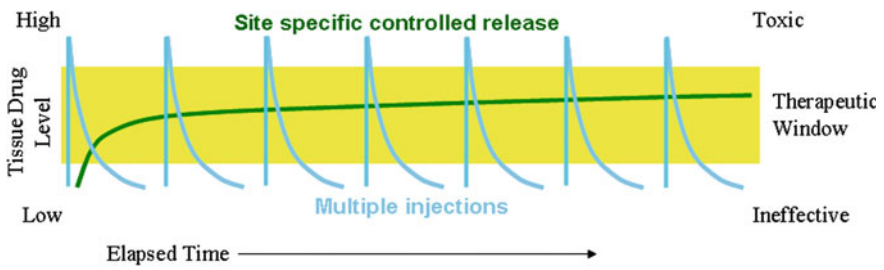

Fig. 18.1 Schematic illustration of drug level in tissue as a function of time. Comparison of multiple injections (blue) with site specific controlled drug delivery (green)

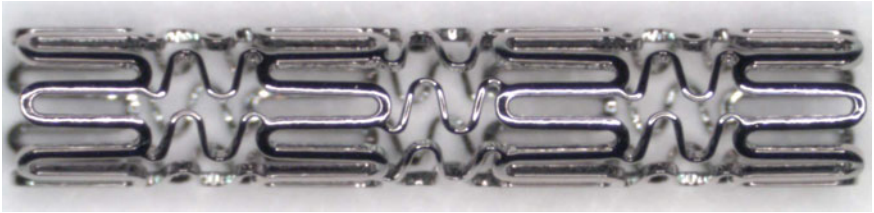

Fig. 18.2 Brightfield microscopy image of drug eluting stent (8 mm long Cordis Cypher® stent)

One option in the treatment of atherosclerosis of the heart involves implantation of a stent (Fig. 18.2), a wire mesh, which when inserted into a blood vessel opens blockages and restores blood flow, while mechanically preventing the re-collapse of the vessel. In some cases, stent implantation causes tissue damage and induces formation of excess scar tissue, which results in re-blockage of the artery (restenosis). Through delivery of an antiproliferative drug, such as rapamycin from a drug-eluting stent (a stent coated with a thin polymer coating containing drug), restenosis events are significantly reduced [4]. Formulation of drug eluting coatings remains a challenge since the coating must be thin and conformal, the polymer matrix must be tailored to incorporate high concentrations of drug and to control the rate or release (elution) of the drug, and the coating must withstand the severe deformations of the stent wires, which occur upon insertion of the stent into the blood vessel. Once the drug has eluted, the healing process should result in encapsulation of the stent wires into healthy tissue within the walls of the blood vessel.

Critical to the development of a successful therapeutic coating is a thorough physical and chemical characterization of the coating prior to implantation (in vitro), along with characterization of the interaction of the coated medical device with tissue after implantation in the body (in vivo). For hydrophilic gel coatings, questions arise as to the coating thickness, uniformity of thickness, and degree of swelling. For drug eluting coatings, additional questions arise as to the homogeneity of mixing of drug and polymer, the polymorphic form of the drug present, and the mechanisms by which the drug elutes from the polymer. As highlighted in this chapter, confocal Raman microscopy provides some insights and answers to these questions.

18.2 Passive Therapeutic Coatings

18.2.1 Coating Thickness

Coating thickness is sometimes surprisingly difficult to accurately measure. Coating durability, degree of swelling, and biochemical efficacy often correlate with coating thickness. From experience, various methods successfully measure coat-

ing thickness, but each method exhibits advantages and disadvantages. Confocal Raman microscopy provides one useful in situ method for the measurement of coating thickness.

Creation of a sharp step between coated and uncoated regions allows the step height (coating thickness) to be measured by electron microscopy, interferometry or atomic force microscopy (AFM) methods. While creation of a clean, sharp step is sometimes possible via scraping or cryo-fracture, the method requires coatings with poor adhesion to the substrate, or coatings, which have significantly different mechanical properties compared to the substrate such that the coating partially cracks off the substrate and creates a step between coated and uncoated regions. However, the method does destroy the sample, and sampling - the ability to measure coating thickness at many locations to gain statistical confidence - is problematic.

If the refractive index of the coating differs significantly from that of the substrate (for example polymer coatings on metal or glass), interferometric methods sometimes successfully measure coating thickness. In certain cases, the interference fringes created by light interacting with the air/coating interface and the coating/substrate interface may allow creation of images of the distribution of coating thickness over a region with nanometer vertical resolution (z) and optical resolution in x-y [5]. In commercially available instruments, the refractive index difference between substrate and coating must be significant (greater than about 0.5) and the coating must be thicker than 1 or 2 μm for the method to be successful.

Confocal Raman microscopy also allows measurement of coating thickness of polymers on various substrates. For example, consider a coating of dry hydrophilic polymer (cross-linked polyvinyl pyrrolidone) on glass. A cross-sectional image created by mapping the intensity of the polymer Raman bands (carbon-hydrogen stretch region where air and glass exhibit no signal) indicates regions where polymer coating is present versus regions where polymer was scraped off the glass (no Raman signal) (Fig. 18.3). Note that the image was created using a 100× microscope objective with a numerical aperture (NA) of 0.90 without application of immersion oil (dry). A plot of the integrated intensity as a function of vertical (z) distance over one section of this image shows a peaked curve (Fig. 18.3). Upon using the assumption that the actual interface appears at 50% of the maximum Raman intensity, the coating thickness in this region is determined to be about 1.8 μm (Fig. 18.3).

The 50% maximum intensity method is applied with the assumption that the vertical resolution at each interface in the confocal Raman measurement is at best about 0.5 μm but likely poorer [6, 7]. Despite the resolution limitations, the thickness measured by confocal Raman microscopy compares favorably with the values obtained the AFM and interferometric methods, for both the coating shown in Fig. 18.3 also for a similar sample with a slightly thicker coating (Table 18.1).

Especially for thicker samples, use of a dry microscope objective becomes problematic. Spherical aberrations occur at the interfaces between the microscope objective, air, and the sample, which compress the vertical axis in the measurement and result in significantly smaller values of coating thickness compared to those obtained from other methods [6, 7]. However, use of oil immersion fluid to reduce spherical aberration is not practical for the polymer coatings examined here, since the coatings

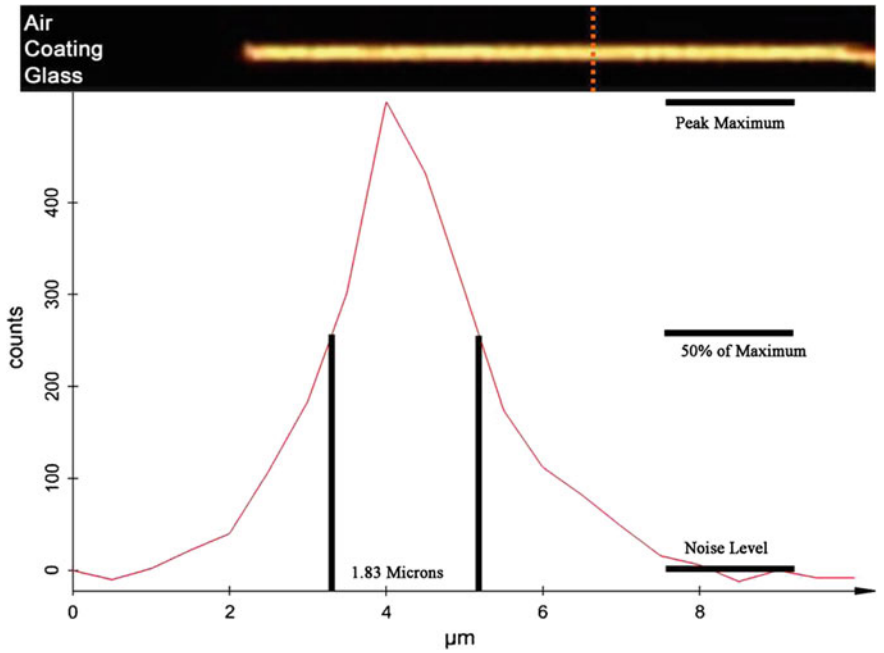

Fig. 18.3 Top: Raman microscopy cross-section image of poly(vinyl pyrollidone) hydrogel coating on glass. Bottom: Profile of Raman signal intensity (2800–3100 rel. cm^{-1} band) through coating along path indicated by dashed red line

Table 18.1 Coating thickness of Poly(vinyl pyrrolidone) hydrogels on glass (µm)

Sample	AFM-Step	I-Step	I-Thickness	Raman	Raman*
1.	2.2	2.2	2.3	1.8	2.7
2.	2.5	2.5	2.9	2.1	3.1

AFM-Step = atomic force microscopy, height of step between coated and uncoated
I-Step = interferometry, height of step between coated and uncoated
I-Thickness = interferometry thickness method (subtraction of fringes at interfaces)
Raman = 50% intensity method shown in Fig. 18.3, 100× dry objective (NA = 0.90)
Raman* = Raman value multiplied by refractive index of polymer (1.53)

absorb immersion oil. Another way to approximately correct for spherical aberrations is to multiply the vertical scale of the confocal Raman measurement by the refractive index of the polymer (1.53 for polyvinyl pyrrolidone). For the coatings examined above, the "corrected" thickness values appear somewhat greater than those obtained with the AFM and interferometry methods, but still within the estimated resolution limits of the Raman method (Table 18.1).

Vapor deposition of parylene, a hydrophobic barrier polymer used in medical device applications, creates coatings of extremely uniform thickness [8]. Knowledge of the mass of coating applied, the density of the coating (1.283 g/cm^3) and

Table 18.2 Coating thickness of Parylene on Silicon Wafer (μm)

Sample	Calculated	AFM-Step	I-Step	I-Thickness	Raman	Raman*
Wafer 1	1.7	1.6	1.5	1.9	1.0	1.7
Wafer 2	5.5	**	4.9	5.2	2.8	4.6

Abbreviations and descriptions as per Table 18.1
Average of 5 measurements per sample
*Raman value multiplied by the refractive index of parylene (1.66)
**too thick to measure with AFM

the dimensions of the substrate allow calculation of the expected coating thickness. For two significantly different coating weights applied to silicon wafers, the AFM and interferometry methods show general agreement with the calculated value of the coating thickness (Table 18.2). However, the Raman intensity method (50% of maximum) yields much smaller thickness values compared to calculated, AFM and interferometry results (Table 18.2). Here especially, correction for spherical aberrations by multiplication of the thickness value by the refractive index for parylene (1.66) results in coating thickness values, which compare favorably with the calculated value (Table 18.2).

For a set of even thicker coatings of polyethylmethacrylate polymer (refractive index = 1.485) on steel substrates, the Raman and interferometry measurements correlate linearly, but again the Raman measurements (dry objective) underestimate the coating thickness significantly (Fig. 18.4).

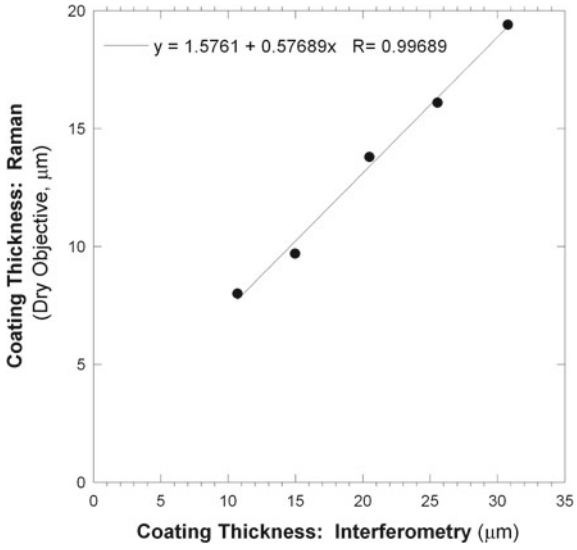

Fig. 18.4 Correlation of coating thickness as measured by Raman microscopy with coating thickness as measured by interferometry (thickness method) for coatings of poly(ethyl methacrylate) on steel

18.2.2 Swelling of Hydrophilic Gel Coatings

While use of an oil immersion object to reduce spherical aberrations is not practical due to oil absorption, use of a water immersion objective on cross-linked hydrophilic gel coatings results not only in a reduction of spherical aberrations, but also allows measurement of the water swelling behavior of a gel coating. Two different cross-linked polyvinyl pyrrolidone coating formulations on glass were imaged dry (dry objective 100×, NA = 0.90) and wet with water (water immersion objective 60×, NA = 1.00). Upon soaking, the Raman signal from the coating (CH-stretch) decreases due to dilution of the coating with water, and the Raman signal extends much farther above the glass surface indicating the gel is swollen (Fig. 18.5).

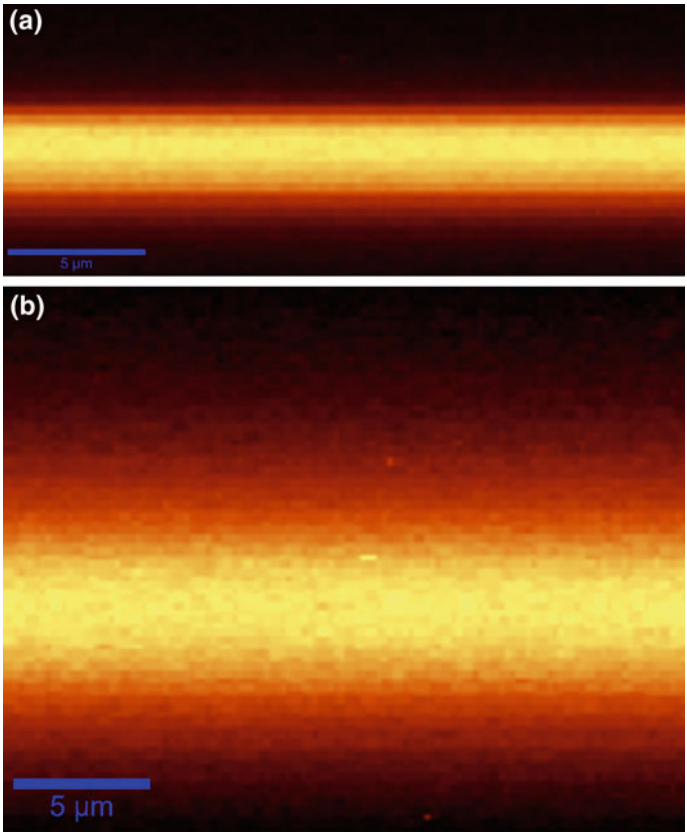

Fig. 18.5 **a** Raman microscopy cross-sectional image of a dry poly(vinyl pyrrolidone) coating on glass as imaged with a 100× dry objective (NA = 0.90). **b** Raman microscopy cross-sectional image of a wet poly(vinyl pyrrolidone) coating on glass as imaged with a 60× water immersion objective (NA = 1.00)

Table 18.3 Swelling of Poly(vinyl pyrrolidone) Hydrogels

Formula	Thickness dry (μm)	Thickness wet (μm)	Swelling ratio
1.	4.9	8.3	1.7
2.	1.8	5.5	3.0

From these images, thickness values were calculated, and the swelling ratio (wet thickness/dry thickness) estimated (Table 18.3). Formula 1 appears to be more cross-linked (swells less) than Formula 2 (Table 18.3).

18.3 Active Therapeutic Coatings

18.3.1 Coating Morphology

The passive therapeutic coatings discussed above usually contain one type of cross-linked hydrophilic polymer. On the other hand, active therapeutic coatings for drug delivery are often blends of drug(s) with hydrophobic polymer(s). Coatings of drugs alone usually exhibit little mechanical strength and often release drug too quickly, but upon blending with polymers, good mechanical strength and controlled release of the drug is possible. Upon optimization of the drug-polymer interaction, the polymer should slow the diffusion of water into the coating and thus slow the diffusion of drug out of the coating.

Upon blending multiple ingredients, coating morphology (microstructure) becomes important. The degree of dispersion of drug within the coating influences the mechanical strength of the coating: coarse dispersion of drug likely yields weaker coatings since the drug itself exhibits little mechanical strength. Note that with fine dispersion, drugs may act as plasticizers [9].

The morphology of the coating also strongly influences the mechanisms and rate of drug elution. If the polymer provides a diffusional barrier to the drug, as the degree of mixing between drug and polymer increases, the rate of drug elution should slow. However, not only is mixing critical, but also important is the physical form (polymorphic form) the drug assumes within the coating. Drugs may exist in various polymorphs: a non-crystalline (glassy) amorphous form, various crystalline forms with different crystal lattice spacings, or in a crystalline form incorporating some solvent or water (solvate or hydrate) [10]. These drug polymorphs may dissolve at different rates and thus influence the overall elution rate [10].

In particular, drug in the glassy amorphous form exhibits unique properties. Upon cooling molten liquid drug at a high cooling rate, a supercooled liquid may form, which upon further cooling freezes into a metastable glass (at a glass transition temperature). At lower rates of cooling, the drug will crystallize. Compared to the crystalline state, amorphous drug exhibits higher internal energy, and thus may exhibit

greater rates of dissolution, greater solubility and greater bioavailability [10, 11]. However, the amorphous drug may also exhibit greater chemical reactivity along with a tendency to spontaneously crystallize [10, 11].

Recent work indicates that polymers can stabilize the amorphous state of a drug, but that the stabilization is kinetic rather than thermodynamic [12, 13]. The inherent solubility of drug in polymer is usually low, but significant supersaturation is possible in some cases. Polymers reduce molecular mobility and thus increase the kinetic barriers to crystallization [12, 13]. Note that an amorphous drug/polymer mixture might be a molecular "solution" of drug in polymer, but could be a dispersion of amorphous drug domains in polymer. In x-ray diffraction, amorphous drug and polymers appear as a background signal without sharp spectral features, which complicates separation of the components in a mixture. However, in Raman microscopy, amorphous drug, crystalline drug and polymers often exhibit spectra with unique spectral features, which allow separation of the signals and hence the corresponding components in the sample.

As demonstrated below, confocal Raman microscopy helps to answer the pharmaceutics questions regarding drug polymorph form within drug/polymer coatings. Raman microscopy shows the degree of mixing of drug within polymer matrices, and Raman spectra often uniquely fingerprint the polymorphic forms of drugs within coatings.

18.3.2 Drug Mixed with Single Polymer: Morphology and Elution

In an effort to better understand the relationships between the drug morphology (degree of mixing, polymorphs) and elution behavior, the steroid dexamethasone was mixed with a series of polymers whereby the hydrophobic nature of the polymer was systematically varied. Upon increasing the alkyl chain length of poly(alkyl methacrylate) polymers, the polymer becomes more hydrophobic. A series of poly(alkyl methacrylate) polymers ranging from poly(ethyl methacrylate) (alkyl chain length = 2) to poly(octadecyl methacrylate) (alkyl chain length = 18) were mixed with dexamethasone at 5, 15 and 33 wt% concentration and spray coated onto stents from solutions in the solvent tetrahydrofuran (THF).

At first the coatings were observed with an optical microscope under white light illumination. Using different modes (brightfield, darkfield and polarized light), regions of clear and cloudy coating were identified, and the presence and frequency of birefringent (crystalline) regions qualitatively noted. The resulting "morphology map" plots the relationship between formulation variables (dexamethasone concentration and polymer type) and the observations from optical microscopy (Fig. 18.6).

Overall, the morphology map indicates that upon increasing dexamethasone concentration and/or increasing the alkyl chain length of the polymer, the appearance of the stent coatings progresses from clear to cloudy to birefringent (Fig. 18.6). In

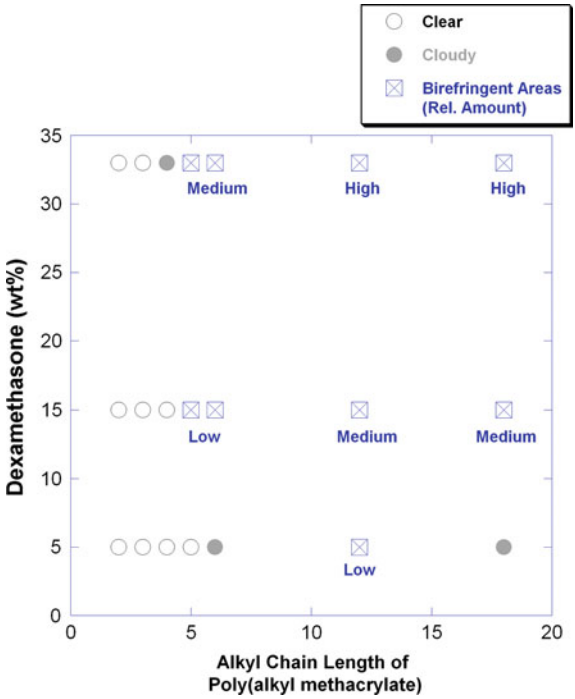

Fig. 18.6 Qualitative evaluation of coatings of dexamethasone in various poly(alkyl methacrylate) on stents via optical microscopy. Observations of clear, cloudy and birefringence coatings as a function of dexamethasone concentration and alkyl chain length (carbon number) of the poly(alkyl methacrylate)

other words, drug/polymer miscibility decreases at higher drug concentrations and with more hydrophobic polymers.

Optical microscopy provides a low resolution overview of coating morphology, but Raman microscopy probes the nature of the clear/cloudy/birefringent morphologies at higher spatial resolution. Cross-sectional Raman images perpendicular to the stent wire allow mapping of the distribution of the ingredients in the stent coatings from the outer coating/air surface down to the inner coating/metal wire (stent) surface.

The micro-Raman spectrum obtained at a particular pixel in a Raman image of a stent coating contains information on the local composition of drug and polymer at that spatial location, along with information on the polymorphic form of the drug present. While the spectra of crystalline dexamethasone and, for example, poly(butyl methacrylate) polymer differ significantly with some unique peaks (Fig. 18.7), the spectra of the two polymorphs of dexamethasone (amorphous and crystalline) differ only subtly with no unique peaks (Fig. 18.8).

Thus, independent images of polymer, amorphous drug and crystalline drug cannot be generated by simple peak integration. In the following, an augmented classical least squares method (aCLS) was applied to the full Raman spectral data set in order to deconvolute the image data into separate images of the distribution of the amorphous and crystalline polymorphs of dexamethasone within the polymer matrix [14].

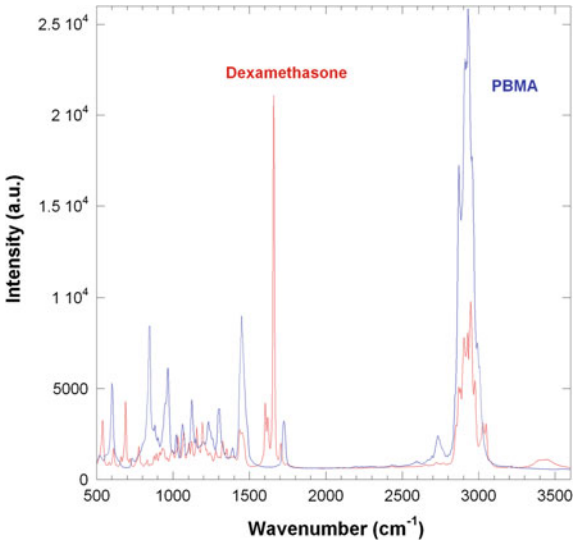

Fig. 18.7 Comparison of the Raman spectra of crystalline dexamethasone (red) and poly(butyl methacrylate), PBMA (blue)

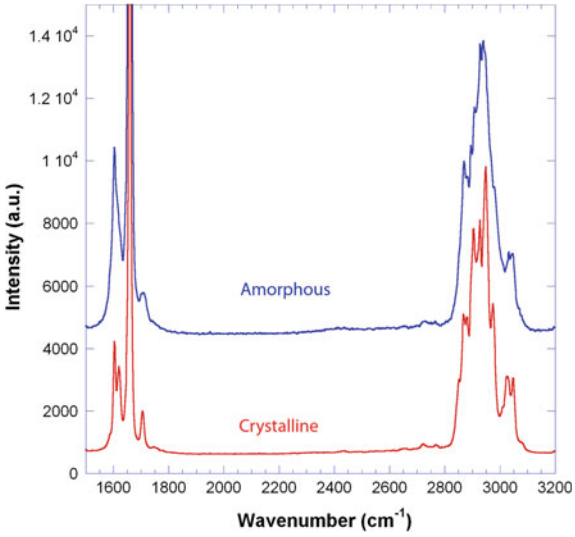

Fig. 18.8 Comparison of the Raman spectra of amorphous (blue) and crystalline (red) dexamethasone

Raman microscopic images were taken of the stent coatings prepared along the formulation path at fixed 33 wt% dexamethasone, but with varying alkyl chain length of the poly(alkyl methacrylate) (Fig. 18.6). Along this formulation path, the coating appearance transitions from clear to cloudy to birefringent (Fig. 18.6). Raman microscopy of the clear coatings at alkyl chain length of 2 or 3 carbons shows homogeneous mixing of amorphous drug within polymer. However, at an alkyl chain length of 4 carbons (polybutylmethacrylate, PBMA), cloudiness appears and Raman microscopy indicates some segregation of amorphous drug and PBMA (Fig. 18.9).

Fig. 18.9 Raman microscopic cross-sectional image of coating of 33 wt% dexamethasone in poly(butyl methacrylate) on stent. Red = Amorphous Dexamethasone, Green = Poly(butyl methacrylate). Image dimension = 100 × 10 μm

This figure shows a cross-sectional image of the coating on a stent. Top of image shows air (dark, no Raman signal), middle of image shows coating (brightly colored), and bottom shows stent metal (dark, no Raman signal). In Fig. 18.9, two images are overlaid: an image of the Raman signal intensity from amorphous dexamethasone (color-coded red) and the image of Raman signal intensity from PBMA polymer (color-coded green). Raman signal intensity is proportional to concentration [15]. Thus, yellow regions (red plus green) are mixtures of dexamethsone plus PBMA: yellow-green regions are relatively richer in PBMA, and orange-yellow regions are relatively richer in dexamethasone (Fig. 18.9). From multiple observations, the regions of cloudier coating in optical microscopy correlate with regions of increased dexamethasone signal in Raman microscopy. While the Raman results indicate some segregation of amorphous dexamethasone into cloudy regions, the aCLS routine applied to the image data did not detect crystalline dexamethasone. Note that in optical microscopy the cloudy regions often appear bluish, which is indicative of scattering from small particulates. The cloudy regions may contain a dispersion of nano-sized amorphous domains, or perhaps contain nano-sized crystalline domains below the detection limit of the Raman method.

Upon further increasing alkyl chain length to 6 (polyhexylmethacrylate, PHMA) the morphology map indicates a significant transition to a "medium" amount of birefringence (Fig. 18.6). The birefringence likely arises from regions of crystalline drug within the coating. Two regions with birefringence were identified with the optical microscope and imaged with the Raman microscope.

In the Raman microscopic images of the two regions (Fig. 18.10), the Raman signal intensities are associated with three colors: red associated with amorphous drug, green associated with crystalline drug, and blue associated with polymer. The Raman images of the PHMA coatings show regions of crystalline drug (green), which correlate with the birefringence observed in optical microscopy (Fig. 18.10). Note, however, that the Raman images distinguish two types of crystalline behavior: crystalline drug present at the outer coating/air surface (Fig. 18.10a), or crystalline drug present at the inner coating/metal surface (Fig. 18.10b). Certainly the two types of crystals will elute differently, since "crystal A" is not covered by a polymer diffusional layer, whereas "crystal B" is.

For the region with crystalline drug near the outer coating/air surface, a bulge appears in the coating. At the bulge, the laser light in the Raman experiment is scattered strongly by the crystals, light does not penetrate below the crystals, and thus the interior region under the crystals appears dark (no Raman signal). On both sides

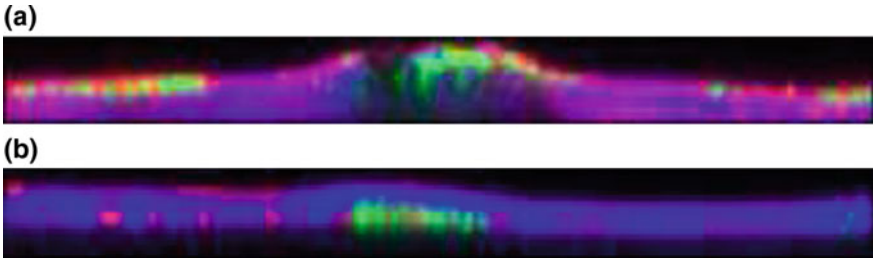

Fig. 18.10 Raman microscopic cross-sectional images of two different birefringent regions of coating of 33 wt% dexamethasone in poly(hexyl methacrylate) on stent. **a** Crystals near outer coating surface: Red = Amorphous Dexamethasone, Green = Crystalline Dexamethasone, Blue = poly(hexyl methacrylate). **b** Crystals near inner stent surface: Red = Amorphous Dexamethasone, Green = Crystalline Dexamethasone, Blue = poly(hexyl methacrylate). Image dimension = 100 × 10 μm

of the bulge in the coating the coating is transparent, and lavender (purple) colored regions indicate significant mixing of amorphous drug (red) with polymer (blue) along with some additional surface segregation of drug into amorphous (orange-red) and crystalline (green) phases.

For the region with crystalline drug near the inner coating/metal interface, a smaller bulge also appears over the crystalline region, and amorphous drug is mixed into the surrounding polymer, along with some surface segregation of amorphous drug present at both the inner and outer surfaces (Fig. 18.10). These images from confocal Raman microscopy yield microstructural information rich in detail, showing the spatial relationships between polymer and the amorphous and crystalline drug regions.

The microstructure revealed by Raman microscopy does correlate with drug elution. Along the path with fixed 33 wt% dexamethasone, upon increasing the alkyl chain length, the overall elution rate increases (Fig. 18.11).

Note that two components of the elution curves are important: the initial amount of drug released in the first 24 h ("burst"), and the rate of release of drug thereafter. The burst increases significantly as amorphous drug crystallizes and separates (demixes) from the polymer, and the polymer is less able to provide a diffusional barrier to the drug (Fig. 18.12).

After the initial burst, the slopes of the elution curves generally increase as alkyl chain length is increased, indicative of increasing diffusivity of the drug within the polymer matrix (Fig. 18.11). Indeed, with increasing alkyl chain length the glass transition temperature decreases systematically for these poly(alkyl methacrylates) and thus the free volume within the polymers increases, which is the likely origin of the increase in elution rate [16]. Note the exception of poly(octadecyl methacrylate). In this case, the octadecyl side chains are now long enough to crystallize and thus inhibit drug diffusion (Fig. 18.11).

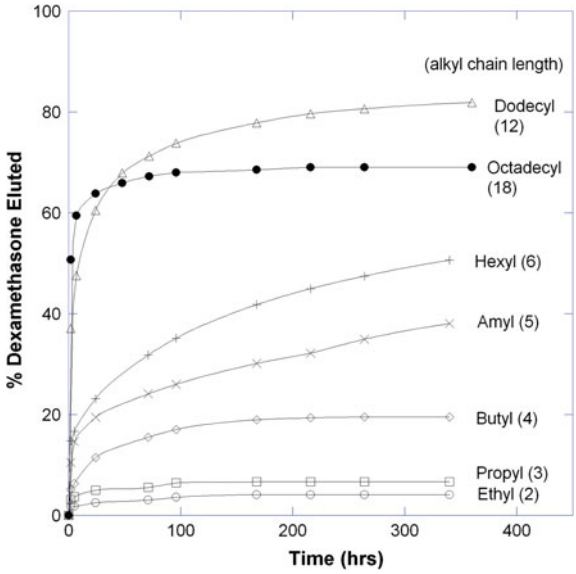

Fig. 18.11 Amount of dexamethasone eluted as a function of time for coatings of 33 wt% dexamethsone in various poly(alkyl methacrylates) on stents

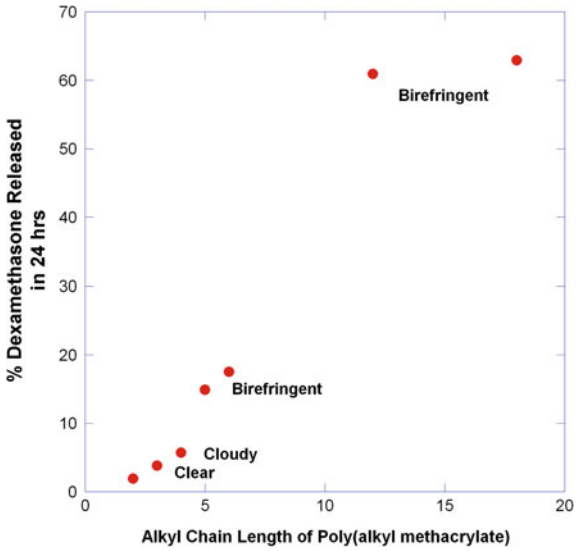

Fig. 18.12 Percent of dexamethasone eluted in the first 24 h ("burst") from coatings of 33 wt% dexamethasone in various poly(alkyl methacrylates) on stents as a function of the alkyl chain length (carbon number) of the polymer

18.3.3 Drug Mixed with Two Polymers: Blending and Layering

In some cases, performance advantages occur upon blending or layering polymers. A reinforced polymer matrix results upon mixing a rubbery polymer with a brittle polymer. A less sticky coating surface results upon layering a non-sticky polymer over the top of a sticky polymer. When mixing drug into blended or layered polymers, various "phases" are possible: amorphous drug mixed into the first polymer, or amorphous drug mixed into the second polymer, or separate phases of pure drug in crystalline or amorphous form. Raman microscopy allows determination of the partitioning of amorphous drug between multiple polymers, or the distribution of drug between layers of polymers.

Consider mixtures of dexamethasone blended into poly(butyl methacrylate) (PBMA), a hard polymer with a high glass transition temperature, and poly(dodecyl methacrylate) (PDMA), a soft polymer with a low glass transition temperature. At a weight ratio of 43.5/43.5/13 of dexamethasone/PBMA/PDMA, a thick layer of coating solution in THF was cast onto a glass slide and allowed to dry slowly with the goal of creating relatively large regions of phase separation. A Raman microscopic planar image of the coating shows round domains of PDMA (blue) dispersed in a continuum of amorphous dexamethasone (red) mixed with PBMA (green) which appears yellow-green and orange (Fig. 18.13). Note that upon closer inspection, some small regions of PDMA mixed with amorphous dexamethasone (purple) appear within the predominantly PDMA (blue) regions (Fig. 18.13).

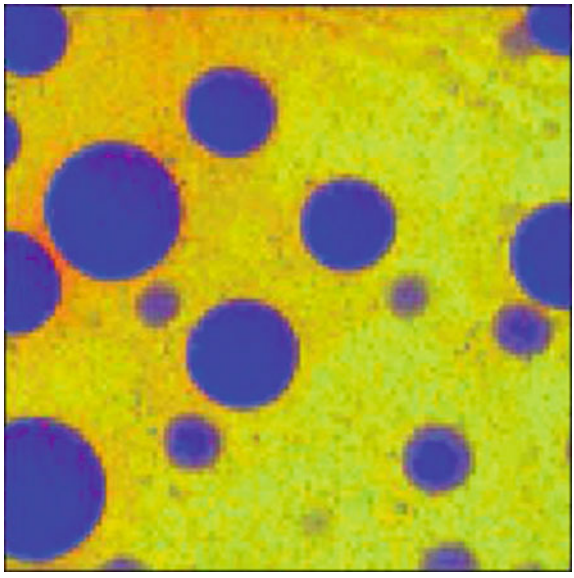

Fig. 18.13 Raman microscopic image of a 43.5/43.5/13 by weight coating of dexamethasone/PBMA/PDMA cast onto glass. Planar image of coating, parallel to glass substrate. Red = Amorphous Dexamethsone, Green = PBMA, Blue = PDMA Image dimension = 100 × 100 μm

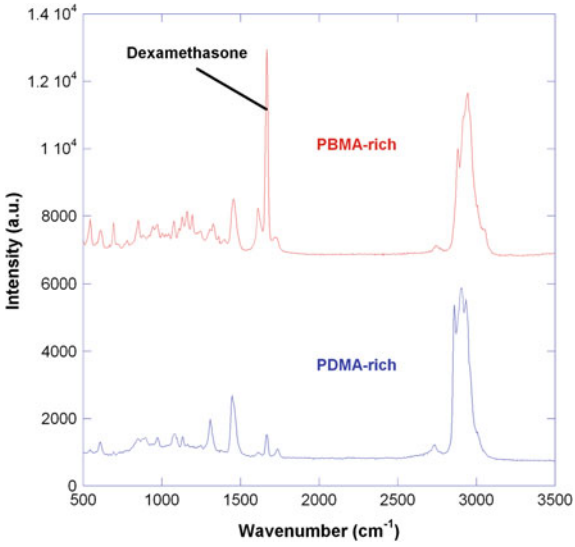

Fig. 18.14 Average micro-Raman spectra obtained for regions rich in PBMA and for regions rich in PDMA from the Raman microscopic image shown in Fig. 18.13

Integration of the micro-Raman spectra over the imaged regions clearly shows the strong preferential partitioning of amorphous dexamethasone into the PBMA-rich phase: The strong dexamethasone Raman peak at 1660 rel. cm^{-1} appears substantially larger in the PBMA-rich regions than in the PDMA-rich regions (Fig. 18.14).

Compared to the slowly drying cast film examined above, a much faster drying process occurs upon spray coating a stent, since multiple thin layers of dried spray droplets are sequentially applied to build up a thick coating. Upon first spray coating the same formulation as discussed above, dexamethasone/PBMA/PDMA, onto a stent, and then overcoating with PBMA alone, a highly microstructured coating is created (Fig. 18.15). With the same color-coding as noted above (amorphous dexamethasone = red, PBMA = green, PDMA = blue), the two-layer coating exhibits three distinct microstructures: a green PBMA-rich layer at the top outer surface of the coating, a yellow-orange PBMA plus dexamethasone layer at the base of the coating, along with blue PDMA-rich blobs dispersed throughout the coating. Surprisingly, the PDMA blobs also appear in the outer PBMA-rich layer, indicating some intermixing between the bottom dexamethasone/PBMA/PDMA layer and the top PBMA layer (Fig. 18.15). The spray coating exhibits similar phase separation to that found in the cast films, albeit at a smaller length scale: small domains of PDMA-rich regions dispersed within a continuum rich in both PBMA and dexamethasone.

In addition to the purely amorphous regions discussed above, a few birefringent regions were found in the stent coatings of dexamethasone/PBMA/PDMA overcoated with PBMA. One of these birefringent regions was imaged in order to determine the distribution of amorphous and crystalline drug within the PBMA/PDMA blend. Since it is difficult to simultaneously overlay images of all four components, three images were created for comparison purposes: a first image showing the rela-

Fig. 18.15 Raman microscopic cross-sectional image of two-layer coating on stent. Bottom coating layer: 43.5/43.5/13 weight% dexamethasone/PBMA/PDMA; Top coating layer: 100 weight% PBMA; Red = Amorphous Dexamethasone, Green = PBMA, Blue = PDMA; Image dimension = 120 × 12 μm

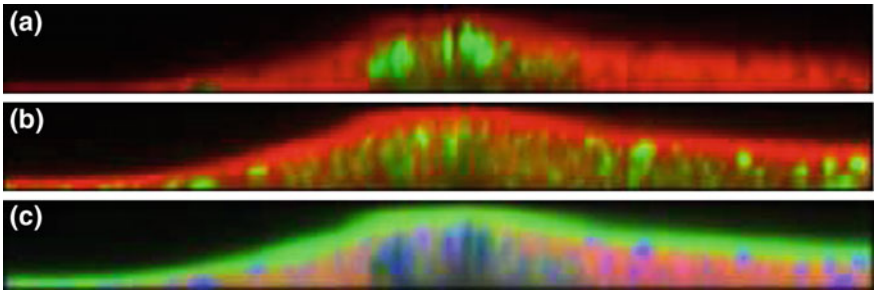

Fig. 18.16 Raman microscopic cross-sectional images of two-layer coating on stent. Bottom coating layer: 43.5/43.5/13 weight% dexamethasone/PBMA/PDMA; Top coating layer: 100 weight% PBMA; **a** Red = Amorphous Dexamethasone, Green = Crystalline Dexamethasone. **b** Red = PBMA, Green = PDMA. **c** Red = Amorphous Dexamethasone, Green = PBMA, Blue = PDMA Image dimensions = 120 × 12 μm

tionship of the two drug forms (Fig. 18.16a), a second image showing the relationship of the two polymers (Fig. 18.16b), and third image showing the relationships between amorphous drug and the two polymers (Fig. 18.16c).

Clearly the first two images show that amorphous and crystalline drug sharply segregate, and that the two polymers sharply segregate into blobs and layers (Fig. 18.16). Around the crystalline region, the Raman microscopic images reveal a microstructure similar to that found in Fig. 18.15: a PBMA-rich layer (green) on top of a PBMA plus dexamethasone layer (yellow-orange), along with dispersed PDMA-rich blobs (blue) (Fig. 18.16). As found within the drug/single polymer mixtures, in the drug/multiple polymer mixtures birefringence is correlated with crystalline regions which appear within bumps (thicker regions) in the coating.

From the comparison of Fig. 18.16a, b, it appears that the crystals formed in regions richer in PDMA than PBMA. As implied in all the results from both cast films and spray coatings, and also in the morphology map of dexamethasone in single polymers, dexamethasone appears much less "soluble" in PDMA than PBMA, and thus dexamethsone likely crystallizes (separates out) at much lower concentrations in PDMA than in PBMA. And, as discussed in the next section, if the drug becomes mobile, regions of PDMA could act as nucleation sites for the transition from amorphous to crystalline dexamethasone.

18.3.4 Drug Mixed with Two Polymers: Exposure to Water

Spin coatings of dexamethasone/PBMA/PDMA on silicon wafers also create the same morphology observed in cast coatings on glass: round PDMA-rich regions dispersed in PBMA plus dexamethasone. However, in spin coatings the size of the PDMA-rich regions is smaller and the overall coating thinner than found for the cast film coatings. In an effort to better understand the early stages of the drug elution process, a spin coating of dexamethasone/PBMA/PDMA was submerged in water and imaged using a water immersion objective. A first Raman image shows the relationship of the two drug forms (Fig. 18.17a), and a second Raman image shows the relationship of the two polymers (Fig. 18.17b).

Small crystals of drug appeared in the coating upon exposure to water for about one hour (Fig. 18.17). However, as Raman microscopy shows, the crystals appear non-uniformly over the coating surface: most of the crystals formed in locations which were PDMA-rich (Fig. 18.17). Apparently, even though a much higher concentration of amorphous dexamethasone mixes with PBMA than with PDMA, the amorphous dexamethasone present in PDMA-rich regions is less stable upon exposure to water, and crystallizes readily upon exposure to water for relatively short periods of time. Water is a strong plasticizer and only small amounts of water are required to reduce the glass transition temperature of an amorphous drug or polymer [10].

In summary, for coatings of dexamethasone in PBMA/PDMA blends, dexamethasone appears much more miscible with PBMA than PDMA. Upon mixing dexamethasone in both PBMA and PDMA simultaneously, dexamethasone prefer-

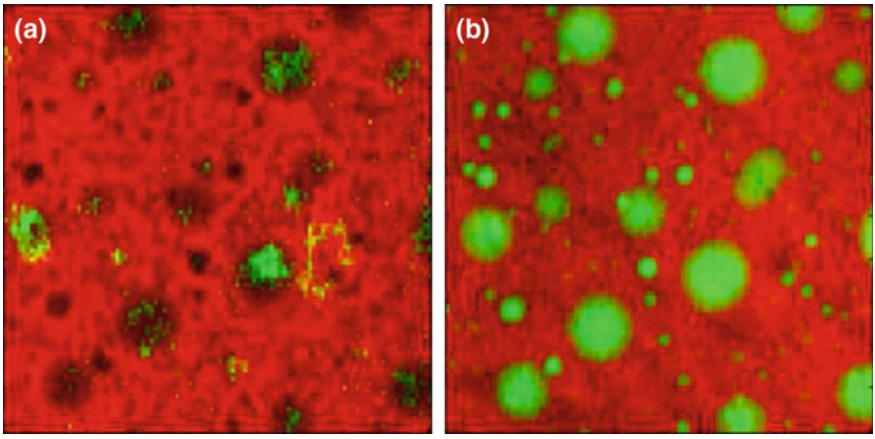

Fig. 18.17 Raman microscopic images of a 43.5/43.5/13 by weight coating of dexamethasone/PBMA/PDMA. Spin coating on silicon wafer soaked for 1 hour in water and imaged with water immersion objective. Planar image of coating, parallel to wafer substrate. **a** Red = Amorphous Dexamethasone, Green = Crystalline Dexamethasone. **b** Red = PBMA, Green = PDMA Image dimensions = 25 × 25 μm

entially partitions into PBMA at a relatively high concentration compared to PDMA (Fig. 18.14). Following exposure of these mixtures to water, crystals of dexamethsone nucleate within PDMA-rich regions (Fig. 18.17).

18.3.5 Drug Mixed with Biodegradable Polymer: Drug Elution with Polymer Degradation

In some cases, the interaction between human tissue and metal yields better biocompatibility than the interaction between tissue and polymer. "Biodegradable" polymers coated onto stents initially control the elution of drug and then erode away, leaving a bare metal surface. Biodegradation occurs through hydrolysis or enzymatic degradation which breaks the polymer into small molecular fragments [17]. Here a common biodegradable polymer, poly (D,L lactide-co-glycolide) or PLGA was mixed with a high concentration (50 wt%) of the drug rapamycin, spray coated onto stents, and the coated stents soaked in buffer at 37 °C. Note that a recently published study on similar mixtures compared the results of x-ray photoelectron spectroscopy (XPS) and time-of-flight secondary ion mass spectrometery (ToF-SIMS) with results from Raman microscopy [18].

Prior to soaking, the 50/50 rapamcin/PGLA coating appeared somewhat cloudy, and cross-sectional Raman microscopic images show some segregation of amorphous rapamycin from the PLGA polymer, with no crystalline rapamycin present (Fig. 18.18). After soaking in buffer for 10 days, chemical analysis of the drug content of the buffer indicate that more than 50% of the drug eluted from the coating. Raman microscopy confirms the chemical analysis: after soaking for 10 days, the average Raman signal due to rapamycin decreases substantially compared to the average signal found prior to soaking, over the regions of the coating imaged with Raman microscopy (Fig. 18.19).

However, Raman microscopic images indicate that the elution is non-uniform: after soaking, the coating exhibits significant non-uniformities in the distribution of

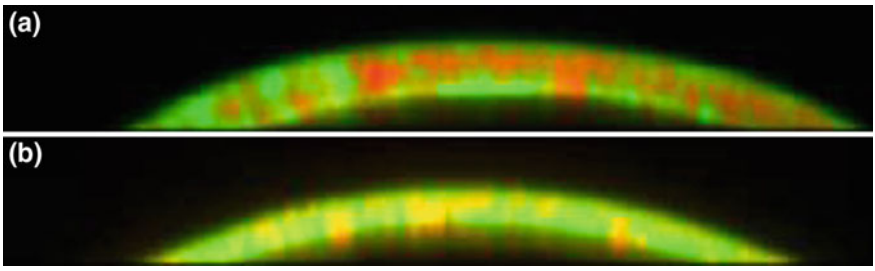

Fig. 18.18 Raman microscopic cross-sectional images of 50 wt% rapamycin in PLGA coated onto a stent. **a** Prior to soaking in buffer. **b** After soaking in buffer for 10 days at 37 °C Image dimensions = 70 × 30 μm

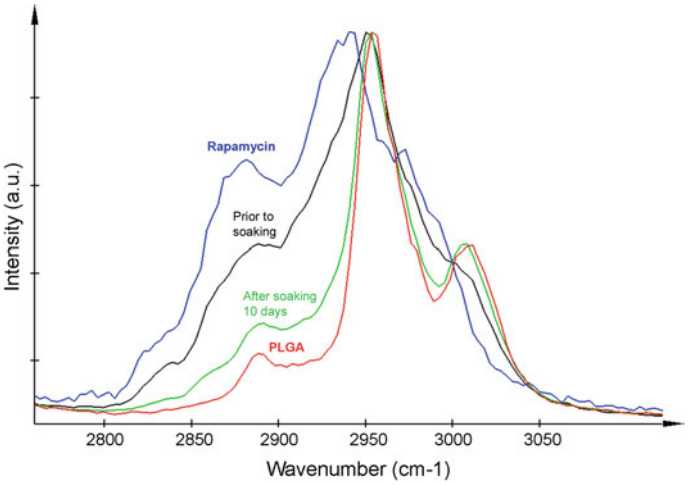

Fig. 18.19 Average micro-Raman spectra over the regions imaged in Fig. 18.18. Comparison of the spectra of coatings of 50 wt% rapamycin in PLGA prior to soaking and after soaking for 10 days with the spectra of rapamycin and PLGA standards

the remaining amorphous rapamycin (Fig. 18.18). Note that the rapamycin does not crystallize during elution, and that no pores or voids appear in the coatings. Upon soaking, not only does drug elute by diffusion, but water also penetrates into the coating. The addition of water likely reduces the glass transition temperature of the PLGA, which perhaps allows "healing" of the polymer as drug elutes.

Comparison of the Raman images before and after soaking for 10 days suggests some decrease in coating thickness occurs (Fig. 18.18). The thickness decrease could be due to biodegradation of PLGA, but is more likely due to elution of significant volumes of rapamycin. After soaking for an additional 22 days (total of 32 days), coating thickness continues to decrease. However, the average Raman spectrum over imaged regions of the coating shows no evidence for chemical changes in the PLGA polymer (Fig. 18.20). Upon hydrolysis, the molecular weight of the polymer remaining in the coating probably decreases [17, 19]. The Raman spectrum of PLGA will change with changes in the copolymer composition and polymer crystallinity, but is not sensitive to changes in molecular weight [20]. Comparison of the Raman spectrum of the coating after soaking for 32 days with the spectra of PLGA polymer (50/50 lactide/glycolide) and poly(D,L lactide) (100/0 lactide/glycolide) suggests no preferential hydrolysis of glycolide or lactide.

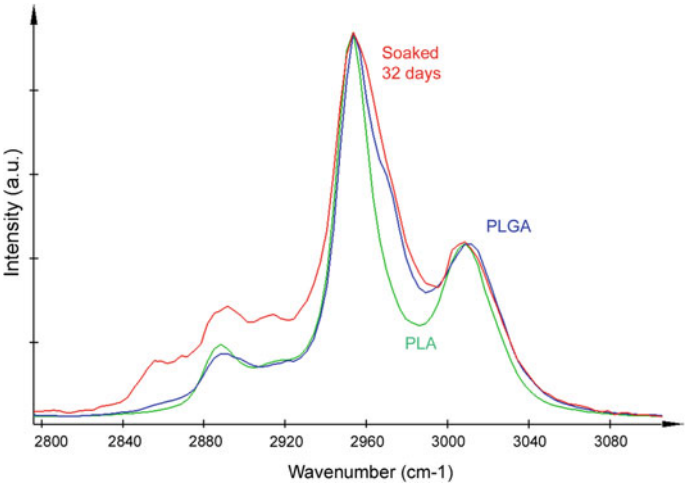

Fig. 18.20 Comparison the Raman spectra of PLA and PLGA standards with the average micro-Raman spectra over an imaged region of a stent coating (50 wt% rapamycin in PLGA coating on stent soaked in buffer for 32 days at 37 °C)

18.4 Summary

In many cases, therapeutic coatings on medical devices provide significant clinical benefits by mediating device/tissue and device/blood interactions. In the development of therapeutic coatings, significant challenges arise in meeting biocompatibility, durability and other performance criteria. As shown in this chapter, confocal Raman microscopy of therapeutic coatings yields important information on the coating thickness, degree of swelling, degree of dispersion of drug, and the polymorphic forms of drugs present within the coatings. Such information helps in the elucidation of the mechanisms by which hydrophilic gel coatings swell, reduce surface friction and increase blood compatibility. This further helps in the elucidation of the mechanisms by which drug elutes from coatings on stents, and how biodegradable coatings on stents erode with time. In particular, confocal Raman microscopy allows characterization of the materials science and pharmaceutics aspects of the amorphous form of drugs. Drug in amorphous form presents both benefits and challenges, and is difficult to characterize with methods other than confocal Raman microscopy.

References

1. B. Ratner, A. Hoffman, F. Schoen, J. Lemons, *Biomaterials Science: An Introduction to Materials in Medicine*, 2nd edn. (Academic Press, San Diego, London, 2004)
2. B. Ratner, S. Bryant, Ann. Rev. Biomed. Eng. **6**, 41 (2004)
3. D. Klee, H. Höcker, Adv. Polym. Sci. **149**, 1 (1999)

4. P. Serruys, A. Gershlick, *Handbook of Drug-Eluting Stents* (Taylor & Frances, London, New York, 2005)
5. G.K.S.W. Kim, Appl. Opt. **38**, 5968 (1999)
6. N. Everall, Spectroscopy **19**, 22 (2004)
7. T. Bridges, M. Houlne, J. Harris, Anal. Chem. **76**, 576 (2004)
8. J. Fortin, T. Lu, *Chemical Vapor Deposition Polymerization* (Kluwer Academic Publishers, Dordrecht, 2003)
9. F. Siepmann, V.L. Brun, J. Siepmann, J. Controlled Release **115**, 298 (2006)
10. R. Hilfiker, *Polymorphism in the Pharmaceutical Industry* (Wiley-VCH, Weinheim, 2006)
11. B. Hancock, G. Zografi, J. Pharm. Sci. **86**, 1 (1997)
12. H. Konno, L. Taylor, J. Pharm. Sci. **95**, 2692 (2006)
13. P. Marsac, S. Shamblin, L. Taylor, Pharm. Res. **23**, 2417 (2006)
14. D. Haaland, E. Thomas, Anal. Chem. **60**, 1193 (1988)
15. M. Pelletier, Appl. Spectrosc. **57**, 20A (2003)
16. M. Beiner, K. Schröter, E. Hempel, S. Reissig, E. Donth, Macromolecular **32**, 6278 (1999)
17. J. Anderson, M. Shive, Adv. Drug Delivery Rev. **28**, 5 (1997)
18. A. Belu, C. Mahoney, K. Wormuth, J. Controlled Release **126**, 111 (2008)
19. A. Hausberger, P. DeLuca, J. Pharm. Biomed. Anal. **13**, 747 (1995)
20. G. Kister, G. Cassanas, M. Vert, Polymer **39**, 3335 (1998)

Chapter 19
Raman Imaging of Plant Cell Walls

Notburga Gierlinger

Abstract To gain a better understanding of plant cell walls, several microscopic and chemical methods have been used for their analysis in recent years. However, a knowledge gap exists about the location, quantity and structural arrangement of molecules on the micrometer scale within the native cell wall. Advances in confocal Raman microscopy and imaging have tackled this problem in a non-invasive way and provide chemical and structural information in-situ with a high spatial resolution ($<0.5\,\mu m$). Examples of high resolution Raman imaging on wood cells are given, showing that changes in polymer chemistry and orientation can be followed within and between different cell wall layers. In horsetail (*Equisetum hyemale*) tissue, in addition to the mapping of plant cell wall polymers, the distribution of amorphous silica is investigated. Area scans from a cross section are included as well as a depth profiling within a silica-rich knob on the outer stem wall.

19.1 Introduction

To gain a better understanding of plant cell walls several microscopic and chemical methods have been applied during the last years. However, a knowledge gap exists concerning the location, quantity and structural arrangement of molecules on the micro level in the native cell wall. Advances in Confocal Raman microscopy and the imaging approach have tackled this problem in a non-invasive way and provide chemical and structural information in-situ with a high spatial resolution ($<0.5\,\mu m$). Examples of high resolution Raman imaging are given on wood cells, showing that changes in polymer chemistry and orientation can be followed within and between different cell wall layers. Chemical images are based on the changes of the integral intensity or band width of Raman bands attributed to specific plant cell wall polymers and cellulose orientation. In addition to the mapping of the plant cell wall polymers, the distribution of amorphous silica is followed and chemical imaging based on a partial least square fit with model spectra (basis analysis) is shown in horsetail tissue (*Equisetum hyemale*).

N. Gierlinger (✉)
Department of Nanobiotechnology, Universität für Bodenkultur Wien,
Muthgasse 11/II 69, 1190, Vienna, Austria
e-mail: burgi.gierlinger@boku.ac.at

J. Toporski et al. (eds.), *Confocal Raman Microscopy*, Springer Series
in Surface Sciences 66, https://doi.org/10.1007/978-3-319-75380-5_19

19.2 Plant Cell Walls

Plant cell walls are complex and dynamic structures and determine cell and plant shape [1]. Built up by incorporation of photosynthetically fixed carbon they represent the most abundant source of terrestrial biomass and renewable energy. Furthermore they are of practical importance for human and animal nutrition and as a source of natural fibers for textiles, materials and paper products. The understanding of plant cell walls is thus of high interest for many practical applications, both from the scientific and biomimetic view, as nature has evolved a big pool of plant cell walls differing in properties according to the desired needs. On a broad view two types of cell walls can be distinguished: primary walls are deposited during cell growth and secondary cell walls after cell growth has ceased. Primary cell walls need to be both mechanically stable and sufficiently extensible to permit cell expansion while avoiding the rupture of cells under their turgor pressure and consist mainly of polysaccharides that can be broadly classified as cellulose, the hemicelluloses and pectins. The latter two classes of cell wall components are often referred to as matrix polysaccharides. Secondary cell walls are deposited after the cessation of cell growth and confer mechanical stability upon specialized cell types such as xylem elements and sclerenchyma cells. These walls represent composites of cellulose and hemicelluloses, and are often impregnated with lignins, an aromatic system composed of phenylpropane units [2–4]. Crystals of cellulose form the microfibrillar foundation in all plant cell walls. Although native cellulose, termed cellulose I, has been one of the most studied subject in polymer science, the biosynthesis and ultrastructure of cellulose are not yet completely resolved [5–8]. The deceptive simplicity of the repeating β-1–4 linking cellobiose unit is not indicative of the complex arrangement of amorphous and crystalline regions at the fibril and fiber level. Within the plant cell wall cellulose is embedded in the matrix polymers, which play an important role in the development of the cell wall [9, 10] as well as for its final properties. The polysacharidic matrix polymers, the hemicelluloses and pectins comprise a variety of different chemical configurations as well as the lignin, the polyphenolic incrusting polymer in secondary plant cell walls.

Furthermore the secondary plant cell wall of wood consists of different sublayers (S1, S2, and S3) formed at different periods during cell differentiation [11]. The S2 layer is the thickest (75–85% of the total thickness of the cell wall) and most important for mechanical stability [12]. Between adjacent cells, a middle lamella layer attached to the primary cell wall ensures the adhesion of a cell to its neighbours. The chemical composition of the cell wall and the alignment of the cellulose microfibrils in the different sublayers show significant inter- and intraspecies variability and determine the different cell wall properties [13].

Most traditional chemical analysis of plant cell walls are destructive, since they require disintegration of the plant tissue. But the functional characteristics of cell walls depend not only on the composition of the cell wall polymers, but also on fine details of their macromolecular structure and conformation, and on their highly ordered architecture at scales from a few nanometers to several microns. Much of

this fine detail is lost when cell wall polymers are fractionated and/or solubilized to be examined by the classical chemical techniques. In addition, sample isolation difficulties arise when small cell wall areas or single layers are of interest, since they have to be carefully excised.

The combination of Raman and infrared spectroscopy with microscopy have developed as an important set of tools in plant cell wall research [14–22], as they allow to acquire information concerning the molecular structure and composition in a native state. Raman microspectroscopy has the advantage that spectra can be acquired on aqueous, thicker yet not opaque samples with a higher spatial resolution. But the impedance of sample autofluorescence, which may hinder the analysis or constrain the quality of the spectra, limited applications on plant tissues, until the development of the NIR-FT (Near infrared-Fourier transformed) -Raman technique [23]. For mapping and imaging of whole plant organs (seeds, fruits, leaves) the lateral resolution ($\sim$10 μm) of the NIR-FT technique is adequate [24–26], whereas for investigations on the lower hierarchical level of cells and cell walls the high resolution gained with a visible laser based system is needed.

19.3 Micro-Raman Spectroscopy of Plant Fibers

Raman applications on plants began with the investigation of cellulose [27–29]. During the last decade Micro-Raman spectroscopy was successfully applied to investigate non-destructively different types of natural cellulosic plant fibers e.g. flax [19, 30–34], cotton [31, 35], jute, ramie, kapok, sisal and coconut fibers [31]. Studies comprise general characterization of fibers [19, 31] as well as analysis of the molecular changes during mechanical processing [36], tensile deformation [37, 38] and chemical treatments [32]. Furthermore the preferential orientation of the functional groups of plant polymers was derived from the response of the relative intensities of characteristic bands with changing polarization of the incident exciting radiation relative to the fiber axis [20, 29]. In plant fibers the intensity of most of the Raman bands assigned to cellulose is strongly dependent on its preferential orientation along the fiber in relation to the polarization direction of the incident exciting radiation. By investigating polarization dependent spectral changes on a fiber with known parallel cellulose microfibril orientation, interpretation and calibration regarding cellulose orientation can be derived for unknown samples and imaging results. Ramie (*Boehmeria nivea*) represents such a model system, as it is composed of almost pure cellulose oriented parallel along the fiber axis. Spectral changes in dependence of the angles of the incident laser polarization were investigated. The most pronounced changes are found for the bands at 1097 and 2898 rel. cm^{-1} (Fig. 19.1). These are assigned to ν_s(C–O–C), mainly related to $\beta(1\rightarrow4)$ glycosidic linkages of the cellulose skeletons, and ν(CH) and $\nu_s(CH_2)$ modes of the glucopyranose rings and to the methylene groups of the glucopyranose side chain, respectively [28, 39]. The effect of orientation has to be taken into account in the data analysis, when spectra of

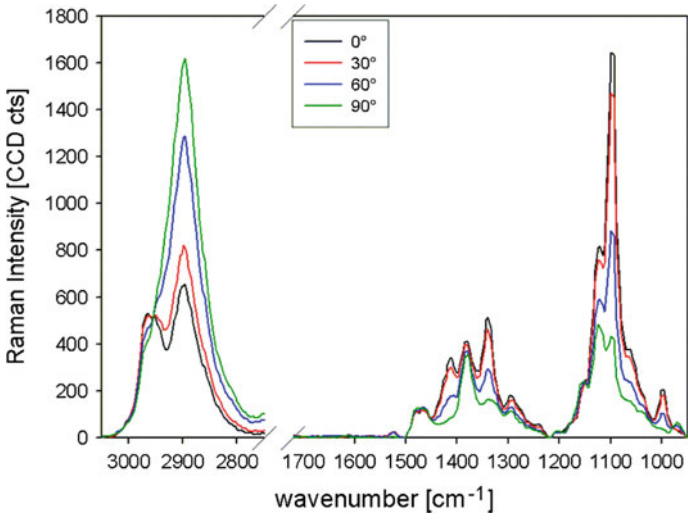

Fig. 19.1 Baseline corrected Raman spectra acquired from a ramie fiber with different polarization directions of the incident laser: 0° (parallel to the fiber), 30°, 60° and 90° (perpendicular to the fiber)

native plant cell walls are acquired with polarized laser irradiation; this is also true for Raman imaging experiments.

19.4 Plant Cell Wall Imaging by Confocal Raman Microscopy

One of the first Raman imaging studies in plant research was carried out on flax stem tissue [19]. Using the NIR-FT-Raman technique area maps were collected in 6–10 μm steps and chemical profiles calculated by integration over specific spectral regions. By this method no information was gained at the cellular level, yet the distribution of the major components (cellulose, lignin, non-cellulosic polysaccharides) was demonstrated for different anatomical tissue types (epidermal tissue, bast, fibers and core) [19]. To investigate changes at the hierarchical level of individual cells and/or cell wall layers, a higher spatial resolution is necessary and, as a consequence, the application of visible laser excitation preferential. In the last years the potential of Raman imaging was demonstrated on wood cell walls [40–42]. A 785 nm near-IR laser-based Raman system was applied to study beech cell walls [42], but also confocal Raman microscopes with 633 nm [40] and 532 nm [41] visible laser excitation wavelengths were used to investigate the wooden cell walls with sub-micron spatial resolution.

19.4.1 Imaging Cellulose Orientation and Lignin Distribution in Wooden Cell Walls

Wooden cell walls consist of 40–50% cellulose, associated with a mixture of hemicelluloses (20–30%), lignin (20–35%), extractives (2–20%) and ash (0.2–3%) [11, 12]. In order to interpret the Raman spectrum of such a multi-component material, not only the contribution of each component needs to be identified, individual Raman bands need to be assigned to component-specific moieties and/or functional groups. Most of black spruce (*Picea mariana*) Raman features could be assigned to cellulose and lignin, however, contributions of hemicelluloses occurred at similar wavenumbers to cellulose and could not be clearly distinguished [43].

As an example of imaging of wooden cell walls, the reaction wood of a tropical wood species (*Laetia procera*) was chosen, because of a highly specialized, non uniform cell wall structure. Reaction wood in general is of interest as these tissues are able to generate tensile stresses of up to 70 MPa, which are able to pull leaning stems and branches upwards [44, 45]. It is still much debated how the mechanism works, consequently this special plant cell wall composition and structure has been of considerable research interest for decades [46–48].

After imaging a sample area of interest, Raman images can be calculated by integrating over bands assigned to e.g. lignin to visualize its distribution within the cell wall [40, 41]. By integrating from 1545–1698 rel. cm^{-1} areas with high lignin content show high intensity (bright yellow, Fig. 19.2a). The compound middle lamella and the cell corners, which glue the wood fibers together, are confirmed as highly lignified areas. The secondary cell wall is intermediately lignified and an unusual layered structure with changing lignin incrustation is visualized (Fig. 19.2a).

Integrating over the ν(CH) and $\nu_s(CH_2)$ modes from 2774–3026 rel. cm^{-1} reflects cellulose amount and/or orientation (Fig. 19.2b) and gives a contrary picture: highest intensity in the secondary cell wall, low between the cells and no clear layering. By restricting the integration to the very orientation sensitive band at 1097 rel. cm^{-1}, two 1 µm thick layers are emphasized in the laser polarization orientation (Fig. 19.2c). Within this region of high intensity the cellulose is supposed to be not oriented parallel along the fiber axis, but with a high angle in respect to the fiber axis. The spectral explanation is that in the investigated cross-section if cellulose is aligned parallel to the fiber axis the ν_s (C–O–C) is low, as excitation is perpendicular to the backbone. When cellulose is aligned with a high angle in respect to the fiber axis, the C–O–C linkage becomes more parallel aligned and therefore the signal is enhanced in the laser polarization direction (Fig. 19.2c). Beside images based on changes of integrated band intensities, also the change in band width can be used to detect and follow molecular changes at the cell wall level (Fig. 19.2d). For the CH-stretching region (2773–3044 rel. cm^{-1}), images reflect mainly changes in the cellulose orientation (Fig. 19.2d). Only the 2898 rel. cm^{-1} band of the overlapping CH-stretching bands raises with changes in orientation and thus also the doublet widths changes in dependence of the orientation (Fig. 19.1). In the cross section the band width is decreasing (signal intensity increasing), when the cellulose is

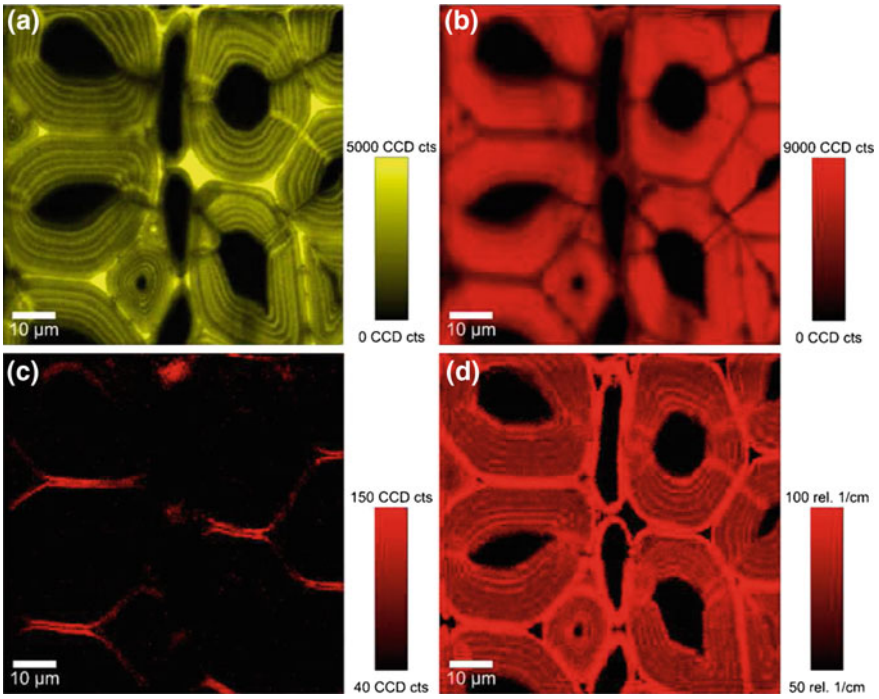

Fig. 19.2 Raman images (80 µm × 80 µm) of a cross-section of tension wood of *Laetia procera* calculated by integrating from 1545–1698 rel. cm^{-1} (**a**, lignin), 2774–3026 rel. cm^{-1} (**b**, cellulose amount and orientation parallel along the fiber) and from 1067 to 1106 rel. cm^{-1} to accentuate the orientation sensitive cellulose band at 1097 rel. cm^{-1} (**c**, cellulose oriented with an high angle in respect to the fiber) and the band width at 50% height of the CH-stretching region (**d**, 2823–2917 rel. cm^{-1})

aligned parallel along the fiber. In this situation the side chain methylene groups are perpendicularly arranged with respect to the cellulose molecule and in plane with the incident light.

When polarized laser light is used in combination with Raman imaging care has to be taken to interpret every intensity change by concentration differences of the cell wall polymers, as changes in the orientation of the molecules may also affect intensity. This may complicate data interpretation, but on the other hand provides insights into changes of orientation of the molecule within the sample [41, 49]. In wood the angle of the cellulose microfibrils in respect to the cell axis is termed microfibril angle (MFA) and of great importance as it was demonstrated to be closely related to the mechanical properties [47, 48].

One major advantage of the imaging approach presented here is that verification of the interpretation (orientation or concentration effect) of imaging results as well as detailed insights can be gained by extracting average spectra of defined areas. So, one has not to rely solely on imaging results, like for example in staining experiments

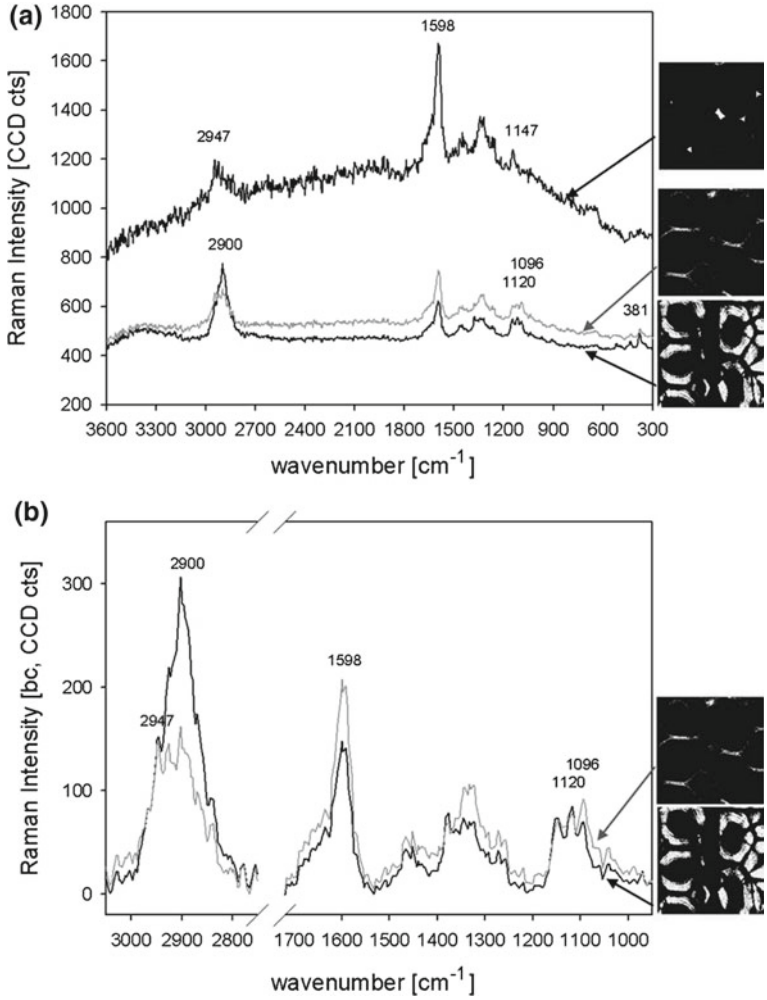

Fig. 19.3 Extracted average spectra of *Laetia procera* Raman images (Fig. 19.2) of (**a**) the cell corner (integral intensity of the band at 1598 rel. cm^{-1} >5000, white area in the upper image and upper black line) and two regions differing in orientation within the secondary cell wall (integral intensity of 1096 rel. cm^{-1} band >100, middle image and gray line; integral intensity of 2900 rel. cm^{-1} band >7000, bottom image and black line) and **b** a zoom into regions of interest of the baseline corrected secondary cell wall spectra

or fast imaging approaches based on the intensity of only one wavelength. Another big advantage is that the image calculation can reveal changes in chemistry and/or orientation at a high spatial resolution. These changes are often not even visible in the light-microscopic images and it would be impossible to place the laser beam accurately on such small regions of interest to resolve these changes. By extracting the spectra after image calculation the spectral information can be gained accurately from very small, defined regions for detailed investigation.

Regions of interest for extracting average spectra can be selected by hand or defined by intensity thresholds based on the calculated chemical images (Fig. 19.2a–d). By selecting a threshold for the lignin intensity above 5000 for example, solely the cell corners are selected (upper picture, Fig. 19.3a) and an average spectrum of the cell corner is calculated (upper black line, Fig. 19.3a).

The cell corner spectrum reflects only lignin characteristic bands and suggests that lignin is the main compound in these areas. Besides, it also shows that lignin causes a high level of background fluorescence, which can disguise small contributions to the Raman spectrum of other polymers present in small amounts, e.g. pectin. In the spectra extracted from the secondary cell walls, the aromatic stretching vibration of lignin at 1598 rel. cm^{-1} is much smaller and fluorescence reduced (spectra on the bottom, Fig. 19.3a). In these spectra characteristic cellulose bands can be found e.g. at 1096 and 1122 rel. cm^{-1}. The two spectra were extracted from zones identified by the imaging approach to differ in cellulose orientation. A zoom in of the CH - stretching region and the fingerprint region bands confirms the opposite trend of the band at 2900 and 1097 rel. cm^{-1} and thus the interpretation as changes of orientation (Fig. 19.3b).

Besides revealing molecular changes within the cell wall layers, the high spatial resolution of confocal Raman microscopy enabled also the characterization of accessory compounds within the lumen of single cells, e.g. lipid droplets in the xylem of trees [50] or spherical storage compounds in wood parenchyma cells [41].

19.4.2 Silica and Cell Wall Composition in Horsetail (Equisetum hyemale)

Minerals and inorganic substances in plants are normally determined as the residues remaining after all the combustible material has been burned off (fully oxidized) and subsumed as ash content. Regrettably, this method does not result in detailed information on the kind of inorganic components. Confocal Raman microscopy studies allow the identification, characterization and spatial localization of inorganic substances in fossil [51–53] and living plants in situ [54–57]. Recent Raman imaging studies were carried out on horsetail samples (*Equisetum hyemale*) [58, 59]. Another common name of the plant is “scouring rush”, a reference to its early use for cleaning pots made possible by its high accumulation of silica up to 25% dry wt [60]. Aspects of processes regarding silica deposition, its association with other biomolecules, as well

as the chemical composition of the outer strengthening tissue still remain unclear, questions which were addressed by Raman imaging [58, 59]. Basis analysis (partial least square fit based on model spectra) was performed in this study, besides the visualization of differences in chemical composition by calculating the integral intensity of selected bands [58]. Average spectra extracted from defined regions of different chemical images seemed to represent almost pure cellulose (hemicellulose), pectin and amorphous silica features and were thus seen as appropriate to be used as model spectra for these compounds. Concluding that the *Equisetum* plant cell walls consist mainly of these compounds, every Raman spectrum in the acquired Raman images is a linear superposition (S) of the spectra of the single compounds. By having the model spectra (basis spectra, B_k) of the single compounds, it is possible to estimate the weighting factor a_k by the least squares fit ($S = \sum a_k B_k$). The weighting factor a_k is proportional to the quantity of the component k in the material and stored in an image. Color coding and combining the different weighting factor images lead to a complete summarizing image of the distribution of the model compounds. The distribution of cellulose, pectin and silica respectively are visualized within one image for every investigated tissue region (Fig. 19.4a–d). Silica accumulation is color-coded blue and confirmed in the knob region (Fig. 19.4a) as well as in a small layer below the cuticula beside the knob region (Fig. 19.4d). In addition it becomes clear that in the epidermal layer below the knob, silica is still detectable in combination with cellulose/hemicellulose, whereas the pectin amount seems to be decreased (Fig. 19.4a, pink color). This is in contrast in the epidermal layer beside the knob where pectin plays the main role (Fig. 19.4d, green). In the epidermis only a small cellulose rich inner ring (red) is found, which becomes continuously thicker inwards and the pectin more and more restricted to the cell corners (Fig. 19.4d). Within the hypodermal sterome the two layered structure, with a pectinized outer ring and an inner ring with highly oriented cellulose comes out (Fig. 19.4b). Further inwards uniform pure cellulose/hemicellulose fibers are found and the pectin is restricted to the CC and middle lamella (Fig. 19.4c).

In the spectrum extracted from the knob region (Fig. 19.4e, blue spectrum) as a main contributions a broad band below 500 rel. cm^{-1}, attributed to amorphous silica, and a band at 976 rel. cm^{-1}, assigned to silanol groups, were found. From this, we concluded that these protrusions were almost pure amorphous, hydrated silica. No silanol group vibration was detected in the silicified epidermal layer below and association with cell wall polymers was indicated.

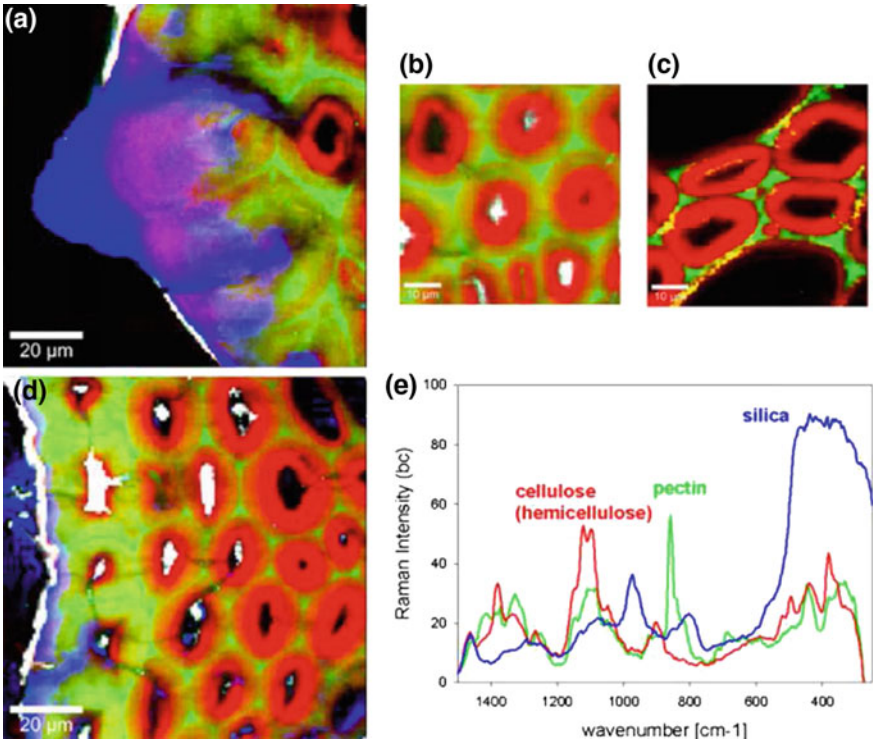

Fig. 19.4 Combined color images (**a**–**d**) from *Equisetum hyemale* derived from a basis analysis (partial least square fit) with average spectra (**e**) extracted from defined regions representing mainly amorphous silica, pectin and cellulose. Blue represents high weighting factor and consequently content for silica, green for pectin and red for cellulose (hemicellulose). The white color shows the cuticular layer and deposits within some lumens of the cells not further investigated [58].

19.5 Outlook

The potential of confocal Raman microscopy/imaging for non-destructive in-situ investigation of plant cell walls has already been demonstrated on various plant tissues. The high spatial resolution allows detection of changes in the cell wall polymer composition and/or orientation on the cell and cell wall level. The Raman imaging approach allows acquiring spectra with short integration time (0.2–2 s), which minimizes problems with sample degradation. The signal to noise ratio of the spectra is sufficient to visualize chemical and orientational changes not visible in the light-optical micrographs. The extraction of average spectra with a better signal to noise ratio from the identified areas of interest can support image interpretation and reveal more details. Conclusions about all cell components can be derived non-destructively at once and in context with structure. This major advantage and potential also comprises a drawback as highly overlapping bands are sometimes difficult to interpret

and conclusions on components with minor amount may be ambiguous. Nevertheless, more experiments on other cell wall variants and selective chemical treatment as well as the combination with other methods (e.g. antibody probes) will improve our understanding of the generated Raman spectra in future.

19.6 Materials and Methods

The Raman mapping experiments shown in this book chapter were done with a Confocal Raman microscope (CRM200, WITec, Ulm, Germany) described in detail together with the sample preparation and data analysis in [41, 58].

Acknowledgements R. Nöske (Potsdam University, Department of Chemistry) is thanked for providing the horsetail sample, B. Clair (Universite Montpellier) for the tropical wood sample and I. Burgert, O. Paris and P. Fratzl (Max Planck Institute of Colloids and Interfaces, Department Biomaterials, Potsdam) for enabling the work. The author acknowledges the APART program of the Austrian Academy of Sciences and the Max Planck Society for funding.

References

1. C. Martin, K. Bhatt, K. Baumann, Curr. Opin. Plant Biol. **4**(6), 540 (2001)
2. A. Boudet, *The Plant Cell Wall—Annual Plant Reviews* (Blackwell Publishing, CRC Press, 2003), chap. Towards an understanding of the supramolecular organization of the lignified wall, pp. 155–178
3. M. Jarvis, M. McCann, Plant Physiol. Biochem. **38**(1/2), 1 (2000)
4. M. O'Neill, W. York, *The Plant Cell Wall—Annual Plant Reviews* (Blackwell Publishing, CRC Press, 2003), chap. The composition and structure of plant primary cell walls, pp. 1–44
5. A. O'Sullivan, Cellulose **4**(3), 173 (1997)
6. R. Atalla, *MIE Bioforum* (UNI Publisher Co., Japan, 1999), chap. The structure of native celluloses, and the origin of their variability
7. R. Brown, I. Saxena, Plant Physiol. Biochem. **38**(1–2), 57 (2000)
8. D. Klemm, B. Heublein, H. Fink, A. Bohn, Angew. Chemie. Int. Ed. **44**(22), 3358 (2005)
9. R. Atalla, J. Hackney, I. Uhlin, N. Thompson, Int. J. Biol. Macromol. **15**(2), 109 (1993)
10. S. Fry, J. Exp. Bot. **40**(1), 1 (1989)
11. C. Plomion, G. Leprovost, A. Stokes, Plant Physiol. **127**, 1513 (2001)
12. D. Fengel, G. Wegener, *Wood: Chemistry, Ultrastructure, Reactions* (Walter de Gruyter & Co., Berlin, 1989)
13. J. Barnett, V. Bonham, Biol. Rev. **79**(2), 461 (2004)
14. M. McCann, M. Hammouri, R. Wilson, P. Belton, K. Roberts, Plant Physiol. **100**(100), 1940 (1992)
15. M. McCann, M. Bush, D. Milionia, P. Sadoa, N. Stacey, G. Catchpole, M. Defernez, N. Carpita, H. Hoft, P. Ulvskov, R. Wilson, K. Roberts, Phytochemistry **57**, 811 (2001)
16. M. Kacuráková, P. Capeka, V. Sasinková, N. Wellner, A. Ebringerova, Carbohydr. Polym. **43**, 195 (2000)
17. D. Stewart, Appl. Spectro. **50**(3), 357 (1996)
18. C. Séné, M. McCann, R. Wilson, R. Crinter, Plant Physiol. **106**, 1623 (1994)
19. D. Himmelsbach, S. Khahili, D. Akin, Vib. Spectrosc. **19**, 361 (1999)

20. R. Atalla, U. Agarwal, Science **227**, 636 (1985)
21. G. Toole, M. Kacurakova, A. Smith, K. Waldron, R. Wilson, Carbohydr. Res. **339**(3), 629 (2004)
22. V. Morris, S. Ring, A. MacDougall, R. Wilson, *The Plant Cell Wall - Annual Plant Reviews* (Blackwell, 2003), chap. Biophysical characterisation of plant cell walls, pp. 55–91
23. B. Schrader, A. Hoffmann, A. Simon, J. Sawatzki, Vib. Spectrosc. **1**(3), 239 (1991)
24. M. Baranska, H. Schulz, P. Rösch, M. Strehle, J. Popp, Analyst **129**(10), 926 (2004)
25. R. Baranski, M. Baranska, H. Schulz, Planta **222**(3), 448 (2005)
26. M. Baranska, H. Schulz, E. Joubert, M. Manley, Anal. Chem. **78**(22), 7716 (2006)
27. R. Atalla, J. Ranua, E. Malcolm, Tappi J. **67**(2), 96 (1984)
28. J. Wiley, R. Atalla, Carbohydr. Res. **160**, 113 (1987)
29. R. Atalla, R. Whitmore, C. Heimbach, Macromolecules **13**(6), 1717 (1980)
30. S. Fischer, K. Schenzel, K. Fischer, W. Diepenbrock, Macromol. Symp. **223**, 41 (2005)
31. H. Edwards, D. Farwell, D. Webster, Spectrochim. Acta Part A Mol. Biomol. Spectrosc. **53**(13), 2383 (1997)
32. A. Jähn, M. Schröder, M. Füting, K. Schenzel, W. Diepenbrock, Spectrochim. Acta Part A Mol. Biomol. Spectrosc. **58**, 2271 (2002)
33. P. Peetla, K. Schenzel, W. Diepenbrock, Appl. Spectrosc. **60**(6), 682 (2006)
34. W. Morrison, D. Himmelsbach, D. Akin, J. Evans, J. Agric. Food Chem. **51**(9), 2565 (2003)
35. Y. Liu, S. Kokot, T. Sambi, Analyst **123**(4), 633 (1998)
36. B. Schrader, H. Klump, K. Schenzel, H. Schulz, J. Mol. Struct. **509**, 201 (1999)
37. N. Gierlinger, M. Schwanninger, A. Reinecke, I. Burgert, Biomacromolecules **7**(7), 2077 (2006)
38. S. Eichhorn, J. Sirichaisit, R. Young, J. Mater. Sci. **36**, 3129 (2001)
39. H. Edwards, D. Farwell, D. Webster, Spectrochim. Acta Part A Mol. Biomol. Spectrosc. **53**(13), 2383 (1997)
40. U. Agarwal, Planta **224**(5), 1141 (2006)
41. N. Gierlinger, M. Schwanninger, Plant Physiol. **140**(4), 1246 (2006)
42. T. Röder, G. Koch, H. Sixta, Holzforschung **58**, 480 (2004)
43. U. Agarwal, S. Ralph, Appl. Spectrosc. **51**(11), 1648 (1997)
44. J. Barnett, G. Jeronimidis, *Wood Quality and its Biological Basis* (Blackwell Scientific Publisher, Oxford, 2003), chap. Reaction Wood, p. 226
45. T. Okuyama, H. Yamamoto, M. Yoshida, Y. Hattori, R. Archer, Ann. Sci. For. **51**, 291 (1994)
46. W. Côté, A. Day, *Cellular Ultrastructure of Woody Plants* (Syracuse University Press, Syracuse, 1965), chap. Anatomy and ultrastructue of reaction wood, pp. 391–418
47. N. Nishikubo, T. Awano, A. Banasiak, V. Bourquin, F. Ibatullin, R. Funada, H. Brumer, T. Teeri, T. Hayashi, B. Sundberg, E. Mellerowicz, Plant Cell Physiol. **48**(6), 843 (2007)
48. H. Yamamoto, M. Yoshida, T. Okuyama, Planta **216**(2), 280 (2002)
49. N. Gierlinger, I. Burgert, NZ J. Forest. Sci. **36**(1), 60 (2006)
50. P. Rösch, H. Schneider, U. Zimmermann, W. Kiefer, J. Popp, Biopolymers **74**(1–2), 151 (2004)
51. D. Dietrich, K. Witke, R. Rossler, G. Marx, Appl. Surf. Sci. **179**(1–4), 230 (2001)
52. K. Witke, J. Gotze, R. Rossler, D. Dietrich, G. Marx, Spectrochim. Acta Part A Mol. Biomol. Spectrosc. **60**(12), 2903 (2004)
53. J. Nowak, M. Florek, W. Kwiatek, J. Lekki, P. Chevallier, E.Z.N. Mestres, E. Dutkiewicz, A. Kuczumow, Mater. Sci. Eng. C-Biomimetic Supramol. Syst. **25**(2), 119 (2005)
54. A. Macnish, D. Irving, D. Joyce, V. Vithanage, A. Wearing, R. Webb, R. Frost, Aust. J. Bot. **51**, 565 (2003)
55. L. Prinsloo, W. du Plooy, C. van der Merwe, J. Raman Spectrosc. **35**(7), 561 (2004)
56. D. Dietrich, S. Hemeltjen, N. Meyer, E. Baucker, G. Ruhle, O. Wienhaus, G. Marx, Anal. Bioanal. Chem. **374**(4), 749 (2002)
57. D. Dietrich, S. Hinke, W. Baumann, R. Fehlhaber, E. Baucher, G. Ruhle, O. Wienhaus, G. Marx, Anal. Bioanal. Chem. **376**(3), 399 (2003)
58. N. Gierlinger, L. Sapei, O. Paris, Planta **227**(5), 969 (2008)
59. L. Sapei, N. Gierlinger, J. Hartmann, R. Nöske, P. Strauch, O. Paris, Anal. Bioanal. Chem. **389**, 1249 (2007)
60. T. Timell, Sven. Papperstidning **67**(9), 356 (1964)

Part VI
Materials Science

Chapter 20
Confocal Raman Imaging of Polymeric Materials

Ute Schmidt, Jörg Müller and Joachim Koenen

Abstract Polymers play an essential role in modern materials science. Due to the wide variety of mechanical and chemical properties of polymers, they are used in almost every field of application and are still a dynamic area in the development of new materials with demanding requirements. Raman spectroscopy is one of the standard characterization techniques used to uniquely determine the chemical composition of a polymer. Modern materials, however, are generally heterogeneous, in which various chemical components or polymorphs of the same chemical species can be present in a very small sample volume. For the analysis of such heterogeneous materials, the combination of Raman spectroscopy with confocal microscopy delivers information about the spatial distribution of the various chemical species with a resolution down to 200 nm. The aim of this contribution is to demonstrate the power of confocal Raman imaging for the characterization of heterogeneous polymeric materials. The first section will deal with polymorphs of polypropylene in polymer films, followed by the nondestructive analysis of polymer blends. A later section will deal with multi-layer polymer coatings and paints and finally, various additives to polymer matrices will be discussed.

20.1 Introduction

The characterization of heterogeneous systems on the microscopic scale continues to grow in importance and to impact key applications in the fields of materials science, nanotechnology and catalysis. The development of advanced polymeric materials for applications such as these requires detailed information about their physical and chemical properties on the nanometer scale. However, some details about the

U. Schmidt (✉) · J. Müller · J. Koenen
WITec GmbH, Lise-Meitner-Strasse 6, 89081 Ulm, Germany
e-mail: ute.schmidt@witec.de

J. Müller
e-mail: joerg.mueller@witec.de

J. Koenen
e-mail: joachim.koenen@witec.de

J. Toporski et al. (eds.), *Confocal Raman Microscopy*, Springer Series in Surface Sciences 66, https://doi.org/10.1007/978-3-319-75380-5_20

phase separation process in polymers are difficult to study with conventional characterization techniques due to the inability of these methods to chemically differentiate materials with sufficient spatial resolution and without damage, staining or preferential solvent washingwq. One technique that has been used successfully in the characterization of heterogeneity in polymers is Atomic Force Microscopy (AFM) [1–4]. AFM can provide spatial information along and perpendicular to the surface of a polymer film with a resolution on the order of 1 nm. The most commonly used AFM imaging mode for polymers is the intermittent contact mode also known as AC Mode or Tapping Mode [5]. In this AFM imaging mode the cantilever is oscillated at its resonance frequency and the topography of the surface is scanned by keeping the oscillation damping constant. A phase image can be recorded simultaneously with the surface topography. In this image, the phase shift between the free oscillation of the cantilever in air and the oscillation while the tip is in contact with the surface is recorded [6]. Since the phase shift depends as much on the viscoelastic properties of the sample as on the adhesive potential between sample and tip, the phase image outlines domains of varying material contrast without describing the nature of the material properties [7–11]. Nevertheless, phase images are often used to characterize polymers at high-resolution [12, 13]. If a composite material consists of compounds with similar mechanical properties, a clear assignment of the phases to the corresponding materials by AFM is quite challenging. To discriminate between materials with similar mechanical properties, additional spectroscopic information is useful. On the macroscopic scale, Raman spectroscopy has become widely used for the characterization of chemical and structural features of polymeric materials [14]. The tremendous value of the Raman effect lies in the fact that the difference in energy between the elastically scattered photons and the Raman shifted photons is caused by the excitation or annihilation of a specific molecular vibration. This energy shift is characteristic for the type and coordination of the molecules involved in the scattering process. Raman spectra provide qualitative and quantitative information about various polymer features [15–17] such as:

- chemical nature: structural units, type and degree of branching, end groups, additives
- conformational order: physical arrangement of the polymer chain
- state of order: crystalline, mesomorphous and amorphous phases
- orientation: type and degree of polymer chain and side group alignment in anisotropic materials.

However, in most spectroscopy setups the spatial resolution is very poor because the excitation laser spot diameter is on the order of 100 μm. Optical microscopy, on the other hand, is capable of providing spatial resolution down to 200 nm using visible light excitation. In a confocal microscope, the light from the sample is detected through a pinhole at the back focal plane of the microscope, giving rise to depth resolution and a strongly reduced background signal [18]. By combining a high-throughput confocal microscope with an extremely sensitive Raman spectroscopy system, it is possible to obtain Raman spectra from extremely small sample volumes down to 0.004 μm^3 as will be shown later. To collect high-resolution Raman images,

the sample is scanned point by point and line by line through the excitation focus [18]. Thus, the Confocal Raman Microscope (CRM) combines the chemical sensitivity of Raman spectroscopy and the high-resolution of confocal microscopy, providing an ideal tool for the characterization of materials in the sub-micrometer range. To achieve the highest resolution, the CRM can be extended with AFM capabilities which enable the user to link the chemical information obtained by confocal Raman spectroscopy with the ultra-high spatial and topographical information acquired by AFM.

The Raman experiments presented in this chapter were performed with a WITec alpha300RA (combined Raman-AFM) using green excitation (532 nm) and a 100×, NA = 0.9 objective. The AFM measurements were done using the same instrument in AFM-AC mode.

20.2 Raman Imaging of Isotactic Polypropylene (IPP)

Polypropylene (PP) is a thermoplastic polymer synthesized from the monomer propylene with the chemical formulas shown in Fig. 20.1. Its dual functionality as plastic and fiber leads to its varied fields of application. As a plastic it is used as reusable containers, stationary plastic parts, laboratory equipment, automotive components, banknotes, etc. As a fiber, polypropylene is used to make ropes, unwoven textiles, packaging materials, etc. The large number of end use applications for PP are due to the ability to tailor grades with specific molecular properties and additives during its manufacturing processes.

The characterization of the morphology of polypropylene fibers in complex structures remains a focus of ongoing research. The crystallinity and the extent of orientation of molecular chains are two of the most important morphological characteristics

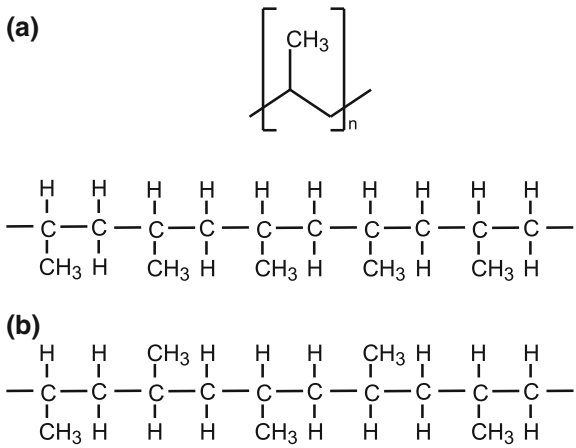

Fig. 20.1 Chemical formula of the polypropylene monomer (**a**) and short segments of polypropylene showing isotactic (upper row) and syndiotactic (lower row) tacticity (**b**)

of the fiber structure that influence the final properties. Raman spectroscopy is one of the many methods used to characterize the microstructure of a semicrystalline polymer. It provides the capability to probe the conformational states of polymer chains in its micro-environment [19–21]. Differences in the Raman spectrum of chains in non-crystalline regions with conformational irregularities or non-helical conformations can be expected [22–25]. A theoretical determination of the vibrational Raman bands of helical polypropylene chains can be found in [26, 27], whereas stress-induced deformations of polypropylene chains are reported in [28, 29]. The structure of a polymer is given by its particular structural arrangement [30]. In isotactic polypropylene, a crystallizable polymer, the structural arrangement is given by the arrangement of crystalline and amorphous domains. The formation of crystalline and amorphous domains is influenced by the crystallization conditions. Crystallization from the unstressed melt results in a randomly nucleated spherulitic structure, whereas crystallization which occurs in an extensional flow field (e.g. during the extrusion process) results in a row-nucleated structure. Depending on the extrusion conditions, bundles of oriented fibers can be formed.

To determine a correlation between the orientation of lammelar rows of isotactic polypropylene and Raman spectra, a uniaxially drawn isotactic polypropylene film (OPP) with a thickness of 50 μm was investigated using polarized Raman spectroscopy. High-resolution atomic force microscopy measurements on such films show a highly oriented fibrillar structure, which is oriented in parallel to the extrusion direction [31]. On this highly oriented isotactic polypropylene film, polarization-dependent Raman spectra were recorded. Figure 20.2 shows a schematic of the four different geometries in which Raman spectra were recorded.

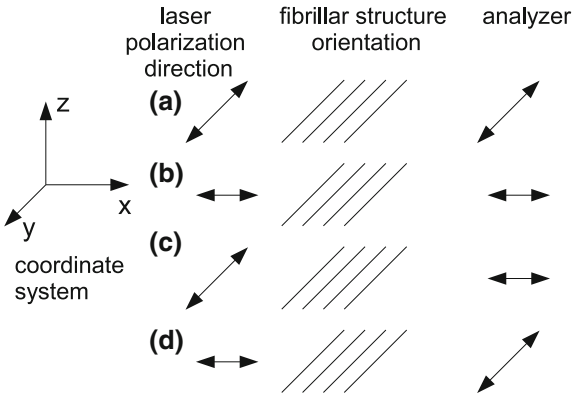

Fig. 20.2 Schematics of the scattering geometry defined in the above shown coordinate system, the incident laser propagates in z-direction. By using a half-wave plate the incident laser light can be polarizes in x- or y-direction. The scattered light is analyzed either in parallel or perpendicular to the polarization direction of the incident laser light. The four possible combinations with respect to the orientation of a one dimensional structure is presented: incident light polarization and analyzer oriented in parallel with the one dimensional structure (**a**), incident light polarization and analyzer oriented perpendicular to the one dimensional structure (**b**), polarization direction of laser and analyzer arranged perpendicular to each other in the two possible arrangements with the one-dimensional structure (**c**, **d**)

The polarized Raman spectra from the OPP film are presented in Figs. 20.3 and 20.4. The spectra result from one sample position. A half-wave plate was used to rotate the polarization of the incident laser light either parallel or perpendicular to the fiber, whereas the scattered light passed through an analyzer either in parallel or perpendicular to the polarization direction of the incident laser light. All recorded Raman spectra were normalized to the bands at 1435 and 1457 rel. cm^{-1}, which are not polarization-dependent. These bands are assigned to methyl group deformations in isotactic polypropylene and show an additional splitting only at very low temperatures [19].

The spectra shown in Fig. 20.3 are recorded in the configuration in which the polarization direction of the incident and scattered laser light are in the same direction, whereas in Fig. 20.4 the spectra recorded in the crossed orientation of laser polarization direction and analyzer are presented. The two later configurations show only minor differences in Raman band intensities as reported before by [20, 32]. Fiber orientation and laser polarization-dependent changes can be clearly observed in the spectra shown in Fig. 20.3. The Raman bands at 809, 841 and 1152, 1169 rel. cm^{-1} are the most characteristic of a directional ordering of the polymer chains in

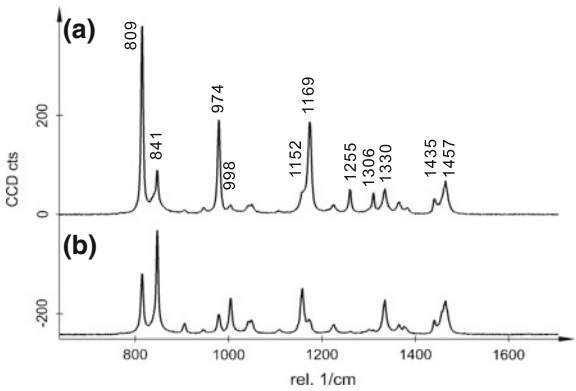

Fig. 20.3 Polarization dependent Raman spectra of uniaxial isotactic polypropylene: polarization direction of laser, fiber and analyzer oriented in parallel (**a**) and polarization direction of laser and analyzer oriented perpendicular to the iPP fibers (**b**)

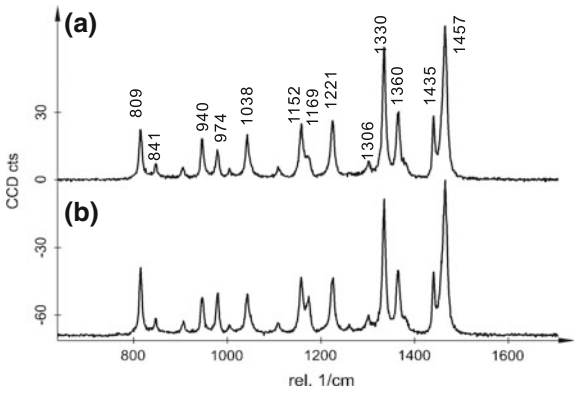

Fig. 20.4 Polarization dependent Raman spectra of uniaxial isotactic polypropylene: polarization direction of laser and fiber oriented in parallel with analyzer perpendicular (**a**) and polarization direction of laser perpendicular and analyzer oriented in parallel to the fiber orientation (**b**)

isotactic polypropylene. Based on normal mode calculations it has been shown that these bands in solid state are associated with the helical chain structure [33, 34].

Considering the above described polarization-dependency of Raman spectra recorded from highly oriented isotactic polypropylene, Raman imaging of polypropylene provides information about the structural arrangement of ordered and disordered polymer chains. Figure 20.5 shows a Raman image of biaxially oriented polypropylene (BOPP). A 2D-array of 100 × 50 single Raman spectra were recorded from a surface area of 50 × 30 μm^2 using a frequency doubled Nd:YAG laser (excitation wavelength 532 nm) and a 100× objective (NA = 0.9). The integration time per single spectrum was 0.1 s. From the 5000 individual spectra, two unique Raman spectra were calculated (Fig. 20.5a). The green spectrum is characteristic for polypropylene fibers oriented parallel to the laser polarization direction, (see Fig. 20.3a), whereas the red spectrum is characteristic for polypropylene fibers oriented perpendicular to the laser polarization direction. The color-coded Raman image (Fig. 20.5b) reveals the oriented fiber bundle. To prove the orientation of such fiber bundles, AFM (Atomic Force Microscopy) measurements were performed on the sample area marked with a frame in Fig. 20.5b. Figure 20.5c shows the topography of the BOPP film, whereas the simultaneously recorded phase image reveals the fiber bundle and the fine fibrillar structure of the BOPP film.

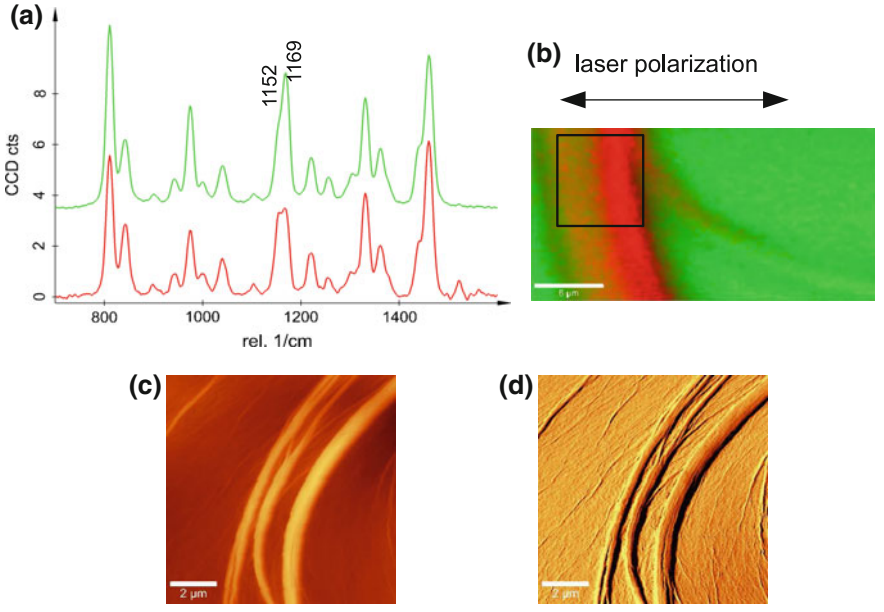

Fig. 20.5 Raman imaging of biaxially oriented polypropylene: Raman spectra (**a**), color-coded Raman image (**b**), AFM topography image (**c**) and AFM phase image (**d**). The scale bar in **b** is 6 µm and in **c** and **d** 2 µm long

The simultaneously recorded phase image reveals much more details of the fine structure of the BOPP film compared to the Raman image. The oriented bundle seems much wider and oriented in a different direction in the Raman image due to the diffraction limited resolution in all three volume directions. The phase image on the other hand is imaging only the surface topography.

Polypropylene films are commonly used as solid dielectrics in high voltage capacitors. Such films are produced by biaxially stretching unstretched molded polypropylene. The surface of such films have an efficiently roughened, fine uneven structure containing crater-like patterns or an isotropic and an anisotropic network structure, which is aligned in the extrusion direction. To obtain more detailed information about the fine structure of such foils, polarized Raman imaging can be employed. By using a polarization rotation (half-wave plate) a surface area can be analyzed using different laser polarization directions, thus determining the different preferential orientation of the spherulitic grains. Figure 20.6 shows the video image recorded on such a foil. The red square marks the area which was scanned for Raman imaging. The spectrometer was equipped with an 1800 grooves/mm grating. Over an area of $15 \times 15\,\mu m^2$, an array of 100×100 Raman spectra was recorded with an integration time of 0.1 s/per spectrum.

The same area was first scanned with the laser polarization and analyzer both oriented horizontally to the x-axis of the image. In a second scan, the same area was scanned with the laser polarization and analyzer oriented both perpendicular to the x-axis of the image. The polarization-dependent Raman spectra of uniaxial isotactic polypropylene (Fig. 20.3) were used as basis spectra for the basis analysis of the recorded 2D spectral arrays [35]. Figure 20.7a shows the distribution of spherulitic structures which are oriented parallel (green) and perpendicular (red) to the laser polarization direction. By rotating the laser polarization direction and analyzer by 90° the image shown in Fig. 20.7b was recorded. In this case, spherulitic structures oriented parallel to the laser polarization direction are shown in yellow, whereas blue was used for perpendicularly oriented spherulitic structures. Figure 20.7c shows

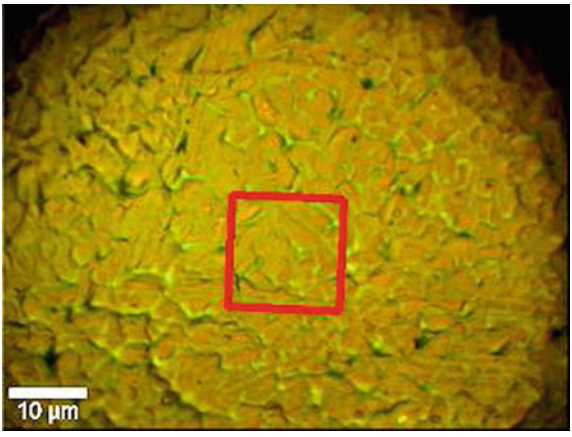

Fig. 20.6 Video image of a polypropylene film used as solid dielectric in capacitors. The red frame marks the area imaged with Raman imaging

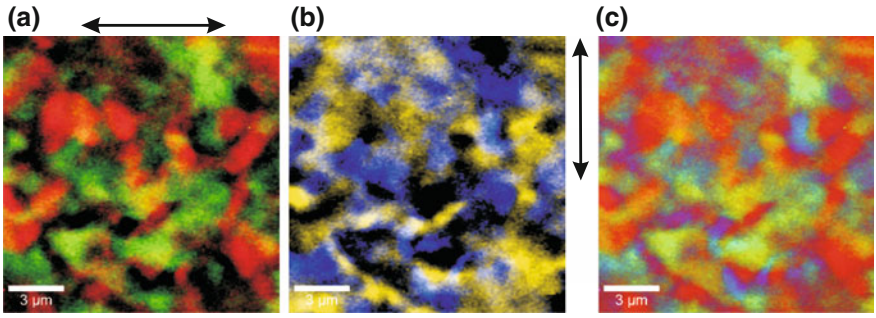

Fig. 20.7 Color coded polarization dependent Raman images of a polypropylene film used as solid dielectric in capacitors: Raman image of polypropylene oriented in parallel and perpendicular to the horizontal (**a**) and vertical (**b**) laser polarization direction and combined color-coded Raman image of all polarization directions

a color-coded image of the various grain orientations detected by using polarized confocal Raman imaging.

The predominant colors in Fig. 20.7c are red and green indicating that one measurement with polarized light is enough to characterize the orientation in such polymer films.

20.3 Raman Imaging of Polymer Blends

Polymer blends are designed to address the needs of different industries and in many cases the relationship between structure, morphology and material properties is crucial for the optimization of material design. Since the beginning of the plastics industry it has been recognized that blending yields materials with property profiles superior to the features of the individual components. A polymer blend is a macroscopically homogeneous mixture of two or more different species of polymer which combine the useful properties of all of the constituents. The technology of blending is now advancing at a rapid pace. There has been progress in the understanding of the behavior of polymer blends, especially the thermodynamics and rheology [36, 37]. New blends are constantly being developed and characterized. The main parameters which influence the properties of a blend are the interface and the morphology. The morphology of a polymer blend indicates the size, shape and spatial distribution of the component phases with respect to each other. The properties, such as: mechanical, optical, rheological, dielectrical, and barrier properties of polymer blends are strongly influenced by the type and granularity of the phase structure. A large variety of analytical methods are used to characterize the morphology of polymer blends. Raman imaging contributes to the analysis of multicomponent polymer systems by visualizing the distribution of individual components based on differences in the unique Raman spectra for different polymeric materials. Domains of different

components in polymer blends are typically of a larger size. In many cases, they are formed during phase separation. Raman imaging provides real-space observation of different coarsening processes and allows direct quantification of phase volume fractions and the computation of domain interface curvatures of various morphologies. A direct assignment of image features to various polymer phases becomes available with a resolution down to 200 nm. Micro-phase separation patterns with spherical, cylindrical, lamellar or micellar morphology, which are characterized by structural factors in the tens of nanometers range can be analyzed by transforming the confocal Raman microscope into an AFM [35, 38].

In the following sections three different blends composed of immiscible polymers, which are at room temperature in either the rubbery or glassy state were investigated. For these studies, thin films of the polymer blends with a thickness of less than 100 nm were prepared by spin-coating solutions containing the polymers onto clean glass cover slides at 2000 rpm.

20.3.1 Raman Imaging of Thin Films of the Polymer Blend: Polystyrene (PS) - Ethyl-Hexyl-Acrylate (EHA)

In this section a polymer blend which consists at room temperature of the glassy state polymer PS and the rubbery state polymer EHA is described.

Figure 20.8a shows the Raman spectra of the pure blend components. Both, PS (blue) and EHA (green) show characteristic band structures around 2800–3000 rel. cm^{-1}, which are associated with C-H stretching and the peak at 1454 rel. cm^{-1} which is characteristic for C-H bending. EHA shows a Raman peak at 1735 rel. cm^{-1} which is characteristic for C=O stretching, whereas PS shows the additional Raman bands associated with the benzene ring modes [39, 40]. These two spectra can be used for the basis analysis of 2-dimensional spectral arrays acquired from the polymer blend.

The variations in the Raman spectra of these two polymers make it possible to distinguish the various polymers from each other when they are blended. The blend of PS-EHA was scanned in Raman spectral imaging mode. Complete Raman spectra were recorded at every image pixel (200×200 spectra) with an integration time of 0.08 s/spectrum. To assign the different polymers in the film, the complete spectra of the two polymers were employed by using basis spectra analysis (see Chap. 5). The distribution of the EHA is shown in Fig. 20.8b, whereas the distribution of PS is represented in Fig. 20.8c. These two complementary Raman images show that PS forms islands surrounded by the EHA matrix. Both polymer phases wet the glass substrate.

High-resolution AFM images recorded on this film are shown in Fig. 20.9. The topography image (Fig. 20.9a) reveals that the PS islands are 40 nm higher than the surrounding EHA phase. The diameter of the PS islands range from 100–1500 nm. The simultaneously recorded phase image (Fig. 20.9b) shows a high phase contrast between the two materials. Brighter areas can be assigned to the harder (glassy)

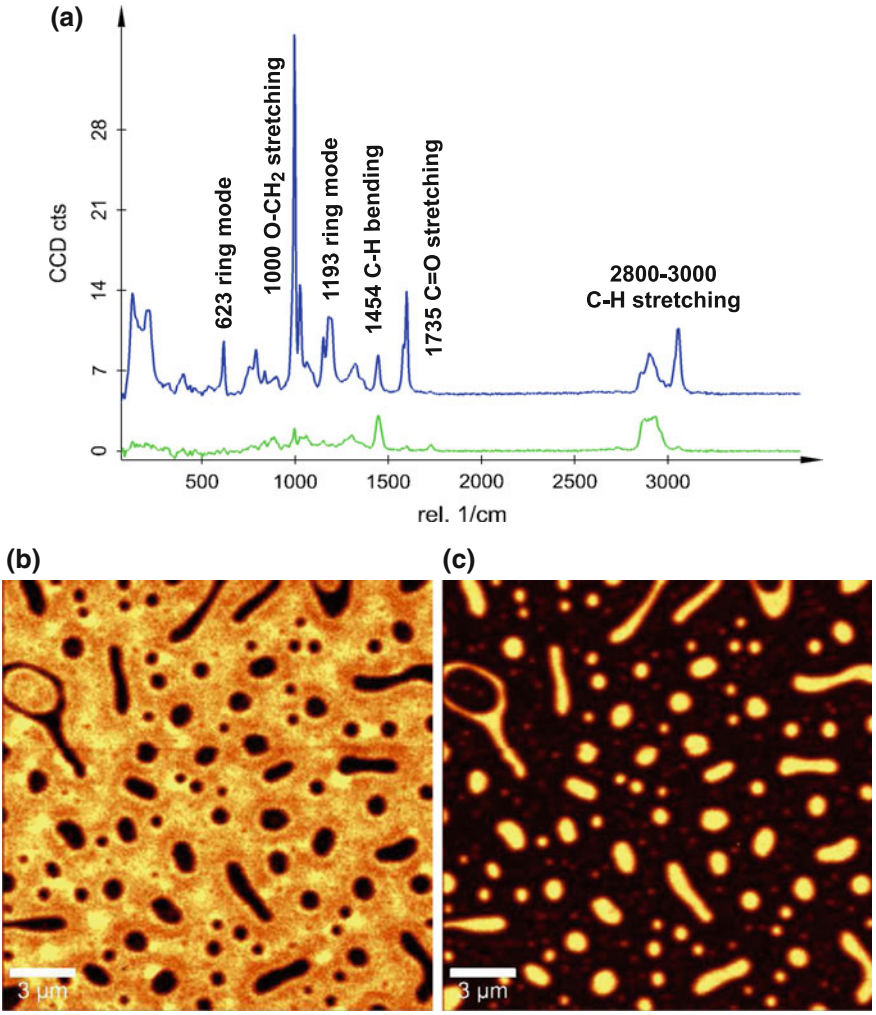

Fig. 20.8 Single Raman spectra of pure PS (blue spectrum) and EHA (green spectrum) (**a**), Raman image of EHA distribution (**b**) and Raman image of PS distribution (**c**)

polystyrene, whereas the soft (rubbery) EHA appears darker. Within the EHA phase a netlike fine structure becomes visible in the phase image.

To determine the overall thickness of the thin film of the polymer blend, the film was scratched with a razor blade and imaged with AFM. Figure 20.10a shows the topography of the scratch and the corresponding height histogram of the image (Fig. 20.10b).

The measured height of the EHA phase of only 30 nm together with the focus spot size of 340 nm shows that a sample volume of less than 0.004 μm^3 is enough to

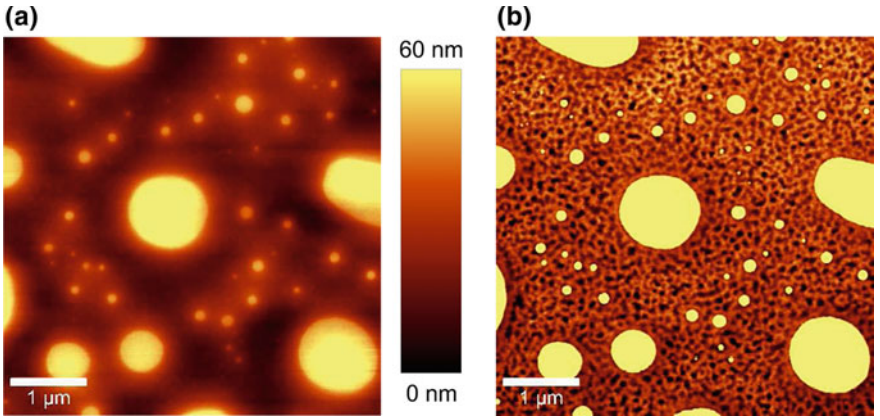

Fig. 20.9 High-resolution AFM AC mode image of the polymer blend PS-EHA: topography image (**a**) and simultaneously recorded phase image (**b**)

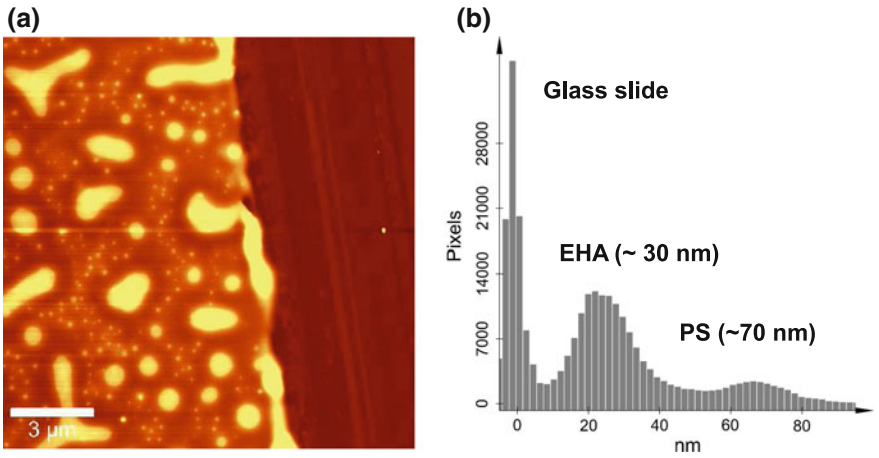

Fig. 20.10 AFM AC mode topography image of the scratched film of PS-EHA (**a**) and histogram of height distribution on the surface (**b**)

identify the chemical species with the confocal Raman microscope using integration times of less than 100 ms/spectrum.

20.3.2 Raman Imaging of Thin Films of the Polymer Blend Ethyl-Hexyl-Acrylate (EHA) - Styrene-Butadiene Rubber (SBR)

In this section a polymer blend consisting of two polymers, which are in the rubber phase at room temperature, is described. A 2D spectral array of 100×50 spectra was acquired from a sample area of $10 \times 5\,\mu m^2$. From the 5000 recorded spectra, two distinct Raman spectra were calculated by using cluster analysis (see Chap. 5 in this book for a more detailed explanation). These spectra are represented in red and green in Fig. 20.11a. The green spectrum shows the characteristic Raman bands of EHA (compare with green spectrum Fig. 20.8a), whereas the red spectrum shows additional Raman bands at 1000 and 3060 rel. cm^{-1} and in the spectral range of 1635–1650 rel. cm^{-1}. The latter Raman bands are associated with C=C stretching and are characteristic for SBR [35]. The differential spectrum between the red and the green spectra is shown in blue in Fig. 20.11a and represents the unique Raman spectrum of SBR [35]. Figure 20.11b shows the Raman image of the distribution of the two detected species within the scanned surface area. The distribution of the pure EHA phase is represented in green and the red color denotes the presence of a mixed phase consisting of EHA and SBR.

To gain insight into the fine structure of the mixed phase consisting of EHA and SBR, high-resolution structural information is required. This can be obtained from high-resolution AFM images. In a previous study it could be shown that phase images recorded on thin films of pure SBR spin-coated on glass substrates reveal a statistical distribution of the hard styrene blocks in the rubbery butadiene matrix [35]. The fine structure of pure EHA wetting the glass substrate is shown in Fig. 20.10b.

AFM images recorded in AC mode on the polymer blend consisting of EHA and SBR reveal a two level topography. The simultaneously recorded phase image is shown in Fig. 20.11c. The netlike structure, characteristic for EHA wetting the glass substrate, could be resolved in the topographic lower regions of the surface. This finding is in good agreement with the elliptic domains consisting of pure EHA found in the Raman image. The topographically elevated structure, consisting of a large network appears featureless if a large area is scanned. The high-resolution AFM image obtained from a smaller scan area (see insert of Fig. 20.11c) reveals a grain-like fine structure in the topographically elevated structure, which is characteristic for SBR. The Raman image showed however, that in these surface areas the two polymers SBR and EHA coexist, thus the SBR phase is formed on top of the EHA layer. By combining confocal Raman imaging with high-resolution AFM imaging, it could be shown that in this polymer blend only EHA is wetting the glass substrate. For this polymer blend only the combination of Raman and AFM imaging reveals the wetting and separation behavior of the two rubbery polymers without selective dissolution of one of the polymer phases.

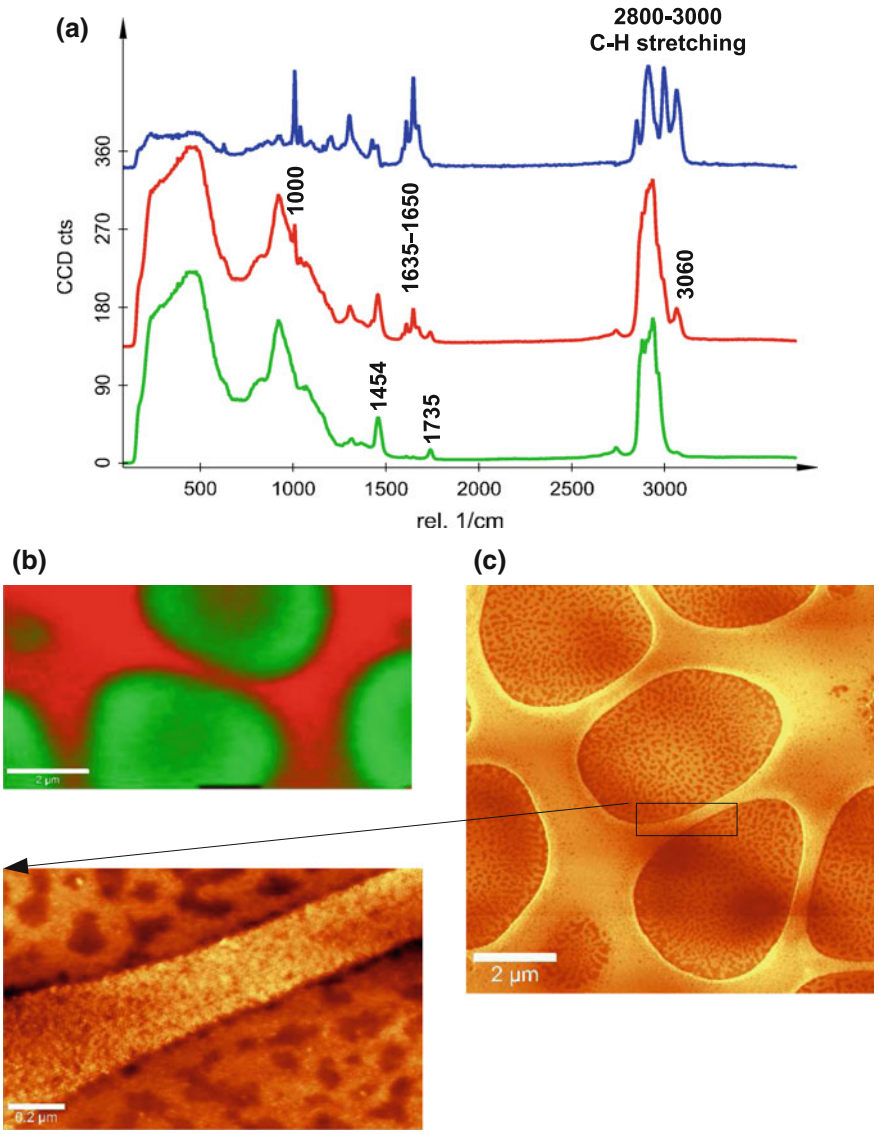

Fig. 20.11 Raman spectra of EHA (green spectrum), a mixed Raman spectrum of EHA+SBR (red spectrum), and the differential spectrum between red and green spectrum revealing the pure SBR Raman spectrum in blue (**a**), color-coded Raman image of the distribution of pure EHA and of the mixed phase EHA+SBR (**b**), and high-resolution AFM phase images of the polymer blend (**c**)

20.3.3 Raman Imaging of Thin Films of the Polymer Blend PS-EHA-SBR

In this section a thin film of a three component polymer blend is described, which at room temperature consists of the two rubbery state polymers EHA and SBR and the glassy state polymer PS.

A 2D spectral array of 128 × 128 spectra was acquired from a sample area of 20 × 20 μm^2 of this polymer film. The spectral array was analyzed using basis analysis. The Raman spectra shown in Fig. 20.12a were used as basis spectra. In the basis analysis technique, each measured Raman spectrum is fitted by a linear combination of a certain number of basis spectra (see also Chap. 5). A color-coded Raman image of the distribution of the three polymer phases is shown in Fig. 20.12b. In this image, blue represents the distribution of PS while the green areas consist of pure EHA. Yellow denotes a mixed phase of EHA and SBR. This image confirms the previously observed phase separation processes: PS, the polymer in the glassy state at room temperature, and EHA, form an interface with the glass substrate, whereas the SBR is formed on top of the EHA phase.

High-resolution AFM images recorded from this blend show that PS is forming a topographically elevated rope-like structure, surrounded by SBR and EHA. A high-resolution AFM phase image (Fig. 20.12c) reveals the fine structures of the three blended polymers. The bright areas of this image can be associated with the hard PS-phase, whereas the dark red reveals the fine structure of EHA, the most adhesive component of the blend. The grain-like fine structure is found again in the SBR layer formed on top of the EHA phase.

A final evaluation of the structural arrangement of the various components of this blend is a confocal Raman depth scan. Figure 20.13 shows a color-coded confocal Raman depth scan performed on this three component polymer blend. For this Raman image a 2D spectral array consisting of 100 × 50 complete Raman spectra was recorded in a plane perpendicular to the surface, similar to a virtual section of the sample. The unique Raman spectra of the blend component (Fig. 20.12a) were used as basis spectra for the basis analysis software tool. Blue and green corresponding to PS and EHA respectively from this image form an interface with the glass substrate, whereas the red SBR phase is formed on top of the green EHA phase.

20.4 Polymer Coatings

Surfaces are coated to give them protection against a hostile environment, to enhance their appearance, or to impart specific properties to the surface. The desired effects can be achieved with coatings ranging from several micrometers to less than one micrometer in thickness. For some surfaces several layers are required to fulfill a specific task, in other cases a specific distribution of materials is needed. Establishing

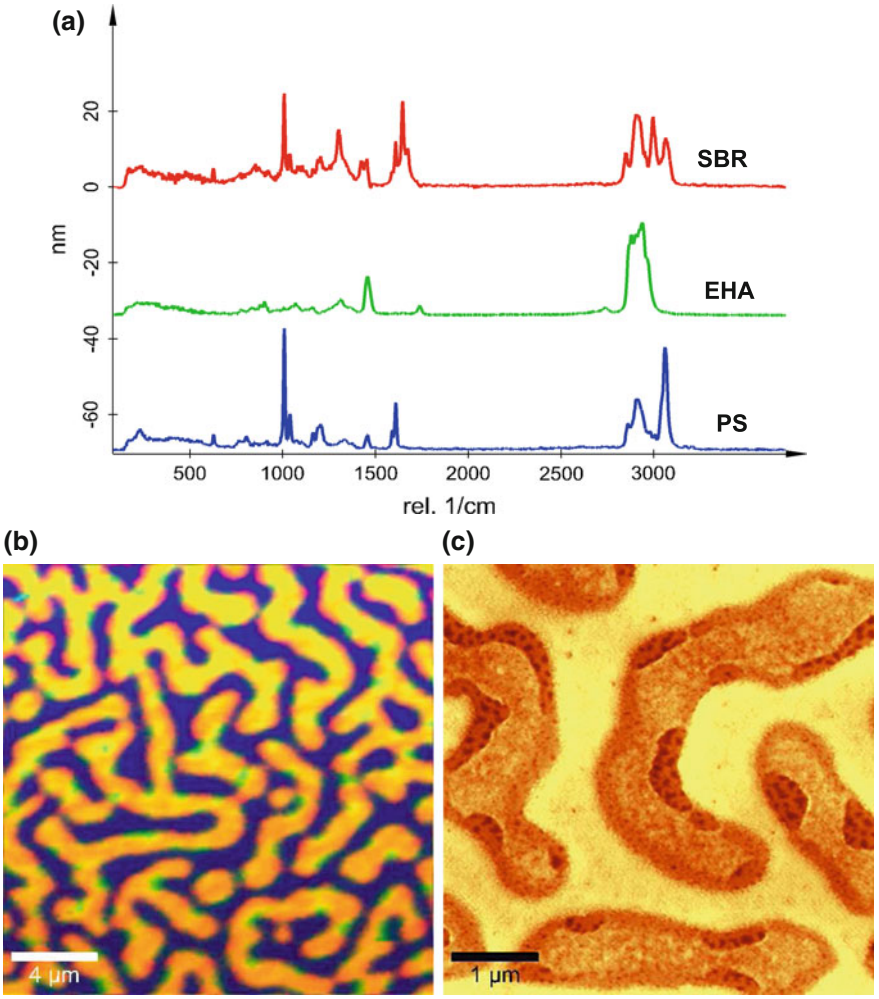

Fig. 20.12 Single Raman spectra of pure PS, EHA, and SBR used as basis spectra for the basis analysis of the 2D spectral array acquired from this sample (**a**), color-coded Raman image of the three component polymer blend (**b**), and high-resolution AFM phase image of this polymer blend (**c**)

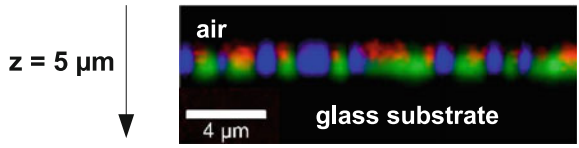

Fig. 20.13 Confocal Raman depth profile of the three component polymer blend consisting of PS (blue), EHA (green), and SBR (red)

the chemical and morphological composition of a surface is therefore a vital step towards understanding its behavior. In the following, several examples of coatings will be presented.

20.4.1 Acrylic Paints

Alkyd and acrylics are used as binders in paints and coatings. These materials produce a shiny, hard finish that is highly water-resistant. Of interest in studying this system are changes in the Raman spectra during the drying process of the paints and the distribution of the two phases within the paint. Figure 20.14 shows Raman spectra recorded from the alkyd phase before drying (a) and in the dry state of the paint (b). The decrease of the Raman bands at 1265 and 3012 rel. cm^{-1} (cis-C=C-H asymmetric stretching bands) and the cis-C=C stretch peak at 1656 rel. cm^{-1} are related to chemical changes during oxidation [41].

Figure 20.15a shows the Raman spectra of alkyd and acrylic latex in their dry state. The small differences in the Raman spectra make it possible to distinguish the two phases in the emulsion. A Raman spectral image consisting of 200 × 200 spectra was recorded from a sample area of 10 × 10 μm^2.

The spectra from Fig. 20.15a were used as basis spectra for the basis spectra analysis of the recorded 2-dimensional spectral array. The resulting color-coded Raman image is presented in Fig. 20.15b. This image indicates that large elliptic domains consisting of alkyd are surrounded by the acrylic latex phase. Figure 20.15c shows the phase image of the dried paint, indicating the stiffer nature of the acrylic latex phase. It also reveals the individual latex spheres, which are smaller than the

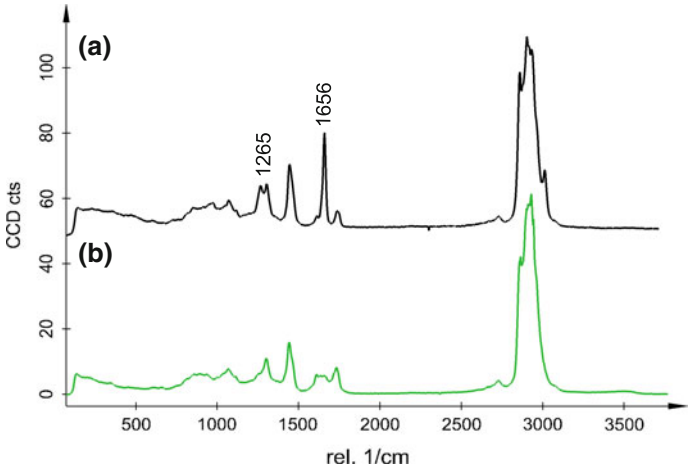

Fig. 20.14 Raman spectra of the alkyd phase before (**a**) and after (**b**) drying of the paint

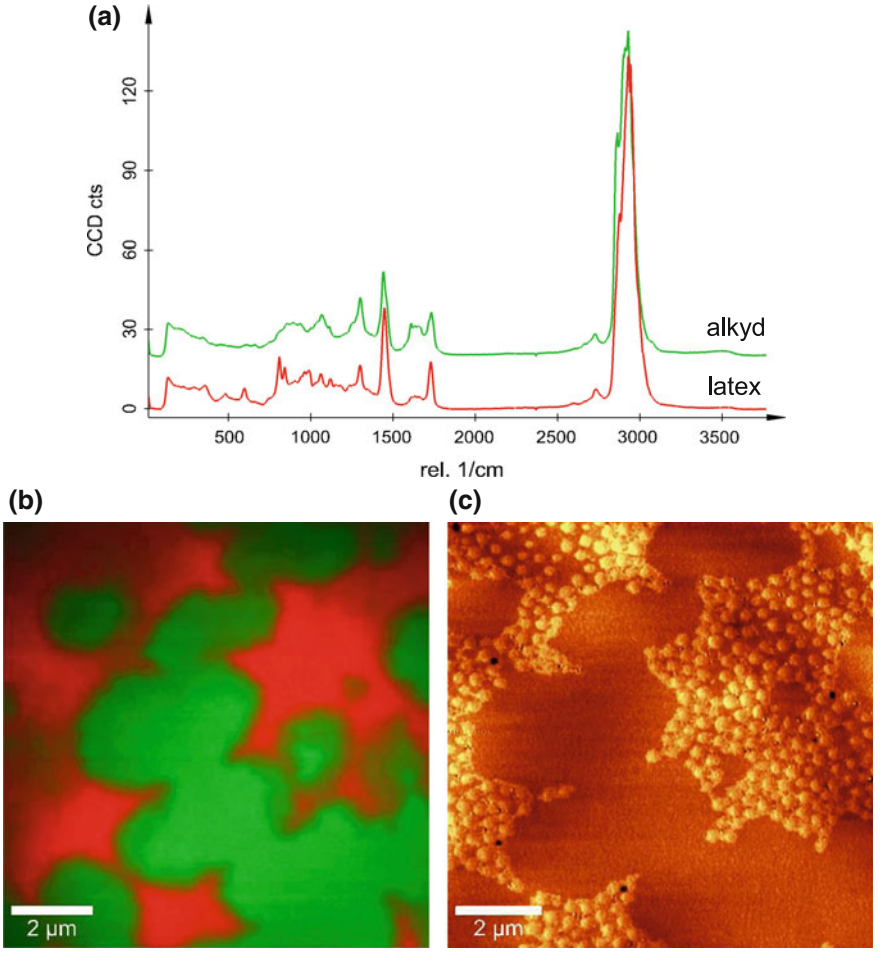

Fig. 20.15 Raman spectra of the alkyd and latex phase in the dry state of the paint (**a**), color-coded Raman spectral image of the paint surface (**b**), and AFM AC mode phase image of the same sample area revealing the spherical latex particles (**c**)

diffraction limit (using an air objective) and are thus not resolved in the confocal Raman image. The diameter of the latex spheres range from 20 to 250 nm.

20.4.2 Adhesives

The use of multi-layered materials for adhesives is now a common practice. Confocal Raman depth scans provide insight into the layered structure of such polymers without any specific sample preparation.

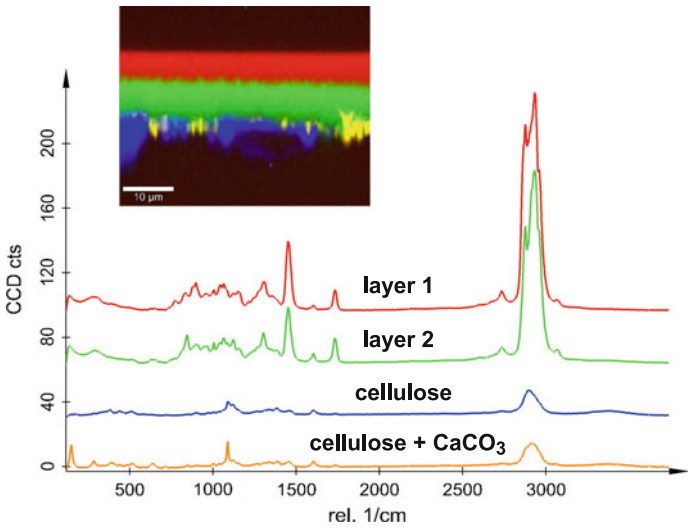

Fig. 20.16 Color coded confocal Raman depth profile of adhesive polymeric layers on a paper substrate

As an example, Fig. 20.16 shows a confocal Raman depth scan performed on an adhesive paper. In this case two polymer layers were applied to the paper surface in order to fulfill the required tasks. The two polymers are immiscible and form a sharp interface (red and green) with the paper beneath (blue and yellow).

20.5 Additives in Polymer Matrices

Nanomaterials are increasingly being used as additives to polymers to simultaneously enhance a variety of properties without sacrificing any qualities of the base polymer.

Additives of inorganic materials in solid form to polymer matrices have a great significance in plastics industry. They are used for a wide variety of purposes, e.g. anti-oxidants, stabilizers, fillers, pigments etc. Anti-oxidants and stabilizers are added in small quantities to prevent degradation of the polymer when it is exposed to air, light and heat. Fillers may be used either simply to produce a cheaper product or to improve the mechanical or electrical properties of the polymeric material. Confocal Raman microscopy allows the allocation of such fillers in the polymer matrix, leading to a better understanding of the properties of the materials. In the following, two examples of fillers are presented.

Fine metal powders and carbon black are commonly added to polymer matrices to improve the electrical, mechanical or thermal properties of the polymers. Figure 20.17 shows a confocal Raman microscopy study of polypropylene with TiO_2 and carbon inclusions. An area of $30 \times 30\,\mu m^2$ of the sample was scanned and a

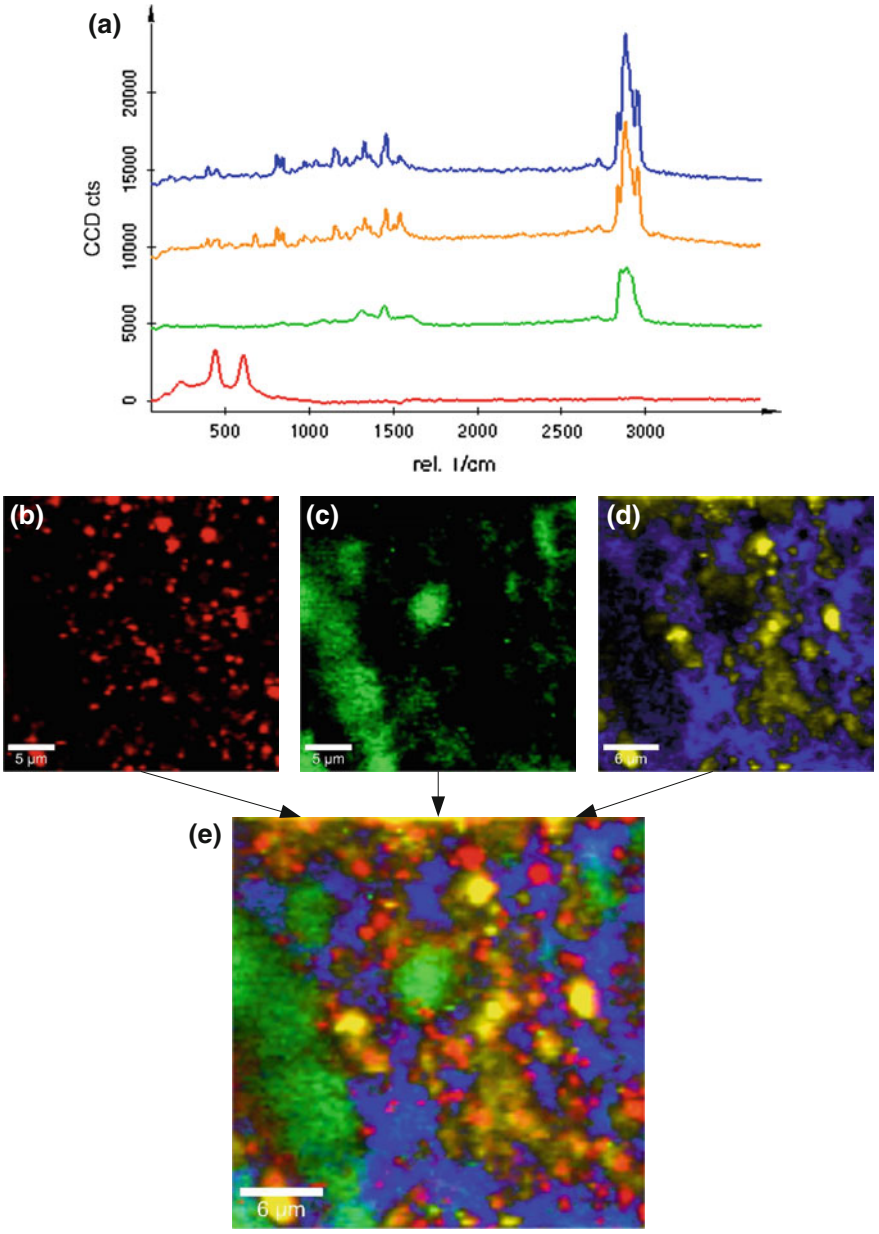

Fig. 20.17 Confocal Raman imaging of additives in a polypropylene matrix: characteristic Raman spectra evaluated from the 2D array of 10,000 spectra using cluster analysis: orientation-dependent PP Raman spectra (blue and yellow), Raman spectrum of amorphous carbon in organic matrix (green) and Raman spectrum of TiO_2 (red) (**a**), distribution of TiO_2 particles (**b**), distribution of amorphous carbon (**c**), distribution of PP (**c**), and color-coded Raman image of the analyzed surface area (**d**)

two-dimensional array of 100 × 100 Raman spectra was acquired with an integration time of 100 ms per spectrum. From this measurement four different spectra were evaluated using cluster analysis. These spectra are presented in Fig. 20.17a. In addition to the orientation-dependent Raman spectra of polypropylene (blue and yellow spectra Fig. 20.17a) the spectrum of TiO_2 (red) and the spectrum of amorphous carbon in an inorganic matrix(green) were extracted by the cluster analysis algorithm.

These spectra were used to evaluate the distribution of each component on the studied sample area using the basis analysis. The weighting factor resulting from the basis analysis denotes the presence of the species in a defined sample volume. Figure 20.17b shows the distribution of TiO_2 on the sample, whereas Fig. 20.17c shows the distribution of amorphous carbon. In Fig. 20.17d the color-coded Raman image of the distribution of polypropylene is presented. By overlaying the images described above and assigning each component the color of the corresponding Raman spectrum, the complete color-coded Raman image can be generated as shown in Fig. 20.17d. From this image it can be clearly seen that the TiO_2 particles adhere to the different oriented polypropylene grains, whereas amorphous carbon forms large clusters with a diameter of up to 6 μm.

Carbon nanotubes (CNTs) have physical properties that exceed those of commonly used materials. With a tensile strength eight times that of stainless steel and a thermal conductivity five times that of copper, CNTs are an obvious choice for creating a new class of composite materials. Their inclusion in a polymer or ceramic matrix holds the potential to enhance the host material's electrical, mechanical, or thermal properties by orders of magnitude, well above the performance possible with traditional fillers such as carbon black or ultra-fine metal powders.

Figure 20.18 shows the distribution of single-walled carbon nanotubes (SWCNTs) in a polymer matrix. For this experiment a diode laser with a wavelength of 785 nm was employed for Raman imaging. An area of 20 × 20 μm^2 was scanned and a two dimensional array of 100 × 100 Raman spectra was acquired with an integration time of 200 ms per spectrum. Figure 20.18a shows the three Raman spectra evaluated with cluster analysis. The Raman spectra of the polymer (red) and two different types of SWCNT's (blue and green) were detected. In this example, only SWCNT's show a Raman band in the spectral range 120–350 rel. cm^{-1}. This Raman band arises from the coherent vibration of the carbon atoms in the radial direction, as if the tube were breathing, and are known as radial breathing modes (RBM). These RBM frequencies (ω_{RBM}) are very useful to identify whether a given carbon material contains SWCNT's and for characterizing the nanotube diameter distribution (d_t) in the sample through use of the relation $\omega_{RBM} = A/d_t + B$, where the A and B parameters are determined experimentally [42, 43]. For typical SWCNT bundles, as expected in this polymer matrix, A = 234 nmcm^{-1} and B = 10 cm^{-1} may be used. The two different ω_{RBM} found in this sample are at 258 and 267 rel. cm^{-1}, corresponding to tube diameters of 0.96 and 0.91 nm respectively. The distribution of these two types of SWCNTs is shown in Fig. 20.18b. The SWCNTs with a diameter of 0.94 nm (green) appear as 2 − 4 μm long rods, whereas the SWCNTs with a diameter of 0.91 nm appear much shorter (0.5 − 1 μm).

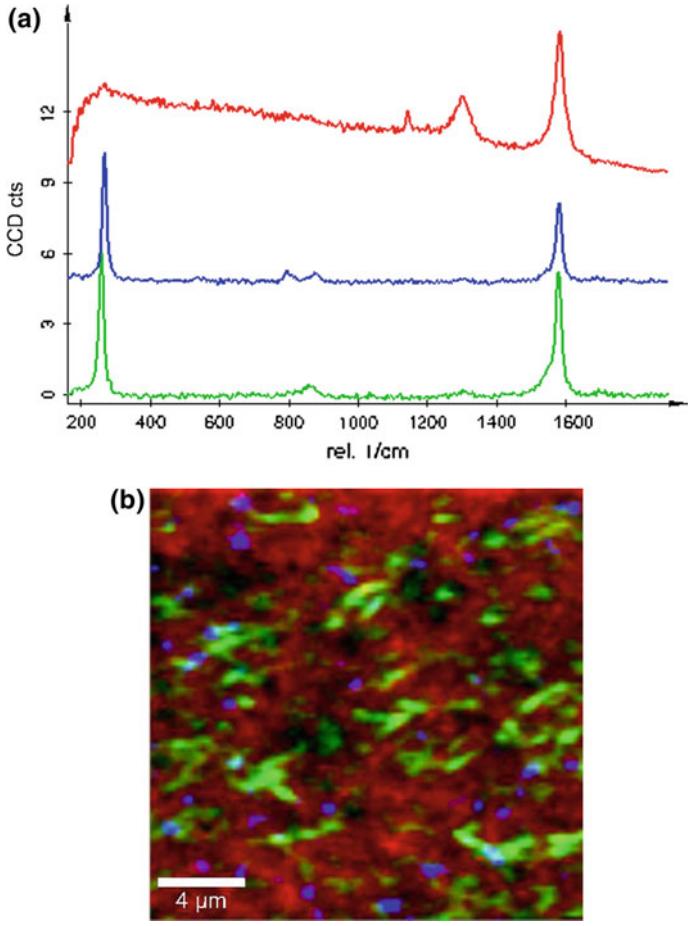

Fig. 20.18 Confocal Raman imaging of the distribution of carbon nanotubes in a polymer matrix: characteristic Raman spectra evaluated from the 2D array of 10000 spectra using the cluster analysis tool of the WITec project software, polymer matrix (red), carbon nanotubes with different diameter (blue, green) (**a**) and color-coded Raman image of the analyzed surface area (**b**)

20.6 Summary

Confocal Raman microscopy is a powerful tool for the characterization of polymeric materials. It could be shown that Raman spectroscopy allows the identification of chemically distinct materials. In combination with a confocal microscope, the distribution of various polymer phases within a polymer matrix can be determined. As shown in Sect. 20.2, confocal Raman microscopy is sensitive to the orientation of long chain polymeric materials, enabling the determination of orientation of fibers when the polarization direction of the excitation laser is known. Polymorphs of a

polymer can be detected and their distribution on the sample visualized. In Sect. 20.3 the combination of confocal Raman microscopy and atomic force microscopy has been demonstrated in the studies of thin films of polymer blends. All studied blends showed a clear phase separation and although the analyzed films were very thin (<100 nm), the sensitivity of the confocal Raman microscope was still high enough to identify the chemical composition of the films with short integration times of 30–100 ms/spectrum.

Structural changes observed with AFM while imaging the polymer films can be linked with the chemical composition from Raman imaging, thus leading to the correlation between chemical composition data and the constructional morphology of the films. Furthermore, due to its confocal setup, the confocal Raman microscope can be used to determine the layered structure of polymer coatings without laborious sample preparation as shown in Sect. 20.4. Additionally, the detection of inorganic materials in a polymer matrix was demonstrated in Sect. 20.5.

Confocal Raman microscopy (especially in combination with AFM) allows the nondestructive characterization of heterogeneous materials. In combination with a suitable software package, chemical identification of sample volumes of only 0.004 μm^3 becomes available at integration times of less than 100 ms per spectrum.

References

1. W. Stocker, J. Beckmann, R. Stadler, J. Rabe, Macromolecules **29**, 7502 (1999)
2. N. Koneripalli, R. Levicky, F.S. Bates, J. Ankner, H. Kaiser, S.K. Satija, Langmuir **12**, 668 (1996)
3. T.J. Morkved, H.M. Jaeger, Europhys. Lett. **40**, 643 (1997)
4. T.S. McLean, B.B. Sauer, J. Polym. Sci. Part B **37**, 85 (1999)
5. T. Zhong, D. Inniss, K. Kjoller, V. Ellings, Surf. Sci. **290**, L688 (1993)
6. S.N. Magonov, V. Elings, M.H. Whangbo, Surf. Sci. **372**, L385 (1997)
7. J. Tamayo, R. Garcia, Appl. Phys. Lett. **71**, 2394 (1997)
8. J. Tamayo, R. Garcia, Appl. Phys. Lett. **73**, 2926 (1998)
9. R. Garcia, J. Tamayo, A. Paolo, Surf. Interface Anal. **27**, 312 (1999)
10. J.P. Cleveland, B. Anczykowski, A.E. Schmid, V.B. Elings, Appl. Phys. Lett. **72**, 2613 (1998)
11. W.W. Scott, B. Bhushan, Ultramicroscopy **97**, 151 (2003)
12. G. Bar, Y. Thomann, R. Brandsch, H.J. Cantow, M.H. Whangbo, Langmuir **13**, 3807 (1997)
13. S. Hild, O. Marti, F. Hollmann, B. Rieger, Europ. Polym. J. **40**, 905 (2004)
14. H.W. Siesler, K. Holland-Moritz, *Infrared and Raman Spectroscopy of Polymers* (Marcel Dekker, New York, 1990)
15. H. Owen, D.E. Battery, M.J. Pelletier, J.B. Slater, SPIEE Proc. **260**, 2406 (1995)
16. E.D. Lipp, R.L. Grosse, Appl. Spectrosc. **52**, 42 (1998)
17. J.F. Aust, K.S. Booksh, M.L. Myrick, Appl. Spectrosc. **50**, 382 (1996)
18. T. Wilson, *Confocal Microscopy* (Academic Press, London, 1990)
19. J.M. Chalmers, H.G.M. Edwards, J.S. Lees, D.A. Long, M.W. Mackenzie, H.A. Willis, J. Raman Spectrosc. **22**, 613 (1991)
20. X. Wang, S. Michielsen, J. Appl. Polym. Sci. **82**, 1330 (2001)
21. A.S. Nielsen, D.N. Batchelder, R. Pyrz, Polymer **43**, 2671 (2002)
22. G.R. Strobl, W. Hagedorn, J. Polym. Sci. Polym. Phys. **16**, 1181 (1978)
23. R. Mutter, W. Stille, G. Strobl, J. Polym. Sci. Pol. Phys. **31**, 99 (1993)

24. P. Hendra, J. Vile, H.A. Willis, V. Zichy, Polymer **25**, 785 (1984)
25. G. Keresztury, E. Foldes, Polym. Test **9**, 329 (1990)
26. E. Lamparska, V. Liegeois, O. Quinet, B. Champagne, ChemPhysChem **7**, 2366 (2006)
27. V.K. Kuppa, J. in't Veld, G.C. Rutledge, Macromolecules **40**, 5187 (2007)
28. K. Tashiro, S. Minami, G. Wu, M. Kobayashi, J. Polym. Sci. Polym. Phys. **30**, 1143 (1992)
29. J.C. Rodriguez-Cabello, J.C. Merino, T. Jawhari, J.M. Pastor, J.M. Pastor, J. Raman Spectrosc **27**, 463 (1996)
30. L. Holliday, *Structure and Properties of Oriented Polymers* (Applied Science Publishers, London UK, 1975), chap. 7
31. S. Hild, A. Rosa, O. Marti, *Scanning Probe Microscopy of Polymers* (Oxford University Press, 1998), p. 110
32. P. Schmidt, J. Dybal, J. Scudla, M. Raab, J. Kratochvil, K. Eichhorn, S.L. Quintana, J.M. Pastor, Macromol. Symp. **184**, 107 (2002)
33. H. Tadokoro, H. Kobayashi, M. Ukita, K. Yasufuku, S. Murahashi, J. Chem. Phys. **42**, 1432 (1965)
34. R.G. Snyder, J.H. Schachtschneider, Spectrochim. Acta **20**, 853 (1964)
35. U. Schmidt, S. Hild, W. Ibach, O. Hollricher, Macromol. Symp. **230**(1), 133 (2005)
36. L. Utracki, *Encyclopaedic Dictionary of Commercial Polymer Blends* (ChemTec Publishing, Toronto, 1994)
37. L. Utracki, *Polymer Blends Handbook* (Kluwer Academic Publishers, Dordrecht, 2002)
38. U. Schmidt, W. Ibach, J. Mueller, O. Hollricher, SPIEProc. **6616**(1), 66160E (2007)
39. H. Kupsov, G.N. Zhizhin, *Handbook of Fourier Transform Raman and Infrared Spectra of Polymers* (Elsevier, Amsterdam, 1998)
40. G. Socrates, *Infrared and Raman Characteristic Group Frequencies* (Wiley, Chichester, 2001)
41. Z.O. Oyman, W. Ming, F. Micciche, E. Oostveen, J. van Haveren, R. van der Linde, Polymer **45**, 7431 (2004)
42. M. Milnera, J. Kürti, M. Hulman, H. Kuzmany, Phys. Rev. Lett. **48**, 1324 (2000)
43. A. Jorio, R. Saito, J.H. Hafner, C.M. Lieber, M. Hunter, T. McCluve, G. Dresselhaus, M.S. Dresselhaus, Phys. Rev. Lett. **86**, 1118 (2001)

Chapter 21
Stress Analysis by Means of Raman Microscopy

Thomas Wermelinger and Ralph Spolenak

Abstract Raman microscopy provides the unique possibility to measure stresses in a fast and uncomplicated way in the sub-micrometer range. The maximal lateral resolution is determined by the laser wavelength. In a Raman spectrum of a deformed or strained material, peak positions are shifted relative to the peak positions of stress-free material. Quantifying these shifts allows the determination of sign and magnitude of internal stresses. Depending on the Raman tensor and therefore on the material's crystal structure, several components of the stress tensor can be measured. Hence, it is not always possible to analyze complicated stress states just by means of Raman microscopy without making adequate assumptions. For transparent Raman-active materials, three-dimensional stress fields can be measured. This chapter will outline the principles of Raman stress measurements and present case studies on ceramics, semiconductors and polymers.

21.1 Introduction

Over the past 20 years Raman microscopy has become a powerful tool for measuring mechanical stresses in the sub-micrometer range. Especially in the semiconductor industry the knowledge of mechanical stresses is a prerequisite for the production of reliable devices. Raman spectroscopy is currently the only laboratory method able to locally measuring mechanical stresses on the micrometer length scale. Alternative methods, which are either based on large scale facilities or are still in the development stages, include X-ray microdiffraction [1], convergent beam electron diffraction with a transmission electron microscope (TEM) [2], electron induced Kossel diffraction with a scanning electron microscope (SEM) [3], or electron backscatter diffraction (EBSD) with an SEM [4]. All of these methods have two aspects in common; they

T. Wermelinger (✉) · R. Spolenak
Laboratory of Nanometallurgy, Department of Materials,
ETH Zurich, Zurich, Switzerland
e-mail: thomas.wermelinger@mat.ethz.ch

R. Spolenak
e-mail: ralph.spolenak@mat.ethz.ch

J. Toporski et al. (eds.), *Confocal Raman Microscopy*, Springer Series
in Surface Sciences 66, https://doi.org/10.1007/978-3-319-75380-5_21

all measure elastic strain in a crystalline material and require the knowledge of its elastic properties to convert strain into stress. All diffraction methods, independent of whether photons or electrons are the probe utilized, directly provide a measure of the lattice parameter of crystalline materials. Raman spectroscopy on the other hand, is a spectroscopy technique which yields the energies of the phonon spectrum. In contrast to diffraction techniques which solely require crystal periodicity, Raman spectroscopy requires a material to be polarizable, which limits the materials choice to ceramics, polymers and semiconductors. Raman studies on metals [5] rely on the mechanical coupling of a Raman active material to the metal and subsequent mechanical modeling. While Raman spectroscopy has traditionally been employed for studies of stress in microelectronic materials [6–10], strain measurements by Raman microscopy and the conversion to mechanical stress is currently being extended to other materials classes and applications. The following chapter thus focuses on the principles of strain measurements by Raman microscopy, its application to Si based materials and novel extensions.

21.1.1 Theoretical Background

Originally, Raman spectroscopy was used for analyzing and characterizing different compositions or phases, but the spectrum itself contains much more information. The Raman effect refers to the inelastic scattering of light due to its interaction with phonons or molecular vibrations. Strain due to mechanical stress affect the frequencies of the Raman-active phonons or molecular vibrations which lead to a shift of the Raman peak positions relative to the stress free peak position [11]. As a simple metaphor one can compare the process to the tuning of a guitar string. The tuning changes the strain and the mechanical stress in the guitar string which leads to a change of the frequency of the vibration and therefore would also lead to a shift of the positions of the Raman peaks. In the following section we will explain the underlying theory of measuring the strain and show how to convert the results into stress. Different methods to measure mechanical stresses in materials with a cubic crystal structure such as silicon will be presented. The stress resolution of the method depends on the stress sensitivity of the Raman peak and the signal-to-noise ratio of the measured signal.

Only certain types of lattice vibrations give rise to Raman scattering. The Raman tensors show which phonons are Raman active and what kind of orientation these phonons have. The Raman tensor can be determined from the crystal structure of the material. According to Louden [12], silicon has three Raman tensors. In the crystal coordinate system $x = [100]$, $y = [10]$ and $z = [001]$ they are:

$$\Delta_1 = \begin{bmatrix} 0 & 0 & 0 \\ 0 & 0 & d \\ 0 & d & 0 \end{bmatrix}, \qquad \Delta_2 = \begin{bmatrix} 0 & 0 & d \\ 0 & 0 & 0 \\ d & 0 & 0 \end{bmatrix}, \qquad \Delta_3 = \begin{bmatrix} 0 & d & 0 \\ d & 0 & 0 \\ 0 & 0 & 0 \end{bmatrix} \tag{21.1}$$

where d is the component different from zero. These components define the intensity of a certain peak. In the case of silicon d is equal in all three tensors.

The total scattering intensity of the phonon modes (I) for a given geometry can be determined from the Raman tensors, Δ_j, and the polarization vector of the incident (e_i) and scattered (e_s) light and is given by

$$I = C \sum_j \left| e_i \cdot \Delta_j \cdot e_s \right|^2 \tag{21.2}$$

where C is a constant. Measuring in a back-scattering mode from a (001) surface the incident as well as the scattered light beam are normal to the surface. In this case Δ_1 and Δ_2 correspond to scattering from the transverse optical phonons (TO), polarized along the x- or the y-axis, respectively. Δ_3 correlates to scattering from the longitudinal optical phonons (LO), polarized along the z-axis. Whether the phonon is longitudinal or transversal depends on the surface from which scattering is observed. Measuring in a back-scattering mode from a (100) surface, Δ_1 corresponds to the LO phonon [6]. The phonons are triply degenerated which means that they have all the same wave number of approximately 520 rel. cm^{-1}.

It follows from (21.2) that different modes can be measured depending on the orientation of the surface and the polarization direction of the light. Table 21.1 shows which of the modes can be obtained for a back-scattering experiment from a (001) surface, (110) surface, or a $(11\bar{2})$ surface.

In a back-scattering configuration for a (001) surface only the longitudinal optical phonon mode is allowed regardless of the polarizations of the incident and the scattered light. In contrast to this, the back-scattering configuration of a (110) as

Table 21.1 Polarization selection rules for back-scattering from a (001), (110) or a $(11\bar{2})$ surface

Polarization		Visible		
e_i	e_s	Δ_1	Δ_2	Δ_3
Back-scattering from (001)				
(100)	(100)	–	–	–
(100)	(010)	–	–	X
$(1\bar{1}0)$	$(1\bar{1}0)$	–	–	X
(110)	$(1\bar{1}0)$	–	–	–
Back-scattering from (110)				
$(1\bar{1}0)$	(001)	X	X	–
$(1\bar{1}0)$	$(1\bar{1}0)$	–	–	X
(001)	(001)	–	–	–
Back-scattering from $(11\bar{2})$				
$(1\bar{1}0)$	(111)	X	X	–
$(1\bar{1}0)$	$(1\bar{1}0)$	–	–	X
(111)	(111)	X	X	X

well as a $(11\bar{2})$ surface allows the excitation of all three Raman modes [8]. In these latter two cases the longitudinal and the transversal phonons can be measured independently from each other. Measuring from a (111) surface, all phonon modes are excited regardless of the polarization of the incident and scattered light [13].

21.1.2 Measuring in Conventional Backscattering Configuration

Strain caused by mechanical stress can influence the frequencies of the Raman mode [8, 11, 14, 15]. In the absence of strain, the triply degenerated phonons lead to a peak at ω_0 = 520 rel. cm^{-1}. Strain changes the phonon vibrations and therefore can lift the degeneracy of the Raman frequencies due to a symmetry reduction of the Raman tensors [8, 16]. This symmetry reduction causes splitting and shifting of the Raman peak. Ganesan et al. [11] showed that if strain is applied to a sample, the frequencies of the three optical phonon modes can be calculated by finding the eigenvalues, λ_j, j = 1, 2, 3, in the following equation

$$\begin{vmatrix} p\varepsilon_{11} + q(\varepsilon_{22} + \varepsilon_{33}) - \lambda_1 & 2r\varepsilon_{12} & 2r\varepsilon_{13} \\ 2r\varepsilon_{21} & p\varepsilon_{22} + q(\varepsilon_{11} + \varepsilon_{33}) - \lambda_2 & 2r\varepsilon_{23} \\ 2r\varepsilon_{31} & 2r\varepsilon_{32} & p\varepsilon_{33} + q(\varepsilon_{11} + \varepsilon_{22}) - \lambda_3 \end{vmatrix} = 0 \quad (21.3)$$

where $p = -1.85\ \omega_0^2$, $q = -2.31\ \omega_0^2$ and $r = -0.71\ \omega_0^2$ are the phonon deformation potentials (PDPs), which are material constants. ε_{ij} are the components of the strain tensor. The frequency of each mode in the presence of strain ω_j $(j = 1, 2, 3)$ of the strained crystal is related to the unstrained frequency, ω_0 by the following relationship:

$$\omega_j^2 = \omega_0^2 - \lambda_j \quad (21.4)$$

or, for the approximation of small strains [8]:

$$\Delta\omega_j = \omega_j - \omega_0 \approx \frac{\lambda_j}{2\omega_0} \quad (21.5)$$

The polarization direction of each mode is given by the eigenvectors of (21.3).

The relation between the strain tensor ε in (21.3) and the stress tensor σ is given by Hooke's law

$$\begin{Bmatrix} \varepsilon_{11} \\ \varepsilon_{22} \\ \varepsilon_{33} \\ 2\varepsilon_{23} \\ 2\varepsilon_{13} \\ 2\varepsilon_{12} \end{Bmatrix} = \begin{bmatrix} s_{11} & s_{12} & s_{12} & 0 & 0 & 0 \\ s_{12} & s_{11} & s_{12} & 0 & 0 & 0 \\ s_{12} & s_{12} & s_{11} & 0 & 0 & 0 \\ 0 & 0 & 0 & s_{44} & 0 & 0 \\ 0 & 0 & 0 & 0 & s_{44} & 0 \\ 0 & 0 & 0 & 0 & 0 & s_{44} \end{bmatrix} \begin{Bmatrix} \sigma_{11} \\ \sigma_{22} \\ \sigma_{33} \\ \sigma_{23} \\ \sigma_{13} \\ \sigma_{12} \end{Bmatrix} \quad (21.6)$$

where $s_{11} = 7.68 \times 10^{-2}$ Pa^{-1}, $s_{12} = -2.14 \times 10^{-12}$ Pa^{-1} and $s_{44} = 12.7 \times 10^{-12}$ Pa^{-1} are components of the elastic compliance tensor. This equation allows the calculation of the developing stresses from the measured strain. In the case of uniaxial stress along the [100] direction, (21.6) leads to the following nonzero components of the strain tensor: $\varepsilon_{11} = s_{11}\sigma_{11}, \varepsilon_{22} = s_{12}\sigma_{11}$ and $\varepsilon_{33} = s_{12}\sigma_{11}$. Solving (21.3) and (21.5) leads to the following results:

$$\begin{aligned} \Delta\omega_1 &= \frac{\lambda_1}{2\omega_0} = \frac{1}{2\omega_0}(ps_{11} + 2qs_{12})\sigma \\ \Delta\omega_2 &= \frac{\lambda_2}{2\omega_0} = \frac{1}{2\omega_0}[ps_{12} + q(s_{11} + s_{12})]\sigma \\ \Delta\omega_3 &= \frac{\lambda_3}{2\omega_0} = \frac{1}{2\omega_0}[ps_{12} + q(s_{11} + s_{12})]\sigma \end{aligned} \tag{21.7}$$

For small strains one can assume that the Raman tensors do not change. According to Table 21.1 only the third Raman mode can be seen, when measuring in a backscattering mode from a (001) surface. Therefore, only $\Delta\omega_3$ has a nonzero value. Similar to the uniaxial case, calculations can be performed assuming biaxial stress ($\sigma_{xx} + \sigma_{yy}$). Then an increase of the Raman frequency corresponds to compressive stress while a decrease of the Raman frequency indicates tensile stress.

The majority of substrates for silicon based microelectronic devices have a (001) surface. As a consequence, the only measurable phonon is the longitudinal optical phonon and information is obtainable only from one parameter, namely for the out-of-plane component. As the stress tensor has six degrees of freedom, it is always necessary to make assumptions about the stress state. To show the importance of a realistic assumption for the stress tensor, three different stress states (hydrostatic, uniaxial along the x-axis, uniaxial along the z-axis) and their influence on the Raman signal are given [17]. In all three cases one supposes a Raman shift of 1cm^{-1}. In the hydrostatic case, the corresponding values are

$$\sigma = -540 \begin{pmatrix} 1/3 & 0 & 0 \\ 0 & 1/3 & 0 \\ 0 & 0 & 1/3 \end{pmatrix} \text{MPa}, \tag{21.8}$$

while if one assumes a uniaxial stress along the x-axis, the value changes to

$$\sigma = -450 \begin{pmatrix} 1\,0\,0 \\ 0\,0\,0 \\ 0\,0\,0 \end{pmatrix} \text{MPa} \tag{21.9}$$

and for uniaxial stress along the z-axis one gets:

$$\sigma = -900 \begin{pmatrix} 0\,0\,0 \\ 0\,0\,0 \\ 0\,0\,1 \end{pmatrix} \text{MPa} \tag{21.10}$$

The large differences among the values have an important consequence. Either the performed measurement is made on samples where the shape of the tensor is already well known, or one has to find a way to overcome the limitation of measuring only one phonon mode. In the following section we will explain how to measure stresses not only for the simple case where one phonon is excited, but we will also show two different ways to overcome experimental limitations.

21.1.3 Off-Axis Raman Spectroscopy

The complete stress tensor for an arbitrary crystal orientation can be determined by tilting the incident beam away from the normal axis while polarizing the incident as well as the scattered beam [18, 19]. This experimental set-up is called off-axis Raman spectroscopy. One has to keep in mind that in this set-up the laser is not focused and therefore the lateral resolution is low. So the method is suitable best for analyzing general stress states.

To detect all three Raman modes from a (001) surface of a silicon wafer, either the incident and/or the scattered light must have electric field components in all three x, y, and z directions to get signal from all three Raman tensors (see Sect. 21.1.2). As another requirement, incident and scattered light beams have to be polarized. If the incident light deviates from the surface normal, all three Raman modes are activated and can be measured. By adjusting the polarizer, one is able to vary the proportion of each mode to the total intensity signal. The correct experimental set-up allows studying a selected phonon mode. Tuning the system allows one to determine all six components of the stress tensor.

In the off-axis Raman spectroscopy it is important to define several experimental parameters, which have to be under direct experimental control. In the case described here four different angles have to be known. The angle between the incident laser and the surface normal Φ is the first important parameter. This angle allows the detection of all three phonon modes due to the non-zero z-component. The orientation of the incident light (α) as well as the scattered light (β) adjusted by a polarizer must be known. Finally, the orientation of the sample (κ) with respect to the incident light is also of high importance (see Fig. 21.1). Once the tilting angle (Φ) is fixed, all the other angles are adjusted to optimize the sensitivity of the apparatus.

Due to the off-axis set-up of the laser, (21.2) has to be adjusted. The final signal intensity at the detector from a given phonon mode can be expressed by the following equation:

$$I = C\left(d_k^H B d_k\right) \tag{21.11}$$

In this notation d_k is a pseudovector. Its components are the nonzero elements of the Raman tensor which only depend on the applied stress but not on the experimental set-up of the system. The superscript H denotes the complex-conjugate (Hermitian) transpose. B is the observation matrix which describes the directions of the vibrations. It depends only on the experimental set-up of the measuring system and on the

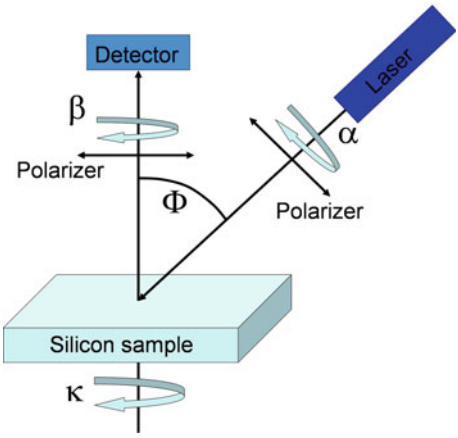

Fig. 21.1 Simplified schematic of an experimental set-up for polarized off-axis Raman spectroscopy. α and β denote the orientation of the polarizer of the incident light and the scattered light, respectively. Φ is the tilting angle between the surface normal and the incident laser light. κ refers to the rotation angle of the silicon sample

material properties, such as refractive index, but it does not depend on applied stress. C is a constant.

It is important to point out that in (21.11) the shape of the spectrum not only depends on the stress but is also a function of the experimental configuration, namely the observation directions given by the observation matrix B. B includes all the parameters which are under experimental control and must be calculated for every configuration (Φ, α, β, κ). By adjusting these parameters, it is possible to selectively measure different phonon vibrations.

As an example, the Raman spectra measured on a silicon wafer with a (001) surface orientation under biaxial stress is shown in Fig. 21.2 [18].

The Raman measurements were taken parallel to the crystallographic axes. As one can see, it is possible to analyze different phonon vibrations in different observation directions. For visualizing the absolute shifts of the Raman peak position a spectrum from the unstressed wafer is plotted as well. The splitting between the two transversal optical phonons in the [100] and [010] direction and the longitudinal phonon in the [001] direction indicates biaxial stress in the wafer.

In conclusion one can say, that polarized off-axis Raman spectroscopy is a characterization method which allows the analysis of the complete stress tensor of a silicon wafer. The largest drawback of the method is the lateral resolution. This problem can be overcome by implementing the method for micro-Raman spectroscopy.

21.1.4 Stress Tensor Analysis in Backscattering Raman Microscopy

We have seen that stress tensor analysis by means of Raman spectroscopy is generally possible, although the presented method does not provide local information about the stress state. To obtain local information about the stress is crucial for

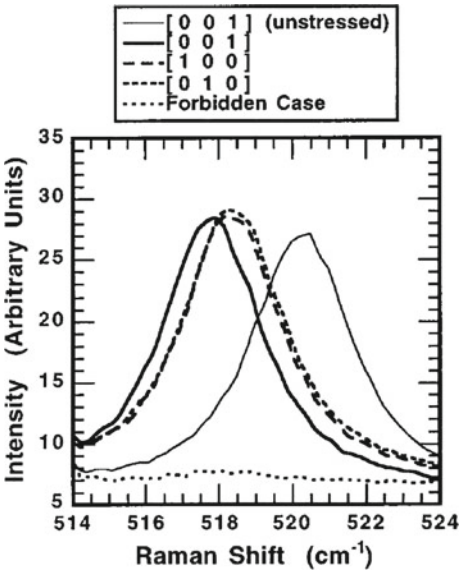

Fig. 21.2 Raman spectra taken with observation directions along the crystallographic axes. All spectra show a significant shift to lower wavenumbers in comparison to the unstressed spectra, which indicates tensile stress. Also a considerable splitting between the two in plane phonons ([100], [010]) and the out of plane phonon [001] can be seen [18]

microelectronics, as it can be the origin of hillocks, voids, and cracks [20]. Therefore a method is required, which allows the measurement of stresses with a lateral resolution in the micrometer range or better. Bonera et al. presented a method to measure different components of the stress tensor with a spatial resolution of 1 m by Raman spectroscopic technique [17, 21].

Equations (21.1) and (21.2) show that one obtains only information from the longitudinal optical phonon from an (001) surface in an ideal back-scattering experiment. The two transversal optical phonons are not excited. In this case, the electric field of the laser light is perpendicular to the surface normal (see Fig. 21.3a). If one uses an objective lens with a large numerical aperture (NA), all three phonons will be excited due to the fact that the incident laser light is no longer polarized perpendicular to the surface normal (Fig. 21.3b). The polarization vector also has a component in the z-axis. The higher the NA, the higher the intensity from the transversal optical phonons will be.

Polarizing the incident as well as the scattered light offers the possibility to measure all three phonon modes separately. Using the Porto notation, these three cases can be written as:

$$\begin{aligned} z(y, y)\bar{z} &\rightarrow \omega_1 \\ z(x, x)\bar{z} &\rightarrow \omega_2 \\ z(y, x \otimes y)\bar{z} &\rightarrow \omega_3 \end{aligned} \tag{21.12}$$

In the Porto notation, the first symbol, z, defines the direction of the in-coming light, while the last symbol, $\bar{z}$, refers to the direction of the scattered light. The $\bar{z}$ implies

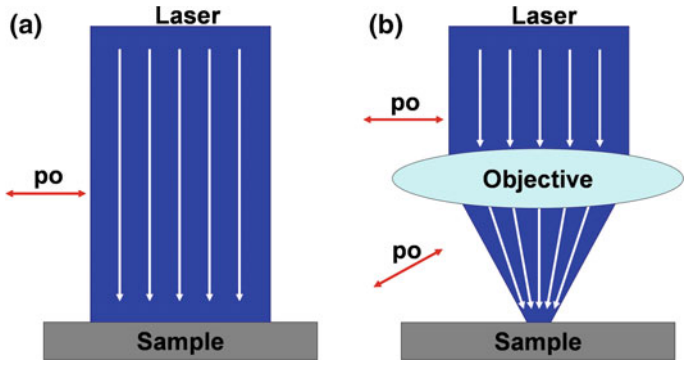

Fig. 21.3 **a** Ideal backscattering configuration. The polarization (po) of the incident laser light is perpendicular to the surface normal. Only the LO phonon is excited. **b** Due to focusing the laser light the polarization vector (po) obtains a component parallel to the surface normal. Therefore all phonon modes are excited

that the scattered light is rotated 180° with respect to z. The first parameter within the parentheses describes the polarization of the incident light, while the second symbol is the polarization direction of the scattered light. Equation (21.12) shows which experimental set-up is required for measuring a certain phonon mode. To study ω_3, which is the LO phonon, no polarizer is needed in the scattered beam. In this case, not only the LO phonon contributes to the total intensity, but also one of the TO phonons. However, in comparison to the intensity of the LO phonon the contribution of the TO phonon is negligible. Therefore, to get information from all three phonon vibrations, one has to measure the same region with all three different polarization states of (21.12). In an unstressed area, ω_1, ω_2 and ω_3 have the same frequency. In stressed areas, the three frequencies are shifted with respect to the unstrained case. The total amount of the shift of the corresponding frequency depends on the actual stress state.

To calculate the stress state, one has to assume that the angles of the unit cells of the crystal do not change and the unit cell remains orthogonal. This assumption results in all nondiagonal values of the stress tensor to vanish.

$$\sigma_{ij} = 0, \qquad i \neq j \tag{21.13}$$

In most cases this assumption is a simplification of the true stress state. Nevertheless, it allows one to measure three of the six components of the stress tensor instead of only one. It is convenient to split the stress tensor into a hydrostatic (σ_h) and a traceless (σ_t) component.

$$\sigma = \sigma_h + \sigma_t \tag{21.14}$$

Using (21.14) simplifies the secular matrix for the strained crystal [see (21.3)] to the following three linear equations:

$$\Delta\omega_j = \frac{(p+2q)(s_{11}+2s_{12})}{2\omega_0}\alpha' \cdot \sigma_h \cdot \alpha + \frac{(p-q)(s_{11}-s_{12})}{2\omega_0}\alpha' \cdot \sigma_t \cdot \alpha \quad (21.15)$$

where $\alpha = x$, y and z; s_{11} and s_{12} are elements of the compliance tensor [see (21.6)]; p and q are phonon deformation potentials. Equation (21.15) allows to determine the stress tensor with a lateral resolution depending on the wave length of the laser and the numerical aperture of the lens.

In conclusion, the above section presents a method to measure stress induced Raman shifts from a silicon surface. The spatial resolution is in the submicrometer range. The method allows to measure different phonon polarizations which belong to different directions in space.

21.2 Case Studies

21.2.1 3-D Raman Spectroscopy Measurements

Stresses and strains are important since they are related to material deformation and failures of devices. The detailed understanding of the stress fields can improve the design of applications to gain highest possible quality and mechanical durability. The most detailed analysis would be a full 3D characterization of the stress state in a material or device. However, at the moment only a few methods, such as 3-D X-ray diffraction microscopy, are known to perform 3D measurements with a resolution at or below the micrometer range [22]. But few such systems are available world wide. Therefore, only a few experiments have been performed to date. An alternative method at a laboratory scale is confocal Raman microscopy.

Sapphire is often used for pressure sensors or in applications for the electronics industry. Therefore it is important to understand the deformation behavior of sapphire single crystals. In this study a sapphire single crystal was used for measuring 3D stress fields around an indent with confocal Raman microscopy [23].

An indent from a Vickers micro indentation was placed on the basal (0001) plane of a sapphire single crystal. The indent had a depth of about 0.5 µm and a diameter of about 4.5 µm (see Fig. 21.4). A confocal Raman microscope (WITec, CRM 200, wavelength: 442 nm) was used to measure the peak shifts around the indent. Due to the confocality of the microscope an exact 3D positioning of the focus spot is feasible [24]. The lateral resolution of the microscope is defined by the Rayleigh equation: $d = 1.22(\lambda_{Laser}/2NA)$ where λ_{Laser} is the wavelength of the laser and NA is the numerical aperture. In the case described here, the lateral resolution is 300 nm.

Figure 21.5 shows the Raman spectra of a sapphire single crystal measured in a backscattering mode from the basal (0001) plane. The visible peaks at 380, 432, 451, 578 and 751 rel. cm^{-1} belong to E_g modes while the peak at 417 rel. cm^{-1} belongs to an A_{1g} mode. With the exception of the peak at 378 rel. cm^{-1}, which belongs to

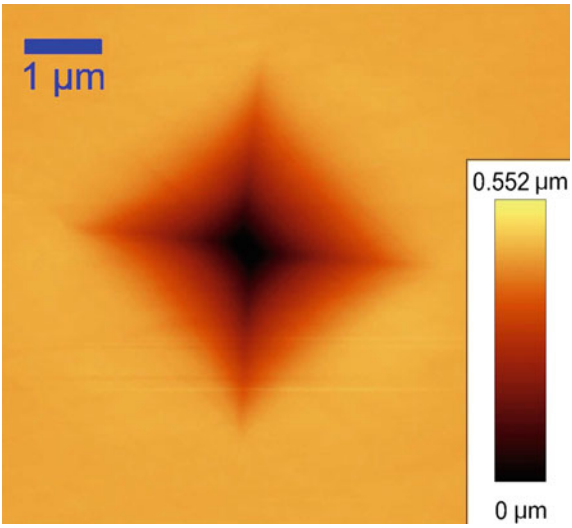

Fig. 21.4 AFM image of the Vickers microindent on the basal C(0001) plane of the Sapphire crystal. The diameter of the indent is about 4.5 µm

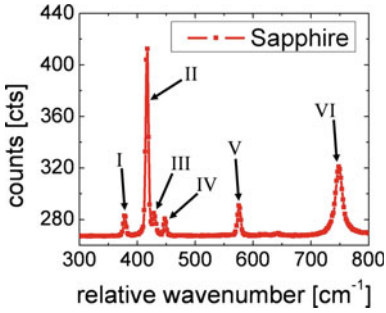

Fig. 21.5 Raman spectrum of a Sapphire single crystal. Arrow I, III, IV, V and VI at 380, 432, 451, 578 and 751 rel. cm^{-1} belong to E_g modes. The peak at 417 rel. cm^{-1} belongs to an A_{1g} mode

a phonon with an in- and out-of-plane component, all peaks belong to out-of-plane phonon vibrations.

Starting from the surface of the sapphire crystal, a stack of xy-scans was taken at different z-positions. All measurements were made with the same x- and y-positions, changing only the z-coordinate by 0.4 µm between scans.

Figure 21.6 shows the shift of the peak at 417 rel. cm^{-1} around the indent starting from the surface of the single crystal down to 2.8 µm. The amount of the peak shift correlates directly to the residual stress. Bright colors correspond to compressive stresses whereas dark colors correspond to tensile stresses. While the indent has fourfold symmetry (see Fig. 21.4) the residual stress field around the indent shows a clear threefold symmetry.

The scans were performed in a backscattering mode with a 100× objective with a numerical aperture NA of 0.9. Therefore, the lateral resolution was 300 nm. The scans had a size of 12×12 µm and consisted of 48 × 48 spectra. All the experiments were done with an integration time per spectra of 4.5 s using a 1800 grooves/mm grating.

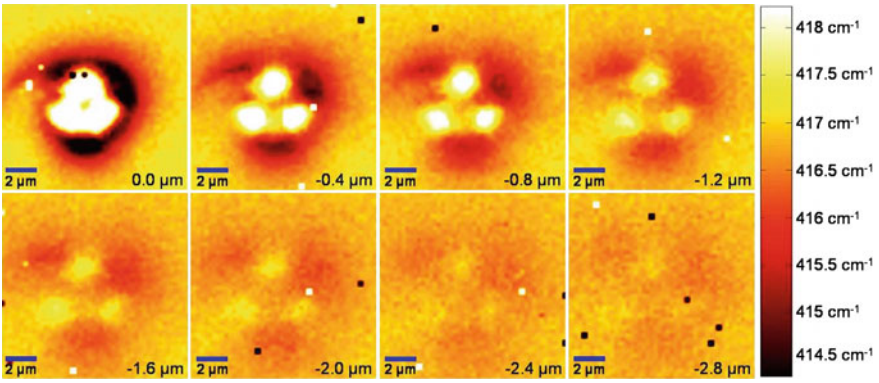

Fig. 21.6 Shift of the peak at 417 rel. cm^{-1} around the indent. High wavenumbers correspond to compressive stress while low wavenumbers correspond to tensile stress. The difference between maps is a distance of 0.4 µm

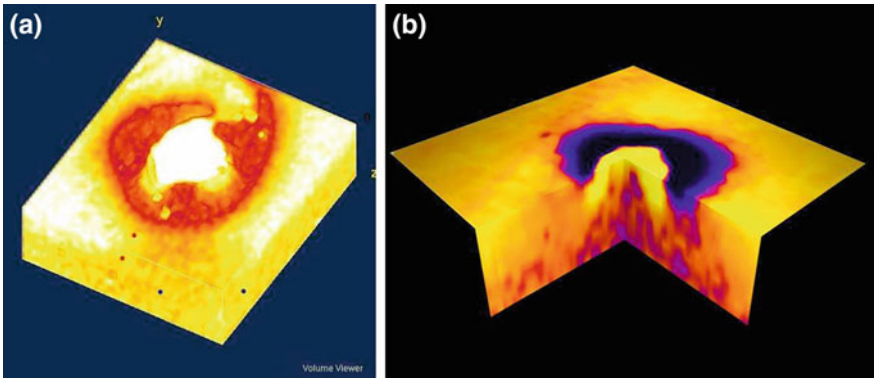

Fig. 21.7 The calculated 3-D stress field around the indent. **a** tensile stresses above a certain threshold are transparent. Only areas with compressive stresses or no stresses are visible in this volume (12 × 12 × 4 µm). **b** bright colors indicate compressive stresses while dark colors correspond to tensile stresses (20 × 20 × 2 µm)

From the stack of images it is possible to visualize the 3-D stress field around the Vickers indent by using an image processing program such as imageJ [25]. Figure 21.7 shows the result of these calculations. However, as the peak at 417 rel. cm^{-1} belongs to an out-of-plane-phonon vibration therefore only out-of-plane stresses are shown.

To understand why an indent with a clear fourfold symmetry leads to a residual stress field with a threefold symmetry one has to consider the deformation behavior of the material. In materials with a hexagonal crystal structure such as sapphire the c/a axis ratio of the unit cell defines the deformation behavior. Figure 21.8 shows the probability for activating a certain slip or twinning system as a function of the angle. The numbers refer to different deformation systems: "1" is a rhombohedral twinning

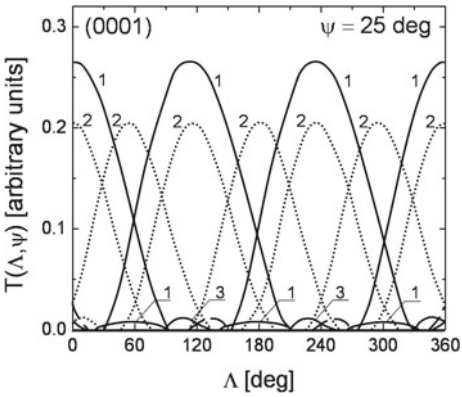

Fig. 21.8 Probability for activating a certain slip or twinning system, T, for all directions Λ around a spherical indent on the (0001) basal plane [26]

system along the {0112} plane, "2" belongs to a basal (0001) twinning system and "3" denotes to a rhombohedral slip system along the $01\bar{1}2$ plane [26].

In this figure Λ describes an angle between the orientation of the indent and the orientation of the sapphire. The solid lines highlight the deformation systems which are activated in the particular experimental set-up. According to Fig. 21.8, the dominating deformation systems involve threefold symmetry. Therefore it is reasonable to assume that the residual stress field will show a similar behavior.

The presented study demonstrated that the residual stress field is not solely influenced by the geometry of the indent. Although the Vickers indent shows fourfold symmetry the stress field shows a clear threefold symmetry. It could be shown that in a transparent sample such as sapphire the 3-D stress field can be measured by means of confocal Raman microscopy, but only out-of-plane phonons could be measured. Therefore, relating this to the previous discussion little can be said about the stress tensor.

21.2.2 ZnO

As shown in the previous section, the confocal Raman microscopy makes it is possible to calculate 3-D stress fields. To get more information about the 3-D stress field, it is important to measure different phonons corresponding to different directions. In the case of zinc oxide, two in-plane phonon vibrations which are perpendicular to each other can be measured.

As in the sapphire study, a single crystal was indented with a Vickers microindenter. In the case of the zinc oxide, the indent was placed on the sidewall of the crystal which was perpendicular to the basal plane. The indent (see Fig. 21.9a) had a diameter of about 7 μm and a depth of about 1.6 μm. Figure 21.9b shows a Raman spectra of zinc oxide (ZnO) taken from the sidewall of the sample. The electrical field of the incident laser light was parallel to the (0001)-axis of the crystal. Arrow II

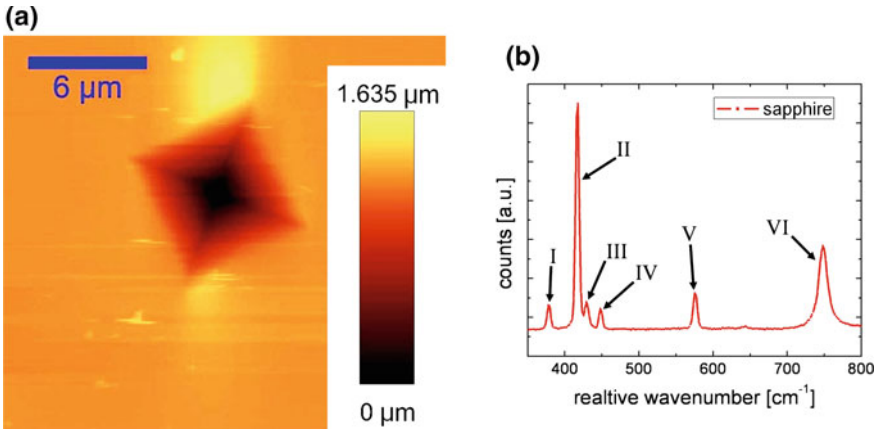

Fig. 21.9 **a** AFM image of the Vickers microindent on the sidewall of the zinc oxide crystal. The diameter of the indent is approximately 7 µm. **b** Raman spectra of ZnO taken from the sidewall of the crystal. The incident laser was polarized parallel to the z-axis of the crystal. The peaks highlighted with arrow II at 378 rel. cm^{-1} and arrow III at 408 rel. cm^{-1} are polarized parallel and perpendicular to the (0001)-axis, respectively. Arrow I at 334 rel. cm^{-1} and arrow IV at 1149 rel. cm^{-1} belong to multiphonon processes

indicates the Raman peak at 378 rel. cm^{-1} which belongs to a phonon vibration of an A_1 mode is polarized parallel to the (0001)-axis. Arrow III points to the Raman peak of an E_1 mode at 409 rel. cm^{-1} which corresponds to a phonon vibration polarized perpendicular to the z-axis [27]. As the phonons are perpendicular to each other, it is possible to analyze two components of the stress tensor. The peaks highlighted with arrow I and arrow IV at 334 and 1149 rel. cm^{-1} belong to multiphonon processes.

Figure 21.10 shows the results of the Raman scans around the indent. The shifts of the Raman peaks at 378 and 409 rel. cm^{-1} are presented. High wavenumbers correspond to compressive stress while low wavenumbers correspond to tensile stresses. The low signal-to-noise ratio of the peak at 409 rel. cm^{-1} results in an image with much more noise than the image from the peak shift of the peak at 378 rel. cm^{-1}. Nevertheless both scans show the same behavior; the residual stress field reveals a twofold symmetry.

As in the sapphire case, the two fold symmetry of residual stresses in zinc oxide can be explained by the deformation behavior. Zinc oxide has a wurtzite crystal structure which belongs to the group of hexagonal crystal systems [28, 29]. Although mechanism of plastic deformation in different hexagonal materials is never exactly equal the behavior still has some similarities. A comparable case of indentation on the $(10\bar{1}0)$ plane of a sapphire single crystal showed that the plastic deformation exhibited a twofold symmetry (see Fig. 21.8) [26]. The numbers in Fig. 21.11 refer to different deformation systems: "1" is a rhombohedral twinning system along the {0112} plane, "2" belongs to a basal (0001) twinning system, "3" denotes a rhombohedral slip system along the $\{0\bar{1}\bar{1}2\}$ plane and "4" is prismatic slip along the $\{\bar{1}2\bar{1}0\}$.

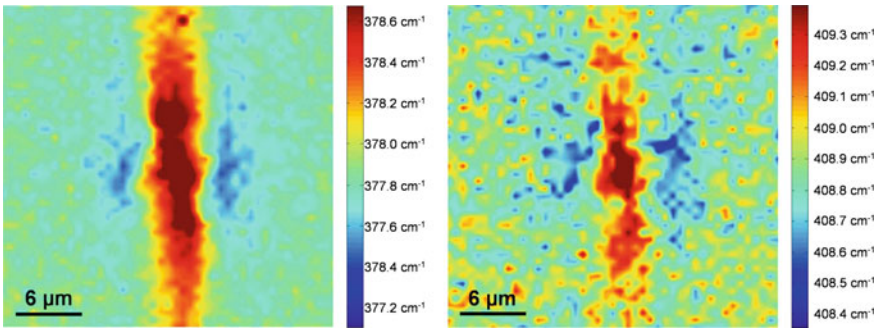

Fig. 21.10 Shift of the peaks at 378 and 409 rel. cm^{-1} around a microindent. High wavenumbers correspond to compressive stresses while shifts to lower wavenumbers indicate tensile stresses. The scan was taken at the surface of the sample

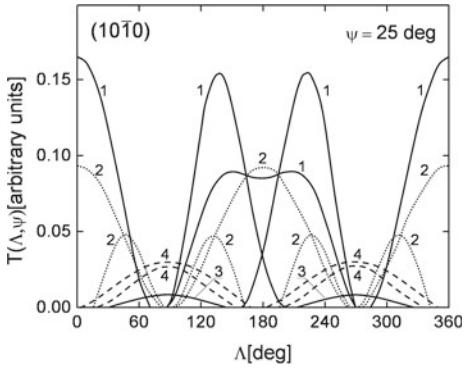

Fig. 21.11 Probability for activating a certain slip or twinning system, T, for all directions Λ around a spherical indent in sapphire on the (10$\bar{1}$0) plane of a ZnO single crystal [26]. All deformation systems are activated

All deformation systems are activated. Summing up the probability for activating certain slip or twinning systems lead to a twofold symmetry. As for sapphire, the twofold symmetry of the plastic deformation leads to the twofold symmetry of the residual stress field around the indent.

Manjon et al. [30] applied hydrostatic pressure to a zinc oxide crystal in a diamond anvil cell. They stated that the stress induced shifts for the peaks at 378 and 409 rel. cm^{-1} are 4.33 and 5.2 cm^{-1} GPa^{-1}, respectively. With these results it is possible to estimate the amount of the residual stresses in two directions which are perpendicular to each other. Taking the maximal peak shifts from the measurements leads to maximal residual stresses of ± 160 MPa parallel to the (0001)-axis and ± 90 MPa parallel to the (0001)-axis. Although the two directions are perpendicular to each other, neither of these directions have to correspond to the principle stress axis. Therefore, one cannot make any assumptions about shear stresses.

21.2.3 The Influence of Stress on the Peak Position of Polymers

So far we have described the influence of stress on the peak position of semiconductors (Si) and ceramics (sapphire and ZnO). But also the Raman peaks of materials other than ceramics and semiconductor are sensitive to applied stress and show similar effects [31–34]. In this section the stress induced peak shift of polyethylene will be discussed.

Ultra high molecular weight polyethylene (UHMWPE) thin films with different draw ratios were tested. The polyethylene was pre-oriented and stretched at an elevated temperature of 135 °C to draw ratios of $\lambda = 20, 40$ and 50. A detailed description of the process is reported elsewhere [35]. The draw ratio is defined as the ratio of the unit length after the deformation, L to and the initial unit length, $L_0 : \lambda = L/L_0$. The drawing leads to a preferred orientation of the polyethylene chains. The degree of the orientation after the stretching process has an influence on the mechanical properties such as the Young's modulus and the strain at breaking. For example, Young's modulus ranges from 40, 70 to 80 GPa for $\lambda = 20, 40$ and 50. Figure 21.12 shows a section of a Raman spectrum of polyethylene. The peak at 1057 rel. cm^{-1} belongs to an asymmetric stretching C–C vibration whereas the peak at 1123 rel. cm^{-1} corresponds to a symmetric stretching C–C vibration. One should note that the resulting peak at 1123 rel. cm^{-1} is the envelope of a "narrow" band and a "broad" band [33]. The peak at 1291 rel. cm^{-1} and the peak at 1375 rel. cm^{-1} belong to a twisting mode and a wagging mode of CH_2, respectively.

To see the influence of applied strain on the Raman spectra of polyethylene stress-strain measurements were carried out using a tensile testing machine. The tensile machine was mounted below a confocal Raman microscope (WITec, CRM 200, wavelength: 442 nm) to measure the Raman signal in situ. The strain was applied parallel to the direction of the drawing process.

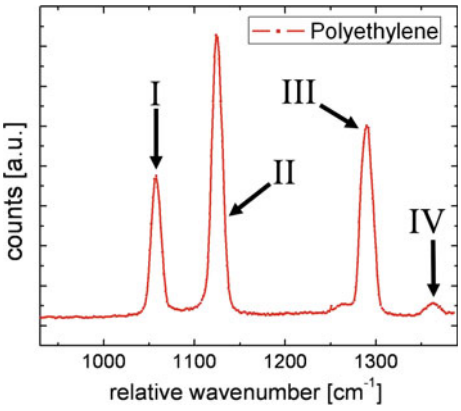

Fig. 21.12 Section of a Raman spectrum of polyethylene. The arrows indicate the following Raman peaks: I: ν_{as} (C–C) asymmetric stretching mode at 1057 rel. cm^{-1}; II: ν_s (C–C) symmetric stretching mode at 1123 rel. cm^{-1}; III: ν_t (CH_2) twisting mode at 1291 rel. cm^{-1} and IV: ω (CH_2) wagging mode at 1375 rel. cm^{-1}

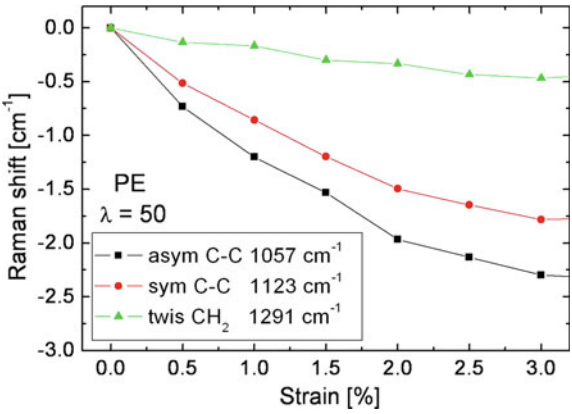

Fig. 21.13 Raman peak shift as a function of applied uniaxial strain for a polyethylene film with a draw ratio of 50

Figure 21.13 shows the Raman shift as a function of applied strain for the polyethylene film made with a draw ratio of 50. Three different peaks were analyzed. For the peak at 1123 rel. cm^{-1}, only the narrow band was analyzed as the broad band at the position did not influence the result. From the figure, one can see that the applied strain leads to a shift to lower wavenumbers. Up to a strain of 2% the shift seems to be linear. For higher strains, the slopes of all three curves change. Furthermore, the three peaks show different strain dependencies. The peak at 1291 rel. cm^{-1} is only altered slightly and has a strain dependence of 0.16 cm^{-1}/%. In comparison the peaks at 1123 rel. cm^{-1} and at 1057 rel. cm^{-1} exhibit a strain dependence of 0.58 cm^{-1}/% and 0.75 cm^{-1}/%, respectively.

The reason for the different strain dependencies is the origin of the peaks. The peak at 1291 rel. cm^{-1} belongs to a CH_2 wagging mode while the peak at 1057 rel. cm^{-1} corresponds to a C–C molecule vibration, which is the backbone bond of the polyethylene. In a tensile experiment the stress is mainly applied on the back bond of the polymer. The C-H bonds of the polymer are like small side arms and are therefore much less affected by the stress.

Figure 21.14 shows the peak shift for the peak at 1057 rel. cm^{-1} for the draw ratios of $\lambda = 20$, 40 and 50 up to 5% strain. The peak corresponds to a C–C backbone vibration. All three samples show the same behavior. With increasing strain the peaks are shifted to lower wavenumbers, but the slope of the peak shift strongly depends on the draw ratio of the film. The higher the draw ratio, the bigger is the slope of the sample.

Highly oriented polymers are assumed to consist of a number of anisotropic units with a uniform stress throughout the aggregate along the orientation axis [36]. Therefore, the macroscopic modulus can be expressed as:

$$\frac{1}{E} = \frac{1}{E_c} + \frac{\langle \sin^2 \theta \rangle}{G} \tag{21.16}$$

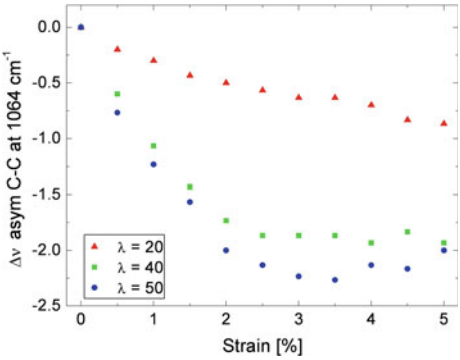

Fig. 21.14 Raman peak shift of the peak at 1057 rel. cm^{-1} as a function of the strain for the three different draw ratios $\lambda = 20$, 40 and 50

where E is the macroscopic Young's modulus, E_c is the average chain modulus, G the macroscopic shear modulus, and $\langle \sin^2 \theta \rangle$ is the mean value of orientation over the chain in the units about orientation axis. Equation (21.16) indicates that the deformation in highly orientated polymer films can be divided into a crystal stretching part (elongation of the polymer chains) and a rotation (shear deformation of small domains containing the chain segment). For high draw ratios the angle θ becomes small and therefore the portion of the rotation in the (21.16) decreases. As a consequence, in highly orientated films applied strain or stress will strongly affect the elongation of the C–C backbone and therefore lead to a peak shift of the corresponding Raman peak. Maximal peak shifts could be obtained in polymer crystals where the chains are perfectly orientated and therefore θ becomes zero.

21.3 Discussion

Strain measurements by means of Raman microscopy have already been shown to be highly useful for applications in microelectronics and microsystems technology. In this application, the standard material is (100)-oriented single crystalline silicon, which is extremely well characterized in terms of mechanical and electronic properties. Also the phonon deformation potentials are well established. Currently, the application of strain measurements by Raman microscopy is being extended to further classes of materials. In these cases, phonon deformation potentials still need to be established. It is therefore important to investigate the advantages and draw-backs of this technique.

The advantages are:

- High lateral resolution
- Depth resolution
- Available in laboratories at moderate cost
- Fast and easy data acquisition
- High strain sensitivity

In contrast the disadvantages include:

- Only certain classes of materials are Raman active
- Phonon deformation potentials are only available for a small set of materials
- Materials need to be transparent for 3D mapping
- Complete strain tensor is difficult to access
- Fluorescence may overshadow Raman peaks

In Table 21.2 the current technique is compared to other techniques for local strain measurements which are mostly based on diffraction. Electron diffraction is available in a laboratory environment, whereas X-ray diffraction requires synchrotron sources for spot sizes in the micrometer range.

The main advantage of Raman microscopy for strain measurements is its speed of acquisition and its ease of use. CBED requires extensive sample preparation and a TEM, Laue microdiffraction requires a synchrotron, which leaves only EBSD and a special Kossel technique which can be attached to SEMs. EBSD, however, has a poor strain resolution and the current state of the Kossel technique lacks automation. Raman microscopy is limited in terms of materials choice (polarizability) and needs the knowledge of phonon deformation potentials to allow for the conversion of peak shift into elastic strain. The conversion of strain into stress by Hooke's law is common to all methods. Complex strain states cannot currently be accessed by Raman microscopy. This draw-back will be overcome in the near future. With regards to lateral resolution, Raman microscopy is on the lower side for the methods com-

Table 21.2 Comparison of the Raman technique for stress measurement to comparable electron and X-ray diffraction based techniques

	Raman	Electron diffraction		X-ray microdiffraction		
		EBSD	CBED	Laue	Mono-chromatic	Kossel
Chromatic lateral resolution (nm)	300	20	5	500	50	500
Depth resolution	500 nm	–	–	1 µm	–	–
Ease of use	Lab based	SEM	TEM	Synchrot.	Synchrot.	SEM
Strain resolution	10^{-4}	10^{-3}	10^{-4}	10^{-4}	10^{-4}	10^{-5}
Time per pixel (s)	0.1	1	1	5	10	10
Materials	Polarizable	Single crystalline	Electron transparent	Single crystalline	Crystalline	Single crystalline
Strain tensor components	1–3	2–5	2–5	5–6	1–2	6

pared. Here, two possibilities are viable. First, near-field optics could be employed to achieve resolutions below 100 nm. The issue with this option is that both near-field optics and the Raman effect strongly attenuate the primary signal and if used in conjunction leave just a few photons of signal to count. The other option is to locally enhance the signal by Plasmon resonances, e.g. by putting metallic nanoparticles of gold or silver in a focused beam [37–39].

In summary, Raman microscopy has been demonstrated to be a fast and relatively easy way to locally measure strains. With a well-developed experimental set-up, more than one component of the strain tensor can be analyzed and certainly new materials will be analyzed in the future. Careful characterization of more materials that exhibit sharp Raman peaks in terms of the phonon deformation potential will enable strain measurements on more and more samples and make this technique useful for general local materials stress analysis.

References

1. N. Tamura, A. MacDowell, R. Spolenak, B. Valek, J. Bravman, W. Brown, R. Celestre, H. Padmore, B. Batterman, J.R. Patel, J. Synchrotron Radiat. **10**, 137 (2003)
2. J. Nucci, S. Kramer, E. Arzt, C. Volkert, J. Mater. Res. **20**, 1851 (2005)
3. J. Bauch, J. Brechbühl, H. Ullrich, G. Meinl, H. Lin, W. Kebede, Cryst. Res. Technol. **34**(1), 71 (1999)
4. R. Keller, A. Roshko, R. Geiss, K. Bertness, T. Quinn, Microelectron. Eng. **75**(1), 96 (2004)
5. Q. Ma, S. Chiras, D. Clarke, Z. Suo, J. Appl. Phys. **78**(3), 1614 (1995)
6. I. Wolf, Semicond. Sci. Technol. **11**, 139 (1995)
7. F. Cerdeira, C. Buchenauer, F. Pollak, M. Cardona, Phys. Rev. B **5**(2), 580 (1972)
8. E. Anastassakis, A. Pinczuk, E. Burstein, F. Pollak, M. Cardona, Solid State Commun. **8**, 1053 (1993)
9. G. Abstreiter, Appl. Surf. Sci. **50**(1–4), 73 (1991)
10. V. Srikar, A. Swan, M. Unlu, B. Goldberg, S. Spearing, J. Microelectromech. Syst. **12**(6), 779 (2003)
11. S. Ganesan, A. Maradudin, J. Oitmaa, Ann. Phys. **56**(2), 556 (1970)
12. R. Loudon, Adv. Phys. **13**(52), 423 (1964)
13. S. Narayanan, S. Kalidindi, L. Schadler, J. Appl. Phys. **82**(5), 2595 (1997)
14. E. Anastassakis, E. Burstein, J. Phys. Chem. Solids **32**(2), 563 (1971)
15. E. Anastassakis, J. Phys. Chem. Solids **32**(2), 313 (1971)
16. I. Dewolf, H. Norstrom, H. Maes, J. Appl. Phys. **74**(7), 4490 (1993)
17. E. Bonera, M. Fanciulli, D. Batchelder, J. Appl. Phys. **94**(4), 2729 (2003)
18. G. Loechelt, N. Cave, J. Menendez, J. Appl. Phys. **86**(11), 6164 (1999)
19. G. Loechelt, N. Cave, J. Menendez, Appl. Phys. Lett. **66**(26), 3639 (1995)
20. S. Hu, J. Appl. Phys. **70**(6), R53 (1991)
21. E. Bonera, M. Fanciulli, D. Batchelder, Appl. Phys. Lett. **81**(18), 3377 (2002)
22. H. Poulsen, S. Nielsen, E. Lauridsen, S. Schmidt, R.M. Suter, U. Lienert, L. Margulies, T. Lorentzen, D. Juul Jensen, J. Appl. Crystallogr. **34**, 751 (2001)
23. R. Nowak, T. Manninen, C. Li, K. Heiskanen, S. Hannula, V. Lindroos, T. Soga, F. Yoshida, JSME Int. J. Ser. A Solid Mech. Mater. Eng. **46**(3), 265 (2003)
24. T. Wermelinger, C. Borgia, C. Solenthaler, R. Spolenak, Acta Mater. **55**(14), 4657 (2007)
25. W. Rasband, Imagej, National Institutes of Health: Bethesda, MD USA. (1997–2007). *Image Processing and Analysis*

26. R. Nowak, T. Sekino, K. Niihara, Philos. Mag. A-Phys. Condens. Matter Struct. Defects Mech. Prop. **74**(1), 171 (1996)
27. T. Damen, S. Porto, B. Tell, Phys. Rev. **142**(2), 570 (1966)
28. F. Decremps, J. Pellicer-Porres, A. Saitta, J. Chervin, A. Polian, Phys. Rev. B **65**(9), 092101 (2002)
29. D. Mead, G. Wilkinson, J. Raman Spectrosc. **6**(3), 123 (1977)
30. F. Manjon, K. Syassen, R. Lauck, High Press. Res. **22**(2), 299 (2002)
31. K. Tashiro, G. Wu, M. Kobayashi, Polymer **29**(10), 1768 (1988)
32. J. Moonen, W. Roovers, R. Meier, B. Kip, J. Polym. Sci. Part B-Polym. Phys. **30**(4), 361 (1992)
33. W. Wong, R. Young, J. Mater. Sci. **29**(2), 510 (1994)
34. V. Mitra, W. Risen, R. Baughman, J. Chem. Phys. **66**(6), 2731 (1977)
35. J. Lefèvre, Ultra-high-performance polymer foils. PhD thesis, ETH Zurich (2008)
36. Y. Ward, R. Young, Polymer **42**(18), 857 (2001)
37. M. Moskovits, Rev. Mod. Phys. **57**(3), 783 (1985)
38. S. Nie, S. Emery, Science **275**(5303), 1102 (1997)
39. L. Zhu, C. Georgi, M. Hecker, J. Rinderknecht, A. Mai, Y. Ritz, E. Zschech, J. Appl. Phys. **101**(10), 104305 (2007)

Chapter 22
Confocal Raman Microscopy Can Make a Large Difference: Resolving and Manipulating Ferroelectric Domains for Piezoelectric Engineering

Fernando Rubio-Marcos, Adolfo del Campo and Jose F. Fernandez

Abstract Ferroelectric materials exhibit spontaneous and stable polarization, which can usually be reoriented by an applied external electric field. The electrically switchable nature of this polarization is at the core of various ferroelectric devices. The following chapter will review the use of Confocal Raman Microscopy (CRM) for the advanced characterization of Lead-free piezoceramics, emphasizing the relationship between structure and piezoelectric properties. In the first part we give a general introduction on the background of the Potassium-Sodium Niobate (KNN) Lead-free piezoceramics for elucidating the phase-structure-performance relationships through a classical approach of Raman spectroscopy. In the second part we reveal the role of the formation of secondary phases in KNN piezoceramics by chemical modifications. This phenomenon is one of the major drawbacks identified in KNN-based systems. In the third part we highlight some practical aspects in the study of ferroelectric domains in KNN-based piezoceramics. Special emphasis is placed on coupling confocal Raman spectroscopy and Atomic Force Microscopy (AFM), demonstrating to being a powerful tool in spatially resolving the structure of ferroelectric domains. Finally, we focus on the light-matter coupling and, consequently, in the relationships between phase boundaries and piezoelectric activity, discuss some existing challenges, suggest possible methods for further improving piezoelectricity, and provide some conclusions.

F. Rubio-Marcos · A. del Campo · J. F. Fernandez (✉)
Electroceramic Department, Instituto de Cerámica y Vidrio,
CSIC, Kelsen 5, 28049 Madrid, Spain
e-mail: jfernandez@icv.csic.es

F. Rubio-Marcos
e-mail: frmarcos@icv.csic.es

J. Toporski et al. (eds.), *Confocal Raman Microscopy*, Springer Series
in Surface Sciences 66, https://doi.org/10.1007/978-3-319-75380-5_22

22.1 Raman Spectroscopy and Confocal Raman Imaging: A Very Useful Technique for the Quick Evaluation of the Structure and the Properties of Lead-Free Piezoceramics

22.1.1 A Classical Approach of Raman Spectroscopy for In Situ Monitoring of Structural Changes

Polymorphic phase boundaries (PPB) in Lead-free piezoelectric materials has attracted significant interest in recent years, in particular because of the unique properties that can be found in their vicinity. It is very difficult to determine the actual phase compositions and types of phase boundaries in a given material. Significant attention has been paid to exploring the origin of high piezoelectricity in Lead-free perovskite oxides with a PPB, by analyzing the phase constituents using different experimental methods.

The $(K_{0.44}Na_{0.52}Li_{0.04})(Nb_{0.86}Ta_{0.10}Sb_{0.06})O_3$ (KNL-NTS) compound is used in this section as a model system to identify the existence of the intermediate phases and thus explain the physical origin for enhanced piezoelectricity around a PPB. KNL-NTS ceramics have been extensively studied as it is one of the most workable Lead-free compositions known to date [1]. The crystallographic structure of the KNL-NTS evolves from a paraelectric cubic (C) phase at high temperatures to a ferroelectric orthorhombic (O) phase at low temperatures, passing through a ferroelectric tetragonal (T) phase. The T to O phase transition gives rise to the PPB, which occurs close to room temperature for this compound (see Fig. 22.1). As a result of the PPB existence, excellent functional properties are achieved in KNL-NTS at room temperature [2]. The PPB temperature can be modulated by chemical modifications, such as the variation of the A/B ratios of the ABO_3 perovskite structure (see panel (a) of Fig. 22.1, where the unit cell of the perovskite structure is shown, in which two different symmetries coexisting at room temperature in the system are illustrated; orthorhombic (O) and tetragonal (T), respectively).

Previous results in KNL-NTS piezoelectric ceramics [3–7] showed that first, the best piezoelectric properties are obtained for the tetragonal symmetry, and second, there is a linear correlation between the tetragonal distortion, c/a ratio, and the piezoelectric properties (see Fig. 22.1e). The amount and distribution of the orthorhombic phase limits the correlation between tetragonality ratio and piezoelectric properties. In addition, obtaining such relationships between the structure and the piezoelectric properties will consequently allow us to understand the parameters leading to the improvement of the properties of these materials. Previous studies showed that not every conventional characterization technique appears suitable for that purpose, yet Raman spectroscopy has already proven to be. In the past, this technique was mainly devoted to fundamental research, but instrumental progress (laser miniaturization, CCD, filters and data processing software improvement) have rendered it a general characterization method. Not only can it provide basic phase identification [8] but

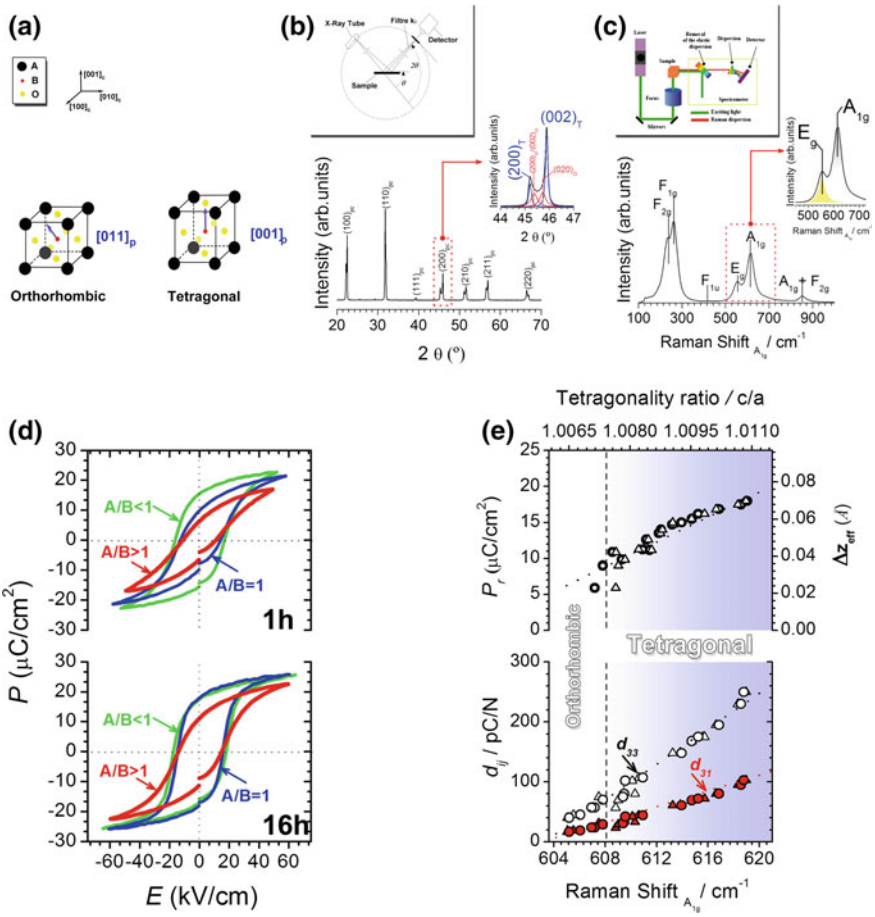

Fig. 22.1 Fast evaluation of the structure and the properties of Lead-free piezoceramics by Raman spectroscopy: **a** Unit cell of the perovskite structure with two different symmetries; orthorhombic (O) and tetragonal (T). **b** XRD diffraction pattern of the structure. **c** An average typical Raman spectrum of the KNL-NTS ceramic. **d** Polarization-field response of the for KNL-NTS ceramics with different A/B ratios. **e** Evolution of the remnant polarization, Pr, and the ionic effective displacement, Δz_{eff}

also subtle spectral alterations can be detected and used to assess nano-scale structural changes [9] and characterize micromechanical behavior. Some specific features can also be used to study charge transfer [10, 11], film orientation [12] or the size of particles or clusters trapped in nano-cavities [13]. Moreover, in our particular case, Raman spectroscopy is a very sensitive tool to study at a local scale the structural deformation of perovskites, which are induced both by the tilting of the BO_6 octahedra and by the cationic displacements.

Here, we have selected the $(K_{0.44+x}Na_{0.52}Li_{0.04})(Nb_{0.86}Ta_{0.10}Sb_{0.04})O_3$ compositions with x = −0.06, 0.00 and 0.04, with the aim of modifying the PPB and

consequently the system properties. This way, the ceramics present different A/B ratios in the ABO_3 perovskite structure, ranging from 0.94 to 1.04. For the sake of clarity, the compositions with A/B = 0.94, 1.00 and 1.04 will be hereafter named respectively as A/B < 1, A/B = 1 and A/B > 1. Three different A/B ratios were studied because previous work demonstrated that these values influence the sinterability of the material [14] and could also produce modifications in the crystalline structure appearing at room temperature [3].

A classical technique to obtain structural information on lead-based piezoceramics with PPB is X-ray diffraction (XRD). The top of Fig. 22.1b represents a sketch of a typical x-ray diffraction equipment. Figure 22.1b shows a typical XRD pattern for a KNL-NTS ceramic, which has a main tetragonal crystal structure with a space group of *P4mm*. The inset of Fig. 22.1b shows a detail of the XRD diffraction pattern in the 2Θ range 44°–47°, corresponding to (002) and (200) peaks of the perovskite structure. It is well known that the tetragonal symmetry (T) of the perovskite phase can be deconvoluted in two Lorentzian peaks, $(002)_T$, and $(200)_T$. In addition, in this sample two peaks located at ~45.4 and ~45.6° (2Θ) which are associated with the orthorhombic symmetry (O), are detected. The presence of peaks indicating tetragonal as well as orthorhombic symmetry is evidence for a PPB. In this model case, the peaks associated with tetragonal symmetry are the more relevant ones. In tetragonal *P4mm* KNL-NTS ceramic, ferroelectricity is mainly due to a relative displacement along the c-axis of the B-cation from its centrosymmetric position in the unit cell and in the oxygen octahedra. In correlation with the B-cation shift, A-ions are also displaced along the fourfold axis of the tetragonal cell. A permanent electric dipole, or ferroelectric polarization, is thus created (blue arrow in Fig. 22.1a). The deviation of the c/a ratio from unity is used as an indication of the presence of the ferroelectric phase. Therefore, we feel that determination of the c/a ratio is a crucial parameter for predicting the functional properties of the ferroelectric ceramics.

In X-ray diffraction, the samples showed an increase of the tetragonality ratio with sintering time and A/B ratios. For the A/B > 1 sample the XRD peak broadening may be caused by the phases' coexistence as well as a low degree of crystallinity. It therefore may be difficult to fully resolve the tetragonality ratio. In contrast, these disadvantages can be minimized using Raman spectroscopy. Raman spectroscopy is a very sensitive tool to study at a molecular scale the structural deformations of perovskites, which are induced both by the tilting of BO_6 octahedra and by the cationic displacements. These structural modifications induce significant changes in internal modes associated with the BO_6 octahedron and thus a modification of the Raman spectra. The main vibrations are associated with the BO_6 perovskite-octahedron [7, 15]. In that case, the vibrations of the BO_6 octahedron consist of $1A_{1g}(\nu_1) + 1E_g(\nu_2) + 2F_{1u}(\nu_3, \nu_4) + F_{2g}(\nu_5) + F_{2u}(\nu_6)$ modes. Figure 22.1c shows an average typical Raman spectrum of the Raman modes associated to the BO_6 octahedron for the KNL-NTS ceramic. Of these vibrations, $1A_{1g}(\nu_1) + 1E_g(\nu_2) + 1F_{1u}(\nu_3)$ are stretching modes and the rest, bending modes. In particular, $A_{1g}(\nu_1)$ and $F_{2g}(\nu_5)$ are detected as relatively strong scattering in systems similar to the one we are studying because of a near-perfect equilateral octahedral symmetry, see insert of the Fig. 22.1c. Raman spectroscopy has been used to evidence the nature of the

crystalline symmetry of the different compositions as function of the stoichiometry (A/B ratio) for both the synthesis powders [16, 17] and the sintered samples [3].

Following the above analysis, we concluded that ferroelectricity is mainly due to a relative displacement along the c-axis of B cation from its centrosymmetric position in the unit cell and in the oxygen octahedra. This relative displacement produces a spontaneous and stable polarization, which can usually be reoriented by an applied external electric field. To verify the ferroelectric behavior at the macroscopic level, a common procedure is to assess the electric field-induced polarization hysteresis loops. Figure 22.1d[1] shows room temperature P-E hysteresis loops of the KNL-NTS ceramics for different A/B ratios at 1 (top) and 16 h (bottom) sintering time, respectively. Well-saturated hysteresis loops with a good square shape are clearly obtained in all samples and an increase in remnant polarization, Pr, with the sintering time is observed for each composition. Moreover, in our case the remnant polarization is shown to be proportional to the tetragonality ratio, as evidenced in Fig. 22.1e.[2]

The most surprising result obtained from Raman spectroscopic investigations is that the evolution of the A1g Raman mode shift is equivalent to the one of the tetragonality ratio calculated from XRD data, as shown in Fig. 22.1e. More important, this fact allows us to gather valuable information about the ionic effective displacement [7, 18], Δz_{eff}, of the active ferroelectric ion (top of Fig. 22.1e), because a larger Raman shift of the A_{1g} mode or a larger tetragonality ratio (c/a) implies a higher value of displacement of the central ion (B^{5+}) from its equilibrium position, Δz_{eff}. In addition, the spontaneous polarization (P_s) is directly proportional to piezoelectric d_{ij} coefficient and therefore a linear relationship between the piezoelectric d_{ij} coefficient and the tetragonality ratio or the wavenumber of the A_{1g} mode is also expected, as shown Fig. 22.1e (bottom).

To summarize the first section, Raman spectroscopy can be used to rapidly determine the tetragonality ratio (c/a) of KNN-based ceramics, since Raman spectra can be taken in few seconds, in contrast to several minutes required for an XRD measurement. Moreover, the quantity of sample required for a Raman measurement is significantly smaller than for an XRD measurement, thus being then a very useful technique for material testing also in industrial processes. And last but not least, Raman spectroscopy has allowed us to establish relationships between the ferroelectric properties (Pr), piezoelectric properties (d_{ij}) and the ionic effective displacement (Δz_{eff}) of the active ferroelectric ion with the wavenumber of the A_{1g} mode (Fig. 22.1e). Knowing and understanding these relationships, Raman spectroscopy can be applied to determinate these parameters and be used as a powerful tool for in situ monitoring their changes under different processing conditions.

[1] Reprinted with permission from [6]. Copyright 2011 The Institute of Electrical and Electronics Engineers (IEE).

[2] Modified and reprinted with permission from [7] Copyright 2011 Wiley.

22.1.2 Raman Imaging: Can It Make a Significant Difference?

The study of a complex system, such as piezoceramic materials, in general is somewhat problematic since there are two main contributions to the macroscopic properties in such piezoelectric materials: the intrinsic and extrinsic contribution. The intrinsic contribution is associated with the crystalline structure, lattice parameter evolution, phase boundary, etc. The extrinsic contribution is mainly associated with the microstructural aspects (i.e. grains, grain boundaries, domains, domain wall motion, etc.). In order to obtain a best possible understanding of the a real-world-sample, both the intrinsic and the extrinsic contributions have to be taken into account. The intrinsic contributions are mainly the tilting of BO_6 octahedra and the cationic displacements at microscopic scales. The extrinsic contributions originate mainly from microstructural features. Confocal Raman Microscopy (CRM) allows us to acquire the microstructural features (extrinsic contribution) at a high spatial resolution and the molecular information at excellent spectral resolution (intrinsic contribution). Besides, with the relatively recent advances in confocal Raman imaging, the identification, distribution, and quantification of all crystalline phases within a ceramic material is now possible at resolution scales ranging from centimeters to nanometers.

As previously mentioned, the identities of crystalline phases play a relevant role with respect to the functional properties of the piezoceramics, and therefore, their identification and distribution can be used to devise new strategies in designing new materials with improved properties. Figure 22.2a shows an optical micrograph of the polished surface of a KNN-based ceramic, aligned perpendicular to the Raman laser (more information about the composition and preparation of this material can be found in [19]). The area of $20 \times 20\,\mu m$ denotes the selected area where the Raman spectra were collected at a plane located just below the surface of the sample, where the Raman intensity was maximized. The acquisition time for a single Raman spectrum was 500 ms, thus the acquisition of a Raman image consisting of 100×100 pixels (10,000 spectra) required 83 min. Features such as Raman peak intensity, peak width or Raman shift can be extracted from recorded Raman spectra using fitting algorithms, such as Gaussian or Lorentzian fits. These can then be used for comparison and display of the information as for example shown in Fig. 22.2b.

Raman spectra having the same Raman shift are classified by colours and the colour intensity corresponds to the Raman intensity of the respective peak. The combination of colours results in an image of the ceramic microstructure, which reveals the presence of both ceramic grains (delimited with a bright dotted line for shake or clarity) and the groups of unit cells with the same orientation (and same crystalline phase), which are called ferroelectric domains. From the colour combination, four grains can be observed (marked as **A**, **B**, **C** and **D** in Fig. 22.2b). These four grains provide different scenarios to study the domain structure (or crystalline phase coexistence) in polycrystalline samples. Grains **A** and **B** are characterized with striped

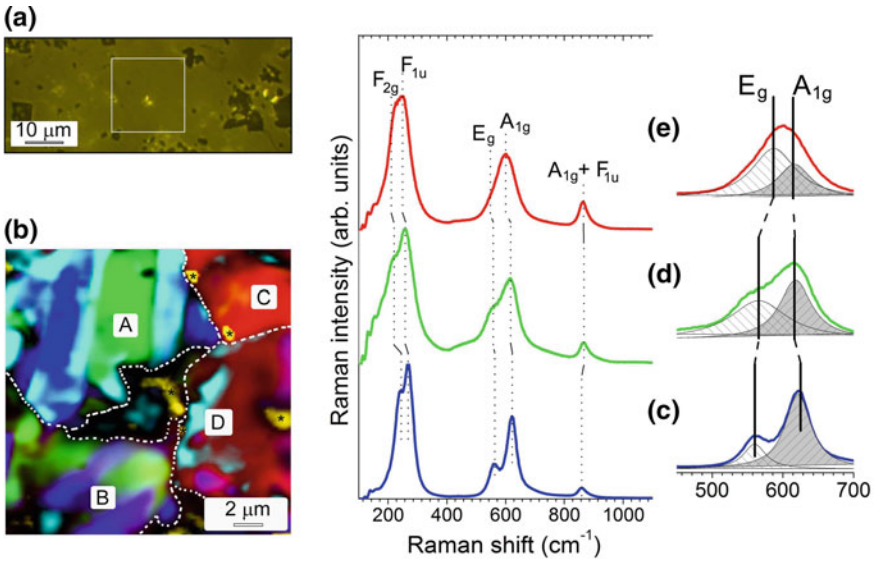

Fig. 22.2 Fast identification of the phase coexistence of Lead-free piezoceramics by Confocal Raman microscopy: **a** Optical micrograph of the polished surface of a KNN-based ceramic. **b** The Raman image of the KNN-based sample exhibiting the domains structure of the ceramic. The colours of the Raman image correspond to the colours of the spectra in (**c**–**e**). The regions delimited by bright dotted lines and marked as A, B, C and D represent four different grains. In addition, a secondary phase in yellow is marked with an asterisk (∗), which will be discussed in the Sect. 22.2. **c**–**e** Main Raman spectra associated with the different colours in (**b**). The inserts show magnified Raman spectra fitted with two Lorentzian peaks, assigned to the E_g (ν_2) and A_{1g} (ν_1) Raman modes, respectively. Reprinted with permission from [19] Copyright 2013 AIP Publishing LLC

domains while grains **C** and **D** are irregularly shaped domains. The colours in the image (Fig. 22.2b) correspond to the colours of their spectra: Fig. 22.2c tetragonal phase (blue); Fig. 22.2d mixing of tetragonal and orthorhombic phases (green) and Fig. 22.2e orthorhombic phase (red), confirming the phase coexistence that previously were observed by Raman spectroscopy at macroscopic scales (Fig. 22.1).

As a relevant result, grains **C** and **D** show irregular domains with the Raman spectra mainly characteristic of an orthorhombic phase. In addition, grain **D** shows small isolated regions inside orthorhombic grains, denoted in the literature as watermark domains [20, 21]. These watermark domains exhibit out-of-plane polarization. It is also worth noting further characteristics revealed by the CRM imaging since it has been possible to detect the presence of a secondary phase (marked with '∗' in Fig. 22.2b), which will be discussed in the following section.

22.2 The Study of (K,Na)NbO_3-Based Lead-Free Piezoelectric Ceramics: Identification of the Secondary Phase Location Using Confocal Raman Imaging

Studies from the very early stages and particularly those on polycrystalline (K,Na)NbO_3-based ceramics have been faced with difficulties in the preparation of the perovskite free of secondary phases. In this section we will reveal the role of the formation of secondary phases in KNN piezoceramics by their chemical modifications. This phenomenon is one of the major drawbacks identified in KNN-based systems. The secondary impurity phase appearance is commonly observed in many of the alkaline niobate based piezoceramics [4–7, 14, 22–25]. In particular, the secondary impurity phases are Li- and K-rich phases [4–7, 23–25]. As a consequence, we reported in previous studies that the chemical modifications with metal oxides (M_2O_n) has an important impact on the perovskite structure [26–31]. The ionic radii of the M_2O_n modulate the degree of lattice distortion, whereas the doping concentration rules the formation of the tetragonal tungsten bronze (TTB) phase [31]. In view of the doping levels, we have demonstrated that the inherent solubility of M_2O_n in the A- or B-sites position of the perovskite is very limited. When the amount of M_2O_n is higher than x = 0.01, M^{n+} ions are supersaturated in the lattice of KNL-NTS, and the excess M^{n+} ions enter on the B-sites of the lattice and favor the formation of the TTB secondary phase. This behavior is associated with a compositional segregation of the alkaline elements during the sintering stage [23, 24, 32]. Moreover, the secondary phase on these ceramics is hard to detect, implying that it could be an amorphous phase formed during sintering, with a high solubility in the system that led to its eventual disappearance with sintering time and/or sintering temperature [5, 33]. By X-ray diffraction, amorphous phases and/or crystalline phases with low concentrations (less than 2% of the main phases) appear as background signal without peak resolution, which complicates separation and localization of the components in the mixture. Nonetheless, in Confocal Raman Microscopy, amorphous phases, crystalline phases with a low concentration, and crystalline main phases often exhibit spectra with unique features. This allows signal separation, and hence, it will help to determine the role of each component for the functional properties of the system.

In the present section, W^{6+} is selected as the dopant of KNL-NTS ceramics. On the basis of its ionic radii [34], the W^{6+} ion ($r_{W^{6+}}$: 0.60Å for a coordination number CN = 6) falls in the size range of the B-site position ($r_{Nb^{5+}}$: 0.64Å, $r_{Ta^{5+}}$: 0.64Å, $r_{Sb^{5+}}$: 0.60Å CN = 6). Considering its valency, W^{6+} can act as a donor-dopant if introduced in the B-site. In order to introduce the W^{6+} ion into the B-site of the perovskite lattice, we selected B-site deficiency with a global formula $(K_{0.44}Na_{0.52}Li_{0.04})[(Nb_{0.86}Ta_{0.10}Sb_{0.04})_{1-x}W_{5x/6}]O_3$, hereafter abbreviated as KNL-$(NTS)_{1-x}W_{5x/6}$ [35].

To verify that the secondary phase formation plays a relevant role in compositional segregation of the alkaline elements during the sintering process, experiments were performed by atomic force microscope (AFM) and CRM. The ceramic with higher

W^{6+} contents, x = 0.05, was chosen to determine the secondary phase appearance. Figure 22.3a depicts an optical microscopy image of the sample with x = 0.05, aligned perpendicularly to the AFM cantilevers. The area of 14 × 14 μm (Fig. 22.3a) delimits the range where topographic information was collected by AFM. Figure 22.3b shows a detailed AFM topographic image of two grains corresponding to the secondary phase structure with plate-like shape. The AFM scans along the white arrow of Fig. 22.3b is illustrated in Fig. 22.3c. The grain associated with the secondary phase (i) has a grain size of ~4 μm and (ii) appears close to grain boundary protrusions (height difference of ~400 nm).

CRM is here combined with AFM in the same experimental setup, thus giving direct correlation between topography and local structure. The selected area is the one previously studied by AFM. As before, Raman spectra having the same Raman shift are classified by colours and the colour intensity corresponds to the Raman intensity of the respective peak. The colour combination results in (i) Raman image

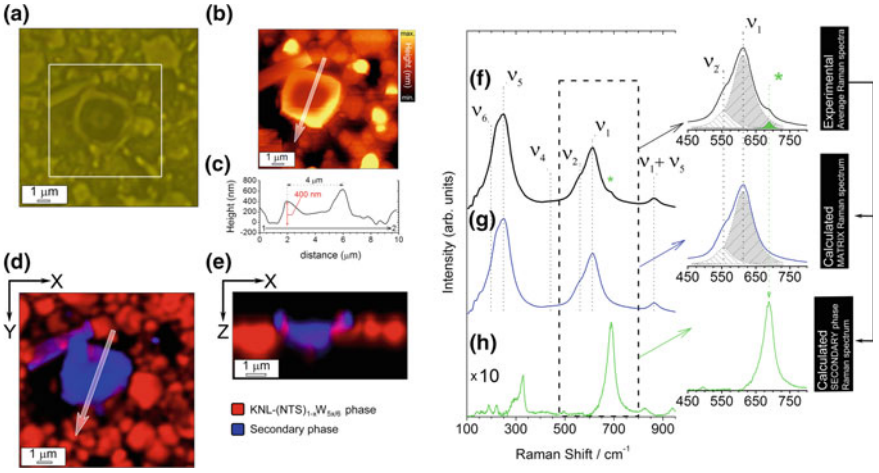

Fig. 22.3 Detection of the secondary phase through confocal Raman microscopy: **a** Optical micrograph of the polished and thermally etched surface of the KNL-$(NTS)_{1-x}W_{5x/6}$ sintered ceramics with x = 0.05. **b** AFM image of KNL-$(NTS)_{1-x}W_{5x/6}$ sintered ceramics with x = 0.05, showing the topography of the secondary phase inside the marked white box of (**a**). **c** AFM topography cross section along the white arrow of (**b**). The white rectangle in the panel (**a**) shows the positions where the XY Raman image is performed and corresponds with the area of previous AFM analysis. The Raman image shows the secondary phase distribution (blue regions) at the surface by colour code (**d**) as well as in the depth scan (**e**). The white arrow in the panel (**d**) shows the position where the XZ Raman depth scan image is performed. **f** Experimental Raman spectra corresponding to a KNL-NTS matrix and a minor secondary phase. This spectrum is fitted to the sum of two spectra: spectrum of the matrix (**g**) and of the secondary phase (**h**). In addition, the isolate Raman spectrum of the secondary phase has been magnified 10 times due to its low Raman intensity compared to the Raman spectrum of the KNL-NTS ceramic (matrix). The inserts in (**f**–**h**) show magnified Raman spectra in the frequency range 450–750 rel. cm^{-1}. Modified and reprinted with permission from [35]. Copyright 2015 Royal Society of Chemistry

of the surface (Fig. 22.3d) and (ii) Raman depth scan image of the cross-section (Fig. 22.3e). From these results we can deduce that there is a clear correlation between the secondary phase region (marked in blue colour) and the protrusion evidenced by AFM. This phenomenon results from the partial retention of the alkali elements (Li, Na, K) induced by the secondary phase formation at high temperatures during the sintering process, which promotes the displacement of the alkaline elements from the main KNL-NTS phase (red region in Fig. 22.3d–e) to the new secondary phase (blue region in Fig. 22.3d–e). As a consequence, we can conclude that the partial retention of the alkaline elements (Li, Na, K) onto the secondary phase, plays an important role in the modulation of functional properties of the system.

Following this section, there are several novel methodological approaches that may deserve further attention. CRM is particularly valuable for delivering information on both the (primary) matrix and the secondary phase. A detailed explanation of how we manage to discriminate the secondary phases, can be followed from Fig. 22.3f–h; the average Raman spectrum of the secondary phase is shown in Fig. 22.3f, which can be indexed on the basis of a phase mixture constituted by a majority of KNL-NTS phase and a minor effect of the secondary phase. The localization of the secondary phase can be observed in Fig. 22.3d, which is displayed as blue regions. As alluded earlier, this secondary phase is hard to detect by corresponding X-ray diffraction pattern. In previous studies concerning the KNL-NTS compounds, we have demonstrated that the secondary phase could be assigned either to $K_3LiNb_6O_{17}$ (KLN) or $K_6Nb_{10.88}O_{30}$ (PDF♯87-1856), both with tetragonal tungsten-bronze type structure (TTB) [5, 26, 31].

We have performed additional analysis to determine the isolated Raman spectrum of the secondary phase. The Raman spectrum discrimination of the secondary phase was calculated from average Raman spectra of KNL-NTS ceramic associated with the secondary phase (Fig. 22.3f). Then, the spectrum is fitted to the sum of two spectra: the first is associated with the matrix Raman spectrum (Fig. 22.3g), as it is well known for the piezoelectric KNL-NTS perovskite systems. The second spectrum is ascribed to the secondary phase with TTB structure (Fig. 22.3h).

To conclude this section, confocal Raman imaging allows the detection of sample characteristics, such as the presence of a secondary phase, which had previously been unobservable using XRD.

22.3 High Spatial Resolution Structure of (K,Na)NbO_3 Lead–Free Ferroelectric Domains

Lead zirconate titanate (PZT) based ceramics are currently enjoying wide use in piezoelectric devices despite lead toxicity. Due to growing environmental and human health concerns, the attention to piezoelectric ceramics has been moving to lead-free materials, in particular to potassium-sodium niobate-based lead-free piezoceramics [(K,Na)NbO_3-based, KNN]. Unfortunately, practical implementations of KNN

ceramics for commercial use are still limited by their inferior electrical and electromechanical properties as compared to their conventional Lead Zirconate Titanate (PZT) counterparts.

Almost all recent efforts contributing to property enhancement in KNN ceramics have been concentrating on chemical optimization through doping [36, 37], in addition to control over the sintering process [36, 38] and domain engineering by control of the poling process [39, 40]. For improving of the properties of KNN, the major concern is the increase of the piezoelectric coefficient d_{33}, which is determined by the electric charge response to a low external mechanical stress under linear conditions. The low mechanical field applied in the d_{33} measurement inhibited the extrinsic contribution of non-180° domain wall motions so the d_{33} values are dominated by the intrinsic (lattice) piezoelectric responses. Thus, the study of domain walls in piezoelectric materials is of high interest for a better understanding of their properties. Only few papers dealing with the ferroelectric domains in KNN and related compositions, such as single crystals [41, 42] and polycrystalline ceramics [43–45], are reported in the literature and they have been performed mainly by using Piezo-Force Microscopy.

Most classical characterization techniques of the ferroelectric domain structure are destructive, since they require the modification of the surface of the ceramic materials. In addition, as it has been mentioned above, the functional properties of the ferroelectric materials depend not only on the structural modification of the lattice distortion (intrinsic contribution) but also on the fine details of their ferroelectric domain configuration (extrinsic contribution) and on their highly ordered architecture at a scale ranging from few nanometers to several microns. Most of these fine details are lost when the surface of the ceramic is modified to be examined by such classical techniques. In order to investigate the structure and distribution of ferroelectric domains, a number of techniques have been commonly applied, among them are scanning probe microscopy (SPM) [43], environmental scanning electron microscopy (ESEM) [46], optical microscopy (OM) [47], transmission electron microscopy (TEM) [48], atomic force microscopy (AFM) [48] and lately, scanning electron microscopy in the backscattered mode (SEM-BS) [44, 49]. In contrast to spectroscopy methods, the above mentioned methods yield no or very limited compositional information and pure knowledge about the topography of the samples is often insufficient for the comprehensive characterization of complex domain structures. Various attempts have been made to combine the high spatial resolution of scanning probe microscopy with chemical information provided by spectroscopic techniques. Methods based on micro Raman spectroscopy give the possibility to study at a local scale the structural deformations of perovskites, which are induced both by the tilting of BO_6 octahedra and by the cationic displacements, as it is known for piezoelectric PZT and PMN-PT[3] perovskite systems [50, 51]. These structural modifications induce significant changes in internal modes associated with the BO_6 octahedron and thus a modification of the Raman spectra. Raman spectroscopy has been used to demonstrate the correlation of the structure and the piezoelectric properties of the

[3]PMN-PT = lead magnesium niobate modified with lead titanate.

materials, and to calculate the effective ionic displacement causing the piezoelectric polarization [7]. By determining both topography (microstructure) and molecular structure (chemical information) simultaneously, confocal Raman microscopy coupled with atomic force microscopy provide molecular-level information about the relationship of the crystalline structure with the domain formation as well with the polarization (Fig. 22.4). For a correct assessment, we need structural and topographic pieces that are at the core of potential technological applications.

As an example of a correct assessment of the ferroelectric domain structure, the Lead-free (K,Na)NbO_3 ceramic prepared by microwave–hydrothermal synthesis was chosen, because its grain size is much larger than commonly obtained by other methods, allowing us to perform studies on single crystals prepared by conventional ceramic method. The ferroelectric domain structure of this system in general is of interest because of its potential technological applications [52]. However, it is still much debated how ferroelectric domain structures affect the functional response of the material. Consequently this issue has been of considerable research interest in the last decades.

22.3.1 Simultaneous Determination of Topographic and Structural Features by CRM Coupled with AFM

Study of the domain structure was performed by Optical Microscopy and Atomic Force Microscope. Figure 22.4a depicts an optical microscopy image of the chemically etched KNN sample aligned perpendicularly to the AFM cantilevers. The domain structure is mainly composed of striped regions, vertically aligned in the image, containing in their interior 180° parallel domains. The domains in adjacent stripes present an angle of about 90°, indicating that a 90° domain wall appears between the vertical stripes shown in Fig. 22.4a. The area of 40 × 40 μm (marked as white box in the Fig. 22.4a) delimits the range where topographic information was collected by AFM. Figure 22.4b shows a detailed AFM topographic image of the domain structure. The topography analyses, Fig. 22.4c, confirm that the 90° domains (stripes) width ranged from 8 to 16 μm (90° domain walls are marked by dashed lines). Meanwhile, inside each striped area the domain width is smaller and varies from one strip area to another. Inside the 2–3 area (Fig. 22.4b) the domains are ∼450 nm in width and ∼32 nm in height, Fig. 22.4d, in contrast with the area 3–4, where domains are ∼1.4 μm in width and ∼100 nm in height, Fig. 22.4e. The domain density is thus different between stripe areas, indicating a relevant difference in the crystallographic orientations.

As we have highlighted in this section, both topographic and structural (chemical) information must be taken into account simultaneously to understand the nature of the micrometric domains in KNN ceramics.

CRM is here combined with AFM in the same apparatus, thus giving direct correlations between topography and local structure. The Raman spectra are collected

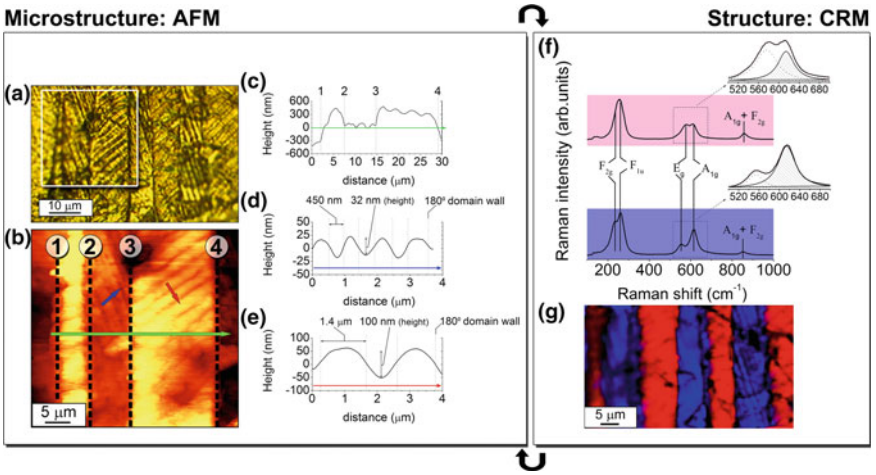

Fig. 22.4 Determination of both topographic and structure features simultaneously by CRM coupled with AFM: **a** Optical image of KNN ceramic after chemical etching, which shows a complex domain structure. **b** AFM image of the same sample showing the domain structure as consequence of the different chemical etching rate of the crystallographic orientations. **c–e** AFM line scans along the arrows marked in (**b**). **c** The AFM scan (green arrow) shows three regions separated by 90° domains walls, with a step height at these 90° domain walls of ~400 nm. **d**, **e** Height profiles corresponding to the arrows marked with blue and red colour in the image shown in (**b**). **f** Average Raman spectra of adjacent striped domains separated by a 90° domain wall. The inserts show magnified Raman spectra and Lorentzian fits of domain structures in the frequency range between 500 and 700 rel. cm^{-1}. These spectra are fitted to the sum of two Lorentzian peaks, ascribed to the E_g (ν_2) and A_{1g} (ν_1) Raman modes, respectively. **g** Raman image of domains structure of the KNN exhibiting clear differences between average spectra of adjacent striped domains separated by a 90° domain wall. The Raman image was derived by integration of the total spectral intensity from 100 to 1000 rel. cm^{-1}. Modified and reprinted with permission from [52]. Copyright 2012 Royal Society of Chemistry

at a plane located just below the surface of the sample where the Raman intensity is maximized (because CRM is very sensitive to surface topography and large differences in signal intensity could be originated from nanoroughness). The selected area (60 × 40 μm) is the one previously studied by optical microscopy (Fig. 22.4a). The acquisition time for a single Raman spectrum was 1.5 s/pixel (Fig. 22.4f). Thus the Raman image consisting of 60 × 40 pixels (2400 spectra) required 60 min for the planar-section (Fig. 22.4g). Features such as Raman peak intensity, peak width or Raman shifts are fitted with algorithms in order to compare information and to represent the derived Raman image. The assignments of the observed Raman modes, both symmetry and nature (first and second order), are summarized in the first part of this chapter. Figure 22.4f shows the average Raman spectra obtained in two adjacent strip areas separated by a 90° domain wall. Clear differences can be observed on the shape of both spectra, particularly in the 600 rel. cm^{-1} region. A detail of the BO_6 octahedron stretching E_g (ν_2) and A_{1g} (ν_1) Raman modes of the perovskite is magnified in the respective inserts in Fig. 22.4f and fitted to the sum of two Lorentzian

peaks. The A_{1g} (ν_1) Raman mode located at ~612 rel. cm^{-1} is a symmetric mode so it is observable for the different crystal orientations and is usually an intense mode, while the E_g (ν_2) Raman mode at ~550 rel. cm^{-1} is an anti-symmetric Raman mode along the polar direction (perpendicular to the oxygen octahedral basal plane). The E_g (ν_2) Raman mode is less intense than the A_{1g} (ν_1), but is magnified when the Raman polarization is parallel to in plane polarization. Then, it can be said that the polar direction is parallel to the sample plane surface in those regions (in red colour) of the sample presenting the red spectrum shown in Fig. 22.4f, while the blue spectrum represent a ferroelectric domain region with out-of-plane polarization.

In Fig. 22.4g, a colour-coded image indicates sample regions where the Raman spectra correspond to the ones presented in Fig. 22.4f (red and blue colour regions respectively). Raman spectra having same Raman shift are classified by colours and the colour intensity corresponds to the Raman intensity. As can be seen in this image, adjacent stripes present different Raman spectra. The studied Raman modes are certainly coupled and the determination of crystal orientation in adjacent striped regions cannot be determined unequivocally with the above measurement only. However, this measurement shows that there are relevant differences related to the polarization direction in the stripe regions corresponding to alternations of in-plane and out-of-plane orientations. This allows the confirmation of a 90° domain wall between adjacent stripe regions, as previously expected based on the topography. This example demonstrates the sensitivity and applicability of the Confocal Raman technique for detecting the presence of domains at the micro-scale.

22.3.2 Insights into the Details of the Ferroelectric Domain Structure

In addition to the domain identification, CRM allows a determination of the nature of domain walls and correlation between the structure and piezoelectric properties. Raman spectra have been measured following a line crossing perpendicularly the 180° domains in a stripe region where in-plane polarization is predominant (region marked in red in Fig. 22.4f and corresponding to red spectrum, see also the marked blue line in Fig. 22.5). In Fig. 22.5b, c we show the BO_6 octahedron Raman modes in two adjacent 180° domains, marked by A and B points in Fig. 22.5a. The differences in E_g and A_{1g} Raman modes intensity presumably account for different polar orientations, while the variations in the Raman shift of modes associated to the BO_6 octahedron allow determining changes in polarization, which are associated with modification of the constant force of the octahedron due to deformation or stress. It is worth noticing that there are two characteristic aspects in the E_g and A_{1g} Raman shift evolution along the line crossing the domains. First, the peaks shift in different directions (a polarization change), probably attributed to differences in polarization orientation, which is compensating between both modes. Second, the Raman shift amplitude in the E_g Raman mode is nearly 4 times higher than the one in the A_{1g}

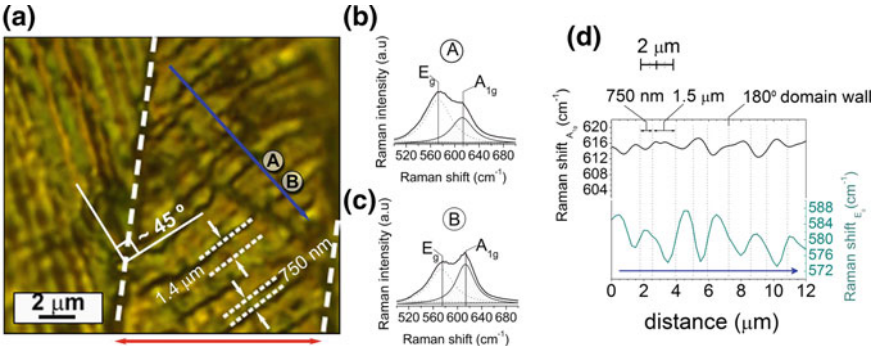

Fig. 22.5 Characterization of the 180° domain walls by confocal Raman spectroscopy: **a** Optical microscopy image of KNN ceramic samples, with two domains separated by a 90° domain wall. The 180° domain walls under analysis are present at a 45° angle to the 90° domain wall; note that the 180° domains located on the left of the 90° domain wall fail to preserve the symmetry and the angle is slightly lower than 45°. The width of the 180° domains is in the range of 750–1500 nm. **b**, **c** Magnified Raman spectra and Lorentzian fits of domain structures in the frequency range between 500 and 700 rel. cm^{-1} corresponding to the points labelled (A) and (B) in the image shown in (**a**). These spectra are fitted to the sum of two Lorentzian peaks, ascribed to the E_g (ν_2) and A_{1g} (ν_1) Raman modes, respectively. **d** Evolution of the A_{1g} and E_g modes which were measured following the blue arrow marked in the panel (**a**). Reprinted with permission from [52]. Copyright 2012 Royal Society of Chemistry

Raman mode. These evidences indicate that, in addition to the polar orientation change, the value of cell distortion is also modified and therefore the polarization changes (in value as well as in orientation). The alternating polarization differences in 180° domains tetragonal templates are resolved by 60° and 120° orthorhombic domains, which resulted in T-O alternating domains, coexistent in the in-plane-polarization region.

22.3.3 Some Clues About the Origin of the Ferroelectric Domain Structure: The Stress Sensitivity of Raman Spectroscopy

As mentioned above, at room temperature KNN presents a crystallographic structure composed of coexisting orthorhombic (O) and tetragonal (T) phases, a phenomenon known as Polymorphic Phase Boundary (PPB). The high temperature tetragonal structure formed at the T_c (cubic-tetragonal transition) acts as domain template of the room temperature orthorhombic structure. The change of the polarization direction of the orthorhombic structure implies a crystal lattice strain that is governed by the existing tetragonal domain configuration. The internal stress results in the appearance of an unusual polarization relaxation at the 90° domain wall in $(K,Na)NbO_3$ ceramics (Fig. 22.6).

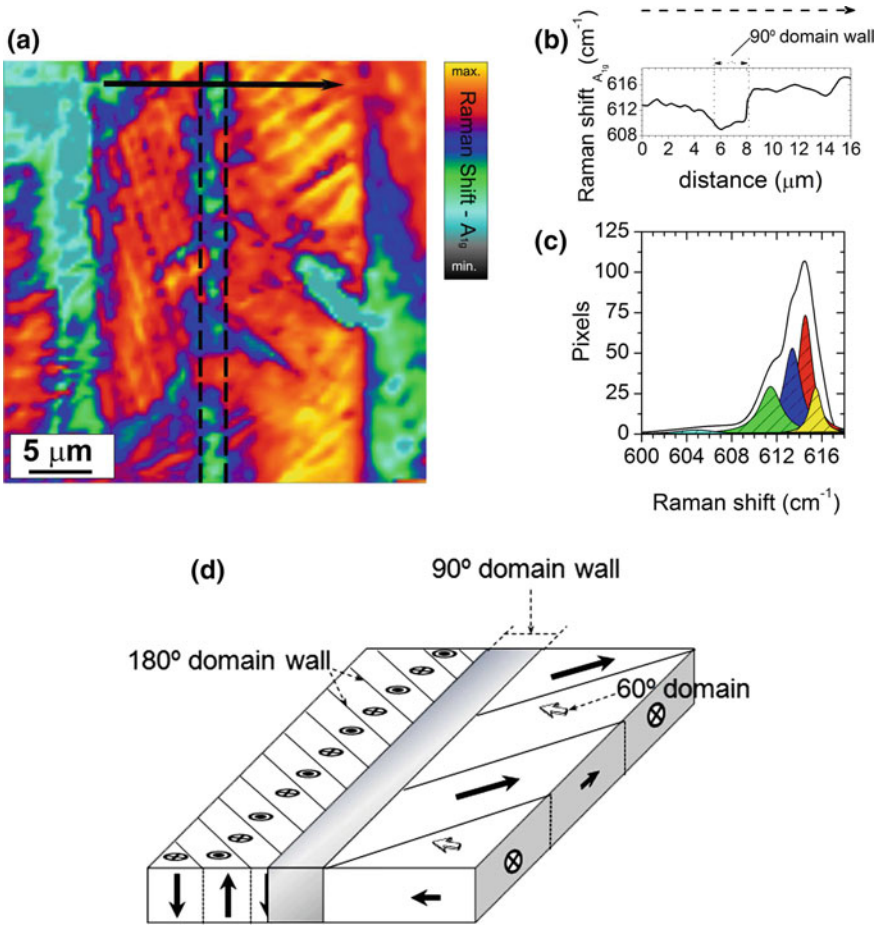

Fig. 22.6 Stress analysis around complex domain structures: **a** Color coded Raman image showing the Raman shift of the A_{1g} mode. **b** Evolution of the A_{1g} mode Raman shift following the arrow marked in (**a**). **c** Statistical analysis of the number of spectra corresponding to different Raman shift values of the A_{1g} mode. **d** Schematic representation of the three-dimensional domain structure. Reprinted with permission from [52]. Copyright 2012 Royal Society of Chemistry

Taking advantage of the stress sensitivity of Raman spectroscopy, we used Confocal Raman maps to monitor the distortion of the oxygen octahedra originated by the appearance of the ferroelectric domains. In Fig. 22.6a we show the Raman shift of the A_{1g} mode over two adjacent stripe regions. The evolution of the A_{1g} mode, in Fig. 22.6b, shows clearly an abrupt decreasing in the Raman shift of this mode that occurs at the 90° domain wall. The occurrence of alternating regions with T and T-O domains, as a result of the new crystalline structural distortions, must be accommodated at such 90° domain boundary. The decrease of polarization at the 90°

domain walls is consequence of such stress, which can be evaluated by statistical analysis of the A_{1g} mode Raman shift of all spectra shown in Fig. 22.6c.

To sum up, we feel that the methodology proposed here is a powerful tool to evaluate complex domain structures, which allows imaging of the ferroelectric domains with high spatial resolution and therefore it offers the opportunity to build a simple model that explain the nature of domain walls and correlation between the structure and piezoelectric properties (Fig. 22.6d).

22.4 A Potential Technological Application: Ferroelectric Domain Wall Motion Induced by Polarized Light

In the last section we will elucidate the surprising ability to move ferroelectric domain walls of a $BaTiO_3$ (BTO) single crystal by varying the polarization angle of a coherent light source [53]. Along the different sections of this chapter, we have emphasized that ferroelectric materials are characterized by exhibiting spontaneous and stable polarization, which can usually be reoriented by an applied external electric field. Various ferroelectric devices rely on the electrically switchable nature of this polarization, such as nonvolatile ferroelectric random access memory (FeRAM). In such memory devices, the storage of data bits is achieved by motion of domain walls that separate regions with different polarization directions. Therefore, an external voltage pulse can switch the polarization between two stable directions, representing "0" and "1". This behavior is responsible for a read/write process that can be completed within nanoseconds. The major drawback of FeRAM is that it requires a circuitry access, limiting their practical implementations for commercial use due to their difficult integration into devices as compared to their conventional magnetic random access memory counterparts. Consequently, there is a need for a method for switching the polarization of ferroelectric materials without the need of a circuitry access.

The engineering of ferroelectric domains is now advancing at a rapid pace. There has been progress in the understanding of the behavior of ferroelectric domain walls, especially on the control of their movement. New research studies are ongoing in order to find effective methodologies capable of modulating ferroelectric domain motion. Recently, in a pioneering study, T. Sluka and co-workers [54] demonstrated the correlation between the existence of "strongly" charged domain walls (sCDW) in ferroelectric $BaTiO_3$, and their enhanced electromechanical properties (electron-gas-like conductivity while individual domains remained excellent insulators). Therefore, the discovery of this stimulant behavior from sCDW described for BTO-based materials and the potential technological applications from these enhanced functionalities raises a need for an efficient and non-invasive method to switch ferroelectric domains without the need of electrical connections or physical contact, for example, by means of an electrostrictive film.

22.4.1 Resolving the Origin of the $BaTiO_3$ Complex Domain Structure

As we have shown in the previous section, a large variety of methods are used to characterize the ferroelectric domain structure. For that, it is crucial to know both structural and topographic properties that are at the core of engineering of ferroelectric domains. AFM and Raman imaging contribute to the analysis of the ferroelectric domain structures by visualizing the distribution of the individual domains based on the differences in the characteristic Raman spectra of each one them.

In an effort to shed light on the relationship between the switching of ferroelectric domains and their functional properties (e.g. the storage of data bits), we have chosen a $BaTiO_3$ (BTO) single crystal as a model case. The BTO single crystal used in this study was produced by top-seeded solution growth (TSSG) and provided by PIKEM Ltd (UK). The $5 \times 5 \times 1\,mm^3$ BTO crystal was grown with (100) orientation, or a-plane. The single-crystal was polished using $1\,\mu m$ diamond paste, and then cleaned with acetone and ethanol before characterization. No further thermal and/or chemical etching was used to reveal the domain structure, thus avoiding topographic artifacts induced by these processes. The sample was maintained at $T > 25\,°C$ during the AFM and CRM measurements.

A basic identification of the structure and of the crystalline orientation of the single crystal reveals that the sample presents a tetragonal symmetry and two different crystallographic orientations, (001) or c-plane and (h00) or a-plane [53]. At first the BTO single crystal was characterized from a topographical point of view by optical microscopy and AFM (Fig. 22.7a–d). The morphology map indicates that the domain structure is mainly composed of domains of 40–50 μm width and adjacent domains appear alternately as protrusions and troughs (height difference of $\sim$120 nm) (Fig. 22.7c). The AFM scan also reveals the domain boundary topography, associated with soft transitions (Fig. 22.7d). Moreover, such transitions are asymmetric: left boundary of the protrusions presents a characteristic step (1.5–3 μm), while this step is not observed for right boundary.

Although the topography is an essential pillar for the determination of the domain structure, CRM allows studies at a local scale of the structural deformations of perovskites, induced both by the tilting of BO_6 octahedra and by the cationic displacements [52]. CRM is here combined with AFM in the same apparatus, thus giving direct correlations between topography and local structure (Fig. 22.7e, f). The Raman spectra are collected at a plane located just below the surface of the sample where the Raman intensity is maximized. The selected area ($150 \times 30\,\mu m$) is the same previously studied by AFM (Fig. 22.7b). The acquisition time for a single Raman spectrum was 1 s (1 pixel). Thus the Raman image consisting of 150×30 pixels (4500 spectra) required 75 min for the planar-section. Features such as Raman peak intensity, peak width or Raman shifts are fitted with algorithms in order to compare information and to represent the derived Raman image. The assignments of the observed Raman modes, both symmetry and nature (first and second order), are summarized in the Table 22.1.

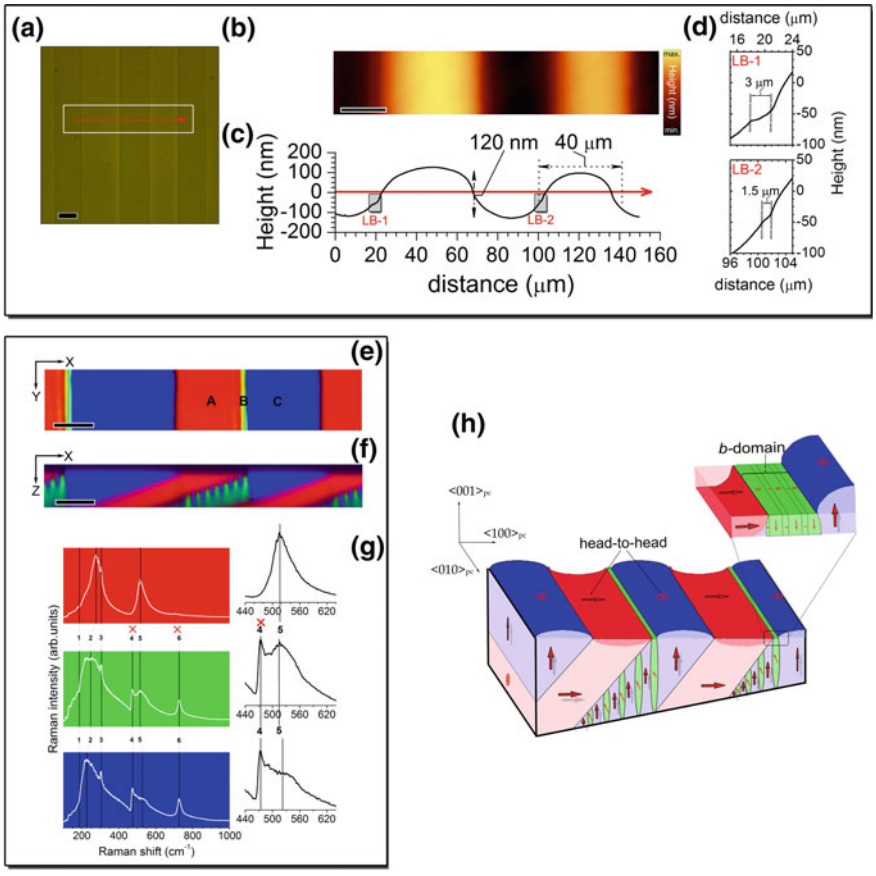

Fig. 22.7 Resolving the $BaTiO_3$ complex domain structure: **a** Optical micrograph of the domain structure. **b** AFM image of BTO crystal, showing the domain topography inside the marked white box of (**a**). Scale bar, 20 μm. **c** AFM topography scan along the red arrow of (**a**). **d** Detail of the domain boundary topography, corresponding to the left boundaries LB-1 and LB-2 of panel (**c**). The Raman image showing the domain distribution at the surface (recorded in the white rectangle marked in (**a**)) by colour code (**e**) as well as in the depth scan (**f**). Raman spectra having the same spectral shift are shown using the same colour and the colour intensity correlates with the Raman intensity. Scale bar, 20 μm. **g** Main Raman spectra of BTO Raman image associated with the three different colours: red = a-domain, blue = c-domain, green = b-domain, collected at the points marked as A, B, and C in panel **e**, respectively. The numbers next to the vibrational peaks represent the main atomic motions (see Table 22.1 for assignments). The inserts show magnified Raman spectra, ascribed to the 4 and 5 Raman modes, respectively. **h** The Figure displays a schematic illustration of the domain structure, which has been built by combining the AFM and Raman imaging information, shown in (**a**–**d**) and (**e**–**g**) respectively. Modified and reprinted with permission from [53]. Copyright 2015 Nature Publishing Group

Table 22.1 Raman modes and their mode symmetry assignments in tetragonal $BaTiO_3$ single crystal. The table summarizes both symmetry and nature (first and second order), of the Raman modes of the $BaTiO_3$ phase. According to the nuclear site group analysis, Raman active phonons of the tetragonal P4*mm* (C_{4v^1}) crystal symmetry are represented by $3A_1 + B_1 + 4E$. Long-range electrostatic forces induce the splitting of transverse and longitudinal phonons, which results in split Raman active phonons represented by $3[A_1\ (TO) + A_1\ (LO)] + B_1 + 4[E\ (TO) + E\ (LO)]$

Raman Shift rel. cm^{-1}	Symmetry	Abbreviated number	References
36	E(TO)	1	[55–59]
170	A_1(TO)	1	[56–61]
180	E(TO_2), E(LO)	1	[55–59]
185	A_1(LO)	1	[56–61]
210–270	A_1(TO_2)	2	[56–61]
305	E($TO_3 + LO_2$)	3	[55–59]
305	B_1	3	[55–59]
463	E(LO_3)	4	[55–59]
475	A_1(LO_2)	4	[56–61]
486	E(TO_4)	4	[55–59]
518	E(TO_5)	5	[55–59]
520	A_1(TO_3)	5	[56–61]
715	E(LO_4)	6	[55–59]
720	A_1(LO_3)	6	[56–61]

Raman spectra having the same Raman shift are classified by colours and the colour intensity corresponds to the Raman intensity. The combination of colours results in a Raman image of the surface (Fig. 22.7e) and a Raman depth scan image of the cross-section (Fig. 22.7f). Figure 22.7g shows the average Raman spectra obtained in adjacent domains: A (red) and C (blue) points. The a-domains (so called because its (100) crystallographic orientation) are easily detectable since they are characterized by the annihilation of two Raman modes (4 and 6 in Fig. 22.7g), while the presence of the both Raman modes is attributed to the c-domains (so called because its (001) crystallographic orientation). With the aid of optical microscopy and confocal Raman microscopy, mappings of the domain structure are obtained at the surface and deeper within the sample (Fig. 22.7e, f, respectively). Two well-known types of domains are identified by their characteristic Raman peak (a- and c-domains) and we also found a new type of domain (green colour, point B in Fig. 22.7e), which appears at the surface like a domain boundary. For the sake of simplicity, we will use hereafter the term b-domain to refer to this boundary. From their Raman signature, the b-domains (green colour, point B in Fig. 22.7e) appear clearly as a combination of both the a-domain and c-domain that could be explained as a bundle of subdomains. Indeed, recent studies have revealed the existence of a-c-subdomain structure in thin single-crystalline slices of $BaTiO_3$, referred as "superdomains" [62]. The formation of complex domains accounts for the existence of stress in thin layers, that usually relax for thicknesses >100 nm. In addition, this fact can produce a small onset of

electrostatic potential across the two sides of a 90° domain wall, which should have a dominant effect on the migration of charges that accumulates electron and oxygen vacancies at domain walls. As a relevant result, we believe that the b-domains clearly appear in the a-c-domain wall due to crystalline stress higher in the a-c-domain wall than in the c-a one. Due to the boundary conditions of the crystal surface, the c-domain protrudes accordingly with out-of-plane distortion, while the a-domain is depleted. AFM (Fig. 22.7a–d) and Raman imaging information (Fig. 22.7e–g) help in the building of a simple model of the complex domain structure (Fig. 22.7h) by which it is possible to explain the origin of the appearance of a new type of domain on the BTO. The scheme shows a domain structure composed of a-domains and c-domains with a head-to-head configuration of the polarization vectors, which are represented in red and blue colours respectively. The head-to-head configuration maximizes the internal stress close to the domain wall. As a consequence of this internal stress the a-c-domains are hindered by b-domains, which are represented in green colour. The insert of the b-domains structure shows how internal stress at the domain wall is minimized by a bundle of alternate a-domain and c-domain.

22.4.2 "In Situ" Ferroelectric Domain Switching Using a Polarized Light Source: A Potential Technological Application

Following the above analysis and interpretation, the b-domains are associated with a significant stress degree and according to the literature by an uncompensated charge [63]. Strongly charged domain walls (sCDW) generate photovoltages that could imply an interaction of photons with the accumulated charge. Consequently, a response of the sCDW related either to charge or stress redistribution could be expected when exposed to light. In addition, as we noted in the introduction of this section, an emerging application of ferroelectric materials are FeRAM devices, where the polarization switching of the ferroelectric domain is the key to the storage of data bits.

To explore such possibilities, in situ observations of polarization switching are carried out by applying polarized light. In all cases the incident light is normal to the sample surface and the polarization direction of light parallel to the surface. The angle between the polarization of light and the depth scan direction varies with increments of $\Delta\Theta = 15°$ between $\Theta = 0°$ and $\Theta = 90°$. The scanning direction is always perpendicular to the a-c-domain wall. Thus, in the a-domain case the polarization of light and consequently its associated electric field (E) is parallel to in plane polarization for $\Theta = 0°$ (E parallel to P) and perpendicular for $\Theta = 90°$. Therefore, the electric field has no effect on the polarization vector of BTO-cell for $\Theta = 0°$ (E and P are parallel) and has a maximal impact for $\Theta = 90°$ (E and P are perpendicular). Thus, for the a-domain, the effect of the electric field could imply an in-plane rotation of the polarization vector that remains parallel to the crystal surface even with re-orientation of its polarization direction under polarized light.

For the c-domain, the polarization of light is always perpendicular to the out-of-plane polarization. Whatever the Θ angle, the electric field associated to polarized light has the same effect. For the b-domains, a combination of both behaviors is expected as a result of the bundle of a-c-subdomains. Thus b-domains are probably the most sensitives to electric field and thus to the polarized light.

Figure 22.8a–g shows a sequential depth scan Raman images obtained for various Θ angles. The D-E-line serves as a guide to the eye to follow the domain motion. Clearly, ferroelectric domains move along the X axis for both the b-domains (green) and the c-domains (blue). When the polarized light reaches $\Theta = 90°$, the Raman spectrum of the c-domain evolves toward b-domain (Fig. 22.8a–g), accounting for a structural change. The a-domain (red), located on top surface of the sample, ap-

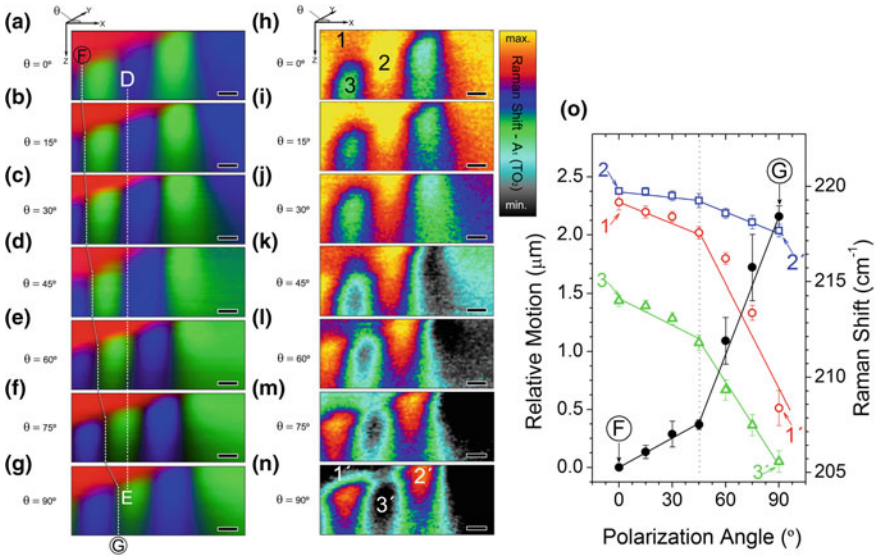

Fig. 22.8 Motion of ferroelectric domains under polarized light: **a–g** Sequence of Raman depth scan images showing the switching of the c-domains and b-domains in the BTO cross section for different angles of light polarization between 0° → 90°. The scheme localized at the top of (**a**) represents the angle Θ of the polarized light in the XY plane. Additionally, on the left of each image the light polarization angle value is indicated (**a–g**). The scale bar is 1 μm. **h–n** Sequence of Raman shift depth scans images showing the Raman shift at each pixel corresponding to the $A_1(TO_2)$ Raman mode 2 in Table 22.1. The colour code of the bar corresponds to maximum (220 rel. cm^{-1}) and minimum (205 rel. cm^{-1}) values of Raman shift of (**h–n**). The relative motion of domain is illustrated along the line marked as F → G in (**a–g**), and is plotted in black as a function of the polarization angle (Θ) in (**o**). The error bars show the standard deviation (σ) of the relative motion from the measurement for each angle of light polarization on a given sample. Moreover, panel **o** also shows the Raman shift evolution for three main points in the complex domain structure representing a-domain, a-c-domain wall and b-domain which are inscribed as 1→1', 2→2' and 3→3' in (**h–n**), respectively. The error bars show the standard deviation of the Raman shift evolution for three main points in the domain structure for each angle of light polarization on a given sample. Reprinted with permission from [53]. Copyright 2015 Nature Publishing Group

pears as unchanged. The local change of domain configuration seems to imply the displacement of the b-domain (green) to the detriment of the c-domain (blue). This observation supports our previous hypothesis of charged b-domains: these charges are highly sensitives to electric field and associated to the motion of domain walls.

However, it is noteworthy that the domain wall motion observed here implies a modification of tetragonality and polarization, at least at local scale. As we have demonstrated along the sections presented here, the Raman shift is an indicator of the crystal stress and correlates with both tetragonality and polarization [7, 64]. Indeed, a modification of the chemical environment (atomic displacement, local stress …) changes the force constants of chemical bonds and thus modify the phonon frequency of some Raman modes (Raman shift). By analogy with the visible spectrum and compared to references, a Raman shift increase of the Raman peak frequency is called "blueshift" (higher energy of phonon), while a Raman shift decrease is called "redshift". Raman shifts reveal chemical bond variations in the BO_6 octahedron, associated with the crystalline stress: we used confocal Raman imaging to understand this complex domain structure. The $A_1(TO_2)$ Raman active phonon is a symmetrical mode, which is detected as relatively strong scattering signal in BTO because of a near-perfect equilateral octahedral symmetry. Figure 22.8h–n display depth scans Raman shift images related to the $A_1(TO_2)$ Raman mode, for the different light polarization angles as indicated. Raman shifts as large as ca. $15\,cm^{-1}$ (from 205 to 220 rel. cm^{-1}) are determined in the complex domain structure. The Raman shift also evolves with the light polarization angle, with a translation of the domain structure, as stated above. The b-c-domain walls move and the region with local charge accumulation moves accordingly, undergoing redshift with increasing Θ. The redshift seems to be more relevant for $\Theta > 45°$ and the most relevant redshift occurs in the a-domain, indicating stress relief, or to some extent a structural modification of the crystal lattice. As a whole, the domain structure promotes a polarization reduction by the effect of the polarized light that stimulated the domain motion.

Figure 22.8o summarizes the extent to which the domain position is affected by the light polarization angle. This relative motion is illustrated by using as a reference the line F → G in Fig. 22.8a–g. This analysis shows that the relative motion of the domains is approximately $2.16 \pm 0.09\,\mu m$ when the light polarization direction changes from 0 to 90°. Accordingly, the relative domain displacement presents two different regimes as a function of the light polarization angle. From 45 to 90° the relative motion approximately triplicates the one observed between 0 and 45°, Fig. 22.8d–g. In addition, there is a progressive change of the c-domain nature that reaches the top of the single crystal surface, which for the observed region becomes a b-domain in nature. The previous experiments are attempted in two ways: the first one, the light polarization angle increasing in steps of 15° from 0° → 90° and thereafter decreases from 90° → 0°. For the second one, the light polarization angle randomly switches between the selected steps. In all cases the domain motion is reversible and remains within the error bars of Fig. 22.8o. In addition, the experiments are performed on different days and different regions along the complex domain structure, reaching similar results that confirm the reproducibility.

To summarize this final section, we demonstrate how polarized light with a wavelength of 532 nm can induce the motion of ferroelectric domain walls of a $BaTiO_3$ single crystal without any physical contact. It is worth pointing out that this stimulant behavior observed here could have potential technological applications leading to a non-contact read-out method in FeRAM devices or remote control of piezoelectric actuators.

22.5 Outlook

Raman spectroscopy can be used to establish relationships correlating the functional properties and crystalline phase changes (i.e. intrinsic contribution) on ferroelectric materials, respectively. Being a fast measurement technique and requiring only small quantities of sample material it is a powerful technique for material testing, also for industrial applications and processes. In combination with confocal microscopy, the identification and distribution of crystalline phases can be used to design new ferroelectric materials with improved properties.

Confocal Raman Microscopy (CRM) allows us to acquire at high resolution the microstructural features such as the ultrastructure of the ferroelectric domain configuration (extrinsic contribution) and their highly ordered architecture at a scale ranging from few nanometers to several microns. For a correct assessment, it is necessary to determine both the structural and topographic features that are at the core of potential technological applications. To facilitate that, we took advantage of the combination of CRM (chemical information) with AFM, (topographic information), to obtain molecular-level information on the relationship of the crystalline structure with the domain formation as well with the effect of polarization.

Finally, one of the most important points of this chapter is the demonstration that advanced measuring techniques such as CRM (especially coupled with AFM) can be successfully used to resolve and manipulate ferroelectric domains for piezoelectric engineering. As an example, the methodology proposed here has allowed us to demonstrate how polarized light can induce the motion of ferroelectric domain walls of a ferroelectric material without any physical contact. This breakthrough observation could lead to memory devices without electrical connections, by converting light energy directly into ferroelectric domain wall motion on a $BaTiO_3$ single crystal. In more general terms, the coupling between coherent light and the crystal orientation opens up exciting new opportunities for materials science.

Acknowledgements The authors express their thanks to Spanish National Research Council (CSIC) under project NANOMIND CSIC 201560E068. F. R-M is also indebted to MINECO for a "Ramon y Cajal" contract (ref: RyC-2015-18626), which is co-financed by the European Social Fund. Finally, many of the results summarized in the present chapter have been achieved with the support and collaboration of the numerous people. They are (in alphabetic order) Prof. Miguel A. Bañares, Prof. Miriam S. Castro, Mr. Carlos A. Fernández-Godino, Dr. Rigoberto López-Juárez, Dr. Pascal Marchet, Dr. Leandro Ramajo, and Dr. Juan J. Romero.

References

1. A. Safari, M. Abazari, K. Kerman, N. Marandian-Hagh, E.K. Akdoğan, IEEE Trans. Ultrason. Ferroelectr. Freq. Control **56**(8), 1586 (2009)
2. E. Akdogan, K. Kerman, M. Abazari, A. Safari, Appl. Phys. Lett. **92**(11), 2908 (2008)
3. F. Rubio-Marcos, M.G. Navarro-Rojero, J.J. Romero, P. Marchet, J.F. Fernández, IEEE Trans. Ultrason. Ferroelectr. Freq. Control **56**(9), 1835 (2009)
4. F. Rubio-Marcos, P. Ochoa, J. Fernandez, J. Eur. Ceram. Soc. **27**(13), 4125 (2007)
5. F. Rubio-Marcos, P. Marchet, T. Merle-Mejean, J. Fernandez, Mater. Chem. Phys. **123**(1), 91 (2010)
6. F. Rubio-Marcos, P. Marchet, J. Romero, J.F. Fernandez, IEEE Trans. Ultrason. Ferroelectr. Freq. Control **58**(9), 1826 (2011)
7. F. Rubio-Marcos, M. Banares, J. Romero, J. Fernandez, J. Raman Spectrosc. **42**(4), 639 (2011)
8. M. Navarro-Rojero, J. Romero, F. Rubio-Marcos, J. Fernandez, Ceram. Int. **36**(4), 1319 (2010)
9. F. Rubio-Marcos, A. Quesada, M. García, M. Banares, J.G. Fierro, M.S. Martín-Gonzalez, J.L. Costa-Krämer, J. Fernández, J. Solid State Chem. **182**(5), 1211 (2009)
10. A. Cabot, A. Dieguez, A. Romano-Rodrıguez, J. Morante, N. Barsan, Sens. Actuators B: Chem. **79**(2), 98 (2001)
11. P. Cassoux, D. de Caro, L. Valade, H. Casellas, S. Roques, J.P. Legros, Synth. Met. **133**, 659 (2003)
12. G.J. Fang, K.L. Yao, Z.L. Liu, Thin Solid Films **394**(1), 63 (2001)
13. V.V. Poborchii, Solid State Commun. **107**(9), 513 (1998)
14. M. Matsubara, T. Yamaguchi, W. Sakamoto, K. Kikuta, T. Yogo, S.I. Hirano, J. Am. Ceram. Soc. **88**(5), 1190 (2005)
15. K.I. Kakimoto, K. Akao, Y. Guo, H. Ohsato, Jpn. J. Appl. Phys. **44**(9S), 7064 (2005)
16. F. Rubio-Marcos, J. Romero, M.S. Martín-Gonzalez, J. Fernández, J. Eur. Ceram. Soc. **30**(13), 2763 (2010)
17. F. Rubio-Marcos, J. Romero, J. Fernandez, J. Nanopart. Res. **12**(7), 2495 (2010)
18. S. Abrahams, S. Kurtz, P. Jamieson, Phys. Rev. **172**(2), 551 (1968)
19. F. Rubio-Marcos, A. Del Campo, J. Fernández, J. Appl. Phys. **113**(18), 187215 (2013)
20. R. López-Juárez, O. Novelo-Peralta, F. González-García, F. Rubio-Marcos, M.E. Villafuerte-Castrejón, J. Eur. Ceram. Soc. **31**(9), 1861 (2011)
21. S.Y. Cheng, N.J. Ho, H.Y. Lu, J. Am. Ceram. Soc. **89**(7), 2177 (2006)
22. K.I. Kakimoto, I. Masuda, H. Ohsato, J. Eur. Ceram. Soc. **25**(12), 2719 (2005)
23. Y. Wang, D. Damjanovic, N. Klein, E. Hollenstein, N. Setter, J. Am. Ceram. Soc. **90**(11), 3485 (2007)
24. Y. Wang, D. Damjanovic, N. Klein, N. Setter, J. Am. Ceram. Soc. **91**(6), 1962 (2008)
25. J. Acker, H. Kungl, M.J. Hoffmann, J. Am. Ceram. Soc. **93**(5), 1270 (2010)
26. F. Rubio-Marcos, J. Romero, M. Navarro-Rojero, J. Fernandez, J. Eur. Ceram. Soc. **29**(14), 3045 (2009)
27. F. Rubio-Marcos, P. Marchet, X. Vendrell, J. Romero, F. Rémondière, L. Mestres, J. Fernández, J. Alloy. Compd. **509**(35), 8804 (2011)
28. F. Rubio-Marcos, P. Marchet, J.R. Duclère, J. Romero, J. Fernández, Solid State Commun. **151**(20), 1463 (2011)
29. F. Rubio-Marcos, P. Marchet, J. Romero, J. Fernández, J. Eur. Ceram. Soc. **31**(13), 2309 (2011)
30. F. Rubio-Marcos, J. Reinosa, X. Vendrell, J. Romero, L. Mestres, P. Leret, J. Fernández, P. Marchet, Ceram. Int. **39**(4), 4139 (2013)
31. F. Rubio-Marcos, J.J. Romero, J.F. Fernández, P. Marchet, Appl. Phys. Express **4**(10), 101501 (2011)
32. X. Vendrell, J. García, F. Rubio-Marcos, D. Ochoa, L. Mestres, J.F. Fernández, J. Eur. Ceram. Soc. **33**(4), 825 (2013)
33. F. Bortolani, A. del Campo, J.F. Fernandez, F. Clemens, F. Rubio-Marcos, Chem. Mater. **26**(12), 3838 (2014)

34. R.T. Shannon, Acta Crystallogr. Sect. A: Cryst. Phys. Diffr. Theor. Gen. Crystallogr. **32**(5), 751 (1976)
35. L. Ramajo, M. Castro, A. del Campo, J. Fernandez, F. Rubio-Marcos, J. Mater. Chem. C **3**(16), 4168 (2015)
36. J. Rödel, W. Jo, K.T. Seifert, E.M. Anton, T. Granzow, D. Damjanovic, J. Am. Ceram. Soc. **92**(6), 1153 (2009)
37. J. Wu, D. Xiao, J. Zhu, Chem. Rev. **115**(7), 2559 (2015)
38. M. Matsubara, T. Yamaguchi, K. Kikuta, S.I. Hirano, Jpn. J. Appl. Phys. **44**(1R), 258 (2005)
39. K. Wang, J.F. Li, Adv. Funct. Mater. **20**(12), 1924 (2010)
40. F. Rubio-Marcos, J.J. Romero, D.A. Ochoa, J.E. García, R. Perez, J.F. Fernandez, J. Am. Ceram. Soc. **93**(2), 318 (2010)
41. Y. Inagaki, K.I. Kakimoto, I. Kagomiya, J. Eur. Ceram. Soc. **30**(2), 301 (2010)
42. D. Lin, Z. Li, S. Zhang, Z. Xu, X. Yao, Solid State Commun. **149**(39), 1646 (2009)
43. R.P. Herber, G.A. Schneider, S. Wagner, M.J. Hoffmann, Appl. Phys. Lett. **90**(25), 252905 (2007)
44. D. Grüner, Z. Shen, J. Am. Ceram. Soc. **93**(1), 48 (2010)
45. J.H. Cho, Y.H. Lee, B.I. Kim, J. Ceram. Process. Res. **11**(2), 237 (2010)
46. S. Zhu, W. Cao, Phys. Rev. Lett. **79**(13), 2558 (1997)
47. A. Benčan, E. Tchernychova, M. Godec, J. Fisher, M. Kosec, Microsc. Microanal. **15**(05), 435 (2009)
48. J. Kling, X. Tan, W. Jo, H.J. Kleebe, H. Fuess, J. Roedel, J. Am. Ceram. Soc. **93**(9), 2452 (2010)
49. E. Soergel, Appl. Phys. B **81**(6), 729 (2005)
50. K. Lima, A. Souza Filho, A. Ayala, J. Mendes Filho, P. Freire, F. Melo, E. Araújo, J. Eiras, Phys. Rev. B **63**(18), 184105 (2001)
51. J. Lima, W. Paraguassu, P. Freire, A. Souza Filho, C. Paschoal, A. Zanin, M. Lente, D. Garcia, J. Eiras et al., J. Raman Spectrosc. **40**(9), 1144 (2009)
52. F. Rubio-Marcos, A. Del Campo, R. López-Juárez, J.J. Romero, J.F. Fernández, J. Mater. Chem. **22**(19), 9714 (2012)
53. F. Rubio-Marcos, A. Del Campo, P. Marchet, J.F. Fernández, Nat. Commun. **6** (2015)
54. T. Sluka, A.K. Tagantsev, P. Bednyakov, N. Setter, Nat. Commun. **4**, 1808 (2013)
55. M. DiDomenico Jr., S. Wemple, S. Porto, R. Bauman, Phys. Rev. **174**(2), 522 (1968)
56. U.D. Venkateswaran, V.M. Naik, R. Naik, Phys. Rev. B **58**(21), 14256 (1998)
57. P. Dobal, R. Katiyar, J. Raman Spectrosc. **33**(6), 405 (2002)
58. Y. Shiratori, C. Pithan, J. Dornseiffer, R. Waser, J. Raman Spectrosc. **38**(10), 1288 (2007)
59. Y. Shiratori, C. Pithan, J. Dornseiffer, R. Waser, J. Raman Spectrosc. **38**(10), 1300 (2007)
60. A. Pinczuk, W. Taylor, E. Burstein, I. Lefkowitz, Solid State Commun. **5**(5), 429 (1967)
61. G. Burns, B.A. Scott, Solid State Commun. **9**(11), 813 (1971)
62. P. Sharma, R.G. McQuaid, L.J. McGilly, J.M. Gregg, A. Gruverman, Adv. Mater. **25**(9), 1323 (2013)
63. L. Hong, A. Soh, Q. Du, J. Li, Phys. Rev. B **77**(9), 094104 (2008)
64. G. Gouadec, P. Colomban, Prog. Cryst. Growth Charact. Mater. **53**(1), 1 (2007)

Part VII
Correlative Microscopy

Chapter 23
RISE: Correlative Confocal Raman and Scanning Electron Microscopy

Guillaume Wille, Ute Schmidt and Olaf Hollricher

Abstract RISE, the combination of Raman Imaging and Scanning Electron microscopy is a promising technique that adds chemical information to the high resolution imaging capability of electron microscopy. By automatically transferring the sample from the electron beam to a separate Raman position inside the vacuum chamber, Raman molecular imaging can be performed without compromising SEM performance. Chemical information can be acquired with a resolution down to 300 nm and results obtained with both techniques can be overlaid with high precision.

Acronyms

BSE	BackScattered Electrons (SEM imaging mode)
BF	Bright Field (STEM imaging mode)
CRM	Confocal Raman Microscopy
CRSEM	Confocal Raman in SEM
DF	Dark Field (STEM imaging mode)
EBSD	Electron BackScattered Diffraction
EDS	Energy Dispersive X-ray Spectroscopy
EPMA	Electron Probe Micro Analyzer (SEM-based analytical system equipped with 3–5 WDS)
ESEM	Environmental Scanning Electron Microscope (allowing for a gaseous environment in the specimen chamber - working under dry gas or H_2O vapour pressure from a few Pa up to more than 1 kPa allows for the

G. Wille (✉)
BRGM, 3 Avenue Claude Guillemin, BP 36009, 45060 Orleans Cedex 2, France
e-mail: g.wille@brgm.fr

U. Schmidt · O. Hollricher
WITec GmbH, Lise-Meitner-Strasse 6, 89081 Ulm, Germany
e-mail: ute.schmidt@witec.de

O. Hollricher
e-mail: olaf.hollricher@witec.de

J. Toporski et al. (eds.), *Confocal Raman Microscopy*, Springer Series in Surface Sciences 66, https://doi.org/10.1007/978-3-319-75380-5_23

	option of collecting electron micrographs of specimens that are "wet", uncoated or both)
eV	Electron-Volt (energy unit equal to the energy of 1 electron accelerated by a tension of 1 volt)
LV-SEM	Low Vacuum Scanning Electron Microscope (allowing for a gaseous environment in the specimen chamber - working under dry gas pressure from a few 40 Pa to several hundred Pa)
Raman	often used as Raman Spectroscopy
SCA	Structural and Chemical Analyzer, interfaced with SEM from Renishaw
SEM	Scanning Electron Microscope
SE	secondary electrons (SEM imaging mode also named SEI: Secondary Electron Imaging)
SPM	Scanning Probe Microscopy
STEM	Scanning Transmission Electron Microscope (transmission Electron imaging in the SEM)
TEM	Transmission Electron Microscope
TOF-SIMS	Time Of Flight Secondary Ion Mass Spectroscopy
WDS	Wavelength Dispersive X-ray Spectroscopy

23.1 Introduction

The characterization of a material, whether natural or synthetic, usually requires a combination of different analytical methods whose data interconnection will lead to the requested information. A SEM equipped with various accessories, detectors (SE, BSE, CL…) and microanalysis tools (EDS, WDS, EBSD) is a powerful device for the characterization of materials and provides information on morphology, chemistry, texture and crystallography. Micro-Raman spectroscopy, another major analytical method in materials science, uses inelastic light scattering to extract valuable information on chemical bonds, molecular structure and crystallinity.

These two techniques appear to be essential and complementary for the microcharacterization of morphology and elemental and structural chemical properties of materials and minerals. Data provided by the SEM and associated techniques (EDS, EBSD) are mainly images whereas Raman imaging is well suited to combining data from both SEM and Raman. Therefore the combination of both techniques in a unique analytical system and the application of image correlation techniques for combining data is a promising tool.

23.2 Combining Scanning Electron Microscopy and Confocal Raman Spectroscopy

In recent years, numerous technical developments have made possible the combination of several analytical techniques in a single device. Thus, Raman spectroscopy has been combined with techniques as varied as, for example, Atomic Force Microscopy (AFM) [1–3], LIBS [4] and micro-X-Ray Fluorescence (μXRF) [5].

SEM imaging (combined with microanalytical techniques such as EDS, WDS or EBSD) and micro-Raman spectroscopy have been combined for materials characterization in several recent studies. Switching from one to the other is often considered to be problematic. This led to the idea of incorporating SEM and Raman spectroscopy within a single device [6, 7].

23.2.1 SEM and SEM-Based Microanalysis

Scanning Electron Microscopy (SEM) is a high-resolution imaging technique. An electron beam accelerated by an electrical voltage (from several tens of V to 30 kV) scans the area of interest on the sample. Several electron-matter interaction emissions are generated (see Fig. 23.1) and detected by specialized detectors. The detected signal is synchronized with the beam scan to provide images. Various images and data can then be obtained from the SEM, providing a wide range of information on the nanometer scale.

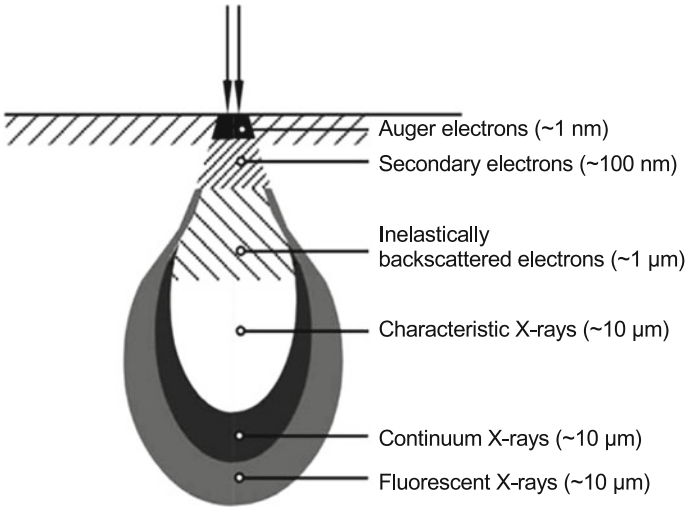

Fig. 23.1 Interaction volumes and depth range for the main types of emissions in SEM [8]

Secondary Electron (SE) and Back Scattered Electron (BSE) imaging are the most common imaging modes carried out in the SEM. SE are low-energy electrons (by convention $<50\,eV$) generated by the energy transfer from an electron of the beam to a "core electronic level" electron in atoms of the sample. SE images provide high-resolution (up to 1 nm or better) information on the sample shape, dimensions and surface topography. The most common detector is known as an "Everhart-Thornley" detector (named for T.E. Everhart and R.F.M. Thornley, inventors) [9]. Various detectors have been developed for specific applications, including high-resolution (detectors inserted in the objective lens), low vacuum or environmental mode.

BSE ($>50\,eV$) are primary beam electrons that have been deflected by interaction with atoms (core electronic levels) to such an extent that their path actually takes them back up through the sample surface. BSE imaging is frequently considered to be the "chemical imaging" approach, but other information can be obtained from the BSE detector, such as topography or crystal orientation.

Other imaging modes are also available in the SEM. Cathodoluminescence (CL) is a photonic emission in the visible and near-visible light range under the electron beam. This technique is widely used for the characterization of crystal growth, zonation (chemical heterogeneity of a crystal) and crystallography of samples in geology, materials science and the semiconductor industry. It is also commonly employed for imaging and wavelength spectral analysis.

Scanning Transmission Electron Microscopy (STEM) employs a specific type of detector installed on the SEM to observe thin sections of materials in parallel with Transmission Electron Microscopy (TEM).

SEM can be combined with chemical microanalysis (Energy Dispersive X-ray Spectrometry - EDS, or Wavelength Dispersive X-ray Spectrometry - WDS). Characteristic X-rays are emitted during the relaxation process following the secondary electron (SE) emission which are then detected in an energy or wavelength dispersive manner. These techniques make it possible to determine - qualitatively and quantitatively - the elemental composition of the sample on the micrometer scale. Sub-micrometer scale can be obtained under low voltage conditions [10].

Crystallographic analysis can also be provided by an SEM-based technique called EBSD (Electron Back-Scattered Diffraction). The electron beam is diffracted by the crystal lattice planes and the diffraction bands are collected by a special camera equipped with an electron-sensitive scintillator (i.e. phosphor deposited on glass). The pattern is automatically indexed for the determination of the crystal phase and orientation. EBSD spatial resolution is approximately several tens of nanometers. Widely used for metallurgical samples (micro-texture, strain measurements, etc.), EBSD is increasingly popular and applied to the characterization of all crystalline materials, including geological samples, especially when combined with EDS data [11].

23.3 Confocal Raman Imaging

The principles of Raman spectroscopy and confocal microscopy as well as their combination are outlined in previous chapters in this volume. Details on the achievable lateral and depth resolution are additionally provided and are therefore not repeated here. However, in preparation for the results presented later in this chapter some basic properties often illustrated through confocal Raman imaging should be emphasized:

- An image generated by calculating the peak intensity or the integral of a specific Raman band displays the distribution of the relative amount of a chemical compound.
- An image generated by calculating the peak shift displays modifications in the crystal structure (such as the presence of atoms in substitution or insertion in the crystal network, internal strain, etc.).
- An image generated by calculating the peak width displays the degree of crystallinity or the strain homogeneity within the sampled volume and can be used for the differentiation of crystalline and amorphous phases.

23.4 Combining SEM/EDS and Confocal Raman Spectroscopy

23.4.1 Correlation of SEM and Raman Information

Integrating several techniques into a single instrument provides multiple advantages for sample analysis in many applications. The SEM has developed into a micro-laboratory with the integration of several technologies in the SEM chamber, from a cryo-stage for observing frozen aqueous samples, mechanical and electrical tests, micro-X-ray fluorescence, focused ion beam or, more recently, time-of-flight secondary ion mass spectrometry (TOF-SIMS) or even scanning probe Microscopy (SPM).

Many studies combining micro-Raman spectroscopy and SEM/EDS microscopy are listed in the literature for various applications such as geoscience [12, 13], archaeometry [14], materials science [15] or environmental science [16] to name but a few. This combination of techniques is frequently beneficial for solids characterization due to the contributions of each of these techniques:

- SEM imaging modes provide information about morphology, size, chemistry and crystallography on the nanometer scale.
- Microanalysis (using EDS and/or WDS) provides local information on the elemental composition of solids on the micrometer scale.
- EBSD provides local information on the crystal nature and orientation of crystalline solids on the nanometer scale, but requires a high quality polishing not necessary for SEM, EDS or Raman spectroscopy.

- Raman spectroscopy provides structural information on minerals, such as crystal structure and polymorphism, the influence of trace elements on crystal structure and the presence of chemical species such as hydroxides, carbonates, organic compounds, fluid inclusions, etc.

In many cases, these applications are based on the use of two separate analytical systems followed by the correlation of data. But in some cases, severe difficulties occur, for example in locating the same area using different observation modes with different resolutions or locating micrometric particles or phases with optical microscopy.

Geological samples are good examples of these difficulties as the nature and distribution of phases and particle sizes in these samples are often complex and heterogeneous. In these cases, the use of a micro-Raman spectrometer based on optical microscopy can make particle and phase recognition difficult or impossible. Transparent minerals, zonation (heterogeneous distribution of minor elements in a unique mineral phase) or small particles or areas are not easily seen using visible light illumination and the location of areas of interest is often difficult in optical microscopy as compared to SEM imaging (observation modes and resolution). Ambiguous locations for the two analyses may lead to ambiguous results.

23.4.2 Toward an Integrated Solution

To overcome this difficulty, Truchet and Delhaye [6, 17] were the first to propose and describe a system that makes possible the collection of Raman spectra directly within an electron microscope or an electron microprobe microanalyser (EPMA). Collecting Raman spectra within the SEM can provide numerous benefits:

- Accurate coupling of imaging (from various detecting modes of the SEM) and microanalysis (for example, chemical composition variation from BSE or CL detectors and EDS/WDS microanalysis) with the Raman spectrum location [18]
- Ability of SEM imaging modes to precisely locate micrometric or sub-micrometric phases with similar optical properties that cannot be differentiated using optical microscopy [19].

Commercial systems for coupling Raman imaging and SEM have been available since the early 2000s. The first examples were based on the use of a mirror inserted under the pole piece (objective lens) of the SEM to focus the laser beam onto the sample surface and redirect the signal to the spectrometer. Such systems have been successfully used for the characterization of biological samples [19, 20], individual particles [21–23], forensic applications [24], mineralogical samples [18, 25, 26] and archaeo-materials characterization [25, 27].

These systems achieve a lateral resolution of approximately 1.5 μm [25] and allow only point to point spectral acquisition. Line scanning can be achieved only by an SEM stage scan or a dedicated stage fixed on the SEM stage. However, these systems have a number of drawbacks, as mentioned by several authors [23, 25], such as:

(a) a severe loss in detected intensity of the Raman-in-SEM system (versus a conventional micro-Raman spectrometer to which the system is connected) and
(b) influence of cathodoluminescence on the detected signal when using SEM and Raman together.

Moreover, the depth resolution varies depending on the optical properties of the sample [25]. The insertion of the retractable mirror under the pole piece also requires the retraction of any detector placed at this position, such as the BSE or CL detector. In this case, a special safety procedure is required to avoid a collision between the BSE detector and the mirror as they are being inserted. In addition, depending on the geometric configuration of the system, the mirror arm may partially mask the other detectors. A smart choice of SEM and detector configuration [25] can partially solve this problem, even if, in principle, any SEM is compatible with this system (except small specialized configurations such as tabletop SEMs).

23.4.3 Confocal Raman in the SEM

As the resolution of an optical microscope is determined by the numerical aperture (NA) of the excitation/collection optics, an optical microscope requires nearly the entire space above the sample to be efficient. Therefore a microscope objective must be placed offset from the electron beam column to not occupy too much valuable space. In case of the parabolic mirror approach this problem is solved by drilling a hole in the mirror to let the electron beam pass freely onto the sample. On the other hand a parabolic mirror has several disadvantages that make a high-resolution microscope objective far superior in terms of resolution, confocality and collection efficiency [7, 28, 29].

The parallel setup, in which the microscope objective is placed some distance away parallel to the electron column, uses the SEM stage for precisely repositioning the sample between Raman and SEM optics, which takes only a few seconds (see Fig. 23.2). The primary advantage is that the user benefits from the capabilities and performance of a conventional confocal Raman microscope, particularly in terms of resolution, confocality and signal intensity without affecting the performance of the SEM itself.

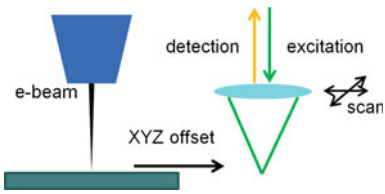

Fig. 23.2 RISE parallel setup

23.5 Correlative Confocal Raman/SEM Imaging

23.5.1 Confocal Raman Microscopy in an SEM

The confocal Raman imaging technique consists of Raman spectroscopy collected through a confocal microscope. The area of interest on the sample is scanned with a piezoelectric scanner point by point and line by line, and a complete Raman spectrum is collected at each point. In contrast to standard setups the objective is scanned rather than the sample, which leaves the sample positioned unaltered. This method provides an "image-spectra" in 4D (x, y, Raman shift, intensity) or in case of optically transparent samples even a 5D (x, y, z, Raman shift, intensity) data cube. Due to the confocal microscope configuration, the detector collects only Raman information from the focal plane with spatial resolution at the diffraction limit of the excitation wavelength. Furthermore, a good depth resolution is provided by the confocal setup. This configuration also allows for depth profiles and 3D Raman imaging [30].

For Raman imaging, a full spectrum is collected at each point of the scanned area and then analyzed with the software to provide images of the area. As a result, the integration time for each pixel is a critical parameter. For example, when acquiring an image consisting of 200×200 pixels with an integration time of 1 s per spectrum, the total acquisition time is approximately 11 h. A high-efficiency system is therefore required to reduce the integration time significantly. As an example, a reduction in integration time to 0.05 s corresponds to the reduction of the complete scan duration to 30 min.

To achieve high confocal Raman spatial resolution with high collection efficiency, a vacuum-compatible objective with certain specifications is necessary, in particular a high numerical aperture (according to Abbe's law, the higher the NA, the lower the diffraction limit). A large working distance is required to facilitate the translation between SEM and CRM positions and limit the risk of collision. The solution adopted for the WITec RISE (Raman Imaging and Scanning Electron) microscope is a $100\times$ objective with an NA of 0.75 and a working distance of 4 mm. With this objective, a lateral resolution of about 400 nm is obtained with a green (532 nm) excitation laser [29].

23.5.2 Choice of SEM for Integration with a Confocal Raman Microscope

23.5.2.1 Conventional or Low-Vacuum SEM

An SEM is normally operated under vacuum with a chamber pressure of a few milliPascals. To avoid having a charge built-up on the surface of nonconductive samples, the surface is usually coated with a conductive layer. Two different types of coating layers are common: several nanometers of a metal (Au, Pt, Au/Pd, Pt/Pd…)

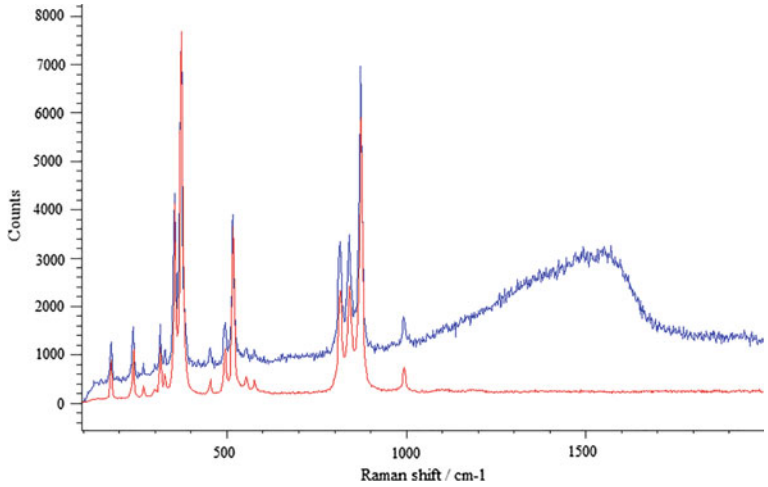

Fig. 23.3 Raman spectra of andradite $Ca_3Fe_2Si_3O_{12}$ non-coated (red)/carbon-coated (blue) (from [25])

or 10–20 nm of carbon. Due to the strong X-ray absorption of heavy metals, carbon is preferred for elemental microanalysis (EDS, WDS).

For Raman analysis however, coating the sample should be avoided. Even a thin layer of metal reflects and absorbs some energy of the excitation laser and therefore reduces the Raman signal. The absorbed power can also heat the sample and cause thermal damage to sensitive samples such as polymers. A carbon coating also absorbs light and therefore reduces the signal and the carbon layer itself shows its signature as a broad double peak between 1000 and 1600 rel. cm^{-1} in the Raman spectrum (Fig. 23.3).

Sometimes this carbon background is visible in areas which have been previously analysed with the SEM. The origin is commonly called "contamination," a thin carbon layer due to the cracking of organic molecules (related to the cleanliness of vacuum, chamber, sample…) under the electron beam can also be visible in the Raman spectra.

There are ways to avoid conductively coating samples for SEM investigation. In a high-vacuum SEM, the solution could be to reduce the high voltage to below a value that depends on the nature of the sample (1 or 2 kV in general). But using a very low acceleration voltage comes at a price. First of all, under low voltage conditions modification of SE and BSE contrasts are observed and it may become difficult to interpret the images: there might even be a contrast inversion compared to high voltage imaging [31]. Another problem is that EDS or WDS microanalysis is not possible under low voltage conditions [10, 32].

The most efficient solution is to analyze non-conductive samples under low-vacuum conditions. A low vacuum SEM is designed to work under a few Pascals (up to several hundred Pa) of pressure from various gases, commonly air or nitrogen.

Using this "low-vacuum" mode (LV), a conductive coating is not necessary as the charge neutralization of the sample surface is ensured by collisions between it and gas molecules. Under LV conditions, it is possible to work at any high voltage appropriate for SEM imaging and EDS (WDS) microanalysis. The only change in SEM imaging is the use of a different SE detector. Indeed, the conventional E-T detector is unusable in a degraded vacuum and therefore different technical solutions have been developed to allow SE detection under LV conditions [33]. EDS microanalysis is also possible, although it is slightly more complex than under high vacuum conditions due to dispersion of the electron beam from the pole piece exit to the sample surface as a result of collisions between electrons from the incident beam and molecules of the LV gas (also called the "skirt" effect). However, unlike the on-axis setup, no detector is masked by the coupling system, and therefore no specific geometry is required to perform SEM imaging and EDS microanalysis [25].

23.6 Application Examples of CRM Coupled to SEM

23.6.1 Raman-SEM (RISE) Analysis of Graphene

The mechanical isolation of single-layer graphene with the help of adhesive tape in 2004 [34, 35] kicked off the rapid growth in research on materials consisting of only one or a few layers of atoms, defined as 2D materials. Different from bulk matter, they display interesting semiconducting characteristics that inspired an extensive exploration of their structural, electronic and optical properties. While graphene is still the most prominent example of a single-layered semiconducting material, other 2D materials such as transition metal dichalcogenides (TMDCs) and black phosphorus also possess sizeable bandgaps.

Confocal Raman imaging is an ideal method for studying 2D thin films, revealing their molecular characteristics through a non-destructive and fast procedure. It is used to discern the orientation of their layers and to investigate defects, strain and functionalization, as their Raman properties are determined by molecular bonds, relative orientation and number of layers. Their morphological details can be ideally visualized with other high-resolution microscopy methods such as SEM. By correlating the information of both approaches, 2D materials can be even more thoroughly analyzed.

In Fig. 23.4, SEM (a) and RISE (c) images of a CVD-grown graphene sheet deposited on a Si/SiO_2 substrate are presented. The RISE image is an overlay of the SEM image with a color-coded Raman image. The layer numbers were deduced from the Raman spectra (Fig. 23.4b). The colors used represent a single layer (blue, dark green) with different grades of defects and more than one layer (light green, red). The RISE image highlights the large amount of defects in the blue area, in good agreement with the high-resolution SEM image while the silicon substrate is color coded yellow.

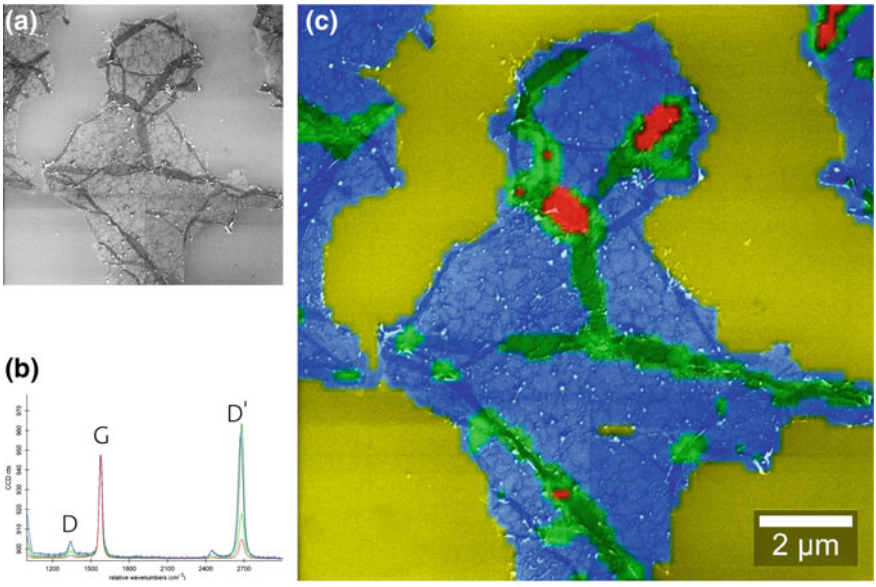

Fig. 23.4 WITec RISE CRM microscopy measurement of a CVD-grown graphene film: **a** SEM SE image of the graphene film revealing defects in the surface structure **b** Main Raman spectra identified through peak width and intensity (**c**) corresponding color-coded RISE confocal Raman image in the SEM (yellow: Silicon substrate) - Image parameters: $20 \times 20\,\mu m^2$, 150×150 pixels = 22,500 spectra, integration time 0.05 s/spectrum [29, 36]

23.6.2 RISE Microscopy of MoS_2

RISE microscopy reveals structure as well as crystalline and exciton dynamics of few-layered transition metal dichalcogenides (TMDCs). CVD-grown monolayers of MoS_2 form triangular two-dimensional crystals. Twin crystals of MoS_2 on Si/SiO_2 appear in the SEM image as star-shaped forms (Fig. 23.5b). The Raman spectra of MoS_2 monolayers show the characteristic E^1_{2g} and A_{1g} Raman band modes of MoS_2 at 385 and 403 rel. cm^{-1}, respectively (Fig. 23.5a). With an increasing number of layers the two Raman bands drift apart due to in-plane and out-of-plane (inter-layer) vibrations.

Here the green spectrum indicates monolayer MoS_2, while the blue and red spectra signify edges and defects, respectively. The spectral information was used to create a Raman image which was overlaid on the SEM image to result in a RISE image (Fig. 23.5c). The grain boundaries visible in the SEM image correlate perfectly with the areas where Raman signals indicate crumpled or overlapping edges, highlighting the effectiveness of RISE imaging for characterizing MoS_2 crystals.

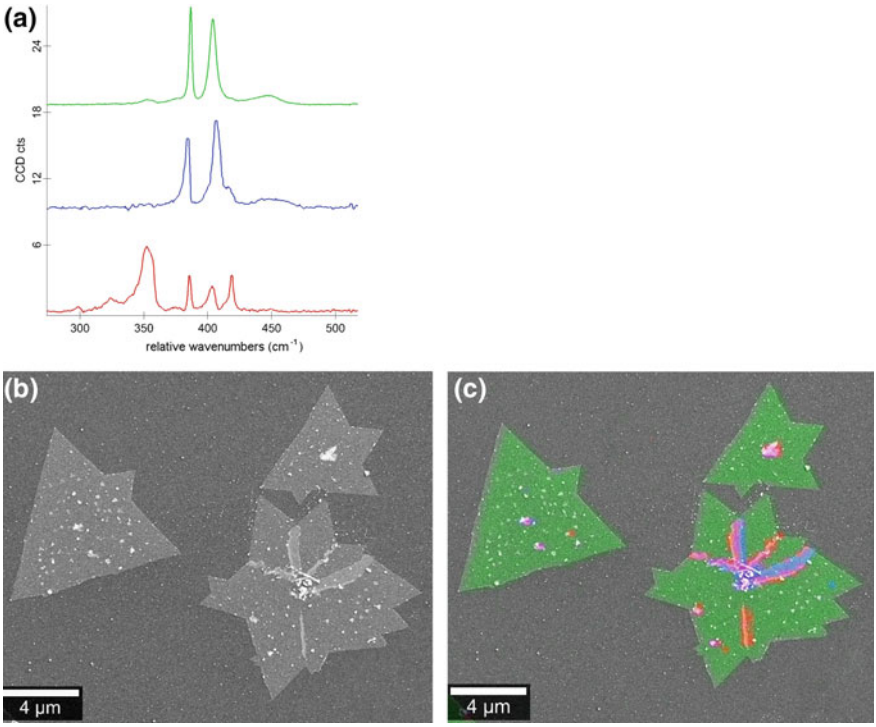

Fig. 23.5 RISE microscopy of MoS_2 crystals. **a** Raman spectra of MoS_2: green = 1L MoS_2, blue and red = edges and defects. **b** SEM image of MoS_2 crystals. **c** Color-coded Raman image derived from the spectral information overlaid on the SEM image to produce the RISE image. Sample courtesy of Ting Yu, Nanyang Technological University, Singapore

23.6.3 Geoscience Application Example: Mineral Characterization of an Asbestos Fiber Bundle

Asbestos is a commercial term or regulatory definition (in Europe, directive 2009/148/CE [39]) applied to a group of six naturally occurring minerals (seven in the French overseas special territory New Caledonia, i.e. fibrous antigorite) that have grown with a specific crystalline structure and exhibit characteristics of flexibility, high tensile strength, large surface area, electrical resistance and resistance to heat and chemical degradation. Asbestos is a group of mineral fibers with special morphological characteristics, especially:

- Length $> 5\,\mu m$, width $< 3\,\mu m$, ratio of length/width > 5
- Parallel edges
- Specific shapes of the ends of the fibers.

After a century of use in many manufactured goods (more than 3000 commercial products), asbestos was banned by almost every country in the world. But because

asbestos is a group of naturally occurring minerals, countries with deposits of these minerals thought it necessary to assess the risk posed by natural asbestos in the environment.

Several problems are inherent in the characterization of naturally occurring asbestos as compared to asbestos in manufactured goods. One is sample characterization, which requires the evidence of three main characteristics; morphology, chemistry and crystallography. Asbestos in manufactured goods is mainly (>90 %) chrysotile, one of the six varieties classified as asbestos. It is easy to recognize it by TEM analysis due to the morphology of the fibers, which look like a rolled sheet of paper 40–70 nm in diameter. Moreover, in a natural sample, the presence of various minerals together with amphibole fibers sometimes (with a similar composition) in the same sample makes the identification harder than for manufactured goods, and the risk of error is high, especially because of the risk of confusion between true fibers and sub-micrometric cleavage fragments of amphiboles [37]. This challenge requires new analytical procedures. In this context, coupling SEM - EDS with confocal Raman imaging is a novel analytical solution that can provide morphological information from SEM, chemical composition from EDS and crystallographic information from Raman spectroscopy. Correlative SEM/EDS and confocal Raman-in-SEM imaging has been successfully used to characterize the cross-section of an actinolite fiber bundle containing other mineral phases.

A sample of naturally occurring mineral fibers was collected in the north of Corsica (France) as shown in Fig. 23.6.

Thin sections of the rock sample were prepared for SEM - EDS analysis. As asbestos fibers are very thin and mixed with other mineral phases with a similar chemical composition, numerous analytical difficulties resulted, including a wide range of elemental composition as determined by EPMA. A cross section of the fiber bundle was prepared by placing it in resin then cutting it perpendicularly to the fibers and polishing it. SEM observations show that the bundle is made of fibers of several tens to several hundreds of nanometers in diameter, with another mineral phase beside or between fibers (see Fig. 23.7). Due to their small dimensions, it is difficult to determine the composition but confirmation of the mineral phases is necessary.

Raman spectroscopy was used to determine the mineralogical nature of the two phases (Fig. 23.8).

To determine the location of the different phases in the sample, a BSE detector was used to collect an SEM image. The bundle section was then transferred to the Raman measurement position in the SEM, and the grey scale image of the BSE was used to acquire spectra from the different parts of the sample. Based on the EDS analyses and Raman spectra, two mineral phases can be identified by comparing Raman spectra to databases: an amphibole called actinolite (monoclinic) $Ca_2(Mg,Fe)_5Si_8O_{22}(OH)_2$ (whose fibrous occurrences are classified as asbestos) and talc $Mg_3Si_4O_{10}(OH)_2$, whose composition is similar to that of anthophyllite (orthorhombic) or amosite (monoclinic) $(Mg,Fe)_7Si_80_{22}(OH)_2$ (whose fibrous occurrences are classified as “asbestos” - Amosite is the name given to the asbestiform variety of the mineral grünerite). These bands are described in the literature as lattice

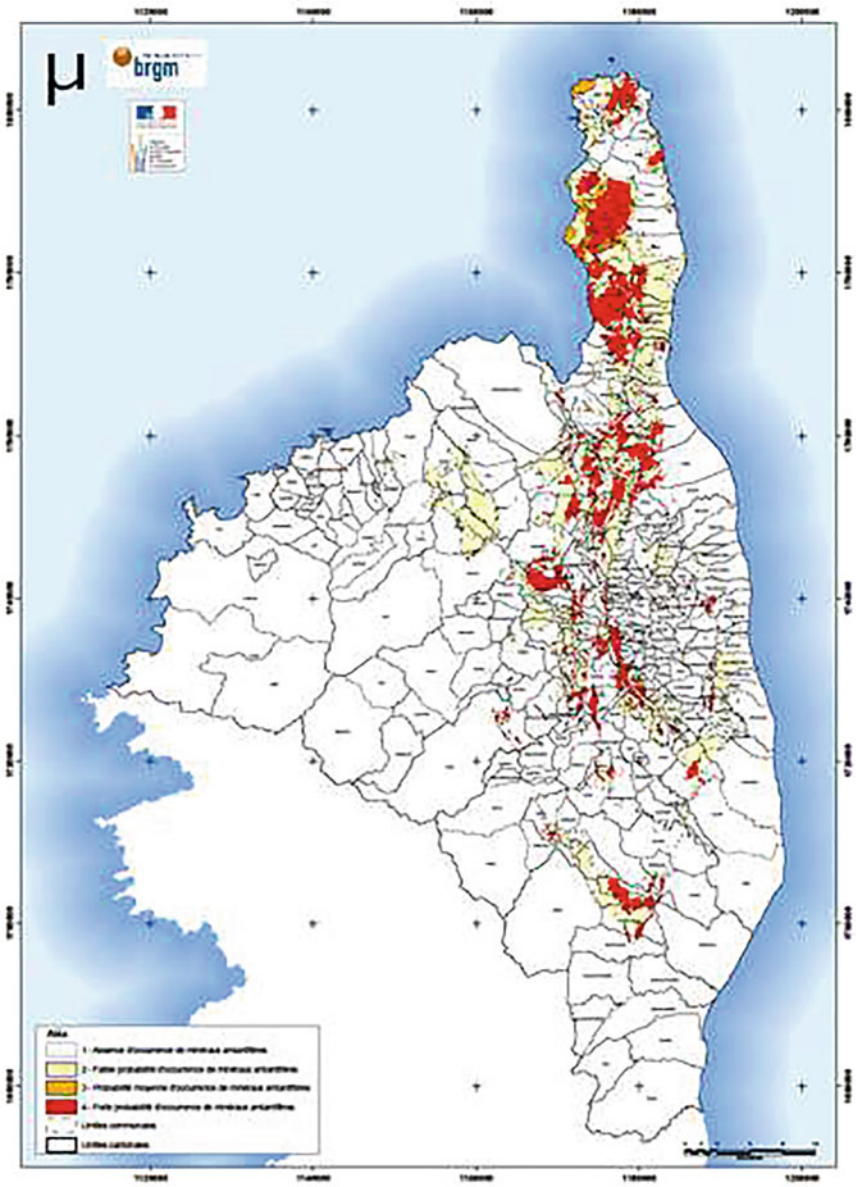

Fig. 23.6 Environmental asbestos hazard map of northern Corsica, France - Red color corresponds to an abundance of natural asbestos (BRGM Infoterre [38])

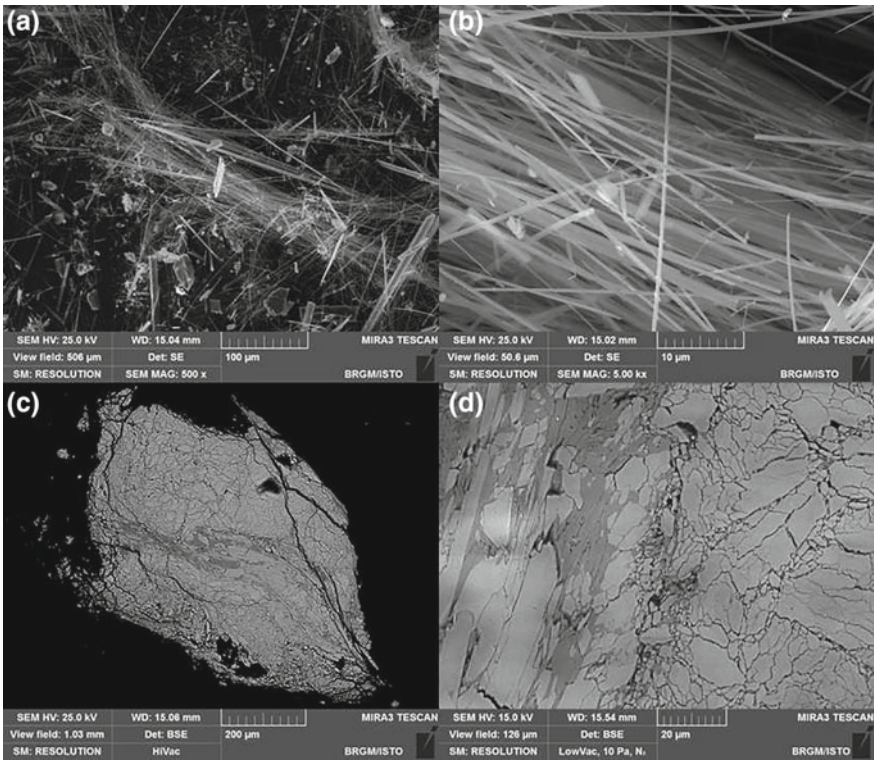

Fig. 23.7 SEM observation of actinolite fibers (**a**, **b**) and cross section of an embedded fiber bundle (**c**, **d**) showing sub-micrometer "asbestiform" fibers

modes and an illustration of the difference in crystal structure is shown in Fig. 23.9. These minerals can also be identified through EPMA by analyzing pluri-micrometric grains. But in the case of the cross section of asbestiform fiber bundles, the fiber diameter is below the volume WDS can analyze. Identification of these mineral phases by EPMA is thus only possible if large grains are present in the sample; otherwise only an approximate composition is obtained.

The Raman spectra of the two phases can be distinguished in the 150–250 rel. cm^{-1} range, where talc shows only one Raman peak at 198 rel. cm^{-1} while actinolite shoes a group of three peaks at approximately 165, 185 and 230 rel. cm^{-1}. These differences make it possible to differentiate the two phases with Raman imaging. The confocal Raman system implemented in the SEM has a lateral resolution of well under 0.5 µm, much sharper than that obtained by SEM-EDS/EPMA analysis at 10–15 rel. cm^{-1} kV (estimated by Monte-Carlo simulation to be about 1.5–2 µm). The result of a confocal Raman-in-SEM analysis of the cross section of a fiber bundle containing sub-micrometric fibers (less than 500 nm in diameter) is presented in Fig. 23.10.

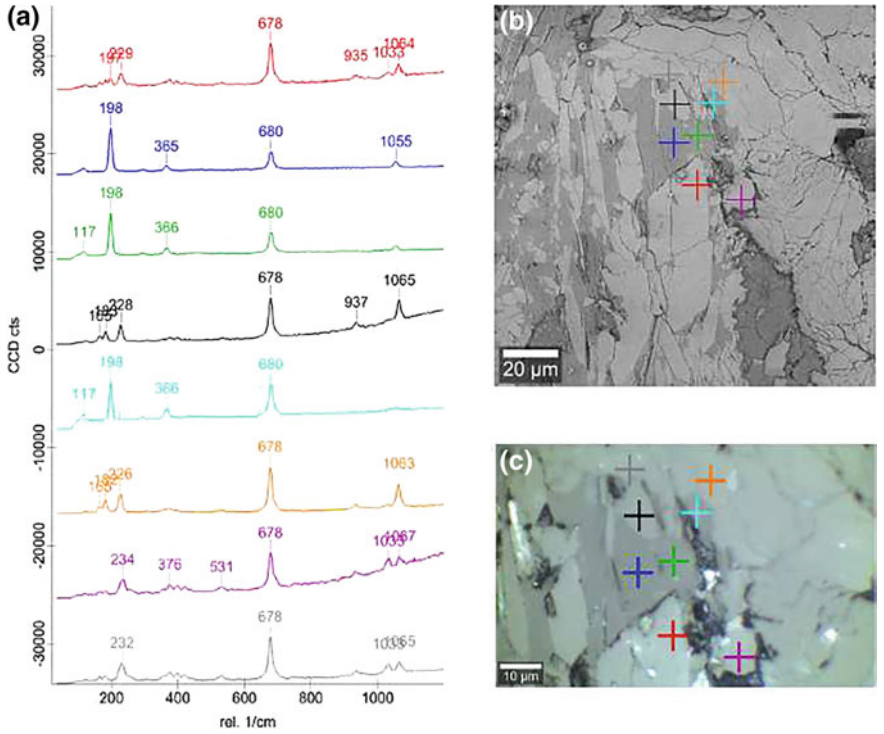

Fig. 23.8 Raman spectra (**a**) acquired from the positions marked in the SEM image (**b**) and the white light image (**c**)

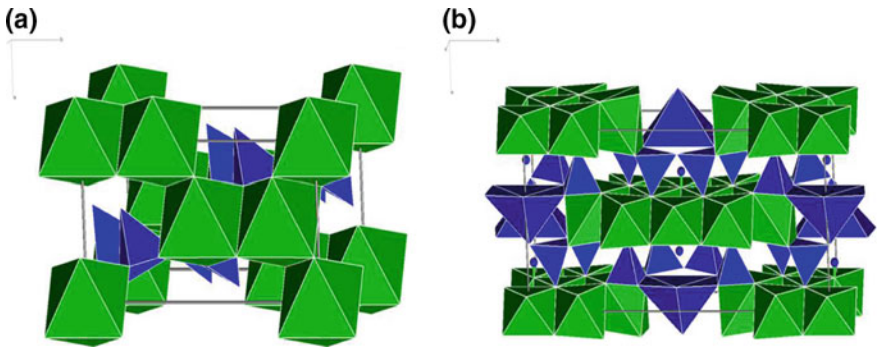

Fig. 23.9 Crystal structure of talc (**a**) and actinolite (**b**)

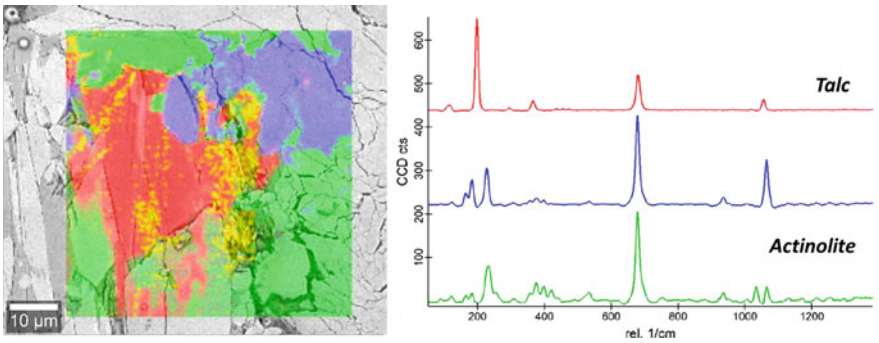

Fig. 23.10 Color-coded Raman image (red: talc/blue, green: actinolite/yellow: fluorescence) overlaid on SEM (BSE) image

Talc and actinolite phases are shown in red and blue/green, respectively, in the Raman image and their surface ratio can therefore be calculated. No other phase was detected in the sample, so the connection to the SEM BSE image is helpful in extrapolating for a larger area of the sample. In addition, differences in the actinolite phase were observed and are shown in green and blue. A subtle difference is observed on several peaks, such as in the group of peaks at approximately 200 rel. cm^{-1}, attributed to $(SiO_4)^4-$ vibrations and the group of peaks attributed to Mg–OH vibrations [39].

23.6.4 Geoscience Application Example: Drill Core Sample

Mineral phases of a rock section from a core drill sample were analyzed in the next example. The dominant rock type is diorite. The sample had no need to be treated or vaporized but was only sectioned with a diamond saw under water. This reduces the risk of contamination of the surface, which is of great importance not only for geological drill core samples but also for objects acquired from the deep sea.

Figure 23.11a shows the SEM image of a small sample area using the backscattered electron detector of the SEM.

The same area was analyzed using EDX (Fig. 23.11b). The distribution of elemental groups indicates the presence of three distinct minerals. Single Raman spectra could be acquired from the three different areas (Fig. 23.11e), three of which show the characteristic Raman bands for quartz, epidote and plagioclase.

This is in good agreement with the elemental composition obtained by EDX. Raman spectra of the three primary minerals were evaluated using cluster analysis. In addition to these spectra, four others were detected, two of which could indicate different grain orientations within the phases of epidote and plagioclase, respectively. The spatial distribution of the minerals is shown in the color coded RISE image (Fig. 23.11d), in which the colors of the Raman image match the colors of the spectra.

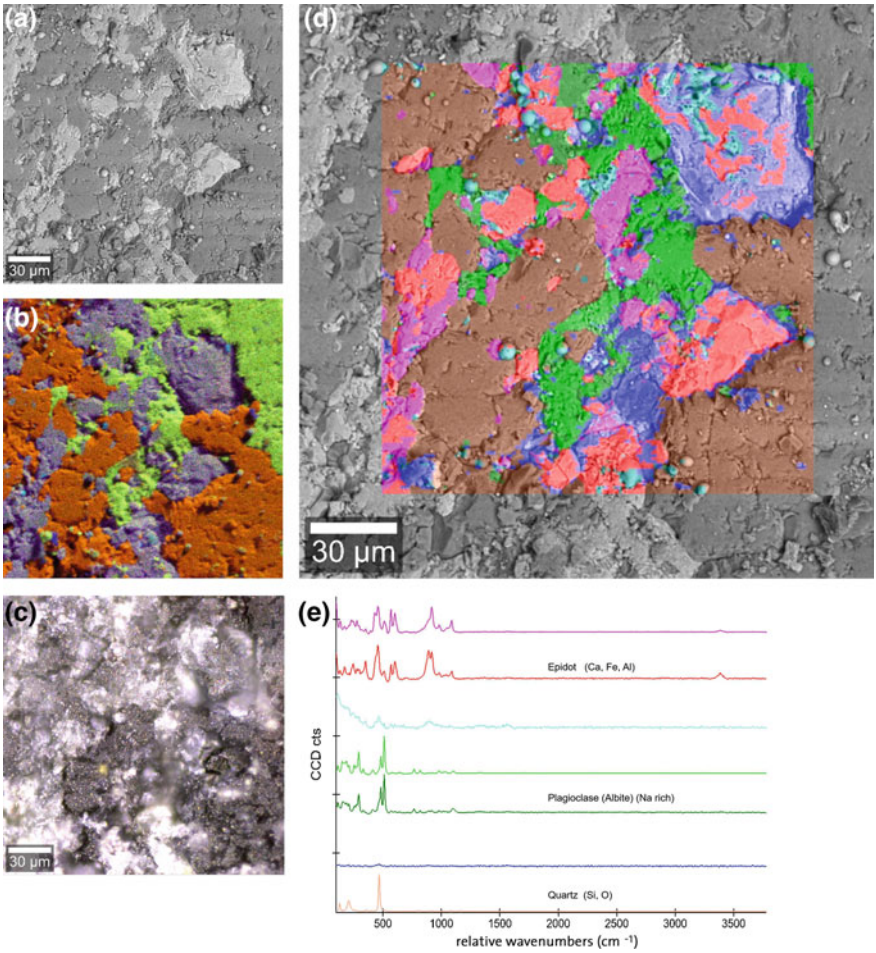

Fig. 23.11 A mineral phase of a diorite rock section. **a** SEM image **b** overlay of SEM and EDX image. Three element groups could be distinguished with EDX: Si, O: orange; Ca, Fe, Al: grey-purple; Na; green. **c** White light microscopy image from the same sample area. **d** Raman spectral image overlaid with the SEM image. **e** Raman single spectra acquired from the three distinct regions with the characteristic Raman bands of quartz (brown), epidot (red) and Plagioclase (green). Image parameters: $100 \times 100\,\mu m^2$, 150×150 pixels = 22,500 spectra, integration time 0.08 s per spectrum. Sample courtesy by Christiane Heim, Geoscience Centre GZG, Dept. Geology, University of Göttingen, Germany

Not only could the mineral phase distribution be detected, but also small grains within a mineral phase. Figure 23.11c shows the white light image acquired from the same sample area as the SEM image. It clearly shows the different appearance of identical areas in SEM and optical microscopy, which is why it is difficult to retrieve the sample area when using two stand-alone instruments.

23.6.5 RISE Analysis of Polymorphs: Correlating Structure with Chemical Phases

With SEMs it is possible to identify materials consisting of different atoms using a common combination with EDX (energy- dispersive X-ray spectroscopy). It cannot however distinguish between different modifications of chemically identical materials (polymorphs). As the manner of atomic bonding greatly influences the structure and properties of a material, visualizing not only morphology but also identifying its molecular architecture is important. RISE microscopy accomplishes both of these tasks as demonstrated with the analysis of TiO_2 polymorphs (Fig. 23.12). TiO_2 is studied intensively because of its interesting chemical and optical properties and is widely employed in photo-catalysis, electrochemistry, photovoltaics and chemical catalysis. It is also used as white pigment in tooth paste, sun screen and wall paint and as anode material for lithium-ion batteries. Depending on the application, one crystalline form or the other gains in cations, two of which - anatase and rutile - were examined. For RISE microscopy an SEM image was generated of a 1:1 anatase/rutile powder mixture (Fig. 23.12a). The corresponding confocal Raman image from the same sample area was merged with this SEM image (Fig. 23.12b). It was demonstrated that though the elemental compositions of the modifications anatase and rutile are identical, they can be distinguished from one another by their character-

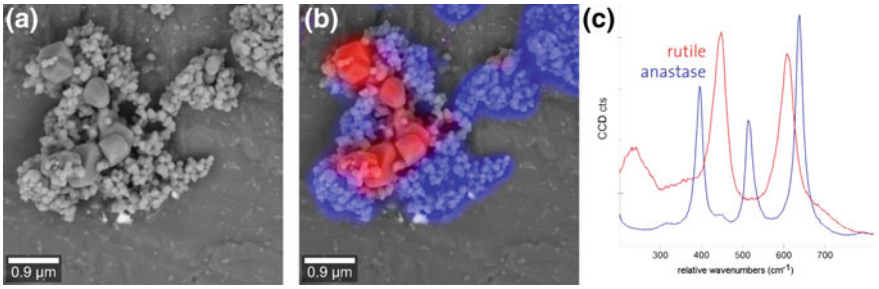

Fig. 23.12 Two modifications of TiO_2, anatase and rutile, were mixed 1:1, ground, dissolved in water and imaged with an SEM (**a**) and a confocal Raman microscope. **b** SEM and Raman images overlaid. **c** In the Raman spectrum anatase (blue) can be easily distinguished from rutile (red). Image parameters: $12 \times 12\,\mu m^2$ scan range, 150×150 pixels = 22,500 spectra, integration time: 0.037 s per spectrum

istic Raman spectra at relative wavenumbers between 300 and 800 (Fig. 23.12c). Both phases were combined in agglomerates, in which rutile accumulated in larger particles than anatase.

23.7 Conclusion

Numerous authors have expressed interest in combining SEM-EDS and Raman spectroscopy for the characterization of materials for many years. The emergence of devices that integrate these techniques in a single analytical system has revealed new capabilities for data correlation. The combination also allows the use of optical microscopy to locate areas of interest to be investigated with SEM imaging and EDS elemental analysis on the micrometric and sub-micrometric scales. The precision and accuracy of Raman analysis is greatly improved by the addition of SEM imaging capabilities (resolution, variety of imaging modes) and combined elemental and structural chemical data. For numerous applications, the use of coupled Raman and SEM systems makes it possible to collect co-located data in difficult cases where separate devices would not be effective. The benefit of an "on-axis" setup has been established by many publications and conferences over the last fifteen years but several limitations restrict its use in characterization laboratories, including being limited to point analysis.

The development of a new confocal Raman-in-SEM imaging system based on a parallel configuration opens up new possibilities. In particular, it meets the expectations of the SEM users in terms of imaging and mapping. SEM and EDS microanalysis provide images and 2D information on the sample, and the addition of 2D Raman data is advisable for an optimized use of such systems. Depth resolution for Raman spectroscopy depends strongly on the optical system. For on-axis systems, it is difficult to evaluate this aspect due to the variation in specific technical configurations. The confocal Raman in the SEM system is equipped with an optical objective, and thus it is possible to connect the confocality of such systems to conventional micro-Raman spectroscopy. The depth resolution aids in collecting accurate surface data. In addition, the use of a confocal Raman system in the SEM introduces new capabilities in terms of depth profiling and 3D data collection. The 3D functionality of the RISE confocal Raman-in-SEM imaging system could open new perspectives for SEM characterization, reducing in many cases the use of more complex and expensive 3D techniques.

Finally, the significant analytical potential of Raman-in-SEM is greatly extended by the development of a true confocal Raman imaging device in the SEM, offering new point analysis, depth profiling, imaging, and 3D capabilities. The combination of SEM imaging modes, EDS microanalysis and confocal Raman imaging makes it possible to greatly extend our capacity to obtain information on morphology, structural chemistry and atomic, molecular and crystal structure on a scale comparable to that of elemental microanalysis.

References

1. F. Sharifi, R. Bauld, G. Fanchini, J. Appl. Phys. **114**(14), 144504 (2013)
2. F. Rubio-Marcos, A. Del Campo, R. López-Juárez, J.J. Romero, J.F. Fernández, J. Mater. Chem. **22**(19), 9714 (2012)
3. F. Foucher, F. Westall, A. Gucsik, *AIP Conference Proceedings*, vol. 1163 (AIP, 2009), pp. 47–58
4. M. Hoehse, D. Mory, S. Florek, F. Weritz, I. Gornushkin, U. Panne, Spectrochim. Acta, Part B **64**(11), 1219 (2009)
5. J. Zieba-Palus, R. Borusiewicz, M. Kunicki, Forensic Sci. Int. **175**(1), 1 (2008)
6. M. Truchet, M. Delhaye. Analytic Microscopy Device, Capable of Forming Both a Raman Probe and an Electronic Probe. INPI patent 2596863-A1, France (1986)
7. A. Van Apeldoorn, Y. Aksenov, M. Stigter, I. Hofland, J. De Bruijn, H. Koerten, C. Otto, J. Greve, C. Van Blitterswijk, J. R. Soc. Interface **2**(2), 39 (2005)
8. W. Werner. Interaction of Electron Beams with Matter (2012)
9. T.E. Everhart, R. Thornley, J. Sci. Instrum. **37**(7), 246 (1960)
10. C. Merlet, X. Llovet, *IOP Conference Series: Materials Science and Engineering*, vol. 32 (IOP Publishing, Bristol, 2012), p. 012016
11. S.I. Wright, M.M. Nowell, Microsc. Microanal. **11**(S02), 672 (2005)
12. H. Yu, H. Zhang, X. Wang, Z. Gu, X. Li, F. Deng, J. Phys. Chem. Solids **68**(10), 1863 (2007)
13. F.L. Theiss, A. López, R. Scholz, R.L. Frost, Spectrochim. Acta Part A Mol. Biomol. Spectrosc. **147**, 230 (2015)
14. T.D. Chaplin, R.J. Clark, M. Martinón-Torres, J. Mol. Struct. **976**(1), 350 (2010)
15. K. Grodecki, I. Jozwik, J. Baranowski, D. Teklinska, W. Strupinski, Micron **80**, 20 (2016)
16. M.P. Nelson, C.T. Zugates, P.J. Treado, G.S. Casuccio, D.L. Exline, S.F. Schlaegle, Aerosol Sci. Technol. **34**(1), 108 (2001)
17. M. Truchet, M. Delhaye, J. Microscopie Spectroscopie Électroniques **13**(2), 167 (1988)
18. N. Maubec, C. Lerouge, A. Lahfid, G. Wille, K. Michel, X. Bourrat, J. Mol. Struct. **1048**, 33 (2013)
19. R.M. Jarvis, A. Brooker, R. Goodacre, Anal. Chem. **76**(17), 5198 (2004)
20. R.M. Jarvis, R. Goodacre, Anal. Chem. **76**(1), 40 (2004)
21. A. Worobiec, S. Potgieter-Vermaak, A. Brooker, L. Darchuk, E. Stefaniak, R. Van Grieken, Microchem. J. **94**(1), 65 (2010)
22. E.A. Stefaniak, F. Pointurier, O. Marie, J. Truyens, Y. Aregbe, Analyst **139**(3), 668 (2014)
23. A. Worobiec, L. Darchuk, A. Brooker, H. Potgieter, R. Van Grieken, J. Raman Spectrosc. **42**(4), 808 (2011)
24. V. Otieno-Alego, J. Raman Spectrosc. **40**(8), 948 (2009)
25. G. Wille, X. Bourrat, N. Maubec, A. Lahfid, Micron **67**, 50 (2014)
26. E.A. Stefaniak, A. Alsecz, R. Frost, Z. Máthé, I.E. Sajo, S. Török, A. Worobiec, R. Van Grieken, J. Hazard. Mater. **168**(1), 416 (2009)
27. I. Guerra, C. Cardell, J. Microsc. **260**(1), 47 (2015)
28. J. Jiruse, L. Sedlacek, M. Rudolf, V. Friedli, F. Oestlund, J. Whitby, Microsc. Microanal. **18**(S2), 638 (2012)
29. J. Jiruše, M. Haničinec, M. Havelka, O. Hollricher, W. Ibach, P. Spizig, J. Vac. Sci. Technol. B, Nanotechnol. Microelectron. Mater. Process. Meas. Phenom. **32**(6), 06FC03 (2014)
30. T. Dieing, O. Hollricher, J. Toporski, *Confocal Raman Microscopy*, vol. 158 (Springer Science & Business Media, Berlin, 2011)
31. P. Lewis, S. Micklethwaite, J. Harrington, M. Dixon, R. Brydson, N. Hondow, *Journal of Physics: Conference Series*, vol. 644 (IOP Publishing, Bristol, 2015), p. 012019
32. D.E. Newbury, J. Res. Nat. Inst. Stand. Technol. **107**(6), 605 (2002)
33. M. Jacka, M. Zadrazil, F. Lopour, Scanning **25**(5), 243 (2003)
34. K.S. Novoselov, A.K. Geim, S.V. Morozov, D. Jiang, Y. Zhang, S.V. Dubonos, I.V. Grigorieva, A.A. Firsov, Science **306**(5696), 666 (2004)

35. K. Novoselov, D. Jiang, F. Schedin, T. Booth, V. Khotkevich, S. Morozov, A. Geim, Proc. Nat. Acad. Sci. U.S.A. **102**(30), 10451 (2005)
36. U. Schmidt, K. Hollricher, P. Ayasse, O. Hollricher, Microsc. Anal. **May/June** (2015)
37. R.J. Lee, B.R. Strohmeier, K. Bunker, D. Van Orden, J. Hazard. Mater. **153**(1), 1 (2008)
38. InfoTerre. Infoterre, le visualiseur des données géoscientifiques. http://infoterre.brgm.fr/
39. N. Gopal, K. Narasimhulu, J. Rao, Spectrochim. Acta Part A Mol. Biomol. Spectrosc. **60**(11), 2441 (2004)

Index

J. Toporski et al. (eds.), *Confocal Raman Microscopy*, Springer Series in Surface Sciences 66, https://doi.org/10.1007/978-3-319-75380-5